

Dissertation

submitted to the
Combined Faculties for the Natural Sciences and for Mathematics
of the Ruperto-Carola University of Heidelberg, Germany
for the degree of
Doctor of Natural Sciences

Submitted by
Dipl.-Phys. Jan Wolfgang Krieger
born in Munich, Germany

Date of oral examination: 23rd July 2014

Mapping Diffusion Properties in Living Cells

Referees: PD Dr. Christoph S. Garbe
Prof. Dr. Ulrich Schwarz

Zusammenfassung: Bildgebung von Diffusionsprozessen in lebenden Zellen

Die Funktion lebender Zellen basiert auf chemischen Reaktionen. Es zeigt sich, dass die Geschwindigkeit dieser Reaktionen durch den Molekültransport in der Zelle limitiert ist und damit auch wesentlich von der räumlichen Organisation der Zelle abhängt. Zur Untersuchung solcher Transportprozesse wird häufig Fluoreszenz-Korrelations-Spektroskopie (FCS) in Verbindung mit fluoreszenzmarkierten Proteinen angewendet. Hierbei beobachtet man mit Hilfe eines Lasermikroskops die Fluktuationen der Fluoreszenz, die aus einem kleinen Untervolumen ($\sim 1 \mu\text{m}^3$) der Probe emittiert wird. Eine Autokorrelationsanalyse dieser Fluktuationen ermöglicht es, die Konzentrationen und vor allem den Diffusionskoeffizienten der markierten Teilchen zu vermessen. Üblicherweise wird für FCS ein konfokales Mikroskop eingesetzt, das zu jeder Zeit nur ein einziges Volumen beobachten kann. In der vorliegenden Dissertation wurde FCS zu einer bildgebenden Methode weiterentwickelt, indem es mit Lichtscheibenfluoreszenzmikroskopie (SPIM) kombiniert wird. Diese relativ neue Weitfeldmikroskopietechnik ermöglicht es, gezielt eine beliebig positionierbare Ebene ($1 - 3 \mu\text{m}$ dick) in einer Zelle zu beobachten. Durch Einsatz einer schnellen elektronenvervielfachende CCD-Kamera (EMCCD) konnte damit die Bewegung auch relativ kleiner autofluoreszenter Proteine in lebenden Zellen ortsaufgelöst vermessen werden.

Es wird zunächst der Aufbau eines Lichtscheibenmikroskops beschrieben, das für die Anwendung auf SPIM-FCS in einzelnen Zellen optimiert wurde. Verschiedene Testmessungen zeigen die grundsätzliche Anwendbarkeit von SPIM-FCS in in-vitro-Proben und in allen größeren Kompartimenten lebender Zellen (Zellkern, Zytoplasma, Zellmembran). Anschließend wird die Eignung verschiedener kommerziell erhältlicher Kameras als Bildsensor für SPIM-FCS-Messungen verglichen. Nach aktuellem Stand bieten EMCCD-Kameras den besten Kompromiss aus Photosensitivität und erreichbarer zeitlicher Auflösung ($\sim 500 \mu\text{s}$). Zusätzlich zu diesen linearen Kameras wird auch der Einsatz von Bildsensoren aus Einzelphoton-Lawinenphotodioden (SPAD arrays) untersucht. Diese bieten gegenüber EMCCD-Kameras eine deutlich höhere Zeitauflösung ($1 - 10 \mu\text{s}$) und wären damit ideale Detektoren für SPIM-FCS. Allerdings erreichen sie noch nicht die gleiche Photosensitivität. Zwei verschiedene Sensoren wurden ausführlich charakterisiert und konnten erfolgreich für erste SPIM-FCS Messungen von gelösten Fluoreszenzfarbstoffen eingesetzt werden. In einem weiteren Schritt wurde SPIM-FCS um eine Kreuzkorrelations-Analyse erweitert (SPIM-FCCS), die es zum ersten Mal erlaubt, auch Interaktionen zwischen verschiedenen markierten, cytosolischen Molekülen in Zellen zu kartieren. Dazu werden die Fluoreszenz-Fluktuationen aus zwei unterschiedlichen Farbkanälen einer Kreuz-Korrelations-Analyse unterzogen. Eine messbare Kreuz-Korrelation ergibt sich nur, wenn zwei unterschiedlich markierte Moleküle in der Probe eine Bindung eingehen und sich gemeinsam bewegen.

Schließlich konnten die entwickelten Verfahren auf verschiedene zelluläre Systeme angewendet werden. Durch die Kartierung der Mobilität von inerten Molekülen verschiedener Größe konnte unter anderem die Viskosität des Mediums in verschiedenen Zellen bestimmt werden. Eine räumliche Abhängigkeit der Mobilität konnte nur in Nukleoli nachgewiesen werden. Außerdem wurde ein wichtiger Schritt im Remodellierungszyklus des Keratin-Zytoskeletts in Zellen untersucht. Als dritte Anwendung demonstrieren SPIM-F(C)CS-Messungen an verschiedenen Chromatin-assoziierten Molekülen die Dynamik des Zellkerns. Eine Bildgebung der Mobilität von markierten Histon-Proteinen ließ Rückschlüsse auf Organisation des Chromatins zu. Außerdem wurde die Aktivität des nuklearen Rezeptors RXR und eines Transkriptionsfaktors vermessen.

Diese Dissertation wurde zwischen Juli 2008 und Mai 2014 am Deutschen Krebsforschungszentrum (DKFZ) unter der Betreuung von Prof. Dr. Jörg Langowski und PD Dr. Christoph Garbe erstellt.

Abstract:

Mapping Diffusion Properties in Living Cells

The function of living cells is based on chemical reactions. It has been shown that the velocity of these reactions is limited by the molecular transport in the cell. Therefore also the spatial organization of a cell plays a major role. In order to investigate such transport processes, fluorescence correlation spectroscopy (FCS) is often used in combination with fluorescently labeled proteins. In FCS a small subvolume of the cell ($\sim 1 \mu\text{m}^3$) is observed with a laser-based microscope. The fluctuations of the fluorescence, emitted from this subvolume, are acquired. An autocorrelation analysis of these fluctuations reveals the concentrations and diffusion coefficients of the labeled particles. Usually, FCS is implemented using a confocal microscope, which can observe only a single spot at any time. For this thesis, FCS was extended to an imaging method, by combining it with light sheet fluorescence microscopy (SPIM). This relatively new widefield microscopy technique allows to observe an arbitrarily positionable, thin plane (diameter: $1 - 3 \mu\text{m}$) in the cell. By using a fast electron-multiplying charge-coupled device (EMCCD) camera, the combination of SPIM and FCS allowed to map the motion also of relatively small autofluorescent proteins in living cells.

At first, the setup of a light sheet microscope is described. This microscope was designed and optimized for SPIM-FCS measurements in living cells. Several test measurements show the applicability of SPIM-FCS to in vitro samples and to all larger compartments of a living cell (nucleus, cytoplasm, cellular membrane). Afterwards, the usability of several commercially available cameras as image sensor for SPIM-FCS measurements is assessed. At the time of writing, EMCCD cameras offer the best trade-off between photosensitivity and achievable temporal resolution ($\sim 500 \mu\text{s}$). In addition to these linear cameras, also the use of single-photon avalanche diode (SPAD) arrays is investigated. These offer a significantly better temporal resolution ($1 - 10 \mu\text{s}$) than current EMCCD cameras, which would render them the ideal image sensor for SPIM-FCS. However, they do not yet reach the photo-sensitivity of EMCCDs. Two different SPAD arrays were characterized in detail and first successful SPIM-FCS measurements of solute fluorescent molecules could be demonstrated.

In a second step, SPIM-FCS was extended by a cross-correlation analysis (SPIM-FCCS), which allowed for the first time to map the interactions of differently labeled cytosolic molecules in living cells. For this purpose, the cross-correlation function between the fluorescence fluctuations from two different color channels is analyzed. A non-zero amplitude of this cross-correlation function is found only, if the differently labeled molecules interact and move together.

Finally, the methods developed during this project were applied to different cellular systems. The mapping of the mobility of inert tracer molecules of different sizes allowed to measure the viscosity of the cytoplasm in different cells. A position-dependence of this mobility could only be found in the nucleoli. In addition, an important step in the remodelling cycle of the keratin intermediate filament system was investigated. As a third application, SPIM-F(C)CS measurements of different chromatin-associated proteins demonstrated the dynamics in the cellular nucleus. Mobility maps of labeled histone proteins revealed the organization of chromatin in interphase nuclei. In addition, the activity of the nuclear receptor RXR and a transcription factor were mapped.

This dissertation was conducted under the supervision of Prof. Dr. Jörg Langowski and PD Dr. Christoph Garbe at the German cancer research center (DKFZ) between July 2008 and Mai 2014.

Contents

I. Introduction	1
1. Imaging transport processes in living cells	3
1.1. Eukaryotic cells	3
1.2. Reaction kinetics in living cells	5
1.3. Transport processes in living cells	6
1.3.1. Normal diffusion	6
1.3.2. Anomalous diffusion	8
1.3.3. Directed transport and superdiffusion	10
1.4. Measuring transport in living cells	10
1.4.1. Single particle tracking	10
1.4.2. Observing the transition into equilibrium	11
1.4.3. Fluorescence fluctuation techniques	12
1.5. Aim of the thesis	15
1.6. Own Contributions	16
1.7. Outline of the thesis	17
II. Methods	19
2. Fluorescence labeling techniques	21
2.1. Fluorescence	21
2.2. Triplet transitions and phosphorescence	22
2.3. Photobleaching and photoswitching	23
2.4. Chemical fluorophores	23
2.5. Fluorescent proteins	24
2.6. Quantum dots	26
3. Fluorescence microscopy	27
3.1. Basic fluorescence microscopy	27
3.1.1. Principle	27
3.1.2. Focus properties and resolution	28
3.1.3. Multi-color fluorescence microscopy	30
3.2. Confocal fluorescence microscopy	30
3.2.1. Principle	30
3.2.2. The pinhole in confocal microscopy	31
3.2.3. Focus properties and resolution	31
3.3. Light sheet microscopy	33
3.3.1. Principle	33
3.3.2. Focus properties and resolution	34
3.3.3. Typical image artifacts in light sheet microscopy	35

3.3.4.	A short history of light sheet microscopy	37
4.	Photodetectors	39
4.1.	Photon counting detectors	39
4.1.1.	Single-photon avalanche diodes	39
4.1.2.	Statistics of photon counting detectors	40
4.1.3.	Single-photon avalanche diode arrays	41
4.2.	Linear detectors	43
4.2.1.	Introduction	43
4.2.2.	CMOS cameras	43
4.2.3.	CCD cameras	44
4.2.4.	EMCCD cameras	45
4.2.5.	Statistics of linear image sensors	46
4.3.	Comparison of image sensors	48
5.	Measuring diffusion: fluorescence fluctuation techniques	51
5.1.	Introduction to fluorescence correlation spectroscopy	51
5.1.1.	Single point measurements	51
5.1.2.	Fluorescence correlation spectroscopy on a confocal microscope	52
5.1.3.	Imaging fluorescence correlation spectroscopy	52
5.2.	Modeling fluorescence in a microscope	54
5.3.	Theory of fluorescence correlation spectroscopy	56
5.3.1.	The FCS autocorrelation function	56
5.3.2.	Zero-lag correlation and particle numbers	56
5.3.3.	The concentration correlation factor	57
5.3.4.	Normal diffusion	59
5.3.5.	Anomalous diffusion	62
5.3.6.	Arbitrary mean squared displacement	63
5.3.7.	Sample translation or flow	64
5.4.	Fluorescence cross-correlation spectroscopy	66
5.4.1.	Measuring directed motion: Two-focus cross-correlation	66
5.4.2.	Measuring molecular interactions: Two-color cross-correlation	69
5.5.	Artifacts in fluorescence (cross-)correlation spectroscopy	73
5.5.1.	Photophysics	73
5.5.2.	Constant background signal	74
5.5.3.	Detector afterpulsing	75
5.5.4.	Fluorophore depletion	76
III.	Development of a SPIM-FCS/FCCS instrument	79
6.	Hardware setup of the SPIM	81
6.1.	Optics setup	81
6.1.1.	Overview	81
6.1.2.	Light sheet shaping	83
6.1.3.	Transmission illumination	85
6.1.4.	Detection system	85
6.2.	Sample chamber and sample mounting	88
6.2.1.	Sample Chamber	88
6.2.2.	Temperature control	90

6.2.3.	Sample mounting	90
6.3.	Characterization of the optics	93
6.3.1.	Measuring light sheet properties	93
6.3.2.	Measuring the molecular detection efficiency	96
6.3.3.	Imaging capabilities of the SPIM	98
6.4.	SPAD arrays	99
6.4.1.	SPAD arrays used in this thesis	99
6.4.2.	Readout	100
6.4.3.	Characterization of the SPADs	101
6.4.4.	Microlens arrays on <i>SwissSPAD</i>	103
6.4.5.	Influence of microlenses on the SPAD array performance	104
7.	Data processing and instrument control software	107
7.1.	Imaging FCS/FCCS data evaluation	107
7.1.1.	Overview	107
7.1.2.	Background and bleach correction	108
7.1.3.	Calculation of correlation functions	110
7.1.4.	Model parameter estimation	114
7.1.5.	Maximum entropy data analysis	115
7.2.	Single particle tracking	116
7.3.	The data evaluation software QuickFit 3.0	116
7.4.	Instrument control for a SPIM	117
8.	Evaluation of the SPIM for FCS measurements	119
8.1.	Alignment and calibration procedure for FCS measurements	119
8.2.	Determination of absolute diffusion coefficients	122
8.3.	Particle concentration measurements in SPIM-FCS	126
8.4.	Anomalous Diffusion with complex MDE shapes	132
8.5.	Artifacts in SPIM-FCS	132
8.5.1.	Stripe artifacts in SPIM-FCS	132
8.5.2.	Artifacts due to sample bags	134
8.5.3.	Changing the thickness of the light sheet	135
8.6.	Applicability to live-cell measurements	136
8.7.	Comparison of different linear image sensors	141
8.8.	Using SPAD arrays for SPIM-FCS	145
8.8.1.	SPIM-FCS using <i>Radhard2</i>	145
8.8.2.	SPIM-FCS using <i>SwissSPAD</i>	146
8.8.3.	Afterpulsing in <i>SwissSPAD</i>	148
8.8.4.	Concluding remarks	150
8.9.	Summary of the chapter	150
9.	Evaluation of the SPIM for FCCS measurements	151
9.1.	Alignment procedure for 2-color FCCS measurements	151
9.2.	Simulation of a misalignment in 2-color FCCS	153
9.3.	Comparison with confocal 2-color FCCS	155
9.4.	Absolute concentration measurements with 2-color FCCS	156
9.5.	Applicability of 2-color FCCS in live-cells	157
9.6.	Flow measurements with 2-focus SPIM-FCCS	161
9.7.	Summary of the chapter	163

IV. <i>In vivo</i> applications	165
10. Macromolecular dynamics in live cells	167
10.1. Protein mobility in live cells	167
10.2. Mobility of different inert tracer molecules	167
10.2.1. Tracer molecules	167
10.2.2. Measurement protocol	168
10.2.3. Results	169
10.3. Diffusion in different cell lines	173
10.4. Conclusions	174
11. Keratin dynamics	175
11.1. The keratin intermediate filament system	175
11.2. The free pool of keratin precursors	177
11.3. SPIM-FCS measurements of the free pool of keratin precursors	178
11.4. Discussion of the results	182
12. Dynamics and interaction of chromatin-associated proteins	183
12.1. Histone Dynamics	183
12.1.1. Introduction	183
12.1.2. Measurement protocol	184
12.1.3. Results	184
12.2. The AP-1 transcription factor system	187
12.2.1. Introduction	187
12.2.2. Measurement protocol	187
12.2.3. Results	190
12.3. Nuclear receptors	191
12.3.1. Introduction	191
12.3.2. Measurement protocol	191
12.3.3. Results	192
12.4. Conclusions	193
V. Summary	195
13. Summary	197
VI. Appendix	201
A. Materials and methods	203
A.1. List of used materials and suppliers	203
A.2. Cell culture protocols	206
A.2.1. Cell growth and transfection	206
A.2.2. Cell types	210
A.3. SPIM sample mounting protocols	212
A.3.1. Preparation of sample bags for liquid samples	212
A.3.2. Preparation of a gel cylinder for bead scans	213
A.3.3. Preparation of cover slips for adherent cells	213

B. Simulation software	215
B.1. Fluorescence correlation spectroscopy simulations	215
B.2. Macromolecular crowding	217
B.3. Numerical integration for the PSF of a microscope	219
B.4. Beam propagation method	219
C. Formulary	223
C.1. Fourier transform	223
C.2. Convolution	223
C.3. Statistical measures	224
C.4. Recalibration of diffusion coefficients to a different temperature	224
C.5. Estimation of diffusion coefficients for particles of different geometries	224
Nomenclature	227
List of Figures	235
List of Tables	241
Bibliography	243

Part I.
Introduction

1. Imaging transport processes in living cells

1.1. Eukaryotic cells

All known living organisms consist of one or more cells. The name cell stems from Latin *cella* meaning small room or storeroom [1]. This section will give a simplified overview of the eukaryotic cell and describes the constituents that play a role throughout this thesis. A detailed picture can be found in any textbook on cellular biology, e.g. Ref. [2]

Figure 1.1 shows a sketch of an eukaryotic cell, as it is e.g. found in all mammals and other higher organisms. These cells are typically between 10 μm and 100 μm in diameter. All cells are separated from their environment by a bio-membrane consisting of a phospholipid double-layer. They are filled with the cytoplasm, a dense aqueous solution, which contains several small molecules, such as salt ions, sugars, lipids and amino acids. Also many biological macromolecules, such as proteins and nucleic acids are dissolved in the cytoplasm. Some of these macromolecules form large assemblies with specific functions, ranging from macromolecular complexes consisting of a few proteins to complete organelles

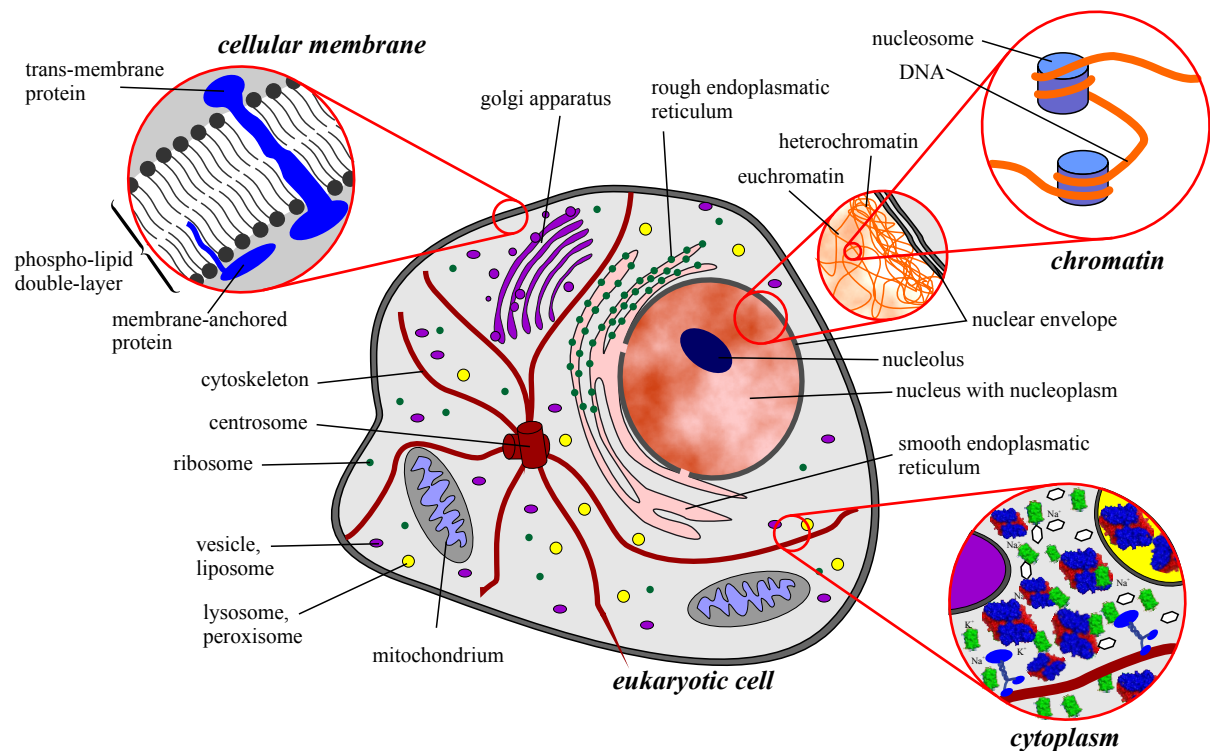


Figure 1.1. | Sketch of an eukaryotic cell. The insets show (in clock-wise order) the cellular membrane, the chromatin and a DNA strand wound around a nucleosome and a view of the densely packed cytoplasm.

of several 100 nm in size.

The cell further contains small compartments, called organelles, which carry out specific functions. All organelles are surrounded by their own single- or double-layered phospholipid membrane, which allows them to maintain specialized chemical conditions on their inside. For instance, lysosomes and peroxisomes contain proteins that would be toxic for the cell, if they were free in the cytoplasm. Mitochondria keep a lower pH value on their inside, than in the cytoplasm. Many forms of membrane enclosed vesicles are used to store and transport proteins, nutrients and waste.

The membranes, which surround the organelles, as well as the whole cell, are usually interspersed with a large number of proteins. These membrane-bound and trans-membrane proteins are used for instance to transport molecules across the membrane. They can also alter and influence the structure of the membrane or take part in directing and transporting the organelles inside the cell. Membrane-associated proteins also play a major role in sensing the environment. For instance, the presence of certain molecule in extracellular space is detected by a trans-membrane receptor molecule, which then activates a cascade of biochemical reactions inside the cell.

The functioning of a cell is based on proteins. These are biological polymers, which consist of a chain of amino acids and are folded into higher-order structures. They perform diverse tasks, that range from maintaining the cellular structure with a cytoskeleton, cargo transport and cell motility with motor proteins to digestion and energy production. Many proteins simply catalyze reactions that would also take place without their presence, but at a significantly lower rate. Proteins also form the cellular machines that allow for reproduction and manufacturing of new proteins. The function of many proteins depends heavily on their 3-dimensional structure and not only on their amino acid sequence.

The cell also contains a system for information storage, processing and transport: the nucleic acid polymers deoxyribonucleic acid (DNA) and ribonucleic acid (RNA). Each DNA molecule consists of a linear sequence of four different nucleic acids cytosine (C), guanine (G), adenine (A) and thymine (T). They are connected by a sugar-phosphate backbone. In a cell DNA forms a double-helix of two complementary strands (dsDNA), which is stabilized by hydrogen bonds between the complementary nucleic acid pairs C-G, and A-T. A few large DNA molecules with several million basepairs – the chromosomes – form the central information storage in the cell. Amongst other functions, these molecules encode the amino acid sequence of every protein, which is present in the cell. During cell division, a copy of these DNA molecules is produced and transferred to the daughter cell.

The live-span of a cell basically consists of a succession of two phases: during interphase, the cell follows its basic functions, grows, and finally replicates the DNA molecule, before it enters the mitosis phase (M). During mitosis the cell divides into two daughter cells. This cycle is illustrated in Fig. 1.2. Interphase can be split up into four phases. The major part of interphase is made up by the G_1 -phase. Here the cell grows, follows its basic functions. It also accumulates nutrients that are required for cell division. During the synthesis phase (S-phase), the cell duplicates its chromosomes and the centrioles, which are protein complexes that organize the micro-filament network of the cell. After S-phase, a second growth phase, G_2 , follows. At the end of G_2 , the nuclear envelope breaks down and the two centrosomes move to opposite ends of the cell. Then the chromatin condenses into chromatids, which are attached to fibers that are connected to the two centrosomes. Finally the centrosomes pull the sister chromatids apart. To conclude the cell division, cytokinesis divides the remaining constituents of the cell in equal parts between the two separating daughter cells, which then reform their nuclei.

During interphase, the chromosomes are packed into the cellular nucleus, a large organelle (diameter about 10 μm), which is enclosed by a double-layered phospholipid double-membrane. The chromatin needs to be compacted into higher order structures in order to fit into the tiny volume of a nucleus. A single human cell contains DNA molecules with an overall length of around 2 m. The volume of the molecule itself corresponds to a sphere of approximately 2 μm in diameter. Free in solution, such DNA polymers would form a roughly spherical conformation with a diameter of around 100 μm [3]. Further compaction is prevented by entropic forces and the stiffness of the polymer. In order to overcome

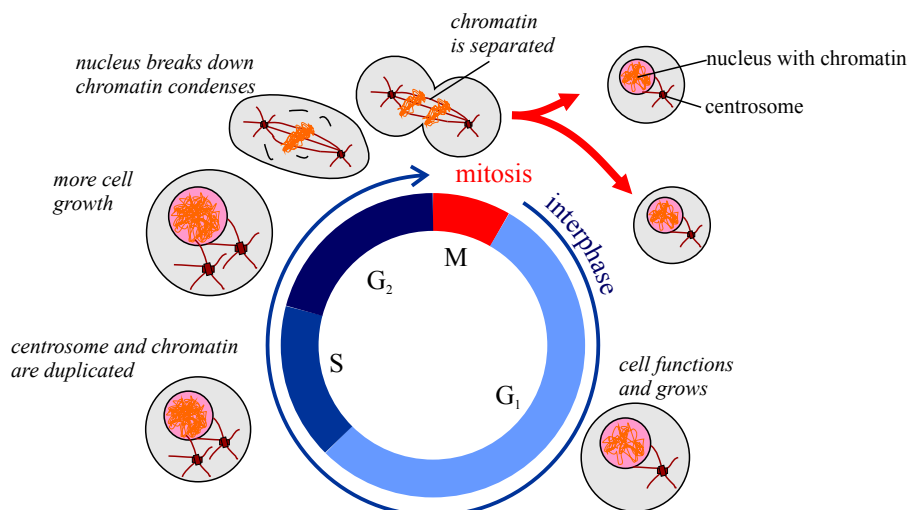


Figure 1.2. | **Illustration of the cell cycle.** Cell cycle phases are denoted by letter inside the inner circle: mitosis (M), growth phases (G_1/G_2), synthesis phase (S).

these limitations and compress the full genomic DNA into the nucleus, external forces are required. Eukaryotic cells use a protein-DNA complexes called nucleosome, to perform the first stage of this compaction process (Fig. 1.1, top right inset). They consist of a core structure made up of eight histone proteins, around which ~ 150 basepairs or ~ 50 nm of DNA are wound in approximately 1.8 turns. The complete structure is only around 10 nm in diameter, which is significantly less than the DNA segment length and its persistence length. In a second step, histones can mediate the formation of higher-order structures.

Special proteins can read, copy and repair DNA molecules. To synthesize a protein, its amino-acid sequence is transcribed from the chromatin to an RNA molecule by a protein complex, known as RNA polymerase. This short RNA molecule is then transported out of the nucleus and into a ribosome. The latter is a large complex of proteins, DNA and RNA, which finally translates the amino acid sequence, encoded on the RNA, into a protein. A group of three nucleic acids encodes for one of the ~ 20 different amino acids that are used to build up all proteins.

The number of proteins of a certain species that are present in a cell, is controlled by the transcription process. Special proteins e.g. from the group of transcription factors and nuclear receptors, help to initiate DNA transcription. They can also operate as sensors, that inhibit or stimulate the transcription machinery. This way a complex network of proteins and protein-protein and protein-DNA interactions is built up, which controls and regulates the function of the whole cell. The packing state of DNA also plays a major role in regulation, as DNA can only be transcribed if it can be made accessible by unwrapping it from nucleosomes. For instance, during interphase, a part of the chromatin is highly compacted at the periphery of the nucleus. DNA transcription is effectively prevented by this hetero-chromatin conformation.

1.2. Reaction kinetics in living cells

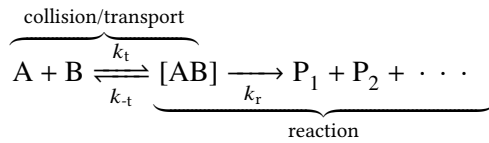
The small volume of a cell allows it to maintain a high concentration of molecules, although each protein species is only present in a small number. For instance, many proteins exist only as $10^3 - 10^6$ copies per cell. Another example is the genomic DNA of a human cell, which consists of only 46 double-helices. Still the small volume of the cells allows for chemical reactions to efficiently take place.

A typical mammalian cell has a diameter of $d_{\text{cell}} = 20 \mu\text{m}$ and a volume of $V_{\text{cell}} \approx 4000 \mu\text{m}^3 = 4 \cdot 10^{-12} \text{ l}$.

protein	reaction	k_r [s^{-1}]	$\tau_{r,1/2}$ [ms]
pepsin	$\text{Phe-Gly} \xrightarrow{+\text{H}_2\text{O}} \text{Phe} + \text{Gly}$	0.5	1400
fumarase	$\text{fumarate} \xrightarrow{+\text{H}_2\text{O}} \text{malate}$	$8 \cdot 10^2$	0.9
carbonic anhydrase	$\text{HCO}_3^- + \text{H}^+ \longrightarrow \text{H}_2\text{O} + \text{CO}_2$	$4 \cdot 10^5$	0.002

Table 1.1. | Examples of reaction rates k_r and half-life times $\tau_{r,1/2}$ for enzyme-catalyzed reactions. Values taken from Ref. [4].

The concentration c of the reagents typically is $10^{-12} - 10^{-6}$ mol/l, which corresponds to around $2 \cdot 10^3 - 2 \cdot 10^9$ molecules per cell. The corresponding averaged inter-particle distance is $d_{\text{mm}} = 0.55 \cdot c^{-1/3}$ [5, 6], which is in the range of 6600 – 66 nm. This distance is larger than the typical size of the molecules (e.g. single-atom ions: 0.2 nm, sugars: 0.5 – 1 nm, proteins: 1 – 10 nm). When modeling chemical reactions in a cell, therefore also the transport process has to be included. First two (or more) molecules A, B have to get in close proximity and form a complex [AB]. Then they react to form one or more products P_1, P_2, \dots [7, 8]:



The transport process is modeled by two rate constants k_t and k_{-t} for the formation and dissociation of the complex [AB]. They quantify the number of formation or dissociation events that take place per second at given concentrations of the molecules. These reaction rates depend mainly on the transport properties of the molecules. If two molecules have met and formed a complex [AB], the final step of the reaction may take place, which transforms [AB] into the products P_1, P_2, \dots . This is described by a reaction rate k_r . The typical timescale, on which a reaction takes place can be calculated as the reaction half-life time $\tau_{r,1/2} = \ln(2)/k_r$. Values for k_r and $\tau_{r,1/2}$ for typical molecules vary significantly, as shown in Tab. 1.1. Assuming a constant concentration of the intermediate [AB] (steady-state approximation), an effective reaction rate can finally be obtained [8]:

$$k_{\text{eff}} = \frac{k_t \cdot k_r}{k_{-t} + k_r}. \quad (1.2.1)$$

In the limiting case that the reaction step is much faster than the transport step, i.e. $k_r \gg k_t, k_{-t}$, the overall reaction velocity $k_{\text{eff}} \rightarrow k_t$ is limited by the transport process. This is called kinetic perfection and many biological reactions belong to this class [7].

1.3. Transport processes in living cells

1.3.1. Normal diffusion

Three typical transport processes in a living cell are shown in Fig. 1.3. Figure 1.3(a) illustrates the simplest process, which is the free random Brownian motion (BM) of molecules. It can be pictured as a drunkard's walk through the gel-like environment of the cytoplasm and is, in fact, one of the most important transport processes in the cell. The observed particle is driven by perpetual collisions with surrounding molecules, mostly water. In each collision a small and random amount of momentum is transferred to the particle, which slightly changes its direction and velocity. Over longer timescales, this leads to the quivering motion, shown in Fig. 1.3(a) [9–15].

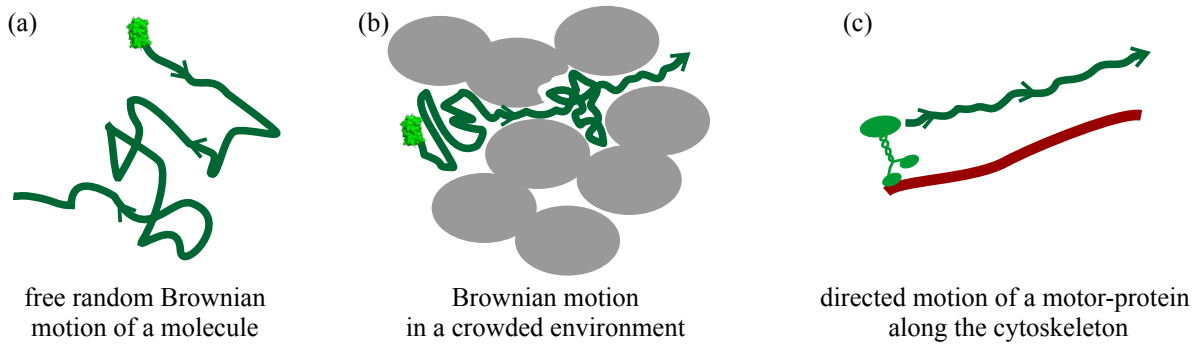


Figure 1.3. | Typical transport processes in a cell

The random nature of Brownian motion requires a statistical analysis of the trajectories. A good quantity to describe the global behavior of the molecules, is the mean squared displacement (MSD). It can be defined using a time average over the trajectory $\vec{r}(t)$ of a single particle:

$$\text{MSD}(\tau) := \lim_{T \rightarrow \infty} \frac{1}{T} \cdot \int_0^T |\vec{r}(t + \tau) - \vec{r}(t)|^2 dt. \quad (1.3.1)$$

The MSD measures the average (squared) distance that a particle travels during a time lag τ . If Brownian motion takes place in a viscous medium, it gives rise to normal diffusion, which is characterized by a linear MSD [10]

$$\text{MSD}(\tau) = 2d \cdot D \cdot \tau. \quad (1.3.2)$$

Here D is the diffusion coefficient of the particles, which move in a d -dimensional space. For random motion, D plays the same role as the velocity for linear motion. Together with Eq. (1.3.2), it defines how far a particle can move (on average) within a given time. If the particles are spherical with hydrated radius R_h , the diffusion coefficient has a simple analytical form (“Einstein relation”) [10]:

$$D = \frac{k_B \cdot T}{6\pi \cdot \eta_{\text{visc}} \cdot R_h}, \quad (1.3.3)$$

where k_B is Boltzman’s constant, T is the absolute temperature and η_{visc} is the dynamic viscosity of the medium, in which the particles move. Expressions for the diffusion coefficients of differently shaped particles are summarized in appendix C.5.

With the Einstein relation Eq. (1.3.3), it is possible to give a first estimate for transport times of a typical molecule inside a cell. Table 1.2 summarizes diffusion coefficients for different particles. The hydrodynamic radii in this table are typical values for different kinds of particles in living cells. The viscosity was assumed to be $\eta_{\text{visc,cell}} \approx 3 \text{ mPa} \cdot \text{s}$, as measurements of $\eta_{\text{visc,cell}}$ in cells give values, which are a factor 2 – 10 lower than the viscosity of water [16–19]. The table also contains the average times τ , which one of these particles needs to cover typical distances r in the cell. These are comparable to the reaction half-life times in Tab. 1.1, which shows that diffusion is an effective transport process for reactions in living cells.

particle	R_h [nm]	D [$\mu\text{m}^2/\text{s}$]	average time τ [ms] to travel a distance r		
			$r = 66 \text{ nm}$	$r = 660 \text{ nm}$	$r = 10 \mu\text{m}$
small molecules	0.5	151	0.007	0.7	165
small proteins	2	38	0.03	2.9	661
large proteins	10	7.6	0.14	14	3304
small vesicles	50	1.5	0.72	72	16523
large vesicles	500	0.2	7.2	720	165230

Table 1.2. | Transport timescales for the diffusion of several typical particles inside a living cell over a given distance r . The diffusion coefficient D is calculated by Eq. (1.3.3) from the hydrodynamic radius R_h , the temperature $T = 273 \text{ K} + 37^\circ\text{C}$ and the viscosity $\eta_{\text{visc}} = 3 \text{ mPa} \cdot \text{s}$. The times τ are calculated using $\tau = r^2/(6D)$ (Eq. 1.3.2).

1.3.2. Anomalous diffusion

The environment in a cell is densely crowded. Figure 1.3(b) shows a particle, which moves through such a medium. A large part of its surrounding is occupied by other molecules and therefore inaccessible to the particle. If the fraction $V_{\text{excluded}}/V_{\text{cell}}$ of excluded volume is large enough, it severely hinders the random motion of particles. It was demonstrated that in this case the MSD is no longer a linear function, as in Eq. (1.3.2), but has to be described by a power-law [20–25]:

$$\text{MSD}(\tau) = 2d \cdot \Gamma \cdot \tau^\alpha \quad \text{with } 0 < \alpha < 1. \quad (1.3.4)$$

Here α is the anomaly parameter and Γ is the generalized or anomalous diffusion coefficient. Note that Γ inherently depends on α , as its units are $[\Gamma] = \text{m}^2/\text{s}^\alpha$. Eq. (1.3.4) implies that a crowded environment does not simply reduce the diffusion coefficient, but leads to a significantly different behavior of the particles. Figure 1.4 shows a comparison of the MSD for normal and anomalous diffusion.

Figure 1.5 shows results obtained from a simulation of the movements of tracer particles in a crowded environment. The crowdiers occupy a partial volume V_{excluded} out of a total volume V_{all} and their position does not change over time (“swiss-cheese model”). The simulation procedure is detailed in appendix B.2. For small crowder concentrations, the trajectory shown in Fig. 1.5(a) samples a large fraction of the simulational box. For high crowder concentrations the trajectory is strongly confined. Figure 1.5(a) shows $\text{MSD}(\tau)$ curves obtained from these simulations (solid lines). The excluded volume fraction $V_{\text{excluded}}/V_{\text{all}}$ is color-coded from green to light blue. Dashed lines show ideal MSDs for normal (magenta) and anomalous (red) diffusion. With increasing $V_{\text{excluded}}/V_{\text{all}}$, the diffusion on timescales $\tau > 10^{-5} \text{ s}$

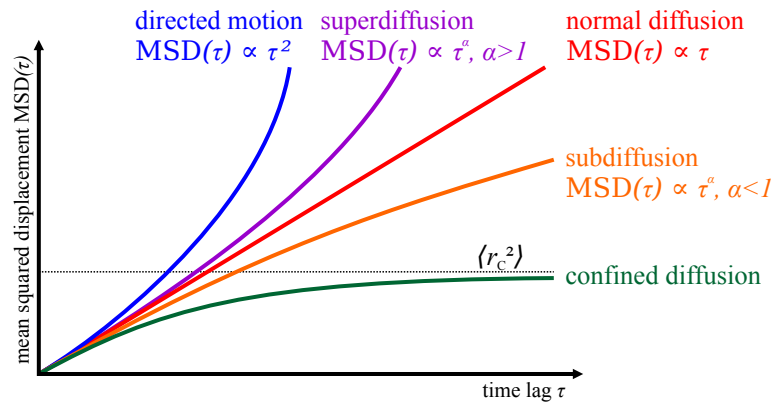


Figure 1.4. | Mean squared displacements for different types of transport.

changes from normal to anomalous. On faster timescales $\tau < 10^{-6}$ s, the motion is normal for most examples. Here the particles move inside the pores between the crowdors, but do not yet “feel” the excluded volume.

Anomalous diffusion has been reported for the 3-dimensional motion of many different molecules in cells and also for the 2-dimensional motion of membrane-bound proteins (e.g. [22, 23, 26–31]). A good review of theoretical and experimental results is given in Ref. [25]. The anomaly parameters reported for diverse cellular systems typically range between $\alpha = 0.5$ and 0.9. Often experiments are not interpreted in terms of anomalous diffusion. Then typically one or two separate effective diffusion coefficients for different timescales are reported (e.g. [27, 32, 33]). Also the viscosities η_{visc} , that were used for Tab. 1.2, are such effective quantities.

In some cases, the excluded volume fraction is so large, that some particles are trapped in sub volumes, which they cannot leave at all. On large timescales, the MSD is then limited by the squared characteristic radius of these subvolumes $\langle r_c^2 \rangle$. This kind of diffusive motion is usually called confined or corralled diffusion. The MSD can then be written as [34–36]

$$\text{MSD}(\tau) = \langle r_c^2 \rangle \cdot \left(1 - A_1 \cdot \exp \left[-A_2 \cdot \frac{2d \cdot D\tau}{\langle r_c^2 \rangle} \right] \right). \quad (1.3.5)$$

here A_1 and A_2 are constants that describe the geometry of the confining spaces. Figure 1.4 shows how this MSD model levels off to $\langle r_c^2 \rangle$.

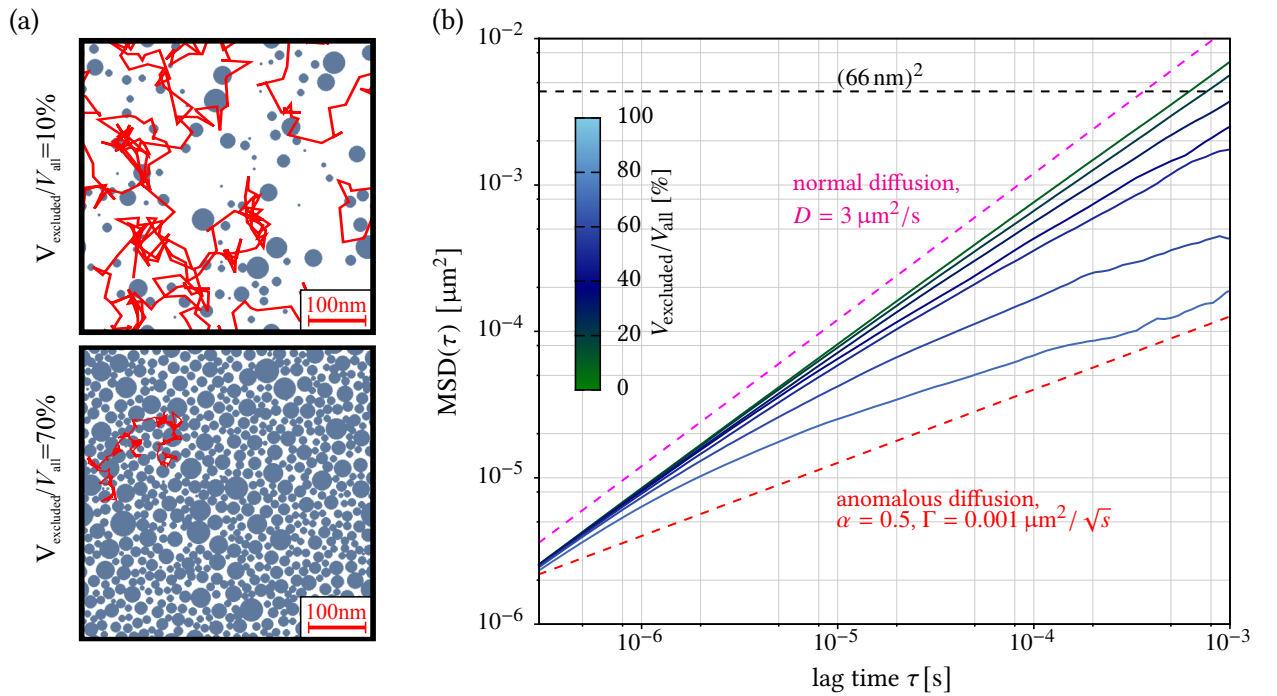


Figure 1.5. | Anomalous transport in an environment with a given amount of excluded volume.

(a) Distribution of fixed crowdors (gray) and example trajectories of a tracer particles (red). (b) MSD of tracer particles with diameter 8 nm for different excluded volume fractions $V_{\text{excluded}}/V_{\text{all}}$. The dashed magenta and red lines indicate normal and anomalous diffusion. This plot was created with the simulation from appendix B.2 using non-moving crowdors.

1.3.3. Directed transport and superdiffusion

A closer look at Tab. 1.2 shows that for larger particles, such as vesicles (diameter: a few 10 nm to a few 100 nm), diffusion might not be fast enough to transport them to their destination inside the cell in a sufficiently short time. An example is axonal transport of synaptic vesicles in a nerve cell. Here neurotransmitter molecules are packaged into small vesicles (diameter: ~ 50 nm). These have to be transported from the Golgi network to the synapses of a nerve cell. The latter two are connected by the axon, which can have a length of a few millimeters up to meters. If this was performed by diffusion only, transport durations of more than 200 h for 1 mm or 20,000 h for 10 mm would be reached. This does not suffice to sustain the functionality of the nerve cell.

Cells use active transport to overcome the described problem. Motor proteins, e.g. from the kinesin, myosin or dynein families, move vesicles and even larger organelles, such as mitochondria, along cytoskeletal filaments [2, 37–39]. The segregation of chromatids during mitosis is also performed by motor proteins [39]. In plant cells the complete cytoplasm is kept in motion (“cytoplasmic streaming”). Myosin-coated organelles drag the cytoplasm along, while they move along actin filament bundles which are anchored in the cell membrane.

Motor proteins use adenosine triphosphate (ATP) as an energy source and exert forces of a few 10^{-12} N per molecule [40]. Resulting transport velocities have been reported to be in the range of $0.1 - 1 \mu\text{m/s}$ for vesicles in live cells [37, 41, 42]. This is more than a factor 100 faster than normal diffusion (see timescales in Tab. 1.2). Cytoplasmic streaming even reaches flow velocities of up to $100 \mu\text{m/s}$ [43].

As mentioned above, active transport is characterized by a velocity v , which directly relates the traveled distance to the elapsed time τ :

$$\langle \Delta r \rangle(\tau) = \lim_{T \rightarrow \infty} \frac{1}{T} \cdot \int_0^T [\vec{r}(t + \tau) - \vec{r}(t)] dt = v \cdot \tau. \quad (1.3.6)$$

Also the mean squared displacement (MSD) of a particle, which undergoes directed motion can be expressed in terms of v [21]:

$$\text{MSD}(\tau) = v^2 \tau^2. \quad (1.3.7)$$

The MSD of normal diffusion (Eq. 1.3.2) and directed transport (Eq. 1.3.7) can both be seen as special cases of the anomalous MSD: normal diffusion with $\alpha = 1$ and active transport with $\alpha = 2$. Motions in the regime $\alpha > 1$ are usually called superdiffusive, as the MSD increases faster than in normal diffusion [21]. In cell biology, superdiffusion has been reported in connection with active transport (see e.g. [44]). For such cases, it is assumed that periods of directed motion are interspersed with periods of normal or subdiffusive motion. This can happen, when e.g. vesicles are dragged over certain distances by motor proteins, then uncouple from them and perform Brownian motion, until they hit the next motor protein.

1.4. Measuring transport in living cells

Several experimental methods exist, that allow to measure the stochastic cellular transport processes described above. In all these methods, the first step consists of labeling the molecules of interest, so that they can be distinguished from their environment. All the techniques discussed in this thesis use fluorescent molecules as tags. Therefore fluorescence microscopy is applied to observe the labeled molecules in the cell.

1.4.1. Single particle tracking

A straightforward approach is single particle tracking (SPT). Here only few particles are labeled, so that they can be followed independently, as shown in Fig. 1.6(a) [45–48]. SPT is implemented either on a

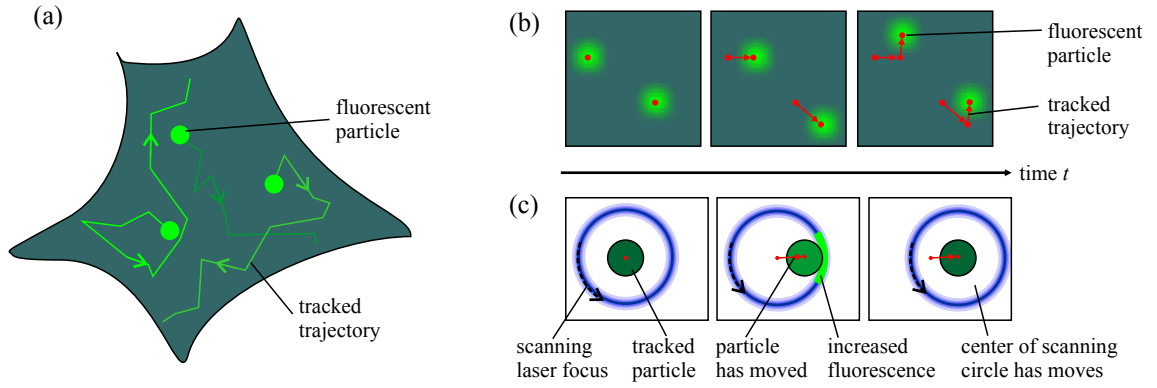


Figure 1.6. | (a) Principle of single particle tracking (SPT). (b) SPT in an image series. (c) SPT on a laser scanning microscope.

widefield microscope with a camera or on a point-scanning device. In the first case, shown in Fig. 1.6(b), a time series of images is recorded and the position of the single labeled particles is identified in each frame (blue dots). In a second step, the positions are combined to trajectories, by joining positions that are near to each other in subsequent frames. Finally the trajectories can be used to extract statistical properties of the random motion, such as the MSD. This approach was used for instance to determine the motion of membrane-bound receptors [49], the trafficking of viruses in living cells [50], or chromatin dynamics during interphase [51]. It was also applied to track whole cells inside a developing zebrafish embryo [52]. As in all microscopy techniques, that are based on the localization of single spots, the spatial resolution of SPT is a factor 2 – 10 better than the optical resolution of the microscope [36, 53].

Newer techniques for SPT use point-scanning (confocal) microscopes, as shown in Fig. 1.6(c). These microscopes detect only the fluorescence, which is excited in the small focal volume. The focus is then scanned in a fast circular motion around a single fluorescent particle [47]. If the particle crosses the circle, a small intensity peak is observed and the focus can be shifted, so the particle is again in its center. Finally the trajectory is reconstructed from the positions of the focus.

1.4.2. Observing the transition into equilibrium

Apart from SPT, which relies on the resolvability of single particles, it is also possible to measure diffusion in samples with a higher concentration of labeled molecules. These methods can be classified into two groups, based on whether the observed system is in an equilibrium or a non-equilibrium state on the timescale of observation. If the observed organism is in a non-equilibrium state, the concentration distribution $c(\vec{r}, t)$ will show macroscopic changes on larger time and length scales. In a simple case these changes are described by the diffusion differential equation

$$\frac{\partial c(\vec{r}, t)}{\partial t} = D \cdot \vec{\nabla}^2 c(\vec{r}, t), \quad (1.4.1)$$

which is a direct consequence of the Brownian motion (BM). For more complex cases, other differential equations may apply. The concentration $c(\vec{r}, t)$ can be directly observed with a microscope, as the fluorescence intensity is proportional to the concentration: $F(\vec{r}, t) \propto c(\vec{r}, t)$. With the help of Eq. (1.4.1), the diffusion coefficient and other properties of the random motion can be extracted from the measured $F(\vec{r}, t)$.

The non-equilibrium state may either be of natural origin or it is induced by the experimenter. Examples for naturally occurring non-equilibria are the redistribution of certain proteins during a signaling cascade [54], or changes in the structure of the cytoskeleton [55]. A large field of application

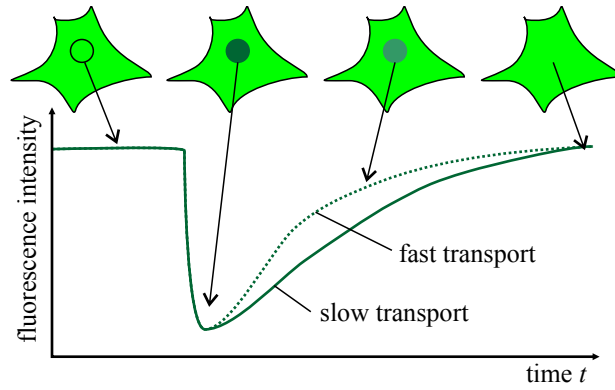


Figure 1.7. | Illustration of fluorescence recovery after photo bleaching.

is also the observation of Ca^{2+} waves during stimulus propagation in nerve cells [56–58]. Here a Ca^{2+} -sensitive fluorescent dye is used to make the distribution of Ca^{2+} -ions visible. Other methods rely on artificially induced non-equilibria. Often the cell is perturbed by bleaching the fluorescent molecules in a given region and observing, how fluorescence is recovered, when labeled molecules diffuse back into the bleached region [59, 60]. This method, called fluorescence recovery after photo bleaching (FRAP), is illustrated in Fig. 1.7. It has been applied to measure the diffusion of molecules in the cytosol, the nucleus and in the cellular membrane [61–63]. FRAP can also be used to measure reaction kinetics [64]. Several variants of FRAP have been developed, where one monitors the fluorescence loss in the environment of the bleached region [65, 66], or the bleaching process itself [67].

1.4.3. Fluorescence fluctuation techniques

The methods described so far, need to either discriminate single particles, or extract information from a transition of the system between a non-equilibrium and an equilibrium state. Such a transition is shown in Fig. 1.8(a). First the average concentration (dashed red curve) decreases until an equilibrium concentration $\langle c(\vec{r}) \rangle_t$ is reached. In such an equilibrium state, the system does not change anymore and differential equations like Eq. (1.4.1) can no longer be used to determine the parameters of the dynamics. However, if the system is observed on a shorter timescale (thin red curve), fluctuations $\delta c(\vec{r}, t)$ around the average intensity $\langle c(\vec{r}) \rangle_t$ become apparent:

$$c(\vec{r}, t) = \langle c(\vec{r}) \rangle_t + \delta c(\vec{r}, t), \quad \text{with} \quad \langle \delta c(\vec{r}, t) \rangle_t = 0. \quad (1.4.2)$$

These statistical fluctuations $\delta c(\vec{r}, t)$ are caused by the random process, that drives the dynamics of the system (e.g. Brownian motion). This section describes a class of methods that analyze these fluctuations. Such methods were also used throughout this thesis. The fluctuations $\delta c(\vec{r}, t)$ are measured by observing a small subvolume V_{obs} of the sample (red circle in Fig. 1.8a), which contains only a few 10 to a few 100 particles at any time. The statistical processes, that drive the dynamics of the system, are imprinted in the statistical properties of $\delta c(\vec{r}, t)$. For instance the number of particles $N(t) = c(t) \cdot V_{\text{obs}}$ in the observation volume obeys Poissonian statistics. Therefore the average concentration can be extracted from the variance of the fluctuations, as $\langle \delta c(\vec{r}, t)^2 \rangle_t = \langle c(\vec{r}) \rangle_t$.

While particles move randomly in and out of the observation volume V_{obs} , they create temporal correlations in $\delta c(\vec{r}, t)$. If a particle resides in V_{obs} for a certain time τ_{D} , the fluctuations are no longer statistically independent on that time scale. The retention time τ_{D} directly depends on the MSD of the single particles and the characteristic size w_{obs} of V_{obs} (e.g. the diameter of the red circle in Fig. 1.8a),

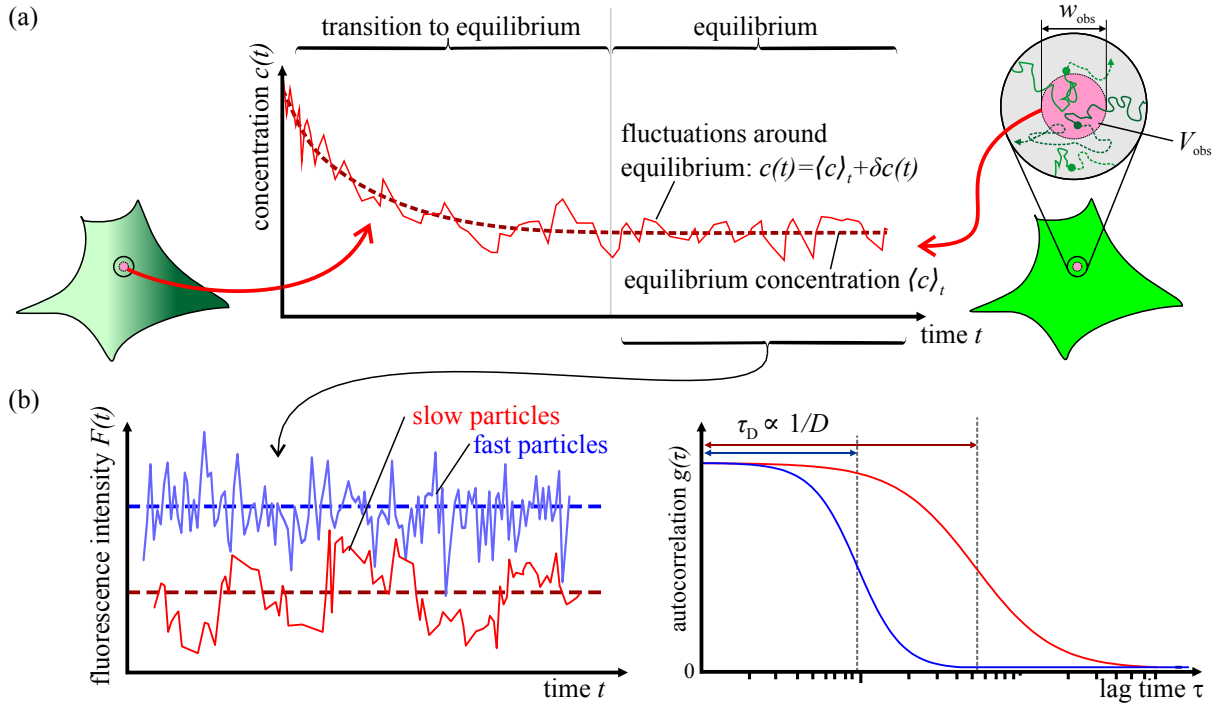


Figure 1.8. | (a) Transition of the time-dependent concentration into an equilibrium state. (b) Illustration of fluorescence correlation spectroscopy

via the equation

$$\text{MSD}(\tau_D) \stackrel{!}{=} w_{\text{obs}}^2 \quad \xrightarrow{\text{normal diffusion}} \quad \tau_D \propto \frac{w_{\text{obs}}^2}{D}. \quad (1.4.3)$$

As shown in Fig. 1.8(b), the time τ_D can directly be measured as the decay time of the (normalized) autocorrelation function of the fluorescence intensity fluctuations $F(t) = \langle I \rangle_t + \delta F(t)$ in V_{obs} :

$$g(\tau) = \frac{\langle F(t) \cdot F(t + \tau) \rangle_t}{\langle F \rangle_t^2} - 1 = \frac{\langle \delta F(t) \cdot \delta F(t + \tau) \rangle_t}{\langle F \rangle_t^2}. \quad (1.4.4)$$

Here $F(t) \propto c(t)$ and $\delta F(t) \propto \delta c(t)$. This method is called fluorescence correlation spectroscopy (FCS). It was first described by Magde et al. in 1974 [68, 69]. Today it is typically implemented on a confocal microscope (see Fig. 1.9a), which observes a focal volume $V_{\text{obs}} = 0.2 - 0.6 \mu\text{m}^3$ with a typical diameter on the order of $w_{\text{obs}} = 500 \text{ nm}$ [70]. Therefore FCS does not require to average over larger volumes in the sample, as it was (implicitly) done in SPT and fluorescence recovery after photo bleaching. single-photon avalanche diodes (SPADs) or photo-multiplier tubes are used as detectors in the confocal microscope. With suitable data acquisition electronics, they allow to measure $F(t)$ and $g(\tau)$ with a temporal resolution of $\sim 10 - 100 \text{ ns}$. With specialized electronics, $g(\tau)$ can be resolved even on the picosecond timescale [71].

FCS is widely used to determine concentrations and diffusion coefficients in solution (see e.g. [72] for a good review) and in different compartments of cells (see e.g. [17, 73–77]). It was also applied to more complex phenomena, like anomalous diffusion [22, 26, 27], active transport [37, 78] and the internal motion of polymers [79–83]. As Eq. (1.4.4) will contain contributions from any process that changes the fluorescence intensity of a particle in V_{obs} , FCS can be applied to observe photo-physical blinking processes [84–86], which are present in most fluorescence dyes, or reactions that change the brightness

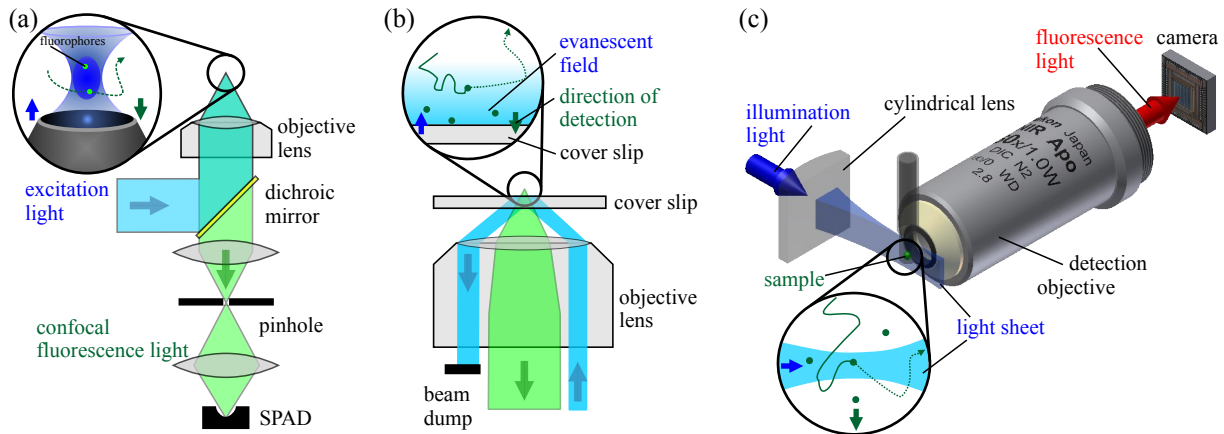


Figure 1.9. | (a) Confocal microscope. (b) total internal reflection fluorescence (TIRF) microscope. (c) light sheet fluorescence microscope (LSFM).

of a fluorophore. If the illumination light is linearly polarized the rotation of the dipole vector of a fluorophore can be observed [87–90].

FCS has been extended to a cross-correlation analysis of the intensities $F_g(t)$ and $F_r(t)$, measured in two color-channels g and r simultaneously [91–94]:

$$g_{gr}(\tau) = \frac{\langle \delta F_g(t) \cdot \delta F_r(t + \tau) \rangle_t}{\langle F_g \rangle_t \cdot \langle F_r \rangle_t}. \quad (1.4.5)$$

This technique is called fluorescence cross-correlation spectroscopy (FCCS). Typically two molecular species of interest are specifically labeled with two differently colored dyes. Then the crosscorrelation amplitude $g_{gr}(0)$ is proportional to the concentration of molecules that carry both dyes. This technique can be used to measure molecular interactions and binding reactions *in vitro* and *in vivo* (see e.g. [73–76, 93, 95, 96]).

All the FCS variants and implementations mentioned above are limited to measurements on a single spot. As the cell is a non-uniform, complex environment, several attempts have been made to extend FCS and FCCS to an imaging method. The first approaches used the scanning capabilities of confocal microscopes to move the focus quickly in a circle [97] or along a line [98]. The repetition rates are typically on the order of $\sim 1000 \text{ s}^{-1}$. In this way simultaneous measurements on 10 – 100 positions are possible. In addition, consecutive measurements on several spots in a cell have been used, either with many pixels and short dwell times [99], or at fewer pixels, but with longer dwell times and consequently less noisy autocorrelation curves [27, 33]. To achieve simultaneous measurements in many positions, variants of confocal microscopy were used: line-confocal detection [100, 101] and spinning-disk microscopy [102, 103]. In these variants cameras were used as fluorescence detectors, which are generally slower than SPADs. They reach a temporal resolution on the order of $100 \mu\text{s}$ for a single line or $0.5 - 2 \text{ ms}$ for larger areas. To improve the limited temporal resolution, SPAD arrays have been used [104–107]. These combine between 2×2 and 32×32 SPADs on a single silicon microchip with fast readout electronics, which allows for a temporal resolution of $10 \mu\text{s}$ or better. In order to achieve small observation volumes, multi-confocal setups were used, that create between 2 and 1024 laser foci simultaneously. The fluorescence from the foci is imaged onto the SPAD arrays, so each focus coincides with a single SPAD. Such systems have just recently (in 2013) been shown to be applicable to live-cell measurements [107]. The complex optical setup and alignment of these instruments renders them hard to operate by non-expert users.

An alternative route to imaging fluorescence correlation spectroscopy (imaging FCS) is the use of wide-field microscopes in combination with high-sensitivity cameras. In 2007 Kannan et al. have

shown that FCS can be performed in an imaging mode on a total internal reflection fluorescence (TIRF) microscope [108]. This setup is illustrated in Fig. 1.9(b). An evanescent wave is used to illuminate only a 100 – 200 nm thin layer above a glass cover slip. This leads to a low background signal, which is a prerequisite for an FCS analysis. The technique was successfully used to analyze the diffusion in biological membranes, where τ_D is on the order of milliseconds [109–116]. The low penetration depth of an evanescent wave, limits the systems that can be observed with TIRF microscopy mostly to such membrane systems.

In 2010 Wohland et al. pioneered the use of light sheet microscopy to perform imaging FCS [117]. The principle of a light sheet fluorescence microscope (LSFM) is shown in Fig. 1.9(c) [118, 119]. A cylindrical lens is used to form a thin sheet of light, which only illuminates a 1 – 2 μm thin slice in the sample. Detection is done perpendicular to this light sheet with a second microscope objective, that projects the image onto a fast camera. This wide-field microscopy technique has low background and the detection volumes are small enough to successfully perform an FCS analysis ($V_{\text{obs}} = 1 - 2 \mu\text{m}^3$). In contrast to TIRF microscopy, the light sheet may be placed anywhere in the sample, not just at the interface to a glass cover slip. Light sheet microscopes are also not as complex as multi-confocal setups and since 2013 they are available commercially. The combination of light sheet microscopy and FCS is usually termed single plane illumination fluorescence correlation spectroscopy (SPIM-FCS). It was used to study the dynamics of chromatin associated proteins [120, 121].

In addition to FCS and FCCS that correlate the signals from a single focus in time, also spatial crosscorrelation has been used to measure diffusion. As the MSD describes how far particles move in a certain time, also spatial correlations are imprinted on the fluorescence fluctuations $\delta F(\vec{r}, t)$. This can be exploited by calculating a spatial or spatio-temporal cross-correlation function:

$$g_{\text{ICS}}(\tau, \vec{\xi}) = \frac{\langle \delta F(\vec{r}, t) \cdot \delta F(\vec{r} + \vec{\xi}, t + \tau) \rangle_{t, \vec{\xi}}}{\langle F \rangle_{t, \vec{\xi}}^2}. \quad (1.4.6)$$

The averaging is now done over space and in some cases over time, as indicated by the index in $\langle \cdot \rangle_{t, \vec{\xi}}$. Techniques using a spatial correlation like in Eq. (1.4.6) are generally called image correlation spectroscopy (ICS) methods. As they usually require only a simple post-processing of images or image series from confocal or wide-field microscopes, they have been applied in many variants to several cellular systems [122–129]. As the camera-based imaging FCS described above, most ICS methods are limited in their temporal resolution by the used image sensors. Furthermore the spatial cross-correlation in Eq. (1.4.6) implies an inherent averaging over larger parts of the images. Therefore the spatial resolution of ICS is generally one order of magnitude lower than that of imaging FCS, as described above.

1.5. Aim of the thesis

The aim of this thesis project was to develop an instrument, that allows to map molecular mobility and interactions in living cells. The intended application was to determine the mobility of different inert tracer molecules, such as oligomers of the enhanced green fluorescent protein (eGFP), nuclear receptors and transcription factors, as well as chromatin in a live cell. Imaging FCS was chosen as the fundamental method, as it allows to measure the mobility parameters of these molecules at many positions in the cell simultaneously and with sufficient spatial resolution. It was implemented on a light sheet microscope, which can be applied to image any part of a cell. This SPIM-FCS technique was advanced in cooperation with Thorsten Wohland and co-workers (NUS, Singapore), who published a first implementation in 2010 [117].

1.6. Own Contributions

For this thesis a light sheet microscope was designed, which is optimized for SPIM-FCS measurements in living cells (see chapter 6). Its optics was tailored to yield a thin light sheet ($1/e^2$ -width: $\sim 2.5 \mu\text{m}$) and a small focal volume over a field of view of $\sim 50 \mu\text{m}$. The parameters are matched to the approximate size of living cells (diameter: $10 - 50 \mu\text{m}$, height: $\sim 10 \mu\text{m}$). The microscope is equipped with a fast EMCCD camera, which allows for SPIM-FCS measurements of most fluorescently labeled proteins in living cells. The selection of this camera type is based on a thorough comparison of different commercially available cameras, which was published in

[130]: AP. Singh¹, JW. Krieger¹, J. Buchholz, E. Charbon, J. Langowski, and T. Wohland. **The performance of 2D array detectors for light sheet based fluorescence correlation spectroscopy.** *Opt. Express*, 21(7):8652–8668, 2013. doi:10.1364/OE.21.008652.

These results are detailed in section 8.7. They show, that at the time of writing, EMCCD cameras offer the best trade-off between photosensitivity and temporal resolution.

The initially published simple SPIM-FCS theory (see Ref. [117]) was extended to cover different transport processes, including directed flow and anomalous diffusion (see chapter 5). Also, a set of data evaluation methods had to be developed, that allow to evaluate the huge amount of data, that is recorded in each SPIM-FCS measurement (typically 100,000 frames with 128×20 pixels each). These techniques are described in chapter 7. They need to be sufficiently robust, so that model fits and all other tasks can be performed without detailed supervision by the user. All methods were implemented in a freely available², user-friendly software QUICKFIT 3.0. This program also controls the selective plane illumination microscope (SPIM).

The newly built microscope and SPIM-FCS were applied to several different test systems, in order to characterize the prospects and limitations of the technique. In this way it could be shown, that SPIM-FCS is able to measure absolute diffusion coefficients without requiring an external calibration standard, as it is customary in confocal FCS [130]. After this fundamental characterization, SPIM-FCS could be applied to several cellular systems (chapters 10-12). One particular example is the keratin intermediate filament system. Here a pool of free filament precursors could be quantified in living cells (see chapter 11). These measurements needed to be performed at positions between large and bright filament bundles, that are present throughout the whole cell. With single-point confocal FCS this would pose a cumbersome effort, since the cell constantly moves during the measurement. The motion will impair a large fraction of the consecutive FCS measurements. In SPIM-FCS the data acquisition process is parallelized, since hundreds or thousands of autocorrelation curves are acquired simultaneously. This way, a large number of evaluable measurements were left in each cell, even if the pixels that were impaired by cell motions were excluded.

A second application for SPIM-FCS were measurements on the nuclear receptor RXR. Its function was investigated in a cooperation with the group of Gyuri Vámosi (university of Debrecen, Hungary). Here SPIM-FCS was used to show that the interaction of RXR with chromatin seems to be homogeneously distributed over the whole cellular nucleus. A brief summary of these results can be found in section 12.3. They were published in:

[121]: P. Brazda, JW. Krieger, B. Daniel, D. Jonas, T. Szekeres, J. Langowski, K. Toth, L. Nagy, and G. Vamosi. **Ligand binding shifts highly mobile retinoid x receptor to the chromatin-bound state in a coactivator-dependent manner, as revealed by single-cell imaging.** *Molecular and Cellular Biology*, 34(7):1234–1245, 2014. doi:10.1128/MCB.01097-13.

For most of the SPIM-FCS measurement, shown in this thesis, a fast EMCCD camera was used. It has a high photosensitivity, but only a limited temporal resolution of $0.33 - 1 \text{ ms}$. This is not fast enough to resolve the diffusion of small molecules reliably (e.g. of single chemical fluorescent dyes, or fluorescent

¹equally contributing first authors

²<http://www.dkfz.de/Macromol/quickfit>

proteins in solution). Therefore the use of fast SPAD arrays as image sensors was thoroughly assessed during this thesis work. These experimental image sensors achieve a temporal resolution of 1 – 10 μ s, which is 1-2 orders of magnitude faster than the EMCCD cameras. This way SPAD arrays would allow for the reliable measurement also of small fluorescent particles. Two different chips were used: *Radhard2* and *SwissSPAD*. Both were designed by the group of Edoardo Charbon (TU Delft/EPFL Lausanne). For the early model *Radhard2*, the principal applicability to SPIM-FCS measurements of very bright samples could be demonstrated. This was characterized and described in two publications: Ref. [130] (see above) and

[131]: J. Buchholz, JW. Krieger, G. Mocsár, B. Kreith, E. Charbon, G. Vámosi, U. Keschull, and J. Langowski. **FPGA implementation of a 32x32 autocorrelator array for analysis of fast image series.** *Optics Express*, 20(16):17767, 2012. doi:10.1364/OE.20.017767.

However, due to its low photosensitivity, the *Radhard2* chip could not be applied to fluorescent proteins or live-cell samples. During the last months of the PhD project, this problem was addressed by the new chip *SwissSPAD*, which exhibits a significantly larger array (512 \times 128 SPADs), higher photosensitivity and has microlenses, that concentrate the incident light onto the sensors (see sections 6.4 and 8.8). Using *SwissSPAD*, SPIM-FCS measurements of molecules, that are labeled with a single chemical fluorophore (Alexa-488) became feasible. Nevertheless, an application to auto-fluorescent proteins in live cells could not be achieved so far.

Within the last two years of the thesis project, the microscope was extended with a second excitation laser and a dual-view optics. In this way, spatially resolved dual-color FCCS became possible for the first time. This new technique was termed single plane illumination fluorescence cross-correlation spectroscopy (SPIM-FCCS) and was published in:

[132]: JW. Krieger³, AP. Singh³, CS. Garbe, T. Wohland, and J. Langowski. **Dual-color fluorescence cross-correlation spectroscopy on a single plane illumination microscope (SPIM-FCCS).** *Optics Express*, 22(3):2358, 2014. doi:10.1364/OE.22.002358.

It allows for the first time to simultaneously map molecular interactions and mobilities in a complete slice of a living cell. In Ref. [132], it was also demonstrated, that SPIM-F(C)CS is not only applicable to the cytoplasm and the nucleus of living cells, but also to the membrane.

In the course of the thesis work, several simulation programs were developed and some of them are described in appendix B. Of particular importance was an FCS/FCCS simulation, which was used to test the SPIM-FCCS models, developed in this thesis. Also the effects of several experimental artifacts were explored using this program. As a side project, it was combined with a Brownian dynamics simulation of DNA dynamics. This allowed for a deeper understanding of experimental results published by Shusterman et al. [81]. The findings of this study are summarized in:

[82]: T. Wocjan, JW. Krieger, O. Krichevsky, and J. Langowski. **Dynamics of a fluorophore attached to superhelical DNA: FCS experiments simulated by brownian dynamics.** *Physical Chemistry Chemical Physics*, 11(45):10671, 2009. doi:10.1039/B911857H.

1.7. Outline of the thesis

In the following chapter 2 the fluorescent dyes and labeling techniques are introduced, that were used throughout this thesis. Fluorescence microscopy and especially light sheet fluorescence microscopy are described in chapter 3. Chapter 4 gives an overview of the different types of image sensors, that were used for the measurements. After these basics, chapter 5 details the theory of fluorescence correlation spectroscopy (FCS) and fluorescence cross-correlation spectroscopy (FCCS), especially the variants used for SPIM-F(C)CS.

³equally contributing first authors

In the second part of this thesis, the experimental realization of SPIM-FCS/SPIM-FCCS is outlined. At first, chapter 6 describes a selective plane illumination microscope (SPIM), which was tailored for SPIM-FCS measurements in single cells. Here also the basic characterization of the microscope (resolution, light sheet thickness etc.) is presented. Chapter 7.3 then summarizes the data processing methods, used to evaluate the measurements. Finally chapters 8 and 9 present several test measurements, performed with the described setup. In addition, several artifacts are discussed, that can arise in such measurements. The measurement of concentrations and molecular interactions are also detailed.

The third part of the thesis presents applications of the SPIM-FCS/SPIM-FCCS instrument to live-cell measurements. Chapter 10 shows measurements on the dynamics of different molecules in the complex and dynamic environment of a cell. Chapter 11 presents measurements on the dynamics of the keratin intermediate filament system and shows a first quantification of a free pool of keratin precursor molecules. Finally, in chapter 12, measurements of the mobility of several chromatin-associated proteins are described.

Part II.

Methods

2. Fluorescence labeling techniques

In this thesis all methods used to measure transport processes rely on fluorescence labeling of the molecules of interest. This allows one to sensitively detect and track only a specific species of particles. The remaining bulk of cellular constituents is rendered virtually invisible for the measurement. This chapter will give a short introduction into fluorescence and accompanying processes (sections 2.1–2.3). Three classes of fluorescent dyes are introduced in the last three sections: chemical fluorophores in section 2.4, fluorescent proteins in section 2.5 and quantum dots in section 2.6.

2.1. Fluorescence

Fluorescence is the emission of a photon by a molecule after its excitation by an incident photon. It can be understood considering the different energy states of the molecule, represented in a Jablonski diagram, as shown in Fig. 2.1. The energy spectrum splits up into quantized electronic states S_ν of energy E_ν , numbered by the quantum number ν , where S_0 is called ground state and S_1, S_2, \dots are called excited states. Each of these electronic states further splits up into a large set of oscillatory and rotational substates that differ only slightly in energy. In complex fluorescent molecules, like the ones used here, these states are so dense that they seemingly form a continuum.

A photon of wavelength λ_{ex} (or angular frequency ω_{ex}) carries an energy of

$$E_{\text{photon}} = \hbar\omega_{\text{ex}} = \frac{h \cdot c_0}{\lambda_{\text{ex}}}, \quad (2.1.1)$$

where h is Planck's constant, $\hbar = h/(2\pi)$ and c_0 is the speed of light in vacuum. If E_{photon} matches the energy difference between two states S_0 and S_1 , an electron in S_0 may absorb the photon and is excited into S_1 . Typically the electron then resides in a vibro-rotational substate S_1^* , which quickly decays without emission of further photons into the excited ground state S_1 . The energy is transformed into heat, e.g. by collisions with solvent molecules. After some time the electron decays back from S_1 into a state S_0^* with $\nu = 0$. The energy difference is emitted as a new photon with wavelength $\lambda_{\text{fl}} > \lambda_{\text{ex}}$. Again the electron subsequently decays into the ground state S_0 without emitting a photon. The difference between the peak excitation and fluorescence wavelengths is called Stokes shift:

$$\Delta\lambda_{\text{Stokes}} = \lambda_{\text{ex}} - \lambda_{\text{fl}}. \quad (2.1.2)$$

It is typically between 10 nm and 100 nm. The band structure of the energy states leads to broadened absorption and emission peaks, as shown in the spectra in Fig. 2.1(b).

The timescale of an excitation transition is typically a few femtoseconds, whereas internal relaxation happens within picoseconds. Both processes are much faster than typical fluorescence lifetimes, which are in the range of nanoseconds.

After excitation into the state S_1 , there are two decay channels with associated transition rates: Either the energy is lost by emitting a fluorescence photon with rate Γ , or by a non-radiative decay with rate k_{nr} (green dashed lines in Fig. 2.1a). These rates are usually summarized into two numbers, specific to each fluorophore: The fluorescence lifetime

$$\tau_{\text{fl}} = \frac{1}{\Gamma + k_{\text{nr}}} \quad (2.1.3)$$

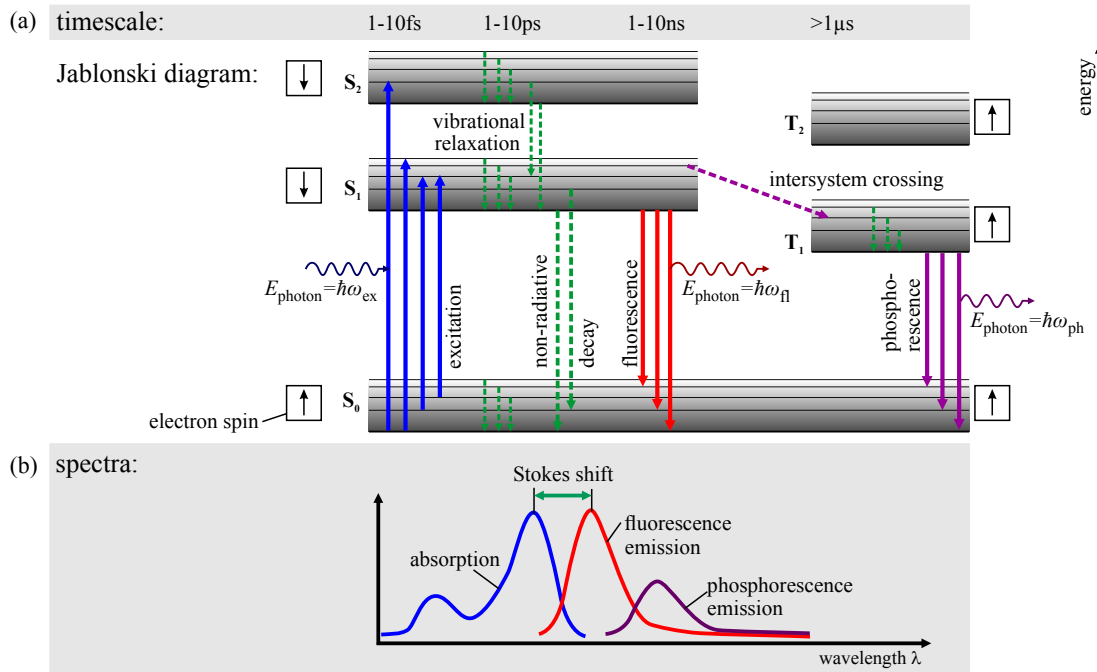


Figure 2.1. | Jablonski diagram of a fluorescent molecule. S_ν and T_ν denote singlet and triplet states for the quantum number ν . Solid lines are transitions with absorption or emission of a photon (horizontal wavy line). Non-radiative transitions are sketched as vertical or inclined dashed lines.

describes the average lifetime of the excited state, whose population $n_{S_1}(t)$ decays exponentially:

$$n_{S_1}(t) = n_{S_1}(0) \cdot e^{-t/\tau_{fl}}. \quad (2.1.4)$$

The second important property is the quantum yield q_{fluor} , which relates the number of absorbed photons $N_{\text{photon, abs}}$ to the number of emitted fluorescence photons $N_{\text{photon, fl}}$:

$$q_{\text{fluor}} \equiv \frac{N_{\text{photon, fl}}}{N_{\text{photon, abs}}} = \frac{\Gamma}{\Gamma + k_{\text{nr}}}. \quad (2.1.5)$$

The absorption process alone is typically characterized by the absorption cross-section σ_{abs} of a single molecule, or by its molar extinction coefficient $\epsilon_{\text{abs}} = N_A \cdot \sigma_{\text{abs}} / \ln(10)$ ($[\epsilon_{\text{abs}}] = 1 \text{ M}^{-1} \text{ m}^{-1}$). These quantities describe the loss in intensity $I(x)$ along a path x in a sample containing the molecules at concentration c :

$$I(x) = I(0) \cdot \exp(-\sigma_{\text{abs}} \cdot c \cdot N_A \cdot x) = I(0) \cdot 10^{-\epsilon_{\text{abs}} \cdot c \cdot x}, \quad (2.1.6)$$

where $I(0)$ is the incident intensity and N_A is Avogadro's number. This relation is called "Lambert-Beer law".

2.2. Triplet transitions and phosphorescence

So far the spin of the electrons was not taken into account. Initially the molecular ground state S_0 is populated by two electrons with anti-parallel spins. The overall spin is then 0 and the multiplicity is 1. Therefore the state is called singlet state. The quantum mechanical selection rules for pure electronic dipole transitions forbid a flip its spin during the transition. So only other singlet states S_1, S_2, \dots may be reached.

In addition to the spectrum of singlet states, also a spectrum of triplet states T_ν exists, which is illustrated in Fig. 2.1(a). These have an overall spin of $1\hbar$ and a multiplicity of 3, hence the name. Since in complex molecules the mentioned selection rules do not apply absolutely, transitions between singlet and triplet states become possible (“intersystem crossing”). Due to the spin-flip, their probability is lower than for transitions between two singlet states, which leads to a prolonged lifetime τ_T of the triplet states. Typical values for this triplet lifetime τ_T are on the order of microseconds for the dyes used in this thesis. The delayed photons emitted by the transition $T_1 \rightarrow S_1$ are called “phosphorescence” to distinguish them from fluorescence. The phosphorescence emission spectrum is red-shifted, as compared to the fluorescence spectrum (see Fig. 2.1b). In effect, the triplet dynamics will appear as an on-off blinking of the fluorescence of each fluorophore on a typical timescale of τ_T , as no more fluorescence photons are created, while the fluorophore stays in T_1 .

2.3. Photobleaching and photoswitching

A fourth decay channel from an excited state of a fluorophore is “photobleaching”. During this process the chemical structure of the fluorophore changes. These changes are typically non-reversible or very long-lived and change the spectrum of the fluorophore, rendering it non-fluorescent at a given excitation wavelength. The fluorophore then seems to be switched off after the photobleaching has occurred. Such transitions may also be initiated by the chemical environment of the fluorophore, e.g. by a pH-dependent protonation reaction of some fluorescent proteins [85, 133]. Such dyes may be used as intra-cellular sensors, e.g. for the pH. Special fluorescent dyes also can be switched between an on- and an off-state by a third illumination wavelength [134].

2.4. Chemical fluorophores

Many molecules, that are fluorescent in the visible spectral range, share the common feature of having a large system of conjugated π -electrons [137]. These electrons are only weakly bound to the molecule and visible photons have enough energy to excite them. The binding energy is typically decreasing with increasing size of the π -system, shifting their absorption and fluorescence into the red spectral range [137]. A large variety of synthetic dyes are available, that are based on this principle.

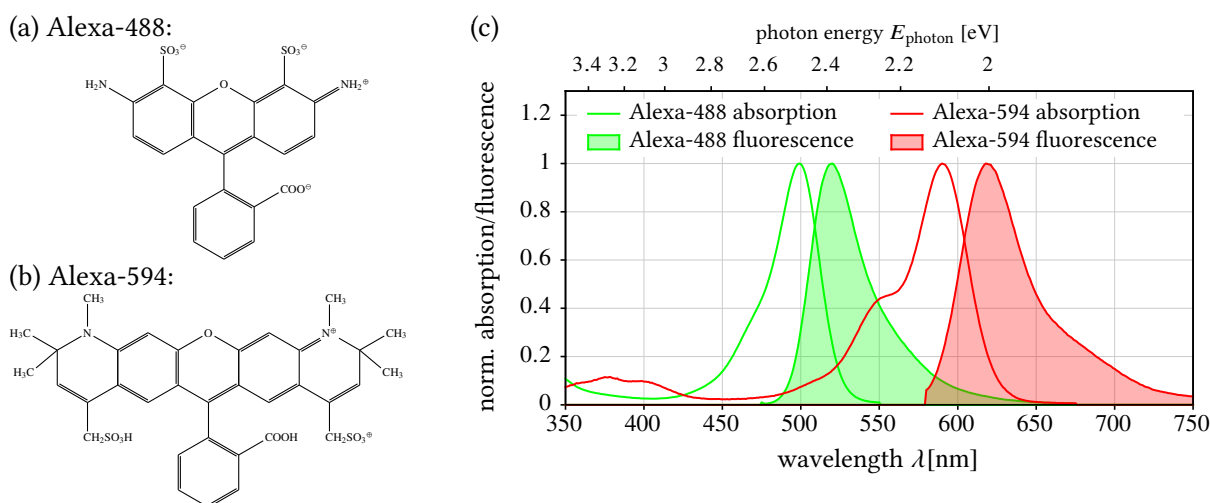


Figure 2.2. | Molecular structures (a,b) and absorption and fluorescence spectra (c) of Alexa-488 and Alexa-594 dyes. The molecular structures and the spectra were taken from [135, 136].

dye	$\lambda_{\text{abs,max}}$ [nm]	$\lambda_{\text{fl,max}}$ [nm]	$\Delta\lambda_{\text{Stokes}}$ [nm]	ϵ_{abs} [M ⁻¹ cm ⁻¹]	q_{fluor} [%]	$\epsilon_{\text{abs}} \cdot q_{\text{fluor}}$ [mM ⁻¹ cm ⁻¹]
chemical fluorophores						
FITC	495	519	24	75,000	92	69
Alexa-488	495	519	24	73,000	92	67
Alexa-594	590	617	27	92,000	66	61
fluorescent proteins						
wtGFP	395	504	9	25,000	79	20
eGFP	488	507	19	56,000	60	34
eYFP	514	527	13	83,400	61	51
dsRed	556	586	30	35,000	10	3.5
mRFP1	584	607	23	44,000	25	11
quantum dots						
QDot-525	—	525	—	130,000 ^a	29	38
QDot-565	—	565	—	290,000 ^a	—	—
QDot-585	—	585	—	530,000 ^a	21	111
QDot-655	—	655	—	2,900,000 ^a	—	—

^a: at excitation with 488 nm

Table 2.1. | **Spectroscopic properties of some fluorescent dyes.** $\lambda_{\text{abs,max}}$ is the wavelength of maximum absorption, $\lambda_{\text{fl,max}}$ is the fluorescence maximum, $\Delta\lambda_{\text{Stokes}}$ the Stokes shift, ϵ_{abs} is the extinction coefficient and q_{fluor} is the fluorescence quantum yield. The parameter $\epsilon_{\text{abs}} \cdot q_{\text{fluor}}$ is an empirical measure of the brightness (fluorescence photons emitted from a given solution at given illumination). Data was taken from Refs. [139–143].

The two dyes Alexa-488 and Alexa-594 were used for many experiments described in this thesis. Figure 2.2 shows their chemical structure and absorption as well as fluorescence spectra and Tab. 2.1 summarizes their basic spectroscopic properties. Alexa-488 absorbs blue and emits green light, whereas Alexa-594 absorbs orange and emits red light. The π -electron system is distributed over four C_6 -rings for Alexa-488 and six rings for Alexa-594, which demonstrates the red-shifting effect of the larger π -system.

These fluorescent molecules are available with diverse side chains, that allow labeling of different molecules of interest. Some of these sidechains can bind covalently and specifically to thiol ($-\text{SH}$) or amine ($-\text{NH}_2$) residues of amino acids. This allows to label specific positions in a protein. Also short single-stranded DNA oligo-nucleotides, that are labeled at one end with a fluorescent dye, are commercially available. Larger labeled DNA strands can be built from these, if they are used as primers in a polymerase chain reaction (PCR). A last class of samples used for this thesis are fluorescent microspheres. They are made of polystyrene or latex, and fluorescent molecules are embedded in their matrix. For example, the fluorescence of microspheres F8803 produced by Invitrogen with a diameter of 100 nm is equivalent to around 7400 fluorescein isothiocyanate (FITC) molecules [138]. FITC is a widely used yellow-green fluorescent dye, which is comparable to Alexa-488.

2.5. Fluorescent proteins

In addition to the synthetic fluorescent dyes discussed in the previous section, a large family of auto-fluorescent proteins exist [140, 144]. They were derived from wildtype green fluorescent protein (wtGFP) which was extracted in 1962 from the jellyfish *Aequorea victoria* [145]. Later, the original protein was mutated at a few amino-acids in order to change its color or improve its brightness and photo-stability. The molecular structure of wtGFP is illustrated in Fig. 2.3(a). It is composed of a barrel of β -sheets, which is about 4 nm long and 3 nm in diameter. This barrel surrounds and protects the chromophoric

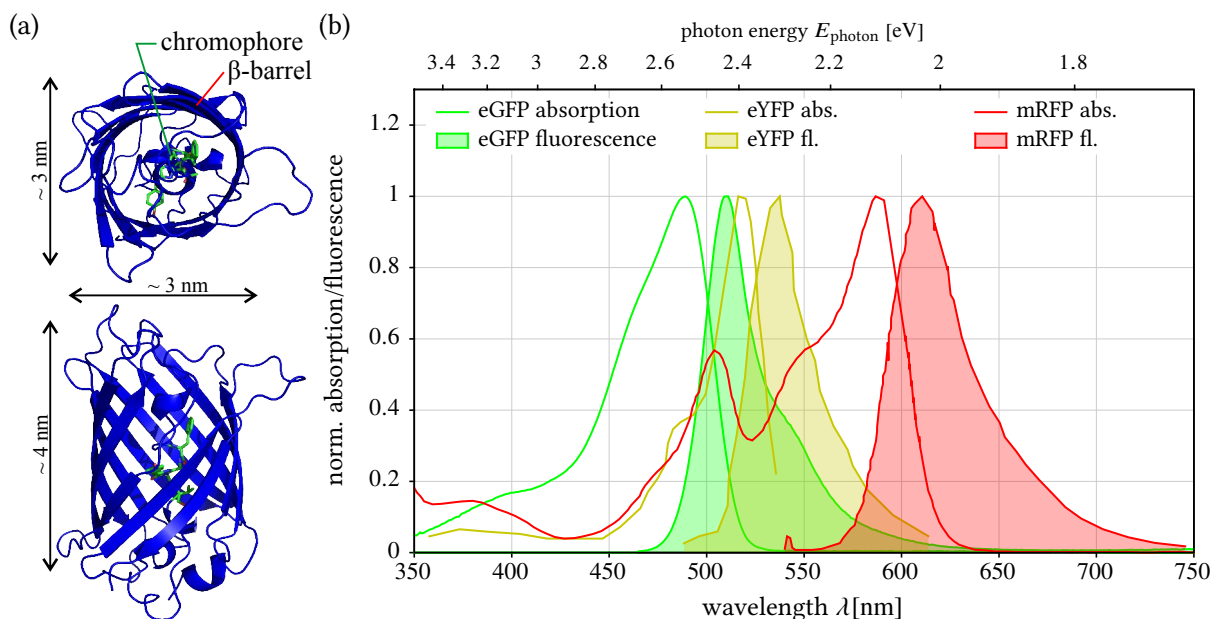


Figure 2.3. | (a) Molecular structure of wtGFP. (b) Absorption and fluorescence spectra of the fluorescent proteins eGFP, eYFP and mRFP1. The crystal structure of wtGFP was taken from [148] and rendered with PyMol. Spectra were taken from Refs. [139, 140, 147, 149, 150].

group, which is responsible for the fluorescence. In wtGFP the chromophore is formed by a reaction of three peptide residues that also interact with other peptide residues in their vicinity [146].

For this thesis, mainly the enhanced green fluorescent protein (eGFP), the enhanced yellow fluorescent protein (eYFP) and the monomeric red fluorescent protein (mRFP1) were used. Their spectra are shown in Fig. 2.3 and their spectroscopic properties are summarized in Tab. 2.1. The first two dyes were derived from wildtype green fluorescent protein (wtGFP) and mRFP1 is a monomeric form of the red fluorescent protein DsRed, which was extracted from the coral *Discosoma* [147].

Fluorescent proteins have the advantage that they can be transfected into live cells, which subsequently express (i.e. produce) the fluorophore. Transfection means that the genetic code of the fluorescent protein is inserted into a DNA plasmid, which also contains promoter sites that initiate the transcription of the new gene. This technique can also be used to label a specific protein inside the cell, if its genetic code is known. In this case, both genes are positioned one after the other on the plasmid and a short linker between the two is inserted. After transfection, the cell will express the protein of interest, linked to the fluorescent label. Care has to be taken to not disturb the function of the labeled protein by the fluorophore. Typically transfection is only a transient process, i.e. the new gene is not integrated into the cells genome and the plasmids transfected into a cell will dilute during cell division. Finally the transfection and thus also the fluorescence is lost after several generations. A stable transfection is in some cases possible by adding a second gene to the plasmid that contains a resistance against a toxin. A very small amount of cells will actually incorporate the plasmid DNA into their genome. Using the resistance, these few cells may selectively proliferate. After some generations they form a new cell line, which does no longer loose the transfected gene. This process is called “stable transfection” to distinguish it from the previously described “transient transfection”.

Fluorescent proteins typically show a fast triplet blinking. In addition they often also exhibit an on-off blinking of the fluorescence on longer timescales. The fluorophore of eGFP can undergo a reversible protonation reaction, which changes the absorption spectrum of the dye and renders it dark, if excited around 488 nm [85]. The distribution of fluorophores in protonated and non-protonated states is

determined by the pH of the surrounding solution. Some red fluorescent proteins also show fluctuations that depend on the excitation intensity [133]. These are explained by photo-induced, reversible structural changes in the fluorescent proteins.

2.6. Quantum dots

A third class of fluorescent dyes are nanoscale semiconductor quantum dots (QDots). The structure of the QDots, which were used for this thesis, is shown in Fig. 2.4(a). A CdSe crystal core ($\varnothing = 2 - 10$ nm) is covered with a layer of ZnS, which isolates it from the environment. For protection, the core is encased in polymer layer, which may be modified with charged side chains to make the QDots water-soluble [144, 151–153]. In addition, reactive groups can be attached to the polymer layer, which allow specific labeling of biomolecules, as explained for chemical dyes in section 2.4.

The fluorescence of QDots is based on exciting electrons from the valence band into high-energy states of the conduction band (see Fig. 2.4b). The broad, unoccupied conduction band gives rise to an also broad excitation spectrum (see Fig. 2.4c). The excited electron-hole pairs behave like quantum mechanical particles in a box. The energy of their quantized states E_n decreases with increasing size L of the box (or QDot), as $E_n \propto 1/L^2$ [154]. Typically the electron first drops non-radiatively to an energy state near the lower edge of the conduction band. The pair then recombines and emits a fluorescence photon. As fluorescence transitions only take place between states near the band edges, the emission spectrum is narrow. The dependence of the exciton energies on the size of the quantum dot can be used to tune its spectral properties. A CdSe/ZnS dot with a diameter of $\varnothing = 2.3$ nm emits in the blue spectral range, whereas a larger dot with $\varnothing = 5.5$ nm emits red light [152].

Quantum dots have a very high extinction coefficient of $10^5 - 10^6 \text{ M}^{-1} \text{ cm}^{-1}$ at blue excitation wavelengths. They do not bleach even after hours of excitation [151]. A disadvantage is their very complex blinking dynamics: intermittent “off” periods have been observed on timescales between 200 μs and several 100 s [86, 155, 156]. These dark states are believed to be related to surface traps in the QDot. In contrast to chemical fluorophores or fluorescent proteins, the decay of these dark states was found to follow a power law. Therefore no finite lifetimes can be defined [86, 155, 156].

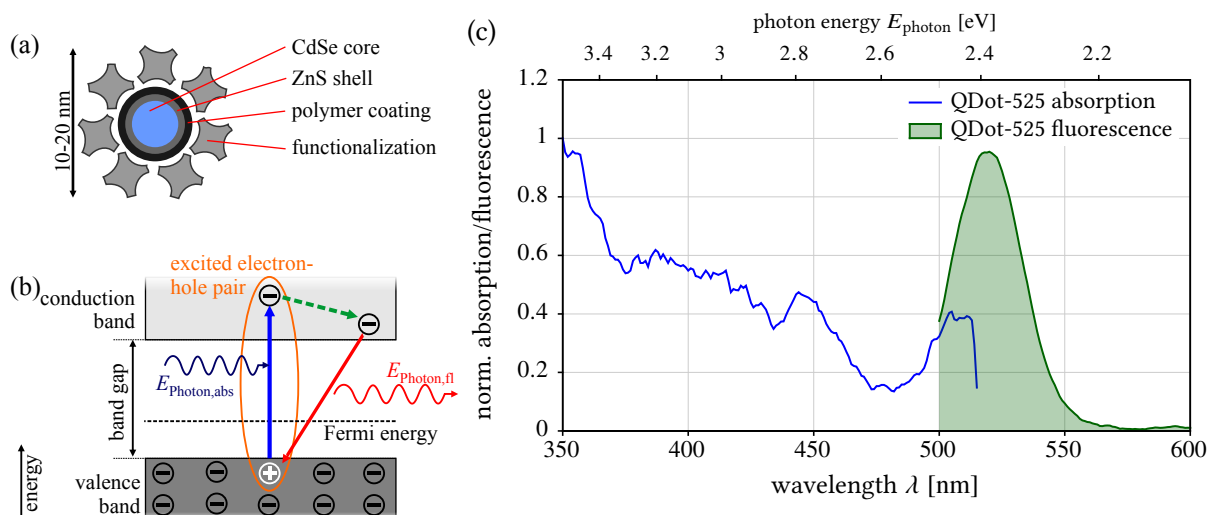


Figure 2.4. | Properties of CdSe/ZnS quantum dots. (a) Cross drawing of a typical CdSe/ZnS QDot. (b) Simplified energy band diagram. (c) Absorption and fluorescence spectrum of Invitrogen QDot525 ITK.

3. Fluorescence microscopy

As shortly described in section 1.4, fluorescence fluctuations from a small volume of the sample ($\sim 1 \mu\text{m}^3$ in size) are evaluated to yield transport properties. In order to observe such small volumes, microscopic techniques are necessary. Fluorescence is used to specifically label the molecular species of interest. Section 3.1 gives a general introduction to fluorescence microscopy. Section 3.2 describes confocal microscopy, which is commonly used for FCS. Finally section 3.3 introduces light sheet microscopy, which is the main microscopy technique used in this thesis.

3.1. Basic fluorescence microscopy

3.1.1. Principle

All fluorescence microscope can be generally divided into two parts: the excitation beam path and the detection beam path. In many cases these two parts also share some of their components. Figure 3.1(a) shows the optical setup of a typical epi-fluorescence microscope. The excitation beam (blue beam in Fig. 3.1a) is projected through the objective lens into the sample. It is slightly expanded in the object plane, so that the whole field of view is illuminated uniformly. The fluorescence light (red beam in Fig. 3.1a) is generated in the sample and collected with the same objective lens. It is separated from the excitation light using a dichroic mirror, which transmits long wavelengths and reflects short wavelengths. A detection filter further narrows the detected band of the light spectrum, so that only the emission of the

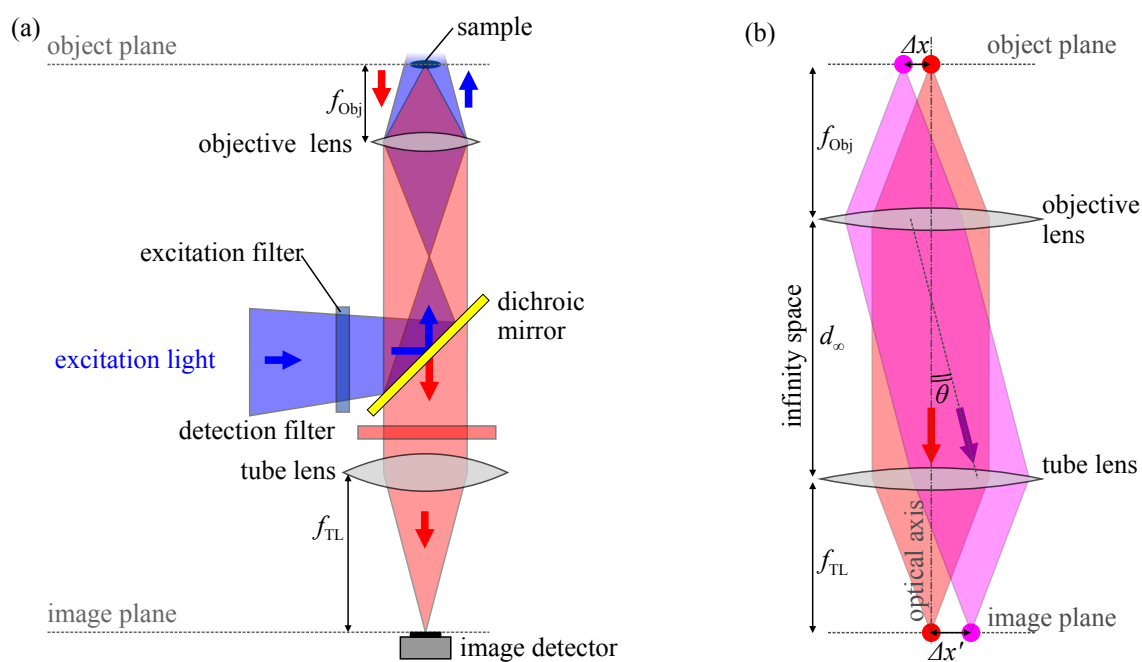


Figure 3.1. | (a) Basic setup of an epi-fluorescence microscope and (b) principle of infinity-corrected optics.

fluorophore of interest is detected. Then a tube lens projects the light onto the imaging detector (camera).

Figure 3.1 shows a special configuration of the detection beam path. Between the objective lens and tube lens, the detected light is collimated, i.e. focused into infinity (“infinity space”). Here additional optical components, such as filters, can easily be introduced into the microscope without impairing its optical properties. Today these infinity-corrected microscopes are common in most applications. The principle of such a beam path is illustrated in Fig. 3.1(b) in more detail: two fluorescent molecules (red and magenta circles) are positioned in the image plane. Due to the fast rotation of most molecules, their fluorescence light is emitted equally distributed into all spatial directions. A fraction of this light is collected by the objective lens. As the objective is positioned exactly one focal length f_{Obj} from the object plane, the fluorescence light is collimated by the lens. If the fluorescent molecule is shifted a distance Δx from the optical axis of the system, the light is still collimated, but exits the lens under an angle θ with [157]:

$$\Delta x = f_{\text{Obj}} \cdot \tan \theta. \quad (3.1.1)$$

After another distance d_{∞} the tube lens with focal length f_{TL} focuses the light onto the image sensor, where the displacement $\Delta x'$ from the optical axis is given by:

$$\Delta x' = f_{\text{TL}} \cdot \tan \theta. \quad (3.1.2)$$

Combining Eq. (3.1.1) and Eq. (3.1.2), the lateral magnification of the infinity-corrected microscope is:

$$M_{xy} = \frac{\Delta x'}{\Delta x} = \frac{f_{\text{TL}}}{f_{\text{Obj}}}. \quad (3.1.3)$$

3.1.2. Focus properties and resolution

The resolution of optical imaging is limited by diffraction at the apertures of the used lenses. This means that a point source in the object plane is not imaged into a point in the image plane, but into a small blurred circle, an “Airy disc”. This general property of optical systems can be described by a convolution of the fluorophore distribution in the object plane $c(\vec{r}, t)$ with the point spread function PSF(\vec{r}) of the system:

$$I(\vec{r}, t) = c(\vec{r}, t) \otimes \text{PSF}(\vec{r}). \quad (3.1.4)$$

Here PSF(\vec{r}) describes the 3-dimensional shape of the Airy disc. An analytical approximation of the point spread function (PSF) is possible, using diffraction theory [158]. With the general principle of reversibility of optical paths, the problem of calculating the detection PSF is equivalent to calculating the intensity distribution around the focus of a lens, which focuses an incident plane wave. Applying Debye diffraction theory the electrical field distribution $h(\vec{r})$ around the focus is then expressed as an integral over plane waves, which converge onto the focus (green lines in Fig. 3.2a):

$$h(\vec{r}) = -\frac{i}{\lambda} \cdot A_0 \cdot \iint_{\Omega} \exp\left(-\frac{2\pi \cdot i}{\lambda} \cdot \vec{q}(\Omega) \cdot \vec{r}\right) d\Omega. \quad (3.1.5)$$

Here \vec{r} is the position relative to the focus, A_0 is a normalization constant and \vec{q} is the unit vector along the direction of propagation of the plane wave. The integration is performed over all points Q on the spherical phase plane in the lens, expressed as the solid angle Ω .

The lens is characterized by its focal length f_{Obj} and aperture diameter d_{Obj} . From these parameters, the numerical aperture NA is calculated for a medium of refractive index n :

$$\text{NA} := n \cdot \frac{d_{\text{Obj}}}{f_{\text{Obj}}} = n \cdot \sin(\alpha) \quad \text{with} \quad \text{NA} \leq n. \quad (3.1.6)$$

Here 2α is the opening angle of the lens. The numerical aperture describes the focussing power of the lens. The spherical symmetry of the lens implies a spherical symmetry also of the resulting PSF. Introducing two general coordinates

$$u \equiv u(z) = \frac{2\pi\text{NA}^2}{n\lambda} \cdot z \quad \text{and} \quad v \equiv v(x, y) = \frac{2\pi\text{NA}}{\lambda} \cdot \sqrt{x^2 + y^2}. \quad (3.1.7)$$

the Eq. (3.1.5) becomes [158]:

$$h(u, v) = -\frac{2\pi i}{\lambda} \cdot \frac{\text{NA}^2}{n^2} \cdot A_0 \cdot \exp\left(\frac{i\text{NA}^2 u}{n^2}\right) \cdot \int_0^1 J_0(v\rho) \cdot \exp\left(-\frac{i u \rho^2}{2}\right) \cdot \rho \, d\rho. \quad (3.1.8)$$

Here $J_0(\cdot)$ is the Bessel function of the first kind, with order 0. This integral can be evaluated numerically and the PSF is finally obtained as the absolute square value of the field amplitude $h(u, v)$:

$$\text{PSF}_{\text{fl}}(\vec{r}) = |h(\vec{r})|^2. \quad (3.1.9)$$

Some example plots of a PSF calculated with Eq. (3.1.9) are shown in Fig. 3.2(b).

For the special cases of the PSF along a coordinate axis (z -axis: $x = y = v = 0$, x/y -axis: $z = u = 0$), simplified analytical forms can be given [158]:

$$\text{PSF}_{\text{fl}}(u, 0) \propto \left[\frac{\sin(u/4)}{u/4} \right]^2, \quad \text{PSF}_{\text{fl}}(0, v) \propto \left[\frac{2J_1(v)}{v} \right]^2. \quad (3.1.10)$$

From Eq. (3.1.10), the size of the focus can be calculated. It is given as $1/e^2$ -half widths $w_{\text{fl},xy}, w_{\text{fl},z}$ of the central maximum:

$$w_{\text{fl},xy} \approx 0.82 \cdot \frac{\lambda}{\text{NA}}, \quad w_{\text{fl},z} \approx 2.80 \cdot \frac{n \cdot \lambda}{\text{NA}^2}. \quad (3.1.11)$$

This definition is usually used in literature on fluorescence correlation spectroscopy and will be used throughout the rest of this thesis.

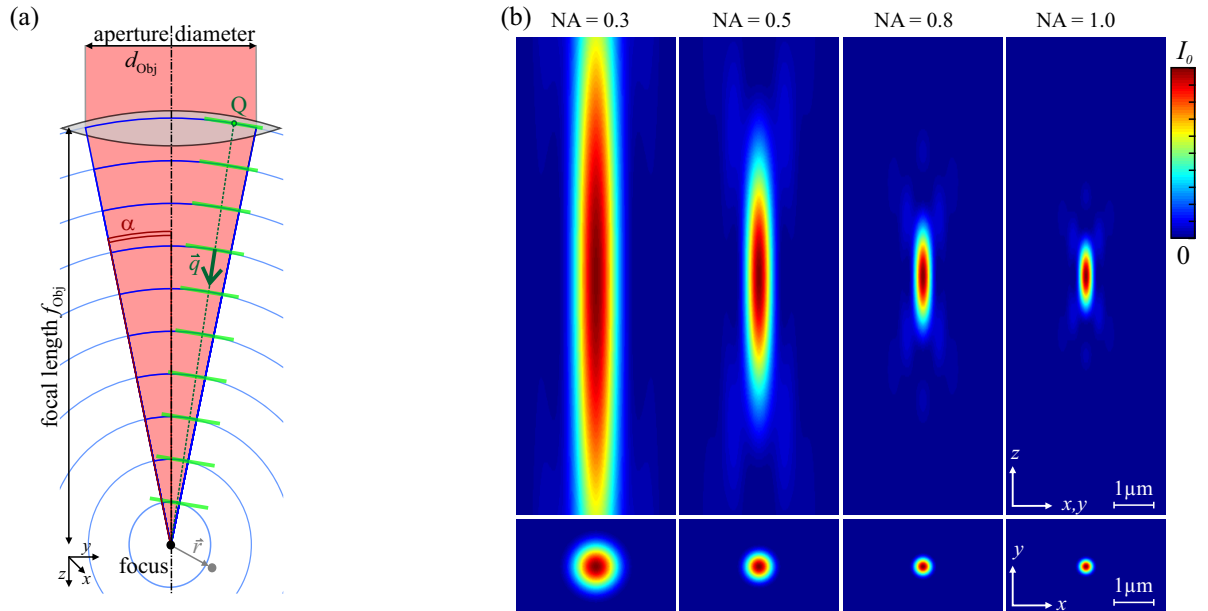


Figure 3.2. | (a) Definition of the quantities used to calculate the PSF of a focusing lens. (b) Point spread function of a fluorescence microscope for different numerical apertures NA. The images in (b) were plotted by integrating Eq. (3.1.8) numerically, using MATLAB (see appendix B.3). The other parameters were $n = 1.33$ (water) and $\lambda = 525$ nm (green light).

3.1.3. Multi-color fluorescence microscopy

Figure 3.3 illustrates two possible modifications of a fluorescence microscope, that enable it to detect two different color channels simultaneously. In the Fig. 3.3(a), a dichroic mirror (DC) splits the fluorescence light onto two image sensors, each equipped with its own tube lens (TL). In Fig. 3.3(b) a special “dual-view optics” is shown, which images the two color channels side-by-side onto the same image sensor [159]. This dual-view optics consists of two additional lenses behind the tube lens of the microscope. They form a second infinity space, in which the fluorescence light is spectrally split into two collimated beams by a dichroic mirror (DC). The beams are incident on the final lens under different angles that can be adjusted using two mirrors (AM) in the beam path. According to Eq. (3.1.1), the different incidence angles of the color channels lead to two laterally shifted images on the image sensor. To prevent the two color channels from overlapping, an adjustable aperture (AA) is introduced in the image plane of the microscope, where the camera would usually sit. It limits the image to a size that exactly fills half of the image sensor. With the two adjustable mirrors (AM), the two images can be moved independently.

The illumination also needs modification: two light sources are used to excite two different fluorophores, e.g. a laser at $\lambda_{\text{ill}} = 488 \text{ nm}$ for eGFP and a second laser at $\lambda_{\text{ill}} = 568 \text{ nm}$ for mRFP1. As these are typically combined to one excitation beam, the (single-band) dichroic mirror needs to be replaced by a multi-band dichroic mirror, intended for the reflection of both laser wavelengths.

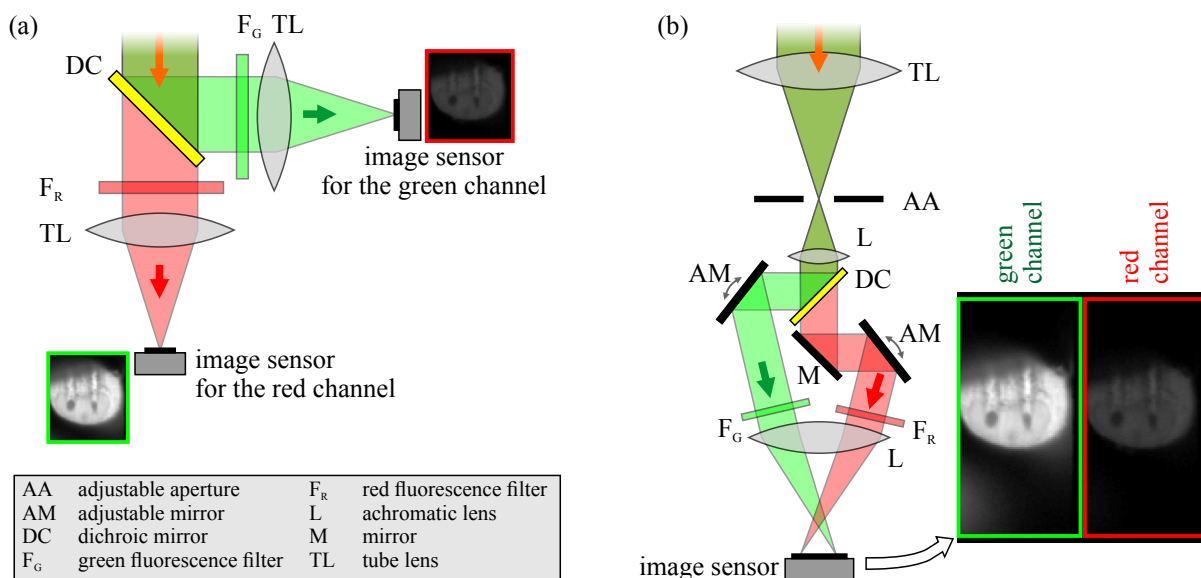


Figure 3.3. | Two versions of dual-color detection. In (a) the light is split into two image sensors and in (b) a “dual-view” optics images the two color channels onto one image sensor.

3.2. Confocal fluorescence microscopy

3.2.1. Principle

An epi-fluorescence microscope has a reasonable lateral resolution, but suffers from bad contrast. Fluorescence is also excited above and below the focal plane, because the excitation light passes through the whole sample. Some of this light is collected by the detection objective and appears as a background signal (“out-of-focus light”). This effectively reduces the contrast. The confocal microscope overcomes this problem by excluding the emitted out-of-focus light with a pinhole. It also has a slightly improved lateral resolution. The disadvantage of using a pinhole is, that most confocal microscope can only observe a single point at every time. Therefore images have to be built up sequentially by scanning the

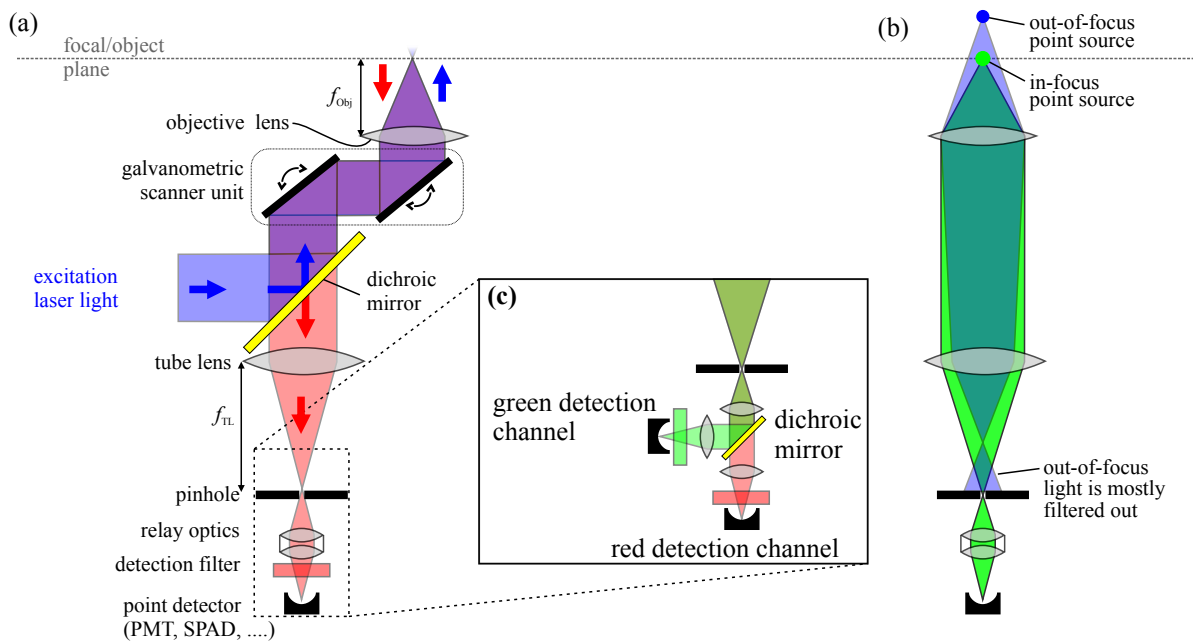


Figure 3.4. | (a) Schematic setup of a confocal microscope. (b) Out-of-focus light exclusion with a pinhole. (c) Modification for dual-color-detection. The schematic in (b) is simplified from the version in (a), by removing the illumination beam path and the galvanometric scanner.

observed point through the sample. This introduces an inherent time-structure into the images and limits the maximum frame rate during image acquisition. Figure 3.4(a) shows a schematic of a typical confocal microscope.

3.2.2. The pinhole in confocal microscopy

Out-of-focus light cannot pass the pinhole, as shown in Fig. 3.4(b). Any fluorescence light, emitted from points below or above the object plane (blue circle in Fig. 3.4b), will not be focused in the plane of the pinhole, but will be imaged onto an area, exceeding the size of the pinhole. So only a tiny fraction of this light will pass the pinhole towards the detectors. In contrast light from the image plane (green circle in Fig. 3.4b) is focused exactly onto the plane of the pinhole and thus can completely pass on to the detectors. This resulting suppression of out-of-focus light is often referred to as depth-sectioning or z -sectioning.

Figure 3.4(c) shows how a confocal microscope can be extended to detect two different fluorophores simultaneously. A dichroic mirror is added behind the pinhole, which splits the emitted fluorescence onto two light sensors. As for the multi-color fluorescence microscope, the excitation beam splitter has to be a multi-band device.

3.2.3. Focus properties and resolution

Collimated excitation light is focused by the objective lens into a small illumination focus, described by the point spread function $PSF_{ill}(\vec{r})$. Only in this tiny volume, fluorophores are excited. The red-shifted fluorescence photons are collected with the same objective. The focus is now described by a detection point spread function $PSF_{det}(\vec{r})$, which will be generally the same as $PSF_{ill}(\vec{r})$, but slightly larger due to the longer wavelength. The fluorescence emission is then separated from the excitation light using a dichroic mirror and focused onto a tiny pinhole, positioned in the image plane of the tube lens. Only light, which passes the pinhole is finally imaged onto a point-detector. Typically photo multiplier tubes

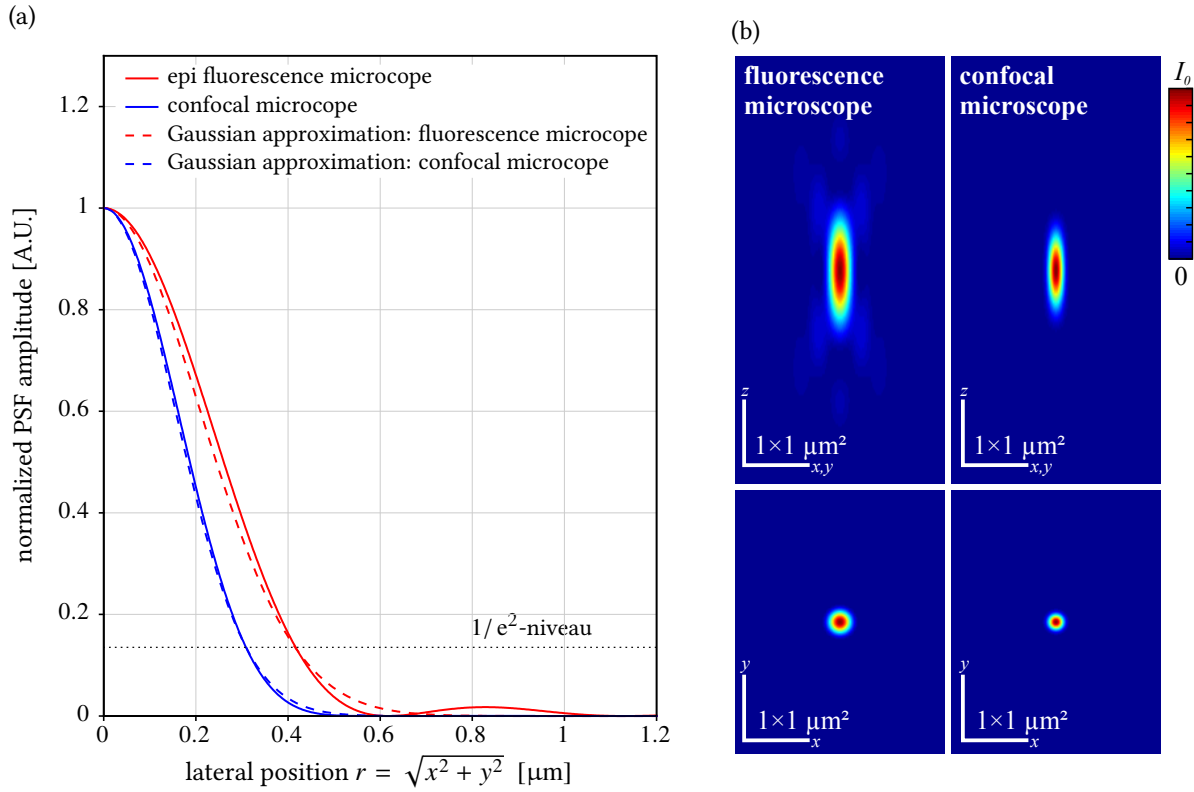


Figure 3.5. | (a) Cut through the PSF of an epi-fluorescence and a confocal microscope in the focal plane. (b) PSF of an epi-fluorescence and a confocal microscope. The improvement in resolution is clearly visible. In addition a suppression of the sidelobes can be seen. The functions are plotted for $\lambda_{\text{ill}} = 488 \text{ nm}$, $\lambda_{\text{fl}} = 525 \text{ nm}$, $\text{NA} = 1.0$, $n = 1.33$ (water). The Gaussian approximations are plotted as a Gaussian function with its $1/e^2$ -width given by Eq. (3.1.11).

or single-photon avalanche diodes (SPADs) are used to detect the fluorescence light. The sample is usually scanned with a motorized stage, or better with a galvanometric scanners in the infinity space of the microscope. The PSF of the complete system is finally given by:

$$\text{PSF}(\vec{r}) = \text{PSF}_{\text{ill}}(\vec{r}) \cdot \text{PSF}_{\text{det}}(\vec{r}). \quad (3.2.1)$$

This equation signifies that fluorescence can only be detected from a position \vec{r} , if a certain probability exists, that a fluorophore is excited at \vec{r} and that the light emitted at \vec{r} is actually imaged onto the detector. The two PSFs in Eq. (3.2.1) can be approximated by the PSF of a fluorescence microscope (see Eq. 3.1.10). If the wavelengths of illumination λ_{ill} and of fluorescence λ_{fl} are averaged into an effective wavelength

$$\lambda_{\text{eff}} = \frac{\lambda_{\text{ill}} + \lambda_{\text{fl}}}{2}, \quad (3.2.2)$$

the confocal PSF can simply be modeled as:

$$\text{PSF}_{\text{confocal}}(\vec{r}) = \text{PSF}_{\text{fl}}^2(\vec{r}). \quad (3.2.3)$$

Figure 3.5 compares the PSFs of a confocal and an epi-fluorescence microscope. Using Eq. (3.2.3), the $1/e^2$ -half width of the PSF of a confocal microscope can be estimated numerically (cf. Eq. (3.1.11) on

p. 29 for the same estimates for an epi-fluorescence microscope):

$$w_{\text{confocal,xy}} \approx 0.61 \cdot \frac{\lambda_{\text{eff}}}{\text{NA}} \approx 0.74 \cdot w_{\text{fl,xy}}, \quad w_{\text{confocal,z}} \approx 2.09 \cdot \frac{n \cdot \lambda_{\text{eff}}^2}{\text{NA}^2} \approx 0.75 \cdot w_{\text{fl,z}}. \quad (3.2.4)$$

These results are consistent with equations given e.g. in Refs. [160, 161].

The square in Eq. (3.2.3) leads to an effective suppression of sidelobes in the PSF, as shown in Fig. 3.5(a). Therefore the PSF of a confocal microscope can often be approximated by a 3-dimensional Gaussian function. The improvement in PSF size over a widefield fluorescence microscope in Eq. (3.2.4) is approximately a factor $1/\sqrt{2} \approx 0.71$, which can be derived analytically for a Gaussian approximation of the PSF: the product of two Gaussian functions with $1/e^2$ -widths w_{ill} and w_{det} , is again a Gaussian with the $1/e^2$ -width:

$$\frac{1}{w_{\text{sys}}^2} = \frac{1}{w_{\text{ill}}^2} + \frac{1}{w_{\text{det}}^2} \quad \xrightarrow{w_{\text{ill}} \approx w_{\text{det}}} \quad w_{\text{sys}} = \frac{w_{\text{ill}}}{\sqrt{2}}. \quad (3.2.5)$$

3.3. Light sheet microscopy

3.3.1. Principle

Confocal microscopy (cf. section 3.2) leads to an improvement in resolution and the z -sectioning capability, when compared to widefield fluorescence microscopes, but it is unable to perform simultaneous

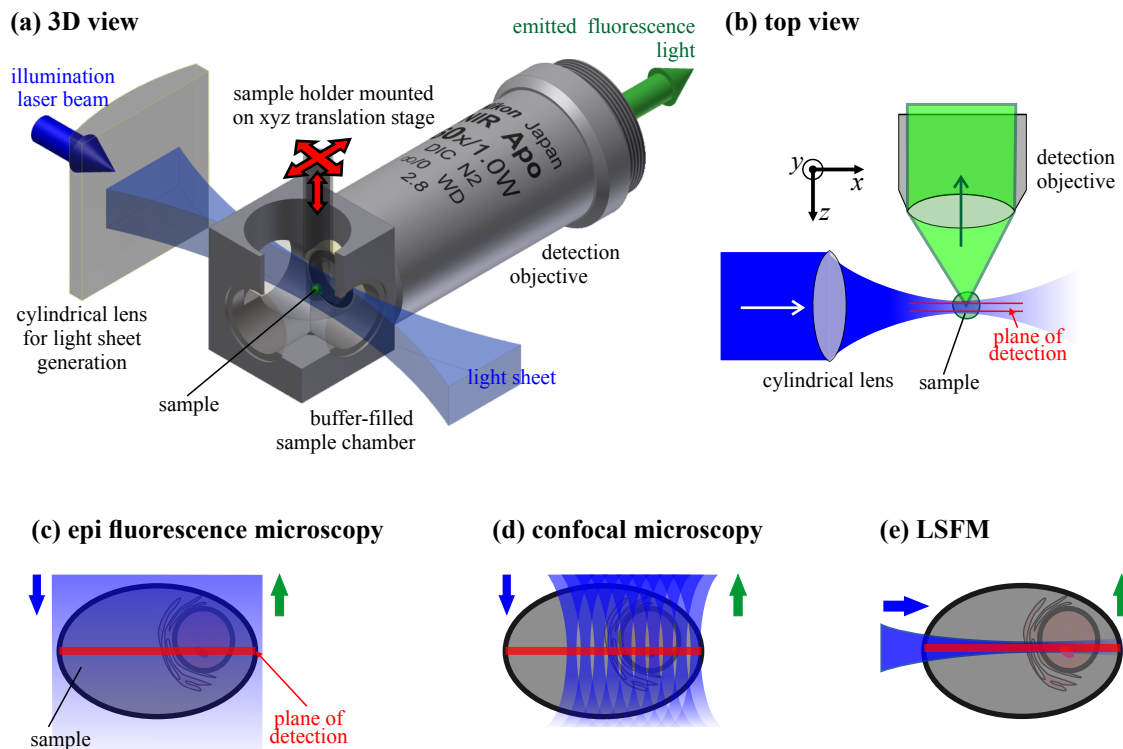


Figure 3.6. | Principle of light sheet fluorescence microscopy in a 3-dimensional view (a) and a top view (b) and comparison of the illumination schemes of epi-fluorescence microscopy (c), confocal fluorescence microscopy (d) and light sheet microscopy (e). In (c-e) the red line marks the image plane of the detection optics; green and blue arrows indicate direction of illumination and detection.

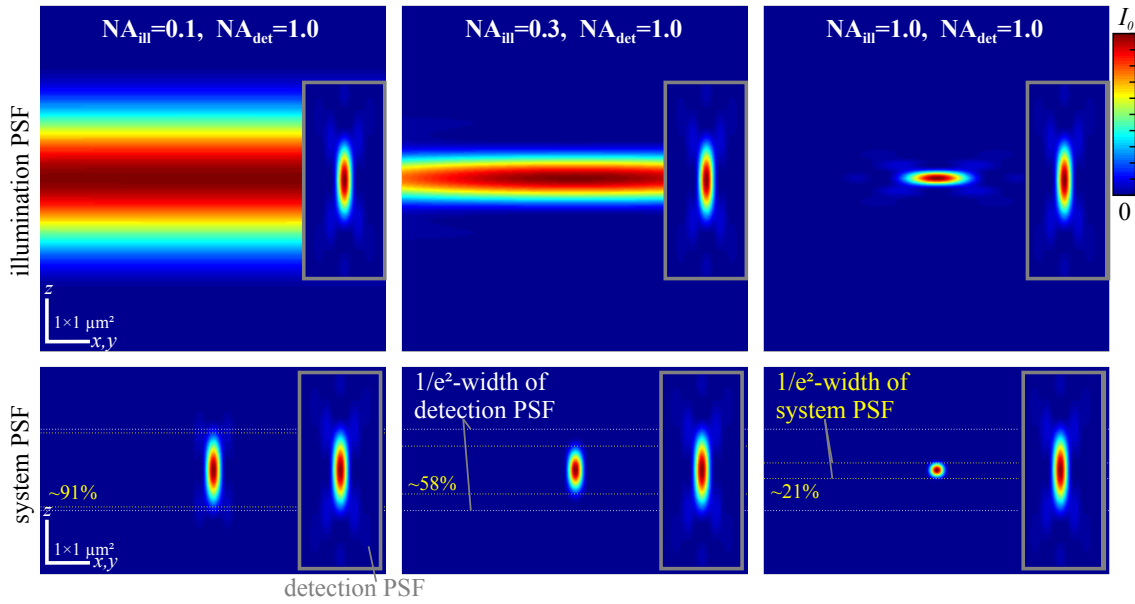


Figure 3.7. | Examples of the system PSF of a light sheet fluorescence microscope with a numerical aperture $NA_{\text{det}} = 1.0$ for detection and different numerical apertures $NA_{\text{ill}} \in \{0.1, 0.3, 1.0\}$ for illumination. For comparison the illumination PSF is shown as insets. White dotted lines indicate the $1/e^2$ -width of the detection PSF and yellow dotted lines indicate the $1/e^2$ -width of the final PSF. Yellow numbers give the relative decrease in focus size and thus the improvement in longitudinal resolution. The illumination light wavelength was $\lambda_{\text{ill}} = 488$ nm, the fluorescence wavelength was $\lambda_{\text{fl}} = 525$ nm and the immersion medium was water ($n = 1.33$).

measurements in all points of the image plane. Lightsheet fluorescence microscopy can be seen as a compromise between confocal and epi-fluorescence microscopy. It is a widefield illumination-method that allows measuring all image points simultaneously with a single image sensor. At the same time it strongly improves z -sectioning, compared to a standard epi-fluorescence microscope.

The principle of light sheet microscopy is shown in Fig. 3.6(a,b). A cylindrical lens is used to focus light only in one direction, forming a line focus, which is referred to as light sheet. The latter is then superimposed to the object plane of an infinity-corrected fluorescence microscope, which is oriented perpendicular to the light sheet. In contrast to the other microscopy techniques described so far, two separate lenses are used for illumination and detection. The thickness of the light sheet is typically chosen to match the z -extent of the detection PSF. In this way excitation of fluorescence above or below the image plane is avoided (cf. Fig. 3.6e), the z -sectioning is improved and out-of-focus light is not generated. In contrast, when using epi-fluorescence microscopes or confocal microscopes, the excitation light travels through the whole thickness of the sample, thereby generating fluorescence above and below the focal object plane. Thus light sheet microscopy strongly reduces fluorophore bleaching and photo-damage in parts of the sample that are not imaged. This permits an observation of the same sample over more than 24 h [118].

As in epi-fluorescence microscopy, dual-color detection can be implemented using a dual-view optics or two cameras. For dual-color illumination two different lasers are coupled into the same excitation beam path.

3.3.2. Focus properties and resolution

The system PSF of a LSFM can be calculated again using the results for an epi-fluorescence microscope. As for the confocal microscope, the PSF of the complete system is the product of an illumination PSF

($\text{PSF}_{\text{ill}}(\vec{r})$) and detection PSF ($\text{PSF}_{\text{det}}(\vec{r})$):

$$\text{PSF}(\vec{r}) = \text{PSF}_{\text{ill}}(\vec{r}) \cdot \text{PSF}_{\text{det}}(\vec{r}). \quad (3.3.1)$$

Both single PSFs are again modeled by Eq. (3.1.8) and Eq. (3.1.9), with $1/e^2$ -widths $w_{\text{ill,xy}}, w_{\text{ill,z}}$ for illumination and $w_{\text{det,xy}}, w_{\text{det,z}}$ for detection. Note that these widths are given in the frame of reference of each objective, but these are perpendicular to each other. Figure 3.7 shows examples of illumination and detection PSFs, as well as the resulting system PSF in a top-view, as in Fig. 3.6(b). As in Eq. (3.2.5), the widths of the final system PSF can be approximated as:

$$w_{\text{LSFM,xy}} = w_{\text{det,xy}}, \quad (3.3.2)$$

$$w_{\text{LSFM,z}} = \frac{1}{\sqrt{1/w_{\text{det,z}}^2 + 1/w_{\text{ill,xy}}^2}}. \quad (3.3.3)$$

So the lateral resolution is not improved over that of an epi-fluorescence microscope. In contrast, the longitudinal resolution $w_{\text{LSFM,z}}$ depends on the light sheet thickness $w_{\text{ill,xy}}$. If $w_{\text{ill,xy}}$ is comparable to or smaller than $w_{\text{det,z}}$, the longitudinal resolution is improved. In Fig. 3.7, the relative improvement is given as yellow numbers. If two objectives of equal numerical aperture are used for detection and illumination, the improvement in longitudinal resolution is nearly 5-fold (see right column in Fig. 3.7).

A second important figure in light sheet microscopy is the usable field-of-view (FOV). As the illuminating beam is focused perpendicular to the direction of detection, its depth of field or longitudinal extent $w_{\text{ill,z}}$ limits the range over which fluorescence is excited effectively in the image plane. For instance, if the illumination objective has the same numerical aperture as the detection objective (third case in Fig. 3.7), this leads to a small longitudinal focus size. At the same time, if the detection PSF is shifted by more than 2–3 of its diameters, the illumination intensity has already dropped below 20%, as $w_{\text{ill,z}} = 1.82 \mu\text{m}$. The first two examples are better in that respect: they do not offer as strong an improvement in z -resolution, but the FOV is larger and can accommodate a complete sample of considerable size ($w_{\text{ill,z}} = 20.2 \mu\text{m}$ for $\text{NA}_{\text{ill}} = 0.3$ and $w_{\text{ill,z}} = 182 \mu\text{m}$ for $\text{NA}_{\text{ill}} = 0.1$). In all cases, good z -sectioning is still retained, as the lateral width of the illumination profile ($w_{\text{ill,xy}} = 1.3 \mu\text{m}$ for $\text{NA}_{\text{ill}} = 0.3$ and $w_{\text{ill,xy}} = 4 \mu\text{m}$ for $\text{NA}_{\text{ill}} = 0.1$) grows slower with numerical aperture than the longitudinal width. In the first sample though, the illumination PSF is so thick, that considerable sidelobe contributions from the detection PSF are visible. So when designing a LSFM for a specific sample, a tradeoff between sidelobes, z -sectioning and FOV has to be found.

3.3.3. Typical image artifacts in light sheet microscopy

Light sheet microscopy typically suffers from a specific image artifact called stripe artifact. This consists of several dark stripes, that are visible in the images and are parallel to the direction of propagation of the illumination light. Figure 3.8(a) shows a schematic illustration and a real example.

As shown in Ref. [162], these stripes can be explained by light scattering from particles distributed throughout the sample and whose refractive indexes differ slightly from their environment. Several structures of live-cells are candidates for such particles: lipid droplets, organelles and vesicles that contain a different environment than the surrounding cytoplasm, or regions of high protein density, such as nucleoli. In larger samples, also the complete cellular nucleus can act as a scatterer.

One method to reduce stripe artifacts during imaging is to pivot the light sheet, i.e. to quickly change its direction of incidence, as illustrated in Fig. 3.8(b). This reduces the shadows behind the scattering objects to a certain degree [163].

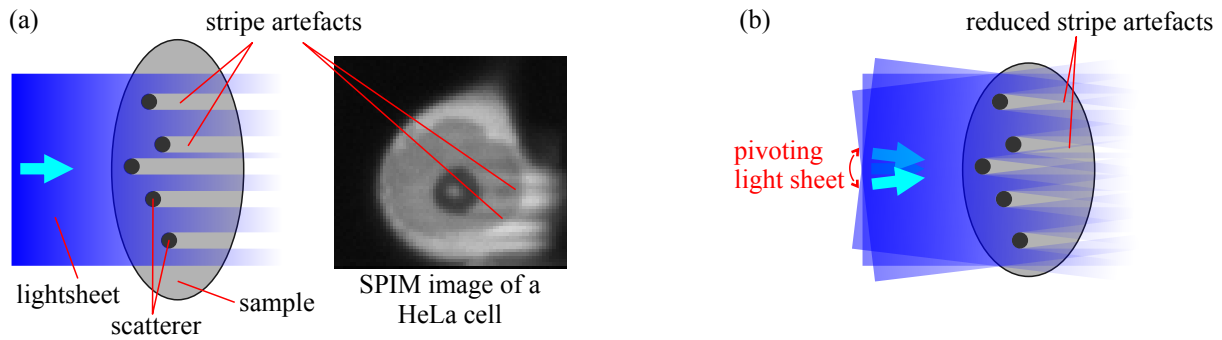


Figure 3.8. | (a) Stripe artifacts in light sheet microscopy. (b) Pivoting of the light sheet, which is used to reduce stripe artifacts. Note: A different version of this figure has been created by myself for the Wikipedia article on light sheet microscopy: https://en.wikipedia.org/wiki/File:Lsfm_stripes.svg.

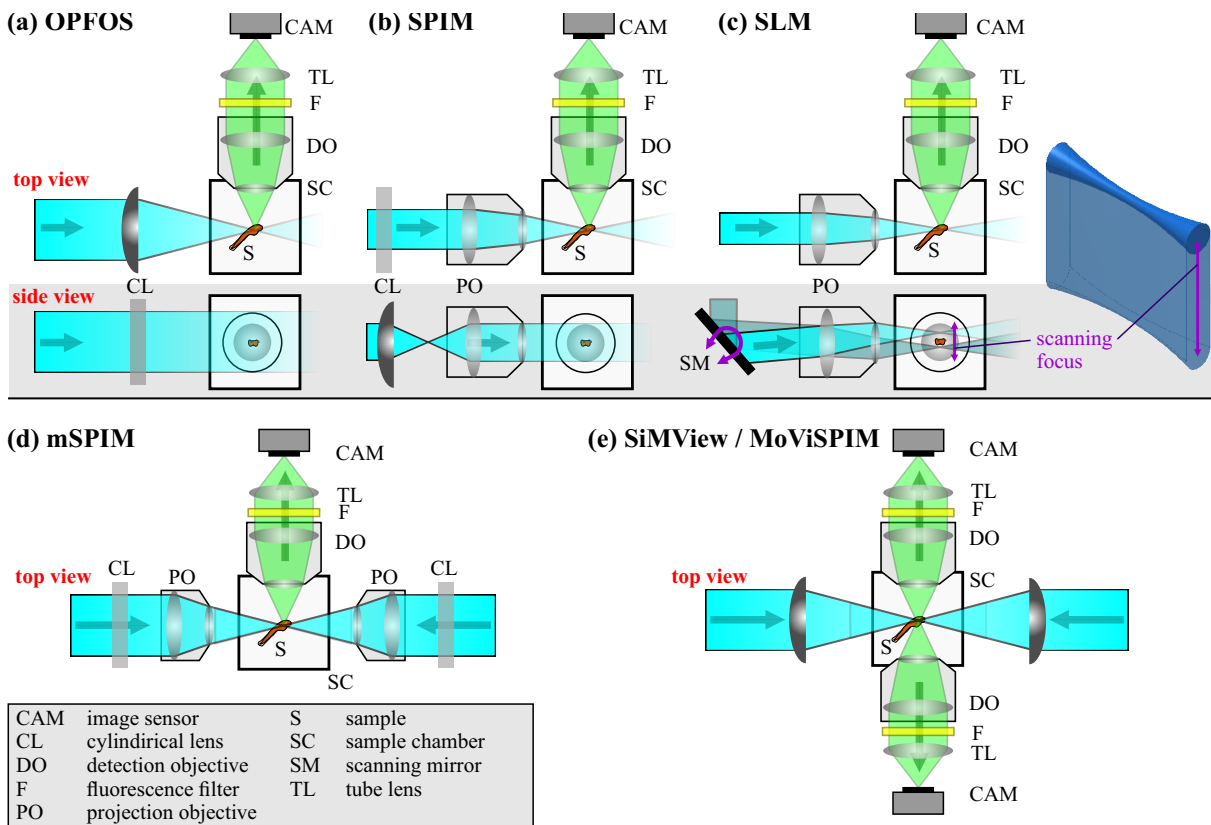


Figure 3.9. | Overview of different schemes of light sheet microscopes implemented in the last 20 years. (a) orthogonal-plane fluorescence optical sectioning (OPFOS), (b) selective plane illumination microscope (SPIM), (c) scanning light sheet microscope (SLM), (d) multi-directional selective plane illumination microscopy (mSPIM), (e) multi-view selective plane illumination microscope (SiMView/MoViSPIM)

Note: A different version of this figure has been created by myself for the Wikipedia article on light sheet microscopy: https://en.wikipedia.org/wiki/File:Lsfm_methods.svg.

3.3.4. A short history of light sheet microscopy

Light sheet microscopy has been reintroduced to biological and bio-physical research within the last 20 years. It is based on the dark field microscopy technique called “ultramicroscopy” (German: *Spalt-ultramikroskop*), developed around 1902 by Richard Adolf Zsigmondy, an austro-hungarian chemist, and Henry Siedentopf, a german physicist at the Carl Zeiss company [164]. Here the sample is also illuminated with a sheet of light. Instead of the fluorescence light, as in an LSM, the light scattered by the particles in the sample is observed perpendicularly. R.R. Zsigmondy used this ultramicroscope to study suspensions of nano-sized particles [165] and received the Nobel prize in 1925 [166]. Also Jean Perrin used this new ultramicroscope for his observations on Brownian motion [167].

In 1993 Voie et al. published a first fluorescence version of the ultramicroscope under the name orthogonal-plane fluorescence optical sectioning (OPFOS) [168]. The light sheet in an OPFOS setup is directly formed by a cylindrical lens (cf. Fig. 3.6 and Fig. 3.9a). Only a limited range of cylindrical lenses are commercially available and these are not very well corrected for optical aberrations, such as chromatic and spherical errors. There the light sheet width was limited to about 20 μm .

In 2004 Huisken et al. replaced the cylindrical lens by a combination of a cylindrical and a standard microscope objective lens (cf. Fig. 3.9b) [118]. This type of setup is referred to as selective plane illumination microscope (SPIM). The parameters of the light sheet in this type of microscope are completely determined by the objective lens PO and do not depend on the cylindrical lens CL [119]. This allows for a resolution on the order of micrometers longitudinally and few hundred nanometers laterally. This type of setup was also implemented during this thesis and a detailed description is given in section 6.1.

In a later version, the cylindrical lens was completely removed from the setup by quickly scanning a round laser beam up and down in the image plane, as shown in Fig. 3.9(c). The scanned beam appears as a light sheet if the camera integrates over several scanning cycles [52]. Instead of Gaussian laser beams, also other electro-magnetic field modes can be used for scanned light sheets. Gauss-Bessel [169, 170] and asymmetric Airy beams [171] were shown to improve the usable field-of-view of the microscope by increasing the penetration depth of the light sheet into strongly scattering samples. They can also provide thinner light sheets in some cases.

Another method to improve the penetration depth of light sheet microscopy is two-sided illumination using two light sheets as shown in Fig. 3.9(d) [163]. Later it was combined with two-sided detection, as shown in Fig. 3.9(e) [172, 173]. This allows for faster data acquisition of 3-dimensional multi-view data sets, as the sample is imaged from two sides simultaneously.

All LSM variants presented so far are based on the standard planar setup, as illustrated in Fig. 3.6 and Fig. 3.9. Here, the samples are mounted hanging from above. Other geometries have been proposed, in which the sample is mounted on a horizontal support. Figure 3.10(a) shows an inverted selective

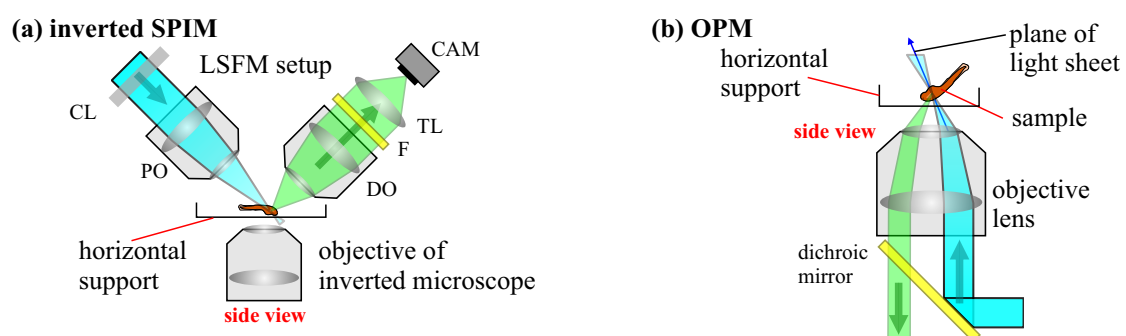


Figure 3.10. | Two LSFM variants with a horizontal support for the samples: (a) inverted selective plane illumination microscope (iSPIM) and (b) oblique plane microscopy (OPM).

plane illumination microscope (iSPIM) setup: the whole SPIM has been rotated and positioned on top of an upright microscope [120, 174, 175]. Figure 3.10(b) shows an oblique plane microscopy (OPM), where the light sheet is projected by the same objective as used for detection [176, 177]. The excitation light enters the objective at its periphery and leaves it under a very steep angle $\geq 60^\circ$, illuminating a thin slice of the sample. All these variants allow to use standard sample mounting techniques. In addition they allow to extend an existing standard microscope with light sheet microscopy capabilities.

4. Photodetectors

This chapter introduces the photo sensor used in this thesis. They are divided in two groups. Section 4.1 introduces photon counting detectors. Linear detectors, such as most commercially available digital cameras, are introduced in section 4.2. Both these parts also contain a discussion of the statistical properties of the respective detectors. Finally the properties of different image sensor types are compared in section 4.3.

4.1. Photon counting detectors

4.1.1. Single-photon avalanche diodes

In confocal microscopes single-photon avalanche diodes (SPADs) are frequently used as photo-detectors, especially when fluorescence fluctuation methods are to be employed. These devices produce a strong electrical output pulse for each detected photon. An incident photon creates an electron-hole pair (or excitation) in the semiconductor crystal with a certain probability. This pair is then multiplied by repeated impact-ionization in a strong electrical field, which is applied to the detector. Finally a whole avalanche of secondary electrons reaches the electrodes and creates a current spike for each single photon [178–180].

Figure 4.1(a) shows a sketch of a typical SPAD built from four differently doped layers of semiconductor. The photons are absorbed and create the first exciton in a large and lightly p-doped region (“i(p)” in the figure). The electron then drifts towards the amplification region, which consists of a strongly doped pn-junction. This drifting process is driven by a reverse bias voltage U_{bias} over the diode and is limited by collisions of the electrons with the semiconductor lattice. The reverse bias voltage generates a very high electric field $|\vec{E}(x)|$ over the relatively small amplification region, where impact ionization creates up to millions of secondary electrons.

While the reverse voltage gets higher, the amplification increases, until it gets virtually infinite if U_{bias} rises above the breakdown voltage U_{break} . In this case the avalanche is self-sustaining and the SPAD is

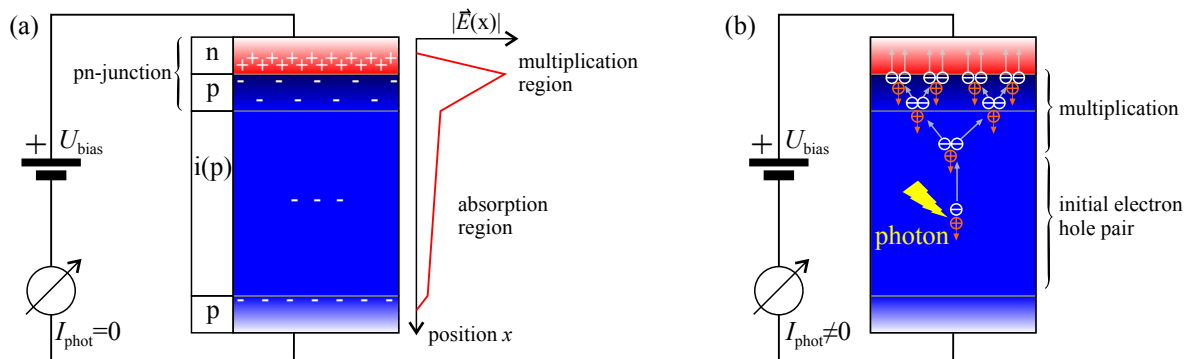


Figure 4.1. | (a) Cross-section of a typical single-photon avalanche diode, showing the charge distribution in the device. (b) Formation of an avalanche of electron-hole pairs in a single-photon avalanche diode.

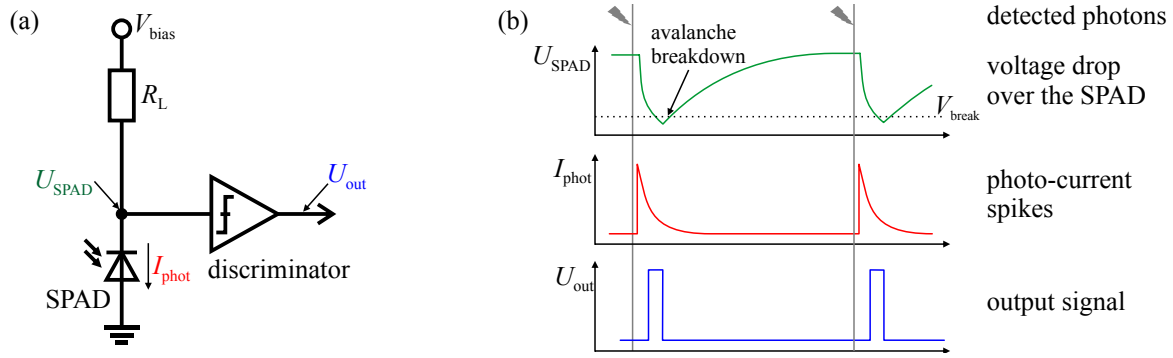


Figure 4.2. | (a) Passive quenching circuit for a single-photon avalanche diode. (b) Signals in that circuit.

said to operate in Geiger or photon counting mode. After a photon has hit the diode, the output current increases sharply within nanoseconds. This initial edge of the current defines the photon arrival time. It is measured with an electronic discriminator circuit. As stated above, the avalanche is self-sustaining in the Geiger mode, i.e. the photo current would stay high after the detection and eventually destroy the device. Thus the diode has to be “quenched” to stop the avalanche and reset the diode for the next photon. There are two major ways of quenching:[180]

1. **active quenching:** An active electronic circuit detects the increase in photocurrent and reduces the reverse voltage U_{bias} below U_{break} .
2. **passive quenching:** Figure 4.2 shows a passive quenching circuit, in which a resistor R_L is placed in series with the SPAD and the reverse bias voltage source. Each photocurrent pulse I_{phot} leads to a voltage drop over R_L , which reduces the voltage over the diode $U_{\text{bias}} - R_L \cdot I_{\text{phot}}$ below U_{break} . This quenches the avalanche. Afterwards the bias is rebuilt, by recharging the diode capacitance $C_d \approx 1 \text{ pF}$ over R_L .

In both cases the reverse bias voltage over the SPAD is reduced below the operation range for a short time after each detected avalanche. During this “dead time” (typically 100 ns), no further photons can be detected. To reduce the dead time of passively quenched SPADs, a transistor can be used to short R_L [181, 182]. This technique is called active recharge.

Impurities and other lattice defects can trap charge carriers from an avalanche with a low probability. These may be released after the avalanche has ended and cause a second avalanche for one incident photon. This behavior is called afterpulsing and has to be taken into account, when evaluating the output signals of a SPAD. In some devices this afterpulsing has been reported to follow a power-law timing [105, 183, 184].

4.1.2. Statistics of photon counting detectors

Single photon detectors, such as SPADs, generate a strong electrical output pulse for most of the incident photons, but not for all. The detection probability of photons is called quantum efficiency and is denoted by η_{det} . The output is a series of pulses at times $t_i: \{t_0, t_1, \dots\}$. These pulses can be either stored and processed directly, or counted during regularly spaced periods $[t, t + \Delta t_{\text{exp}}]$ to yield an intensity time-trace $N_{\text{photon}}(t)$ with arbitrary temporal resolution Δt_{exp} . Assuming a mean photon flux Φ , the average number of photons detected by the detector during Δt_{exp} is given by:

$$\langle N_{\text{photon}}(t) \rangle_t = \left\langle \int_t^{t+\Delta t_{\text{exp}}} \sum_i \delta(t_i - t') dt' \right\rangle_t = \eta_{\text{det}} \cdot \Phi \cdot \Delta t_{\text{exp}}. \quad (4.1.1)$$

The number of actually detected photons N_{photon} obeys Poissonian statistics. The variance of the number of detected photons then equals the mean photon number:

$$\text{Var}(N_{\text{photon}}) = \langle N_{\text{photon}} \rangle. \quad (4.1.2)$$

SPADs also have a certain dark count rate, i.e. they fire output pulses although there has not been an incident photon. These pulses are caused by avalanches that are started by thermal fluctuations and by afterpulsing. The resulting dark count rate \dot{N}_{dark} can be reduced by cooling the device. The corresponding dark count signal is characterized by a Poissonian distribution with mean $N_{\text{dark}} = \eta_{\text{det}} \cdot \dot{N}_{\text{dark}} \cdot \Delta t_{\text{exp}}$ and variance $\sigma_{\text{dark}}^2 = N_{\text{dark}}$. The complete statistical properties of the detected signal is then:

$$\langle N_{\text{photon, det}} \rangle = \eta_{\text{det}} \cdot (\langle N_{\text{photon}} \rangle + \dot{N}_{\text{dark}} \cdot \Delta t_{\text{exp}}), \quad (4.1.3)$$

$$\text{Var}(N_{\text{photon, det}}) = \text{Var}(N_{\text{photon}}) + \sigma_{\text{dark}}^2 = \eta_{\text{det}} \cdot (\langle N_{\text{photon}} \rangle + \dot{N}_{\text{dark}} \cdot \Delta t_{\text{exp}}). \quad (4.1.4)$$

4.1.3. Single-photon avalanche diode arrays

In recent years, arrays of SPADs have been developed, that allow for single-photon imaging at high frame-rates [185–193]. These sensors contain up to 65,536 SPADs on a single complementary metal oxide semiconductor (CMOS) chip. In some devices quenching and readout electronics is also integrated on the same chip.

Figure 4.3(a) shows a simple SPAD array with three circular diodes. All connections of each SPAD are accessible on the outside. Such arrays have been demonstrated with eight SPADs (diameter: $d_{\text{SPAD}} = 50 \mu\text{m}$) in a row at a pixel pitch of $a_{\text{sensor}} = 250 \mu\text{m}$ [194, 195]. Readout and quenching completely relies on external electronics.

From these early devices, imaging detectors were derived, which combine several pixels into a larger array (see Fig. 4.3b). The SPADs themselves are still circular. Typically the pixels are row-addressable

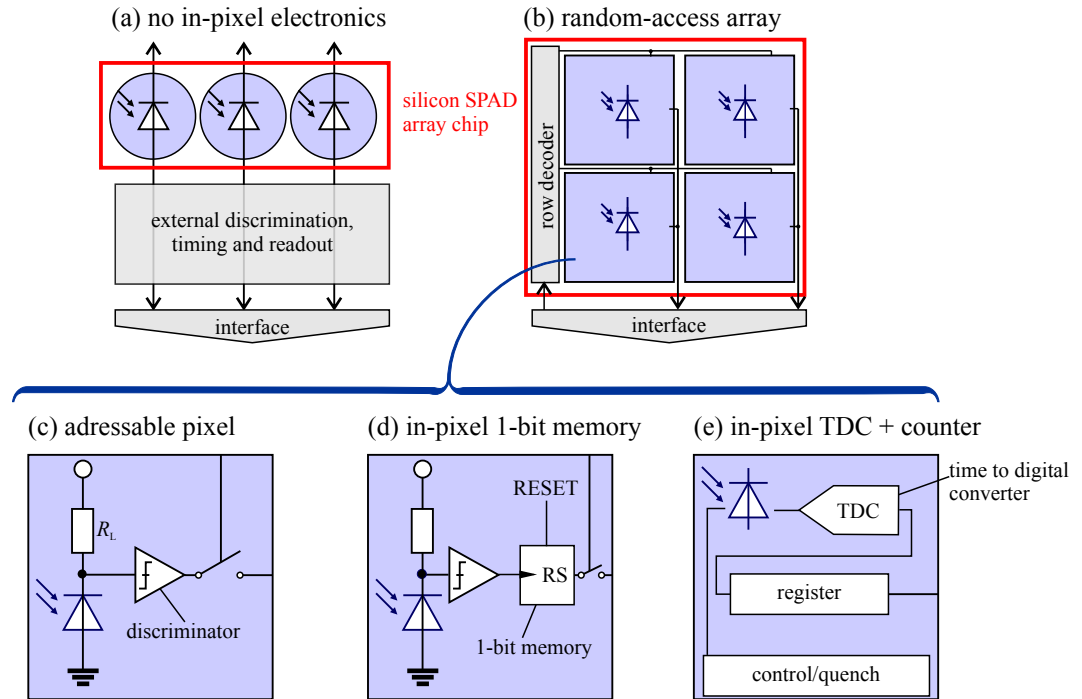


Figure 4.3. | (a,b) Different structures and (c-e) Different pixel designs of SPAD array image sensors.

and a readout line for every column is provided. It is connected to a computer interface or further external data processing electronics. The first imaging detector of this kind was published in 2005 [196]. It contained a 32×32 array of SPADs and the discriminator was integrated into the pixels ($a_{\text{sensor}} = 58 \mu\text{m}$, $d_{\text{SPAD}} = 4 \mu\text{m}$, see Fig. 4.3(c) for the pixel structure). It was used for 3D time-of-flight (TOF) imaging. For this method the arrival times of short light pulses, that are reflected by the observed scene, are measured with picosecond accuracy. These arrival times can then be converted into a depth map. This pulse timing method can also be applied for the measurement of fluorescence lifetimes τ_{fl} (see section 2.1), by illuminating a fluorophore sample with short laser pulses [188]. A histogram of the delays between the laser pulses and detected fluorescence photons yields τ_{fl} .

The SPAD arrays described so far were not designed to read many SPADs simultaneously at high temporal resolution. In these arrays a single row of pixels is selected before each measurement. To obtain a full image the selected row is moved slowly over the chip. In order to get rid of the inherent time structure caused by this method, additional electronics is required, which stores the events in each pixel between two readouts.

The simplest sensors rely on fast readout and contain only a one bit memory per pixel. The stored information is, whether there has been at least one photon since the last readout or not (see Fig. 4.3(d) and Refs. [186, 192, 193]). If two or more photons are detected by the SPAD between two consecutive readouts, they are still only counted as one. The probability for such missed photons decreases with increasing readout speed. The SPAD arrays used in this thesis are of this type.

Other high-functionality sensors incorporate a time-to-digital converter (TDC) into each column [185] or pixel [187]. This is illustrated in Fig. 4.3(e). A TDC is an electronic circuit which can measure the photon arrival time with picosecond precision, thus the sensor can be used to measure several arrival-times simultaneously. Tisa et al. reported a sensor, with a TDC and an 8-bit counter in each pixel. This device can be used either as a camera, which can count more than one photon in each exposure, or for simultaneous measurements of arrival time [190].

The in-pixel electronics limits the space that is available for the SPAD. Therefore a trade-off has to be found between the available functionality and the ratio between sensitive area and the complete pixel

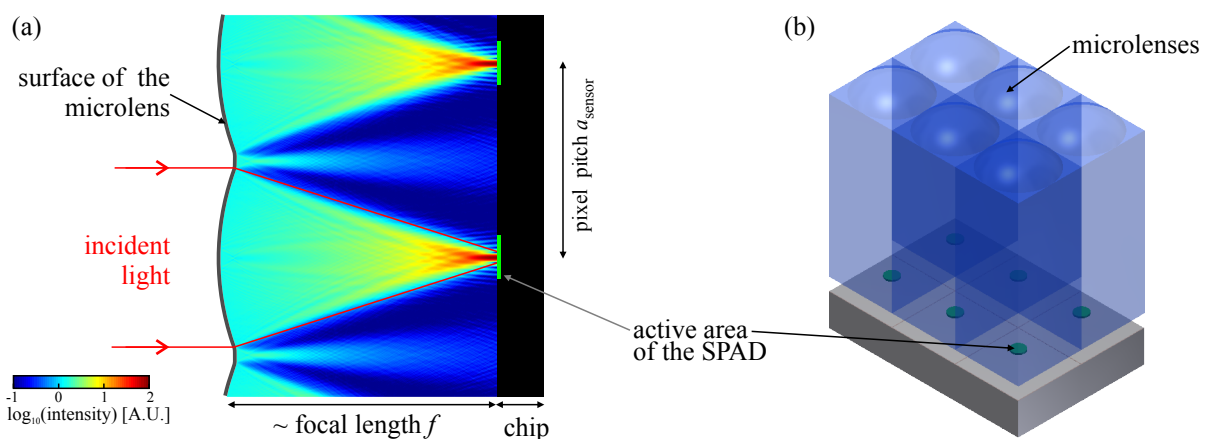


Figure 4.4. | (a) Intensity distribution in a microlens array for an image sensor with low fill factor. (b) 3-dimensional illustration of the microlens array and the sensor. The light intensity distribution in (a) is shown on a clipped logarithmic color scale. It was calculated using the beam propagation method, detailed in appendix B.4 for a spherical lens of radius $r = 80 \mu\text{m}$ and refractive index $n_1 = 1.4$.

area. This ratio is called fill-factor

$$\text{FF} := \frac{\text{active area}}{\text{pixel area}} = \frac{\pi \cdot (d_{\text{SPAD}}/2)^2}{a_{\text{sensor}}^2}. \quad (4.1.5)$$

For instance the sensor described in Ref. [190] contains a TDC and a counter in each pixel and has a round SPAD of diameter $d_{\text{SPAD}} = 20 \mu\text{m}$ at a pixel size of $a_{\text{sensor}} = 100 \mu\text{m}$. This results in a fill-factor as low as 3.1%. So most of the incident photons never have a chance to be detected by a SPAD. Sensors with such low fill factors can be combined with microlens arrays mounted directly on the chip, as shown in Fig. 4.4. These microlenses focus the light incident on each pixel onto the light-sensitive area. At a given photon flux, this increases the number of detected photons by a factor 3 – 10 [197]. Microlenses are typically produced by applying a non-solidified polymer onto the chip. Then a mold is used to shape the lenses while the polymer is cured.

4.2. Linear detectors

4.2.1. Introduction

The photon detectors described so far, generate a series of countable pulses. This section will describe “linear” detectors, which generate a measurable photocurrent I_{phot} . The latter is (ideally) proportional to the incident photon flux Φ and the detector quantum efficiency η_{det} . Such detectors are used e.g. in charge-coupled device (CCD) cameras and CMOS cameras. Also all simple photodiodes and SPADs driven below their breakdown voltage belong to this class. The measurement principle of linear detectors is typically based on separation of electron hole pairs created in the depletion region of a pn-junction in a semiconductor crystal. These photoinduced charges lead to a directly measurable photocurrent, which linearly depends on the incident photon flux:

$$I_{\text{phot}} = \eta_{\text{det}} \cdot \Phi \cdot q_e, \quad (4.2.1)$$

where q_e is the charge of an electron. A more detailed analysis is given in section 4.2.5. In typical image sensors, the photoinduced charges are accumulated in a potential well in the device, until they are read out after an exposure time Δt_{exp} . In that case the number of photoelectrons is given by:

$$N_e = \frac{I_{\text{phot}} \cdot \Delta t_{\text{exp}}}{q_e}. \quad (4.2.2)$$

Comparing this to the previous section, a SPAD can be seen as a linear sensor, which is coupled to an amplifier with near-to-infinite amplification.

4.2.2. CMOS cameras

CMOS cameras¹ combine several photodiodes in a 2-dimensional array to form an image sensor (see Fig. 4.5). Each pixel is separately addressable and readable [198]. In addition to the photodiode, each pixel also contains additional transistors, which are used to read and amplify the photoelectrons, reset the photodiode for a new exposure and perform the addressing and readout (“active pixel”). As in SPAD arrays, the additional electronics in each pixel (typically 3-5 transistors) lower the fill factor and microlenses are often used on CMOS camera chips to compensate for this. Another possible solution are back-illuminated sensors. Here the pixel electronics is stacked above the photodiode and the substrate is thinned down, so light can penetrate the photodiode from the back.

¹The name originates from the complementary metal oxide semiconductor process, these silicon chips are typically produced in. More accurately the name active pixel sensor should be used.

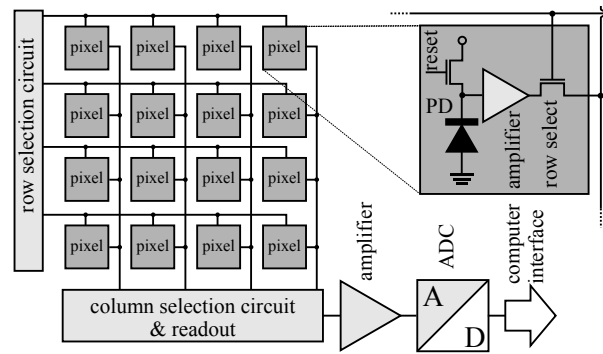


Figure 4.5. | Structure of a typical CMOS image sensor. The inset shows a simplified electronic circuit of a single pixel. Figure adapted from Ref. [198].

The readout is typically organized by first addressing a single row in the sensor and then reading its pixels one by one. The photo-induced charges, accumulated in each pixel during exposure, are amplified during readout. Then they are digitized by an analog-to-digital converter (ADC) and the digital value is transferred to a computer for further processing. After reading all pixels in a row, they are reset and a new exposure begins. This typical operation mode of a CMOS sensor is called “rolling shutter”. It can lead to image artifacts, if fast moving objects cross several rows during a single full-frame read-out cycle. In modern image sensors an additional transistor is added to each pixel, which transfers the photoelectrons from the photodiode to a storage gate for subsequent reading [199]. This global shutter removes the rolling shutter artifacts. However the readout of the full frame needs a certain amount of time Δt_{read} during which the sensor has to be inactive to prevent different integration times for different rows. This limits the number of detectable photons, especially in high-speed applications at low light levels. Here the rolling shutter mode is advantageous.

In recent years, a new generation of CMOS image sensors have been developed, which are called scientific complementary metal oxide semiconductor camera (sCMOS). These combine large sensors (4-5.5 million pixels), high-speed and low-noise readout. A modern pixel structure allows for a global shutter mode in some devices and the use of microlenses leads to a high fill factor [199, 200]. They are optimized for low-light scientific applications such as fluorescence microscopy.

4.2.3. CCD cameras

A second type of analog linear sensors are charge-coupled device (CCD) cameras. In contrast to CMOS cameras, these do not contain active pixels, but are a 2-dimensional array of metal-insulator-semiconductor (MIS) photo gates (see Fig. 4.6a). If a voltage is applied to the metal contacts, a potential well is formed in the silicon chip, which can be used to accumulate photo-induced electrons. After the exposure, varying voltage pattern is applied to the MIS gates, that shifts the charges off the chip (see Fig. 4.6b). A detailed description of these sensors is e.g. given in Refs. [201, 202].

Simple CCD sensors are organized as shown in Fig. 4.6(c). Here the charges are shifted vertically into the readout register. The content of the readout register is then shifted horizontally out of the chip, where it is amplified and digitized with an ADC. Finally the digitized photoelectron counts are transferred to a computer for further processing. This scheme has the disadvantage, that the image will smear during transport, as additional photoelectrons are created during the shifting process. This problem is overcome by interline or frame-transfer sensors (see Fig. 4.6d,e), which store the charges in additional light-shielded areas. In an interline sensor, the photo charges are first shifted from the photodiodes into vertical, shielded shift registers. Their content is subsequently shifted into the main readout register. In a frame-transfer sensors, a second shielded CCD array is positioned next to the

sensitive area. At the beginning of the readout process, the full image is quickly shifted into this storage area. This minimizes the smear. Then the content of the storage area is read out and digitized, while the sensitive area accumulates the next frame. Both methods reduce the smear artifacts and allow the sensor to integrate the next frame during the readout phase, minimizing the non-active period between frame integrations.

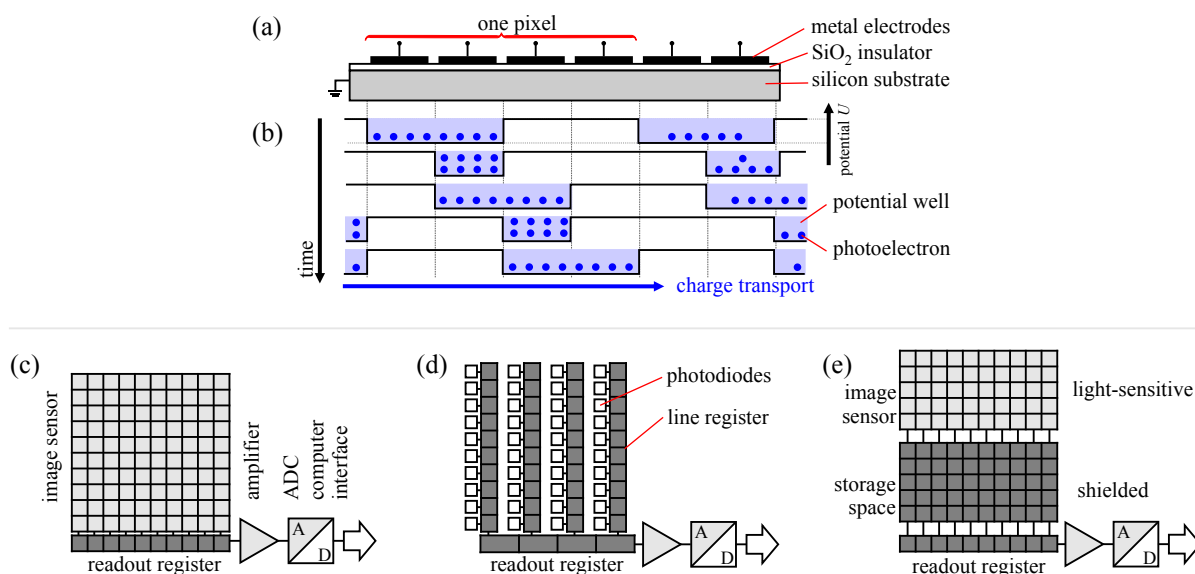


Figure 4.6. | (a,b) Operation of a CCD structure as a shift register for charges. (c) CCD sensor with a single readout register. (d) Interline transfer sensor. (e) Frame-transfer CCD sensor. Figure adapted from Refs. [198, 201, 202].

4.2.4. EMCCD cameras

The sensitivity of CCD image sensors can be enhanced by an on-chip gain mechanism. A second shift register is inserted between the readout register and the external amplifier, as shown in Fig. 4.7(a). This register works like a standard CCD register, but uses higher voltages during part of the shift process (see Fig. 4.7b). This creates potential wells, which are deep enough to cause a multiplication of the photo electrons by impact ionization. Therefore it is called electron-multiplication (EM) register and the whole sensor is called electron-multiplying charge-coupled device (EMCCD). Due to the exponential nature of the repeated impact ionization process, very high amplification factors can be achieved and even single photon counting experiments are possible with EMCCD sensors [203].

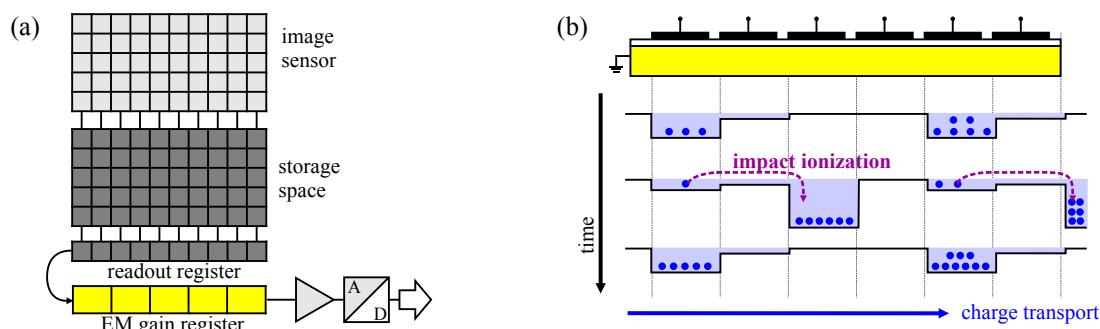


Figure 4.7. | (a) Structure of a frame-transfer EMCCD image sensor. (b) Electron multiplication process in an EM gain register. Figure adapted from Ref. [202, 204].

4.2.5. Statistics of linear image sensors

This section will discuss the statistics of linear image sensors. As explained in section 4.2.1, the photocurrent $I_{\text{phot}}(t)$ generated in a pixel is typically accumulated over a period Δt_{exp} and then read out. The readout process includes a gain mechanism and a quantification of the photo-induced charges by an ADC. All three steps need to be modeled, in order to understand the statistics of such image sensors.

Photons hit the sensor and are detected with a probability η_{det} . Each detected photon is described by its arrival time t_l and generates exactly one photoelectron. In sensors with an amplifier, this charge is amplified by a factor G_l . For EMCCD cameras or SPADs, which are driven below their breakdown voltage, the gain is itself a random variable with average $\langle G_l \rangle = \bar{G}$ and variance σ_G^2 . Then the time series of photoelectrons, that leave the sensor, can be written as:

$$N_{e,\text{det}}(t) = \sum_l G_l \cdot \delta(t - t_l). \quad (4.2.3)$$

The accumulation process during the exposure time Δt_{exp} can be written as

$$N_e(t) = \int_t^{t+\Delta t_{\text{exp}}} N_{e,\text{det}}(t') dt' = \int_t^{t+\Delta t_{\text{exp}}} \left[\sum_l G_l \cdot \delta(t' - t_l) \right] dt'. \quad (4.2.4)$$

With this definitions, the average number of detected photoelectrons in each pixel can be calculated as

$$\langle N_e \rangle = \bar{G} \cdot \eta_{\text{det}} \cdot \Phi \cdot \Delta t_{\text{exp}}, \quad (4.2.5)$$

where Φ is the incident photon flux on a single pixel. Due to the statistical independence of the gain and photodetection processes, the variance of the random variable Eq. (4.2.4) is finally given by

$$\text{Var}(N_e) = \langle N_e^2 \rangle - \langle N_e \rangle^2 = \eta_{\text{det}} \cdot \Phi \cdot \Delta t_{\text{exp}} \cdot \langle G^2 \rangle = \eta_{\text{det}} \cdot \Phi \cdot \Delta t_{\text{exp}} \cdot \mathcal{F}^2 \cdot \langle G \rangle^2. \quad (4.2.6)$$

In the last step the excess noise factor \mathcal{F}^2 was introduced, which is defined as [178]:

$$\mathcal{F}^2 := \frac{\langle G^2 \rangle}{\langle G \rangle^2} = 1 + \frac{\sigma_G^2}{\bar{G}^2}. \quad (4.2.7)$$

This factor quantifies the increase in signal noise by a stochastic gain process over a non-stochastic amplification. For sensors with a non-stochastic amplification (e.g. an operational amplifier in front of the ADC only), the excess noise factor is $\mathcal{F}^2 = 1$, as $\sigma_G^2 = 0$. For EMCCD cameras it is typically $\mathcal{F}^2 = 2$ [205].

A linear analog-to-digital converter (ADC) is used to quantify the photoelectrons. Its output signal $I_{\text{ADC}}(t)$ is quantized into $2^{\mathcal{R}_{\text{ADC}}}$ different values, where $\mathcal{R}_{\text{ADC}} = 1, 2, \dots$ is the resolution of the ADC in bits. The output units of an ADC are commonly called analog-to-digital converter units (ADUs). The digitization is modeled by a conversion factor \mathcal{A}_{ADC} , which is given in units of ADUs per photo electron:

$$I_{\text{ADC}}(t) = \left\lfloor \mathcal{A}_{\text{ADC}} \cdot N_e(t) + \frac{1}{2} \right\rfloor \quad \text{with} \quad \mathcal{A}_{\text{ADC}} = \frac{1}{N_{\text{max}}/2^{\mathcal{R}_{\text{ADC}}}}. \quad (4.2.8)$$

Here $\lfloor \cdot \rfloor$ denotes rounding to the next lower integer number and N_{max} is the number of electrons represented by the highest ADC value $I_{\text{ADC}} = 2^{\mathcal{R}_{\text{ADC}}} - 1$.

Also without incident light, all linear image sensors show a small background signal. It is most often created by a combination of thermally induced charges and offset signals in the readout process. This

background signal is quantified by its mean $\langle N_{\text{back}} \rangle$ and variance σ_{back}^2 . Then Eqs. (4.2.5, 4.2.6) are rewritten as [206, 207]:

$$\langle N_e \rangle = \langle N_{\text{back}} \rangle + \bar{G} \cdot \eta_{\text{det}} \cdot \Phi \cdot \Delta t_{\text{exp}} \quad (4.2.9)$$

$$\text{Var}(N_e) = \sigma_{\text{back}}^2 + \underbrace{\eta_{\text{det}} \cdot \Phi \cdot \Delta t_{\text{exp}} \cdot \mathcal{F}^2 \cdot \langle G \rangle^2}_{=: \sigma_{\text{photon}}^2}. \quad (4.2.10)$$

The additive background noise term σ_{back}^2 in Eq. (4.2.10) can be separated into several contributions:

1. **dark current:** Thermally created electron hole pairs are indistinguishable from photo-induced electrons, so they are subject to the same amplification processes. Their contribution to the image and noise is:

$$\langle N_{\text{dark}} \rangle = \bar{G} \cdot \dot{N}_{\text{dark}} \cdot \Delta t_{\text{exp}}, \quad \sigma_{\text{dark}}^2 = \bar{G}^2 \cdot \dot{N}_{\text{dark}} \cdot \Delta t_{\text{exp}}. \quad (4.2.11)$$

Here \dot{N}_{dark} is the rate of dark current electrons, which typically decays exponentially with decreasing temperature (Boltzman distribution) until a low bias value is reached [198]. Therefore this noise contribution can be effectively reduced by cooling the image sensor.

2. **clock-induced charges:** In CCD and EMCCD cameras, the shifting process may induce additional electrons, which are treated like an additional dark current. These can be minimized by careful design of the readout scheme. The average number of clock-induced electrons is N_{cic} per readout cycle. Due to the Poissonian nature of the process, its variance is

$$\sigma_{\text{cic}}^2 = \bar{G}^2 \cdot N_{\text{cic}}. \quad (4.2.12)$$

3. **readout noise:** The readout noise does not depend on the signal level and summarizes the noise imposed by the readout electronics (external amplifier etc.). It is characterized by a vanishing mean and a standard deviation of σ_{read} electrons per readout cycle. This contribution is typically the limiting factor in most image sensors. Only in EMCCD cameras it is of minor importance, as the on-chip amplification is done before the external electronics and pushes the signal level above the readout noise level. The readout noise can be reduced by lowering the readout speed of the sensors, the use of low-noise electronic circuits, or by adding additional averaging filters. All these options effectively limit the readout speed of the camera.
4. **quantization noise:** The digitization noise σ_{ADC} is caused by the limited resolution of the ADC, which images several input values on the same output value (cf. Eq. (4.2.8)). The maximal error is typically one least significant bit or $1/\mathcal{A}_{\text{ADC}}$ electrons. It can be shown that the standard deviation of this contribution is given (in units of electrons) by [208, 209]

$$\sigma_{\text{ADC}} = \frac{1}{\mathcal{A}_{\text{ADC}} \cdot \sqrt{12}}. \quad (4.2.13)$$

Typically the resolution of the ADC is high enough, so that this error is negligible.

All noise contributions can finally be summarized in the signal-to-noise ratio (SNR), which relates the background corrected signal intensity to the noise standard deviation:

$$\text{SNR} := \frac{\langle \mathcal{A}_{\text{ADC}} \cdot N_e \rangle}{\sqrt{\text{Var}(\mathcal{A}_{\text{ADC}} \cdot N_e)}} = \frac{\mathcal{A}_{\text{ADC}} \cdot \eta_{\text{det}} \cdot \Phi \cdot \bar{G}}{\mathcal{A}_{\text{ADC}} \cdot \sqrt{\sigma_{\text{photon}}^2 + \sigma_{\text{dark}}^2 + \sigma_{\text{cic}}^2 + \sigma_{\text{read}}^2 + \sigma_{\text{ADC}}^2}}, \quad (4.2.14)$$

Using the different results obtained above, this yields:

$$\text{SNR} = \frac{\mathcal{A}_{\text{ADC}} \cdot \eta_{\text{det}} \cdot \Phi \cdot \Delta t_{\text{exp}} \cdot \bar{G}}{\sqrt{\mathcal{A}_{\text{ADC}}^2 \cdot \bar{G}^2 \cdot \mathcal{F}^2 \cdot (N_{\text{cic}} + N_{\text{dark}} \cdot \Delta t_{\text{exp}} + \eta_{\text{det}} \cdot \Phi \cdot \Delta t_{\text{exp}}) + 1/12 + \mathcal{A}_{\text{ADC}}^2 \cdot \sigma_{\text{read}}^2}} \quad (4.2.15)$$

If the image sensor contains an on-chip amplifier (e.g. an EM-gain register) and a readout amplifier in front of the ADC, the average gain \bar{G} will be the product of both amplification factors. As the off-chip amplifier typically uses a non-stochastic amplification scheme (e.g. an electronic operational amplifier), the excess noise factor \mathcal{F}^2 will only be influenced by the on-chip amplification. The off-chip amplifier noise is contained in the readout noise.

In addition to the noise of each single pixel, it is important to be aware of the nonuniformity of most image sensors, which is often called fixed pattern noise. In CMOS sensors, each photodiode and the transistors in every pixel may have slightly different performance. This leads to a pixel-to-pixel variation of the detected signal, even at uniform illumination. In CCD and EMCCD cameras, variations in the performance of the shift registers and MIS photosensors lead to a comparable effect [206].

4.3. Comparison of image sensors

An important factor in image sensors for low light applications, such as fluorescence microscopy, is the quantum efficiency η_{det} . Figure 4.8 shows η_{det} of different image sensor types as a function of the wavelength λ of the incident light. The figure includes front- and back-illuminated CCD and CMOS sensors, as well as a SPAD array. Back-illuminated sensors generally reach values above 90%, but are available only for a few technologies, due to their high production costs. Fluorescent dyes in the green to red spectral range ($\lambda = 500 \dots 700$ nm) were used for this thesis. All image sensors have their maximum η_{det} close to the green spectral range and still a significant η_{det} for red light.

Another important parameter of image sensors is the signal-to-noise ratio that can be reached with a given number of incident photons. Figure 4.9 compares the theoretical SNR for different camera types. For comparison an ideal image sensor is shown as a black dashed line. It is limited only by the

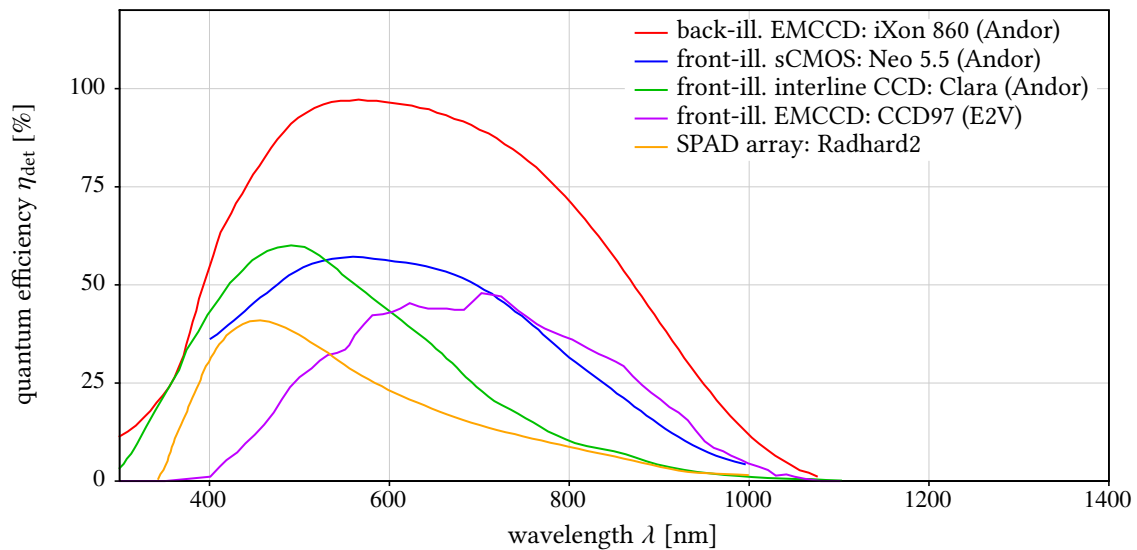


Figure 4.8. | Quantum efficiency η_{det} of different image sensors, as a function of the light wavelength λ . Data was taken from Refs. [189, 200, 210, 211].

photon-noise. At high light levels, the performance of all sensor types approaches that of an ideal image sensor. Only EMCCD cameras (blue line) show a lower SNR in this regime, due to the excess noise, caused by their stochastic amplification process. At low light levels, only EMCCD, sCMOS cameras (green line) and SPAD arrays (magenta line) are viable choices. The use of standard CCD sensors (red line) is precluded by their high readout noise. At very low light levels, close to one incident photon per exposure, SPAD arrays perform best and EMCCD cameras are a good choice due to their on-chip gain process. sCMOS cameras are a good choice at slightly higher light levels, as their SNR is not limited by a stochastic gain process.

In summary SPAD arrays would be the ideal image sensor for low-light applications, such as fluorescence microscopy. Their disadvantage is the complex readout and the fact, that SPAD arrays are not yet available commercially. Also their detection efficiency for red light is limited. The next best sensors for low light applications are EMCCD and sCMOS cameras. Normal CCD or CMOS cameras show good performance only at high light levels or low frame rates. Their advantage is the relatively low price, compared to sCMOS, EMCCD and SPAD array cameras.

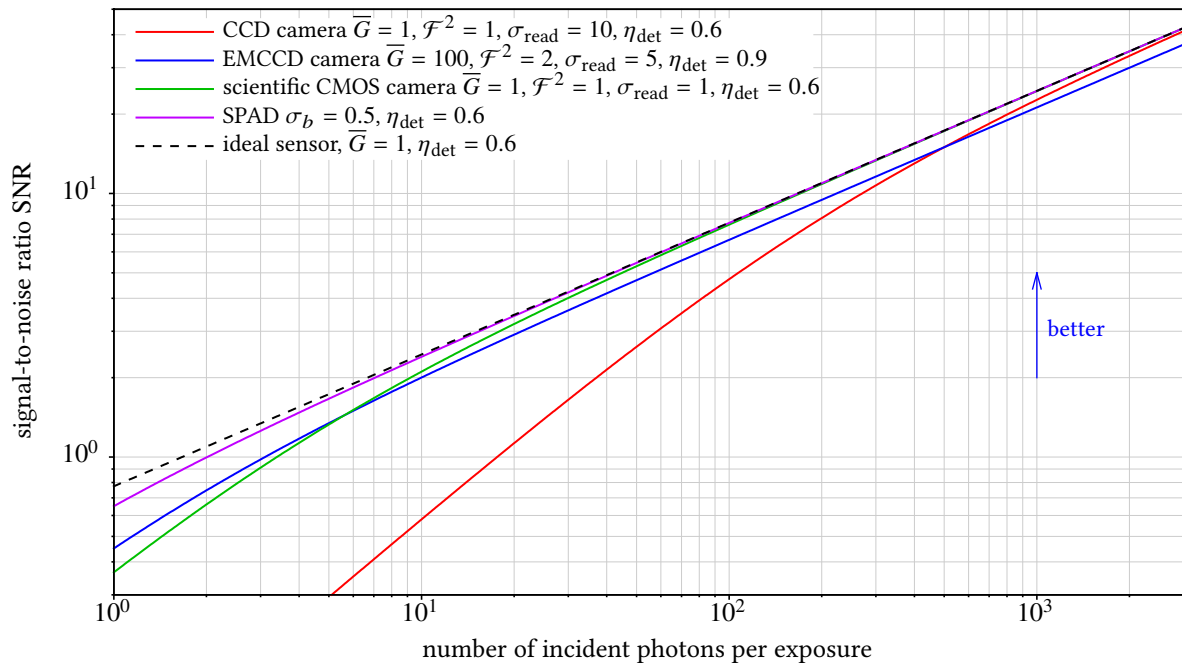


Figure 4.9. | Theoretical signal-to-noise ratios of different image sensors. The parameters for different sensors were taken from [200]. Eq. (4.2.15) was used for the plots.

5. Measuring diffusion: fluorescence fluctuation techniques

This chapter will present the theory of fluorescence correlation spectroscopy (FCS) and fluorescence cross-correlation spectroscopy (FCCS) for confocal and light sheet microscopes. Its form is based on the presentation in Refs. [93, 96] and it was also used in our article Ref. [132]. For the autocorrelation analysis, this form is a bit more complex than usually seen in FCS publications, but it yields the same results. Its advantage will be evident in section 5.4: the FCCS auto- and cross-correlation functions can be written in a compact and unified form.

5.1. Introduction to fluorescence correlation spectroscopy

5.1.1. Single point measurements

As already mentioned in section 1.4, the method of choice to determine protein mobility in living cells in this thesis work was fluorescence correlation spectroscopy (FCS). It was introduced in 1974 by Magde, Elson, and Webb in Refs. [68, 69, 78]. As shown in Fig. 5.1, fluorescence is excited and detected in a tiny subvolume (a few μm^3) of the sample containing only few particles $N(t)$ at any time. The measured fluorescence intensity $F(t)$ is proportional to this particle number. Due to the diffusive motion of the particles, $N(t)$ is permanently fluctuating around its mean value $\langle N \rangle$. This is represented as:

$$N(t) = \langle N \rangle + \delta N(t) \quad \Rightarrow \quad F(t) = \langle F \rangle + \delta F(t) \quad \text{with} \quad \langle \delta N(t) \rangle = \langle \delta F(t) \rangle = 0. \quad (5.1.1)$$

Here $\delta N(t)$ and $\delta F(t)$ represent the fluctuations of the particle number and the fluorescence intensity. Depending on the speed of motion (diffusion coefficient), the particle number fluctuates “faster” or “slower”. This can be quantified using an autocorrelation analysis. The normalized FCS autocorrelation

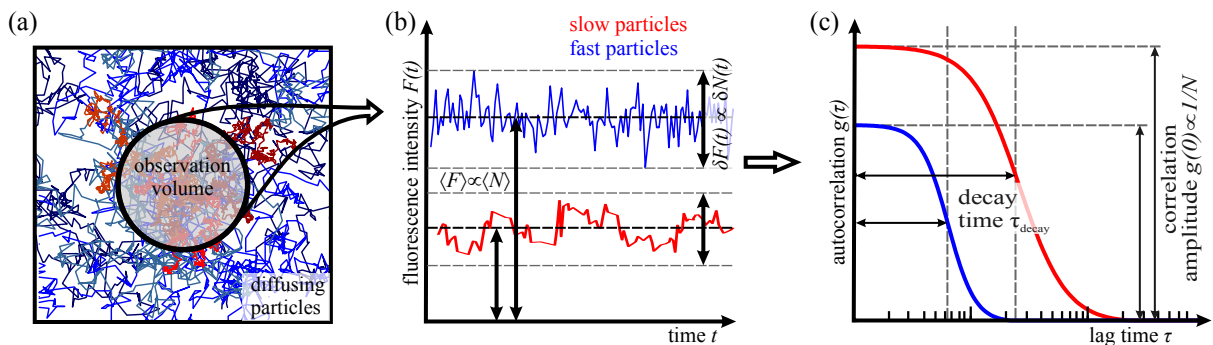


Figure 5.1. | **Illustration of the principle of FCS.** (a) Sample with particles moving with different diffusion coefficients (fast: blue, slow: red). The circle indicates the observation volume. (b) Fluorescence intensity, as measured from the sample in (a), showing the fluorescence fluctuations $\delta F(t)$ around the mean intensity $\langle F \rangle$. (c) Autocorrelation functions $g(\tau)$, calculated from the intensity traces in (b). The decay times τ_{decay} are defined by $g(\tau_{\text{decay}}) = g(0)/2$.

function is defined as

$$g(\tau) = \frac{\langle \delta F(t) \cdot \delta F(t + \tau) \rangle}{\langle F \rangle^2} = \frac{\langle F(t) \cdot F(t + \tau) \rangle}{\langle F \rangle^2} - 1, \quad \tau > 0. \quad (5.1.2)$$

where the averaging operation $\langle \cdot \rangle$ is defined as a time average:

$$\langle F(t) \rangle = \lim_{T \rightarrow \infty} \frac{1}{T} \cdot \int_0^T F(t) dt. \quad (5.1.3)$$

The autocorrelation function $g(\tau)$ measures the similarity of the signal $F(t)$ to its time-shifted version $F(t + \tau)$. If the fluctuations are completely random white noise, the correlation function is $g(\tau) \propto \delta(\tau)$, which is 0 for all time lags $\tau > 0$. If $F(t)$ contains a non-random component, the correlation will be non-zero over a lag-time range, which is characteristic for the non-random process. In FCS the non-random fluctuations are caused by Brownian motion of fluorescent particles, which implies a typical dwell time of the particles in the observation volume of (cf. Eq. (1.3.2) (p. 7)):

$$\tau_D \propto \frac{(\sqrt[3]{V_{\text{obs}}})^2}{D}. \quad (5.1.4)$$

During this time, the presence of a single particle causes a self-similarity in the fluctuations, which manifests itself as a decay of the autocorrelation function from a zero-lag amplitude $g(0) > 0$ to $g(\infty) = 0$. The half-life time τ_{decay} of this decay is approximately given by τ_D from Eq. (5.1.4).

The zero-lag amplitude $g(0)$ of the autocorrelation function Eq. (5.1.2) yields the average particle number in the observation volume, as

$$g(0) = \frac{\langle \delta F^2(t) \rangle}{\langle F \rangle^2} \propto \frac{\langle \delta N^2(t) \rangle}{\langle N \rangle^2} = \frac{1}{\langle N \rangle}. \quad (5.1.5)$$

In the last step, the Poissonian nature of the randomly fluctuating particle number $N(t)$ was used, which dictates that $\langle \delta^2 N(t) \rangle \equiv \text{Var}(N(t)) = \langle N \rangle$.

5.1.2. Fluorescence correlation spectroscopy on a confocal microscope

Today FCS is typically implemented using confocal microscopes (see section 3.2) with a very small observation volume ($V_{\text{obs}} \approx 0.2 - 0.6 \mu\text{m}^3$), and fluorescence is detected by single-photon avalanche diodes (SPADs) (cf. section 4.1). The acquired fluorescence intensity time-trace $F(t)$ is correlated using either specialized digital electronics or a software correlator. In a final step, analytical model functions are used to determine the average particle number $\langle N \rangle$, the diffusion coefficient D (via the decay time τ_{decay}) and other properties of the molecular motion, such as flow speeds, anomalous diffusion exponent, kinetic reaction rates.

5.1.3. Imaging fluorescence correlation spectroscopy

Confocal FCS measurements are limited to a single detection focus due to the nature of the used confocal microscope. For this thesis, FCS was implemented on a selective plane illumination microscope (SPIM) with fast image sensors, such as SPAD arrays and fast EMCCD cameras. This combination allows to perform imaging fluorescence correlation spectroscopy (imaging FCS) measurements also of fast diffusing molecules. These measurements result in maps of mobility parameters and yield extensive statistics for each single sample. The new combination of SPIM and FCS, termed single plane illumination fluorescence correlation spectroscopy (SPIM-FCS), has been introduced by Wohland et al. in 2010 [117]

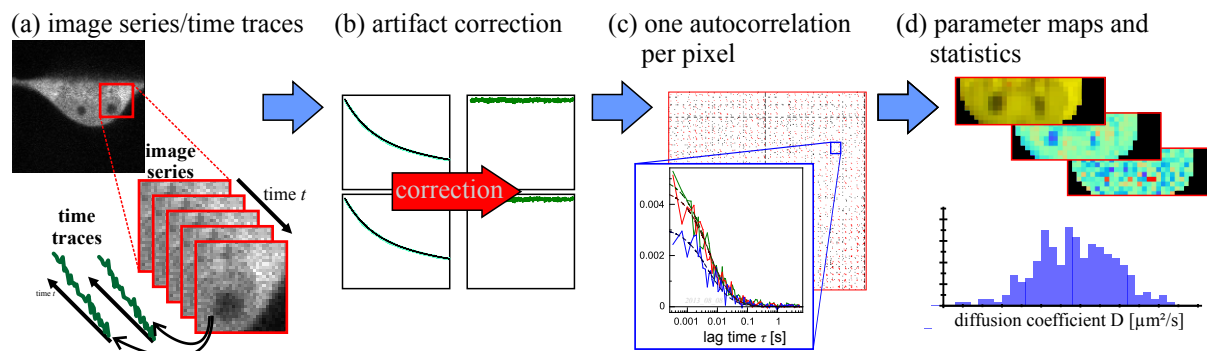


Figure 5.2. | Illustration of the principle of imaging FCS.

and first applications to single cells were reported in [120, 121]. Besides SPIMs, also TIRF microscopes have been successfully used for imaging FCS [108]. This combination was called imaging total internal reflection fluorescence correlation spectroscopy (ITIR-FCS).

The principle of imaging FCS is illustrated in Fig. 5.2. At first, an image series is acquired with high temporal resolution. The frame repetition time Δt_{frame} should be at least one order of magnitude smaller than the FCS decay time of the observed particles. To give an example, $\tau_{\text{decay}} \approx 0.1 - 1$ ms for small and $\tau_{\text{decay}} \approx 10$ ms for large proteins in living cells (see section 8.2). To achieve such high readout rates of the image sensor, a region of interest (ROI) is typically chosen from the full frame. With EMCCD and CMOS cameras, frame repetition times in the range of $\Delta t_{\text{frame}} = 0.3 - 1$ ms can be achieved. SPAD arrays are much faster and reach frame repetition times in the microsecond range.

An image stack of $\approx 50,000$ frames is recorded and processed according to Fig. 5.2(b-d). Initially, artifacts such as an offset due to a background intensity or the effect of fluorophore photobleaching are corrected for. Then a statistical estimator of the analytical autocorrelation function in Eq. (5.1.2) is calculated. Finally a non-linear least squares fit is used to extract the parameters of interest (e.g. decay times, diffusion coefficients or particle number) from the measured autocorrelation of every pixel. These parameters can be displayed as parameter maps, showing their spatial variation across the sample. Such maps can also be used to calculate parameter statistics over the whole sample or regions of interest (ROIs).

Outline of the chapter

The rest of this chapter will introduce the theoretical framework of FCS as well as of two-color and pixel-pixel FCCS, which allows not only for the measurement of particle mobility, but also for molecular interactions and spatial correlations. At first, section 5.2 explains how the fluorescence excitation, emission and measurement in a microscope are modelled. In section 5.3 the full theory of FCS is developed. It is applied to the case of a confocal and of a SPIM microscope. In section 5.4 the theory is expanded to 2-focus and 2-color FCCS. The final section 5.5 treats typical artifacts in FCS and FCCS, such as photophysics, background fluorescence and fluorophore bleaching.

5.2. Modeling fluorescence in a microscope

The theoretical framework of FCS starts from a simplified model of the fluorescence microscope, which is used to acquire the data. Figure 5.3 illustrates this model. It will be explained in detail throughout this section.

The sample of volume V_{sample} contains $N_{\text{sample},\chi}$ particles of species χ that move randomly. The motion of each particle $i = 1 \dots N_{\text{sample}}(\chi)$ is described by its trajectory $\vec{r}_i(t)$. The trajectories are typically not known exactly, but their statistics, such as the mean squared displacement (MSD), is known. Finally, the local particle concentration distribution of species χ can be written as

$$c_{\chi}(\vec{r}, t) = \frac{1}{V_{\text{sample}}} \cdot \sum_{i=1}^{N_{\text{sample},\chi}} \delta[\vec{r} - \vec{r}_i(t)]. \quad (5.2.1)$$

The particles are illuminated by some kind of illumination optics (e.g. a confocal microscope or a SPIM) with an intensity distribution $I_{\gamma}(\vec{r})$. The index $\gamma \in \{g, r, \dots\}$ denotes the color channel of the microscope, e.g. $\gamma = g$ for excitation at 488 nm and detection in the range of [500...550] nm to observe eGFP, or $\gamma = r$ for excitation at 568 nm and detection at [600...700] nm for mRFP1. An absorption cross-section $\sigma_{\text{abs},\gamma,\chi}$ and a fluorescence quantum yield $q_{\text{fluor},\gamma,\chi}$ is assigned to each species. Then the amount of fluorescence emitted by a single fluorophore of species χ at position \vec{r} into channel γ can be written as

$$I_{\gamma}(\vec{r}) \cdot \sigma_{\text{abs},\gamma,\chi} \cdot q_{\text{fluor},\gamma,\chi}.$$

The detection optics is described by a detection efficiency distribution $\Omega_{\gamma}(\vec{r})$ and a detection efficiency $\eta_{\text{det},\gamma}$. The latter summarizes any signal loss due to optical surfaces or filters in the detection beam path. The distributions $I_{\gamma}(\vec{r})$ and $\Omega_{\gamma}(\vec{r})$ are not observable independently, so they are usually combined into a single function, called molecular detection efficiency function (MDE):

$$\text{MDE}_{\gamma}(\vec{r}) := I_{\gamma}(\vec{r}) \cdot \Omega_{\gamma}(\vec{r}). \quad (5.2.2)$$

This function is proportional to the rate of fluorescence photons expected from a fluorophore at position \vec{r} . Its actual form for a given microscopy setup can be calculated from the PSFs of the microscope (see

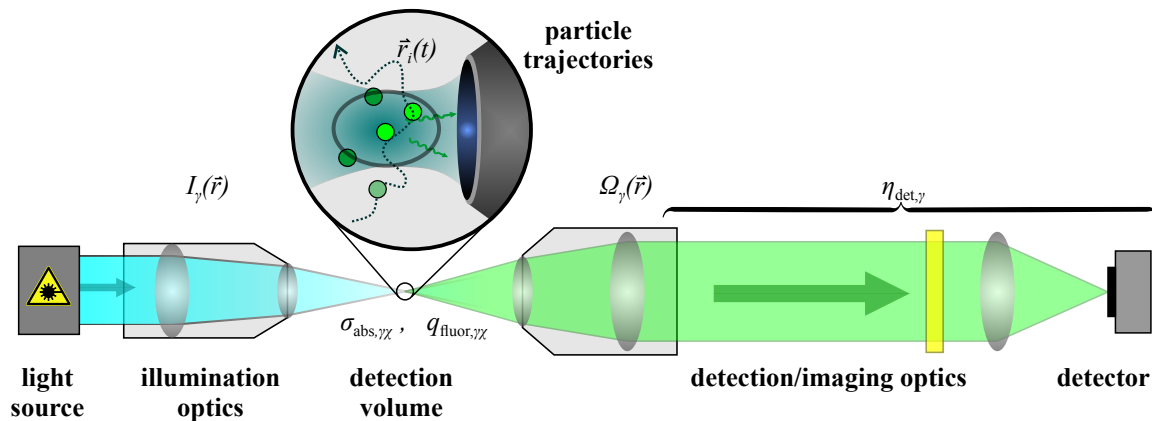


Figure 5.3. | Schematic of the optics model used for the derivation of FCS theory. The illumination optics focuses light into an intensity distribution $I_{\gamma}(\vec{r})$. The detection optics is characterized by its detection probability distribution $\Omega_{\gamma}(\vec{r})$ and the detection efficiency $\eta_{\text{det},\gamma}$. The sample is modeled as a set of particles with trajectories $\vec{r}_i(t)$. To each species an absorption cross-section $\sigma_{\text{abs},\gamma,\chi}$ and a fluorescence quantum efficiency $q_{\text{fluor},\gamma,\chi}$ is assigned.

chapter 3). The geometry of the detectors (e.g. square pixels of a camera) also may need to be taken into account. For confocal setups a 3-dimensional, rotationally symmetric Gaussian function with width w_γ and height z_γ is a good approximation, as shown in section 3.2.3:

$$\text{MDE}_{\text{confocal},\gamma}(\vec{r}) = I_0 \cdot \exp\left(-2 \cdot \frac{x^2 + y^2}{w_\gamma^2} - 2 \cdot \frac{z^2}{z_\gamma^2}\right). \quad (5.2.3)$$

In Refs. [117, 130] and section 3.2.3 it is argued, that a properly designed and aligned SPIM has a PSF with negligible sidelobe contributions. So the PSF can also be approximated by a Gaussian function. Still the finite size of the quadratic camera pixel has to be taken into account for the final form of the MDE:

$$\text{MDE}_{\text{SPIM},\gamma}(\vec{r}) = I_0 \cdot (h_{\text{pixel}} \otimes \text{PSF}_{\text{SPIM},\gamma})(\vec{r}) = \iint_{-a/2}^{a/2} \text{PSF}_{\text{SPIM},\gamma}(\vec{r} - \vec{r}') \, dx' \, dy', \quad (5.2.4)$$

where a is the width of the pixel in the object plane, \otimes denotes convolution and $h_{\text{pixel}}(\vec{r})$ is the characteristic function, describing a camera pixel:

$$h_{\text{pixel}}(\vec{r}) = \delta(z) \cdot \begin{cases} 1 & -\frac{a}{2} \leq x \leq \frac{a}{2} \quad \wedge \quad -\frac{a}{2} \leq y \leq \frac{a}{2} \\ 0 & \text{else} \end{cases}. \quad (5.2.5)$$

The convolution integral in Eq. (5.2.4) can be solved analytically:

$$\text{MDE}_{\text{SPIM},\gamma}(\vec{r}) = I_0 \cdot \frac{\left[\text{erf}\left(\frac{a-2x}{\sqrt{2} \cdot w_\gamma}\right) + \text{erf}\left(\frac{a+2x}{\sqrt{2} \cdot w_\gamma}\right)\right] \cdot \left[\text{erf}\left(\frac{a-2y}{\sqrt{2} \cdot w_\gamma}\right) + \text{erf}\left(\frac{a+2y}{\sqrt{2} \cdot w_\gamma}\right)\right]}{\left[2 \cdot \text{erf}\left(\frac{a}{\sqrt{2} \cdot w_\gamma}\right)\right]^2} \cdot \exp\left(-2 \cdot \frac{z^2}{z_\gamma^2}\right) \quad (5.2.6)$$

As shown in Fig. 5.4, this MDE deviates significantly from a Gaussian function, if a is significantly larger than the size w_γ of the PSF.

Finally, the results of this section can be combined into the fluorescence time trace expected from a fluorophore concentration $c_\chi(\vec{r}, t)$ (see Eq. 5.2.1):

$$F_\gamma(t) = \iiint_{-\infty}^{\infty} \text{MDE}_\gamma(\vec{r}) \cdot \sum_{\chi \in \mathbb{S}} \eta_{\text{det},\gamma} \cdot \sigma_{\text{abs},\gamma,\chi} \cdot q_{\text{fluor},\gamma,\chi} \cdot c_\chi(\vec{r}, t) \, dV. \quad (5.2.7)$$

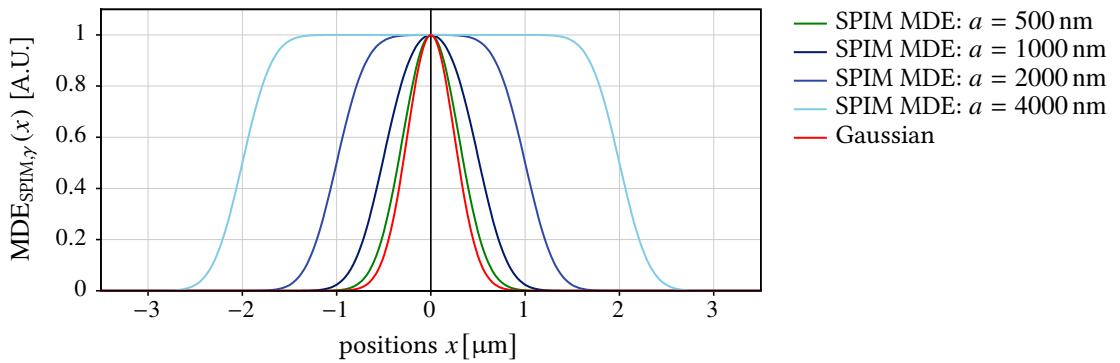


Figure 5.4. | Plots of cuts through the MDE of a SPIM in Eq. (5.2.6) along one coordinate axis. For all plots, the PSF width was $w_\gamma = 500$ nm.

The factors $\eta_{\text{det},\gamma}$, $\sigma_{\text{abs},\gamma,\chi}$ and $q_{\text{fluor},\gamma,\chi}$ are not distinguishable in a FCS experiment, so they are summarized into a single detection efficiency $\eta_{\gamma,\chi}$ of a fluorophore of species $\chi \in \mathbb{S}$ in channel γ :

$$\eta_{\gamma,\chi} \equiv \eta_{\text{det},\gamma} \cdot \sigma_{\text{abs},\gamma,\chi} \cdot q_{\text{fluor},\gamma,\chi} \quad (5.2.8)$$

Then Eq. (5.2.7) can be simplified to

$$F_\gamma(t) = \iiint_{-\infty}^{\infty} \text{MDE}_\gamma(\vec{r}) \cdot \sum_{\chi \in \mathbb{S}} \eta_{\gamma,\chi} \cdot c_\chi(\vec{r},t) \, dV. \quad (5.2.9)$$

As shown in Eq. (5.1.2), the autocorrelation function is written in terms of signal fluctuations $\delta F_\gamma(t)$ around a mean intensity $\langle F_\gamma \rangle$. These can be expressed in a form analogous to Eq. (5.2.9), if the concentration dynamics $c_\chi(\vec{r},t)$ is also split into a fluctuation part and an average concentration:

$$c_\chi(\vec{r},t) = \langle c_\chi \rangle + \delta c_\chi(\vec{r},t). \quad (5.2.10)$$

Due to the linearity of Eq. (5.2.9), this finally yields:

$$\delta F_\gamma(t) = \iiint_{-\infty}^{\infty} \text{MDE}_\gamma(\vec{r}) \cdot \sum_{\chi \in \mathbb{S}} \eta_{\gamma,\chi} \cdot \delta c_\chi(\vec{r},t) \, dV. \quad (5.2.11)$$

5.3. Theory of fluorescence correlation spectroscopy

5.3.1. The FCS autocorrelation function

For a color channel γ , the FCS autocorrelation function is defined as

$$g_\gamma(\tau) = \frac{\langle \delta F_\gamma(t) \cdot \delta F_\gamma(t + \tau) \rangle}{\langle F_\gamma \rangle^2}. \quad (5.1.2)$$

Using the results in Eqs. (5.2.9, 5.2.11) this can be rewritten as:

$$g_\gamma(\tau) = \frac{\sum_{\chi \in \mathbb{S}} \eta_{\gamma,\chi}^2 \iiint_{-\infty}^{\infty} \iiint_{-\infty}^{\infty} \text{MDE}_\gamma(\vec{r}) \cdot \text{MDE}_\gamma(\vec{r}') \cdot \langle \delta c_\chi(\vec{r},t) \cdot \delta c_\chi(\vec{r}',t + \tau) \rangle \, dV \, dV'}{\left(\sum_{\chi \in \mathbb{S}} \eta_{\gamma,\chi} \cdot \iiint_{-\infty}^{\infty} \text{MDE}_\gamma(\vec{r}) \cdot \langle c_\chi(\vec{r},t) \rangle \, dV \right)^2}. \quad (5.3.1)$$

Here, the linearity of the integration and averaging $\langle \cdot \rangle$ was used. Furthermore, it was assumed that the concentration fluctuations from two different molecular species χ and χ' are statistically independent, i.e. $\langle \delta c_\chi(\vec{r},t) \cdot \delta c_{\chi'}(\vec{r},t) \rangle = 0$.

5.3.2. Zero-lag correlation and particle numbers

The Poissonian nature of the particle number (or concentration) in the focus dictates for $\tau = 0$:

$$\langle \delta c_\chi(\vec{r},t) \cdot \delta c_\chi(\vec{r}',t) \rangle \equiv \langle \delta c_\chi^2(\vec{r},t) \rangle \cdot \delta(\vec{r} - \vec{r}') = \langle c(\vec{r},t) \rangle \cdot \delta(\vec{r} - \vec{r}'), \quad (5.3.2)$$

where the factor $\delta(\vec{r} - \vec{r}')$ signifies, that single particles are non-interacting and therefore, also statistically independent. Therefore they are only correlated to themselves and not to other particles nearby. Using

Eq. (5.3.2) and further assuming that the concentration does not change significantly over the observation volume (described by the MDE), i.e. $\langle c_\chi(\vec{r}) \rangle \equiv \langle c_\chi \rangle$, the zero-lag autocorrelation amplitude becomes:

$$\begin{aligned}
 g_\gamma(0) &= \frac{\sum_{\chi \in \mathbb{S}} \eta_{\gamma,\chi}^2 \cdot \langle c_\chi \rangle \cdot \iiint_{-\infty}^{\infty} \text{MDE}_\gamma^2(\vec{r}) \, dV}{\left(\sum_{\chi \in \mathbb{S}} \eta_{\gamma,\chi} \cdot \langle c_\chi \rangle \cdot \iiint_{-\infty}^{\infty} \text{MDE}_\gamma(\vec{r}) \, dV \right)^2} = \\
 &= \frac{\sum_{\chi \in \mathbb{S}} \eta_{\gamma,\chi}^2 \cdot \langle c_\chi \rangle \cdot \iiint_{-\infty}^{\infty} \text{MDE}_\gamma^2(\vec{r}) \, dV}{\left(\sum_{\chi \in \mathbb{S}} \eta_{\gamma,\chi} \cdot \langle c_\chi \rangle \right)^2 \cdot \left(\iiint_{-\infty}^{\infty} \text{MDE}_\gamma(\vec{r}) \, dV \right)^2} \stackrel{\mathbb{S}=\{\chi\}}{=} \frac{1}{\langle c_\chi \rangle} \cdot \frac{\iiint_{-\infty}^{\infty} \text{MDE}_\gamma^2(\vec{r}) \, dV}{\left(\iiint_{-\infty}^{\infty} \text{MDE}_\gamma(\vec{r}) \, dV \right)^2}. \quad (5.3.3)
 \end{aligned}$$

In the last step, a single species χ was assumed. Introducing the effective volume

$$V_{\text{eff},\gamma} := \frac{\left(\iiint_{-\infty}^{\infty} \text{MDE}_\gamma(\vec{r}) \, dV \right)^2}{\iiint_{-\infty}^{\infty} \text{MDE}_\gamma^2(\vec{r}) \, dV} \quad (5.3.4)$$

of the MDE, the zero-lag amplitude of the autocorrelation function can be written in terms of a particle number $\langle N_\chi \rangle = \langle c_\chi \rangle \cdot V_{\text{eff},\gamma}$ within this volume:

$$g_\gamma(0) = \frac{\sum_{\chi \in \mathbb{S}} \eta_{\gamma,\chi}^2 \cdot \langle c_\chi \rangle \cdot V_{\text{eff},\gamma}}{\left(\sum_{\chi \in \mathbb{S}} \eta_{\gamma,\chi} \cdot \langle c_\chi \rangle \cdot V_{\text{eff},\gamma} \right)^2} = \frac{\sum_{\chi \in \mathbb{S}} \eta_{\gamma,\chi}^2 \cdot \langle N_\chi \rangle}{\left(\sum_{\chi \in \mathbb{S}} \eta_{\gamma,\chi} \cdot \langle N_\chi \rangle \right)^2} \stackrel{\mathbb{S}=\{\chi\}}{=} \frac{1}{\langle N_\chi \rangle}. \quad (5.3.5)$$

For confocal and light sheet microscopes, the MDEs were defined in section 5.2. The integrals in the effective volume in Eq. (5.3.4) can be calculated analytically for these specific MDEs:

$$\text{confocal:} \quad V_{\text{eff},\gamma} = \pi^{3/2} \cdot w_\gamma^2 \cdot z_\gamma, \quad (5.3.6)$$

$$\text{SPIM:} \quad V_{\text{eff},\gamma} = \frac{\sqrt{\pi} \cdot a^2 \cdot z_\gamma}{\left[\text{erf}\left(\frac{a}{w_\gamma}\right) + \frac{w_\gamma}{\sqrt{\pi} \cdot a} \left(e^{-a^2/w_\gamma^2} - 1 \right) \right]^2}. \quad (5.3.7)$$

5.3.3. The concentration correlation factor

In the autocorrelation function Eq. (5.3.1) the particle dynamics is fully described by the concentration correlation factor

$$\langle \delta c_\chi(\vec{r}, t) \cdot \delta c_\chi(\vec{r}', t + \tau) \rangle =: \phi_\chi(\vec{r}, \vec{r}', \tau) \equiv \phi_\chi(\vec{r} - \vec{r}', \tau). \quad (5.3.8)$$

It quantifies the amount of correlation at a time-lag τ between the concentration fluctuations at two positions \vec{r} and \vec{r}' . The last equivalence in Eq. (5.3.8) states that $\phi_\chi(\cdot, \cdot)$ only depends on the difference in positions, i.e. the whole system is shift-invariant in space. If the system of interest is furthermore isotropic, the self correlation function only depends on the length $\|\vec{r} - \vec{r}'\|$, i.e. $\phi_\chi(\vec{r}, \vec{r}', \tau) \equiv \phi_\chi(\|\vec{r} - \vec{r}'\|, \tau)$. Note that generally these assumptions are not necessarily true, but on the small scales of FCS measurements they usually are assumed to apply.

The concentration correlation factor is (up to prefactors) equivalent to the van-Hove self correlation function of the particles [25, 212, 213], which is given in terms of single-particle trajectories $i = 1, 2, \dots, N$ as [213]:

$$P_\chi(\vec{r}, \vec{r}', \tau) = \frac{1}{N} \cdot \left\langle \sum_{i=1}^N \delta(\vec{r}' - \vec{r} + \vec{r}_i(0) - \vec{r} - (\vec{r}_i(\tau) - \vec{r})) \right\rangle. \quad (5.3.9)$$

Here, $P_\chi(\cdot, \cdot, \cdot)$ can be interpreted as the probability to find a particle at position \vec{r}' at time τ , if it was initially at position \vec{r} . Specific forms of $P_\chi(\cdot, \cdot)$ can be calculated as the Green's function or propagator of the partial differential equation (PDE), which governs the dynamics of $c_\chi(\vec{r}, t)$. A simple example for the PDE is the diffusion equation in Eq. (1.4.1) (p. 11). The Green's function is defined as the solution of the PDE for the initial condition $c_\chi(\vec{r}, 0) = \delta(\vec{r})$ [214]. It can be used to calculate the solution $c_\chi(\vec{r}, \tau)$ of the PDE for an arbitrary initial condition $c_\chi(\vec{r}, 0)$ at any time $\tau > 0$:

$$c_\chi(\vec{r}, \tau) = c_\chi(\vec{r}, 0) \otimes P_\chi(\vec{r}, \tau) = \int \cdots \int c_\chi(\vec{r}', 0) \cdot P_\chi(\vec{r}, \vec{r}', \tau) \, d^d r'. \quad (5.3.10)$$

Here \otimes denotes a convolution and d is the dimension of the space, in which the motion takes place. Finally, the concentration correlation factor is given by

$$\phi_\chi(\vec{r}, \vec{r}', \tau) = \langle \delta c_\chi(\vec{r}, t) \cdot \delta c_\chi(\vec{r}', t + \tau) \rangle = \langle c_\chi \rangle \cdot P_\chi(\vec{r}, \vec{r}', \tau). \quad (5.3.11)$$

With these definitions, Eq. (5.3.1) can be slightly rewritten:

$$g_\gamma(\tau) = \frac{\sum_{\chi \in \mathbb{S}} \eta_{\gamma, \chi}^2 \langle c_\chi \rangle \iiint_{-\infty}^{\infty} \iiint_{-\infty}^{\infty} \text{MDE}_\gamma(\vec{r}) \cdot \text{MDE}_\gamma(\vec{r}') \cdot \phi_\chi(\vec{r}, \vec{r}', \tau) \, dV \, dV'}{\left(\sum_{\chi \in \mathbb{S}} \eta_{\gamma, \chi} \langle c_\chi \rangle \right)^2 \cdot \left(\iiint_{-\infty}^{\infty} \text{MDE}_\gamma(\vec{r}) \, dV \right)^2} = \frac{\sum_{\chi \in \mathbb{S}} \eta_{\gamma, \chi}^2 G_\gamma^\chi(\tau)}{\left(\sum_{\chi \in \mathbb{S}} \eta_{\gamma, \chi} \langle c_\chi \rangle \right)^2}. \quad (5.3.12)$$

In this form a non-normalized correlation function

$$G_\gamma^\chi(\tau) := \frac{\langle \delta F_\gamma^\chi(t) \cdot \delta F_\gamma^\chi(t + \tau) \rangle}{\eta_{\gamma, \chi}^2 \cdot \left(\iiint_{-\infty}^{\infty} \text{MDE}_\gamma(\vec{r}) \, dV \right)^2} = \frac{\langle c_\chi \rangle \cdot \iiint_{-\infty}^{\infty} \iiint_{-\infty}^{\infty} \text{MDE}_\gamma(\vec{r}) \cdot \text{MDE}_\gamma(\vec{r}') \cdot \phi_\chi(\vec{r}, \vec{r}', \tau) \, dV \, dV'}{\left(\iiint_{-\infty}^{\infty} \text{MDE}_\gamma(\vec{r}) \, dV \right)^2} \quad (5.3.13)$$

of the fluctuations $\delta F_\gamma^\chi(t)$ caused by a single species χ in a channel γ is introduced.

The next subsections will give the exact mathematical form of $\phi_\chi(\vec{r}, \vec{r}', \tau)$ and the FCS autocorrelation functions $G_\gamma^\chi(\tau)$ and $g(\tau)$ for different situations frequently encountered in FCS measurements.

5.3.4. Normal diffusion

The most common dynamics in FCS is normal diffusion, as introduced in section 1.3.1. Here, the particle concentration dynamics $c_\chi(\vec{r}, t) = \langle c_\chi \rangle + \delta c_\chi(\vec{r}, t)$ is governed by the diffusion equation Eq. (1.4.1):

$$\frac{\partial (\langle c_\chi \rangle + \delta c_\chi(\vec{r}, t))}{\partial t} = D_\chi \cdot \vec{\nabla}^2 (\langle c_\chi \rangle + \delta c_\chi(\vec{r}, t)) \quad \Rightarrow \quad \frac{\partial \delta c_\chi(\vec{r}, t)}{\partial t} = D_\chi \cdot \vec{\nabla}^2 \delta c_\chi(\vec{r}, t). \quad (5.3.14)$$

The Green's function of this PDE is

$$P_\chi(\vec{r}, \vec{r}', \tau) = \frac{1}{(4\pi D_\chi \tau)^{3/2}} \cdot \exp\left(-\frac{(\vec{r}' - \vec{r})^2}{4D_\chi \tau}\right). \quad (5.3.15)$$

With this result and the MDEs in Eqs. (5.3.6, 5.3.7), the FCS autocorrelation function for normal diffusion can be calculated. The MDEs as well as Eq. (5.3.15) can be separated into three factors that depend solely on a single direction x , y or z . Therefore, also the autocorrelation function separates into three directional components:

$$G_\gamma^X(\tau) = \langle c_\chi \rangle \cdot G_{\gamma,x}^X(\tau) \cdot G_{\gamma,y}^X(\tau) \cdot G_{\gamma,z}^X(\tau). \quad (5.3.16)$$

Each directional factor is defined by

$$G_{\gamma,x}^X(\tau) = \frac{\int_{-\infty}^{\infty} \int_{-\infty}^{\infty} \text{MDE}_{\gamma,x}(\xi) \cdot \text{MDE}_{\gamma,x}(\xi') \cdot \phi_{\chi,x}(\xi, \xi', \tau) d\xi d\xi'}{\left(\int_{-\infty}^{\infty} \text{MDE}_x(\xi) d\xi\right)^2}. \quad (5.3.17)$$

Here the directional components of $\text{MDE}_\gamma(\vec{r})$ and of $\phi_\chi(\vec{r}, \vec{r}', \tau)$ are denoted by an additional index x .

Confocal FCS: For a 3-dimensional Gaussian MDE (Eq. 5.2.3), the directional factor in Eq. (5.3.17) is given for the x and y direction by

$$G_{\gamma,x}^X(\tau) = \frac{1}{\sqrt{\pi} \cdot w_\gamma} \cdot \left(1 + \frac{4D_\chi \tau}{w_\gamma^2}\right)^{-1/2}. \quad (5.3.18)$$

The factor for the z direction is of the same form, but with w_γ replaced by z_γ . From this the non-normalized correlation function is easily calculated:

$$G_\gamma^X(\tau) = \frac{\langle c_\chi \rangle}{\pi^{3/2} w_\gamma^2 z_\gamma} \cdot \left(1 + \frac{4D_\chi \tau}{w_\gamma^2}\right)^{-1} \cdot \left(1 + \frac{4D_\chi \tau}{z_\gamma^2}\right)^{-1/2}. \quad (5.3.19)$$

The final FCS normalized correlation function is then given by:

$$g_\gamma(\tau) = \frac{1}{\langle c_\chi \rangle \cdot \pi^{3/2} w_\gamma^2 z_\gamma} \cdot \left(1 + \frac{4D_\chi \tau}{w_\gamma^2}\right)^{-1} \cdot \left(1 + \frac{4D_\chi \tau}{z_\gamma^2}\right)^{-1/2}, \quad (5.3.20)$$

which can be reformulated to

$$g_\gamma(\tau) = \frac{1}{\langle N_\chi \rangle} \cdot \left(1 + \frac{\tau}{\tau_{D,x}}\right)^{-1} \cdot \left(1 + \frac{\tau}{(z_\gamma/w_\gamma)^2 \cdot \tau_{D,x}}\right)^{-1/2}. \quad (5.3.21)$$

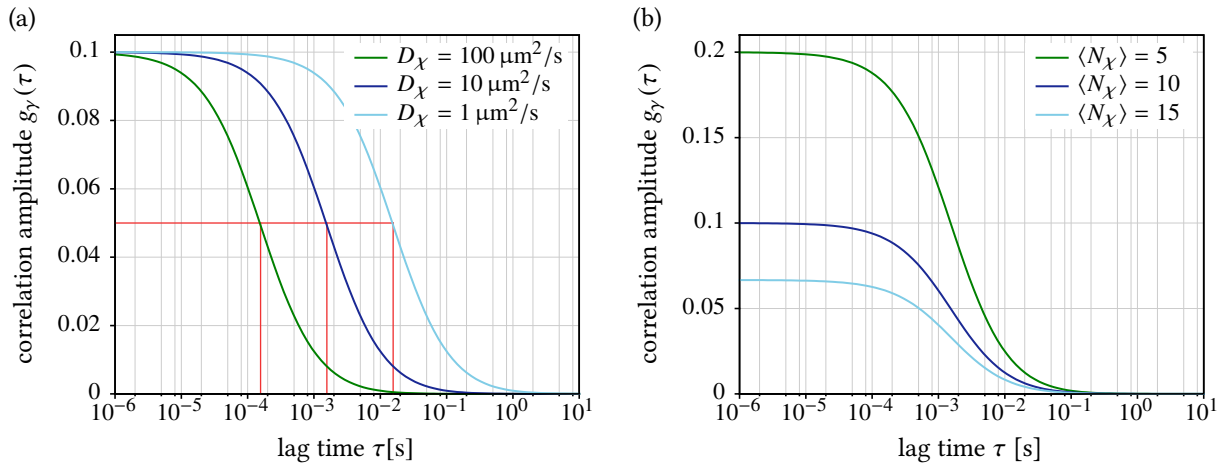


Figure 5.5. | **Plots of the autocorrelation function for a confocal microscope and 3-dimensional normal diffusion, as defined in Eq. (5.3.20).** In (a) the diffusion coefficient is varied, whereas in (b) the average particle number changes. In (a) the red lines indicate the diffusion correlation time $\tau_{D,\chi}$ as defined by Eq. (5.3.22) for each of the curves. Fixed parameters: $\langle N_\chi \rangle = 10$, $D_\chi = 100 \mu\text{m}^2/\text{s}$; MDE parameters: $w_\gamma = 250 \text{ nm}$, $\kappa_\gamma = 6$.

Here $\langle N_\chi \rangle$ is the average number of particles in a focal volume as given by Eq. (5.3.6) and $\tau_{D,\chi}$ is the diffusion correlation time (cf. Eq. (1.4.3), p. 13) with

$$\tau_{D,\chi} = \frac{w_\gamma^2}{4D_\chi}. \quad (5.3.22)$$

This $\tau_{D,\chi}$ is the average dwell time of particles in the observation volume and also the half decay time of $g_\gamma(\tau)$. Figure 5.5 illustrates the function $g_\gamma(\tau)$ for a single species χ for different the diffusion coefficients and the particle numbers. The red lines in Fig. 5.5(a) indicate $\tau_{D,\chi}$ for the different cases. They demonstrate that $g_\gamma(\tau_{D,\chi}) = g_\gamma(0)/2$. Figure 5.5(b) illustrates the general dependence $g_\gamma(0) = 1/\langle N_\chi \rangle$ of the zero-lag amplitude on the average particle number $\langle N_\chi \rangle$ in the focal volume.

SPIM-FCS: For a SPIM-MDE as in Eq. (5.2.6) the volume integrals are also separable. Along the z -axis, the MDE is Gaussian, so the component $G_{\gamma,z}^\chi(\tau)$ is given by Eq. (5.3.18), as in the confocal case. The x - and y -component are:

$$G_{\gamma,x}^\chi(\tau) = G_{\gamma,y}^\chi(\tau) = \frac{1}{a} \cdot \left\{ \text{erf} \left(\frac{a}{\sqrt{4D_\chi\tau + w_\gamma^2}} \right) \frac{\sqrt{4D_\chi\tau + w_\gamma^2}}{a \cdot \sqrt{\pi}} \left[\exp \left(-\frac{a^2}{4D_\chi\tau + w_\gamma^2} \right) - 1 \right] \right\}. \quad (5.3.23)$$

So the final 3-dimensional result is:

$$G_\gamma^\chi(\tau) = \frac{\langle c_\chi \rangle}{\sqrt{\pi} \cdot z_\gamma \cdot a^2} \cdot \left\{ \text{erf} \left(\frac{a}{\sqrt{4D_\chi\tau + w_\gamma^2}} \right) + \frac{\sqrt{4D_\chi\tau + w_\gamma^2}}{a \cdot \sqrt{\pi}} \left[\exp \left(-\frac{a^2}{4D_\chi\tau + w_\gamma^2} \right) - 1 \right] \right\}^2 \cdot \left(1 + \frac{4D_\chi\tau}{z_\gamma^2} \right)^{-1/2}. \quad (5.3.24)$$

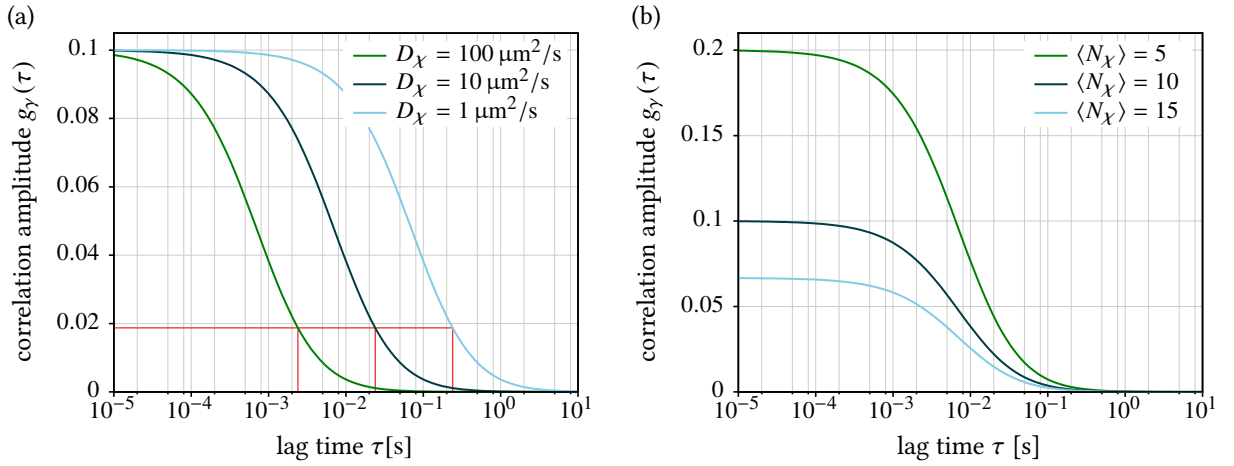


Figure 5.6. | Plots of the SPIM-FCS autocorrelation function for 3-dimensional normal diffusion, as defined in Eq. (5.3.25). In (a) the diffusion coefficient was varied, whereas in (b) the average particle number changes. In (a) the red lines indicate the diffusion correlation time $\tau_{D,\chi}$ for each of the curves. Fixed parameters: $\langle N_\chi \rangle = 10$, $D_\chi = 10 \mu\text{m}^2/\text{s}$. MDE parameters: $a = 400 \text{ nm}$, $w_\gamma = 500 \text{ nm}$, $z_\gamma = 1200 \text{ nm}$.

The normalized SPIM-FCS autocorrelation function for normal diffusion of a single species then is:

$$g_\gamma(\tau) = \frac{1}{\langle c_\chi \rangle \cdot \sqrt{\pi} \cdot z_\gamma \cdot a^2} \cdot \left\{ \text{erf} \left(\frac{a}{\sqrt{4D_\chi\tau + w_\gamma^2}} \right) + \frac{\sqrt{4D_\chi\tau + w_\gamma^2}}{a \cdot \sqrt{\pi}} \left[\exp \left(-\frac{a^2}{4D_\chi\tau + w_\gamma^2} \right) - 1 \right] \right\}^2 \cdot \left(1 + \frac{4D_\chi\tau}{z_\gamma^2} \right)^{-1/2}. \quad (5.3.25)$$

This is still expressed in terms of absolute concentrations $\langle c_\chi \rangle$ and diffusion coefficients D_χ . Using the effective focal volume $V_{\text{eff},\gamma}$ of a SPIM-MDE, as defined in Eq. (5.3.7), the absolute concentration can be replaced by the number of particles $\langle N_\chi \rangle$ within this volume ($\langle c_\chi \rangle \rightarrow \langle N_\chi \rangle / V_{\text{eff},\gamma}$). Then again the zero-lag autocorrelation amplitude is simply $g_\gamma(0) = 1 / \langle N_\chi \rangle$. Defining a diffusion correlation time $\tau_{D,\chi}$ is not as straightforward, as in the confocal case, since the lateral MDE shape is more complex. The definition sometimes used for the SPIM correlation time is [112, 114]

$$\tau_{D,\chi} = \frac{A_{\text{eff},\gamma}}{4D_\chi}, \quad (5.3.26)$$

where the effective lateral focal area is defined as [112]

$$A_{\text{eff},\gamma} = \frac{\left(\iint_{-\infty}^{\infty} \text{MDE}_\gamma(x, y, 0) \, dx \, dy \right)^2}{\iint_{-\infty}^{\infty} \text{MDE}_\gamma^2(x, y, 0) \, dx \, dy} \stackrel{\text{Eq. (5.2.6)}}{=} \frac{a^2}{\left[\text{erf} \left(\frac{a}{w_\gamma} \right) + \frac{w_\gamma}{\sqrt{\pi} \cdot a} \left(e^{-a^2/w_\gamma^2} - 1 \right) \right]^2}. \quad (5.3.27)$$

This definition does not fulfill $g_\gamma(\tau_{D,\chi}) = g_\gamma(0)/2$, but is still a useful quantity describing the time a particle dwells in the focus. Defining $\tau_{D,\chi}$ with $g_\gamma(\tau_{D,\chi}) = g_\gamma(0)/2$ in an analytically closed form is not possible. Finally, Fig. 5.6 illustrates the SPIM-FCS autocorrelation function Eq. (5.3.25) for different parameter combinations.

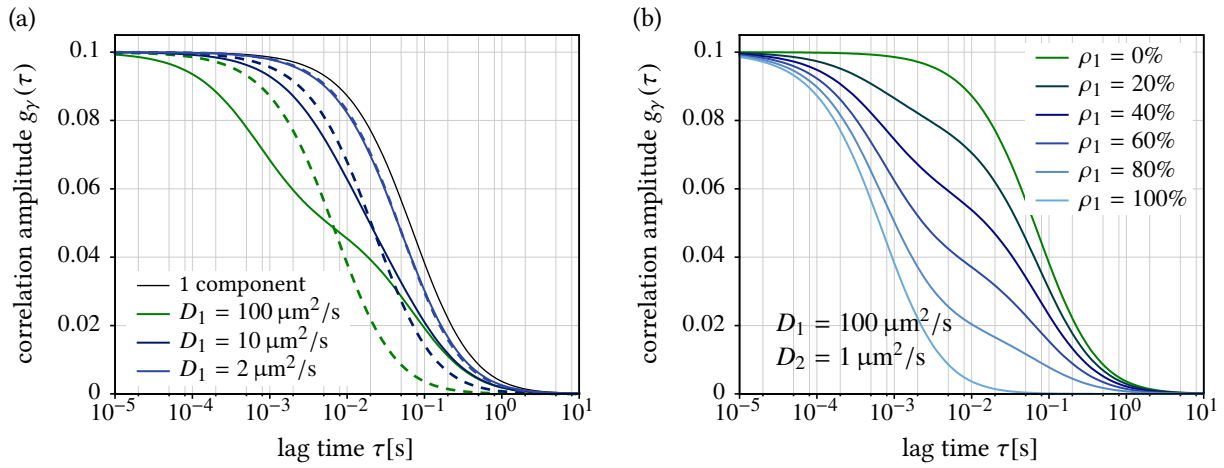


Figure 5.7. | **Plots of the SPIM-FCS autocorrelation function for a two-component system** $\chi = 1, 2$ with $\eta_{\gamma,1} = \eta_{\gamma,2}$, as defined by Eq. (5.3.25). In (a) one diffusion coefficient is fixed to $D_2 = 1 \mu\text{m}^2/\text{s}$ and D_1 is varied, while $\langle N_1 \rangle = \langle N_2 \rangle = 5$. The black line is a one-component model with $\langle N_1 \rangle = 10$ and $D_1 = 1 \mu\text{m}^2/\text{s}$. The dotted lines represent 1-component fits to the 2-component curves. In (b) the diffusion coefficients are fixed to $D_1 = 100 \mu\text{m}^2/\text{s}$, $D_2 = 1 \mu\text{m}^2/\text{s}$ in all curves, but the particle number fraction $\rho_1 := \langle N_1 \rangle / (\langle N_1 \rangle + \langle N_2 \rangle)$ is varied, keeping $\langle N_1 \rangle + \langle N_2 \rangle = 10$. MDE parameters: $a = 400 \text{ nm}$, $w_\gamma = 500 \text{ nm}$, $z_\gamma = 1200 \text{ nm}$.

Lower-dimensional diffusion: Using the separation of the confocal FCS and SPIM-FCS autocorrelation functions into directional components, also lower-dimensional diffusion models are easy to set up. In Eq. (5.3.17) one can easily omit the dimensions, along which no motion takes place. The concentrations $\langle c_\chi \rangle$ then have to be reinterpreted as an areal density, or a line density, depending on the diffusion model.

Multi-component diffusion: Figure 5.7 shows exemplary autocorrelation curves of a 2-component SPIM-FCS autocorrelation model. To simplify the situation, the molecular brightnesses of both species $\chi = 1, 2$ are set equal ($\eta_{\gamma,1} = \eta_{\gamma,2}$). Figure 5.7(a) shows a 2-component model with different combinations of diffusion coefficients (solid lines) and 1-component fits (dotted line) to these. The 1-component fit is hardly distinguishable from the 2-component data if the diffusion coefficients are too close to each other. If the assumption of equal brightnesses holds in a system, the multi-component diffusion model is typically written in terms of an overall concentration $\langle c_{\text{all}} \rangle$ and relative concentrations ρ_χ for each species, with:

$$\langle c_{\text{all}} \rangle := \sum_{\chi \in \mathbb{S}} \langle c_\chi \rangle, \quad \rho_\chi := \frac{\langle c_\chi \rangle}{\langle c_{\text{all}} \rangle} \quad \text{and} \quad \sum_{\chi \in \mathbb{S}} \rho_\chi \stackrel{!}{=} 1. \quad (5.3.28)$$

With these definition, Eq. (5.3.12) can be simplified to:

$$g_\gamma(\tau) = \frac{1}{\langle c_{\text{all}} \rangle^2} \cdot \sum_{\chi \in \mathbb{S}} G_\gamma^\chi(\tau) \quad (5.3.29)$$

5.3.5. Anomalous diffusion

Anomalous diffusion was introduced in section 1.3.2. In FCS the propagator for such anomalous transport processes is typically assumed to be a Gaussian function [22, 23, 27, 32]

$$P_\chi(\vec{r}, \vec{r}', \tau) = \frac{1}{(4\pi\Gamma_\chi\tau^{\alpha_\chi})^{3/2}} \cdot \exp\left(-\frac{(\vec{r}' - \vec{r})^2}{4\Gamma_\chi\tau^{\alpha_\chi}}\right), \quad (5.3.30)$$

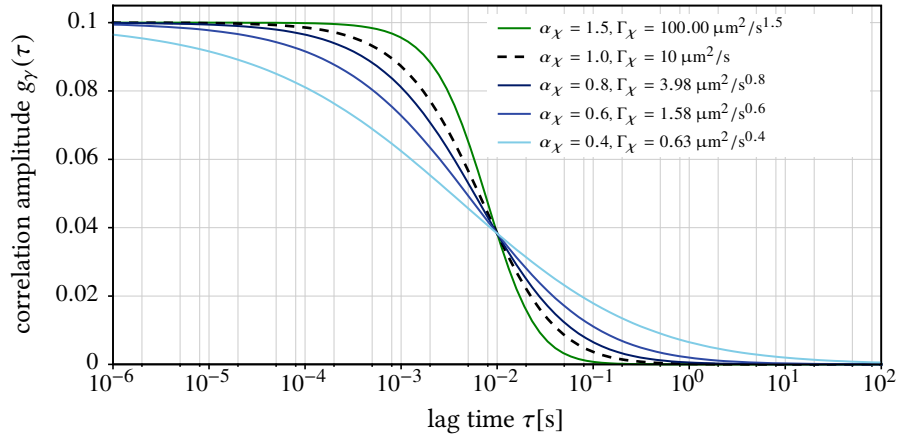


Figure 5.8. | Plots of the SPIM-FCS autocorrelation function for single-component anomalous diffusion, as defined in Eq. (5.3.24). The value of the parameter Γ_χ was chosen, so that the autocorrelation curves coincide at $\tau = 10$ ms: $\Gamma_\chi = 10 \mu\text{m}^2/\text{s} \cdot \tau^{1-\alpha_\chi}$. MDE parameters: $a = 400$ nm, $w_\gamma = 500$ nm, $z_\gamma = 1200$ nm.

with the anomaly parameter α_χ and the generalized diffusion coefficient Γ_χ . This propagator can be used to calculate the confocal non-normalized FCS correlation functions:

$$G_\gamma^\chi(\tau) = \frac{\langle c_\chi \rangle}{\pi^{3/2} w_\gamma^2 z_\gamma} \cdot \left(1 + \frac{4\Gamma_\chi \tau^{\alpha_\chi}}{w_\gamma^2}\right)^{-1} \cdot \left(1 + \frac{4\Gamma_\chi \tau^{\alpha_\chi}}{z_\gamma^2}\right)^{-1/2}. \quad (5.3.31)$$

Note the similar form of this expression and the corresponding expression for normal diffusion in Eq. (5.3.19). Also the SPIM-FCS non-normalized correlation function is very similar to its normal diffusion counterpart in Eq. (5.3.24):

$$G_\gamma^\chi(\tau) = \frac{\langle c_\chi \rangle}{\sqrt{\pi} \cdot z_\gamma \cdot a^2} \cdot \left\{ \operatorname{erf} \left(\frac{a}{\sqrt{4\Gamma_\chi \tau^{\alpha_\chi} + w_\gamma^2}} \right) + \frac{\sqrt{4\Gamma_\chi \tau^{\alpha_\chi} + w_\gamma^2}}{a \cdot \sqrt{\pi}} \left[\exp \left(-\frac{a^2}{4\Gamma_\chi \tau^{\alpha_\chi} + w_\gamma^2} \right) - 1 \right] \right\}^2 \cdot \left(1 + \frac{4\Gamma_\chi \tau^{\alpha_\chi}}{z_\gamma^2}\right)^{-1/2}. \quad (5.3.32)$$

In general, both results can be obtained by the simple substitution $D_\chi \tau \rightarrow \Gamma_\chi \tau^{\alpha_\chi}$.

Figure 5.8 shows plots of SPIM-FCS autocorrelation functions for different anomaly parameters α_χ . For subdiffusion ($\alpha_\chi < 1$) the curves have a flatter slope than the normal diffusion ($\alpha_\chi = 1$). Therefore they also spread out over a significantly larger lag time range. For superdiffusion ($\alpha_\chi > 1$) the correlation function gets increasingly steeper. This behavior represents the flatter, or steeper slope of the MSD.

5.3.6. Arbitrary mean squared displacement

The propagator Eq. (5.3.30) can further be generalized for a motion with an arbitrary mean squared displacement $\text{MSD}_\chi(\tau)$. Under the assumption, that $P_\chi(\vec{r}, \vec{r}', \tau)$ still retains its Gaussian shape, the following definition can be used [80–82, 215]:

$$P_\chi(\vec{r}, \vec{r}', \tau) = \frac{1}{(2\pi \cdot \text{MSD}_\chi(\tau)/3)^{3/2}} \cdot \exp \left(-\frac{(\vec{r}' - \vec{r})^2}{2 \text{MSD}_\chi(\tau)/3} \right). \quad (5.3.33)$$

For example, the confocal normalized autocorrelation function then reads:

$$g_\gamma(\tau; \text{MSD}_\chi(\tau)) = \frac{1}{\langle N_\chi \rangle} \cdot \left(1 + \frac{2 \text{MSD}_\chi(\tau)}{3 w_\gamma^2} \right)^{-1} \cdot \left(1 + \frac{2 \text{MSD}_\chi(\tau)}{3 z_\gamma^2} \right)^{-1/2}. \quad (5.3.34)$$

This form can be used to extract $\text{MSD}_\chi(\tau)$ from an experimentally determined autocorrelation function $\{(\tau_i, \hat{g}_i)\}_{i \in \mathbb{N}}$, by (numerically) solving the equation

$$g_\gamma(\tau_i; \text{MSD}_\chi(\tau_i)) = \hat{g}_i \quad (5.3.35)$$

for $\text{MSD}_\chi(\tau_i)$ at every lag time τ_i . This method was introduced by Shusterman et al. in 2004 to distinguish the internal and the global motion of fluorescently labeled polymer chains [80].

5.3.7. Sample translation or flow

To describe a directed motion (see section 1.3.3) or flow of particles through the focus of the microscope, the advection-diffusion equation is used:

$$\frac{\partial c_\chi(\vec{r}, t)}{\partial t} = -\vec{v} \cdot \vec{\nabla} c_\chi(\vec{r}, t) + D_\chi \cdot \vec{\nabla}^2 c_\chi(\vec{r}, t). \quad (5.3.36)$$

Here the flow is characterized by its velocity vector $\vec{v} = (v_x, v_y, v_z)^T$. The propagator for Eq. (5.3.36) is

$$P(\vec{r}, \vec{r}', \tau) = \frac{1}{(4\pi D_\chi \tau)^{3/2}} \cdot \exp\left(-\frac{(\vec{r}' - \vec{r} - \vec{v} \cdot \tau)^2}{4D_\chi \tau}\right). \quad (5.3.37)$$

This leads to a non-normalized confocal FCS autocorrelation function, which is extended by an exponential factor as compared to the normal diffusion form [37, 78, 216]:

$$G_\gamma^\chi(\tau) = \frac{\langle c_\chi \rangle}{\pi^{3/2} w_\gamma^2 z_\gamma} \cdot \left(1 + \frac{4D_\chi \tau}{w_\gamma^2} \right)^{-1} \cdot \left(1 + \frac{4D_\chi \tau}{z_\gamma^2} \right)^{-1/2} \cdot \exp\left(-\frac{(v_x^2 + v_y^2) \cdot \tau^2}{4D_\chi \tau + w_\gamma^2} - \frac{v_z^2 \cdot \tau^2}{4D_\chi \tau + z_\gamma^2}\right). \quad (5.3.38)$$

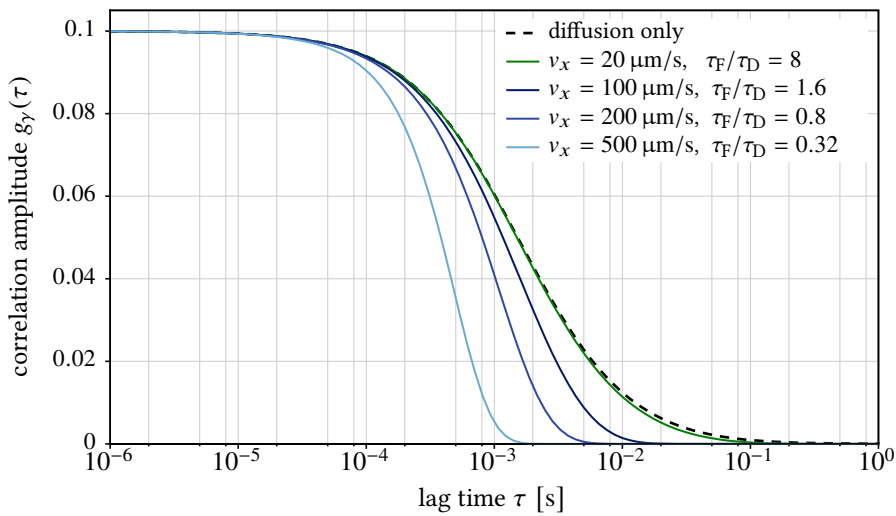


Figure 5.9. | Impact of flow on FCS autocorrelation curves for 3D diffusion in a Gaussian focus.

The correlation time for normal diffusion (black dashed line) is $\tau_D \approx 1.5$ ms. Plot parameters: $\langle N_\chi \rangle = 10$, $D_\chi = 10 \mu\text{m}^2/\text{s}$. MDE parameters: $w_\gamma = 250$ nm, $\kappa_\gamma = 6$.

Again, the SPIM-FCS non-normalized autocorrelation function is more complex, but as for normal diffusion the integrals separate into three direction factors $G_{\gamma}^x(\tau) = \langle c_x \rangle \cdot G_{\gamma,x}^x(\tau) \cdot G_{\gamma,y}^x(\tau) \cdot G_{\gamma,z}^x(\tau)$ with

$$G_{\gamma,x}^x(\tau) = \frac{1}{2a^2} \cdot \left\{ \left[(a - v_x \tau) \cdot \operatorname{erf} \left(\frac{\sqrt{2} \cdot (a - v_x \tau)}{\sqrt{4D_x \tau + w_y^2}} \right) - 2v_x \tau \cdot \operatorname{erf} \left(\frac{\sqrt{2} \cdot v_x \tau}{\sqrt{4D_x \tau + w_y^2}} \right) + (a + v_x \tau) \cdot \operatorname{erf} \left(\frac{\sqrt{2} \cdot (a + v_x \tau)}{\sqrt{4D_x \tau + w_y^2}} \right) \right] + \frac{\sqrt{4D_x \tau + w_y^2}}{\sqrt{2\pi}} \cdot \left[e^{-\frac{2 \cdot (a - v_x \tau)^2}{4D_x \tau + w_y^2}} - 2 \cdot e^{-\frac{2v_x^2 \tau^2}{4D_x \tau + w_y^2}} + e^{-\frac{2 \cdot (a + v_x \tau)^2}{4D_x \tau + w_y^2}} \right] \right\}. \quad (5.3.39)$$

The result for the z -direction is again the same as for a confocal MDE:

$$G_{\gamma,z}^x(\tau) = \frac{1}{\sqrt{\pi} \cdot z_\gamma} \cdot \left(1 + \frac{4D_x \tau}{z_\gamma^2} \right)^{-1/2} \cdot \exp \left(-\frac{v_z^2 \tau^2}{4D_x \tau + z_\gamma^2} \right). \quad (5.3.40)$$

The effect of a flow in the sample can easily be seen in the confocal case, where the exponential term will lead to a faster decay of the autocorrelation function. In the SPIM case the influence is qualitatively the same, but this is obscured by the complex analytical form of the functions. In both cases, the dependence of the autocorrelation function on the flow velocity $\|\vec{v}\|$ is strong, whereas the dependence on the flow direction $\vec{v}/\|\vec{v}\|$ is very weak or non-existent due to the symmetry of the MDE. Therefore the flow direction cannot be determined with single-focus FCS. The methods presented in section 5.4.1 will overcome this problem.

Finally Fig. 5.9 shows exemplary autocorrelation curves for a system with diffusion and flow. It clearly shows the faster decay and changing shape of the autocorrelation function with increasing flow speed. The impact of flow is minor, as long as the typical time to pass the focus by flow

$$\tau_F = \frac{w_\gamma}{\|\vec{v}\|} \quad (5.3.41)$$

is smaller than the diffusion correlation time τ_D .

5.4. Fluorescence cross-correlation spectroscopy

5.4.1. Measuring directed motion: Two-focus cross-correlation

So far the fluorescence fluctuations from a single observation volume were considered to yield mobility parameters of the observed particles. As noted in section 5.3.7, this method is limited, when the velocity and direction of a flow field are to be measured. A way to overcome this limitation is “2-focus fluorescence cross-correlation spectroscopy (FCCS)”. In this method two observation volumes are used, that are displaced by $\vec{\delta} = (\delta_x, \delta_y, \delta_z)^T$ (see Fig. 5.10). Then the fluorescence intensity time traces $F_\gamma(t)$ from both foci $\gamma = l, r$ are measured independently. The autocorrelation functions will be described by the models from section 5.3.7 and the flow velocity $\|\vec{v}\|$ may be extracted from each focus individually. A closer look at the fluorescence intensity traces shows, that the trace from the right focus $F_r(t)$ is a delayed version of the trace from the left focus $F_l(t)$. The delay is given by the time, that the particles need to move from the left to the right focus. For a flow velocity \vec{v} , this delay time is given by $\tau_{Fx} = \|\vec{\delta}\| \cdot \|\vec{v}\|$. This feature of the intensities can be quantified by calculating the spatial cross-correlation function between the two intensity time traces:

$$g_{\gamma\rho}(\tau) = \frac{\langle \delta F_\gamma(t) \cdot \delta F_\rho(t + \tau) \rangle}{\langle F_\gamma \rangle \cdot \langle F_\rho \rangle} = \frac{\langle F_\gamma(t) \cdot F_\rho(t + \tau) \rangle}{\langle F_\gamma \rangle \cdot \langle F_\rho \rangle} - 1, \quad \tau > 0, \quad \gamma, \rho \in \{l, r, \dots\}. \quad (5.4.1)$$

This form includes the autocorrelation as the special case $\gamma = \rho$. Therefore the explicit autocorrelation functions $g_{\gamma\gamma}(\tau)$ and $g_{\rho\rho}(\tau)$ are omitted throughout the rest of this chapter.

In order to determine the actual form of these model functions for imaging fluorescence cross-correlation spectroscopy (imaging FCCS), they are again rewritten in terms of non-normalized cross-correlation factors $G_{\gamma\rho}^X(\tau)$, analogous to Eq. (5.3.12) in section 5.3.3:

$$g_{\gamma\rho}(\tau) = \frac{\sum_{\chi \in \mathbb{S}} \eta_{\gamma,\chi} \eta_{\rho,\chi} \langle c_\chi \rangle \iiint_{-\infty}^{\infty} \iiint_{-\infty}^{\infty} \text{MDE}_\gamma(\vec{r}) \cdot \text{MDE}_\rho(\vec{r}') \cdot \phi_\chi(\vec{r}, \vec{r}', \tau) \, dV \, dV'}{\left(\sum_{\chi \in \mathbb{S}} \eta_{\gamma,\chi} \langle c_\chi \rangle \cdot \iiint_{-\infty}^{\infty} \text{MDE}_\gamma(\vec{r}) \, dV \right) \cdot \left(\sum_{\chi \in \mathbb{S}} \eta_{\rho,\chi} \langle c_\chi \rangle \cdot \iiint_{-\infty}^{\infty} \text{MDE}_\rho(\vec{r}) \, dV \right)} = \frac{\sum_{\chi \in \mathbb{S}} \eta_{\gamma,\chi} \eta_{\rho,\chi} G_{\gamma\rho}^X(\tau)}{\left(\sum_{\chi \in \mathbb{S}} \eta_{\gamma,\chi} \langle c_\chi \rangle \right) \cdot \left(\sum_{\chi \in \mathbb{S}} \eta_{\rho,\chi} \langle c_\chi \rangle \right)}. \quad (5.4.2)$$

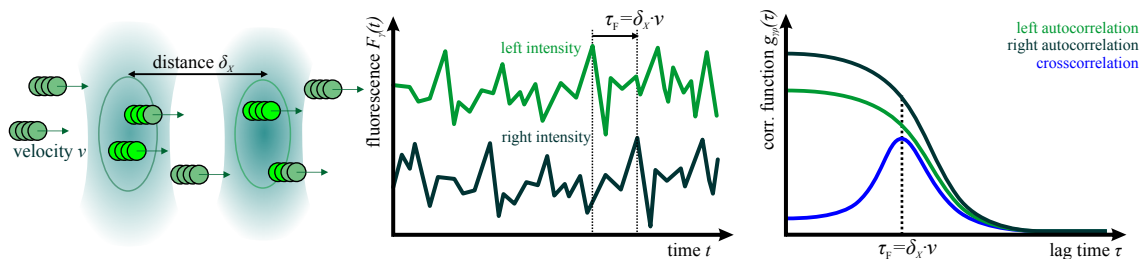


Figure 5.10. | **Illustration of two-focus fluorescence cross-correlation spectroscopy.** Particles move from left to right with a velocity v through two foci, that are separated by a distance δ . The intensity traces are thus shifted by a time $\tau_{Fx} \approx \delta \cdot v$ and the cross-correlation shows a peak at this time τ_{Fx} . The figure shows the idealized case, where $v^2 \tau^2 \gg D\tau \ \forall \tau \gg 0$.

The non-normalized cross-correlation factor $G_{\gamma\rho}^X(\tau)$ is defined as:

$$\begin{aligned} G_{\gamma\rho}^X(\tau) &:= \frac{\langle \delta F_\gamma^X(t) \cdot \delta F_\rho^X(t+\tau) \rangle}{\left(\eta_{\gamma,\chi} \cdot \iiint_{-\infty}^{\infty} \text{MDE}_\gamma(\vec{r}) \, dV \right) \cdot \left(\eta_{\rho,\chi} \cdot \iiint_{-\infty}^{\infty} \text{MDE}_\rho(\vec{r}) \, dV \right)} \\ &= \langle c_\chi \rangle \cdot \frac{\iiint_{-\infty}^{\infty} \iiint_{-\infty}^{\infty} \text{MDE}_\gamma(\vec{r}) \cdot \text{MDE}_\rho(\vec{r}') \cdot \phi_\chi(\vec{r}, \vec{r}', \tau) \, dV \, dV'}{\left(\iiint_{-\infty}^{\infty} \text{MDE}_\gamma(\vec{r}) \, dV \right) \cdot \left(\iiint_{-\infty}^{\infty} \text{MDE}_\rho(\vec{r}) \, dV \right)} \end{aligned} \quad (5.4.3)$$

In both Eqs. (5.4.2, 5.4.3), the molecular brightnesses $\eta_{\gamma,\chi}, \eta_{\rho,\chi}$ and MDEs $\text{MDE}_\gamma(\vec{r}), \text{MDE}_\rho(\vec{r})$ were written with different indices. This accounts for any optical differences between the two foci. The situation is usually simpler, as for both MDEs the same detection filters, illumination intensities and optics are used and therefore also the brightnesses can be assumed to be equal. The MDEs then have the same size, but with a shift $\vec{\delta}$:

$$\eta_{\gamma,\chi} = \eta_{\rho,\chi} \quad \text{and} \quad \text{MDE}_\tau(\vec{r}) = \text{MDE}_1(\vec{r} + \vec{\delta}) \quad \text{or} \quad \text{MDE}_\tau(\vec{r} - \vec{\delta}) = \text{MDE}_1(\vec{r}). \quad (5.4.4)$$

Under these assumptions, the non-normalized cross-correlation factor for a confocal microscope is given by:

$$G_{\gamma\rho}^X(\tau) = \frac{\langle c_\chi \rangle}{\pi^{3/2} w_\gamma^2 z_\gamma} \cdot \left(1 + \frac{4D_\chi \tau}{w_\gamma^2} \right)^{-1} \cdot \left(1 + \frac{4D_\chi \tau}{z_\gamma^2} \right)^{-1/2} \cdot \exp \left(-\frac{(v_x \tau - \delta_x)^2 + (v_y \tau - \delta_y)^2}{4D_\chi \tau + w_\gamma^2} - \frac{(v_z \tau - \delta_z)^2}{4D_\chi \tau + z_\gamma^2} \right). \quad (5.4.5)$$

The normalized cross-correlation function for a single species is then given by

$$g_{\gamma\rho}(\tau) = \frac{1}{\langle N_\chi \rangle} \cdot \left(1 + \frac{4D_\chi \tau}{w_\gamma^2} \right)^{-1} \cdot \left(1 + \frac{4D_\chi \tau}{z_\gamma^2} \right)^{-1/2} \cdot \exp \left(-\frac{(v_x \tau - \delta_x)^2 + (v_y \tau - \delta_y)^2}{4D_\chi \tau + w_\gamma^2} - \frac{(v_z \tau - \delta_z)^2}{4D_\chi \tau + z_\gamma^2} \right). \quad (5.4.6)$$

The non-normalized autocorrelation factors for SPIM-FCCS can be written in terms of three direction factors $G_{\gamma\rho}^X(\tau) = \langle c_\chi \rangle \cdot G_{\gamma\rho,x}^X(\tau) \cdot G_{\gamma\rho,y}^X(\tau) \cdot G_{\gamma\rho,z}^X(\tau)$. Again, the factors for the x - and y direction are equal:

$$\begin{aligned} G_{\gamma\rho,x}^X(\tau) &= \frac{1}{2a^2} \cdot \left\{ \left[(a - v_x \tau + \delta_x) \cdot \text{erf} \left(\frac{a - v_x \tau + \delta_x}{\sqrt{4D_\chi \tau + w_\gamma^2}} \right) - 2(v_x \tau - \delta_x) \cdot \text{erf} \left(\frac{v_x \tau - \delta_x}{\sqrt{4D_\chi \tau + w_\gamma^2}} \right) \right] \right. \\ &\quad \left. + (a + v_x \tau - \delta_x) \cdot \text{erf} \left(\frac{a + v_x \tau - \delta_x}{\sqrt{4D_\chi \tau + w_\gamma^2}} \right) \right\} \\ &\quad + \frac{\sqrt{4D_\chi \tau + w_\gamma^2}}{\sqrt{\pi}} \cdot \left[e^{-\frac{(a - v_x \tau + \delta_x)^2}{4D_\chi \tau + w_\gamma^2}} - 2 \cdot e^{-\frac{(v_x \tau - \delta_x)^2}{4D_\chi \tau + w_\gamma^2}} + e^{-\frac{(a + v_x \tau - \delta_x)^2}{4D_\chi \tau + w_\gamma^2}} \right] \end{aligned} \quad (5.4.7)$$

The factor in z -direction is:

$$G_{\gamma\rho,z}^X(\tau) = \frac{\exp \left(-\frac{(v_z \tau - \delta_z)^2}{4D_\chi \tau + z_\gamma^2} \right)}{\sqrt{\pi} \cdot \sqrt{4D_\chi \tau + z_\gamma^2}}. \quad (5.4.8)$$

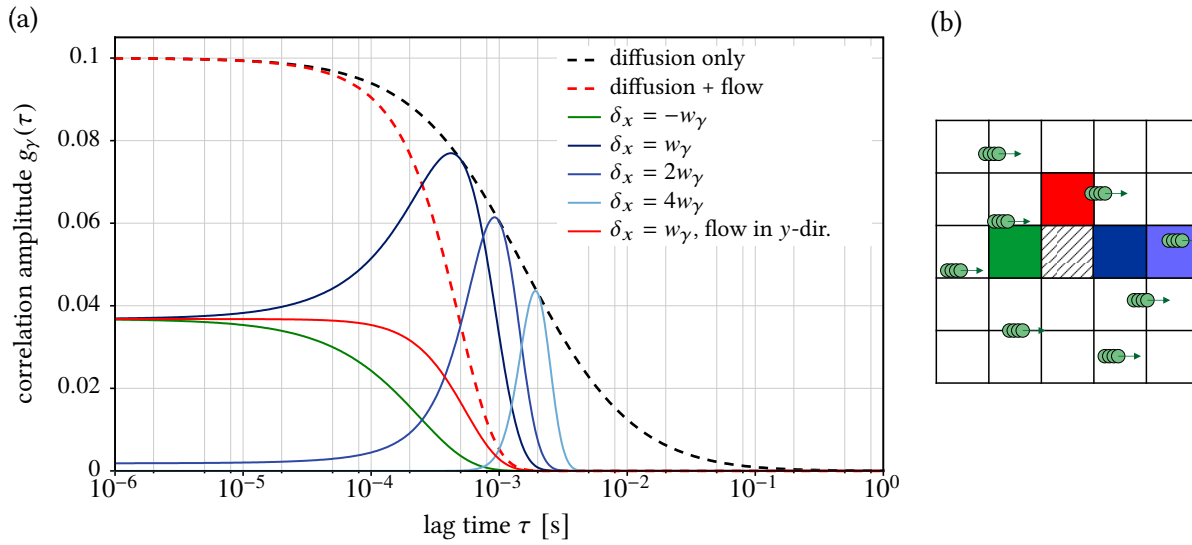


Figure 5.11. | Impact of flow on the FCCS cross-correlation curves for 3D diffusion between two Gaussian foci (Eq. (5.4.6)). Parameters for the plots: $\langle N_{\chi} \rangle = 10$, $D_{\chi} = 10 \mu\text{m}^2/\text{s}$, $\vec{v} = (500, 0, 0)^{\text{T}} \mu\text{m}/\text{s}$. MDE parameters: $w_{\gamma} = 250 \text{ nm}$, $z_{\gamma} = 1500 \text{ nm}$, $\delta_y = \delta_z = 0$. Diffusion correlation time: $\tau_{\text{D}} \approx 1.5 \text{ ms}$. The illustration (b) shows the relative position of the foci (squares on the matrix of the image detector) to the flow and the central pixel (shaded central square). The colors correspond to the graph colors in (a).

Figure 5.11 shows examples of the model function in Eq. (5.4.6). The three blue cross-correlation curves are calculated for an increasing displacement δ_x in the flow direction (dark to light blue). They show the characteristic peak due to the flow and how it moves towards longer lag times with increasing focus distance $\|\vec{\delta}\|$. Also the correlation amplitude and the peak height decrease with $\|\vec{\delta}\|$. The green cross-correlation curve is for a focus displacement $\vec{\delta}$, which is anti-parallel to the flow vector \vec{v} . Since in this case, particles from the first focus never reach the second by flow, no peak is formed. The remaining correlation amplitude is explained by the superimposed diffusive motion only. Compared to the diffusion-only case (black dotted curve) the half decay time is reduced because the flow causes particles to leave the focus faster than solely by diffusion. Finally the red curve shows a cross-correlation

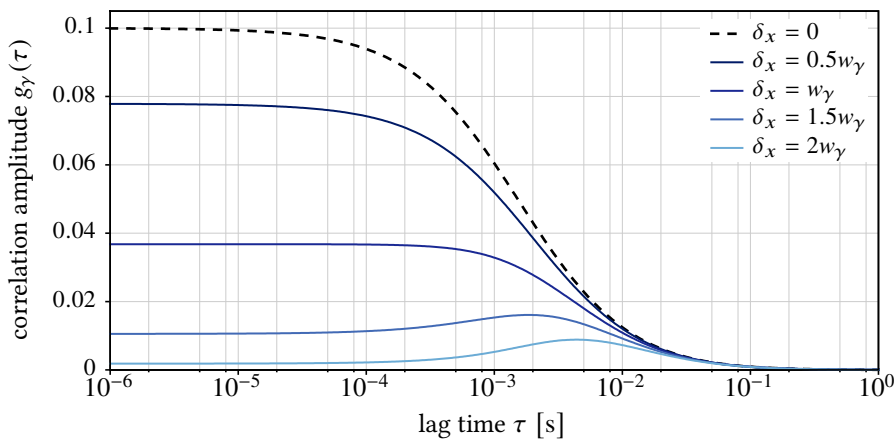


Figure 5.12. | Two-focus FCCS cross-correlation curves for 3D diffusion without flow (Eq. (5.4.6)). Plot parameters: $\langle N_{\chi} \rangle = 10$, $D_{\chi} = 10 \mu\text{m}^2/\text{s}$. MDE parameters: $w_{\gamma} = 250 \text{ nm}$, $z_{\gamma} = 1500 \text{ nm}$.

curve for a focus displacement perpendicular to the flow direction. Here the decay time is similar to that of the autocorrelation curve for diffusion and flow (red dotted line). So for a given flow direction, the cross-correlation curves in four directions differ significantly. This can be used to estimate the speed and the direction of the flow: with two foci, two directions (left/right) may be distinguished. In imaging FCCS a camera is used as detector (see Fig. 5.11b) and the cross-correlations to the four directly neighboring pixels can be calculated. A global fit (see section 7.1.4) can be used to optimize the parameters in five model functions simultaneously: one for the autocorrelation curve and one for each of the four cross-correlation curves between the direct neighbors. Then both planar components of the flow velocity v_x and v_y can be determined. The flow in z -direction can only be assessed, if additional foci are available below and above the focal plane, which is not possible in a typical microscopes.

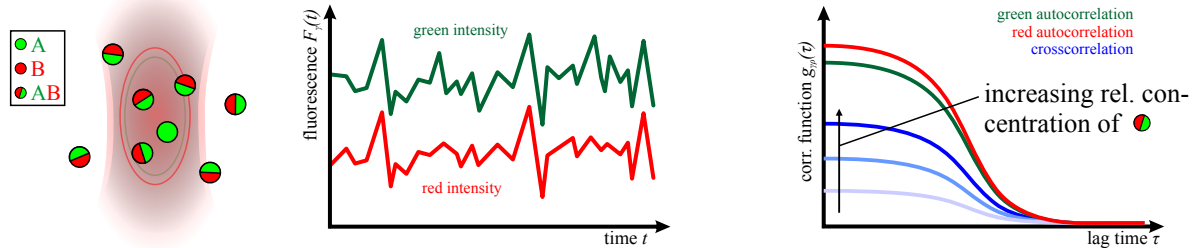
Figure 5.12 shows the 2-focus cross-correlation functions if no flow is present in the sample ($\|\vec{v}\| = 0$). Also in these cases a peak can form, if the displacement $\vec{\delta}$ between the foci is sufficiently large. This peak is related to the time, that particles need to cover the distance $\|\vec{\delta}\|$ by diffusion only.

5.4.2. Measuring molecular interactions: Two-color cross-correlation

A second type of cross-correlation analysis allows to measure molecular interactions between particles, carrying spectrally distinct fluorophores, for instance either a green (A) or a red (B) fluorophore. This “2-color fluorescence cross-correlation spectroscopy (FCCS)” method is illustrated in Fig. 5.13. The cross-correlation analysis is performed between the fluorescence intensities $F_g(t)$ and $F_r(t)$ from two overlapping foci, from which photons in two distinct spectral ranges are detected (in Fig. 5.13(:) green g and red r). If the particles interact, some of them move together (depicted as dimer AB in Fig. 5.13a). This generates a correlation between the signals $F_g(t)$ and $F_r(t)$, which manifests itself as a non-vanishing amplitude $g_{gr}(0)$ of the cross-correlation function. If no interaction is present (see Fig. 5.13b), the signals $F_g(t)$ and $F_r(t)$ are statistically independent and the cross-correlation amplitude is 0.

As shown in Fig. 5.13(a), the cross-correlation amplitude $g_{gr}(0)$ depends on the relative concentration

(a) 2-color cross-correlation: sample with double-labeled particles (●)



(b) 2-color cross-correlation: sample with single-labeled particles only (●, ●)

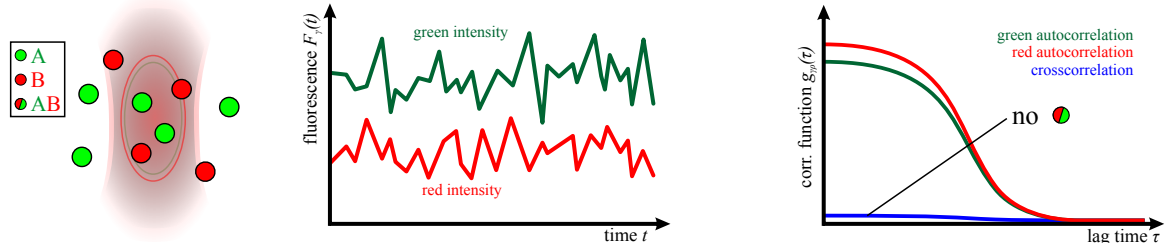
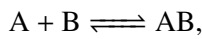


Figure 5.13. | Schematic illustration of two-color fluorescence cross-correlation spectroscopy

(a) Sample with a high fraction of double-labeled molecules. The fluorescence intensity traces show correlated fluctuations resulting in a high cross-correlation amplitude. (b) Sample with single-labeled particles only. The fluorescence time-traces are non-correlated and the cross-correlation amplitude is nearly 0.

of dimers $c_{AB}/(c_A + c_B + c_{AB})$. If only dimers are present, it reaches a maximum level, which is approximately the average between $g_{gg}(0)$ and $g_{rr}(0)$. This dependence is a complicated function, which is linear only to a first approximation. Therefore proper fit models need to be derived, in order to measure the absolute and relative concentrations of each of the three species A, B and AB with 2-color FCCS.

In the framework of FCS/FCCS theory, presented in this chapter, the correlation functions are all of the form given in Eq. (5.4.3). In contrast to two-focus cross-correlation (see section 5.4.1), the constraints in Eq. (5.4.4) are dropped and for both foci $MDE_g(\vec{r})$ and $MDE_r(\vec{r})$ may be different. As (mostly chromatic) aberrations of and misalignment in the optics may lead to an offset $\vec{\delta}$ between the green and the red focus, the shift $\vec{\delta}$ is retained in the model function. Information on the spectral properties of the species $\chi \in \{A, B, AB, \dots\}$ allows to impose new constraints on the molecular brightnesses $\eta_{g,\chi}$ and $\eta_{r,\chi}$. As an example, a simple bi-molecular hetero-dimerization



is used here, although more complex models (including e.g. homo-dimers) may be set up. This model will be applied to several measurements in the remainder of this thesis. The same labeling scheme as above is used: A carries a green fluorescent label, B a red fluorescent label and AB both labels. Then the following set of constraints on the molecular brightnesses may be formulated:

$$\begin{aligned} \eta_{g,A} &\equiv \eta_g & \eta_{g,B} &= 0 & \eta_{g,AB} &= \eta_g \\ \eta_{r,A} &= \kappa_{gr}\eta_g & \eta_{r,B} &\equiv \eta_r & \eta_{r,AB} &= \eta_r + \kappa_{gr}\eta_g. \end{aligned} \quad (5.4.9)$$

Here the brightness of a green fluorophore (either on A or AB) in the green detection channel is denoted by η_g and the brightness of a red fluorophore in the red channel (either on B or AB) by η_r . These quantities can be estimated from the average intensities $\langle F_g \rangle$ and $\langle F_r \rangle$ and the particle concentrations $\langle c_A \rangle$, $\langle c_B \rangle$ and $\langle c_{AB} \rangle$:

$$\eta_{g,A} \equiv \eta_g = \frac{\langle F_g \rangle}{\langle c_A \rangle + \langle c_{AB} \rangle} \quad \text{and} \quad \eta_{r,B} \equiv \eta_r = \frac{\langle F_r \rangle}{\langle c_B \rangle + \langle c_{AB} \rangle}. \quad (5.4.10)$$

The variable κ_{gr} in Eq. (5.4.9) denotes the crosstalk between channels g and r, i.e. the fraction of green

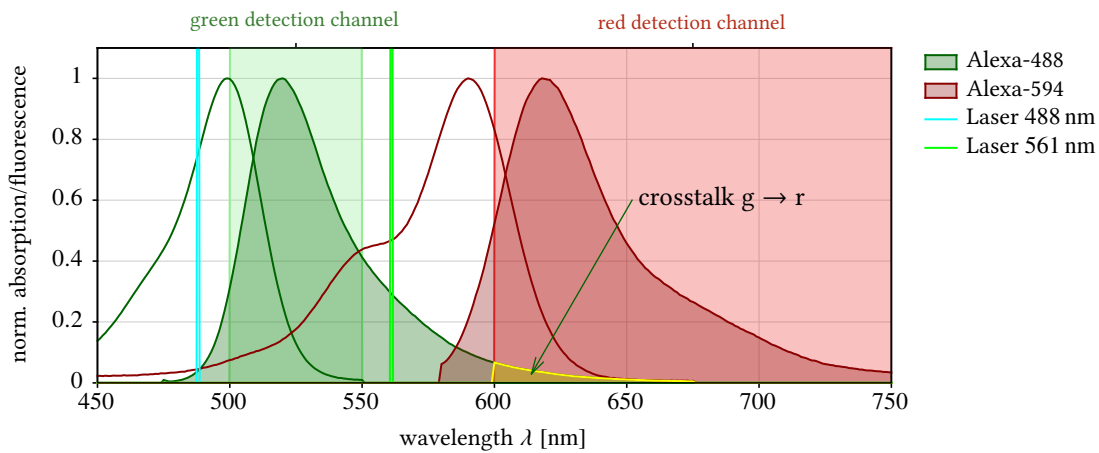


Figure 5.14. | Absorption and fluorescence spectra of Alexa-488 and Alexa-594 together with the excitation laser wavelengths and typical fluorescence emission detection channels. The spectra were taken from [135, 136].

fluorescence detected in the red channel due to imperfect filters and broad emission spectra:

$$\kappa_{\text{gr}} = \frac{\int_0^{\infty} \eta_{\text{g}}(\lambda) \cdot h_{\text{r}}(\lambda) \, d\lambda}{\int_0^{\infty} \eta_{\text{g}}(\lambda) \, d\lambda}, \quad (5.4.11)$$

where $\eta_{\text{g}}(\lambda)$ is the fluorescence spectrum of the green fluorophore and $h_{\text{r}}(\lambda)$ describes the transmission spectrum of the red detection channel. Figure 5.14 shows the absorption and emission spectra of the fluorescent dyes Alexa-488 and Alexa-594. The crosstalk is highlighted in yellow. For Alexa-488, the crosstalk is $\kappa_{\text{gr}} \approx 3.5\%$, if the longpass filter in the red channel starts transmitting at 600 nm. For eGFP the crosstalk is $\kappa_{\text{gr}} \approx 3.8\%$ in that case. The crosstalk from the red to the green channel is usually $\kappa_{\text{rg}} = 0$, as the excitation wavelength for the red channel lies above the green detection window.

Using the constraints in Eq. (5.4.9) and the general FCCS cross-correlation function in Eq. (5.4.2), the normalized FCCS auto and cross-correlation functions can finally be written as:

$$g_{\text{gg}}(\tau) = \frac{\eta_{\text{g}}^2 G_{\text{gg}}^{\text{A}}(\tau) + \eta_{\text{g}}^2 G_{\text{gg}}^{\text{AB}}(\tau)}{\eta_{\text{g}}^2 \cdot (\langle c_{\text{A}} \rangle + \langle c_{\text{AB}} \rangle)^2} \quad (5.4.12)$$

$$g_{\text{rr}}(\tau) = \frac{\eta_{\text{r}}^2 \cdot [G_{\text{rr}}^{\text{B}}(\tau) + G_{\text{rr}}^{\text{AB}}(\tau)] + \kappa_{\text{gr}}^2 \eta_{\text{g}}^2 \cdot [G_{\text{gg}}^{\text{A}}(\tau) + G_{\text{gg}}^{\text{AB}}(\tau)] + 2\kappa_{\text{gr}} \eta_{\text{r}} \eta_{\text{g}} G_{\text{gr}}^{\text{AB}}(\tau)}{(\kappa_{\text{gr}} \eta_{\text{g}} \langle c_{\text{A}} \rangle + (\eta_{\text{r}} + \kappa_{\text{gr}} \eta_{\text{g}}) \cdot \langle c_{\text{AB}} \rangle + \eta_{\text{r}} \langle c_{\text{B}} \rangle)^2} \quad (5.4.13)$$

$$g_{\text{gr}}(\tau) = g_{\text{rg}}(\tau) = \frac{\eta_{\text{g}} \eta_{\text{r}} G_{\text{gr}}^{\text{AB}}(\tau) + \kappa_{\text{gr}} \eta_{\text{g}} \eta_{\text{r}} G_{\text{gr}}^{\text{A}}(\tau) + \kappa_{\text{gr}} \eta_{\text{g}}^2 \cdot G_{\text{gg}}^{\text{AB}}(\tau)}{(\eta_{\text{g}} \langle c_{\text{A}} \rangle + \eta_{\text{g}} \langle c_{\text{AB}} \rangle) \cdot (\kappa_{\text{gr}} \eta_{\text{g}} \langle c_{\text{A}} \rangle + (\eta_{\text{r}} + \kappa_{\text{gr}} \eta_{\text{g}}) \langle c_{\text{AB}} \rangle + \eta_{\text{r}} \langle c_{\text{B}} \rangle)} \quad (5.4.14)$$

The parameters η_{g} and η_{r} are usually estimated “on-the-fly” using Eq. (5.4.10) and the fluorescence intensities $\langle F_{\text{g}} \rangle$ and $\langle F_{\text{r}} \rangle$ measured during the experiment. They can also be determined with separate samples that contain only green or only red fluorophores.

The non-normalized cross-correlation factors $G_{\gamma\rho}^{\text{X}}(\tau)$ have a similar form as the results in the last section 5.4.1. In addition they include the different MDE parameters (e.g. PSF widths w_{r} , w_{g} and PSF lengths z_{g} , z_{r}). For a confocal MDE and normal diffusion with flow the result is:

$$G_{\gamma\rho}^{\text{X}}(\tau) = \langle c_{\text{X}} \rangle \cdot \sqrt{\frac{8}{\pi^3}} \cdot \frac{\exp\left(-\frac{2(v_{\text{x}}\tau - \delta_{\text{x}})^2 + 2(v_{\text{y}}\tau - \delta_{\text{y}})^2}{8D_{\text{X}}\tau + w_{\gamma}^2 + w_{\rho}^2} - \frac{2(v_{\text{z}}\tau - \delta_{\text{z}})^2}{8D_{\text{X}}\tau + z_{\gamma}^2 + z_{\rho}^2}\right)}{(8D_{\text{X}}\tau + w_{\gamma}^2 + w_{\rho}^2) \cdot \sqrt{8D_{\text{X}}\tau + z_{\gamma}^2 + z_{\rho}^2}}, \quad (5.4.15)$$

where $\vec{\delta} = (\delta_{\text{x}}, \delta_{\text{y}}, \delta_{\text{z}})^{\text{T}}$ is the shift between the foci.

For 2-color SPIM-FCCS, the pixels are assumed to have the same size a in both color channels. The cross-correlation factor is again a product of three directional factors $G_{\gamma\rho}^{\text{X}}(\tau) = \langle c_{\text{X}} \rangle \cdot G_{\gamma\rho, \text{x}}^{\text{X}}(\tau) \cdot G_{\gamma\rho, \text{y}}^{\text{X}}(\tau) \cdot G_{\gamma\rho, \text{z}}^{\text{X}}(\tau)$, with equal expressions for the x - and y direction:

$$\begin{aligned} G_{\gamma\rho, \text{x}}^{\text{X}}(\tau) = & \frac{1}{2a^2} \cdot \left\{ \left[(a - v_{\text{x}}\tau + \delta_{\text{x}}) \cdot \operatorname{erf}\left(\frac{\sqrt{2} \cdot (a - v_{\text{x}}\tau + \delta_{\text{x}})}{\sqrt{8D_{\text{X}}\tau + w_{\gamma}^2 + w_{\rho}^2}}\right) - \right. \right. \\ & \left. \left. - 2(v_{\text{x}}\tau - \delta_{\text{x}}) \cdot \operatorname{erf}\left(\frac{\sqrt{2} \cdot (v_{\text{x}}\tau - \delta_{\text{x}})}{\sqrt{8D_{\text{X}}\tau + w_{\gamma}^2 + w_{\rho}^2}}\right) + (a + v_{\text{x}}\tau - \delta_{\text{x}}) \cdot \operatorname{erf}\left(\frac{\sqrt{2} \cdot (a + v_{\text{x}}\tau - \delta_{\text{x}})}{\sqrt{8D_{\text{X}}\tau + w_{\gamma}^2 + w_{\rho}^2}}\right) \right] + \right. \\ & \left. + \frac{\sqrt{8D_{\text{X}}\tau + w_{\gamma}^2 + w_{\rho}^2}}{\sqrt{2\pi}} \cdot \left[e^{-\frac{2(a - v_{\text{x}}\tau + \delta_{\text{x}})^2}{8D_{\text{X}}\tau + w_{\gamma}^2 + w_{\rho}^2}} - 2 \cdot e^{-\frac{2(v_{\text{x}}\tau - \delta_{\text{x}})^2}{8D_{\text{X}}\tau + w_{\gamma}^2 + w_{\rho}^2}} + e^{-\frac{2(a + v_{\text{x}}\tau - \delta_{\text{x}})^2}{8D_{\text{X}}\tau + w_{\gamma}^2 + w_{\rho}^2}} \right] \right\}. \quad (5.4.16) \end{aligned}$$

The expression for the z -direction is:

$$G_{\gamma\rho,z}^{\chi}(\tau) = \sqrt{\frac{2}{\pi}} \cdot \frac{\exp\left(-\frac{2(v_z\tau - \delta_z)^2}{8D_{\chi}\tau + z_{\gamma}^2 + z_{\rho}^2}\right)}{\sqrt{8D_{\chi}\tau + z_{\gamma}^2 + z_{\rho}^2}}. \quad (5.4.17)$$

In all cross-correlation factors above (confocal and SPIM), anomalous diffusion may be introduced by the replacement $D_{\chi}\tau \rightarrow \Gamma_{\chi}\tau^{\alpha}$. Lower-dimensional diffusion is implemented by leaving out one or two of the directional factors. Finally multi-component diffusion can be represented by a sum of two or more $G_{\gamma\rho}(\tau)$, which are parametrized with different diffusion coefficients.

Figure 5.15(a) shows plots of the two autocorrelation curves $g_{gg}(\tau)$, $g_{rr}(\tau)$ and the cross-correlation curve $g_{gr}(\tau)$ in Eqs. (5.4.12)-(5.4.14) for different relative dimer concentrations. The non-normalized cross-correlation function Eq. (5.4.15) for a 3-dimensional Gaussian MDE was used. The small cross-correlation amplitude in the first example is caused by the crosstalk, which was assumed to be 5% in these plots. The different amplitudes of the autocorrelation curves are caused by different MDE parameters for the two foci. From left to right the relative dimer concentration increases, and so does the amplitude of the cross-correlation function. Figure 5.15(b) shows a plot of the correlation-function amplitudes as a function of the relative dimer concentration. It depicts the non-linear dependence of the cross-correlation amplitude on $\langle c_{AB} \rangle$. The impact of a crosstalk decreases for increasing relative dimer concentration. Comparable curves can be obtained from the SPIM-FCCS model function.

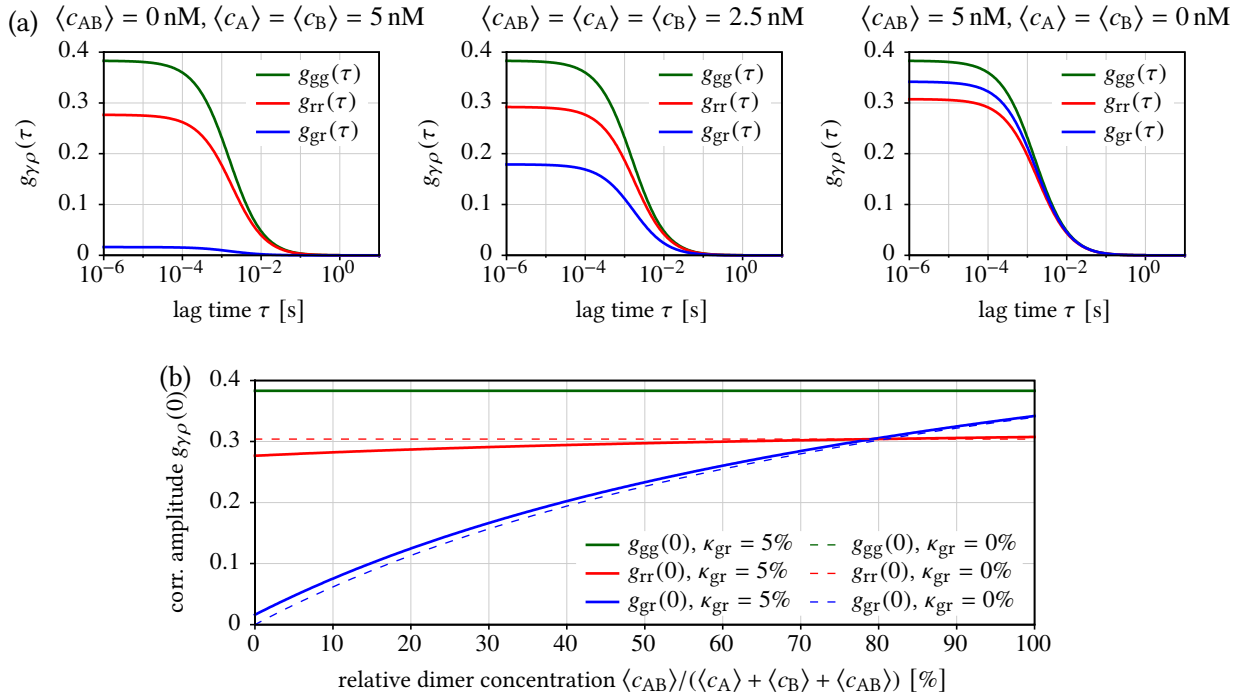
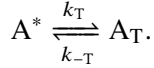


Figure 5.15. | (a) 2-color FCCS correlation curves for different concentrations of monomers (A,B) and dimers (AB). (b) Dependence of the zero-lag amplitudes $g_{\gamma\rho}(0)$ of the different correlation functions on the relative dimer concentration $\langle c_{AB} \rangle / (\langle c_A \rangle + \langle c_B \rangle + \langle c_{AB} \rangle)$ with $\langle c_A \rangle + \langle c_B \rangle + \langle c_{AB} \rangle = 5$ nM and $\langle c_A \rangle = \langle c_B \rangle$. The system equations (5.4.12)-(5.4.14) were used together with the model for a 3-dimensional Gaussian MDE in Eq. (5.4.15). Parameters: $D_A = D_B = D_{AB} = 10 \mu\text{m}^2/\text{s}$, $w_g = 250$ nm, $z_g = 1500$ nm, $w_r = 270$ nm, $z_r = 1620$ nm, $\vec{\delta} = 0$, $\eta_g = \eta_r = 1$, $\kappa_{gr} = 5\%$

5.5. Artifacts in fluorescence (cross-)correlation spectroscopy

5.5.1. Photophysics

So far the influence of the particle motion on the FCS autocorrelation curves was discussed. These motions lead to changes in fluorescence intensity, which are detected by FCS. As FCS is sensitive to any process, that causes such intensity fluctuations, also triplet state dynamics (see section 2.2) and other blinking dynamics in the fluorophores may be detected. Here it is assumed that the blinking results from kinetics in a two-state system with a fluorescent (bright) state A^* and a dark state A_T :



Here k_{-T} is the backward reaction rate and k_T the forward reaction rate. The population dynamics of such a reaction system is described by a set of two linear ordinary differential equations:

$$\frac{dc_{A^*}}{dt} = -k_T \cdot c_{A^*} + k_{-T} \cdot c_{A_T} \quad \text{and} \quad \frac{dc_{A_T}}{dt} = +k_T \cdot c_{A^*} - k_{-T} \cdot c_{A_T}. \quad (5.5.1)$$

The relative equilibrium population θ_T of the fluorescent species A^* can be calculated from $dc_{A^*}/dt = dc_{A_T}/dt = 0$ and the conservation of particle number $c_{A^*} + c_{A_T} = 1$:

$$\theta_T = \frac{k_{-T}}{k_T + k_{-T}} \quad (5.5.2)$$

Solving the system of differential equations Eq. (5.5.1) with the initial conditions $c_{A^*}(0) = 1$ and $c_{A_T}(0) = 0$ yields the time-dependent concentration of the fluorescent species A^* :

$$c_{A^*}(t) = \frac{k_T}{k_T + k_{-T}} + \left(1 - \frac{k_T}{k_T + k_{-T}}\right) \cdot e^{(k_T + k_{-T}) \cdot t} = (1 - \theta_T) + \theta_T \cdot \exp\left(-\frac{t}{\tau_T}\right). \quad (5.5.3)$$

In the last step, the equilibrium population θ_T was used and the lifetime τ_T of the dark state was introduced:

$$\tau_T = \frac{1}{k_T + k_{-T}}. \quad (5.5.4)$$

In FCS this means that in a system with $\langle N_\chi \rangle$ particles in the focus that may undergo a photophysical blinking reaction, at any time only $\theta_T \cdot \langle N_\chi \rangle$ particles are visible. On timescales much larger than τ_T , this effectively reduces the molecular brightness $\eta_{\gamma,\chi}$ with no influence on the single-species autocorrelation curve. In contrast, if the observed lag times τ are of the same order as τ_T , the triplet dynamics will show up as an additional exponential decay term in the autocorrelation function. To write this in an analytical form, the PDEs, which describe the motion of the particles have to be extended with the reaction dynamics in Eq. (5.5.1). Usually the contributions by molecular motion and by blinking are separable and an ansatz of the form $\delta c_\chi(t) \cdot \delta \phi_\chi(t)$ can be used. Here $\delta c_\chi(t)$ describes fluctuations due to particle motion and $\delta \phi_\chi(t)$ describes fluctuations due to blinking. As $\delta c_\chi(t)$ and $\delta \phi_\chi(t)$ are statistically independent, also the concentration autocorrelation separates into two independent factors

$$\langle \delta c_\chi(t) \cdot \delta c_\chi(t + \tau) \rangle \cdot \langle \delta \phi_\chi(t) \cdot \delta \phi_\chi(t + \tau) \rangle \propto G_\chi^X(\tau) \cdot T^X(\tau).$$

The second factor has to fulfill the boundary conditions $T^X(0) = 1/(1 - \theta_T)$ and $T^X(\infty) = 1$. Together with Eq. (5.5.3) this finally yields the following substitution rule to incorporate a blinking process into an FCS autocorrelation curve [72, 84, 217]:

$$G_{\gamma\gamma}^X(\tau) \rightarrow G_{\gamma\gamma}^X(\tau) \cdot T^X(\tau) \quad \text{with} \quad T^X(\tau) = \frac{1 - \theta_{T,\chi} + \theta_{T,\chi} \cdot \exp[-\tau/\tau_{T,\chi}]}{1 - \theta_{T,\chi}}. \quad (5.5.5)$$

Figure 5.16 illustrates the effect of blinking dynamics on a FCS autocorrelation function. The additional decay component is easily distinguishable, as long as the blinking and diffusion timescales differ significantly.

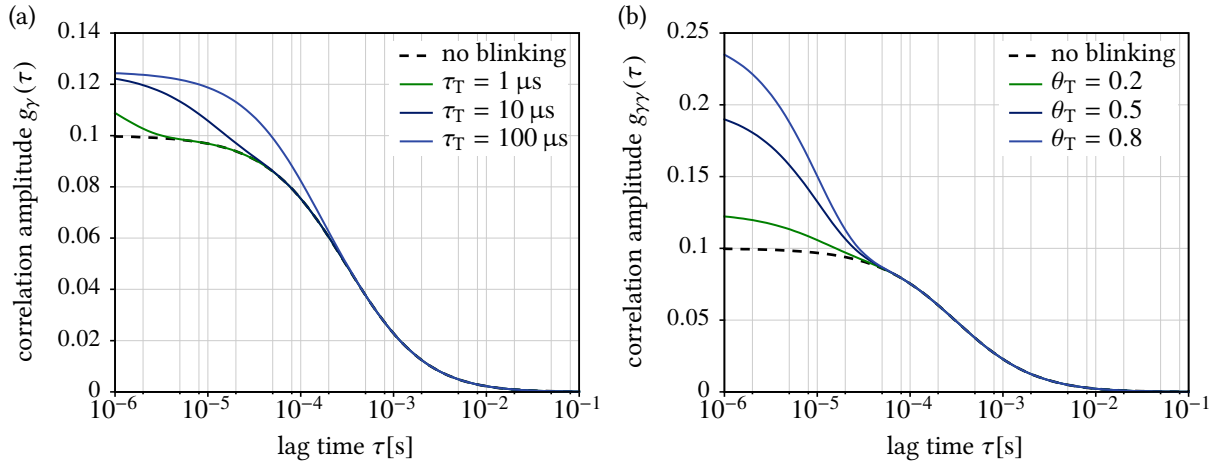


Figure 5.16. | Influence of fluorophore blinking on the confocal FCS autocorrelation function for 3D diffusion. Plot parameters: $\langle N_x \rangle = 10$, $D_x = 50 \mu\text{m}^2/\text{s}$, $\kappa_\gamma = 6$, $w_\gamma = 250 \text{ nm}$. In (a): $\theta_T = 0.2$ and in (b): $\tau_T = 10 \mu\text{s}$.

5.5.2. Constant background signal

One of the most common artifacts in FCS/FCCS is a constant offset $F_{\text{back},\gamma}$ on the average fluorescence signal. This is usually caused by the dark count rate of the used detectors, by an artificial offset of a camera or simply by non-shielded ambient light. When an offset is present, the measured fluorescence signal $F_{\text{meas},\gamma}(t)$ can be formally split into three contributions:

$$F_{\text{meas},\gamma}(t) = F_{\text{back},\gamma} + F_\gamma(t) = \underbrace{\langle F_\gamma \rangle + F_{\text{back},\gamma}}_{=: \langle F_{\text{meas},\gamma} \rangle} + \delta F_\gamma(t). \quad (5.5.6)$$

Here $F_\gamma(t) = \langle F_\gamma \rangle + \delta F_\gamma(t)$ is the signal emitted by the fluorescing particles and $\langle F_{\text{meas},\gamma} \rangle$ is the actually measured offset. The fluctuations $\delta F_\gamma(t)$ are not altered by the background signal. In most situations the background is negligible $F_{\text{back},\gamma} \ll \langle F_\gamma \rangle$. But especially at low concentrations and dim fluorophores, it can have a significant influence. The FCCS cross-correlation function $g_{\gamma\rho}(\tau)$ from Eq. (5.4.1) (p. 66) can be extended to incorporate $F_{\text{back},\gamma}$. Then it is denoted as the measured cross-correlation function $g_{\text{meas},\gamma\rho}(\tau)$, to distinguish it from the ideal function $g_{\gamma\rho}(\tau)$:

$$\begin{aligned} g_{\text{meas},\gamma\rho}(\tau) &= \frac{\langle \delta F_\gamma(t) \cdot \delta F_\rho(t + \tau) \rangle}{(\langle F_\gamma \rangle + F_{\text{back},\gamma}) \cdot (\langle F_\rho \rangle + F_{\text{back},\rho})} = \\ &= \underbrace{\frac{\langle F_\gamma \rangle \cdot \langle F_\rho \rangle}{(\langle F_\gamma \rangle + F_{\text{back},\gamma}) \cdot (\langle F_\rho \rangle + F_{\text{back},\rho})}}_{\text{background contribution}} \cdot \underbrace{\frac{\langle \delta F_\gamma(t) \cdot \delta F_\rho(t + \tau) \rangle}{\langle F_\gamma \rangle \cdot \langle F_\rho \rangle}}_{\text{ideal cross-correlation } g_{\gamma\rho}(\tau)}. \end{aligned} \quad (5.5.7)$$

Figure 5.17 shows the magnitude of this background contribution in the special case of an autocorrelation function ($\gamma \equiv \rho$). The relative change in correlation amplitude due to the background is less than 2%, if $F_{\text{back},\gamma}/\langle F_\gamma \rangle < 1\%$, which is typically not detectable within the measurement error. For $F_{\text{back},\gamma}/\langle F_\gamma \rangle < 5\%$, this change is $< 10\%$ and therefore still negligible.

A correction of the background contribution is possible, if $F_{\text{back},\gamma}$ and $\langle F_\gamma \rangle$ are known. The background is typically measured before the actual experiments, using a sample without fluorescent particles. The fluorescence intensity $\langle F_\gamma \rangle = \langle F_{\text{meas},\gamma} \rangle - F_{\text{back},\gamma}$ can be estimated from the average intensity $\langle F_{\text{meas},\gamma} \rangle$

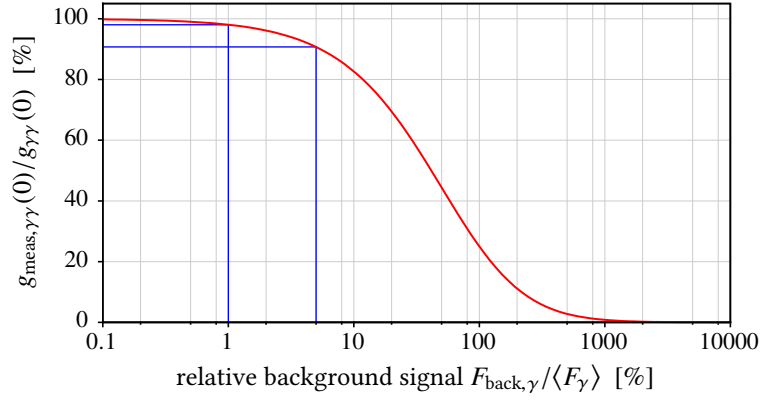


Figure 5.17. | Influence of a constant background signal on the FCS autocorrelation amplitude $g_{\gamma\gamma}(0)$.

measured during the data acquisition. Then Eq. (5.5.7) can be further rewritten:

$$g_{\text{meas},\gamma\rho}(\tau) = \frac{(\langle F_{\text{meas},\gamma} \rangle - F_{\text{back},\gamma}) \cdot (\langle F_{\text{meas},\rho} \rangle - F_{\text{back},\rho})}{F_{\text{meas},\gamma} \cdot F_{\text{meas},\rho}} \cdot \frac{\langle \delta F_{\gamma}(t) \cdot \delta F_{\rho}(t + \tau) \rangle}{\langle F_{\gamma} \rangle \cdot \langle F_{\rho} \rangle}. \quad (5.5.8)$$

In this form, the reduction of the correlation amplitude can be incorporated in any fit model, or it can be corrected for before the evaluation.

5.5.3. Detector afterpulsing

Afterpulsing is a common artifact in single photon detectors, such as SPADs or photomultiplier tubes (see section 4.1.1). In FCS it becomes visible as a fast decay in the first few measured lag times τ . In Ref [218] Zhao et al. propose a theoretical treatment of this artifact. Each incident photon has a certain probability $p_{\text{AP}}(\tau)$ to emit an afterpulse after a timespan τ . The function $p_{\text{AP}}(\tau)$ typically decays very fast on the timescale of a few microseconds [105, 219]. Then the measured fluorescence intensity $F_{\text{meas},\gamma}(t)$ can be written as a function of the afterpulse-free intensity $F_{\gamma}(t)$ and $p_{\text{AP}}(\tau)$ [218, 219]:

$$F_{\text{meas},\gamma}(t) = F_{\gamma}(t) + \int_{-\infty}^0 p_{\text{AP}}(t - t') \cdot F_{\gamma}(t') dt' = F_{\gamma}(t) + \int_0^{\infty} p_{\text{AP}}(t') \cdot F_{\gamma}(t - t') dt'. \quad (5.5.9)$$

The time-averaged intensity is slightly higher than the ideal intensity:

$$\langle F_{\text{meas},\gamma} \rangle = \langle F_{\gamma} \rangle + \underbrace{\langle F_{\gamma} \rangle \cdot \int_0^{\infty} p_{\text{AP}}(t') dt'}_{=:A} = (1 + A) \cdot \langle F_{\gamma} \rangle. \quad (5.5.10)$$

Here $A < 1$ is the absolute probability that an incident photon generates an afterpulse. It can be shown that afterpulsing is an additive effect on the autocorrelation curve [218]:

$$g'_{\gamma}(\tau) \approx g_{\gamma}(\tau) + G_a \cdot p_{\text{AP}}(\tau) \quad (5.5.11)$$

Here G_a is a constant with $G_a \propto 1/\langle F_{\gamma} \rangle$, i.e. at a high number of incident photons, afterpulsing is less important. In that case other contributions to the correlation function outweigh the correlation by the

afterpulses. Fit functions, that are often used to describe $p_{AP}(\tau)$ are:

$$p_{AP}(\tau) = p_0 \cdot \exp\left(-\frac{\tau}{\tau_{AP}}\right) \quad \text{or} \quad (5.5.12)$$

$$p_{AP}(\tau) = p_0 \cdot \tau^{-\beta_{AP}}. \quad (5.5.13)$$

Here τ_{AP} and β_{AP} describe the shape of the decay functions and p_0 is the amplitude of the decays. The latter is usually combined with G_a into a single fit parameter. With Eq. (5.5.11), afterpulsing can be incorporated into any FCS model function. The decay parameters τ_{AP} and β_{AP} can be determined in an independent experiment with a light source with no inherent intensity correlations (e.g. a filament lamp, or light emitting diode (LED)), or from the dark count signal. As the shape $p_{AP}(\tau)$ only depends on detector properties, these parameters may subsequently be used to describe the afterpulsing in an FCS measurement, which uses the same detector. Then only the amplitude p_0 needs to be a free fitting parameter.

Another method to remove afterpulsing is to split the fluorescence signal onto two detectors. The autocorrelation function is then estimated as the cross-correlation between these detectors. As the afterpulsing contributions of the two detectors are statistically independent, they will not appear in the cross-correlation function. Thus also two-color or two-focus cross-correlation functions are free of afterpulsing artifacts.

5.5.4. Fluorophore depletion

As mentioned in section 2.3 many fluorophores bleach after a certain lifetime, if they are illuminated with light of their excitation wavelength. This causes artifacts in FCS/FCCS. Two regimes have to be distinguished: If particles bleach while they are inside the illuminated focus, the measured diffusion times $\tau_{D,\chi}$ are reduced and diffusion coefficients $D_\chi \propto 1/\tau_{D,\chi}$ are overestimated, as particles seem to dwell shorter the focus. This model can be used as long as the average intensity $\langle F_\gamma \rangle$ stays constant over time. It is e.g. valid, as long as enough non-bleached fluorophores are available in the vicinity of the focus and the bleaching probability is small. If these condition are not met, the reservoir of fluorophores is slowly depleted. This leads to a slow decrease of the average intensity $\langle F_\gamma \rangle$ with time. In this case, the autocorrelation analysis is no longer valid, as the intensity time series is no longer stationary. Then also the average variance is not stationary over the whole time series, as the particle number slowly decreases. This case is especially common in LSFM based experiments, because not only a small focal volume, but a whole plane of the sample is bleached.

Ries et al. published a method that can be used to compensate the effect of reservoir depletion [96, 98]. Before calculating the correlation functions, the measured intensity time trace $F_{\text{meas},\gamma}(t)$ is corrected for the bleaching, using a transformation that pins the average intensity to a fixed value and alters the variance, so that it stays constant over the whole time series. The transformation proposed in [98] is:

$$F_\gamma^{(c)}(t) = \frac{F_{\text{meas},\gamma}(t)}{\sqrt{f(t)/f(0)}} + f(0) \cdot \left(1 - \sqrt{f(t)/f(0)}\right), \quad (5.5.14)$$

where $F_\gamma^{(c)}(t)$ is the corrected fluorescence intensity and $f(t)$ is a function, which describes the decay of the fluorescence intensity $F_{\text{meas},\gamma}(t)$. Under the assumption that $F_{\text{meas},\gamma}(t) = F_\gamma(t) \cdot f(t)$, it can be shown that the mean and the variance of $F_\gamma^{(c)}(t)$ equal that of the idealized photon intensity $F_\gamma(t)$ without bleaching. For $f(t)$ any suitable function can be chosen that describes the decay in $F_\gamma^{(c)}(t)$. When low bleaching rates are encountered, a simple single-exponential function is suitable:

$$f(t) = f_0 \cdot \exp(-t/\tau_B). \quad (5.5.15)$$

In FCCS experiments photo-bleaching converts some of the double-labeled molecules into single-labeled molecules. This changes the balance between the two species. Therefore the measured relative cross-correlation amplitude will be lower than expected without bleaching. This effect is not completely compensated by the bleach correction proposed above, as Eq. (5.5.14) is used on each color channel independently. The reduced cross-correlation amplitude has to be taken into account, when interpreting the fit results [98, 220].

Figure 5.18 shows the application of Eq. (5.5.14) to simulated FCS data. If the fluorescence signal does not drop by more than 50%, the bleach correction can fully regain the initial curve. If the bleaching is stronger, the reconstructed correlation amplitude is higher than the ideal amplitude, thus the measured average particle number in the focus is underestimated. The correct diffusion coefficients can however still be extracted from the bleach-corrected autocorrelation curves.

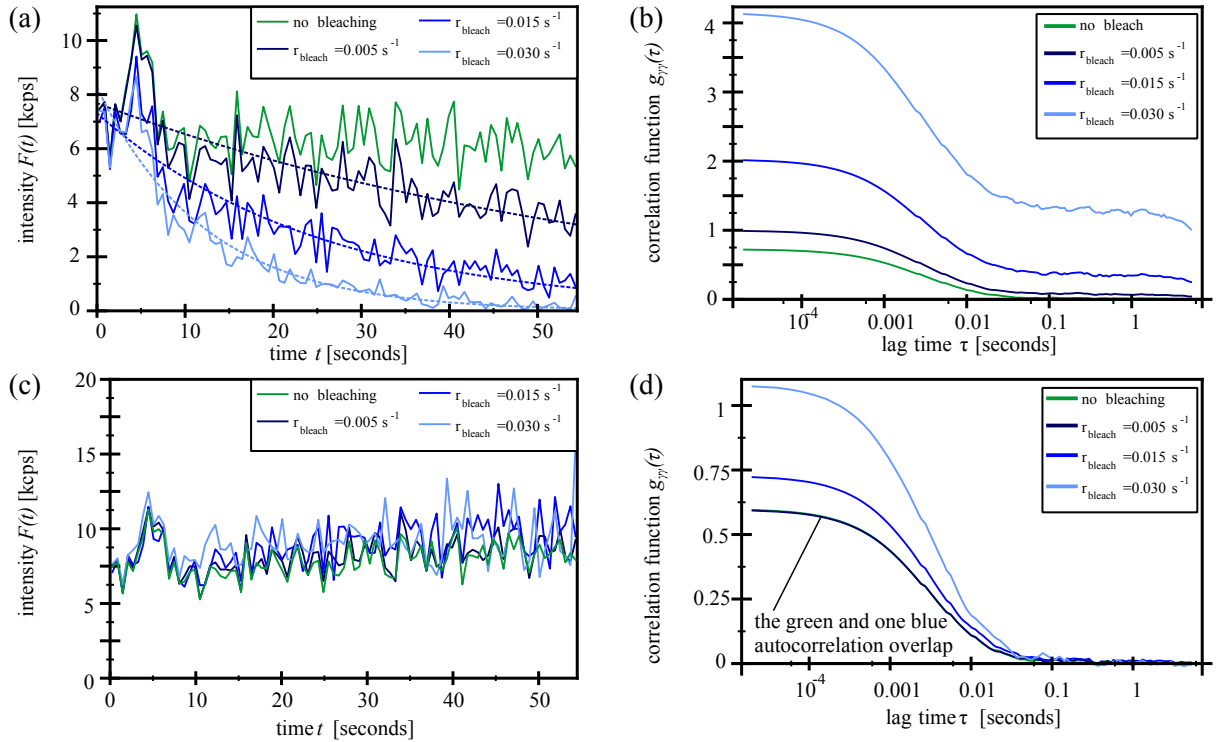


Figure 5.18. | Simulation of SPIM-FCS curves showing a depletion of the fluorophores by bleaching. (a,b) Fluorescence-intensity time-traces and corresponding autocorrelation curves for different depletion rates r_{bleach} . (c,d) The same data as in (a,b), but after a bleach correction with Eq. (5.5.14). Note: The shown autocorrelation curves have a similar noise signature, as they are all created from the same set of simulated particle trajectories. The FCS simulation software in appendix B.1 was used.

Part III.

Development of a SPIM-FCS/FCCS instrument

6. Hardware setup of the SPIM

During this PhD project, a selective plane illumination microscope (SPIM) for application to imaging FCS and imaging FCCS was planned and built. Initially the setup was planned for a SPAD array as image sensor only, but later an EMCCD camera was added. This chapter will describe the complete hardware setup, including the microscope optics in section 6.1. The SPIM sample chamber and the mounting of different samples into the microscope is described in section 6.2. Finally section 6.4 introduces the SPAD arrays used during this thesis, including their readout electronics.

6.1. Optics setup

6.1.1. Overview

An overview of the light sheet microscope, which was built for this thesis, is shown in Fig. 6.1 and Fig. 6.2. The setup is based on the design published by Greger et al. in Ref. [119]. It was modified to match single cells as samples and for the use of EMCCD cameras and SPAD arrays with pixel sizes a in the range of 20 – 30 μm . The microscope is a simple SPIM, as introduced in section 3.3.4. The light sheet is shaped by the combination of a cylindrical lens and an air microscope objective. Two laser beams of different colors are combined for the illumination in a novel way, which allows precise alignment of two differently colored light sheets. A water dipping high-numerical aperture (NA) objective is used to

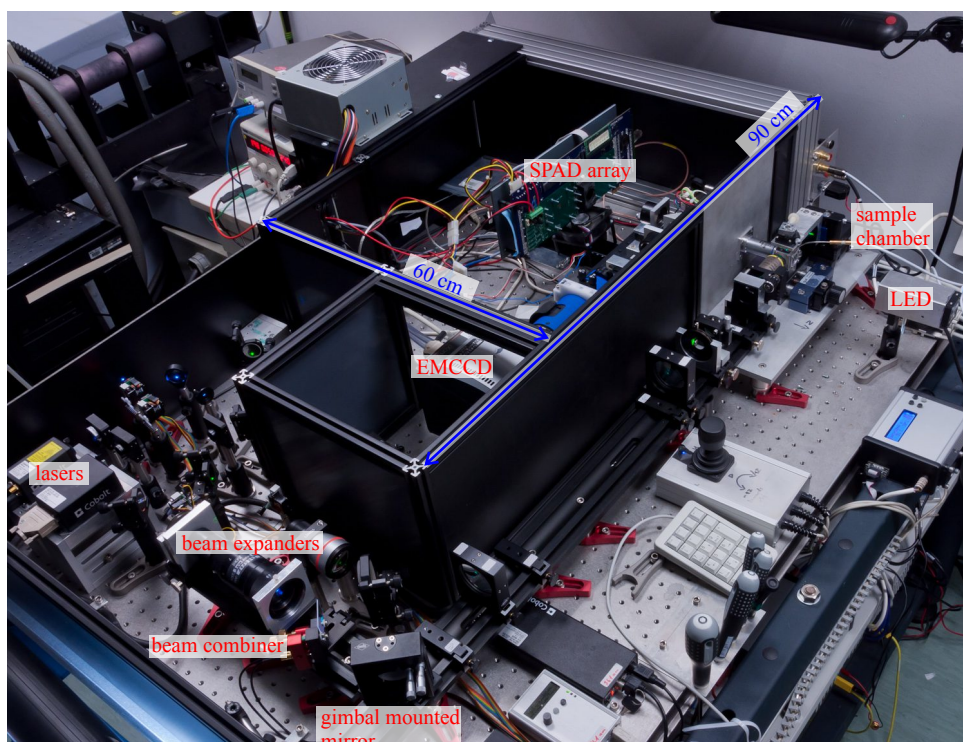


Figure 6.1. | Photograph of the SPIM instrument.

detect fluorescence. Two image sensors are available in two parallel detection beam paths: one path for an Andor iXon X3 860 EMCCD camera and one path for a non-commercial SPAD array. The samples are mounted on motorized linear positioning stages, which allow full sample translation along the x -, y - and z axis (see coordinate systems in Fig. 6.2). The sample is immersed in a buffer solution (e.g. Hank's balanced salts solution (HBSS) or deionized water), which fills a temperature-controlled stainless steel sample chamber. Most components of the microscope are computer controlled, so data acquisition

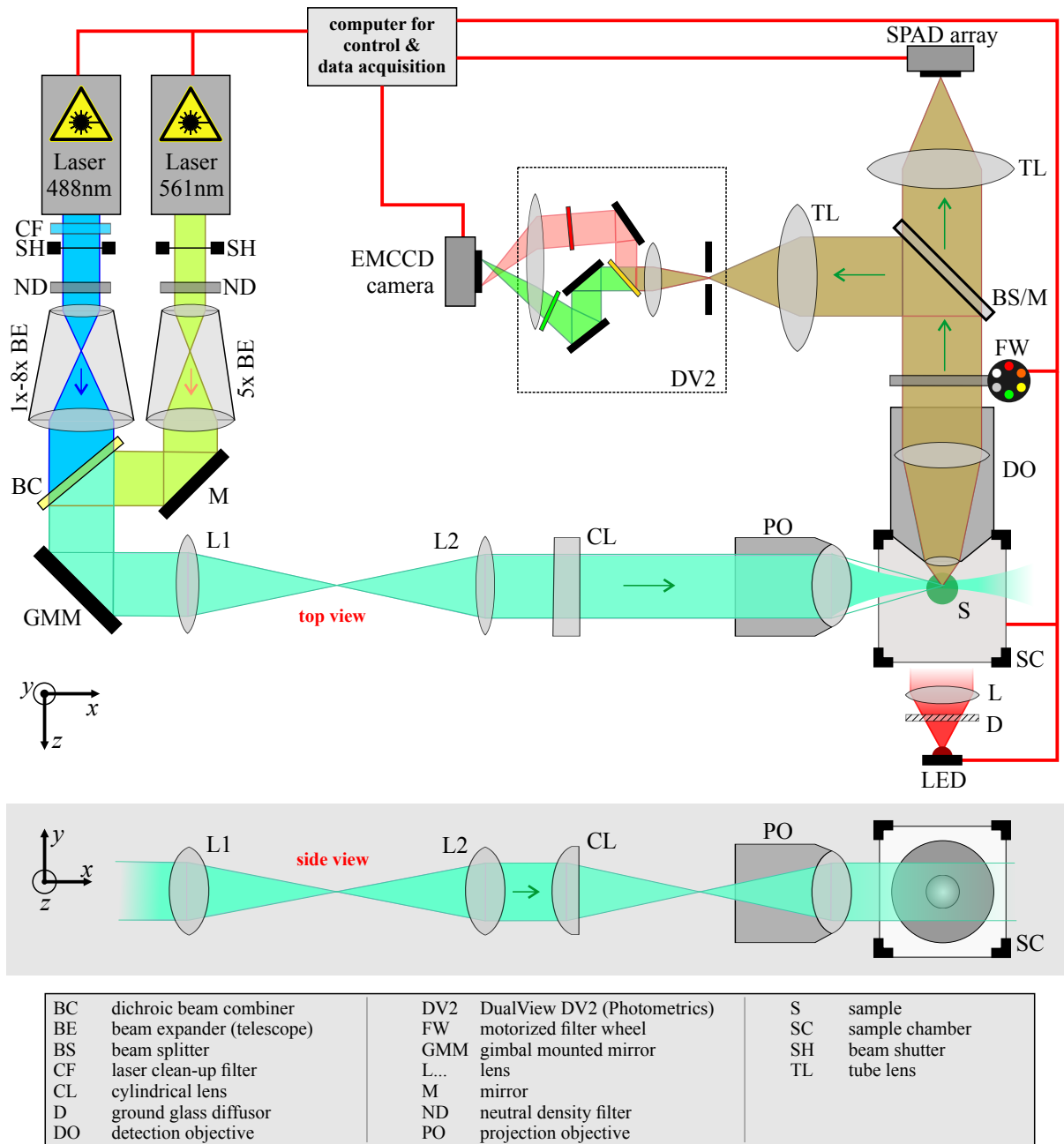


Figure 6.2. | Schematic of the optics and computer control system of the SPIM instrument. The upper part of the image shows a top view of the instrument. The lower, shaded part shows a side-view of the illumination beam path. Optical components are labeled with abbreviations that are explained in the legend. Red lines are signal connection to the control computer. A detailed list of all used components can be found in appendix Tab. A.1.

is mostly automated. Detailed descriptions of each part of the optics will be given in the following subsections and a complete list of the components is available in appendix Tab. A.1.

The microscope has gone through several stages of development with many of the optical components changing. Here the final configuration is described. Previous versions are mentioned only if they are of importance to understand measurements described later in this thesis.

6.1.2. Light sheet shaping

Two lasers can be used simultaneously to excite fluorescence in the sample, a diode laser emitting a maximum output power of 60 mW at 488 nm and a diode-pumped solid state (DPSS) laser emitting a maximum output power of 25 mW at 561 nm. Until end of 2013 the blue laser was a DPSS laser with a maximal output-power of 25 mW and a central wavelength of 491 nm. All of these lasers emit a beam with a clean $TEM_{0,0}$ -mode with a $1/e^2$ -half width of $w_{\text{Laser}} = 0.7$ mm. The blue laser beam is cleaned up with a bandpass filter, as both blue lasers contain a certain amount of green light, which might disturb measurements. The green laser spectrum is sufficiently narrow and no further cleaning is necessary. Both lasers are always operated at their specified output-powers, because in this case the output power and the beam mode are more stable. In order to change the light intensity, the beams are attenuated separately with neutral density filters. Each laser beam can be switched using a custom-built laser shutter consisting of a black anodized aluminum beam dump glued to a model aircraft servo motor.

Before combining the two beams with a dichroic mirror, each beam is expanded 5-fold with a separate beam expander. This allows for a very fine control of the focus of each light sheet separately and ultimately to overlap the two light sheets perfectly. The blue laser beam is used as a reference and the green is combined with it, using a 2" silver mirror and a dichroic beam combiner plate, which is mounted on a kinematic mirror mount with piezo-electric fine adjustment for accurate control. The piezo actuators on the beam combiner are also crucial to allow for a precise overlay of the two light sheets.

After beam expansion and combination, the light sheet is formed, as shown in detail in Fig. 6.3. The

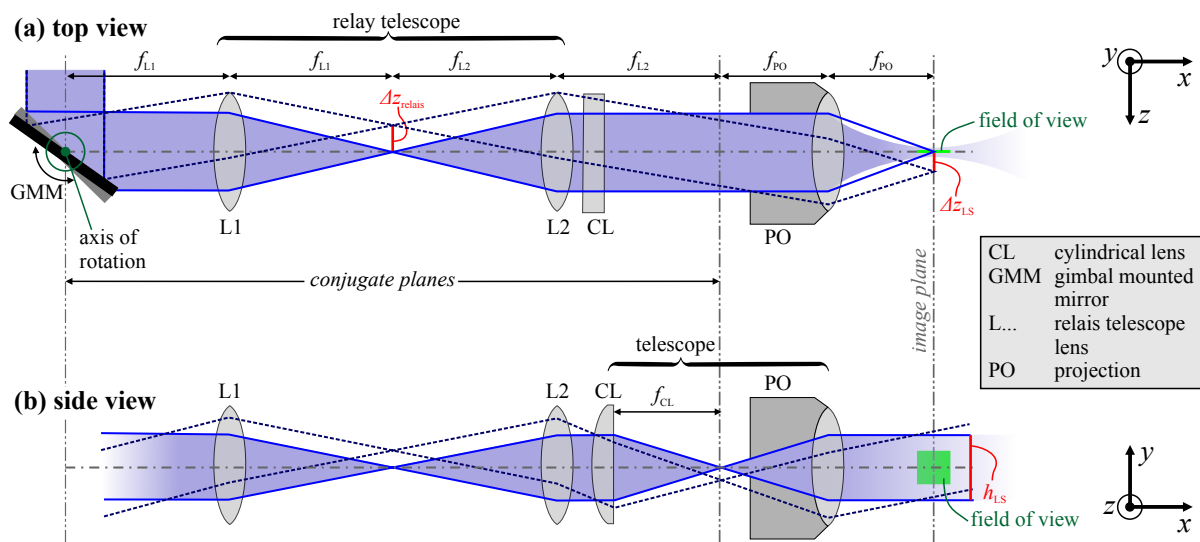


Figure 6.3. | Detailed schematic of the illumination beam path: (a) top view and (b) a side view.

The labels of all optical components are the same as in Fig. 6.2. Δz_{\dots} : beam shifts in z -direction, h_{LS} : the height of the light sheet (y -direction) and f_l : focal lengths of the lens l . The coordinate systems are defined on the right and are the same as in Fig. 6.2. The green line and rectangle represent the field of view of the detection optics.

laser beams are deflected by a gimbal mounted mirror (GMM) and are then relayed via two achromatic lens doublets L1 and L2 with focal lengths $f_{L1} = 150$ mm and $f_{L2} = 250$ mm to an assembly consisting of a cylindrical lens (CL) with focal length $f_{TL} = 150$ mm and the projection objective (PO). The distance of the last two lenses is adjusted, so that the focus of the cylindrical lens coincides with the back-focal point of PO. Viewed from the side, CL and PO form a telescope, which produces a parallel beam. Viewed from the top, the incident laser beam is not affected by the cylindrical lens and the projection objective focuses the light. This method to form a light sheet is described in detail in Ref. [119]. It allows to use high-quality microscope objective lenses for light sheet generation, which produce thinner light sheets with less optical aberrations. In the setup described here, PO is a 10x Nikon microscope objective with a numerical aperture of $NA = 0.3$ and a focal length of $f_{PO} = 20$ mm. The resulting light sheet geometry is sketched in Fig. 6.4. The minimal width w_{LS} of the light sheet in a sample medium with refractive index $n = 1.33$, can then be calculated using Eq. (3.1.11) (p. 29):

$$\lambda = 488 \text{ nm} : w_{LS} \geq 1.33 \mu\text{m} \quad \text{and} \quad \lambda = 561 \text{ nm} : w_{LS} \geq 1.53 \mu\text{m}. \quad (6.1.1)$$

The depth of focus, i.e. the longitudinal $1/e^2$ -half width, is accordingly

$$\lambda = 488 \text{ nm} : d_{LS} \geq 20.2 \mu\text{m} \quad \text{and} \quad \lambda = 561 \text{ nm} : d_{LS} \geq 23.2 \mu\text{m}. \quad (6.1.2)$$

The laser beams are initially expanded 5-fold and then by another factor of f_{L2}/f_{L1} determined by the relay telescope consisting of L1 and L2. The cylindrical lens and the projection objective form a final telescope, which determines the height of the light sheet, as viewed from the side:

$$h_{LS} = 5 \times w_{\text{Laser}} \cdot \frac{f_{L2}}{f_{L1}} \cdot \frac{f_{PO}}{f_{CL}} \approx 0.78 \text{ mm}. \quad (6.1.3)$$

These light sheet parameters fit well to the approximate size of a single mammalian epithelial cell, which is typically about $20 \mu\text{m}$ in diameter and $5 - 10 \mu\text{m}$ high. If the light sheet is approximated by a Gaussian beam, its width along the direction of propagation is given by [178]

$$w_{LS}(x) = w_{LS} \cdot \sqrt{1 + \left(\frac{x}{\text{FWHM}_{LS,z}}\right)^2} \underset{\text{using Eq. (3.1.11)}}{\approx} w_{LS} \cdot \sqrt{1 + \left(\frac{x}{1.58 \cdot d_{LS}}\right)^2}. \quad (6.1.4)$$

At $x = \pm d_{LS}$ the width $w_{LS}(x)$ has increased by a factor ~ 1.18 . As the depth of focus d_{LS} is larger than a single cell, a thin light sheet is achieved everywhere in the sample.

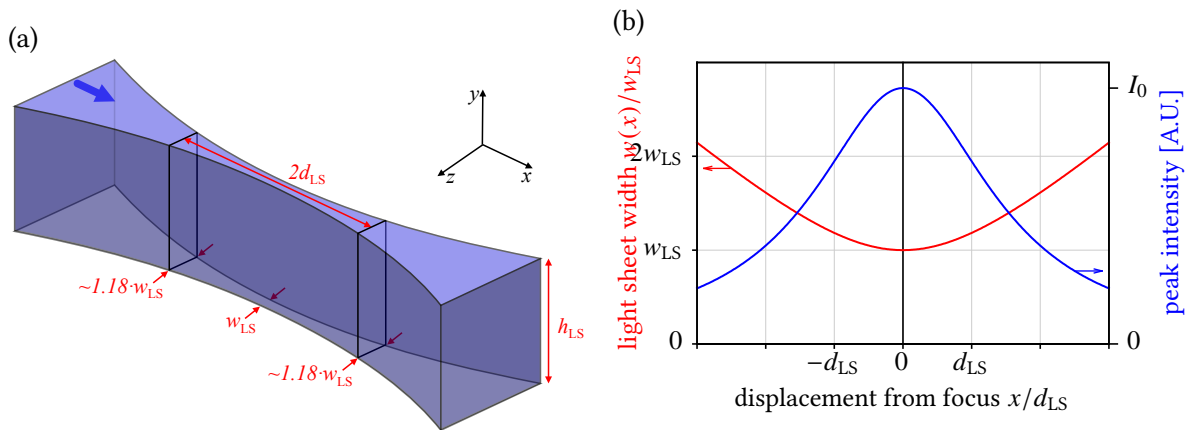


Figure 6.4. | (a) Geometry of a light sheet. (b) Width (blue) and peak intensity (red) of a light sheet as a function of the displacement x from the focus (at $x = 0$). For (b) Eq. (6.1.4) was evaluated.

The relay telescope serves for two purposes. As stated above, it increases the beam width in order to fill the back aperture of PO. In addition it images the pivot point of the gimbal mounted mirror GMM into the back focal plane of the projection objective. As indicated in Fig. 6.3(a), the mirror can be used to move the light sheet in z -direction. If the mirror GMM is tilted by an angle ϕ_{GMM} out of its ideal 45° position, the light sheet moves in z -direction by (cf. Eq. (3.1.1))

$$\Delta z_{\text{LS}} = \frac{f_{\text{PO}} \cdot f_{\text{L1}}}{f_{\text{L2}}} \cdot \tan(\phi_{\text{GMM}}) \underset{\phi_{\text{GMM}} \ll 90^\circ}{\approx} 12 \mu\text{m}/^\circ. \quad (6.1.5)$$

If the pivot point of GMM would not be conjugated to the back-focal point of PO, the shift Δz_{LS} would be the same, but the beam would show aberrations. This would lower the symmetry and quality of the light sheet.

6.1.3. Transmission illumination

In addition to the fluorescence images produced by the light sheet illumination, it is often useful to also acquire additional images with transmission illumination. To this purpose a high-power light emitting diode (LED) and a collimating lens have been added to the SPIM setup (see Fig. 6.2a). The light from the LED is homogenized by a ground glass diffuser. This simple setup generates an approximately uniform illumination of the field of view of the camera. Today high power LEDs are typically driven by switched buck-regulators, which can induce a residual fast blinking of the LED with the switching frequency. This blinking is typically in the range of 10 kHz – 10 MHz and could show up as an oscillation in the measured correlation curves. To circumvent this problem, a fully analog constant current sink was developed and is used to drive the LED. In addition the operating voltage of the circuit is filtered by a low-pass filter.

6.1.4. Detection system

The detection system is shown as an overview in Fig. 6.5 and as a detailed top view in Fig. 6.2(a). A water dipping objective (DO) with $\text{NA} = 1.0$ and a focal length $f_{\text{DO}} = 3.33 \text{ mm}$ is used to collect the fluorescence excited by the light sheet illumination. The objective has a magnification of $60\times$ and a long working distance of 2.8 mm . This gives enough space to mount the samples and to project the light sheet. The microscope is of the infinity corrected type, so the collected light is collimated by the objective (see section 3.1.1). The detection objective DO is fixed to a solid aluminum plate and cannot be adjusted (see Fig. 6.5). As DO does not move, it can easily be sealed against the sample chamber (see section 6.2). The alignment of the light sheet is done with the illumination beam path only. Behind DO, the collected fluorescence light passes a custom-built filter-wheel, with filters that limit the transmitted light to the desired detection range. Outside their transmission window these filters typically suppress any light with an optical density $OD > 5$. In addition, two notch filters can be mounted that specifically suppress the two laser lines with $OD = 4 \dots 6$. Details of the available filters are listed in Tab. A.1 in

sensor	type	format	pixel size a^2	sensor size	a at $60\times$	FOV at $60\times$
iXon X3 860	EMCCD	128×128	$24 \times 24 \mu\text{m}^2$	$3.07 \times 3.07 \text{ mm}^2$	400 nm	$51.2 \times 51.2 \mu\text{m}^2$
Radhard2	SPAD	32×32	$30 \times 30 \mu\text{m}^2$	$0.96 \times 0.96 \text{ mm}^2$	500 nm	$16 \times 16 \mu\text{m}^2$
CHSPAD	SPAD	128×512	$24 \times 24 \mu\text{m}^2$	$3.07 \times 12.29 \text{ mm}^2$	400 nm	$51.2 \times 204.8 \mu\text{m}^2$

Table 6.1. | **Geometric properties of the image sensors used.** The last two columns give the pixel size and the field of view (FOV) in the object plane at a magnification of $60\times$. The magnification is defined by the detection objective and the tube lens of the SPIM. Data for the SPAD arrays was taken from Refs. [186, 192, 193].

the appendix A.1. Finally the light is refocused onto the image sensor with a tube lens (focal length $f_{TL} = 200$ mm). As image sensor either an Andor EMCCD camera iXon X3 860, or one of two available SPAD arrays are used. The EMCCD camera is water cooled, in order to reduce unwanted shaking due to the internal fan. A consumer-grade computer water cooling system is fully sufficient to cool the camera.

The basic geometrical parameters of these sensors are summarized in Tab. 6.1 and details on the SPAD arrays will be given in section 6.4. Again, except for the SPAD array Radhard2, these parameters perfectly match the typical cell size and the parameters of the light sheet. According to Eq. (3.1.11), the detection objective with $NA = 1$ gives an approximate $1/e^2$ -half width of the PSF of

$$\lambda = 525 \text{ nm} : w_{fl,xy} \approx 431 \text{ nm} \quad \text{and} \quad \lambda = 600 \text{ nm} : w_{fl,xy} \approx 492 \text{ nm}.$$

This matches the pixel size of the sensors in the object plane, which is 400 – 500 nm for all image sensors in Tab. 6.1.

As shown in Fig. 6.2(a), the actual setup of the detection optics is more complicated than described above: The fluorescence light is split into two perpendicular beam paths, which allows to use two image sensors simultaneously. The splitting is done with a 50 : 50 beam splitter (BS) on a rotation mount. Each image sensor then has its own tube lens. The beam splitter may also be replaced by a simple mirror, if only the EMCCD camera is used or it can be completely removed, if only the SPAD array is in operation. The beam splitters are mounted on magnetic bases that allow a quick and reproducible replacement also during operation.

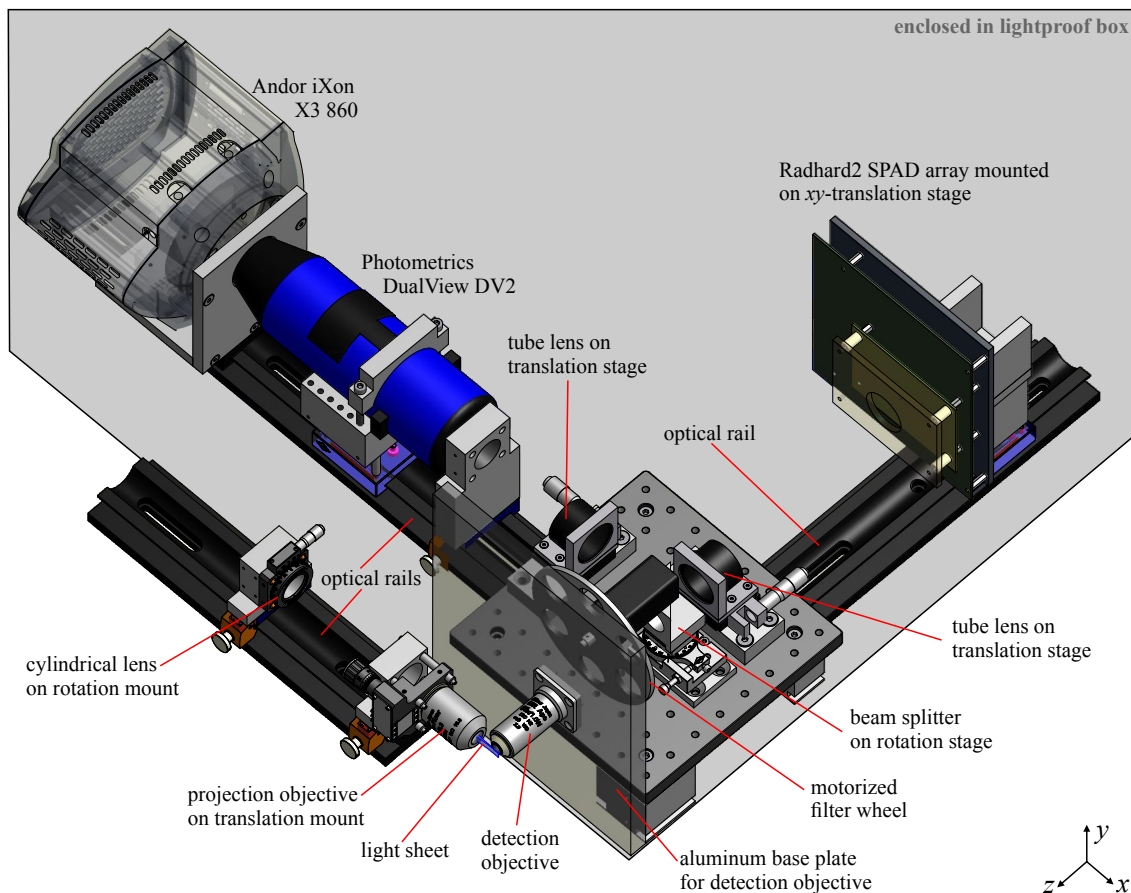


Figure 6.5. | Overview of the detection assembly. The gray area in the background of the figure symbolizes the lightproof box.

All components in the detection beam path are mounted on optical rails that allow to quickly translate them along their respective optical axis and to easily replace any component. Rather than shielding ambient light by tubes around the beam paths, the whole construction is mounted inside a black and lightproof box. This makes alignment and modifications easy, as the position of any components is not limited by tubes. Also the SPAD arrays are simply mounted on top of a printed circuit board without a surrounding “proper” camera housing.

At the time of writing only the beam path of the EMCCD camera is equipped with a commercial dual-view device (Photometrics DualView DV2), as described in section 3.1.3. It is fitted with a filter module that splits the fluorescence light at 565 nm. Emission filters further narrow the detection windows for short and long wavelengths. They are matched to the spectra of eGFP (transmission between 500 nm and 550 nm) and mRFP1 (transmission above 593 nm) and optimized to produce a minimal crosstalk of eGFP into the red channel. The DV2 can be switched to a bypass mode, where the incident light is simply relayed through the whole device. A small loss of a few percent of intensity is still observed, as the light needs to pass two additional lenses. If the DualView is used, the filter wheel is typically set to a 488 nm long pass filter, which does not interfere with the filter set inside the DV2, but suppresses the blue excitation light. The notch filters are still used.

The DualView DV2 needs to be realigned daily to ensure that corresponding pixels in the left and right color channel are imaging the same volume in the object space. This is accomplished by imaging an electron microscopy grid using the transmission illumination. Figure 6.6(a,b) illustrate the geometry of the grids and the adapter used to mount them. The grids are made from a thin copper sheet, that is laminated onto a transparent plastic foil. Two different grids with hole spacing of 16.9 μm and 12.7 μm were used (AGG2785C and AGG2786C, Agar Scientific). Figure 6.6(c) shows an image of a perfectly aligned grid. Two complementary methods were used to better judge how well the green (left) and red

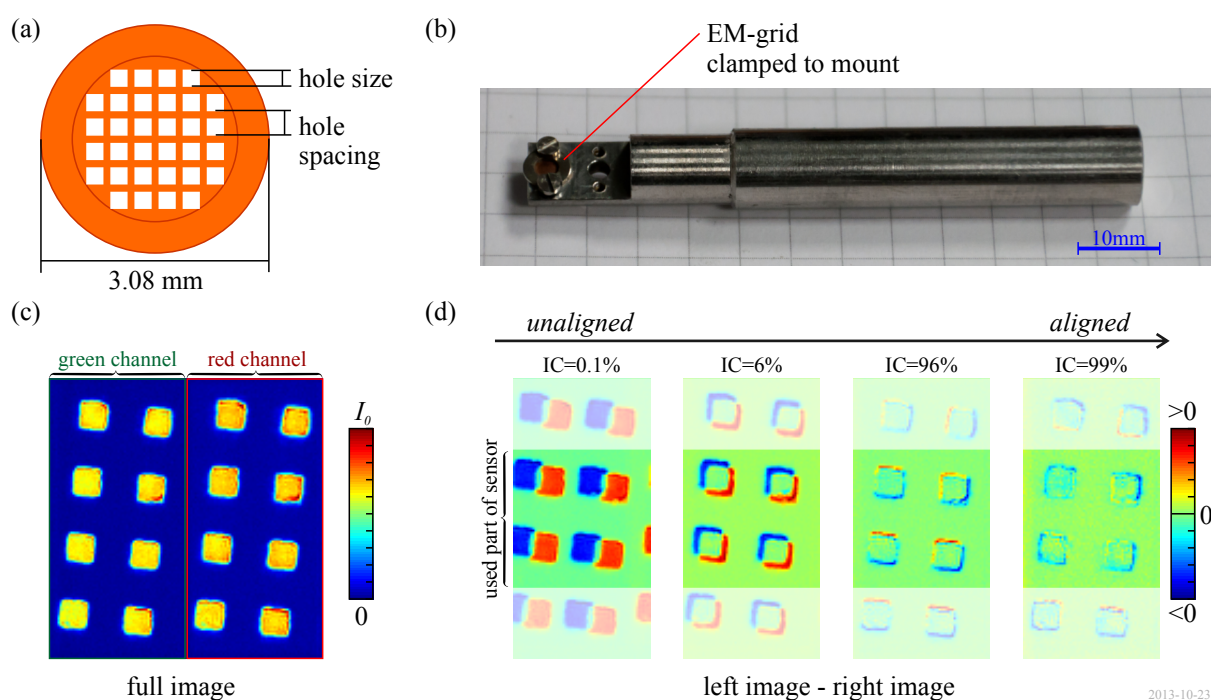


Figure 6.6. | Illustration of the alignment of the DualView DV2. (a) Geometry of the electron microscopy grid. (b) Photograph of the sample holder used to mount the grid. (c) Full frame transmission image of the grid, if the DualView is perfectly aligned. (d) Alignment of the DualView in four steps. For each step, the left half image is subtracted from the right half image and the image cross-correlation coefficient Eq. (6.1.6) is given. All images are shown in false colors.

(right) half images $\{L(x, y)\}$ and $\{R(x, y)\}$ ($x = 1 \dots W$, $y = 1 \dots H$) are aligned. During the alignment, the two half images are subtracted and $\{L(x, y) - R(x, y)\}$ is displayed on a false color scale, as shown in Fig. 6.6(d) and the image cross-correlation coefficient IC is calculated and maximized. The coefficient IC is defined as

$$\text{IC} = \frac{\sum_{x,y} (L(x, y) - \bar{L}) \cdot (R(x, y) - \bar{R})}{W \cdot H \cdot \sqrt{\sigma_L^2 \cdot \sigma_R^2}}, \quad (6.1.6)$$

where \bar{L} and \bar{R} are the average intensities in the left and right half image and σ_L^2 and σ_R^2 are the variances of intensity:

$$\bar{L} = \frac{1}{W \cdot H} \cdot \sum_{x,y} L(x, y) \quad \text{and} \quad \sigma_L^2 = \frac{1}{W \cdot H} \cdot \sum_{x,y} (L(x, y) - \bar{L})^2. \quad (6.1.7)$$

With this setup, the two half images are shifted with the mirrors inside the DualView, until IC is maximized and ideally reaches IC = 100%.

6.2. Sample chamber and sample mounting

6.2.1. Sample Chamber

Finally this section will describe the sample chamber and sample mounting. Both are illustrated in Fig. 6.7. The sample chamber is made from non-corrosive seawater-resistant stainless steel. It can be filled with ~ 7 ml of sample buffer or deionized water. On three sides the chamber is closed by glass windows ($\varnothing = 20 - 22$ mm No.1 cover slips, thickness 0.13 – 0.16 mm). The light sheet and the light from the transmission illumination enter the chamber through these glass windows, therefore they should be of good optical quality. The glass cover slips are pressed against the chamber using aluminum plates and soft o-rings in between. For a better seal, the o-rings were coated with a silicone grease (Baysilicone Paste “low viscous”, GE Bayer Silicones). During longer measurements, a small amount of precipitations accumulates in the sample chamber and also sticks to the glass surfaces. So the windows are typically exchanged before every series of measurements.

Finally the chamber is pushed in ($-z$)-direction against the cone of the water dipping detection objective, using a manual translation stage. Sealing is again done with a soft o-ring which sits in a notch in the sample chamber. Only glass, stainless steel, rubber o-rings and the detection objective are in contact with the liquid inside the sample chamber, preventing any corrosion of the device. If required, the chamber can easily be cleaned and autoclaved.

The sample chamber went through several revisions. First versions were made from aluminum. It turned out that this material caused corrosion problems, especially when deionized water and buffers with higher salt concentrations were used. The passivation layer of aluminum oxide is not resistant enough to protect the material below. Also the sample buffer was slowly polluted with reaction products with the aluminum.

A new version of the sample chamber is currently in planning stage. It will exhibit in- and outlets, that will facilitate the exchange of sample buffer during operation. This will also allow constant perfusion with fresh buffer and an easy control of buffer properties, such as temperature and pH. Finally this would permit the study of samples under changing environmental conditions, for example by adding a drug.

Samples can be mounted in the chamber, hanging from a motorized translation stage. In addition a manual rotation stage allows for full freedom of positioning. For multi-view imaging this manual stage could be replaced with a motorized version. A sample mounting adapter is attached to the rotation

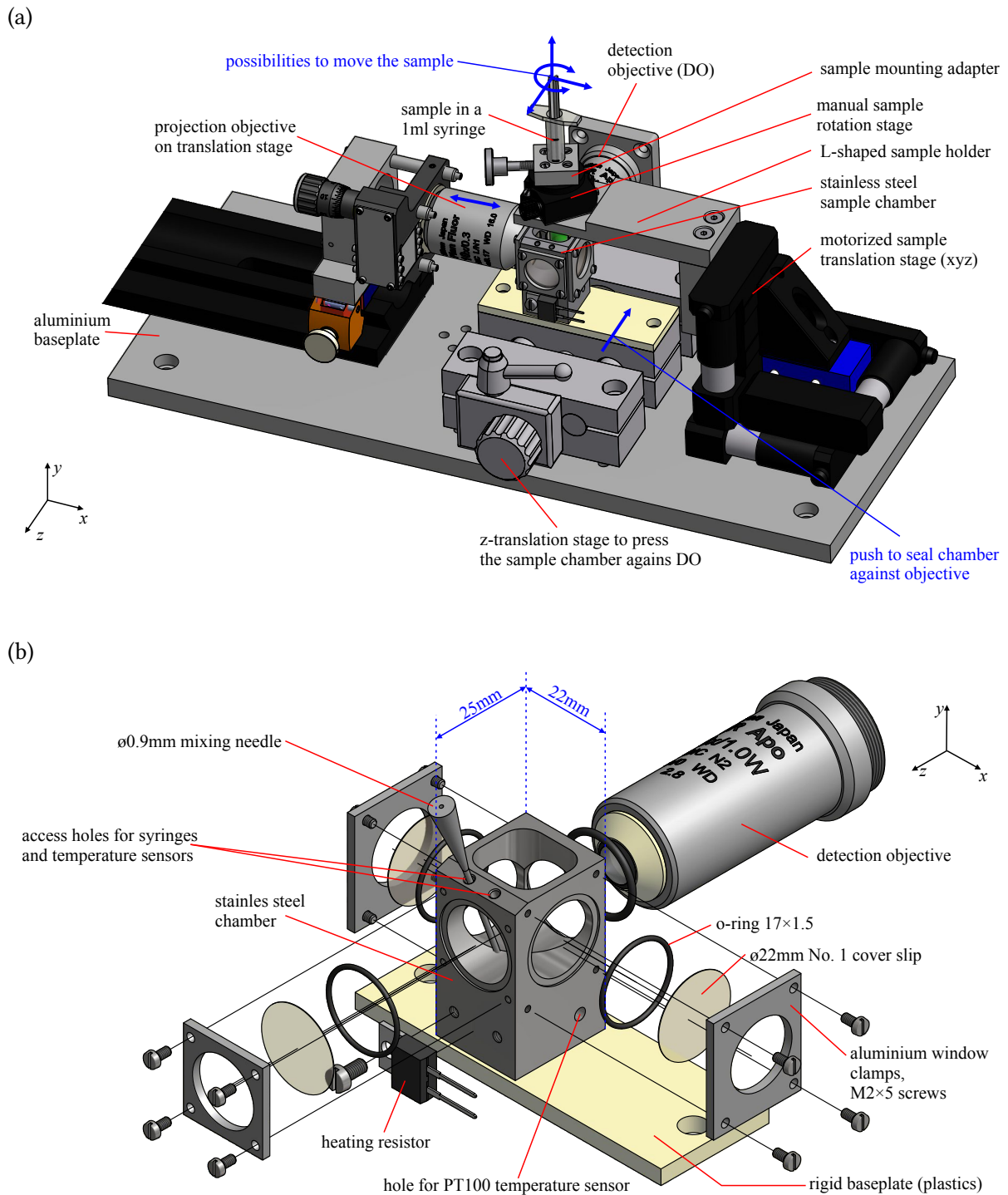


Figure 6.7. | (a) 3D view of the sample chamber and the sample mounting assemblies. (b) Exploded view of the sample chamber.

stage. Different types of sample holders can be fixed to this adapter; a syringe is shown as an example in Fig. 6.7(a). The different possibilities of sample mounting are discussed in detail in section 6.2.3.

Finally the sample chamber features two access holes (see Fig. 6.7b), which allow to use mixing needles ($\varnothing = 0.9$ mm) to exchange the liquid in the chamber. But also a PT100 temperature sensor ($\varnothing = 1.5$ mm) can be inserted in this way.

6.2.2. Temperature control

The temperature of the sample chamber can be stabilized with an external temperature control circuit (PI loop). It uses a resistive heater (resistance: $4.7 - 10 \Omega$), which exerts a heating power of $1 - 10 \text{ W}$. The heater is attached to the base of the chamber. For thermal isolation from the rest of the microscope, the chamber is mounted on a baseplate consisting of plastic material. Two PT100 sensors are mounted in the steel base of the sample chamber and immersed in the sample buffer. Their readout circuits [221] allow to measure the temperature to a precision of $\pm 0.1 \text{ }^\circ\text{C}$ and an accuracy fully determined by the sensor specification (typically $0.3 - 0.5 \text{ }^\circ\text{C}$). The properties of the temperature control system are described in Fig. 6.8. Figure 6.8a shows the heating and cooling of the sample chamber for a target temperature of $38.5 \text{ }^\circ\text{C}$ in its base. Constant temperatures of $(38.1 \pm 0.1) \text{ }^\circ\text{C}$ in the metal base and $(37.2 \pm 0.1) \text{ }^\circ\text{C}$ in the liquid are reached after about 20 min of heating. The temperature drop between the liquid and the base is clearly noted, as well as the delay of a few minutes between the curves. Long-term measurements showed that these temperatures stay constant within the given precision for several hours. In Fig. 6.8(a) the temperature distribution inside the sample chamber is depicted. The samples are mounted in a region (black circle), where a target temperature of $37 \text{ }^\circ\text{C}$ is well achieved. For this measurement a small temperature sensor was moved in 2 mm steps through the sample chamber, while the temperature control circuit was activated. At each position it was allowed to equilibrate with the environment for a few minutes.

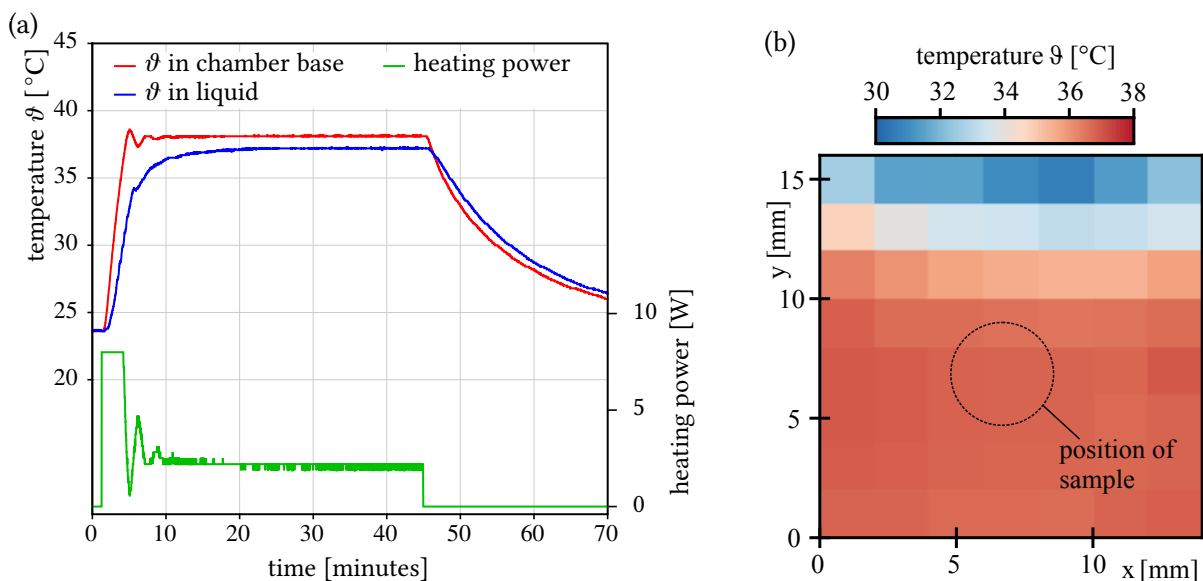


Figure 6.8. | **Properties of the temperature control system: (a) Heating curve and stability of the temperature. (b) Temperature distribution in the sample chamber.** The plot in (a) shows the temperature of the chamber base (red), of the liquid (blue) and the heating power (green), with and without temperature control (target temperature in the chamber base: $38.5 \text{ }^\circ\text{C}$, voltage across the 10Ω heating resistor: 9 V). The data in (b) were obtained by scanning a small temperature sensor in 2 mm steps through the chamber, with activated temperature stabilization. Before the temperature was measured at each point, the sensor was allowed to equilibrate for several minutes.

6.2.3. Sample mounting

The construction of the microscope and the sample chamber requires that the samples are mounted hanging from above. This prohibits to use standard mounting techniques developed for standard microscopes, where the samples are positioned on a horizontal support. Several mounting techniques

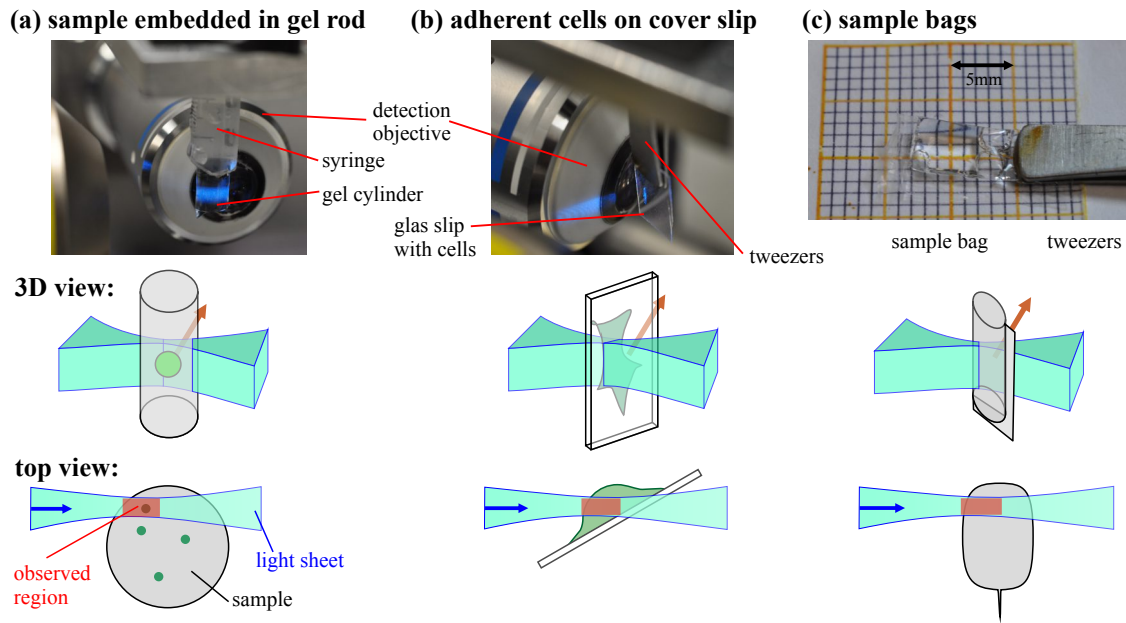


Figure 6.9. | Different methods for sample mounting in a SPIM: (a) samples embedded in a gel cylinder, (b) adherent cells on a cover slip, (c) sample bags for liquid samples.

for the type of SPIM used in this thesis have been discussed e.g. in Refs. [117, 222–224].

The three major mounting methods used here, are depicted in Fig. 6.9. Larger samples, such as embryos or cell spheroids, are commonly embedded in a gel cylinder, extruded from a syringe or a thin capillary. If the gel is prepared from culture medium, cells can easily survive this procedure. Usually low-melting agarose is used, which solidifies only at temperature below 40 °C. Also products, such as PhytaGel (P8169, Sigma-Aldrich) or Gelrite (Carl Roth GmbH) are used, which form a very stiff and clear poly-saccharide gel, if divalent ions (often Mg^{2+}) are present. Here this mounting technique was used for the determination of the PSF of the microscope with fluorescent microspheres (beads). The microspheres were embedded in a 0.5% PhytaGel cylinder, supplemented with 0.1% $MgSO_4$. The gel is extruded from a 1 ml syringe and is scanned in z -direction through the focus (for details, see appendix A.3.29).

Liquid samples, such as fluorophore solutions were mounted in small heat-sealed sample bags (~

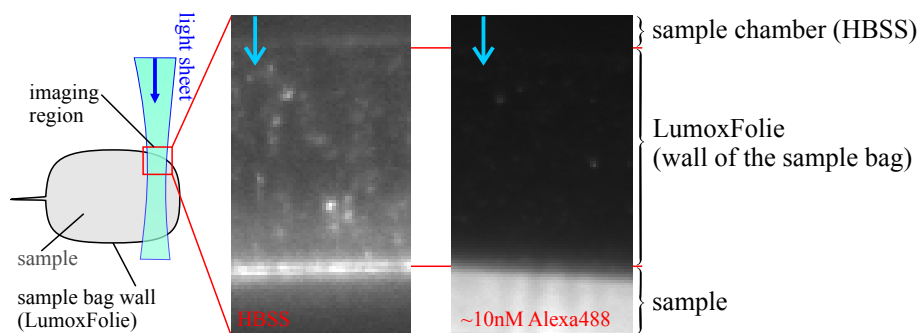


Figure 6.10. | Autofluorescence of sample bags made from LumoxFolie 25 M. The sample bag in (a) is filled with HBSS and the one in (b) with a ~10 nM solution of Alexa-488. The images were taken at high laser power ($\sim 200 \text{ W/cm}^2$), a moderate EM-gain of 50 and an exposure time of 100 ms using an EMCCD camera. The color scaling is different in both images, as can be seen by the virtually invisible autofluorescence on the rhs, if compared to a chemical fluorophore.

$5 \times 10 \times 2 \text{ mm}^3$, see Fig. 6.9c). These bags were prepared from LumoxFolie 25 M (Sarstedt AG & Co, [225]), which has a thickness of $25 \mu\text{m}$. Its refractive index resembles that of water ($n = 1.33$) and its autofluorescence is negligibly low (see Fig. 6.10). These properties make the sample bags virtually invisible to the light sheet and disturb the optical properties of microscope only minimally. LumoxFolie is also resistant to many chemicals, as its chemical structure is comparable to PTFE/teflon. The foil is provided with a functionalized surface: hydrophobic on one and hydrophilic on the other. The bags were heat-sealed using modified soldering tweezers, as described in appendix A.3.1. Each bag was filled with $30 - 50 \mu\text{l}$ of the liquid sample and held by self-closing tweezers.

Most of the biologic measurements for this thesis were performed with living and adherent mammalian cells. These were mounted, as depicted in Fig. 6.9(b) and in more detail in Fig. 6.11. Adherent cells (often epithelial cells) stick to the surface on which they grow, e.g. a glass cover slip or a petri dish. For measurements in a SPIM, cells were grown on small pieces of No. 3 glass cover glasses (size: $\sim 5 \times 10 \text{ mm}^2$, thickness $0.28 - 0.32 \text{ mm}$). A detailed protocol for this mounting technique is provided in appendix A.3.3). Cover slips made of different clear plastic materials were also tested. They showed, however, too much autofluorescence or were not stiff enough to be mounted properly. The glass slips were held by self-closing tweezers that were hanging in the sample chamber from the top. The chamber was filled with a buffer, such as HBSS, which sustains the cells over the duration of the measurements (typically $30 - 90 \text{ min}$ per cover slip). Other cell culture media can also be used, if they are not autofluorescent and do not scatter too much. The scattering is e.g. caused by added fetal calve serum. The medium or buffer should also be free of phenol-red, which is often used as pH indicator and enter the cells. Its spectral properties may interfere with accurate fluorescence measurements. For example, phenol red free RPMI medium has been used successfully for SPIM-FCS measurements. Most of the biologic measurements for this thesis were performed with living and adherent mammalian cells. These were mounted, as depicted in Fig. 6.9(b) and in more detail in Fig. 6.11. Adherent cells (often epithelial cells) stick to the surface on which they grow, e.g. a glass cover slip or a petri dish. For measurements in a SPIM, cells were grown on small pieces of No. 3 glass cover glasses (size: $\sim 5 \times 10 \text{ mm}^2$, thickness $0.28 - 0.32 \text{ mm}$). A detailed protocol for this mounting technique is provided in appendix A.3.3). Cover slips made of different clear plastic materials were also tested. They showed however too much autofluorescence or were not stiff enough to be mounted properly. The glass slips were held by self-closing tweezers that were hanging in the sample chamber from the top. The chamber was filled with a buffer, such as HBSS, which sustains the cells over the duration of the measurements (typically $30 - 90 \text{ min}$ per cover slip). Other cell culture media can also be used, if they are not autofluorescent and do not scatter too much. The scattering is e.g. caused by added fetal calve serum. The medium or buffer should also be free of phenol-red, which is often used as pH indicator and enter the cells. Its spectral properties may interfere with accurate fluorescence measurements. For example, phenol red free RPMI medium has been used successfully for SPIM-FCS measurements.

The bond between typical adherent cells (e.g. HeLa cells or Chinese hamster ovary cell (CHO-K1)) and the glass surface is strong enough so they stay in place throughout a measurement of a few minutes duration. Also the cells consist mostly of water, so the buoyancy partly counteracts a gravitational drag that may pull the cells down the cover slip. So if cell movement is detected, this is an active cellular process.

The glass slip is typically positioned under an angle of less than 45° with respect to the light sheet. This way light is not directly reflected into the detection objective and the cuts through the cells are a bit larger (see Fig. 6.11a). Compared to a standard (fluorescence) microscope, where cells are typically cut in parallel to the plane they grow on, the images of a SPIM look unusual. Examples are shown in Fig. 6.11(b,c). The first image shows a cell expressing eGFP, which is distributed throughout the whole cell. The darker region in the center is the nucleus with the nucleoli. A typical SPIM feature is the flat interface between cell and the glass cover slip, which is nicely visible due to the angled cut through the cell. Figure 6.11(c) shows a cell expressing PMT-eGFP, a fusion protein predominantly enriched in the

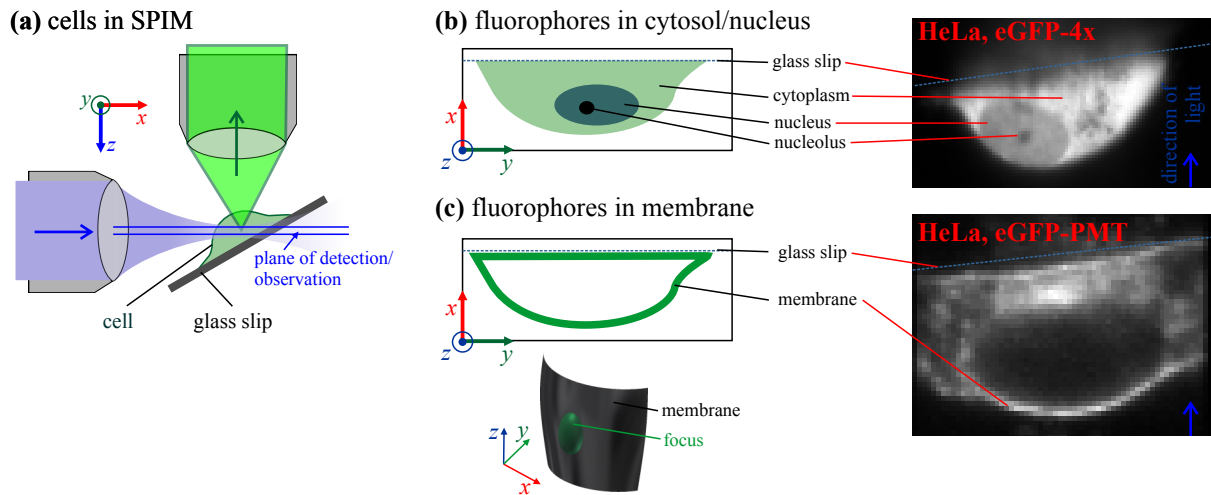


Figure 6.11. | **Details on adherent cells mounted in a SPIM.** (a) shows a top view of the SPIM with the cells mounted in it (not to scale). The light sheet illuminates a thin slice of the cell, which is depicted in (b) for a cell with fluorescent labels in the cytoplasm and in (c) for a cell with a labeled membrane. Compared to a standard fluorescence microscope, the images (rhs column) look unusual, but are explained by the angle under which the cells are sliced.

cellular membranes. Here especially the interface between buffer and cell sticks out as a thin fluorescent line.

6.3. Characterization of the optics

For SPIM-FCS and SPIM-FCCS measurements, an exact knowledge of the optical properties of the used microscope is essential, as these properties are directly used in the model functions described in chapter 5. The characterization described in this section is repeated every day, as the results may be influenced by the daily alignment. Two distinct measurements are performed: First the light sheet properties are directly observed and quantified (see section 6.3.1), then the PSF of the microscope is determined with a z -scan of fluorescent microspheres (see section 6.3.2).

6.3.1. Measuring light sheet properties

The light sheet can be imaged directly with a SPIM, if a mirror is mounted in the sample chamber that reflects the incoming light onto the image sensor [226, 227]. This is illustrated in Fig. 6.12(a). The light sheet can be sampled at different positions in the field of view, by moving the mirror in x -direction. Initially the mirror is positioned in the center of the field of view. This is accomplished by illuminating it with divergent white light through the projection objective. Tiny dirt spots on the mirror surface can be used to exactly position the mirror center in the center of the field of view. Then the blue light sheet is positioned in that center using the gimbal-mounted mirror GMM. Finally the green light sheet is superimposed on the blue one, using the piezo-controlled beam combiner.

The light sheet is imaged at equidistant x -positions of the mirror (step width: $1\ \mu\text{m}$). This results in a series of images, in which the light sheet is at its thinnest in the center and expands as described in section 6.1.2. Side-lobes are especially strong left of the focus. This was shown to be caused by the transmission of the light sheet through a stratified medium (lens \rightarrow air \rightarrow cover glass \rightarrow sample

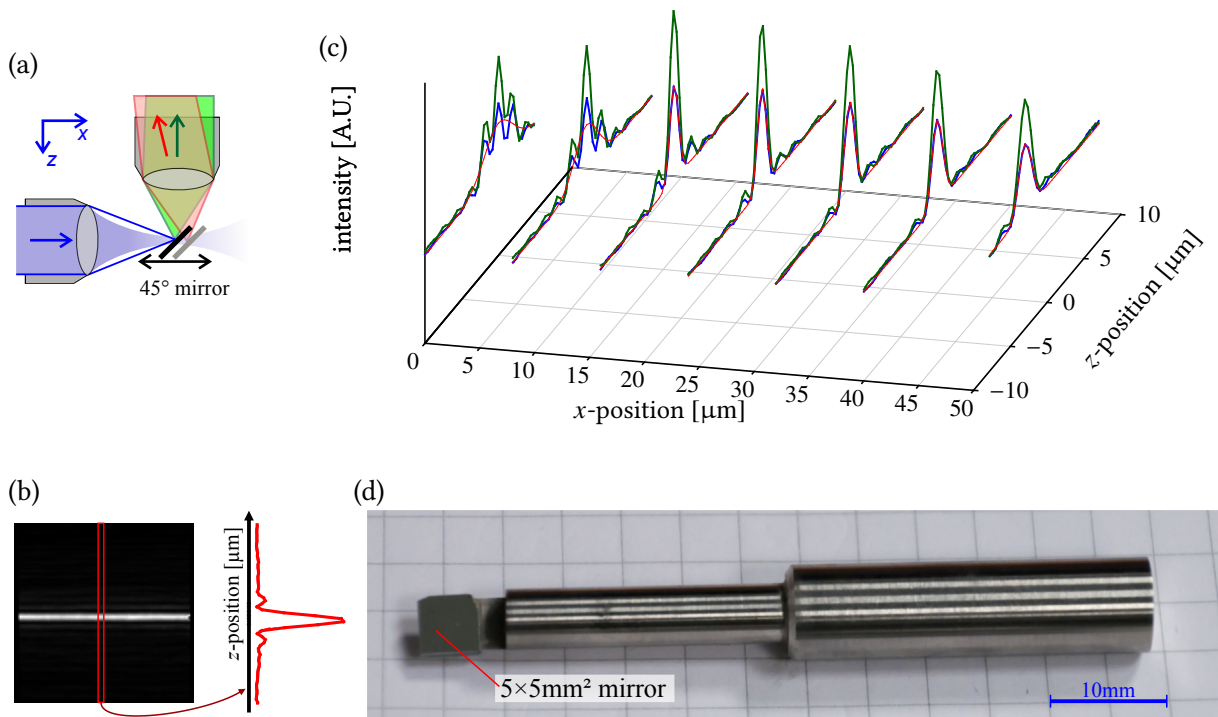


Figure 6.12. | **Light sheet analysis with a mirror.** (a) Principle setup in top-view. (b) Representative image, made with the mirror and a cut through the image, as marked by the red rectangle. (c) Different z -cuts through the light sheet as blue and green solid lines for the blue and green light sheet. Red lines are Gaussian fits to the blue light sheet data. (d) Sample holder with a $5 \times 5 \text{ mm}^2$ silver mirror.

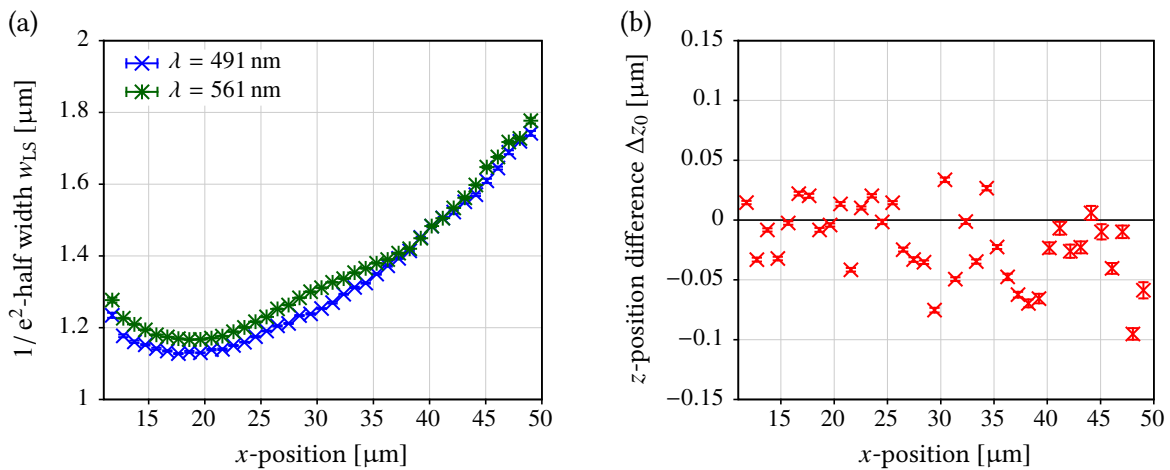


Figure 6.13. | **Typical properties of the light sheet of the SPIM described in this thesis.** (a) $1/e^2$ half width w_{LS} of the blue and green light sheets. (b) Center-center distance $\Delta z_0 = z_{0,491 \text{ nm}} - z_{0,561 \text{ nm}}$ between the maxima $z_{0,491 \text{ nm}}$, $z_{0,561 \text{ nm}}$ of the blue and the green light sheet.

medium) [228–231]. To quantify the properties of the light sheet, a Gaussian function

$$I_{\text{LS}}(z) = I_0 \cdot \exp\left(-2 \cdot \frac{(z - z_0)^2}{w_{\text{LS}}^2}\right) \quad (6.3.1)$$

is fitted to every column in every image of the series, as illustrated in Fig. 6.12(b). Then the parameters of all fits to one image (one x -position) are averaged and plotted, as shown in Fig. 6.13(a).

The projection objective can be moved in x direction to ensure that the thinnest part is a few micrometers left of the center of the field of view ($x = 25 \mu\text{m}$ in Fig. 6.13a,b). This minimizes the light sheet width and keeps the side lobe contributions in the central area $x = 15 \dots 35 \mu\text{m}$ low. Therefore SPIM-FCS measurements in this thesis were typically performed in this central area. The difference $\Delta z_0 = z_{0,491 \text{ nm}} - z_{0,561 \text{ nm}}$ of the center positions $z_{0,491 \text{ nm}}$ of the blue and $z_{0,561 \text{ nm}}$ of the green light sheet can be used to assess how well the laser beams are superimposed. Typically $|\Delta z_0| \leq 100 \text{ nm}$ is achieved, as shown in Fig. 6.13(b).

6.3.2. Measuring the molecular detection efficiency

Also the molecular detection efficiency function (MDE) of the microscope is determined before every measurement. After the light sheets have been aligned as described before, a PhytaGel cylinder containing a small amount of fluorescent microspheres is scanned along the z -direction in steps of 200 nm (see appendix A.3.2 for details on the gel). Figure 6.14 illustrates this method and shows a typical bead image obtained with it. In most measurements multi-fluorescent beads ($\varnothing = 100$ nm, T7279, Invitrogen) were used. Their matrix contains a mixture of four different fluorophores and are visible in both detection channels of the DualView optics.

The bead scan is evaluated using a MATLAB script¹, which performs the following steps:

1. The beads are automatically detected in the image stack, by searching the few brightest pixels in every 10th frame. If the DualView was used, the beads are located in the left half image only and the coordinates are reused for the right half image. The distances between all detected beads in the stack are summarized in a pair-distance matrix. Using this matrix, points are removed until all mutual distances are above a given threshold (typically 3 pixels). From any group of points that are mutually closer than 3 pixels, the brightest point is selected. The remaining points $\{(x_i, y_i, z_i)\}$ are used for further analysis.
2. A region of $\sim 10 \times 10 \times 60$ pixels around each point $\{(x_i, y_i, z_i)\}$ is cut from the whole image stack and several fits are performed to this data. In a DualView image, the following steps are repeated for the same position in the red color channel.
 - a) 1-dimensional Gaussian fits are performed to cuts along the x -, y - and z -axis, which pass through the brightest pixel in the region.
 - b) A 3-dimensional Gaussian fit is performed to the full data set. The Gaussian function has three different major axes, with (sorted) widths w_{large} , w_{mid} and w_{small} . The axes may be tilted and rotated from the basic coordinate axes.
 - c) A 1-dimensional Gaussian fit is performed to every cut along the x - and y - direction for different z -positions. This yields widths $w_x(z)$ and $w_y(z)$. The resulting width curves can be fit to Eq. (6.1.4).
3. The statistics (averages, standard deviations, histograms, etc.) of the results is calculated. In this stage beads are also filtered to exclude outliers and failed fits. The width and height of any bead

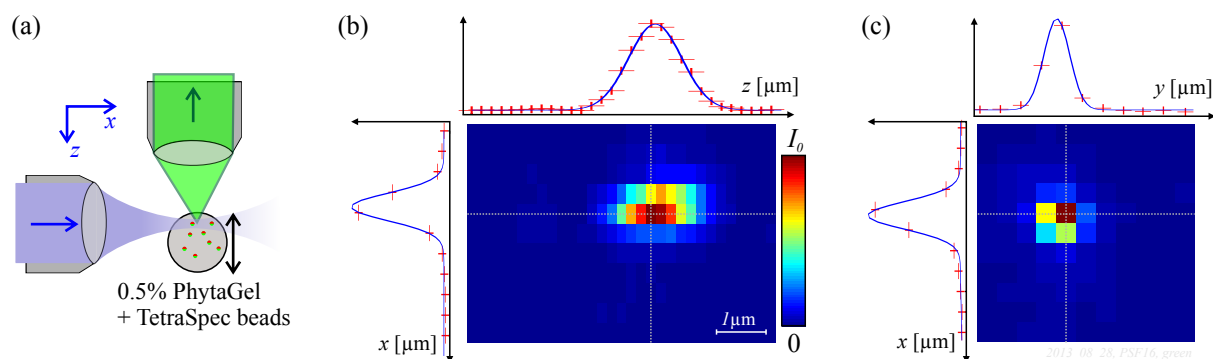


Figure 6.14. | Determination of the MDE of the microscope, using a bead scan. (a) Illustration of the bead scanning process. (b) xz -cut and (c) xy -cut through the MDE of the SPIM described here. Cuts along a single axis are shown besides and above the images.

¹This script is freely available under the terms of the GNU general public license 3.0 under <http://www.dkfz.de/Macromol/quickfit/beadscan.html>.

has to be in a predefined range (e.g. $0.3 \mu\text{m} < w_{\text{large}} < 3 \mu\text{m}$, or $0.1 \mu\text{m} < w_{\text{small}} < 2 \mu\text{m}$). For a stack acquired with the DualView optics, only those beads are used, for which the center-to-center distance $|\vec{\delta}|$ of the 3-dimensional Gaussian fits between the green and red color channel is below $1 \mu\text{m} \approx 3$ pixel.

This bead scan is acquired and evaluated before every day of measurements, in order to check the alignment quality. Also, some parameters of this fit will be used for the later imaging FCS calibration, described in section 8.1. Figure 6.15(a-c) shows a set of representative histograms of the three widths extracted from the 3-dimensional Gaussian fit. Also this evaluation quantifies the overlap of the MDEs in the green and red detection channels, by directly measuring the focus displacement $\vec{\delta} = (\delta_x, \delta_y, \delta_z)^T$. This is shown in Fig. 6.15(d-f). As the histograms and the averages over the plots show, the displacement is zero within one standard deviation. Comparable values are reached over a long timespan, as shown in Fig. 6.16 with bead scan results obtained on 38 days distributed over more than one year.

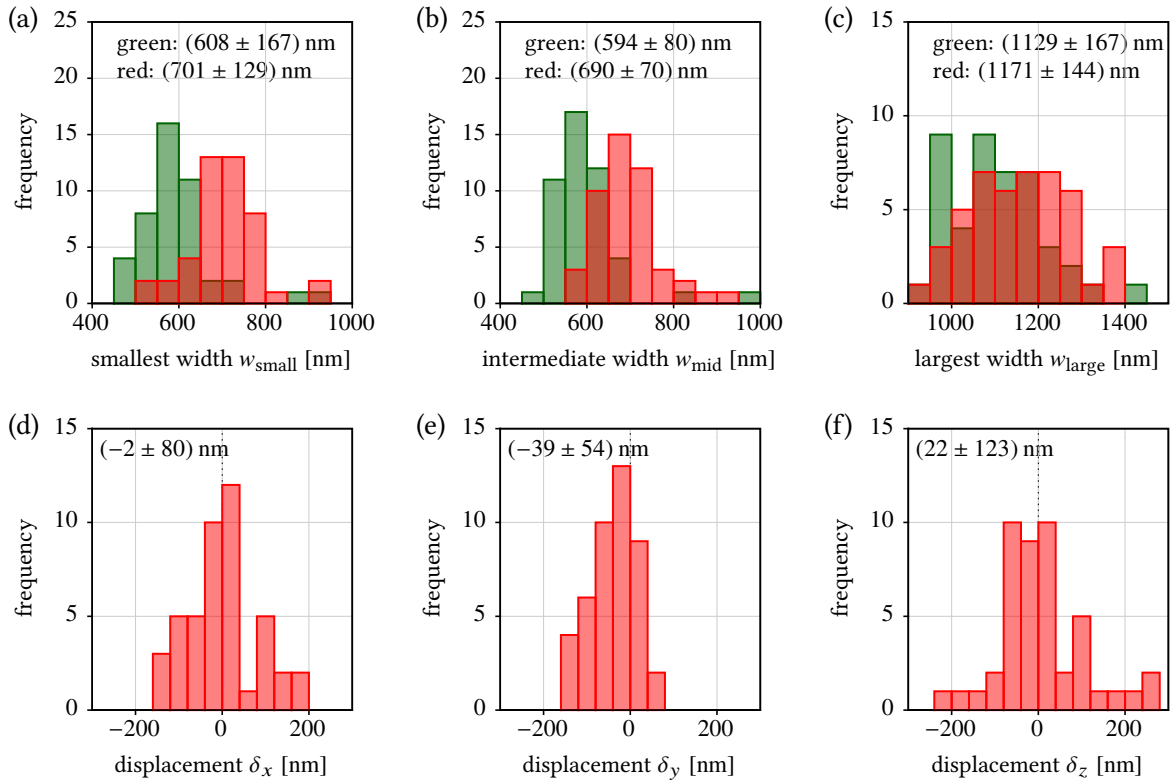


Figure 6.15. | Typical results of a light sheet analysis. (a-c) Histograms of the smallest width w_{small} , the intermediate width w_{mid} and the largest width w_{large} extracted from the 3-dimensional Gaussian fit. (d-f) Histograms of the displacement $\vec{\delta} = (\delta_x, \delta_y, \delta_z)^T$ between beads in the green and red channel. The numbers at the top of the graphs give average and standard deviation of the histograms. Number of beads used for the histograms: 47.

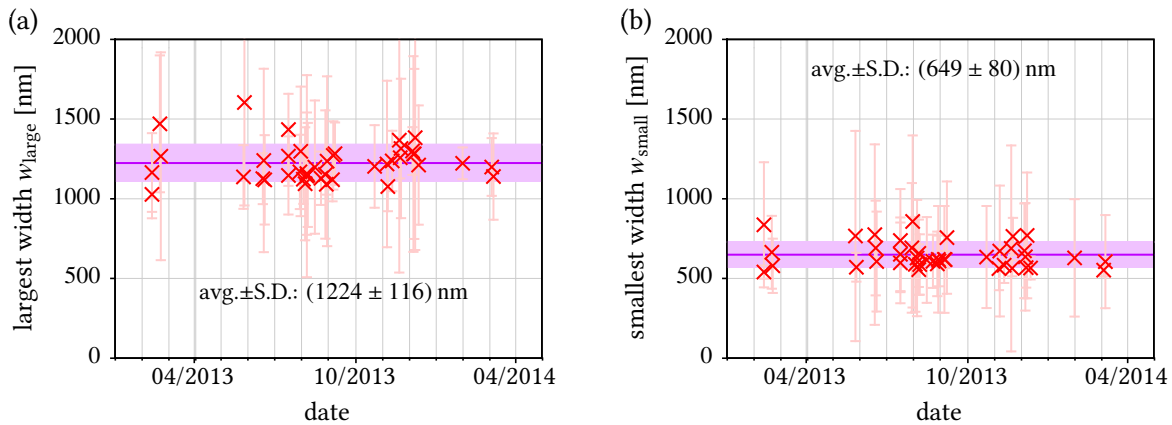


Figure 6.16. | Stability of the MDE parameters over a timespan of more than one year. (a) Mean and standard deviation of the largest and (b) of the smallest width determined in a 3-dimensional Gaussian fit. The violet bands and numbers in the graphs are average and standard deviation over all mean values.

6.3.3. Imaging capabilities of the SPIM

Figure 6.17 shows some representative images acquired with the SPIM described in this chapter. Figure 6.17(a) depicts a mitotic (dying) cell, which expressed a fluorescent dye that is enriched in the cell membrane (PMT-eGFP). A profile along the yellow line demonstrates the resolution of the SPIM. The cellular membrane is only a few nanometers thick, therefore it appears as a single bright pixel, which is blurred only slightly by the PSF (pixel size: $a = 400$ nm, $1/e^2$ -halfwidth of the MDE: ~ 600 nm). Figure 6.17(b,c) show volume renderings of different cells, that were produced from z -stacks. The stacks were acquired at a step-width of 400 nm in order to achieve isotropic pixels. Details on the cell culture protocols can be found in appendix A.2.

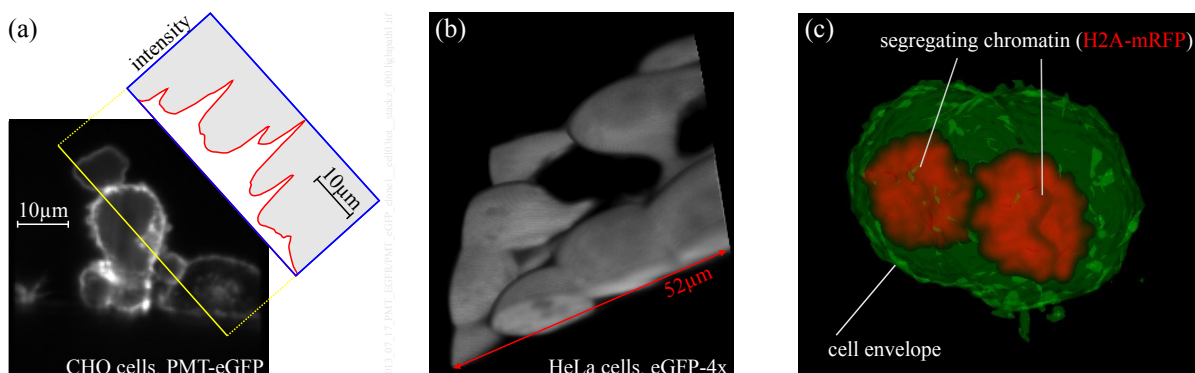


Figure 6.17. | Examples of SPIM images of cells. (a) Single frame showing a mitotic (dying) CHO-K1 cell, which expressed PMT-eGFP. (b) Volume rendering of a group of HeLa cells expressing eGFP-4x. (c) Volume rendering of a HeLa cell during mitosis, expressing H2A-mRFP1. the volume renderings were produced with the “3D Viewer” plugin of Fiji.

6.4. SPAD arrays

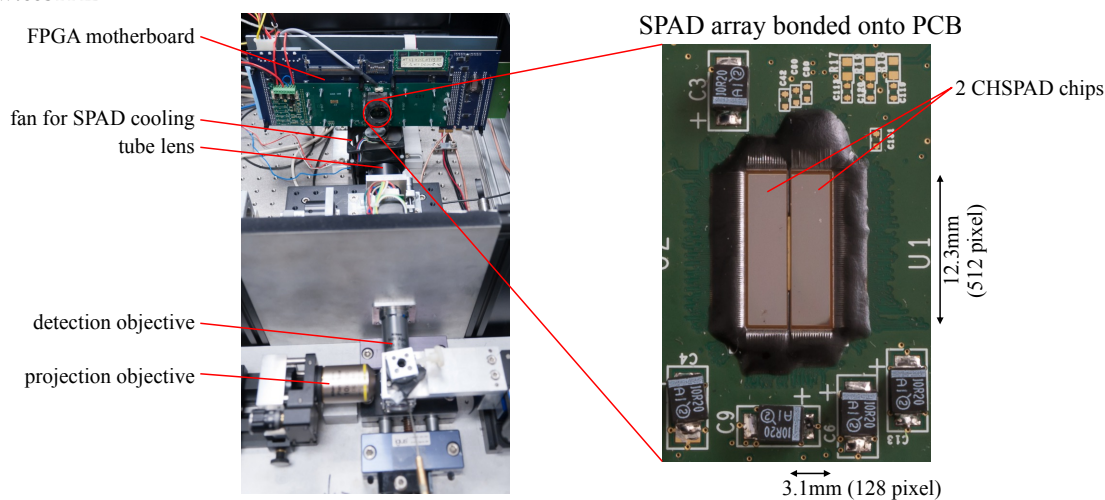
Measurements shown in this section were performed together with Jan Buchholz (DKFZ, Heidelberg) and in part with Samuel Burri (EPFL Lausanne). More details on the SPAD arrays, their readout and applicability to SPIM-FCS will be summarized in Ref. [232].

6.4.1. SPAD arrays used in this thesis

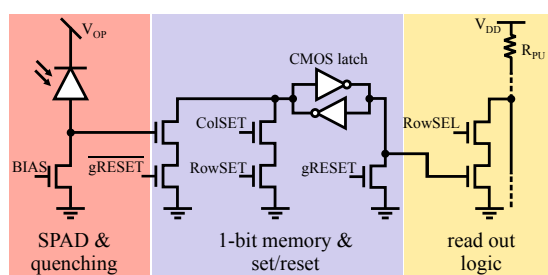
The SPIM described in this thesis is equipped with an EMCCD camera operated at frame rates of 1000 – 5000 fps. The maximal frame rate of EMCCD cameras is mostly limited by the shifting process and the properties of the camera electronics. To achieve better temporal resolution a second detection beam path was implemented, in which the fluorescence light is directed onto an array of single-photon avalanche diodes (SPADs). The structure and operation principle of SPADs and SPAD arrays was described in section 4.1. Figure 6.18(a) shows a photograph of a SPAD array mounted in the microscope and a closeup view of the image sensor. The readout rate of such arrays is typically on the order of 100,000 fps and above. This is fast enough to even resolve the FCS autocorrelation curves of small molecules, like Alexa-488.

In section 4.1.3 different classes of SPAD arrays were introduced, which mainly differed in the amount of in-pixel electronics. Two different SPAD arrays were used during this thesis: An early model called *Radhard2* with 32×32 pixels [186] and an advanced array called *SwissSPAD* with 512×128 pixels [192, 193]. Both devices were designed by and are used in a collaboration with the group of *Edoardo Charbon* at the TU Delft and EPFL Lausanne. They are a compromise between complexity and pixel size.

(a) *SwissSPAD*:



(b) Pixel of *Radhard2*:



(c) Pixel of *SwissSPAD*:

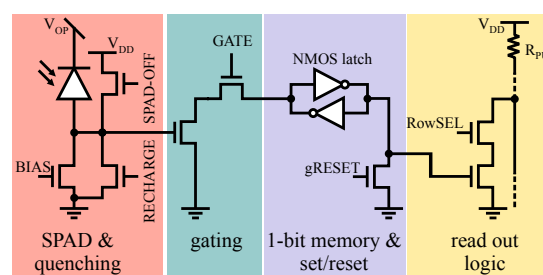


Figure 6.18. | (a) SPAD array *SwissSPAD*, mounted in the SPIM. (b,c) Pixel circuits of the two SPAD arrays (b) *Radhard2* and (c) *SwissSPAD*. Figures (b,c) adapted from [186] and [192, 193].

Each pixel (see Fig. 6.18b,d) contains a SPAD, a passive quenching resistor, a discriminator and a 1-bit memory, that contains 1 if at least one photon has arrived during the last integration-time cycle and 0 else. The passive quenching resistor is implemented using a MOSFET transistor. A small voltage applied to the BIAS input signal will change the drain-source resistance of this transistor. In addition, *SwissSPAD* contains a transistor, which can be used to gate the SPAD, i.e. switch it quickly between a sensitive and insensitive state by disconnecting the SPAD from the 1-bit memory. This feature can be used to measure fluorescence lifetimes, if short windows of sensitivity are placed at different delays from an illumination pulse [193]. *SwissSPAD* also contains a recharge transistor in parallel to the quenching MOSFET. This can be used to shorten the bias resistor for a few nanoseconds and thus reload the SPAD to its operating reverse bias voltage. This active reset of the SPAD is continuously performed every few 100 ns.

property	<i>Radhard2</i>	<i>SwissSPAD</i>
pixels	32×32	512×128
pixel pitch a_{sensor}	$30 \mu\text{m}$	$24 \mu\text{m}$
SPAD diameter d_{SPAD}	$4 \mu\text{m}$	$4 \mu\text{m}$
production process	0.35 μm high-voltage CMOS process	
fill factor FF	1.4%	5%
microlenses		✓
breakdown voltage U_{break}	18.8 V	20.0 V
typical excess bias voltage $U_{\text{excess}} = U_{\text{bias}} - U_{\text{break}}$	3.2 V	4 V
maximum quantum efficiency at typical U_{excess} and $\lambda = 500 \text{ nm}$	40%	34%
median dark count rate at typical U_{excess}	95 Hz	171 Hz (at $\vartheta_{\text{sensor}} = 34^\circ\text{C}$)
minimum full-frame integration time	2.66 μs	6.4 μs
maximum frame rate	376 kfps	156.25 kfps
maximum output-data rate	45.9 MByte/s	1220 MByte/s
maximum usable frame rate	100 kfps	156.25 kfps
maximum readable data rate	12 MByte/s	1220 MByte/s
FPGAs used for readout	Xilinx Virtex-II	Xilinx Virtex-4

Table 6.2. | **Properties of the SPAD arrays *Radhard2* and *SwissSPAD*.** Data was mostly taken from Refs. [186, 192, 193]. The readout rates are explained in more detail in section 6.4.2. The breakdown voltages and dark count rates were measured for this thesis (see section 6.4.3)

6.4.2. Readout

Both arrays – *Radhard2* and *SwissSPAD*– are row-addressable, which means that during readout a single row is selected and the signals of all 32 or 512 SPADs in that row are connected to output pins on the chip. In the case of *SwissSPAD*, there are only 128 output pins, so four neighboring rows share a single pin, using a 4-to-1 multiplexer. Pixel sizes, readout speed and other properties of both sensors are summarized in Tab. 6.2.

The structure of the readout system used for the SPAD arrays is shown in Fig. 6.19. Both arrays are connected to programmable logic chips called field programmable gate array (FPGA). They can be used to implement any logic circuit and provide enough input pins to connect to all signals of the SPAD arrays. In addition to the basic readout, the FPGAs also perform different tasks of data preprocessing, like packaging the raw data stream into frames and some basic corrections for broken pixels. A detailed

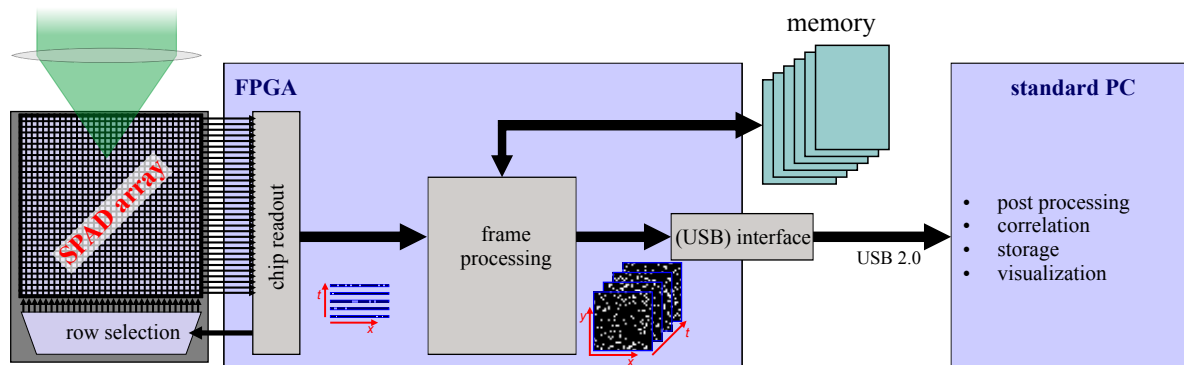


Figure 6.19. | Structure of the readout circuit used for the two SPAD arrays *Radhard2* and *SwissSPAD*.

description of these readout systems will be given in Ref. [232].

For the *Radhard2* chip, *Jan Buchholz* implemented a complete autocorrelator-system, which calculates all $32 \times 32 = 1024$ autocorrelation functions in real-time and transfers them to a control and storage computer [131, 232]. The complete raw data is also available via a second universal serial bus (USB) 2.0 connection, which is fast enough for the ~ 12 MByte/s data rate sourced by the sensor. This system reaches frame rates of 100 kfps for the full 1024 pixels. Higher rates are possible, if only a subset of the pixels is used. The frame rate of 100 kfps is limited by the amount of data that can be processed by the readout system. The chip itself can be read at up to 375 kfps, so a temporal binning stage has been implemented in the FPGA. It sums up three consecutive frames, before the data is sent to the autocorrelators. Transferring the complete raw data set is no longer possible at this frame rate, so only the autocorrelation functions are available [131]. The readout at 375 kfps significantly reduces the probability to count two or more photons, which arrive during a single frame exposure time, as only one.

For *SwissSPAD*, the data rate is more than a factor 100 higher than for *Radhard2*. To accommodate this, the *SwissSPAD* readout system simply stores the frames in a 4 GByte random access memory (RAM) module, which is attached to the FPGA. After the measurement the accumulated data set is transferred via USB 2.0 to a computer, where it is stored to hard disk and the auto- and cross-correlation functions are calculated.

6.4.3. Characterization of the SPADs

The breakdown voltage U_{break} is an important parameter of SPADs, as they operate in single-photon mode only, if biased above U_{break} . Also the quantum efficiency of SPADs directly depends on the amount of excess voltage $U_{\text{excess}} = U_{\text{bias}} - U_{\text{break}}$. Figure 6.20 shows this effect as an increase in detected photons at a given illumination intensity for different values of U_{excess} .

The breakdown voltage of the SPAD arrays used in this thesis was assessed by a series of dark count measurements at different levels of U_{bias} . The probability that a primary electron creates an avalanche in the SPAD is proportional to U_{bias} . Thus also the dark count rate depends linearly on U_{bias} . Avalanches are created and detected, if U_{bias} drops below the breakdown voltage U_{break} . Thus a linear fit to the increase of \dot{N}_{dark} with increasing U_{bias} yields an intercept with the $\dot{N}_{\text{dark}} = 0$ axis, which directly gives the breakdown voltage (see Fig. 6.21b). Breakdown voltages of 18.8 V and 20 V were determined for the *Radhard2* and *SwissSPAD* sensors, used in this thesis, respectively. After removing pixels, that were obviously defunct (see next paragraph), the breakdown voltage is homogeneous over the sensor with a narrow inter-quartile range of 19.9...20.1 V. Figure 6.21(a) shows a histogram of the breakdown voltages as determined in this experiment. From these results the excess bias voltages used for every single chip

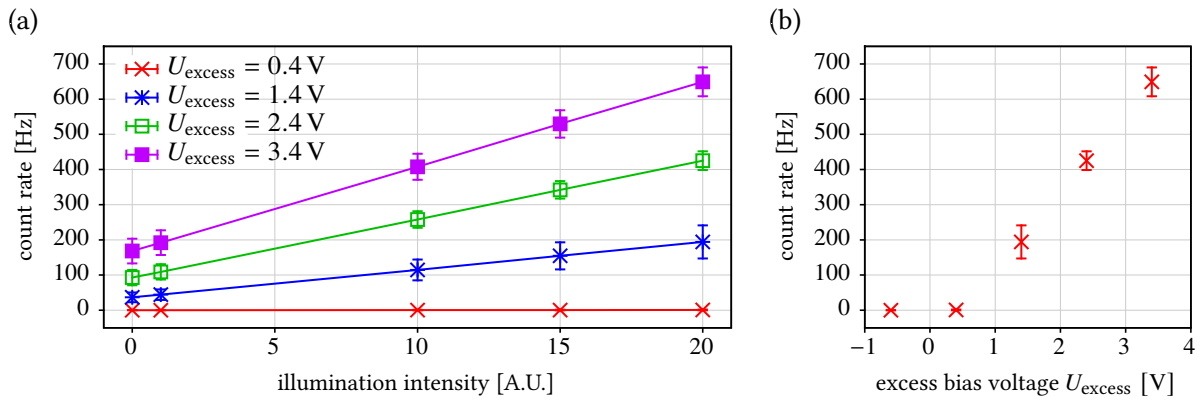


Figure 6.20. | Effect of the excess bias voltage U_{excess} on the quantum efficiency of a SwissSPAD chip without microlenses. (a) Count rate versus illumination intensity at different values of U_{excess} . (b) Count rate versus excess bias voltage at the maximum illumination intensity in (a). Obviously broken pixels were removed from the evaluation. Error bars give average and standard deviation of the intensity in a central region of the chip. Lines are used to guide the eye.

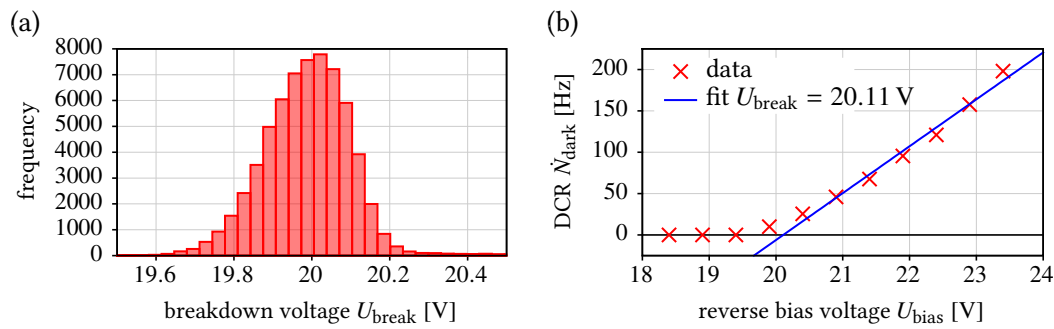


Figure 6.21. | The breakdown voltage of SwissSPAD. (a) Distribution of the breakdown voltage U_{break} of all pixels of a SwissSPAD sensor with microlenses. (b) Example of a fit, used to determine the U_{break} in a single pixel (DCR means dark count rate). The temperature of the SwissSPAD chip was measured to be $\vartheta_{\text{Sensor}} \approx 34^\circ\text{C}$. Obviously broken pixels were removed from the evaluation.

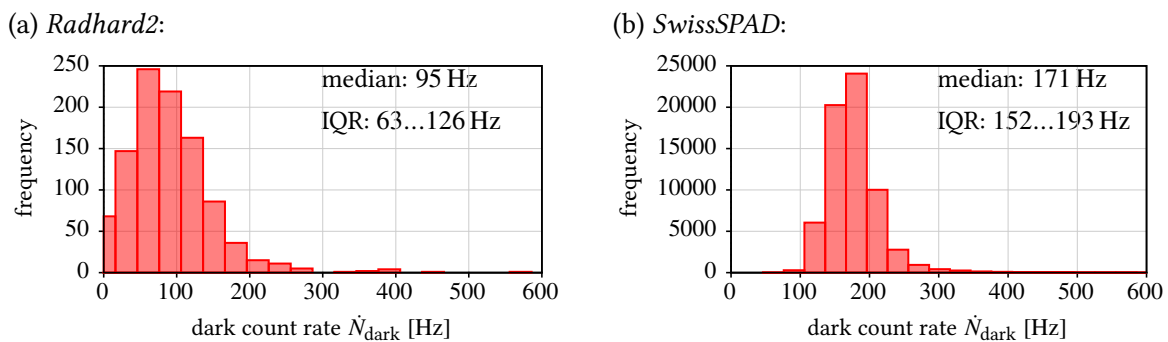


Figure 6.22. | Histograms of the dark count rate of the SPAD arrays *Radhard2* and *SwissSPAD*. The temperature of *Radhard2* was around room temperature $\vartheta_{\text{Sensor}} \approx 24^\circ\text{C}$ and the temperature of *SwissSPAD* was measured to be $\vartheta_{\text{Sensor}} \approx 34^\circ\text{C}$. In each graph the median and the inter-quartile range (IQR) of the distributions is given. Obviously broken pixels were removed from the evaluation.

is chosen and kept constant for all further measurements. For *Radhard2* typically $U_{\text{excess}} = 3.2 \text{ V}$ was chosen and for *SwissSPAD* typically $U_{\text{excess}} = 4 \text{ V}$.

The dark count rate (DCR) \dot{N}_{dark} is an important contribution to the measured signal in a SPAD array and was already used to determine the breakdown voltage. The DCRs were further analyzed at a typical U_{excess} , used for measurements. Figure 6.22 shows two histograms of the measured DCRs for *Radhard2* and *SwissSPAD*. The median DCR was 95 Hz for *Radhard2* and 171 Hz for *SwissSPAD*.

6.4.4. Microlens arrays on *SwissSPAD*

SwissSPAD is equipped with microlenses that increase the effective sensitive area (see section 4.1.3). The geometry of the microlenses is roughly explained in Refs. [193, 197]. Basically a small lens covers each pixel of length $a_{\text{sensor}} = 24 \mu\text{m}$, and focuses the incident light onto the SPAD, which has a diameter of $d_{\text{SPAD}} = 4 \mu\text{m}$. The microlenses have been designed by the company CSEM (Neuchâtel, Switzerland) and built by Süss Microtec AG (Garching, Germany). They are optimized for collimated incident light, which is focused onto the SPAD, as shown in Fig. 6.23(a) on the left. If the incident light is not parallel, the focus will be enlarged at the position of the SPAD and the light concentration efficiency of the microlenses decreases. This effect has been simulated and measured in Ref [197] for a microlens array, comparable to the one on *SwissSPAD*. A raytracing approach was used and a maximum concentration factor of 14 improvement was estimated. In a microscope setup, as shown in Fig. 6.23(b), the image is projected onto the sensor by a final tube lens. This may cause light to hit the sensor not just uncollimated, but also under an off-axis angle α . Then the spot on the chip is moved a distance $\Delta x = f_{\text{TL}} \cdot \tan(\alpha)$, as shown in Fig. 6.23(a) on the right hand side. In the extreme case of this situation, a beam, incident at the upper

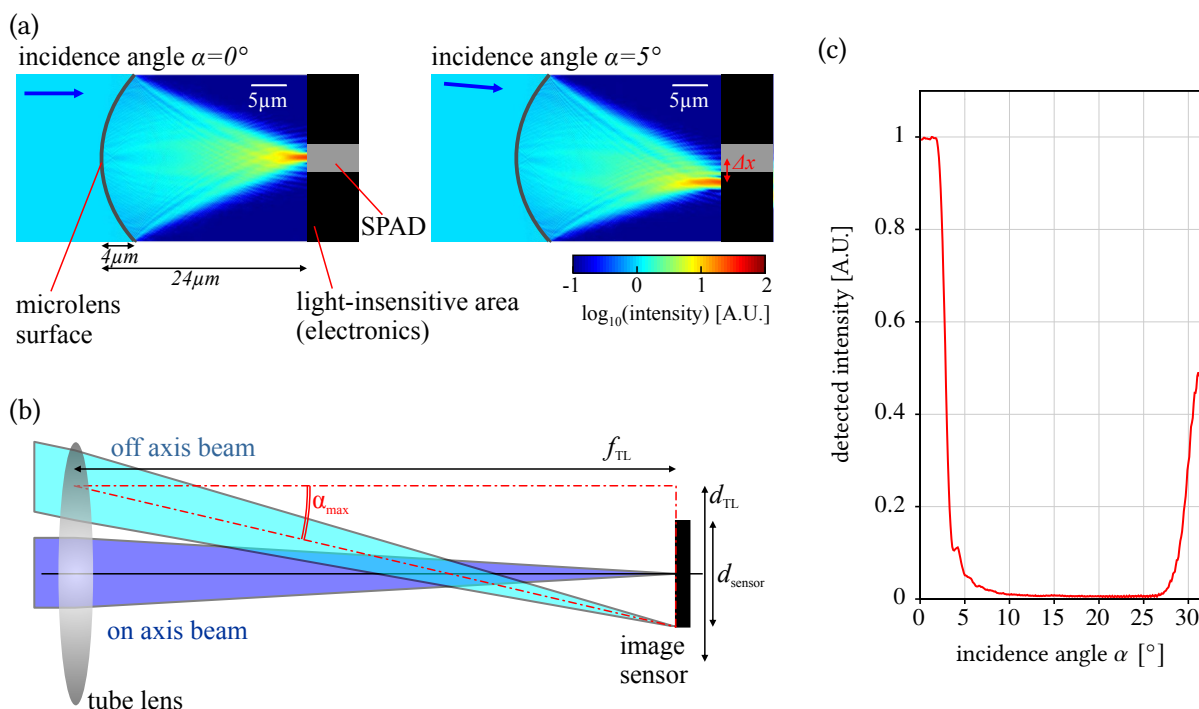


Figure 6.23. | Simulation of the light intensity distribution in a microlens, which is comparable to the microlenses on *SwissSPAD*. (a) Result of the simulation for incident angles of plane waves of $\alpha = 0^\circ$ (left) and $\alpha = 5^\circ$ (right). (b) Sketch on the estimation of the maximum incidence angle of light on an image sensor. (c) Integrated intensity on the SPAD area as a function of the incidence angles α . The simulation was performed with the beam propagation method described in appendix B.4.

border of the tube lens, is focused onto a point at the lower edge of the image sensor (see Fig. 6.23b). The maximum incident angle α_{\max} is then given by

$$\tan(\alpha_{\max}) = \frac{d_{\text{TL}}/2 + d_{\text{sensor}}/2}{f_{\text{TL}}}, \quad (6.4.1)$$

where d_{TL} is the diameter of the tube lens of focal length f_{TL} and d_{sensor} is the width of the sensor. For the *SwissSPAD* in the SPIM described in here ($f_{\text{TL}} = 200 \text{ nm}$, $d_{\text{TL}} = 25 \text{ mm}$, $d_{\text{sensor}} = 12.2 \text{ mm}$), $\alpha_{\max} = 5.3^\circ$ is obtained. This angle leads to a focus shift of $\Delta x \approx 2.3 \mu\text{m}$, if a focal length of around $40 \mu\text{m}$ is assumed for the microlenses. The spot center is then shifted outside of the $4 \mu\text{m}$ SPAD. This situation was simulated for different incidence angles, using the beam propagation method in two dimensions, as described in appendix B.4. Figure 6.23(c) shows the intensity, integrated over the SPAD area, as a function of the incidence angle α . It can be seen that already at an angle of $\alpha \approx 2.8^\circ$ only half of the photons hit the sensitive area. At angles above $\alpha = 25^\circ$ the next microlens in the array focuses a part of its light onto the SPAD. These estimations and simulations may not be completely accurate, because the exact properties of the microlenses are not known or disclosed. Nevertheless, they show that the gain due to the microlenses will be considerably reduced in the outer parts of the sensor. In principle, the microlenses could be shifted to account for the effects described here. This is a possible improvement, planned for the next version of the microlenses, but was not available during this thesis.

6.4.5. Influence of microlenses on the SPAD array performance

When determining the dark count rate and the breakdown voltage, it was mentioned, that “obviously broken pixels were removed”. This will be explained in further detail in this paragraph. The SPAD array sensors are experimental chips that are produced in small numbers, so only few chips are available of each sensor and they cannot be sorted out due to minor problems. Typically these chips have between 0.1% and 2% broken pixels, that output 1 in nearly every exposure (see Fig. 6.24a). These are termed hot pixels and need to be masked before any evaluation. Also broken contacts between the carrier printed circuit board (PCB), which contains the sensor chip, and the motherboard with the FPGAs occurred on

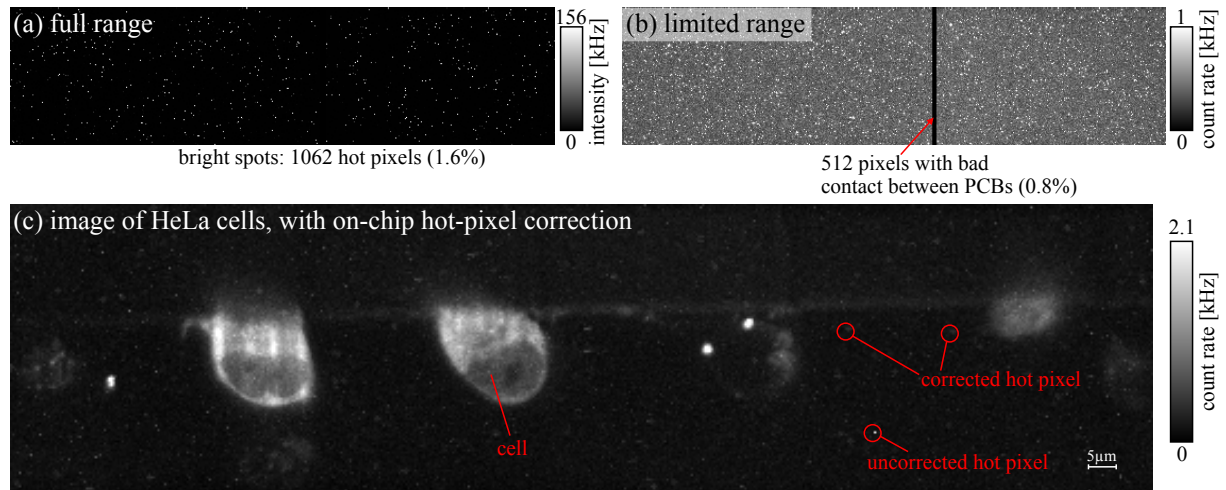


Figure 6.24. | (a,b) Hot pixels and broken columns in the same dark frame, acquired with *SwissSPAD* for two different gray scales (two different color scales!). (c) A SPIM image of HeLa cells expressing eGFP tetramers, acquired with *SwissSPAD* and corrected for broken pixels with the online correction method described in the text. The exposure time was $\Delta t_{\text{exp}} = 419 \text{ ms}$ in all images and $U_{\text{excess}} = 3.5 \text{ V}$ in (a,b) and $U_{\text{excess}} = 4 \text{ V}$ in (c). Hot pixels are classified as pixels with countrates above 2.3 kHz and dark pixels have a countrate below 24 Hz.

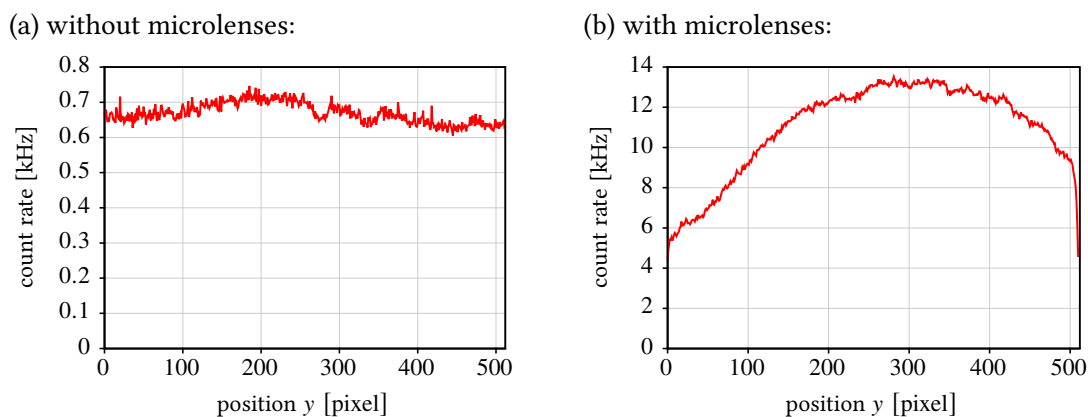


Figure 6.25. | Intensity profile along the longer axis of *SwissSPAD* without microlenses in (a) and with microlenses in (b), at comparable illumination intensities. The data shows the photon counts detected in all 512 pixels of one row of *SwissSPAD* at an approximately even illumination.

some occasions (see Fig. 6.24b). These prevent readout of complete columns of the chip. Finally, for each evaluation the brightest $\sim 2\%$ of the pixels were removed. Jan Buchholz developed an online correction for broken pixels [232]. It is implemented in the same FPGA that is also used for the readout. First, broken pixels are selected either by hand or using a threshold. Then, during each exposure time, the 0 or 1 read from these pixels is ignored and the data from one of the four neighboring pixels is used instead. Which neighboring pixel is used, is randomly changed for each frame. In this way, the broken pixel will effectively output the average over its four neighbors. This method has the advantage that even the broken pixels will output a reasonable autocorrelation curve.

The impact of the microlenses, was also assessed (cf. section 6.4.4). A *SwissSPAD* with and without microlenses was mounted in the SPIM and the transmission illumination LED was used to illuminate the sensor (see Fig. 6.2). The light passed the objective lens and the tube lens on its way, thus simulating the effect of fluorescence light, collected by the microscope. A profile along the 512 pixel-axis of *SwissSPAD* is shown in Fig. 6.25. The intensity on the chip without microlenses varies by about 7% around its average value of 690 Hz, compared to 61% around an average of 9 kHz with microlenses. The strong dependence of the count rate in the chip with microlenses is caused by the increasing incidence angles of the light towards the border of the chip. Therefore, all SPIM-FCS measurements were limited to the bright central part of the sensor ($y = 250\dots 400$ pixel), where the influence of the microlenses is negligible. The discrepancy of a factor of ~ 13 in average intensity is explained by the gain in detected photons by the microlenses and an $\sim 30\%$ lower excess voltage on the sensor without microlenses. In the central region the gain is ~ 18 .

7. Data processing and instrument control software

This section describes the methods for data evaluation and instrument control, which were developed during this project. A single program, called `QUICKFIT 3.0`, was implemented, which serves both purposes. First the data evaluation processes used for imaging FCS and imaging FCCS measurements are described in section 7.1, their implementation in `QUICKFIT 3.0` is subject of section 7.3. In section 7.2, single-particle tracking is described, which was used for some experiments in this thesis. Finally, the instrument control for the SPIM is described in section 7.4.

7.1. Imaging FCS/FCCS data evaluation

7.1.1. Overview

The imaging F(C)CS data evaluation process consists of several stages, as illustrated in Fig. 7.1. The figure also shows how the extent of data is reduced during the processing. The evaluation starts from an image series acquired on a SPIM (or any other suitable microscope) with a given temporal resolution. For measurements in this thesis, that were acquired with an EMCCD camera, each data set typically consists of a series of $10^5 - 10^6$ frames with 128×20 pixels of the fluorescence signal and a second time series of the background signal with $\sim 10^3$ frames. If a SPAD array was used for acquisition, the image size was comparable, but the number of frames was $10^6 - 10^8$.

Initially, the fluorescence image series is corrected for acquisition artifacts: a background signal, the

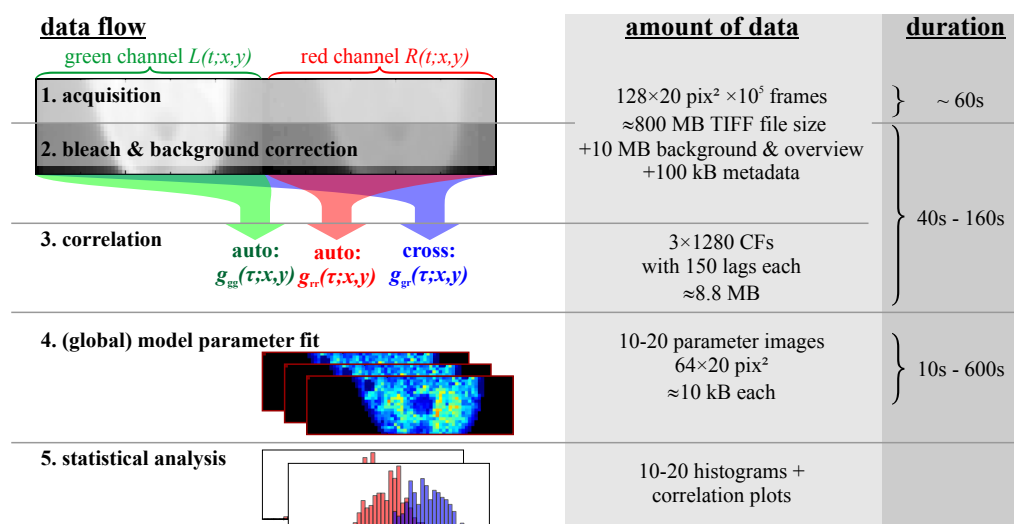


Figure 7.1. | **Evaluation chain for imaging FCCS.** The left column shows the progression from the raw input data to the statistically analyzed results. The mid column gives typical numbers for the size of the data set in each step. The processing times for a typical measurement are given in the column on the right.

camera offset (see section 7.1.2) and bleaching of the fluorophores (see section 7.1.2). This is followed by the calculation of auto- and cross-correlation functions. In addition, a time-averaged “video” with 100 – 1000 frames is produced from the corrected raw data, which allows to observe the behavior of the sample during the measurement (see section 7.1.3). This stage reduces the amount of data by a factor of approximately 100, or even more for SPAD arrays. For the rest of the evaluation the raw data are no longer needed and they can be discarded. Finally, the model functions described in chapter 5 are fitted to the correlation curves and the resulting parameters are stored (see sections 7.1.4 and 7.1.5). These parameters can be displayed as an image and analyzed statistically.

In the remainder of this chapter, image series acquired on a pixel detector of width W and height H will be denoted in the form $F(x, y; t)$, where $x = 1, 2, \dots, W$ and $y = 1, 2, \dots, H$ are the pixel coordinates. If not stated otherwise, the time t is given in units of the frame repetition time Δt_{frame} . Then t is usually an integer number.

7.1.2. Background and bleach correction

Background correction

Before correlation functions are calculated, a background correction is performed. The effect of this artifact on the FCS and FCCS correlation functions has been described in section 5.5.2. In EMCCD measurements the background correction also accounts for the constant offset of typically 100 ADU, which the camera adds to any frame, in order not to clip noisy signals near 0. For the offset correction, the sample illumination is switched off and a second image series $B(x, y; t)$ of a typical length $T_B = 2000$ is acquired with identical camera settings, as in the acquisition of $F(x, y; t)$. Then the background correction is performed, by subtracting the averaged background series from the fluorescence time series $F(x, y; t)$:

$$F(x, y; t) \rightarrow F(x, y; t) - \bar{B}(x, y) \quad \text{with} \quad \bar{B}(x, y) = \frac{1}{T_B} \sum_{t=1}^{T_B} B(x, y; t). \quad (7.1.1)$$

Bleach correction

Especially when measuring fluorescent proteins, a certain amount of bleaching, or more exactly depletion of the reservoir of fluorophores, is observed (see section 5.5.4). As stated there, this effect cannot be incorporated in the fit models, so it is corrected for at this stage, using the correction formula proposed by Ries et al. in Ref. [98]:

$$F(x, y; t) \rightarrow \frac{F(x, y; t)}{\sqrt{f_{xy}(t)/f_{xy}(0)}} + f_{xy}(0) \cdot \left(1 - \sqrt{f_{xy}(t)/f_{xy}(0)}\right). \quad (7.1.2)$$

Here $f_{xy}(t)$ is a function describing the fluorescence decay observed in the pixel (x, y) . For this correction the background-corrected intensity time trace $F(x, y; t)$ is averaged into a series of 100 – 300 equidistant time points $\bar{F}(x, y; t)$. Then the parameters of the model $f_{xy}(t)$ are optimized to best fit $\bar{F}(x, y; t)$. The fit is performed for every pixel separately. Due to the large number of pixels (typically > 1000), a fast fitting procedure is required, which converges reliably, also without supervision.

For the model $f_{xy}(t)$, several options are appropriate. A simple mono-exponential decay was proposed in section 5.5.4. It is typically applicable only in samples, in which bleaching causes an intensity drop of only 10 – 20% over the course of the measurement, such as DNA labeled with chemical fluorophores. The model function is then of the form

$$f_{xy}(t) = f_{0,xy} \cdot \exp\left(-\frac{t}{\tau_{B,xy}}\right), \quad (7.1.3)$$

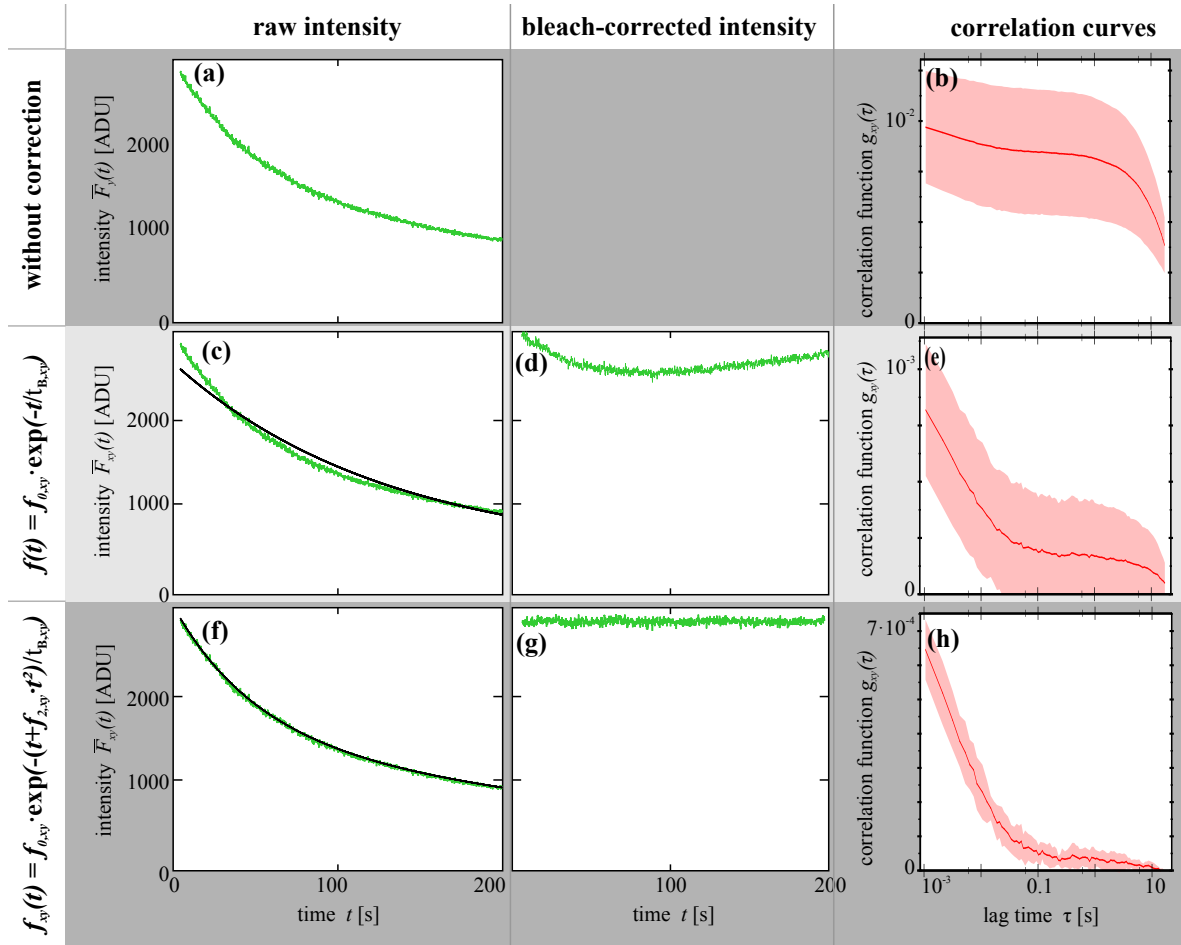


Figure 7.2. | **Example of a bleach correction according to Eq. (7.1.2).** (a,c,f) Uncorrected intensity time traces for one pixel (green) with fitted model function $f_{xy}(t)$ (black). Used models: (c) simple exponential model Eq. (7.1.3), (f) modified model Eq. (7.1.5) with $N_f = 2$. (d,g) Intensity time traces after correction. (b,e,h) Autocorrelation functions obtained after the bleach correction, as average and standard deviation over the curves from 5 consecutive segments of a length of ~ 10.5 s each.

with an amplitude $f_{0,xy}$ and a decay time $\tau_{B,xy}$. For more complex systems, such as living cells, a double-exponential model would be more appropriate [109, 233, 234]:

$$f_{xy}(t) = f_{0,xy} \cdot \exp\left(-\frac{t}{\tau_{B,xy}}\right) + f'_{0,xy} \cdot \exp\left(-\frac{t}{\tau'_{B,xy}}\right). \quad (7.1.4)$$

An unsupervised fit of this model often does not converge. Therefore an extended mono-exponential model has been successfully used throughout this thesis:

$$f_{xy}(t) = f_{0,xy} \cdot \exp\left(-\frac{1}{\tau_{B,xy}} \cdot \left[t + \sum_{i=2}^{N_f} f_{i,xy} \cdot t^i\right]\right). \quad (7.1.5)$$

Here the mono-exponential function with a single decay time $\tau_{B,xy}$ has a polynomial of degree N_f between 2 and 4 as argument. The polynomial coefficients are denoted as $f_{i,xy}$.

Fitting was performed in a multi-step scheme to guarantee a reliable convergence: first the measured intensity $\bar{F}(x, y; t)$ was logarithmized, as the exponential fit then reduces to a simple regression in the

case of Eq. (7.1.3) and a polynomial fit for Eq. (7.1.5). For the polynomial case, the fit was split into N_f fits, where first only the mono-exponential parameters were optimized, then these were taken as starting values for a fit with a parabola and so forth, until the full degree of the desired polynomial was reached. A Levenberg-Marquardt non-linear least-squares fitting algorithm was used in all steps [235–237]. The initial starting parameters were obtained from a robust regression analysis of $\log(\overline{F}(x, y; t))$ using the outlier-robust iteratively reweighted least squares (IRLS) algorithm [238].

Figure 7.2 shows an example for bleaching in a SPIM-FCS measurement of a cell expressing eGFP. The laser intensity was set to a value of approximately 100 W/cm^2 . Figure 7.2(a) shows the decay of the measured intensity $\overline{F}(x, y; t)$ for a single pixel and Fig. 7.2(b) its autocorrelation curve. The mono-exponential and the modified mono-exponential model ($N_f = 2$) were used to correct for this bleaching. Resulting fits, corrected intensities and autocorrelation curves are shown in the second and third column of the figure. The mono-exponential fit already removes most of the bleaching, but there is still a considerable offset present in the autocorrelation curve (Fig. 7.2e). It is caused by the U-shaped corrected fluorescence intensity, see Fig. 7.2(d). The final fit with a polynomial of degree $N_f = 2$ is good enough to cause a straight fluorescence signal and a smoothly decaying autocorrelation function. The remaining long-term decay is due to movements of the cell.

7.1.3. Calculation of correlation functions

After correction for background and bleaching, the normalized FCS or FCCS auto- and cross-correlation functions are calculated. On a pixelated image sensor, the general spatial cross-correlation function can be defined as:

$$g(\tau, \delta_x, \delta_y; x, y) = \frac{\langle F(x, y; t) \cdot F(x + \delta_x, y + \delta_y; t + \tau) \rangle_t}{\langle F(x, y; t) \rangle_t \cdot \langle F(x + \delta_x, y + \delta_y; t) \rangle_t}. \quad (7.1.6)$$

Here τ is the lag time, given in units of Δt_{frame} , and (δ_x, δ_y) is the shift between the two observation volumes, given in numbers of pixels. The autocorrelation functions are included by the special case $\delta_x = \delta_y = 0$.

Two-color acquisitions are done using a dual-view optics (see sections 3.1.3 and 6.1.4), which images the two color channels side-by-side on a single image sensor, as shown in Fig. 7.3. The image stack $F(x, y; t)$ is split into two separated stacks $L(x, y; t)$ (left) and $R(x, y; t)$ (right), as indicated in the figure. Finally the two-color cross-correlation functions are defined as:

$$g_{\text{gr}}(\tau; x, y) = \frac{\langle L(x, y; t) \cdot R(x, y; t + \tau) \rangle}{\langle L(x, y; t) \rangle \cdot \langle R(x, y; t) \rangle} \equiv g(\tau, W/2, 0; x, y). \quad (7.1.7)$$

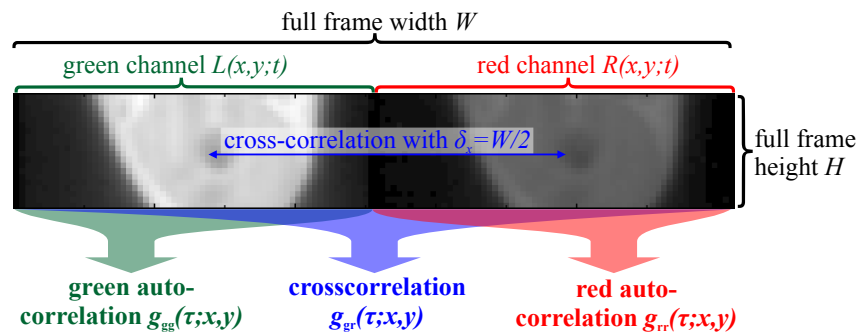


Figure 7.3. | Illustration of the splitting of a single frame from an FCCS measurement.

The last equivalence signifies, that $g_{\text{gr}}(\tau; x, y)$ can also be written as a special case of the spatial cross-correlation (Eq. 7.1.6) of the full image stack. In that case the focus shifts are set to $(\delta_x, \delta_y) = (W/2, 0)$ or $(\delta_x, \delta_y) = (0, H/2)$, depending on the orientation of the image splitting optics.

The averages in Eq. (7.1.6) and Eq. (7.1.7) are temporal averages over infinite times:

$$\langle F \rangle = \lim_{T \rightarrow \infty} \int_0^T F(t) dt. \quad (7.1.8)$$

As a measurement $F(x, y; t)$ consists of a finite number T_F of frames, only a statistical average of such averages can be estimated from a measurement:

$$\langle F \rangle(x, y) = \frac{1}{T_F} \cdot \sum_{t=1}^{T_F} F(x, y; t). \quad (7.1.9)$$

The same is true for the cross-correlation function in Eq. (7.1.6). A good statistical estimator, which was also used throughout the thesis, is [239, 240]

$$\hat{g}_{\text{sym}}(\tau, \delta_x, \delta_y; x, y) = \frac{\frac{1}{T_F - \tau} \cdot \sum_{t=1}^{T_F - \tau} F(x, y; t) \cdot F(x + \delta_x, y + \delta_y; t + \tau)}{\left[\frac{1}{T_F} \cdot \sum_{t=1}^{T_F} F(x, y; t) \right] \cdot \left[\frac{1}{T_F - \tau} \cdot \sum_{t=\tau}^{T_F} F(x + \delta_x, y + \delta_y; t) \right]}. \quad (7.1.10)$$

The special form of normalization in Eq. (7.1.10) is called “symmetric normalization”. Note that the two averages in the denominator extend over two different ranges, whereas a naïve implementation would extend the sums in the normalization over the whole image stack:

$$\hat{g}_{\text{naïve}}(\tau, \delta_x, \delta_y; x, y) = \frac{\frac{1}{T_F - \tau} \cdot \sum_{t=1}^{T_F - \tau} F(x, y; t) \cdot F(x + \delta_x, y + \delta_y; t + \tau)}{\left[\frac{1}{T_F} \cdot \sum_{t=1}^{T_F} F(x, y; t) \right] \cdot \left[\frac{1}{T_F} \cdot \sum_{t=1}^{T_F} F(x + \delta_x, y + \delta_y; t) \right]}. \quad (7.1.11)$$

In this version the three sums extend over the measurement time asymmetrically and the initial part $[1 \dots \tau]$ and the final part $[T_F - \tau \dots T_F]$ of the measurement have different statistical weights [239, 240]. Schätzel et al. showed that both estimators are statistically biased, but Eq. (7.1.10) is favorable, as it better accounts for the finite time series [239].

The expression (7.1.10) can be used to estimate $g(\tau, \delta_x, \delta_y; x, y)$ for an arbitrary value of τ . In FCS and FCCS the autocorrelation functions typically span several decades (e.g. $\tau = 10^{-6} \dots 10$ s). Therefore, a linear grid of τ -values is impractical, as it would result in millions of data points. Hence logarithmically spaced τ -values are used, in order to cover the whole desired lag time range by 100...500 estimates, which are equally distributed over all decades.

The computational cost of calculating Eq. (7.1.10) for $N_\tau = 100 \dots 500$ values of τ is on the order of $\mathcal{O}(N_\tau \cdot N_F)$. This results in long run times of the algorithm, because for each τ , large sums over nearly the whole time series have to be calculated. Therefore the multi- τ algorithm is often used. This algorithm estimates $g(\tau, \delta_x, \delta_y; x, y)$ for semi-logarithmically spaced lag times $\tau \equiv \tau_{s,p}$ with $s = 0 \dots S - 1$ and $p = 0 \dots P - 1$. The series $\tau_{s,p}$ consists of S blocks of P linearly spaced lags $\tau_{s,0} \dots \tau_{s,P-1}$. Initially, the spacing of the lag times equals the frame repetition time Δt_{frame} . It is multiplied by an integer number

m from block s to block $s + 1$:

$$\begin{aligned}\tau_{s,p} &= \tau_{s,0} + p \cdot m^s \cdot \Delta t_{\text{frame}} \\ \tau_{s+1,0} &= \tau_{s,p-1} + m^s \Delta t_{\text{frame}} \\ \tau_{0,0} &= \Delta t_{\text{frame}}.\end{aligned}$$

Typical parameters are $m = 2$ and $P = 8$ or $P = 16$. The number of blocks S is then chosen in such a way, that the full desired lag time range is covered by $\tau = \Delta t_{\text{frame}} \dots \tau_{\text{max}}$ and $\tau_{\text{max}} < T_F$. For EMCCD measurements ($\Delta t_{\text{frame}} \approx 500 \mu\text{s}$, $T_F \approx 60 \text{ s}$) typically $S = 8..13$ blocks are used. This yields a maximum lag time of 1..33 s.

The multi- τ algorithm uses a clever scheme to implement the correlation, which continuously reduces the size of the sums in Eq. (7.1.10): for each linear block s , the algorithm directly calculates the sums in Eq. (7.1.10) for P lag times $\tau = \tau_{s,0} \dots \tau_{s,p}$. In between blocks the data is reduced by binning m measurements together: $F(x, y; t) + \dots + F(x, y; t + m - 1)$. This effectively reduces the length of the time series by a factor m . Then the next linear block is calculated on this binned time series. It can be shown that this averaging step with $m = 2$ allows to perform the calculation of an arbitrary number of blocks S in the same time that is required to calculate two blocks without averaging. Then the algorithmic complexity is reduced to $\mathcal{O}(2P \cdot N_F)$ for any $S \geq 2$ [131]. The argument we made in Ref. [131] to prove this claim is as follows. The first block $s = 0$ needs a computation time Δt_{lin} . Then each subsequent block s needs a computation time $\Delta t_{\text{lin}}/m^{s+1}$, and the overall computation time is finally given by:

$$\underbrace{1 \cdot \Delta t_{\text{lin}}}_{\text{1st lin. block}} + \underbrace{\frac{1}{2} \cdot \Delta t_{\text{lin}}}_{\text{2nd lin. block}} + \underbrace{\frac{1}{4} \cdot \Delta t_{\text{lin}}}_{\text{3rd lin. block}} + \dots \leq \sum_{n=0}^{\infty} \frac{1}{2^n} \cdot \Delta t_{\text{lin}} = 2 \cdot \Delta t_{\text{lin}}. \quad (7.1.12)$$

This algorithm is also ideally suited for implementation in hardware, such as on a field programmable gate array (FPGA). It was used to perform an on-line autocorrelation for all 1024 pixels in the SPAD array *Radhard2* at a maximum readout rate of 10^5 fps [131]. An optimized implementation allows to reach the same performance on modern central processing units (CPUs), as these can parallelize several multiply and accumulate steps [232].

The averaging step in a multi- τ correlator saves a lot of computation time, but also introduces an additional error in the estimator Eq. (7.1.10). For continuous time series $F(x, y; t)$ the binning step can be written as a convolution with a rectangular filter kernel $h_{\text{rect}}(t; m^s \cdot \Delta t_{\text{exp}})$ of width $m^s \cdot \Delta t_{\text{exp}}$. The filter kernel is defined as

$$h_{\text{rect}}(t; \Delta T) = \frac{1}{T} \cdot \begin{cases} 1 & |t| < \Delta T/2 \\ 0 & \text{else} \end{cases}. \quad (7.1.13)$$

The correlation function for any $s > 0$ is then given by

$$\begin{aligned}g'(\tau, \delta_x, \delta_y; x, y) &= \\ &= \frac{\left\langle \left[F(x, y; t) \otimes h_{\text{rect}}(t; m^s \Delta t_{\text{exp}}) \right] \cdot \left[F(x + \delta_x, y + \delta_y; t + \tau) \otimes h_{\text{rect}}(t + \tau; m^s \Delta t_{\text{exp}}) \right] \right\rangle}{\left\langle F(x, y; t) \otimes h_{\text{rect}}(t; m^s \Delta t_{\text{exp}}) \right\rangle \cdot \left\langle F(x + \delta_x, y + \delta_y; t) \otimes h_{\text{rect}}(t; m^s \Delta t_{\text{exp}}) \right\rangle}. \quad (7.1.14)\end{aligned}$$

The normalization is not affected by this averaging, but the correlation factor in the numerator is. As convolution and correlation are linear operations, they can be interchanged. Finally, the correlation function in Eq. (7.1.14) can be expressed as a convolution of the true function Eq. (7.1.7) with a triangular filter $h_{\text{triangle}}(t; m^s \cdot \Delta t_{\text{exp}}) = h_{\text{rect}}(t; m^s \cdot \Delta t_{\text{exp}}) \otimes h_{\text{rect}}(t; m^s \cdot \Delta t_{\text{exp}})$ [241, 242]:

$$g'(\tau, \delta_x, \delta_y; x, y) = g(\tau, \delta_x, \delta_y; x, y) \otimes h_{\text{triangle}}(t; m^s \cdot \Delta t_{\text{exp}}). \quad (7.1.15)$$

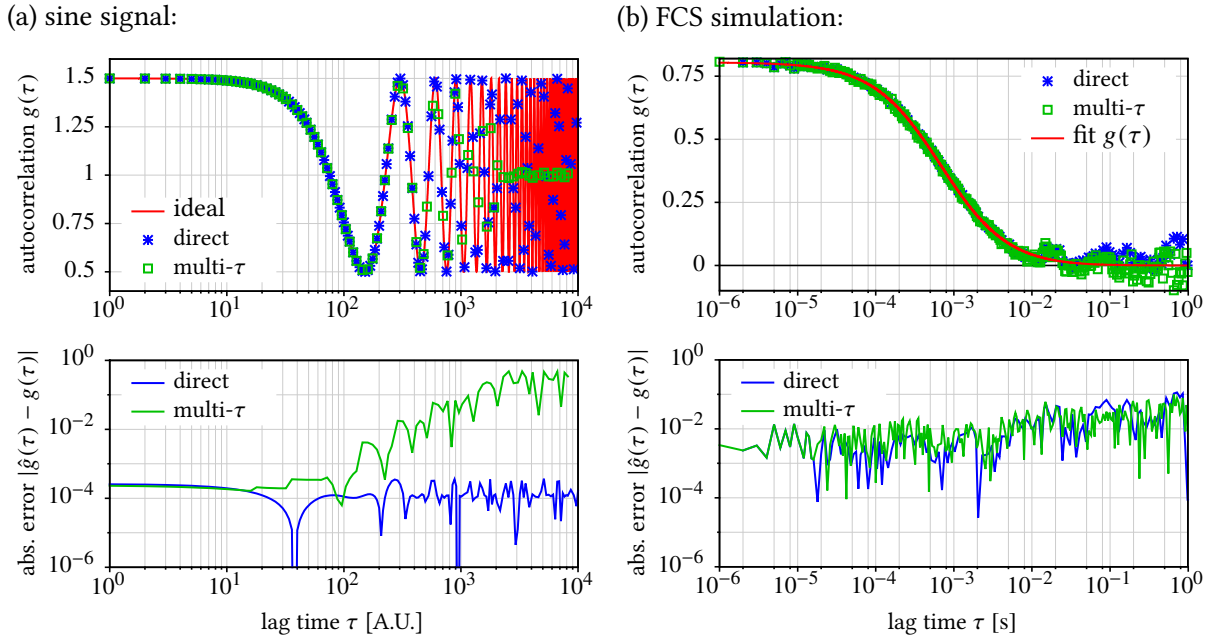


Figure 7.4. | **Effect of triangular averaging in a multi- τ correlation on the estimated correlation curve.** (a) Autocorrelation curve estimated from a sine signal with different correlators. (b) Autocorrelation curve estimated from an FCS simulation with different correlators. The upper graphs show the estimated correlation curves together with the theoretical expectation or a fit (solid red lines). The lower graphs show the absolute deviation of the estimates $\hat{g}(\tau)$ from the ideal curves $g(\tau)$.

Note that the width of both filters increases with the block number s , so that the error is larger at longer lag times. Figure 7.4(a) shows a sine signal that has been correlated either with a multi- τ correlator or by directly evaluating Eq. (7.1.10). The lower graph shows the absolute error between the calculated correlation function and the ideal signal. For the direct correlation, the error stays low, whereas it increases towards 1 for the multi- τ correlator. Figure 7.4(b) shows the same curves as Fig. 7.4(a), however for a simulated FCS data set. Here the averaging error is of minor importance, because the correlations have typically decayed towards 0 for large lag times. Details of the FCS simulation are described in appendix B.1.

Sometimes it is useful to estimate the statistical error, which is introduced by calculating the autocorrelation function using Eq. (7.1.10). It can for instance be used as a statistical weight in a model fit (see section 7.1.4). Some theoretical work has been done on the estimation of such errors [240, 242–244]. Koppel proposed an analytical expression, which requires the true correlation function, or fitting model to be known [243]. A method, that does not require any knowledge about the sample, is to estimate the statistical error from consecutive measurements directly. For this purpose, complete background- and bleach-corrected time series $F(x, y; t)$ is then split into N_{segments} segments of equal length. These are then correlated independently. The average and the standard deviation over the segments are finally used as estimates for the correlation function and its error, respectively. If the time series is stationary, this estimate is reliable. If not, the correlation curves for each segment will scatter wildly, causing a large error and a deformed average. In some cases this can be corrected by excluding some of the segments from the average. Note that this can be done without recorrelating the image series.

7.1.4. Model parameter estimation

The final step of an imaging FC(C)S analysis is model fitting. The models that were used throughout this thesis, were introduced in chapter 5. Fitting is performed for each pixel separately. In imaging FCS only one autocorrelation curve estimate $\hat{g}(\tau, \delta_x, \delta_y; x, y)$ is available for each pixel. Then the fit parameters are obtained by solving the least-squares optimization problem

$$\vec{\beta}^*(\delta_x, \delta_y; x, y) = \arg \min_{\vec{\beta}} \underbrace{\sum_{i=1}^{N_\tau} \left[\frac{\hat{g}(\tau_i, \delta_x, \delta_y; x, y) - g(\tau_i, \delta_x, \delta_y; \vec{\beta})}{\sigma_i(x, y)} \right]^2}_{=: \chi^2(\vec{\beta})}. \quad (7.1.16)$$

Here τ_i is the set of N_τ lag times at which the autocorrelation curve has been estimated. The fit model $g(\tau_i, \delta_x, \delta_y; \vec{\beta})$ depends on the set of parameters $\vec{\beta}$ that are optimized (e.g. diffusion coefficients, particle concentrations etc.). The $\sigma_i(x, y)$ are estimates of the statistical error associated with each $\hat{g}(\tau_i, \delta_x, \delta_y; x, y)$ (see last section). Note that the model does not explicitly depend on the coordinate (x, y) in the data set.

In an imaging FCCS data set, several auto- and cross-correlation functions are available for each pixel:

- for two-color FCCS: two autocorrelations $\hat{g}_{gg}(\tau; x, y)$ and $\hat{g}_{rr}(\tau; x, y)$ for the green and the red focus and one cross-correlation $\hat{g}_{gr}(\tau; x, y)$ between the two color channels.
- for two-pixel FCCS: one autocorrelation $\hat{g}(\tau, 0, 0; x, y)$ for the central pixel and any number of cross-correlations $\hat{g}(\tau, \delta_x, \delta_y; x, y)$ to neighboring pixels (for four direct neighbors: $\hat{g}(\tau, 0, -1; x, y)$, $\hat{g}(\tau, 0, 1; x, y)$, $\hat{g}(\tau, -1, 0; x, y)$, $\hat{g}(\tau, 1, 0; x, y)$).

Typically, the models presented in section 5.4 contain parameters, that reappear in the auto- and cross-correlation models. For instance, in the 2-color case for a binding reaction $A + B \rightleftharpoons AB$, the diffusion coefficients and concentrations of each species contribute to each of the three correlation curves. Therefore a global fitting approach is used, which finds the optimum set of parameters, that minimize the global least-squares problem:

$$\vec{\beta}^*(x, y) = \arg \min_{\vec{\beta}} \sum_{\substack{(\delta_x, \delta_y) \in \\ \{(0,0), \dots\}}} \sum_{i=1}^{N_\tau} \left[\frac{\hat{g}(\tau_i, \delta_x, \delta_y; x, y) - g(\tau_i, \delta_x, \delta_y; \vec{\pi}_{\delta_x, \delta_y}(\vec{\beta}))}{\sigma_i(\delta_x, \delta_y; x, y)} \right]^2. \quad (7.1.17)$$

Here, the curves are parametrized by their shift vector (δ_x, δ_y) . The parameter vector $\vec{\beta}$ comprises all parameters appearing in any of the fit models $g(\dots)$, and $\vec{\pi}_{\delta_x, \delta_y}(\vec{\beta})$ selects the subset of parameters, that are used for the model for a specific value of (δ_x, δ_y) . The variant of Eq. (7.1.17) for two-color cross-correlation is accordingly:

$$\vec{\beta}^*(x, y) = \arg \min_{\vec{\beta}} \sum_{\substack{\gamma\rho \in \\ \{gg, rr, gr\}}} \sum_{i=1}^{N_\tau} \left[\frac{\hat{g}_{\gamma\rho}(\tau_i; x, y) - g_{\gamma\rho}(\tau_i; \vec{\pi}_{\gamma\rho}(\vec{\beta}))}{\sigma_{\gamma\rho, i}(x, y)} \right]^2. \quad (7.1.18)$$

All optimization problems described in the last paragraph are least-squares problems with a relatively low number of parameters, typically between 2 and 20. So standard least squares optimization algorithms can be used. In most cases the Levenberg-Marquardt fit (LM fit) method [235–237] converges sufficiently well and fast, if good starting values are available. This is true even in the case of thousands of fits per data set, which are performed without supervision. Several methods have been used for this thesis to ensure good convergence of the algorithms:

- In order to obtain reasonable starting values for $\vec{\beta}$, a set of average correlation curves, calculated from the mean over all useable pixels, is first fitted with supervision. Then these fit results are used as starting values for all single-pixel fits.
- Typically the fit is repeated 2 – 4 times in each pixel, using the results of the last fit as initial values for the following one.
- An LM fit often gets stuck in local minima of the $\chi^2(\vec{\beta})$ landscape, if its starting values are far apart from the ideal solution. Therefore a different optimization algorithm can be applied to find good starting values for the LM fit. For this thesis, a stochastic optimizer was used that implements the principle of “simulated annealing” [245]. Although it gives good results, it typically has much longer runtimes, than an LM fit.
- In some cases it also helps to relax the model constraints. For instance, a two-color FCCS dimerization model may be modified to not enforce the same three diffusion coefficients D_A , D_B and D_{AB} in each of the three correlation curves. Six parameters may be used instead, which comprise two diffusion coefficients for each color channel {gg, rr, gr} (see section 12.2.2 for details). Then these six parameters are not linked over the whole data set. This generally improves the performance of the fit algorithm, as more degrees of freedom are available. Despite its better convergence, this method may complicate the interpretation of the fit results.

7.1.5. Maximum entropy data analysis

The software implementation of the maximum entropy method was done by Niko Schnellbacher during an internship under my supervision.

Often several components χ of different diffusion coefficients D_χ are present in a sample, and the relative concentration of each of these components is to be estimated from an FCS measurement. A simple approach to this problem is to set up a model as in Eq. (5.3.12) (p. 58), which contains one summand for each anticipated component. As an alternative approach, the maximum entropy data evaluation (MaxEnt) method can be used. It was modified for application in FCS in Refs. [246, 247]. Instead of writing the autocorrelation function Eq. (5.3.12) as a sum over few components, it can be formulated as an integral over a probability distribution $p_{\text{MaxEnt}}(D_\chi)$ of components χ , each with a different diffusion coefficient D_χ :

$$g_\gamma(\tau) = \frac{1}{\langle c \rangle} \int_{D_{\min}}^{D_{\max}} p_{\text{MaxEnt}}(D_\chi) \cdot (G_\gamma^\chi(\tau; D_\chi)/c_\chi) dD_\chi. \quad (7.1.19)$$

The integration is performed over the range of diffusion coefficients $[D_{\min} \dots D_{\max}]$. this range also limits the domain of the distribution $p_{\text{MaxEnt}}(D_\chi)$. The term $(G_\gamma^\chi(\tau; D_\chi)/c_\chi)$ is the correlation factor for a species of diffusion coefficient D_χ and a concentration of $1/V_{\text{eff}}$. Finally, $\langle c \rangle$ is the overall concentration of particles in the sample. As described in Refs. [246, 247] this integral equation can be solved using a numerical method from ref. [248]. This results in an estimate of the distribution $p_{\text{MaxEnt}}(D_\chi)$, but this inversion problem is ill-posed due to the large number of parameters. Therefore a regularization method is used. MaxEnt maximizes the statistical entropy

$$S := \int_{D_{\min}}^{D_{\max}} p_{\text{MaxEnt}}(D_\chi) \cdot \ln[p_{\text{MaxEnt}}(D_\chi)] dD_\chi. \quad (7.1.20)$$

of $p_{\text{MaxEnt}}(D_\chi)$, while minimizing an least squares “data term” $\chi^2(\vec{\beta})$, as given in Eq. (7.1.16). The entropy term leads to a preference of smooth distributions, which do not contain narrow spikes. Typically a regularization parameter allows to balance the data term and the regularization term.

7.2. Single particle tracking

Single particle tracking (SPT) was used as an independent control of diffusion coefficients measured with imaging FCS for this thesis (see section 8.2). In an SPT evaluation, the position of single particles in each frame is determined. As explained in section 3, the particles are not imaged into single bright pixels on the image sensor, but their image is smeared out due to the point spread function (PSF) of the microscope. The SPT algorithms determine the peak position of the image of every particle. As usual in particle-positioning microscopy, this peak position can be determined with higher precision, than the pixel size. The resolution of particle positions is therefore not limited to the pixel size [36, 53].

After the positions of all spots in every frame have been detected, they are connected to longer trajectories $(x_i(t), y_i(t))$ for several particles. Typically two points $(x(t), y(t))$ and $(x'(t+1), y'(t+1))$ are assigned to the same particle, if they moved only a small distance d_{max} between two frames. Finally the mean squared displacement

$$\text{MSD}_i(\tau) = \frac{1}{N_i - \tau} \cdot \sum_{t=1}^{N_i - \tau} \left[(x_i(t + \tau) - x_i(t))^2 + (y_i(t + \tau) - y_i(t))^2 \right] \quad (7.2.1)$$

of each trajectory of length N_i is calculated. Then a fit to the MSD for normal or anomalous diffusion (cf. section 1.3)

$$\text{MSD}(\tau) = 4D \cdot \tau \quad \text{or} \quad \text{MSD}(\tau) = 4\Gamma \cdot \tau^\alpha \quad (7.2.2)$$

is performed, yielding the parameters of the motion.

For SPT the 2D PARTICLETRACKER plug-in [249, 250] for the free image processing software FIJI was used in this thesis. The MSDs were calculated and diffusion coefficients were extracted using a MATLAB script. This script also calculates an averaged MSD, from a subset of the trajectories. A set of filter conditions is applied to them that are designed to sort out outliers. For instance nonsensically high or low diffusion coefficients are sorted out. To fit Eq. (7.2.2), an outlier-robust linear regression (IRLS algorithm) was used, which is implemented in the MATLAB method `robustfit()`.

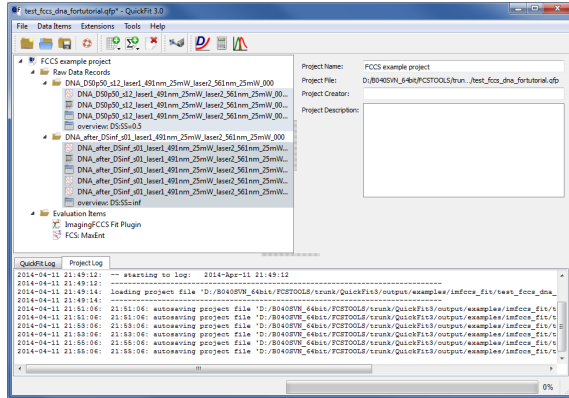
The accuracy and precision, with which the particle positions are estimated, depend mainly on the signal-to-noise ratio (SNR) of the input images. For the algorithm used here, Sbalzarini and Koumoutsakos show, that the positioning accuracy is better than half a pixel, even for low SNRs around 1. For SNRs bigger than 5, the accuracy is even below 0.1 pixels [249]. The precision was shown to always be better than 0.5 pixels. For a typical imaging FCS measurement of fluorescent microspheres at a low concentration, the SNR was 3 or better. Therefore the same image series that are used for an imaging FCS evaluation can be used for SPT, provided the sample is dilute, so that single particles can actually be distinguished.

7.3. The data evaluation software QuickFit 3.0

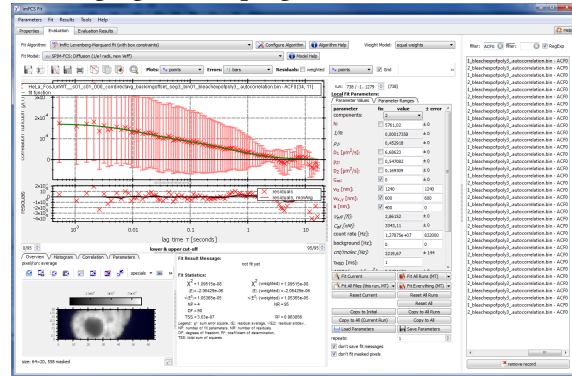
If not noted otherwise, all data evaluation methods were implemented in a software package called QUICKFIT 3.0, which was developed during this thesis. It was designed as a data evaluation software for FCS and imaging FCS techniques and later evolved to include the SPIM instrument control (see next section)¹. The core program provides a project manager that can hold a set of raw data items and a set

¹QUICKFIT 3.0 is available free of charge from <http://www.dkfz.de/Macromol/quickfit/>.

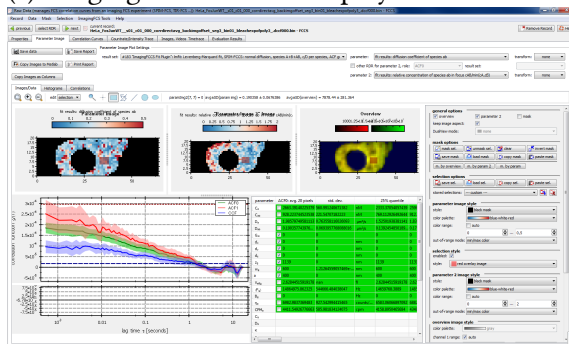
(a) Project management



(b) imaging FCS fit plug-in



(c) imaging FCCS results display



(d) MaxEnt evaluation plug-in

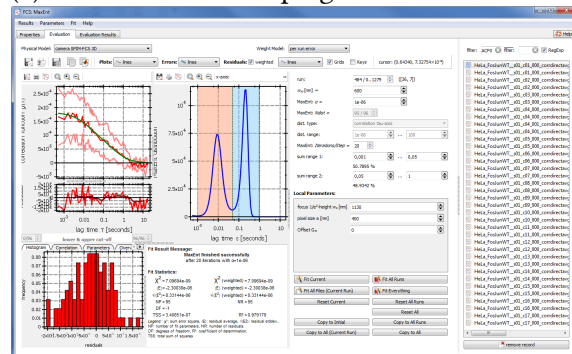


Figure 7.5. | Screenshots of QUICKFIT 3.0.

of evaluation objects that operate on one or more of these raw data items. The project may be saved to disk and reloaded later. It contains links to the actual raw data files and stores all fit results internally. The raw data files are never changed. The functionality of raw data and evaluation items is not defined by QUICKFIT 3.0 itself, but by plug-ins, which are loaded on startup. The open source QT library was used for the graphical user interface of QUICKFIT 3.0. It is completely written in standard C++. Thus the software runs on all important desktop operating systems (MICROSOFT WINDOWS, LINUX and MACOS). Figure 7.5 shows a set of screenshots of QUICKFIT 3.0.

7.4. Instrument control for a SPIM

Later, QUICKFIT 3.0 was extended with a specialized plug-in, that can control the SPIM described in chapter 6. Communication with the different hardware components (cameras, shutters, lasers, stages, etc.) was implemented in separate plug-ins, as shown in Fig. 7.6. In this way, the replacement of old or addition of new computer-controlled devices is easy, as only a new communication plug-in needs to be implemented. The main control-plug-in implements different data acquisition schemes:

- Live-view from the camera
- Acquisition of fast image series for imaging FCS and imaging FCCS data evaluation: This acquisition results in an image series with the principal fluorescence measurement, a set of full-frame overview images with different illumination modes (e.g. transmission and different fluorescence modes), a background image series for background correction. In addition, a set of metadata is stored, which contains user-supplied information about the sample, the complete state of the

microscope (all filters, laser powers, etc.) and additional readings (temperature in the sample chamber, etc.) which were taken during the acquisition.

- Acquisition of arbitrary image stacks: One or more stages are moved and at each position several images are acquired. There is also a possibility to acquire images with different filter and illumination configurations for each position.
- Scripted acquisitions: This allows to control the instrument by a small JAVASCRIPT program and is used to perform automated long-term measurements.

All data is typically written in standard file formats, such as tagged image file format (TIFF), comma separated values (CSV) or simple text files. Therefore the data is readable by most scientific software.

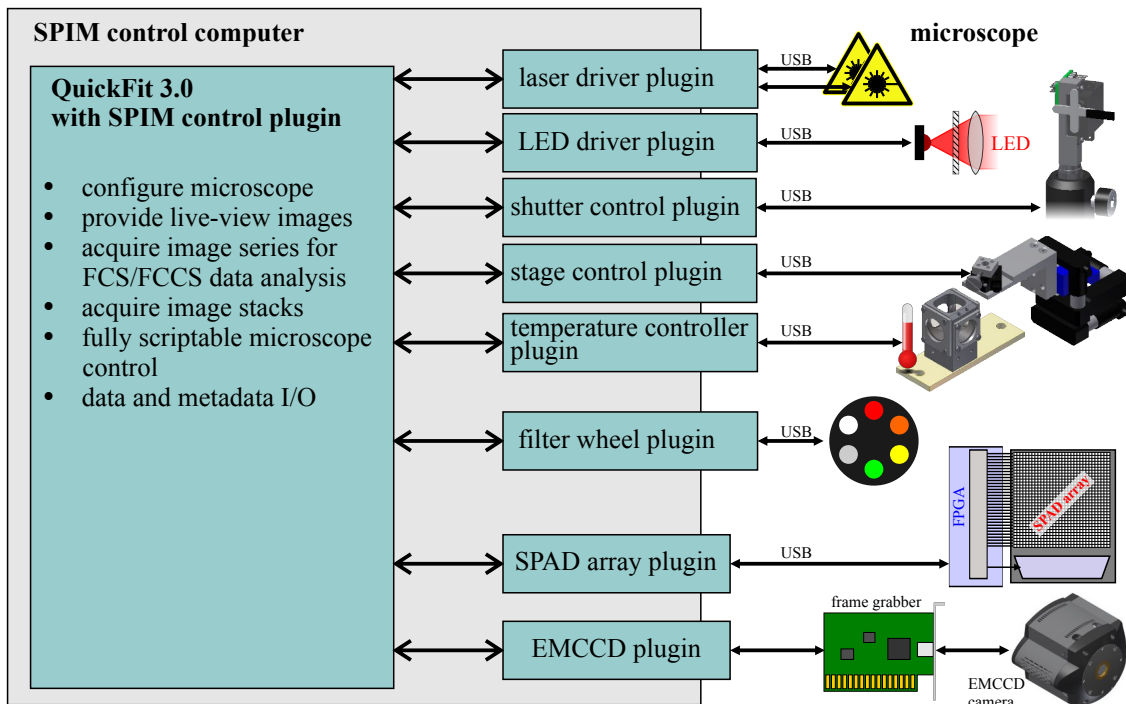


Figure 7.6. | Overview of the SPIM control software and its connections to the microscope.

8. Evaluation of the SPIM for FCS measurements

Measurements in this chapter were performed in part together with Jan Buchholz (DKFZ, Heidelberg) and Anand Pratap Singh (NUS, Singapore).

This chapter recapitulates several test measurements, demonstrating that single plane illumination fluorescence correlation spectroscopy (SPIM-FCS) works correctly and yields reasonable results. At first, the required alignment and calibration methods are described in section 8.1. Sections 8.2-8.4 then discuss how well SPIM-FCS can measure absolute diffusion coefficients, concentrations and the parameters of anomalous diffusion. Several typical artifacts in SPIM-FCS measurements are summarized in 8.5. Section 8.6 discusses the applicability of SPIM-FCS to live cell measurements. Finally, different linear image sensors (section 8.7) and SPAD array sensors (section 8.8) are compared and their usefulness in SPIM-FCS is discussed.

8.1. Alignment and calibration procedure for FCS measurements

Two requirements have to be fulfilled for single-color imaging FCS applications: the light sheet needs to overlap with the image plane as well as possible and the field of view of the detection microscope has to be illuminated with the thinnest part of the light sheet (see section 6.3.1 for more details). Only if these conditions are fulfilled, the microscope can be successfully used for measurements. Therefore a daily alignment of the light sheet microscope according to section 6.3 has to be performed.

The fitting models used in SPIM-FCS depend on parameters, which describe either the sample (concentrations, diffusion coefficients etc.), or describe the molecular detection efficiency function (MDE) of the microscope (pixel size a in the image plane, point spread function (PSF) widths w_g , z_g). The MDE parameters need to be determined before model fitting, as they may change with the day-to-day alignment of the instrument. The pixel size a only depends on the camera parameters and the magnification of the microscope, which does not change significantly when the instrument is realigned. Therefore the nominal pixel size of the camera can simply be divided by the magnification M_{xy} , which is given by the combination of detection objective and tube lens. An accurate value for the PSF height z_g is obtained from a bead scan, as described in section 6.3.2. Typically the average or median $1/e^2$ -half width of the 3-dimensional Gaussian fits is used. This fit also accounts for a slight tilt of the MDE images in the bead scan, which may be caused by an imperfectly aligned sample translation stage. Technically speaking, the bead scan determines the MDE of the microscope, which includes the finite pixel size, but in z -direction, the pixel size plays only a minor role, so that the PSF length z_g can be determined from the bead scan.

Finally the PSF width w_g is calibrated using an FCS measurement. Due to the dependence of the bead scan results on the pixel size, w_g cannot be obtained from these scan results. The calibration also ensures that any artifacts due to the shape of the focus are cleared (see also section 8.3). For the calibration, a SPIM-FCS measurement is performed on an aqueous solution of fluorescent microspheres (e.g. $\varnothing = 100$ nm: T7279, F8794 or F8786, Invitrogen) or a long, fluorescently-labeled DNA. The diffusion in the sample should be slow enough to ensure that most of the decay of the autocorrelation curve is captured by the image sensor with its limited temporal resolution (see section 8.2 for details). Finally,

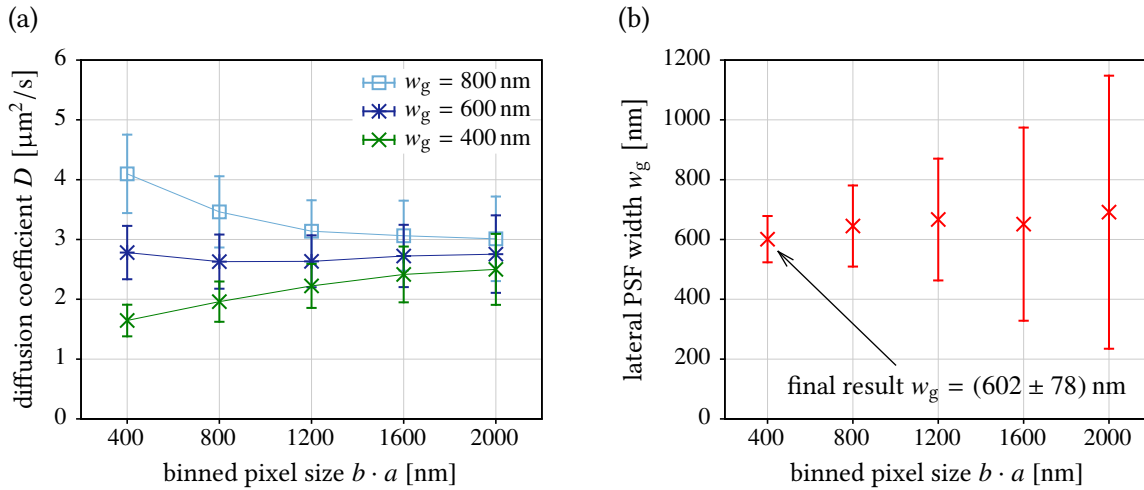


Figure 8.1. | Results of an imaging FCS calibration with increasing pixel size. (a) Plot of the diffusion coefficient D obtained for different pixel sizes $b \cdot a$ and for several test values for the lateral PSF width w_g . (b) Plot of the fit results w_g for different pixel size $b \cdot a$, where $D_{\text{ref}} = 2.76 \mu\text{m}^2/\text{s}$ was fixed. Data points in both graphs show the average and standard deviation over the whole imaging FCS measurement. Sample: TetraSpec multi-fluorescent microspheres ($\varnothing = 100 \text{ nm}$), camera: Andor iXon X3, EMCCD, $a = 400 \text{ nm}$, $z_g = (1138 \pm 100) \text{ nm}$

the PSF width w_g is determined from a fit, in which z_g is fixed to the value from the bead scan and the diffusion coefficient D is fixed to a reference value. In a confocal FCS measurement, D is usually taken from a published reference value, which was obtained with an independent measurement method (e.g. $D_{20^\circ\text{C},\text{W}} = 407 \mu\text{m}^2/\text{s}$ for Alexa-488 [251], or $D_{20^\circ\text{C},\text{W}} = 317 \mu\text{m}^2/\text{s}$ for Alexa-568 [252]).

In imaging FCS, the reference value for D can be determined from the very same measurement, as the known pixel size can be used as a ruler. Therefore no reference value from an independent method is required. On image sensors, such as EMCCD cameras, nearly the whole quadratic pixel is light-sensitive. Therefore the SPIM-FCS models from sections 5.2 and 5.3 stay valid, if $b \times b$ pixels ($b = 1, 2, 3, \dots$) are binned together, before the autocorrelation functions are calculated. The only required change in the model parameters, is the larger pixel size $b \cdot a$, which is introduced by the exchange $a \rightarrow b \cdot a$. If $b \cdot a$ is significantly larger than the (yet unknown) width of w_g of the PSF, the dependence of the fit model on w_g becomes weak. In those cases the dwell time of particles in the focus mainly depends on the longitudinal MDE-size z_g and the pixel size a , so that the diffusion coefficient D can be reliably determined without knowledge of the true value of w_g . This value for D is then used in a second step to determine w_g in a data set with $b = 1$. This method of calibration for imaging FCS was first proposed by Bag et al. in Ref. [114] for ITIR-FCS, and later extended and refined for SPIM-FCS in our publications Refs. [130, 132]. An exact protocol for this “pixel-binning method” is as follows [130]¹:

1. A bead scan is recorded and evaluated to yield the longitudinal PSF width z_g (see section 6.3.2).
2. A SPIM-FCS measurement of the solute test sample in a sample bag is performed. The images should be at least $\sim 20 \times 20$ pixels in size..
3. In the image stack from step 2 is binned into different super-pixels, consisting of $b \times b$ camera pixels (here $b = 1, 2, \dots, 5$). Autocorrelation functions are calculated for each value of b .
4. The reference diffusion coefficient D_{ref} is determined by a fit of the SPIM-FCS model Eq. (5.3.25) (p. 61) to the autocorrelation functions, which were calculated in the last step. In these fits, the pixel size

¹A plugin for QUICKFIT 3.0 is available, which performs this calibration in a semi-automated fashion.

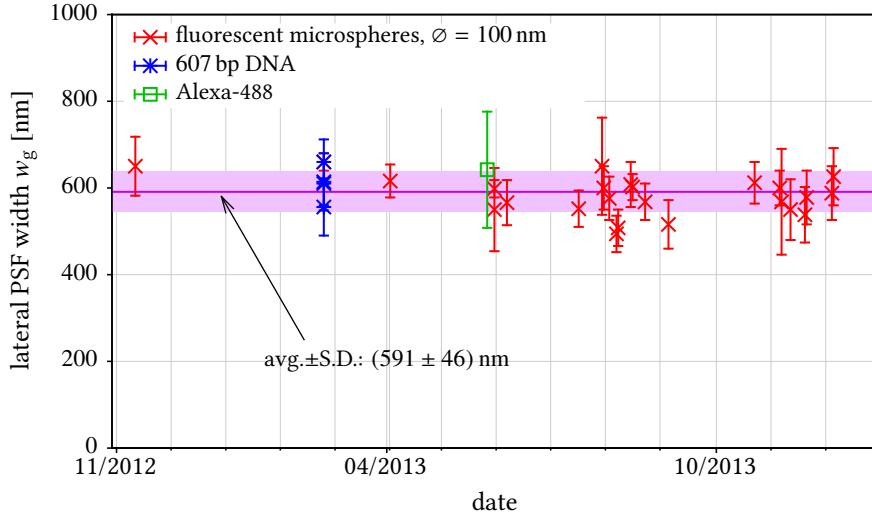


Figure 8.2. | Lateral PSF width w_g over more than one year and for several different calibration samples. The results are shown for the green color channel only. Camera: Andor iXon X3 EMCCD, $\tau_{\min} \approx 500 \mu\text{s}$.

$b \cdot a$ and the PSF length z_g are fixed to their established values. The unknown PSF width w_g is fixed to different test values, which approximately surround the expected value of w_g . For instance, if $w_g \approx 600 \text{ nm}$ is expected, the test values $\{400, 600, 800\} \text{ nm}$ could be used for w_g . Figure 8.1(a) shows a plot of the diffusion coefficients, which are extracted for several values of $b \cdot a$ with this method. With increasing pixel size $b \cdot a$, the influence of the assumed w_g gets smaller and the curves converge to a common value. Finally D_{ref} is determined to be the average of the diffusion coefficients measured at the largest pixel size ($b \cdot a = 2000 \text{ nm}$ and $D_{\text{ref}} = (2.76 \pm 0.26) \mu\text{m}^2/\text{s}$ in Fig. 8.1a).

5. A final fit for the data set with $b = 1$, yields the calibrated lateral PSF width w_g . In that fit D_{ref} from the last step, z_g from the first step and the pixel size $b \cdot a$ are fixed, so only the particle number and w_g are free fit parameters. Exemplary results are shown in Fig. 8.1(b). In that case the calibrated PSF width was $w_g = (602 \pm 78) \text{ nm}$.

A second possible method to determine the lateral PSF width w_g was described in Ref. [130]. Instead of pixel binning, it uses the distance between two cross-correlated pixels as a ruler. The protocol for this method is nearly identical to the protocol above. Instead of the number of binned pixels $b \times b$, the shift between the cross-correlated pixels $\delta_x = b \cdot a$ is varied. Since the amplitude of the cross-correlation function approximately decreases with δ_x as $\exp(-\delta_x^2/w_g^2)$, the significance of the fits decreases accordingly. Therefore the distance δ_x should not be much larger than the expected PSF width w_g . This “shift method” is especially useful for sensors such as SPAD arrays, where the sensitive area is a small circle, instead of a rectangular pixel. If such pixels were binned, the validity of the MDE models in section 5.2 would break down and hence the pixel-binning method cannot be used.

Figure 8.2 shows the stability of the lateral PSF width w_g over more than one year. It summarizes the results of more than 30 calibrations performed for different samples. The values of z_g over a comparable period are shown in Fig. 6.16(a) (p. 98). It can be seen that the average PSF sizes scatter statistically by about 10%. This is caused by day-to-day variations in the alignment. A daily calibration balances these deviations and leads to reliable results. The average PSF size over all data points in Fig. 8.2 was $(591 \pm 46) \text{ nm}$. For comparison, the MDE size, obtained from the bead scans directly, was $(649 \pm 80) \text{ nm}$ (see Fig. 6.16b). As expected, this value is $\sim 10\%$ larger than the value from the SPIM-FCS calibration,

which determines the size of the PSF only.

Figure 8.2 also shows that it is of minor importance, which sample is used for the calibration. All samples shown in the graph yielded comparable results. Even the value obtained for Alexa-488 (green rectangles) agrees with the other results, although only a small part of the decay in the autocorrelation curve is captured by the EMCCD camera (see next section).

8.2. Determination of absolute diffusion coefficients

The calibration described in the last section, enables SPIM-FCS to measure absolute diffusion coefficients. In order to check this claim, the diffusion coefficient D of an aqueous solution of fluorescent microspheres with diameters of 100 nm and 200 nm (F8803 and F8811, Invitrogen) was measured with three different methods: SPIM-FCS, confocal FCS and single particle tracking (SPT). Assuming that the size estimate of the manufacturer is correct, the diffusion coefficient D of these spheres in water at 20 °C can be calculated from Eq. (1.3.3) (p. 7). Also the diffusion correlation time τ_D can be estimated for the used SPIM setup:

$$\begin{aligned} \varnothing = 100 \text{ nm} : & & D_{20^\circ\text{C},\text{W}} = 4.3 \mu\text{m}^2/\text{s}, & & \tau_D \approx 76 \text{ ms} \\ \varnothing = 200 \text{ nm} : & & D_{20^\circ\text{C},\text{W}} = 2.05 \mu\text{m}^2/\text{s}, & & \tau_D \approx 160 \text{ ms}. \end{aligned}$$

The values for τ_D are significantly larger than the temporal resolution $\tau_{\min} = 330 - 530 \mu\text{s}$ of the EMCCD camera (Andor iXon 860), so a large part of the decay of the autocorrelation curves will be acquired in a measurement. This is illustrated with the blue curve in Fig. 8.3(a). The red curves in the same figure show autocorrelation curves from the same sample, obtained however with a confocal microscope. Here

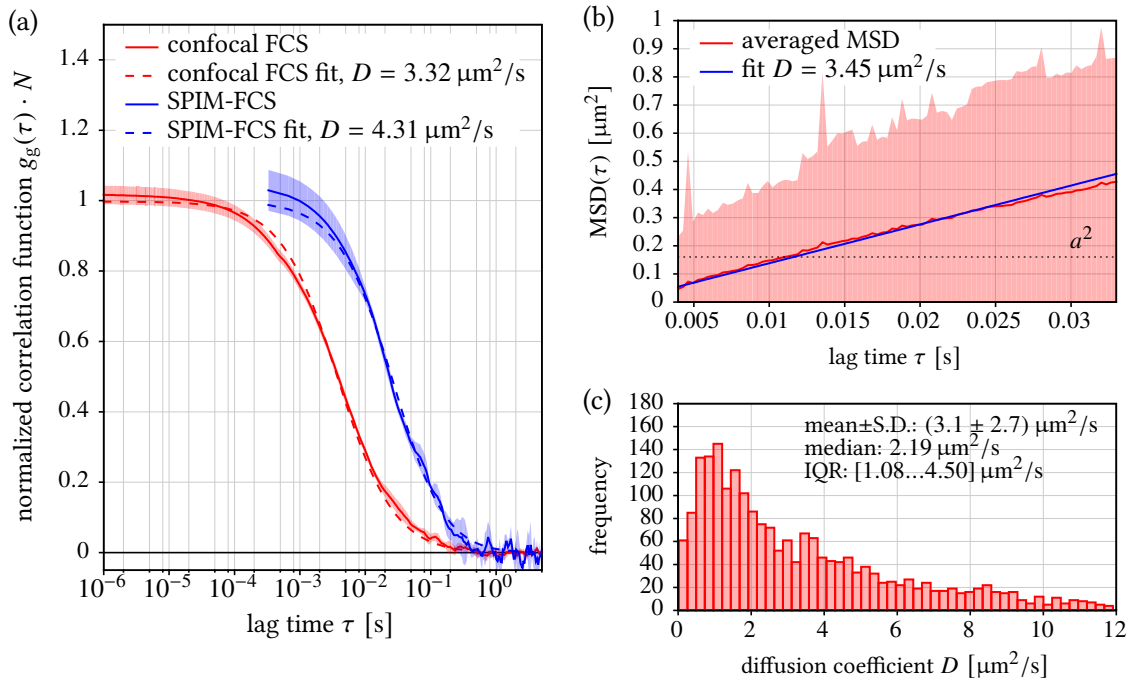


Figure 8.3. | (a) Correlation curves from SPIM-FCS (blue) and confocal FCS measurements (red) on fluorescent microspheres with $\varnothing = 100$ nm. (b) Averaged MSD and (c) diffusion coefficient distribution obtained with SPT on the same sample. In (b) the average and standard deviation over 1690 single-trajectory MSDs are shown in red. The blue line is a fit of the model $\text{MSD}(\tau) = 4D\tau$. (c) shows the distribution of diffusion coefficients, extracted from 2081 single particle MSD curves (IQR = interquartile range).

microsphere diameter	diffusion coefficients $D_{20^\circ\text{C},\text{W}}$ [$\mu\text{m}^2/\text{s}$], obtained with			
	SPIM-FCS	confocal FCS	SPT	theory
100 nm	(3.8 ± 1.1)	(3.0 ± 0.2)	(3.09 ± 0.05)	4.3
200 nm	$(1.9 \pm 0.7)^*$	$(2.10 \pm 0.05)^*$	$(2.05 \pm 0.11)^*$	2.15

* measurements performed by Anand Pratap Singh (NUS, Singapore) on a comparable SPIM, as the one described here.

Table 8.1. | Diffusion coefficients $D_{20^\circ\text{C},\text{W}}$ measured by SPIM-FCS and other methods on two samples of green fluorescent microspheres of different diameter.

the significantly smaller focus ($w_g \approx 250$ nm) leads to a decay of $g(\tau)$ at smaller lag times. Results of an SPT evaluation for the microspheres with $\varnothing = 100$ nm are shown in Fig. 8.3(b,c). Due to the limited accuracy of the SPT algorithm of approximately $\pm a/2$, the MSDs were evaluated only for lag times $\tau > 4$ ms.

Table 8.1 compares the results obtained from SPIM-FCS, from confocal FCS and from a single particle tracking (SPT) evaluation (see section 7.2). As shown by the values in this table, SPIM-FCS yields the

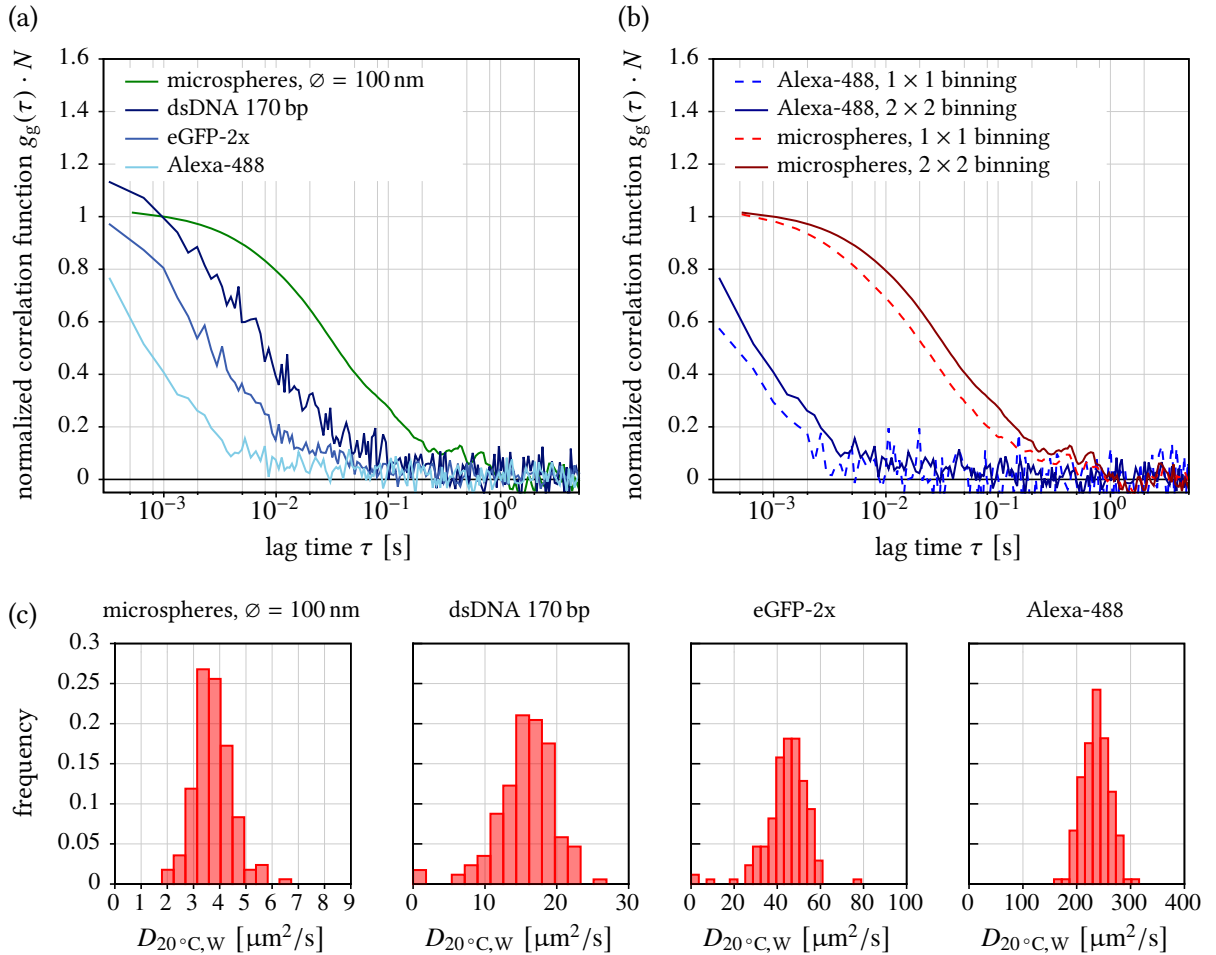


Figure 8.4. | (a,b) Normalized SPIM-FCS autocorrelation functions acquired with an Andor iXon X3 EMCCD camera for different samples and binnings. (c) Histograms of the diffusion coefficients from single SPIM-FCS measurements. In (a,c) 2×2 binning was used. (b) Compares 1×1 binning and 2×2 binning.

same diffusion coefficients (within the errors) as the other two methods. Furthermore, it can be said, that SPIM-FCS yield absolute diffusion coefficients, because it does not rely on external calibration standards. Nevertheless, the theoretical value obtained for the microspheres of $\varnothing = 100$ nm is higher than the measured values. This might be caused by aggregation and swelling of the beads during storage, which is backed by the observation that the diffusion coefficient of fluorescent microspheres from a single batch decreases slowly over the duration of one year.

In order to check the range of diffusion coefficients that can be accurately measured with SPIM-FCS, several samples with different particle sizes and diffusion coefficients were used (see Tab. 8.2 for a summary of the results). Figure 8.4(a) shows normalized autocorrelation curves obtained for a variety of samples: microspheres with $\varnothing = 100$ nm, dsDNA with a length of 170 bp (confocal FCS: $D_{20^\circ\text{C},\text{W}} \approx 27 \mu\text{m}^2/\text{s}$), eGFP dimers (eGFP-2x, confocal FCS: $D_{20^\circ\text{C},\text{W}} \approx 80 \mu\text{m}^2/\text{s}$) and free Alexa-488 molecules (confocal FCS: $D_{20^\circ\text{C},\text{W}} \approx 390 \mu\text{m}^2/\text{s}$). All measurements were performed with an Andor iXon X3 860 EMCCD camera at frame times of $\Delta t_{\text{frame}} = 330 - 560 \mu\text{s}$. A 2×2 binning was applied to each measurement, which increases the size of the focus and therefore extends the correlation time τ_{D} of the particles. This effect is shown in Fig. 8.4(b) on two examples. It can be seen that especially for the fast Alexa-488, a larger part of the slope of the autocorrelation curve is obtained. In addition, the noise on the curves is reduced due to the higher number of photons captured by the larger pixel.

For comparison, Tab. 8.2 also contains the results of confocal FCS measurements for each sample. Figure 8.5 shows these data as a plot, in which ideally all points would lie on the black dotted line. For slow samples ($D_{20^\circ\text{C},\text{W}} < 10 \mu\text{m}^2/\text{s}$) the SPIM-FCS and confocal FCS measurements yield the same values. For faster samples, a bias of the SPIM-FCS results towards lower diffusion coefficients exists. In these cases the temporal resolution is not sufficient and only a part of the slope of the autocorrelation function is captured (see also the examples in Fig. 8.4a). This leads to an underestimation of the diffusion coefficient by the model fit.

Finally, a systematic analysis was performed, which elucidates the influence of the minimum lag time τ_{min} on the fitted diffusion coefficient. A single SPIM-FCS measurement of $\varnothing = 100$ nm microspheres was analyzed by using only lag times $\tau > \tau_{\text{min}}$. Figure 8.5(b) shows the obtained diffusion coefficients, as a function of the ratio between minimum lag time τ_{min} and the diffusion correlation time $\tau_{\text{D}} = (110 \pm 26)$ ms. The value of τ_{D} was obtained at the full temporal resolution $\tau_{\text{min}} = \Delta t_{\text{frame}} = 330 \mu\text{s}$. The plot shows the median and the interquartile range (IQR) of the diffusion coefficients extracted from all pixels. For $\tau_{\text{min}} < \tau_{\text{D}}/30$, the fitted diffusion coefficient depends only weakly on the temporal resolution and the relative error is below 6%. Above this threshold, the relative error rises with increasing τ_{min} . Also the IQR increases, as the noisiness of the autocorrelation curves has a higher impact for low autocorrelation amplitudes $g(\tau)$ near 0. Note however, that all results are still correct within a factor of 2. Sankaran et al. published comparable results for imaging FCS on a total internal reflection fluorescence microscope and for simulations [112]. There the authors suggest to use a minimum lag time of $\tau_{\text{min}} < \tau_{\text{D}}/100$ to obtain reliable diffusion coefficients.

Sample	diffusion coefficients $D_{20^\circ\text{C,W}}$ [$\mu\text{m}^2/\text{s}$], obtained with		
	SPIM-FCS	confocal FCS	theory
dsDNA 28 bp	(66 ± 10)	(84 ± 4)	83
dsDNA 170 bp	(22 ± 3)	(27.3 ± 0.8)	
dsDNA 607 bp	(8.1 ± 5)	(12.7 ± 3.8)	
green microspheres, $\varnothing = 40$ nm	(5.6 ± 1.2)	(5.9 ± 1.4)	10.7
green microspheres, $\varnothing = 100$ nm	(3.8 ± 1.1)	(3.0 ± 0.2)	4.3
multi-colored microspheres, $\varnothing = 100$ nm	(3.1 ± 0.2)		4.3
green microspheres, $\varnothing = 200$ nm	(1.9 ± 0.7)	(2.10 ± 0.05)	2.15
QDot-525 streptavidin ITK	(11.4 ± 1.0)	(22 ± 3)	20 – 40
QDot-565 ITK	(17.7 ± 5.9)	(33.1 ± 2.6)	20 – 40
eGFP-1x	(69.0 ± 18.5)	(102 ± 11)	109
eGFP-2x	(50.8 ± 10.7)	(79.6 ± 7.9)	
eGFP-3x	(34.3 ± 8.7)	(58.1 ± 0.5)	
eGFP-4x	(29.1 ± 5.6)	(55.8 ± 3.1)	
Alexa-488	(270 ± 50)	386	
Alexa-594	(158 ± 96)	257	

Table 8.2. | Summary of diffusion coefficients measured for different samples using SPIM-FCS and confocal FCS. Values are given as $D_{20,W}$ at 20°C with water as solvent (see appendix C.4). All measurements were performed with an Andor iXon X3 860 EMCCD camera with temporal resolution of 330 – 500 μs . Theoretical estimates are given, as explained in appendix C.5 for microspheres of known diameter and for cylindrical molecules (eGFP-monomers: diameter $d_{\text{cyl}} = 3$ nm, length $l_{\text{cyl}} = 4$ nm; 28 bp dsDNA: $d_{\text{cyl}} = 2.5$ nm, $l_{\text{cyl}} = 9.24$ nm).

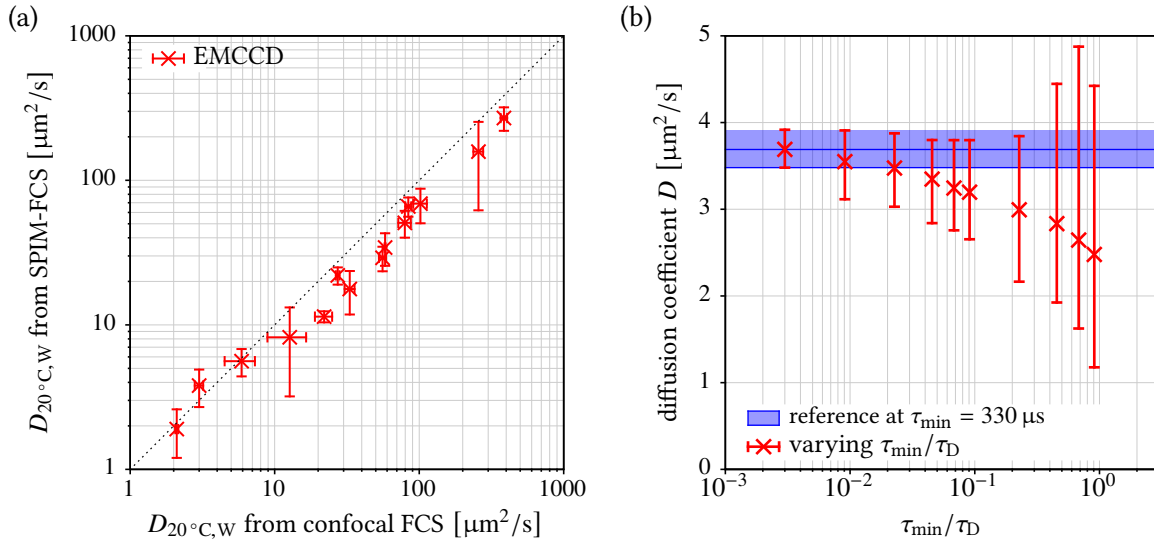


Figure 8.5. | (a) Comparison of diffusion coefficient measured for different samples with SPIM-FCS and confocal FCS. (b) Diffusion coefficient $D_{20^\circ\text{C,W}}$, as a function of ratio between minimum lag time τ_{min} and diffusion correlation time τ_D , measured with SPIM-FCS. The data shown in (a) is the same that is listed in Tab. 8.2. For (b) a SPIM-FCS measurement of green fluorescent microspheres ($\varnothing = 100$ nm) was evaluated taking into account only lag times $\tau \geq \tau_{\text{min}}$, with $\tau_D = 110$ ms resulting from a fit with $\tau_{\text{min}} = 330 \mu\text{s}$. Datapoints are the median and errorbars the IQR of the fit results for pixels from the SPIM-FCS measurement.

8.3. Particle concentration measurements in SPIM-FCS

Besides the diffusion coefficient D , the particle concentration c is the second basic parameter that can be extracted from FCS measurements. The concentration is represented by the zero-lag amplitude $g(0)$, to which the autocorrelation function levels off at small lag times τ (compare also Fig. 5.5(b) on page 60). Therefore the accuracy of a concentration measurement should depend on how well this plateau is represented in the measured lag times. In order to quantify this, the influence of the ratio τ_{\min}/τ_D on the measured concentration was analyzed. Results are shown in Fig. 8.6(a), as median and IQR over all pixels in a SPIM-FCS measurement of an aqueous solution of fluorescent microspheres ($\varnothing = 100$ nm, $\tau_D = (110 \pm 26)$ ms). For large ratios τ_{\min}/τ_D , the estimated concentration and its IQR increase. However, for small minimal lag times $\tau_{\min} < \tau_D/30$ the estimated concentration settles, and the relative deviation from the value at $\tau_{\min} = 330$ μ s is below 10%. Again these results are comparable to the findings in Ref. [112].

To check how well SPIM-FCS performs in concentration measurements, several dilution series were performed using SPIM-FCS and confocal FCS in parallel. Figure 8.6(b) shows the results for three different samples: fluorescent microspheres with $\varnothing = 100$ nm (F8803, Invitrogen), QDot-525 streptavidin ITK (Q10041MP, Invitrogen) and Alexa-488. Each data point represents the mean and standard deviation over all pixels in a SPIM-FCS measurement and ≥ 6 repeats for confocal FCS. Comparable results were obtained on several repeated measurements during two years. A linear relationship between concentration measurements with SPIM-FCS and confocal FCS is obtained over more than three orders of magnitude. The dashed lines in the figure are outlier-robust IRLS fits of a linear function $f(x) = \beta \cdot x$. The resulting slopes were $\beta = 2.995$ for microspheres, $\beta = 2.77$ for QDots. These values are very close to each other, as $\tau_{\min}/\tau_D \approx 3 \cdot 10^{-3}$ for microspheres and $\tau_{\min}/\tau_D \approx 10^{-2}$ for QDots ($\tau_D = (25 \pm 9)$ ms), which is well below the given threshold of $\tau_{\min} < \tau_D/30$. For Alexa-488, the temporal resolution of

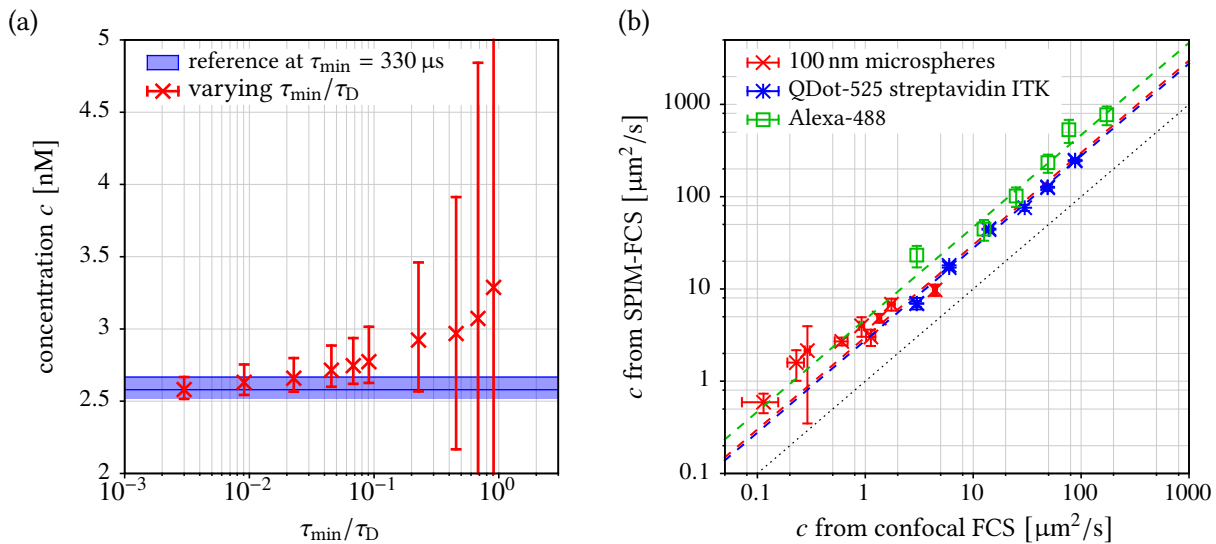


Figure 8.6. | (a) Effect of different ratios τ_{\min}/τ_D on the concentration c , measured with SPIM-FCS. (b) Comparison of concentration measurements with SPIM-FCS and confocal FCS. For (a) a SPIM-FCS measurement of green fluorescent microspheres ($\varnothing = 100$ nm) was evaluated taking into account only lag times $\tau \geq \tau_{\min}$, with $\tau_D = 110$ ms (obtained at $\tau_{\min} = 330$ μ s). Datapoints are the median and errorbars the IQR of the fit results for all pixels from the SPIM-FCS measurement. In (b) the dashed lines are outlier-robust linear fits of $f(x) = \beta \cdot x$ with slopes of $\beta = 2.995$ for microspheres, $\beta = 2.77$ for QDots and $\beta = 4.67$ for Alexa-488. Errorbars are averages over several measurements.

the EMCCD camera is not sufficient and $\tau_D = (3.0 \pm 1.3)$ ms yields $\tau_{\min}/\tau_D \approx 10^{-1}$, which is above the given threshold. Therefore the overestimation of the concentration ($\beta = 4.67$) is even higher than for the microspheres.

In all three dilution series, SPIM-FCS yielded a value of the concentration, which was approximately 3 times higher than the value obtained for the same sample with confocal FCS. If the temporal resolution of the camera is insufficient (as e.g. for Alexa-488), this factor can be even higher. However, the linear relation between confocal FCS and SPIM-FCS persists over several orders of magnitude. Therefore the overestimation can be compensated easily, when a calibration sample of known concentration can be produced. Its true concentration ought to be determined with an independent method, such as absorption spectroscopy, or confocal FCS on a carefully calibrated instrument.

In addition to the limited temporal resolution of EMCCD cameras, several other potential reasons for the described overestimation were identified. They will be explained and analyzed on the next pages. Nevertheless, no single factor could be found, that completely explains $\beta \approx 3$.

An obvious reason for the overestimation of c is the presence of an uncorrected background signal (see section 5.5.2). Before each SPIM-FCS measurement, a background frame is acquired, and is used for background correction. As it is recorded while the illumination is switched off, it cannot account for any direct scattering of illumination light onto the image detector. Such scattered light could be caused for instance by impurities in the sample buffer, or the sample bags themselves. It was measured using sample bags, which are filled with buffer without fluorescent particles. The average intensity of

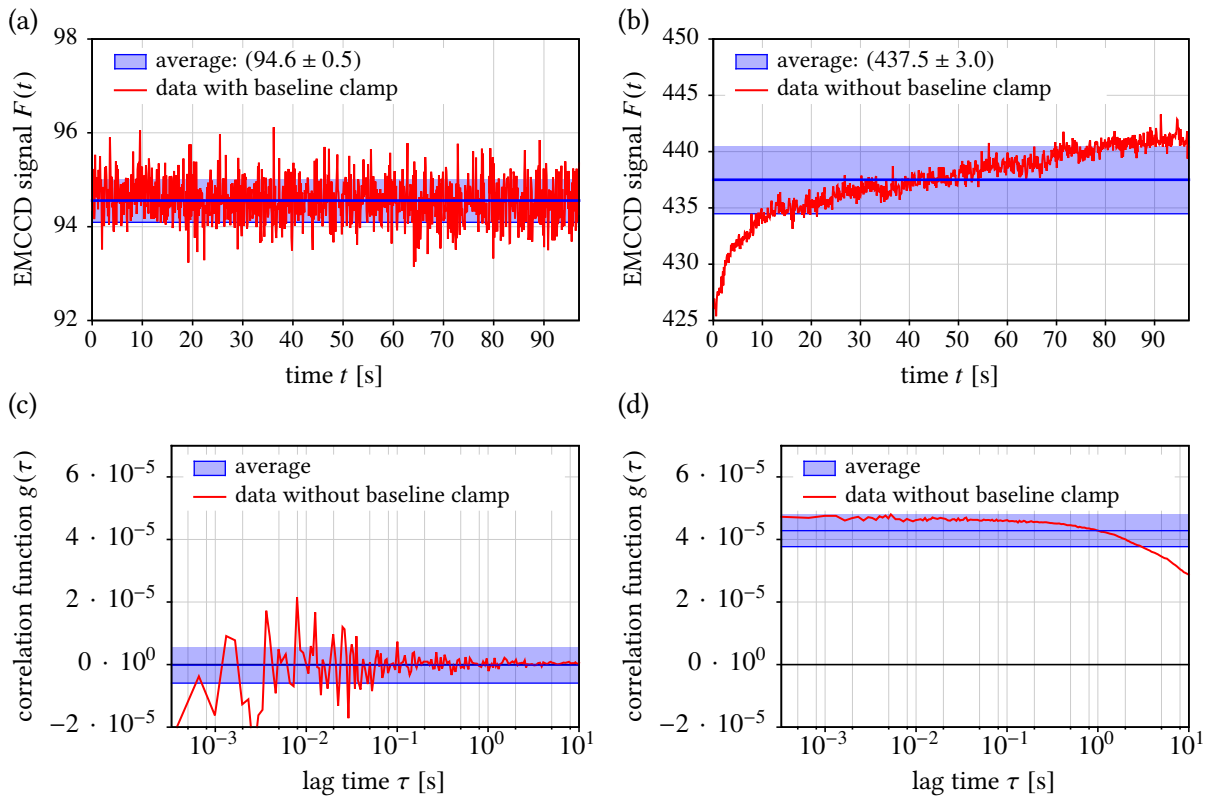


Figure 8.7. | (a,c) EMCCD signal $F(t)$ and autocorrelation function measured on a single pixel of a dark EMCCD camera with the baseline clamp activated. (b,d) The same without activated baseline clamp. The blue lines and ranges show average and standard deviation over the displayed data (red). Measurement parameters: EM-gain setting: 300, $\tau_{\min} = 330 \mu\text{s}$; Evaluation: autocorrelation without background correction.

scattered light at typical settings for the laser and camera is on the order of 2 – 5 ADU for deionized water or clean HBSS. This might considerably change the results for dim samples, such as Alexa-488 or QDots, which exhibited an intensity of 30 – 50 ADU at the lowest concentration, used for the dilution series above. As shown in Fig. 5.17 on page 75, this would already result in an overestimation of the concentration by 10 – 20%. For comparison, the fluorescent microspheres had an average intensity of (180 ± 6) ADU at their lowest concentration. Therefore, the mentioned background signals do not play a significant role here. Even higher background intensities were observed in live-cell measurements, because in this case waste-products and remnants from dead cells tend to pollute the buffer.

A second possible cause for the overestimated concentrations are camera artifacts. EMCCD cameras typically suffer from a drift of their offset value and EM gain, which are caused by temperature drifts in the camera electronics. The Andor iXon X3 860 EMCCD camera, that was used here, compensates these artifacts by a function called “baseline clamp”. It uses the signal from additional, light-shielded pixels to measure and correct the drift. Figure 8.7 shows intensity time-traces and autocorrelation functions, which were measured using a non-illuminated EMCCD camera with and without the baseline clamp activated. The effect of the offset drift without the clamping is clearly illustrated in Fig. 8.7(b). The corresponding autocorrelation of the background would be added to the autocorrelation of the particles. The baseline clamp removes this effect completely from the intensity time-trace and the associated autocorrelation curves (see Fig. 8.7a,c).

Unruh and Gratton suggested in Ref. [253], that the camera gain \bar{G} and the excess noise factor \mathcal{F}^2 might influence the measured concentration also in FCS measurements. This effect was ruled out by simulations of FCS measurements with a detector model that includes the camera noise, as described in section 4.2.5 (see appendix B.1 for details on the simulation). Figure 8.8(a) shows a subset of the simulation results for different values of \bar{G} and of \mathcal{F}^2 . No influence of the different detector parameters on the correlation amplitude was detectable in any of the simulations. This is expected as the camera noise should be non-correlated over time (see section 4.2.5 and Fig. 8.7). Therefore the noise contributions

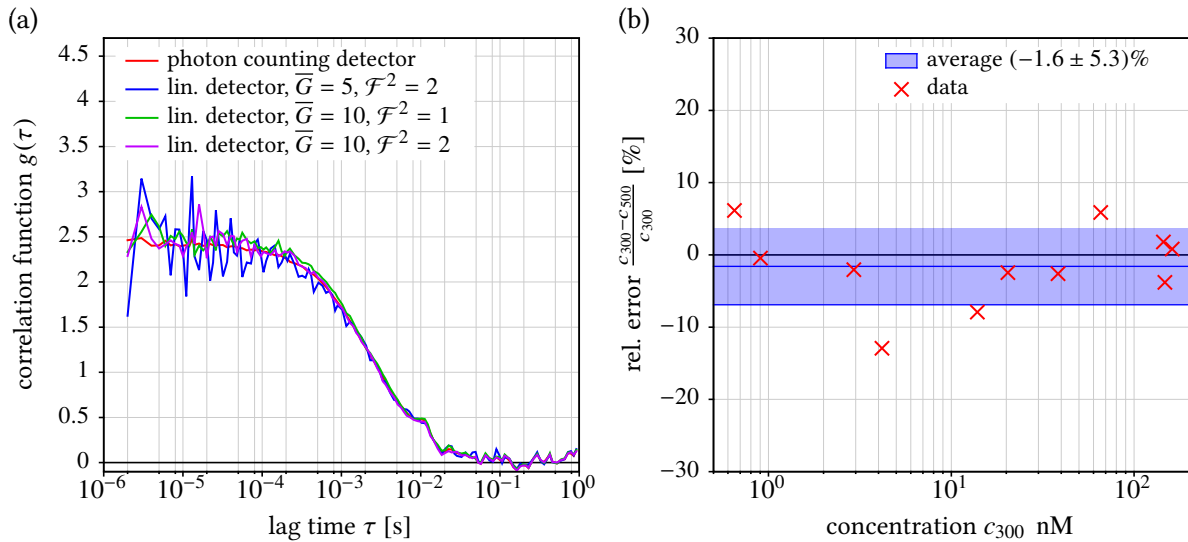


Figure 8.8. | (a) Results of FCS simulations for linear detectors with different gains \bar{G} and excess noise factors \mathcal{F}^2 . (b) Relative error $(c_{300} - c_{500})/c_{300}$ between concentrations c_{300} and c_{500} , measured at an EM-gain setting of 300 and 500, respectively. Simulation parameters for (a): $D = 20 \mu\text{m}^2/\text{s}$, $c = 0.5 \text{ nM}$, $\tau_{\text{min}} = 2 \mu\text{s}$ and for linear detectors: $\sigma_{\text{read}} = 5$. The noise on all curves in (a) has the same shape, as the same trajectories were used for the different detector parameters.

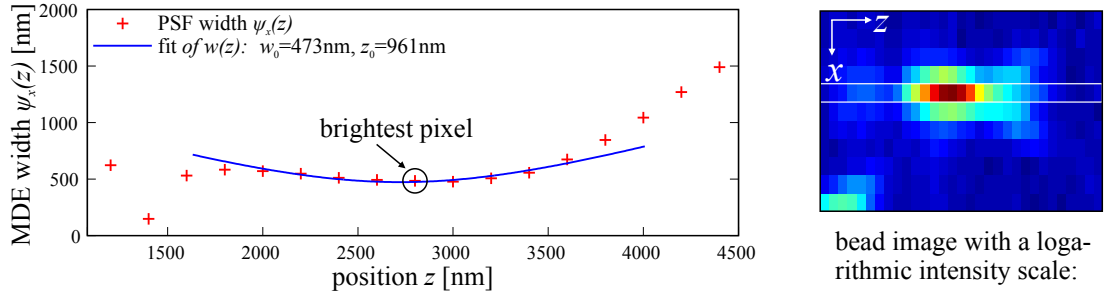


Figure 8.9. | **Representative result of an extended bead scan analysis.** Red data points are the $1/e^2$ -widths $\psi_x(z)$ of the MDE from a beadscan at different z -positions. The blue curve is a fit if $w(z)$ from Eq. (8.3.1) to this data set.

influence the variance of the camera signal, but not its temporal autocorrelation. The only detectable effect on the autocorrelation curves was an increased noise at low lag times, which is due to the read noise σ_{read} of the linear detectors (cf. blue curve in Fig. 8.8). The influence of the EM-gain setting of the camera, which is proportional to \bar{G} , was also tested experimentally. Several different dilutions of QDot-565 were measured at EM-gain settings 300 and 500 on an Andor iXon X3 860 EMCCD camera. Figure 8.8(b) shows the relative deviation between the two measurements for each dilution. The results do scatter, but on average, no influence of \bar{G} could be detected.

Finally, the focus geometry of the SPIM was analyzed more closely. The MDEs assumed for a SPIM in chapter 5 are separable into three factors, each depending only on one coordinate x , y or z . This is mainly a consequence of the assumed 3-dimensional Gaussian shape of the PSF. This assumption allows to successfully obtain absolute diffusion coefficients D . These are measured via the dwell time of particles in the focus, which mostly depends on the smallest dimension of the MDE w_g . The concentration on the other hand, is sensitive to the full focal volume and thereby on all three parameters w_g , z_g and a . For this reason, the bead scans, which were used to determine the focus parameters (see section 6.3.2), were evaluated in more detail. For each bead image, 1-dimensional Gaussian functions were fitted to cuts along the x - or y -axis for different z -positions. For the postulated PSF, the lateral width of the MDE (or PSF) should not depend on the z -position. An example of the $1/e^2$ -widths $\psi_x(z)$, as obtained from the beadscaans, is shown in Fig. 8.9 (red crosses). The width $\psi_x(z)$ significantly increases with increasing distance from the brightest pixel. This feature of the MDE can be understood, if a Gaussian beam is used as a more realistic model for the illumination PSF, than a model using a simple Gaussian function. Such an MDE is defined as [178]:

$$\text{MDE}(x, y, z) = \left(\frac{w_0}{w(z)} \right)^2 \cdot \exp\left(-2 \cdot \frac{x^2 + y^2}{w_0^2(z)}\right), \quad \text{with } w(z) = w_0 \cdot \sqrt{1 + \left(\frac{z}{z_0}\right)^2}, \quad (8.3.1)$$

where w_0 is the beam waist and z_0 is the depth of focus. This function and a simple 3-dimensional Gaussian with similar focus parameters, are shown as a $1/e^2$ -isurface plots in Fig. 8.10. It demonstrates the large difference between the volumes, described by these two functions. In x - and y -direction this MDE(x, y, z) resembles a Gaussian function with z -dependent $1/e^2$ -width $w(z)$. The blue curve in Fig. 8.9 shows a fit of $w(z)$ from Eq. (8.3.1) to the $\psi_x(z)$ measured in the beadscan. This shows that Eq. (8.3.1) is in fact a better approximation of the true PSF shape, than the simple 3-dimensional Gaussian function.

FCS simulations (see appendix B.1) were used to quantify the influence of the true MDE on fit results, which were obtained with a Gaussian model. For this purpose, three focus geometries were set up (see Fig. 8.11):

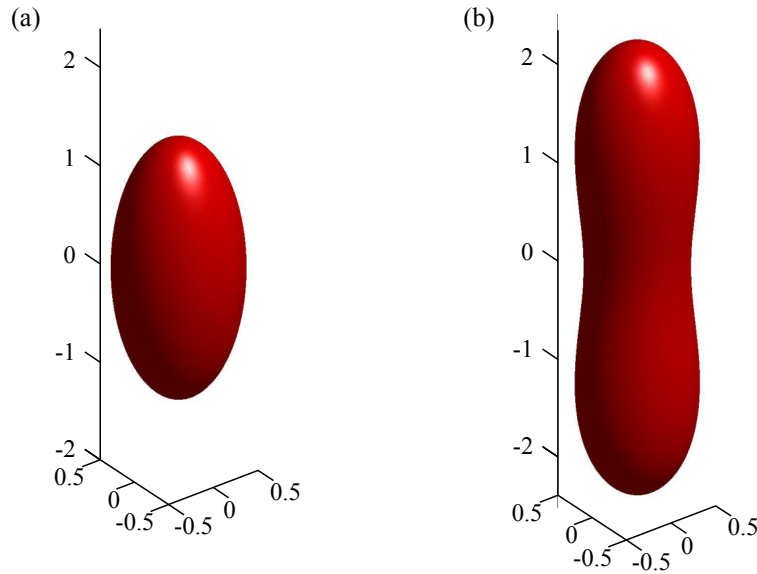


Figure 8.10. | (a) $1/e^2$ -isosurface plot of 3-dimensional Gaussian function. (b) $1/e^2$ -isosurface plot of a Gaussian beam as in Eq. (8.3.1). Parameters: (a) $w_g = 500$ nm, $z_g = 1300$ nm; (b) $w_0 = 470$ nm, $z_0 = 900$ nm

- (a) As a reference, a 3-dimensional Gaussian detection PSF $\Omega(\vec{r})$ was used together with a Gaussian light sheet with a $1/e^2$ -width z_{LS} :

$$I(x, y, z) = I_0 \cdot \exp \left[-2 \cdot \frac{z^2}{z_{LS}^2} \right]. \quad (8.3.2)$$

- (b) A Gaussian beam model (see Eq. 8.3.1) for the detection PSF $\Omega(\vec{r})$ was combined with a Gaussian light sheet Eq. (8.3.2).

- (c) A Gaussian beam model (see Eq. 8.3.1) for the detection PSF $\Omega(\vec{r})$ was combined with a light sheet with side lobes:

$$I(x, y, z) = I_0 \cdot \left(\frac{\sin(\pi \cdot z / z_{LS})}{\pi \cdot z / z_{LS}} \right)^2. \quad (8.3.3)$$

In all cases the pixel size was infinitely small, and the confocal FCS fit models from section 5.3.4 were used for evaluation. The focus parameters w_g and z_g for the fit models were obtained by 1-dimensional Gaussian fits to $MDE(\vec{r})$. Table 8.3 summarizes the results for an FCS simulation of particles with diffusion coefficient $D_{\text{real}} = 50 \mu\text{m}^2/\text{s}$ at different concentrations c_{real} . The diffusion coefficients in all cases were obtained with a relative error below 13%. For the case of a Gaussian focus, also the concentrations were retrieved with an error margin of 12%, showing that the simulation works correctly. For the two other focus shapes, the concentrations were significantly overestimated by 30 – 50%, since the focal volume is underestimated by its Gaussian approximation. This behavior matches well with the observations in the SPIM-FCS measurements: the diffusion coefficient is measured correctly, but the concentration is overestimated.

The findings of the last section suggest to set up SPIM-FCS fit functions, that are modeled around a Gaussian beam PSF as in Eq. (8.3.1). Such models were already proposed for high-precision D and c measurements with confocal FCS by Enderlein et al. [254–256]. Their drawback is that the integrals, that are encountered, when calculating the FCS models, are no longer separable and can no longer be

solved analytically. Numerical integration can be used, when implementing the fit models, but its use makes the fitting process time-consuming. This is a drawback, when fitting thousands of correlation curves, as customary in imaging FCS. Furthermore, it was shown above, that concentrations can be corrected with a simple calibration factor.

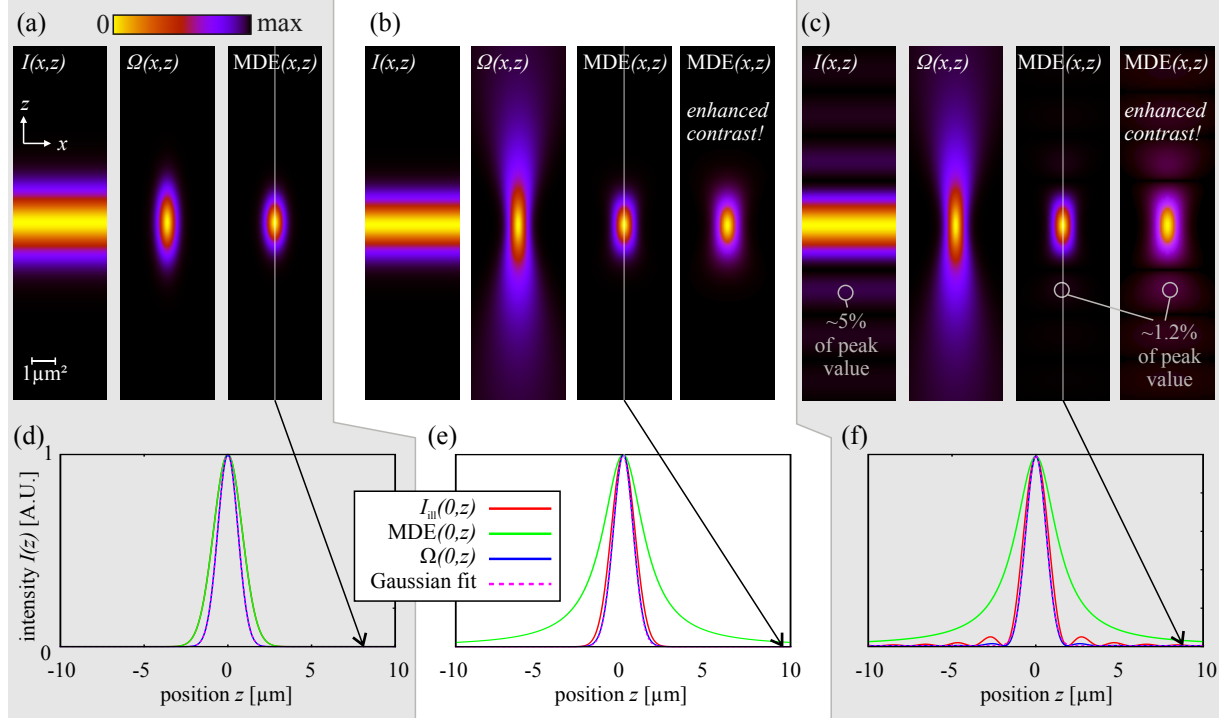


Figure 8.11. | **Different focus geometries used for FCS simulations.** (a,d) A 3-dimensional Gaussian function is used as detection efficiency function $\Omega(x, z)$ and a 1-dimensional Gaussian $I(x, z)$ as light sheet. (b,e) A Gaussian beam is used for $\Omega(x, z)$ and again a 1-dimensional Gaussian as light sheet. (c,f) A Gaussian beam is used for $\Omega(x, z)$ and a slit function for $I(x, z)$. (a-c) shows the functions $I(x, z)$, $\Omega(x, z)$ and $MDE(x, z) = I(x, z) \cdot \Omega(x, z)$. (d-f) shows cuts along the z axis through these functions.

concentration	focus	D [$\mu\text{m}^2/\text{s}$]	$(D - D_{\text{real}})/D_{\text{real}}$	c [nM]	$(c - c_{\text{real}})/c_{\text{real}}$
$c_{\text{real}} = 0.1$ nM	Gaussian focus	53.6	7.2%	0.105	5%
	Gaussian beam	47.5	-5.0%	0.136	36%
	Gaussian beam & sidelobes	48.0	-4.0%	0.141	41%
$c_{\text{real}} = 0.2$ nM	Gaussian focus	52.6	5.2%	0.223	12%
	Gaussian beam	47.1	-5.8%	0.286	43%
	Gaussian beam& sidelobes	48.2	-3.6%	0.295	48%
$c_{\text{real}} = 0.5$ nM	Gaussian focus	56.4	12.8%	0.506	1%
	Gaussian beam	51.5	3.0%	0.657	31%
	Gaussian beam& sidelobes	52.1	4.2%	0.688	38%
$c_{\text{real}} = 1.0$ nM	Gaussian focus	48.2	3.6%	1.074	8%
	Gaussian beam	47.0	-6.0%	1.339	34%
	Gaussian beam & sidelobes	47.1	-5.8%	1.412	41%

Table 8.3. | **Fit results obtained from simulated FCS autocorrelation curves with different focus geometries and for particles with $D_{\text{real}} = 50 \mu\text{m}^2/\text{s}$.**

8.4. Anomalous Diffusion with complex MDE shapes

The discussion of the true shape of the MDE in the last section raises the question, how well anomalous diffusion parameters can be measured with the 3-dimensional Gaussian model described in section 1.3.2. In order to check this, an FCS simulation was used with the same set of focus geometries as in the last section (page 130). In addition, the pixel size was set to $a = 400$ nm in that simulation. The focus parameters were tuned to match those of the SPIM, presented in chapter 6. Trajectories with an anomalous MSD were used as input for these simulations. They were generated for the anomaly parameters $\alpha_{\text{set}} \in \{0.7, 0.8, 0.9, 1.0\}$ by Christian Fritsch (DKFZ, Heidelberg) with the methods described in Ref. [257]. Figure 8.12 shows the results of these simulations. It demonstrates that comparable anomaly parameter α_{fit} is retrieved from fits to the models in Eq. (5.3.31) (p. 63) for the first geometry and Eq. (5.3.32) (p. 63) for the other geometries. The figure also shows the anomaly parameters obtained from the MSDs of the particles directly. The values α from the FCS fits do recover the values from the MSD only in one case. This is most probably due to the low number of only 100 trajectories per α_{set} , that were available for the simulations. Nevertheless, the fact that the same anomaly parameter was regained, independent of the true focus geometry, confirms that the model in section 1.3.2 can be used to measure anomalous diffusion reliably.

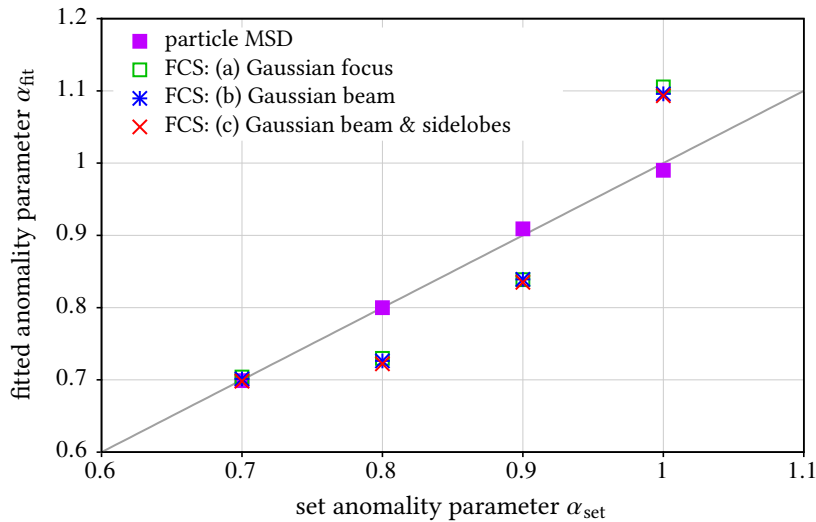


Figure 8.12. | Results of anomalous diffusion FCS simulation. Focus geometries are defined as in section 8.3, page 130. Filled magenta squares are the anomaly parameters obtained via a fit of $\text{MSD}(\tau) = 6\Gamma \cdot \tau^\alpha$ to the MSD of the input trajectories.

8.5. Artifacts in SPIM-FCS

8.5.1. Stripe artifacts in SPIM-FCS

As mentioned in section 3.3.3 (p. 35), light sheet microscopy image often contain stripe artifacts. These are areas of increased or reduced illumination intensity, that are caused by scattering objects in the beam path of the light sheet. These artifacts also have a severe influence on SPIM-FCS measurements and need to be carefully controlled during experiments. Figure 8.13 shows two examples of stripe-artifacts in a SPIM-FCS measurement of QDots in a sample bag and of a cell expressing a labeled protein (β -gal in a rat prostate adenocarcinoma cell (AT-1)). The sample bag had dirt on its plastic foil, which caused the stripes. In the cell, stripes were caused by regions with a slightly different refractive index. In both cases the measured mobility parameters (diffusion coefficient D or diffusion correlation time $\tau_D \propto 1/D$)

as well as the concentration are severely influenced by the stripes.

The facts that especially the concentration is influenced and that concentration and mobility are altered in opposite directions, points to the assumption that the focal volume or its shape is changed in regions, affected by stripe artifacts. This is in agreement with simulations of stripe artifacts that were described in Ref. [162]. There, light propagation was simulated, assuming a sample with average refractive index \bar{n} , which contains a few regions with a slightly altered refractive index $n' = \bar{n} + \delta n(x, y, z)$. Results from a comparable simulation are shown in Fig. 8.14 (see appendix B.4 for details on the simulation method). A small change of n by only 1%, already has a severe impact in the light intensity distribution. At $\delta n/\bar{n} = 2\%$, the shadowing (dark stripes) and focusing (bright stripes) effects of the scattering objects are clearly visible. These changes in light distribution lead to the assumed change in focal volume, as the illumination PSF is severely changed. This in turn, changes the measured concentrations and diffusion coefficients, as the focal volume is not correctly represented by the MDE model in the fitting function and its calibrated parameters.

In live cells, the stripe artifacts can be caused by diverse organelles, or e.g. the nucleolus, which is

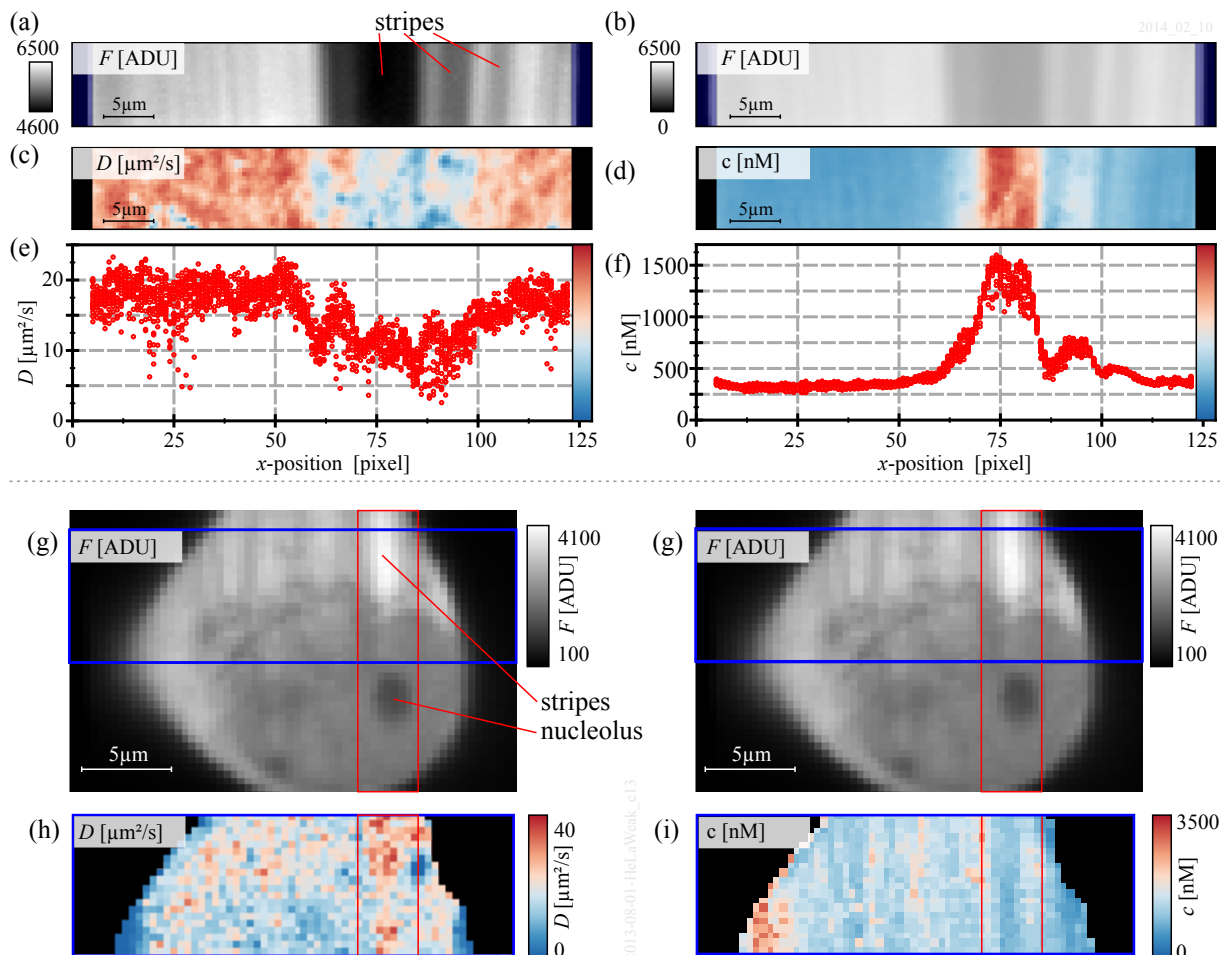


Figure 8.13. | Stripe artifacts in (a-f) a SPIM-FCS measurement of QDot-565 ITK and (g-i) a cell expressing a an eGFP tetramer (eGFP-4x). (a,b) Fluorescence intensity images with dark stripes due to dirt on the sample bag. (c) Map of the diffusion coefficient D . (e) Plot of D vs. x -coordinate. (d) Map of the concentration c . (f) Plot of c vs. x -coordinate. The colorbars for (b,d) are placed on the right of (c,e). (g) Fluorescence intensity image of the cell. (f) Map of the diffusion coefficient D in the cell. (g) Map of the concentration c in the cell. A 1-component normal diffusion fit was used for all samples.

a region of high protein concentration in the nucleus. The latter case is shown in Fig. 8.13(g-i). From phase-microscopic measurements, as e.g. in Refs. [258–260], it is known that the refractive index in cells changes by 2 – 5% between different regions and organelles. This is again in agreement with the qualitative arguments from the simulation above.

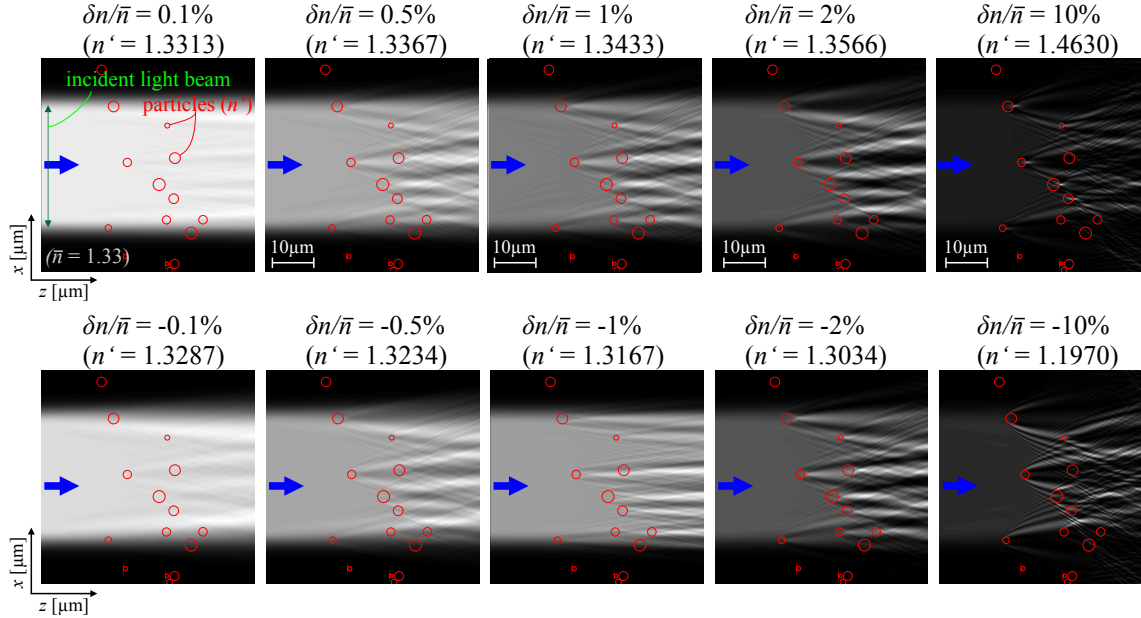


Figure 8.14. | Simulation results of a 2D simulation of light beam propagation in a medium with $\bar{n} = 1.33$, which contains a few circular regions of changed refractive index n' . The simulation method is described in appendix B.4. Blue arrows indicate direction of light propagation. Simulation parameters: light wavelength $\lambda = 488$ nm, spatial resolution 50 nm, simulation domain $51.2 \times 51.2 \mu\text{m}^2$, diameter of the spherical scattering objects (red circles): $(2 \pm 0.5) \mu\text{m}$. After each integration step, the field is normalized, so the contained energy is conserved.

8.5.2. Artifacts due to sample bags

As the last section showed, a small change in refractive index can have large effects on the measurements. Therefore the influence of the sample and the sample mounting on a SPIM-FCS measurement was analyzed. A sample of a 607 bp dsDNA was mounted in a standard sample bag (section 6.2.3 and appendix A.3.1) and SPIM-FCS measurements were performed at different positions x in the sample bag, as shown in Fig. 8.15(a). The results are shown Fig. 8.15(b) for the measured diffusion coefficient D and in Fig. 8.15(c) for the measured concentration c . Both show a clear and opposing dependence on x . This is most probably caused by two effects, that both alter the focal volume. First, there may be mismatches in refractive index between the buffer in the sample chamber, the material in the sample bag and the sample itself. These could alter the size and shape of the light sheet. Also the shape of the sample bag might distort the light sheet. Second, the illumination and fluorescence light both have to travel a certain distance through the sample. During that distance, they may be distorted by absorption and scattering, which again influences the true shape of the MDE. Note that a comparable effect could also occur in cells. Here no perturbing sample bag is present, but there might exist a refractive index mismatch between the interior of the cell and the buffer in the sample chamber, which will have a comparable effect.

To reduce the influence of this artifact, all measurements in sample bags were performed at $x = 200 - 500 \mu\text{m}$ distance from the wall of the bag. As Fig. 8.15(b,c) shows, the parameters only weakly depend on the x in this region. Since also the calibration measurement is performed at this position, the influence of the sample bags on the SPIM-FCS measurement is balanced by this calibration. On the other

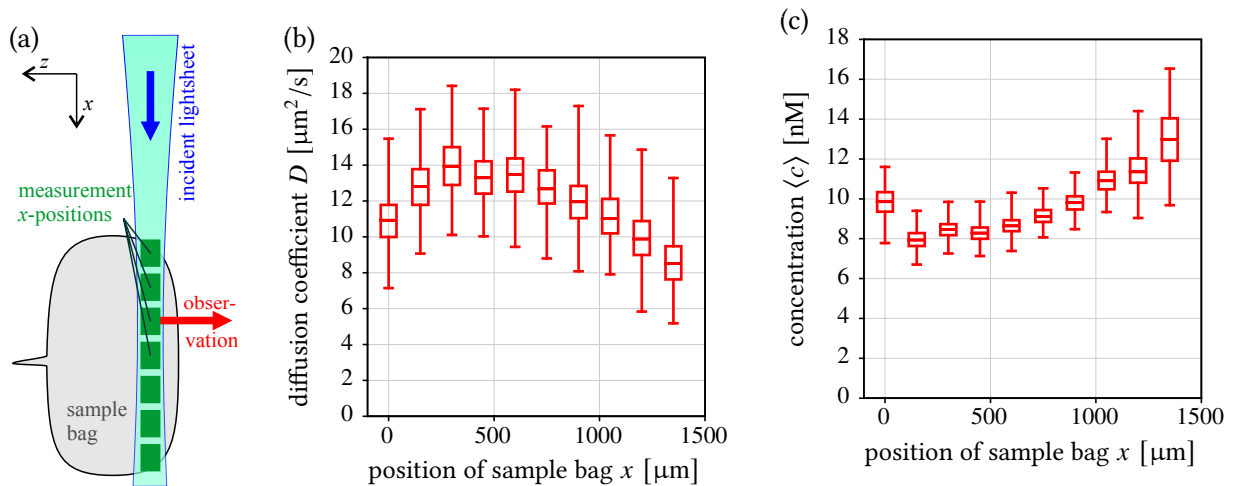


Figure 8.15. | Influence of the sample bags on SPIM-FCS measurements. (b) Diffusion coefficients and (c) particle concentration from SPIM-FCS measurements of a solution of 607 bp DNA, labeled with Alexa-488, acquired with an EMCCD camera. Each data point corresponds to one measurement taken at different positions through the sample bag, as indicated in (a).

hand, the same calibration is used for live cell measurements, where no sample bag is present. Therefore an additional uncertainty of 20 – 40% (from the variations in Fig. 8.15b,c) should be assigned to the absolute parameters obtained in cells. Relative measurements though, are not influenced by this effect.

8.5.3. Changing the thickness of the light sheet

As shown in section 6.3.1, the width of the light sheet changes along the x -axis. Nevertheless, in all measurements shown so far, it was implicitly assumed, that the MDE does not change over the whole field of view. In order to verify this assumption, an Alexa-488-labeled dsDNA fragment (length: 170 bp) was measured with SPIM-FCS and a diffusion coefficient D and a concentration $\langle c \rangle$ were extracted for all 128×6 pixels in the field of view. Figure 8.16 shows average and standard deviation of the measurements

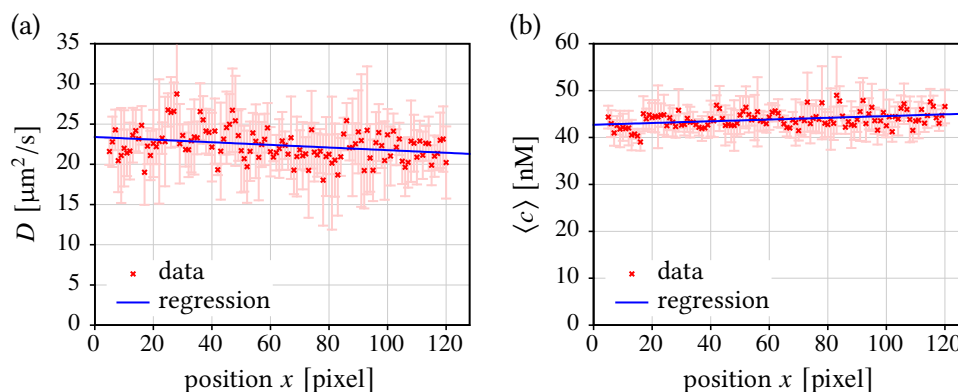


Figure 8.16. | Influence of the width of the light sheet on SPIM-FCS measurements. (a) Diffusion coefficient D and (b) concentration $\langle c \rangle$ as a function of the position x in the field of view, measured from a sample of 170 bp dsDNA, labeled with Alexa-488, acquired with an EMCCD camera. The data points are average and standard deviation over all measurements in one column. Blue lines are linear fits to the data.

in each column. No significant correlation between these fit parameters and the x -position could be detected (correlation coefficients $\rho_{x,D} = -14\%$ and $\rho_{x,\langle c \rangle} = 17\%$). This result is explained by the fact, that the width of the light sheet depends on the x -position (cf. Fig. 6.13a), but the PSF does not. The focal volume is given by the MDE, which is a product of the illumination intensity and the PSF. Therefore the non-changing size of the PSF limits the width of the MDE and the focal volume shows no detectable dependence on x .

8.6. Applicability to live-cell measurements

Cells for this section were prepared by Gabriele Müller (DKFZ, Heidelberg).

This section will demonstrate the applicability of SPIM-FCS to measurements in living cells. The results of SPIM-FCS will be checked by comparing them to results from confocal FCS measurements. As a first example, human cervical carcinoma cells (HeLas) were chosen, which transiently express a monomeric form (eGFP-1x) and a tetrameric form (eGFP-4x) of the enhanced green fluorescent protein (eGFP)² (see appendix A.2 for details on transfection and cell culture protocols). Figure 8.17(a) shows a typical autocorrelation curve for eGFP-4x in a HeLa cell, acquired with confocal FCS. It also contains a fit to this curve. To account for the crowded environment in live cells, a fit model with two normal diffusion components was used. The diffusion coefficient D_{fast} of the faster component is usually interpreted as representing the free motion of the protein in a viscous medium. The slow component describes the effect of crowding in this picture. Dross et al. have published an extensive confocal FCS study on eGFP oligomers in live cells [33], which can serve as a reference for SPIM-FCS measurements. The results from that study are summarized in Fig. 8.17(b). In Fig. 8.17(a), the red rectangle highlights the lag time range, which is accessible to SPIM-FCS with an EMCCD camera ($\tau_{\text{min}} \approx 500 \mu\text{s}$). This range will have to suffice for the SPIM-FCS analysis to yield the correct mobility parameters.

An EMCCD camera with a temporal resolution of $\tau_{\text{min}} = 330 - 560 \mu\text{s}$ was used for all SPIM-FCS measurements in this section. Each measurement was around 60 s long, which is comparable to typical measurements on a confocal microscope. The illumination laser intensity was set to $100 - 150 \text{ W/cm}^2$ at the center of the light sheet, which is roughly a factor 10 lower than typical intensities, used for confocal FCS measurements on cells. At this laser power the fluorescence bleached to $\sim 50\%$ during the complete measurement, which was corrected by the methods described in sections 5.5.4 and 7.1.2. The modified exponential model Eq. (7.1.5) (p. 109) was used for bleach correction. The degree of the polynomial was $N_f = 1 - 4$, depending on the cell. These parameters were also used for most of the cell measurements throughout this thesis.

Figure 8.18 summarizes the results of SPIM-FCS measurements on HeLa cells expressing eGFP-1x and eGFP-4x and shows exemplary maps of the diffusion coefficient D_{fast} and concentration c for eGFP-4x. Figure 8.18(a) depicts two typical autocorrelation curves (solid lines) for eGFP-1x and eGFP-4x together with a two-component normal diffusion fit (dashed line). The fit describes the measured autocorrelation curves very well and the resulting fast diffusion coefficients $D_{\text{fast},20^\circ\text{C}}$ (renormalized to 20°C , see appendix C.4) are given in the plot. Figure 8.18(b) shows a distribution of $D_{\text{fast},20^\circ\text{C}}$ from all pixels in one cell, which expressed eGFP-1x (red) and one cell, which expressed eGFP-4x (blue). The peaks of two distributions are separated and their average values are compatible (within their errorbars) with the expected values in Fig. 8.17(b). Note that these distributions were calculated from a single cell and that cellular FCS measurements typically have a large statistical spread. This is also evident from the large value ranges in Fig. 8.17(b). Therefore at least 10 – 30 cells should be measured and evaluated to obtain statistically significant results. The remaining fit parameters were equal for the monomer and the tetramer. The diffusion coefficient for the slow component $D_{\text{slow},20^\circ\text{C}}$ was in the

²These constructs were kindly provided by M. M. Nalaskowski (university medical center Hamburg-Eppendorf).

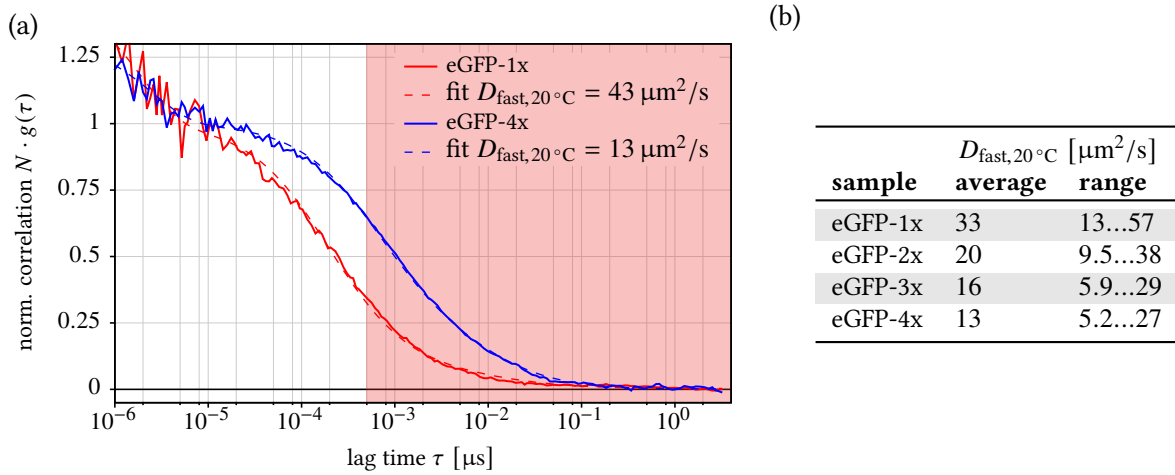


Figure 8.17. | (a) Confocal FCS autocorrelation curve acquired from HeLa cell expressing eGFP-1x or eGFP-4x. (b) Table of diffusion coefficients for eGFP-1x– eGFP-4x acquired with confocal FCS. In (a) the red rectangle highlights the lag time range, which is accessible to SPIM-FCS with an EMCCD camera. Data for (b) taken from Ref. [33] and renormalized to 20 °C (see appendix C.4).

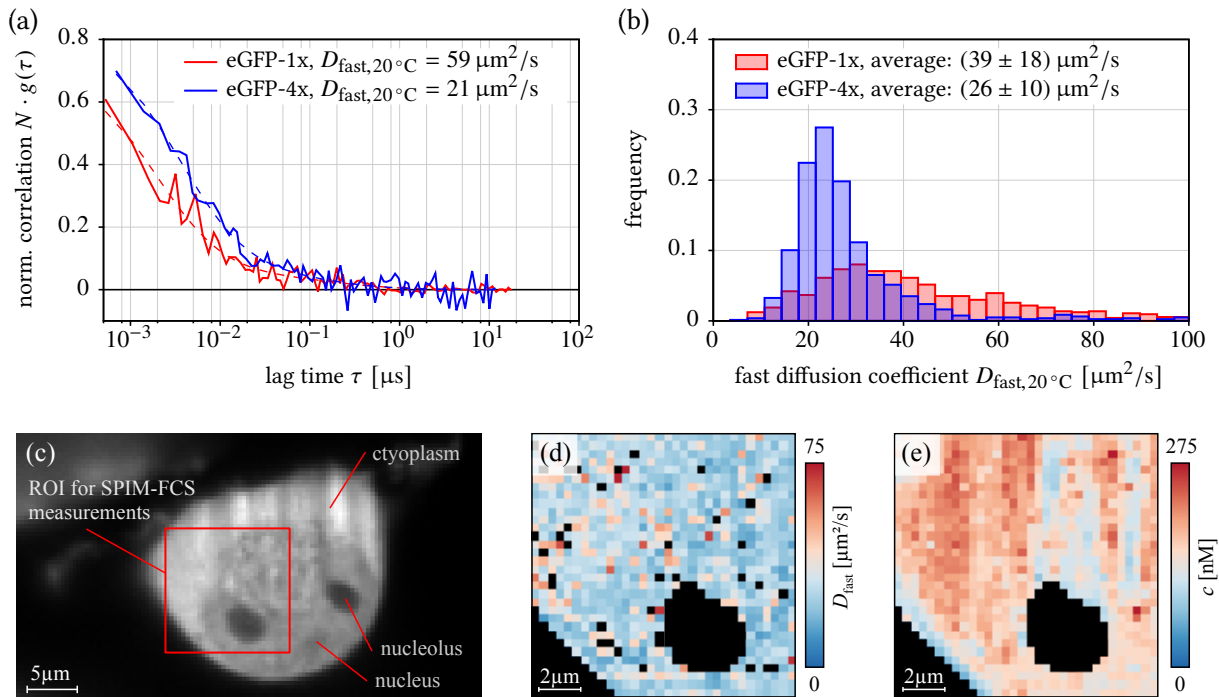


Figure 8.18. | (a) SPIM-FCS autocorrelation curves acquired from HeLa cells expressing eGFP-1x and eGFP-4x with an EMCCD camera. (b) Histograms of fast diffusion coefficient of eGFP-1x and eGFP-4x in the same cells. (c) Fluorescence intensity image of a cell, expressing eGFP-4x. (d) Map of the fast diffusion coefficient D_{fast} and (e) map of the concentration c in the same cell. A SPIM-FCS model for two-component normal diffusion was fitted to the data. Dashed lines in (a) are fits. Data in (a,b) was taken from the cell shown in (c-e). The measure ROI is marked with a red rectangle

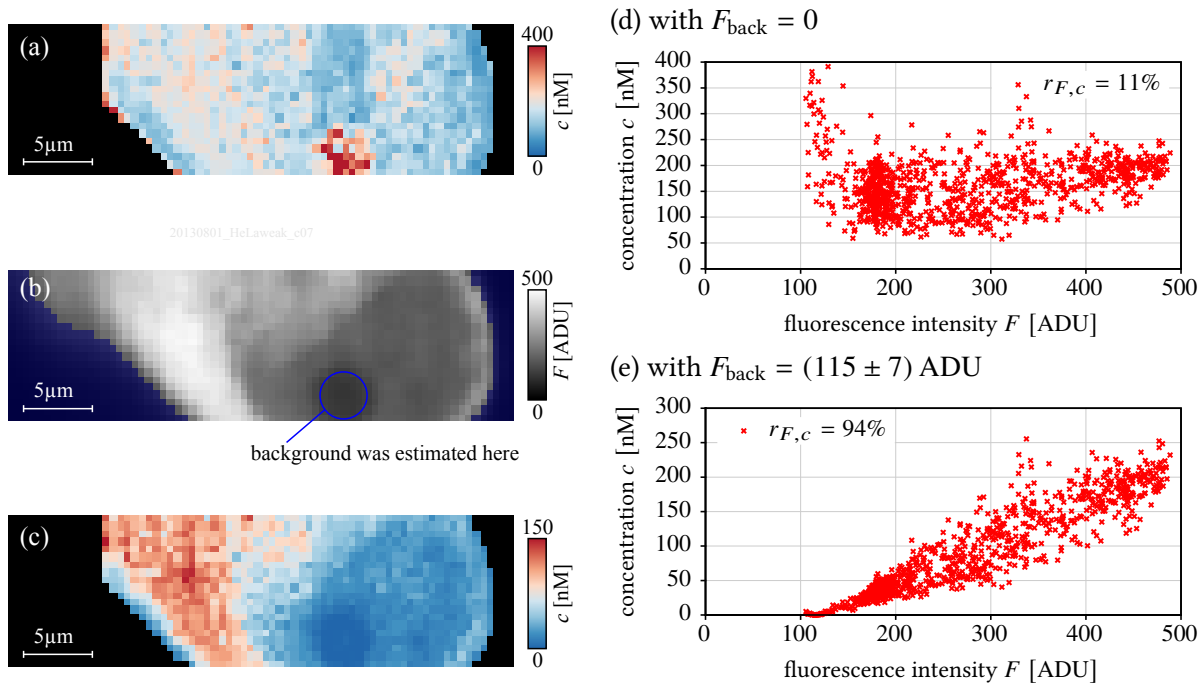


Figure 8.19. | SPIM-FCS measurement of the particle concentration c in a cell, which expressing eGFP-4x. (a) Map of c without a background offset F_{back} . (b) Fluorescence intensity (F) image. (c) Map of c with background intensity F_{back} estimated in the nucleolus (blue circle in b). (d,e) Correlation plot between c and F from (a) and (b). A SPIM-FCS model for two-component normal diffusion was fitted to the data. In (d,e) Pearson’s correlation coefficient $r_{F,c}$ is given.

range of $0 - 1.5 \mu\text{m}^2/\text{s}$ and the fraction of this slow component was $\rho_{\text{slow}} = 5 - 15\%$. Both values are comparable to typical results in confocal FCS. The autocorrelation curves shown in Fig. 8.18(a) are of good quality. In many measurements for this thesis, they were a lot noisier, especially when the samples were labeled with dim fluorophores, such as mRFP1 (see Tab. 2.1, p. 24). In those cases a 2×2 binning proved to be advantageous, as this increases the number of photons detected per pixel, which again improves the quality of the correlation curves.

The last example demonstrated that it is feasible to measure the diffusion coefficient of proteins in the cytoplasm. A closer look needs to be taken to concentration measurements. Figure 8.19 shows the results of SPIM-FCS measurements of a HeLa cell, expressing eGFP-4x. The data was again evaluated with a two-component normal diffusion model. Figure 8.19(a) depicts the map of concentrations as it would be obtained with SPIM-FCS, as described so far. Figure 8.19(c) shows a correlation plot of the fluorescence intensity F versus the measured concentration c . It shows that the two parameters do not correlate well (correlation coefficient $r_{F,c} = 11\%$, see Eq. (C.3.1), p. 224), although they should be perfectly linear. Especially in the nucleolus the measured concentration is much higher than anywhere else. These improperly determined concentrations can be explained by an underestimated background intensity F_{back} , as it was discussed in sections 5.5.2 and 8.3. In order to check this, an estimate of the background intensity was obtained from the nucleolus of the cell (blue circle in Fig. 8.19b, $F_{\text{back}} = (115 \pm 7)$ ADU), where only very few eGFP-4x molecules are present. Therefore these pixels should give an estimate of the background intensity measured in the cell. The fit was repeated, using the background factor explained in section 5.5.2. The new fit results in Fig. 8.19(c,e) show that now the concentration c and the intensity have a very high linear correlation of $r_{F,c} = 94\%$. The concentration map also reproduces all features of the intensity image. However some of the concentrations are mapped close to $c = 0$, which

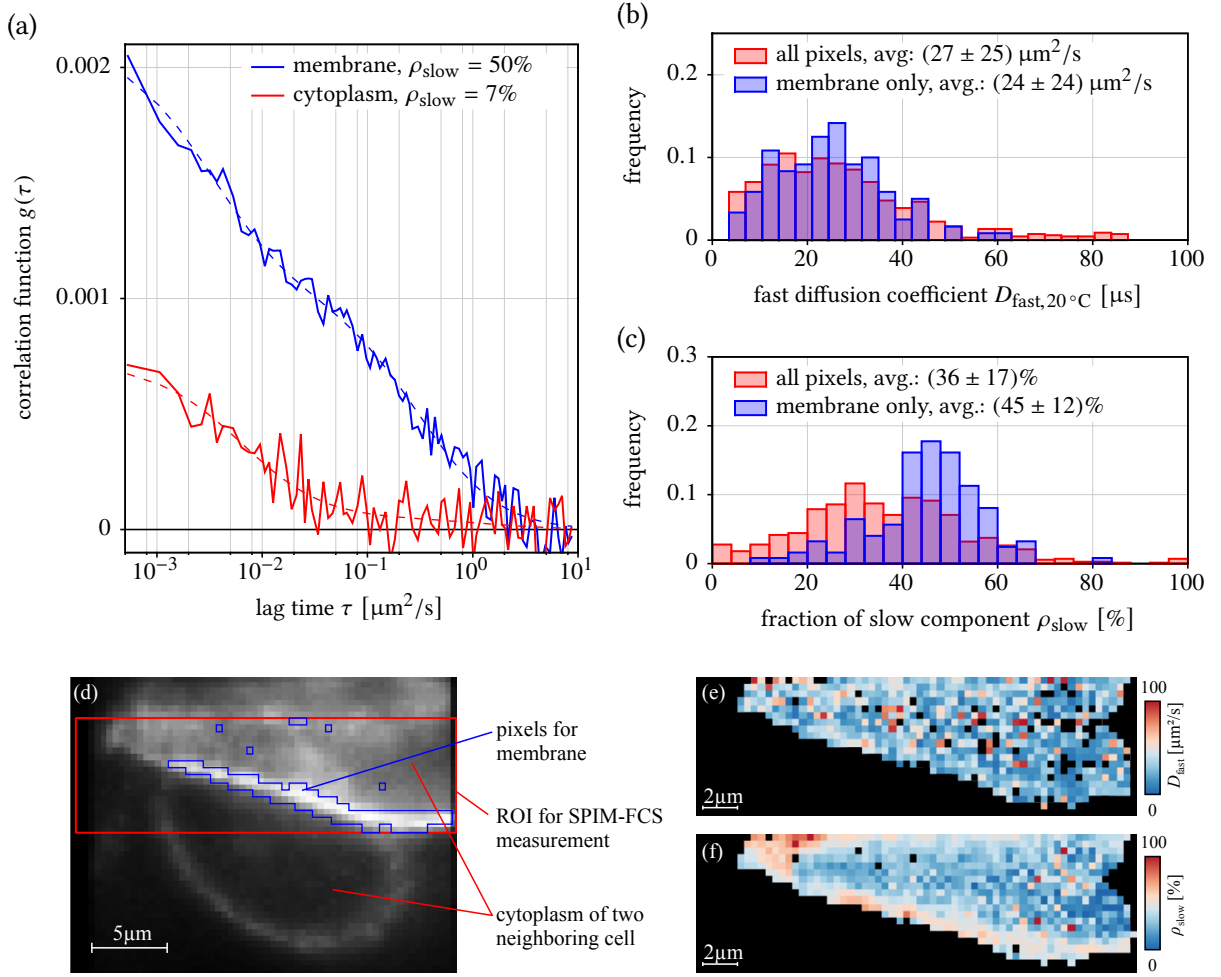


Figure 8.20. | (a) SPIM-FCS autocorrelation curves acquired from CHO-K1 cells expressing PMT-eGFP with an EMCCD camera. (b) Histograms of fast diffusion coefficient. (c) Histogram of the fraction ρ_{slow} of the slow component. (d) Fluorescence image of the cell. (e) Map of the fast diffusion coefficient D_{fast} . (f) Map of the fraction ρ_{slow} of the slow diffusion component. A SPIM-FCS model for two-component normal diffusion was fitted to the data. Dashed lines in (a) are fits. The measure ROI is marked with a red rectangle. The red histograms in (b,c) are over all pixels in the cell and the blue histograms are for the membrane pixels only. These are marked in blue in (d).

is indicative for an overestimated background. Therefore an alternative estimate for the background intensity was obtained from the exterior of the cell: $F_{\text{back}} = (20 \pm 39)$ ADU. This leads to an intermediate correlation between F and c ($r_{F,c} = 50\%$) and all concentrations are shifted to value $c > 0$ (data not shown). Therefore the true background value is possibly in between the two given estimates. This is also compatible with measurements of non-transfected cells, that typically still exhibit a fluorescence signal in the range of 5 – 100 ADU at the same instrument settings as above (data not shown).

In summary these results show that a proper estimate of the background intensity F_{back} is vital for any concentration measurement. In cells this increased background can be caused by a distorted MDE and especially the naturally occurring auto-fluorescence [261]. Since the background signal of whichever source cannot easily be entangled from the fluorescence signal, a proper estimate is hard to achieve. However, both proposed variants (a dark part or the exterior of the cell) yield better results than omitting this background correction. Independent of the chosen estimate for F_{back} , all fits returned the same diffusion coefficient. It was not correlated with either the intensity or the concentration. Therefore a

background correction is not that important, if only the diffusion coefficient is of interest.

Figure 8.20 shows an application of SPIM-FCS to membrane-associated proteins. Chinese hamster ovary cells (CHO-K1s) were transfected with an eGFP, that is fused to the plasma membrane targeting sequence (PMT) of the X-linked retinitis pigmentosa protein PR2³ [76, 262]. This sequence has a high affinity to the cell membrane and anchors most of the eGFPs there. Figure 8.20 shows the results of a SPIM-FCS measurement on that system. The localization to the membrane is clearly visible in the fluorescence intensity image in Fig. 8.20(d), in which the membrane is distinguishable as a thin line around the cell. The interior of the cell is dimmer, but still a significant amount of fluorescence could be measured there. Figure 8.20(a) shows two example autocorrelation curves from this system. The red curve was acquired in a pixel in the cytoplasm. It exhibits a comparable shape and comparable parameters ($D_{\text{fast}} \approx 13 \mu\text{m}^2/\text{s}$, $D_{\text{slow}} \approx 0.1 \mu\text{m}^2/\text{s}$, $\rho_{\text{slow}} \approx 7\%$) to the curves given above for eGFP oligomers. Therefore it most probably originates from PMT-eGFP proteins that freely diffuse in the cytoplasm.

The red curve in Fig. 8.18(a) in contrast was acquired in a pixel on the membrane. This curve also exhibits two diffusing components ($D_{\text{fast}} \approx 27 \mu\text{m}^2/\text{s}$, $D_{\text{slow}} \approx 0.3 \mu\text{m}^2/\text{s}$), but the slow component has a much higher fraction of $\rho_{\text{slow}} \approx 50\%$, than in the blue curve. This effect is even more apparent in the histograms of ρ_{slow} in Fig. 8.18(c). The blue histogram shows only the membrane pixels and the red histogram all pixels. The average of the blue histogram is significantly shifted towards a higher fraction. The same effect is visible in the map of ρ_{slow} shown in Fig. 8.18(f), where the membrane shows up in red, but the cytoplasm is generally blue. The reason for this increased slow fraction is, that in such pixels, the slow fraction represents the diffusion of membrane-bound proteins. In the membrane the diffusion is generally slower than in the cytoplasm and typical diffusion coefficients of intermediately sized particles range between $0.1 \mu\text{m}^2/\text{s}$ and $5 \mu\text{m}^2/\text{s}$ [115]. All these SPIM-FCS results are again compatible with confocal studies on membrane diffusion, as e.g. [76].

In summary these measurements demonstrate that SPIM-FCS is usable for measurements in different compartments of the cell. Even the motion of membrane-bound proteins can be measured and distinguished from that of cytoplasmic proteins. Generally the same diffusion coefficients, as in confocal FCS are obtained. These examples also demonstrate that typical fluorescent proteins are compatible with SPIM-FCS. Therefore the standard labeling techniques of cell biology, i.e. fusion of fluorescent proteins with the protein of interest (see section 2.5) can also be used for SPIM-FCS measurements. Care has to be taken when measuring concentrations. A significant background fluorescence in live-cells, which is hard to quantify, makes concentration measurements in cells hard to interpret. However, at least the order of magnitude of the concentration can be extracted reliably, if the corrections discussed in section 8.3 are applied.

³This construct was kindly provided by Thorsten Wohland (NUS, Singapore).

8.7. Comparison of different linear image sensors

All SPIM-FCS measurements, reported so far, were obtained from an Andor iXon X3 860 EMCCD camera. This camera is used for most SPIM-FCS measurement described in this thesis. It was chosen due to its high sensitivity and low noise at the low light-levels, that are usually encountered in SPIM-FCS measurements (cf. sections 4.2.5 and 4.3). At the time, when this camera was purchased, it was also the fastest available camera for such low-light applications. sCMOS cameras were still in an early stage of development and not yet fully applicable. Nevertheless a series of different linear image sensors was tested for their applicability to SPIM-FCS. The results were published in Ref. [130]. This section will give a short overview, but does not cover SPAD arrays, as these will be discussed in section 8.8 in more detail.

In addition to the Andor iXon X3 860, four other cameras representing different technologies, were tested in the SPIM in Heidelberg, or in a comparable instrument at the NUS in Singapore. Both instruments are usually equipped with an Andor iXon X3 860. Therefore this sensor was used to cross-validate the results between the two labs. The basic camera specifications are summarized in Tab. 8.4. The Evolve-512 is an EMCCD camera with a 4 times larger image sensor, but 33% smaller pixels than the Andor iXon X3 860. Both sensors use back-illuminated sensors, which exhibit a quantum efficiency

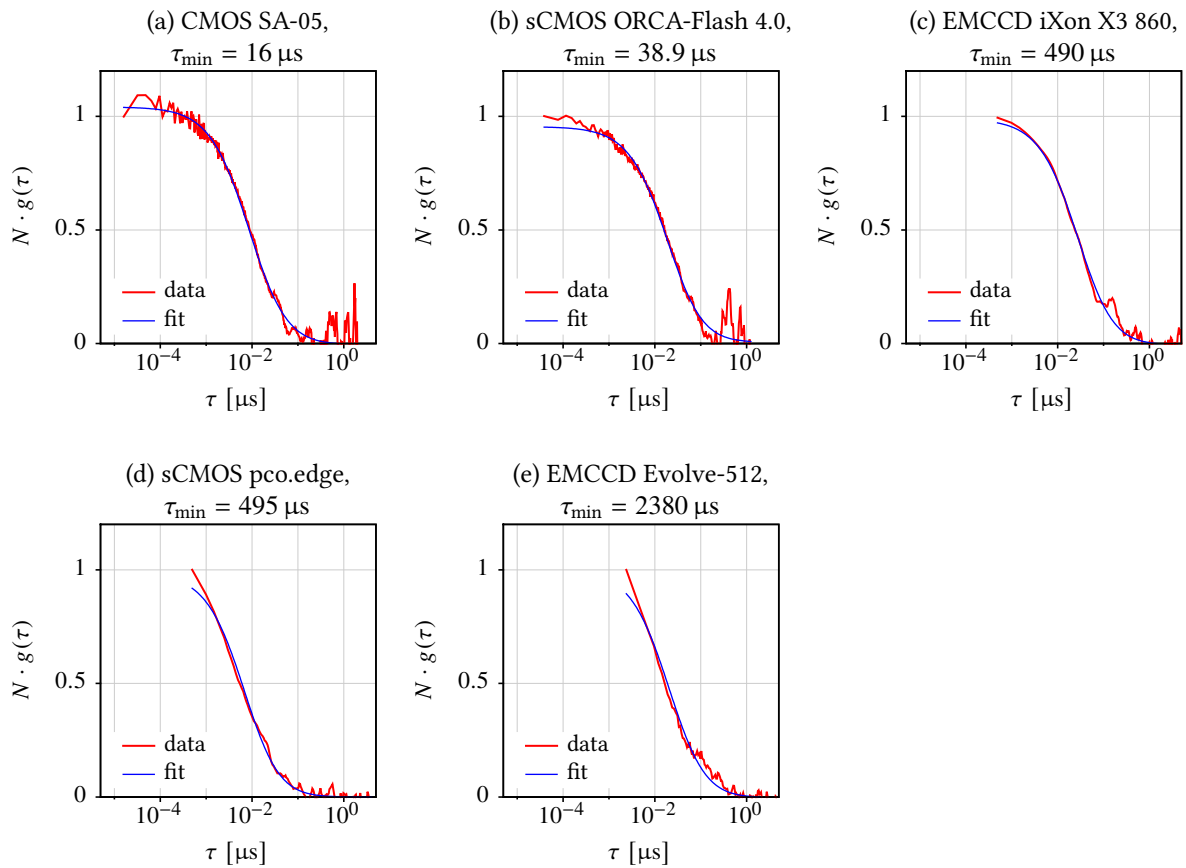


Figure 8.21. | SPIM-FCS autocorrelation curves of green fluorescent microspheres ($\varnothing = 100 \text{ nm}$), obtained with several different cameras. The camera parameters were set, as listed in Tab. 8.4. The readout speed was the maximum speed that was achievable for the given ROIs. The blue lines are fits of Eq. (5.3.25) (p. 61).

camera manufacturer	SA-05 [†] Photon	Orca-Flash 4.0 [†] Hamamatsu	pco.edge 5.5 PCO	iXon X3 860 Andor	Evolve-512 [†] Photometrics	confocal FCS
camera specifications						
technology	CMOS	sCMOS	sCMOS	EMCCD	EMCCD	SPAD
quantum efficiency	35%	70%	54%	95%	95%	55%
$\eta_{\text{det}} @ \lambda = 525 \text{ nm}$	30 – 60	1.3	1.4	< 0.1	< 0.1	—
readout noise $\sigma_{\text{read}} [e^-]$	1024 × 1024	2048 × 2048	2560 × 2160	128 × 128	512 × 512	1
pixel pitch [μm]	20	6.5	6.5	24	16	—
measured MDE properties						
lat. width w_g [nm]	620 ± 62.8	445 ± 32.5	382 ± 64	620 ± 200	574 ± 61.4	232 ± 4
long. width z_g [nm]	1395 ± 45	850 ± 58	810 ± 230	1115 ± 100	1370 ± 37	1856 ± 32
eff. volume $V_{\text{eff}} [\text{fl}]$	3.28	0.96	0.67	2.72	2.69	0.56
acquisition settings						
EM-gain setting	—	—	—	100	100	—
ROI [pixels]	20 × 20	6 × 100	32 × 32	20 × 20	20 × 20	6 runs
exposure time $\Delta t_{\text{exp}} [\mu\text{s}]$	16.6	38.80	486	450	2000	—
frame repetition time	16.8	38.95	495	489	2380	—
$\Delta t_{\text{frame}} [\mu\text{s}]$	—	—	—	—	—	—
acquired frames	165,400	85,000	50,000	60,000	20,000	—
fit results for fluorescent microspheres ($\varnothing = 100 \text{ nm}$)						
$D_{20^\circ\text{C},\text{w}} [\mu\text{m}^2/\text{s}]$	4.43 ± 1.92	4.16 ± 1.84	4.93 ± 1.69	4.20 ± 1.10	3.84 ± 0.78	4.10 ± 0.05
$\beta = c_{\text{measured}}/c_{\text{confocal}}$	—	0.9	4.1	3.5	—	1

[†] measurements performed by Anand Prataph Singh (NUS, Singapore) on a comparable SPIM, as the one described in chapter 6.

Table 8.4. | Properties of the different image sensors and fit results for green fluorescent microspheres ($\varnothing = 100 \text{ nm}$) in water, obtained with each sensor. The camera specifications are given, as provided by the manufacturers. The MDE parameters were obtained, with a bead scan (see section 6.3.2). The last rows give the settings for a SPIM-FCS measurement with a reasonable number of pixels at the smallest usable frame repetition time. The last two rows give the fit results obtained for fluorescent microspheres with these settings. All diffusion coefficients were renormalized to 20 °C and are given as (average ± standard deviation) over the specified number of pixels. The factor $\beta = c_{\text{measured}}/c_{\text{confocal}}$ compares the measured concentration c_{measured} and the concentration c_{confocal} from a confocal measurement.

of up to 95% in the green spectral range. Therefore both cameras exhibit comparable properties in terms of sensitivity, but the iXon camera can be read out faster and collects more photons per pixel. The Photron SA-05 is a high-speed CMOS camera, as it is used for instance in crash tests. It is the camera with the fastest readout, and reaches frame repetition time as low as $\Delta t_{\text{frame}} = 16.8 \mu\text{s}$, but at a significant noise level as it is not optimized for low light applications. This camera also does not directly spool the data to a computer, but fills an on-board RAM, which is then slowly transferred to a host computer after the measurement. The Orca-Flash 4.0 and the pco.edge 5.5 represent the new generation of sCMOS image sensors. Their noise is significantly lower than on other CMOS cameras, but does not completely reach the level of an EMCCD. Although at least the pco.edge supports a global shutter mode, the rolling-shutter is faster and was used for SPIM-FCS measurements on both devices. At the time of the test, the pco.edge could be read at only $\Delta t_{\text{frame}} = 495 \mu\text{s}$, whereas the Orca-Flash 4.0 reached $\Delta t_{\text{frame}} \approx 40 \mu\text{s}$. The sensor of the Orca-Flash 4.0 is also newer than that of the pco.edge and features a higher quantum efficiency in the green spectral range.

A SPIM-FCS measurement of green fluorescent microspheres ($\varnothing = 100 \text{ nm}$, F8803, Invitrogen) was performed on each camera, in order to check their capabilities. Figure 8.21 shows an representative autocorrelation curve from each sensor and Tab. 8.4 lists the diffusion coefficients, that were returned by the fit with a 1-component normal diffusion SPIM-FCS model function (Eq. (5.3.25), p. 61). All these diffusion coefficients are compatible to each other within their errors. Therefore all sensors could be successfully used for SPIM-FCS on the bright microspheres. The parameters of the MDE, required for the SPIM-FCS evaluation, were obtained as usual with a bead scan and are also listed in Tab. 8.4. It was observed that smaller pixels also lead to smaller focal volumes. This can be understood as the small pixels work like a pinhole, that leads to an improved lateral and especially longitudinal focus size.

On the Andor iXon 860, the pco.edge and the Orca-Flash 4.0, a dilution series of the microspheres was measured, as described in section 8.3. The results of these dilution series were comparable to the measurements described in section 8.3. they are reported in Tab. 8.4 as a proportionality factor $\beta = c_{\text{measured}}/c_{\text{set}}$ between the measured concentrations c_{measured} and the concentration measured on a confocal microscope c_{confocal} . Most sensors yield a β close to 3 (cf. section 8.3). Only the Orca Flash 4.0 reached nearly the ideal $\beta = 1$, but the reason for this is unclear. Unfortunately the camera was not available long enough to cross-check the result with a repeat of the experiments.

Finally the pco.edge could also be tested in live-cell measurements. A HeLa cell, which expressed eGFP-4x (see last section for details) was measured at a slightly higher frame repetition time $\Delta t_{\text{frame}} = 761.5 \mu\text{s}$ than above. Figure 8.22 shows representative correlation curves from this measurement, which were obtained with different pixel binning. Also the average over the detected fluorescence intensity during the measurement is shown as images in Fig. 8.22(d-f). It can be seen that the camera images are relatively noisy at 2×2 binning. This has two major reasons. Firstly, the sensor exhibits a higher background noise, as they are not cooled as low as an EMCCD. Secondly, the pixels are smaller and the quantum efficiency is lower than on an EMCCD. In addition the sCMOS cameras do not have an on-chip gain mechanism, therefore less photoelectrons are detected per pixel.

The autocorrelation curves in Fig. 8.22(a-c) are very noisy for 2×2 binning and improve significantly for higher settings. This is most probably also caused by the low number of detected photons (cf. Fig. 8.8 on page 128). Still the quality of the autocorrelation curves of the Andor iXon EMCCD camera is significantly better, than that of the pco.edge, even if they are compared at matching (effective) pixel sizes (Fig. 8.22b,e). Fits of the autocorrelation curves at 8×8 binning gave the following parameters: $D_{\text{fast},20^\circ\text{C}} = (15 \pm 10) \mu\text{m}^2/\text{s}$, $D_{\text{slow},20^\circ\text{C}} = (0.5 \pm 0.4) \mu\text{m}^2/\text{s}$ and $\rho_{\text{slow}} = (23 \pm 15)\%$. The same average values, but with higher standard deviations, were also obtained for lower binning. The fit parameters are compatible with the results discussed in section 8.6. In summary, the sCMOS camera pco.edge could be used for SPIM-FCS also in cells, but its low photon-collection efficiency limits its usability.

In conclusion different linear image sensors are in principle applicable to SPIM-FCS. Nevertheless the EMCCD camera Andor iXon X3 860 still seems to be the best compromise between detection efficiency

and readout speed. The Hamamatsu Orca-Flash 4.0 could pose an alternative, but it could not yet be tested in live-cell measurements. Its use would trade photon detection efficiency against increased readout speed. The next section will test another class of image sensors – SPAD arrays – for use in SPIM-FCS.

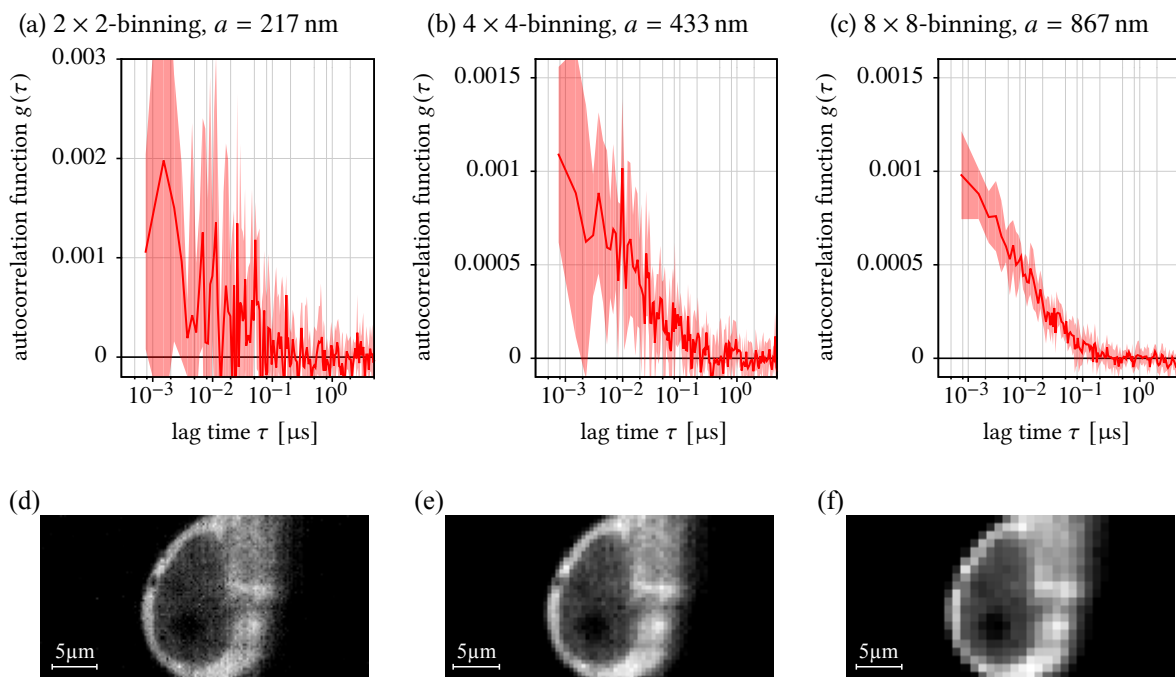


Figure 8.22. | (a-c) Autocorrelation curves from a HeLa cell, expressing eGFP-4x, acquired on a pco.edge sCMOS camera. (d-f) Intensity images of the same cell at different binning stages. The plots show different pixel binning settings. 2×2 -binning was done during acquisition and additional binning was imposed during the correlation step. Minimum lag time and frame repetition time were $\tau_{\min} = 761.5 \mu\text{s}$, exposure time was $\Delta t_{\text{exp}} = 500 \mu\text{s}$. the pixel size a is given above the plots

8.8. Using SPAD arrays for SPIM-FCS

Measurements shown in this section were performed together with Jan Buchholz (DKFZ, Heidelberg) and in part with Samuel Burri (EPFL Lausanne). More details on the SPAD arrays, their readout and applicability to SPIM-FCS will be summarized in Ref. [232].

One goal of this thesis project was to test the applicability of fast SPAD arrays in SPIM-FCS. Two different sensors, *Radhard2* and *SwissSPAD*, were tested, and the results were partly published in Refs. [130, 131]. Their basic properties were already introduced in section 6.4. This section shows how well both sensors perform in SPIM-FCS, at the operation parameters, determined in section 6.4.3.

8.8.1. SPIM-FCS using *Radhard2*

The first sensor, that was tested, was *Radhard2*. Since the SPADs on this chip are only 4 μm in diameter and it does not contain microlenses, its light collection efficiency is very low. Therefore the tube lens in front of the sensor was replaced by a model with a focal length of $f_{\text{TL}} = 100 \text{ nm}$. This decreases the magnification from $60\times$ to $30\times$, but at the same time increases the intensity in the image plane by a factor of 4. The MDE properties are not affected by this replacement, because the SPADs are so small, that the MDE effectively equals the PSF of the microscope, which does not depend on the tube lens, but only on the objective lens. In addition, the laser intensity in the light sheet was typically increased to $200 - 500 \text{ W/cm}^2$, which is a factor 2 – 3 higher than in measurements with an EMCCD camera.

Figure 8.23(a) shows two representative autocorrelation curves, that were obtained with *Radhard2* for fluorescent microspheres ($\varnothing = 100 \text{ nm}$) and for QDot-525 streptavidin ITK. The distributions of the fitted diffusion coefficients (renormalized to 20°C) is shown in Fig. 8.23(b,c). The averages of these distributions are compatible with the diffusion coefficients that were measured for both samples on a confocal microscope: $D_{20^\circ\text{C},\text{W},\text{confocal}}(\text{microspheres}) = (3.0 \pm 0.2) \mu\text{m}^2/\text{s}$ and $D_{20^\circ\text{C},\text{W},\text{confocal}}(\text{QDot-525}) = (22 \pm 3) \mu\text{m}^2/\text{s}$

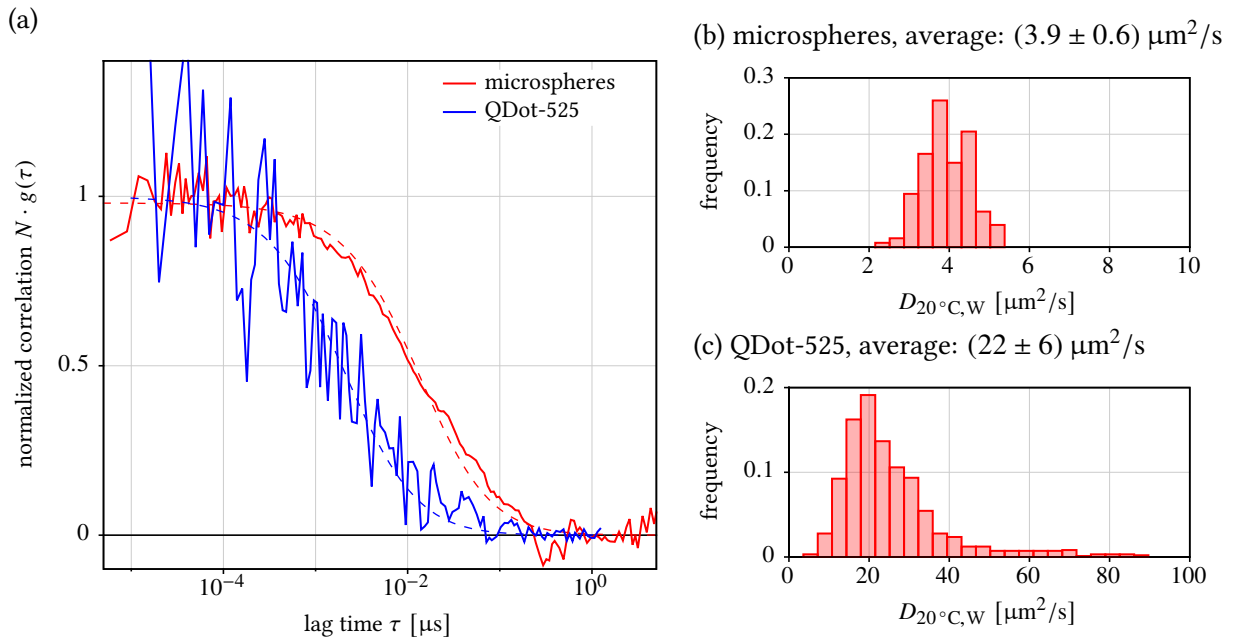


Figure 8.23. | (a) SPIM-FCS autocorrelation curves of fluorescent microspheres ($\varnothing = 100 \text{ nm}$) and QDot-525 streptavidin ITK, obtained with *Radhard2*. (b,c) Distribution of diffusion coefficients, obtained for the two samples. The dashed lines in (a) are fits of Eq. (5.3.25) (p. 61). Average and standard deviation of the distributions in (b,c) are given above the graphs.

(see also Tab. 8.2, p. 125). The diffusion coefficients for QDots is also closer to the confocal measurement, than the estimate from the EMCCD camera. Here the measurement profits from the improved minimum lag time of $\tau_{\min} = 10 \mu\text{s}$.

For the fits, the same model function Eq. (5.3.25) (p. 61) as for confocal measurements was used. As described before, the SPADs are round detectors with a relatively small diameter of only 133 nm in the image plane (at 30 \times magnification). This diameter is significantly smaller than the typical PSF width of the microscope. Therefore the MDE can be represented to a good approximation by a 3-dimensional Gaussian function. This was also checked with bead scans, that were also used to determine the MDE height z_g . The MDE width w_g was then again obtained from a calibration, as described in section 8.1, but with the difference that the absolute diffusion coefficient was either determined with the EMCCD camera, or from a cross-correlation analysis on the sensor (data not shown).

The autocorrelation curve for the QDots is very noisy, compared to the curve for microspheres. This is caused by the low photon count rate of only around 4 – 5 kHz of the QDot-525 sample. Therefore the sensitivity of the *Radhard2* is far too low to make it applicable to measurements of chemical fluorophores or fluorescent proteins. No correlation curves could ever be resolved from these samples.

Also a dilution series of fluorescent microspheres was measured on *Radhard2*. It showed a linear relationship between a confocal reference measurement and the *Radhard2* measurement. the proportionality factor was $\beta = 4.8$, which is even higher than for most linear cameras (see section 8.7). In addition to the reasons already explained for this effect in section 8.3, the *Radhard2* sensors suffers from some specific artifacts, that are only encountered in SPAD arrays. Firstly, the sensor can only count 0 or 1 photons per readout cycle of length $\Delta t_{\text{frame}} = 3 \mu\text{s}$. If more photons are present, they are still only counted as 1. This affects the amplitude of the fluctuations and the absolute count rate and leads to an artificially lowered autocorrelation amplitude and therefore an overestimated particle concentration. Also a certain amount of afterpulsing may occur in SPAD arrays, which shows up as an additional background intensity, which again decreases the autocorrelation amplitude.

8.8.2. SPIM-FCS using *SwissSPAD*

During the last weeks of this thesis project, a new SPAD array has become available: the *SwissSPAD*. It is equipped with microlenses and can be operated at higher excess voltages. In summary this improves the photon detection efficiency by more than a factor of 10 as compared to *Radhard2*. Therefore *SwissSPAD*

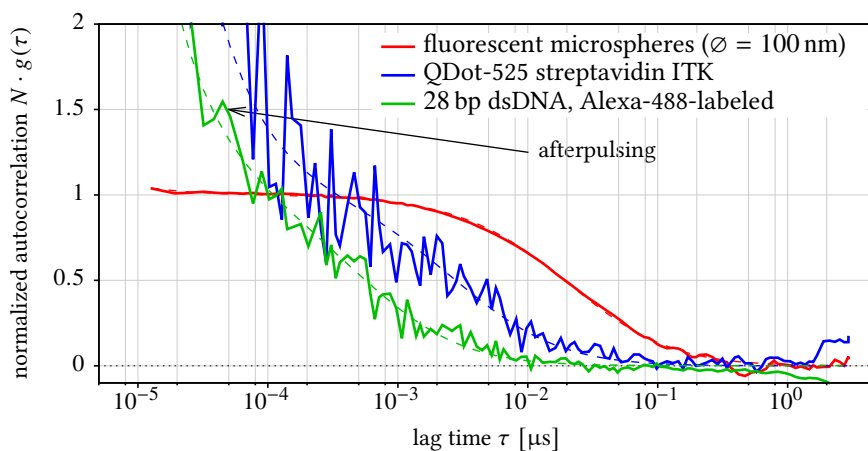


Figure 8.24. | Autocorrelation functions for different samples, acquired with the SPAD array *SwissSPAD*. Dashed lines are one-component fits to the curves. Minimum lag time was $\tau_{\min} = 6.4 \mu\text{s}$.

Sample	SPIM-FCS: <i>SwissSPAD</i> $D_{20^{\circ}\text{C},\text{W}}$ [$\mu\text{m}^2/\text{s}$]	confocal FCS $D_{20^{\circ}\text{C},\text{W}}$ [$\mu\text{m}^2/\text{s}$]	theoretical $D_{20^{\circ}\text{C},\text{W}}^{(\text{theo})}$ [$\mu\text{m}^2/\text{s}$]
dsDNA 28 bp	(83 ± 34)	(84 ± 4)	83
QDot-525 streptavidin ITK	(21 ± 12)	(22 ± 3)	20 – 40
QDot-565 ITK	(22 ± 9)	(33.1 ± 2.6)	20 – 40
green μ spheres, $\varnothing = 100$ nm	(3.3 ± 0.4)	(3.0 ± 0.2)	4.3

Table 8.5. | Summary of diffusion coefficients measured for different samples using the SPAD array *SwissSPAD* and comparison to data from an Andor iXon X3 860 and confocal FCS. Values are given as $D_{20,\text{W}}$ at 20 °C with water as solvent. Minimum lag time with *SwissSPAD* was $\tau_{\text{min}} = 6.4$ μs . See Tab. 8.2 for further details on the measurement with the EMCCD camera and the theoretical estimates.

was also mounted with the standard tube lens ($f_{\text{TL}} = 200$ nm) and the same laser intensities, as for an EMCCD camera were used (i.e. 100 – 200 W/cm^2). *SwissSPAD* can be read with a minimum lag time of $\tau_{\text{min}} = 6.4$ μs could be achieved. This improved sensor allows to also measure dim samples, which are labeled with chemical fluorophores, such as Alexa-488. Figure 8.24 shows some representative autocorrelation curves for fluorescent microspheres, QDot-525 and Alexa-488-labeled dsDNA. Table 8.5 summarizes the diffusion coefficients that were returned by imaging FCS fits to the model function Eq. (5.3.24) (p. 60). In order to account for the steep ascent of the autocorrelation curves at low lag times, an afterpulsing term was added to the model. This will be discussed in detail in section 8.8.3 below. All diffusion coefficients could be acquired with good accuracy, as compared to confocal reference measurements. Also measurements in live cells were attempted, but with no big success, as no evaluable autocorrelation curves could be acquired so far.

Also two dilution series were measured with *SwissSPAD*, one for fluorescent microspheres and one for QDots-525 streptavidin ITK. The results are shown in Fig. 8.25. They demonstrate, that the measured concentration is proportional to a reference measurement. The proportionality factors were again around $\beta = 3$. The overestimation is again explained by an underestimated focal volume (see section 8.3) and an increased background due to afterpulsing.

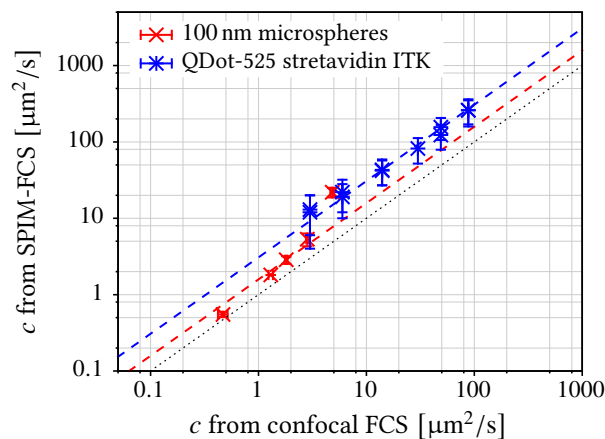


Figure 8.25. | Comparison of concentration measurements with SPIM-FCS with the SPAD array *SwissSPAD* and confocal FCS. The dashed lines are outlier-robust linear fits of $f(x) = \beta \cdot x$ with slopes of $\beta = 1.58$ for microspheres, $\beta = 3.07$ for QDots. Errorbars are averages over several measurements.

8.8.3. Afterpulsing in SwissSPAD

All curves in Fig. 8.5 show a steep ascent of the autocorrelation function towards small lag times. This is caused by a correlating background signal, which is most probably attributed to an afterpulsing in the SPADs. This effect is further analyzed in this section and parameters for its correction are obtained. Figure 8.26(a,b) shows an autocorrelation analysis of the dark count signal, measured with an occluded sensor. If this signal would only consist of thermally created avalanches, the autocorrelation would be flat, as also seen for the dark signal of an EMCCD camera in Fig. 8.7. The decaying autocorrelation in Fig. 8.26(a,b) contradicts this simple model. It can be explained by additional avalanches that are caused by afterpulses. As discussed in section 4.1.1, these follow close to their respective causative pulse. Therefore they cause the more than 100-fold increase in the autocorrelation function between the first two lag times ($\hat{g}(\tau_{\min}) \approx 100 \cdot \hat{g}(2\tau_{\min})$), which is illustrated in Fig. 8.26(a).

Figure 8.26(b) shows the same data, as in Fig. 8.26(a), but without the first lag time channel $\hat{g}(\tau)$. If all avalanches would occur shortly (within one τ_{\min}) after their causative avalanche, at least this curve should be flat. But also on this smaller scale, a now weaker and slower decay of the autocorrelation amplitude can be observed. The reason for this decay is not completely clear. A possible explanation are deeply trapped photoelectrons, that are only released 10 – 100 μs after the initial avalanche. Also

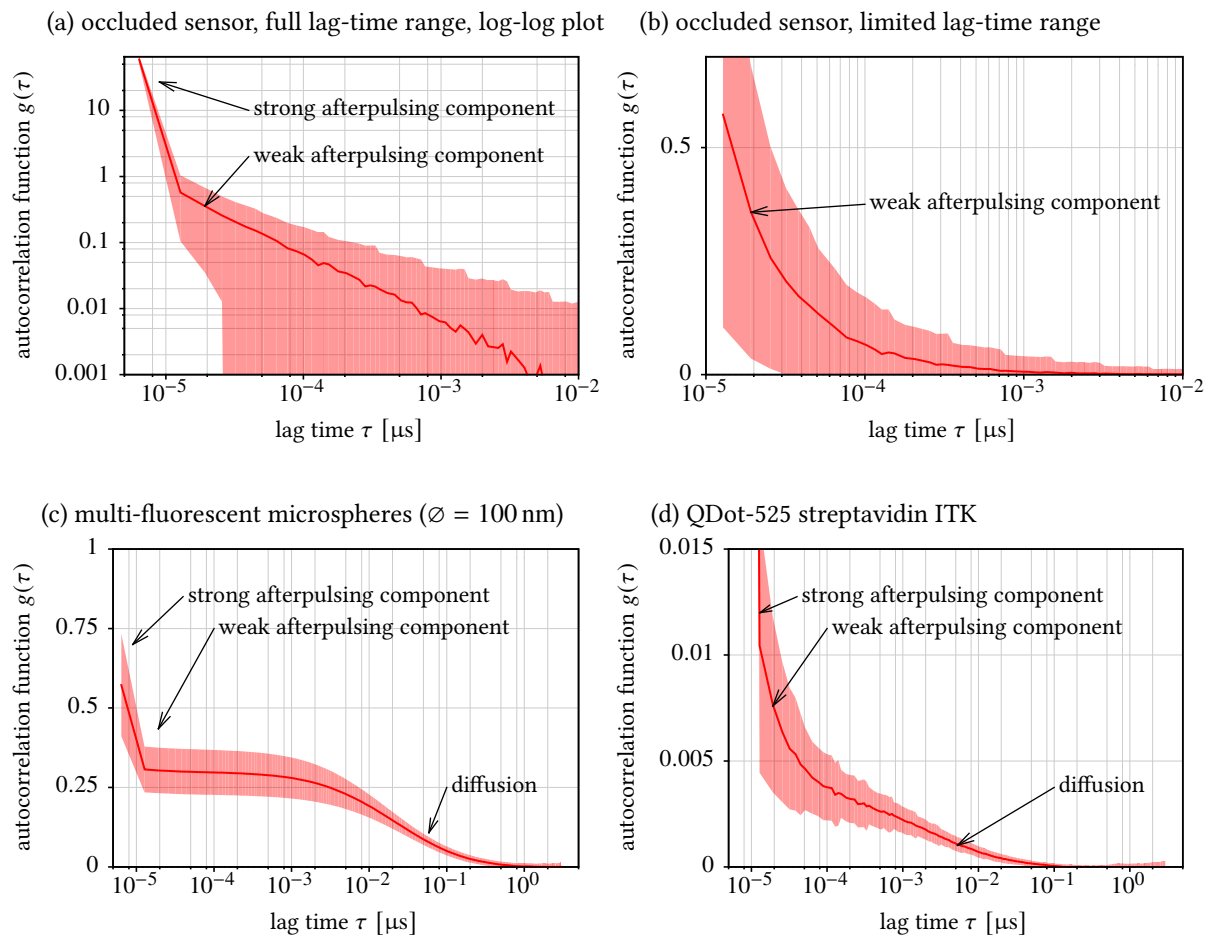
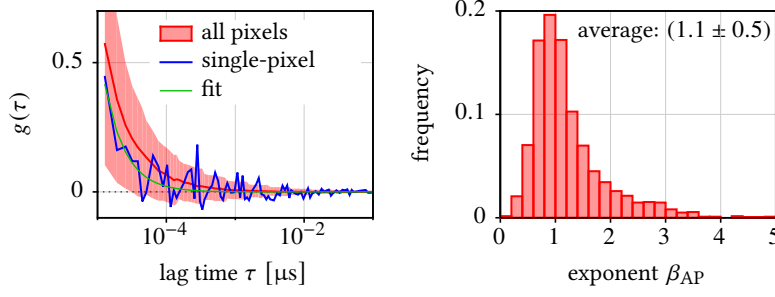
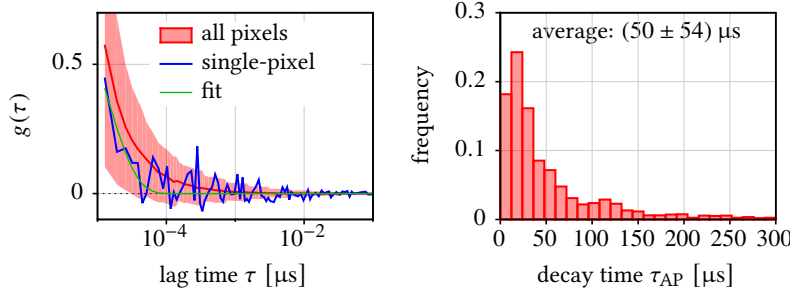


Figure 8.26. | Autocorrelation functions from the SPAD array SwissSPAD, that show afterpulsing. Graphs show average and standard deviation over (a,b) all pixels (512×4) or (c,d) the central 128×4 pixels. Minimum lag time was $\tau_{\min} = 6.4$ μs

(a) power-law fit $g(\tau) = a_0 \cdot \tau^{\beta_{AP}}$, $\chi^2 = (0.44 \pm 0.09)$:



(b) mono-exponential fit $g(\tau) = a_0 \cdot \exp(-\tau/\tau_{AP})$, $\chi^2 = (0.44 \pm 0.09)$:



(c) double-exponential fit $g(\tau) = a_0 \cdot \exp(-\tau/\tau_{AP,0}) + a_1 \cdot \exp(-\tau/\tau_{AP,1})$, $\chi^2 = (0.41 \pm 0.08)$:

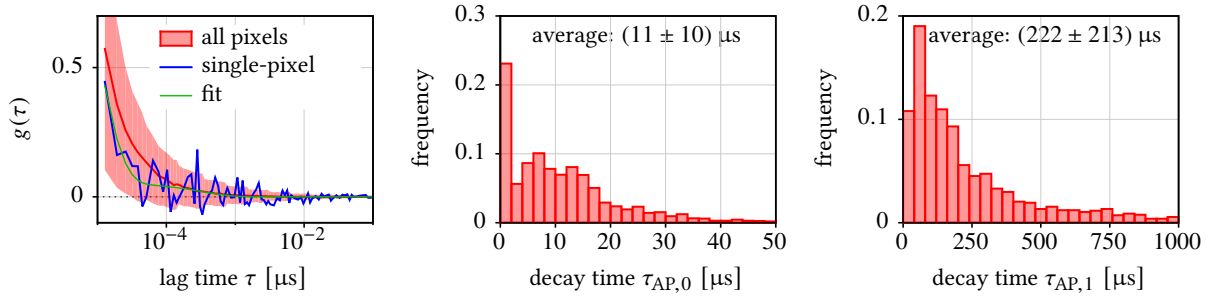


Figure 8.27. | Evaluation of afterpulsing in the SPAD array *SwissSPAD*: (a) with a power-law fit, (b) with a mono-exponential fit and (c) with a double-exponential fit. First plot in each row: autocorrelation curves measured on an occluded sensor. Second/third plot: distribution of selected fit parameters over the central 512×4 pixels. The fit quality χ^2 are average and standard deviation over all pixels (see Eq. (7.1.16), p. 114). Minimum lag time was $\tau_{\min} = 6.4 \mu\text{s}$

a connection to the active recharging in the *SwissSPAD* pixels was observed in a set of preliminary experiments. These showed that the amplitude of the decay is influenced by the timing and frequency of the recharge during a single exposure.

Figure 8.26(c,d) show the averaged autocorrelation curves over all pixels in two representative SPIM-FCS measurements. The effect of the afterpulsing is easily distinguished in both curves. For the bright fluorescent microspheres (Fig. 8.26c), the slow decay from Fig. 8.26(b) is hardly seen and the strong component increases the first value on the autocorrelation curve moderately. For the dimmer quantum dots, $\hat{g}(\tau_{\min})$ was highly increased and was cut therefore from the curve. Then the weak afterpulsing component remains as a steep increase of $\hat{g}(\tau)$ towards $\tau = 2\tau_{\min}$.

As mentioned before, this artifact can be corrected with an additional term in the autocorrelation functions. The basic theory of detector afterpulsing was already described in section 5.5.3. There it was

shown that an additional summand needs to be added to the FCS model function, which is mostly defined by the afterpulsing probability distribution $p_{AP}(\tau)$. Also several possible models for this $p_{AP}(\tau)$ were proposed. To determine the best model, the afterpulsing in Fig. 8.26(b) was analyzed with three different models: a power-law decay, a mono- and a double-exponential decay. The results are summarized in Fig. 8.27. For each model, an exemplary fit is shown together with histograms (over all pixels) of the characteristic parameters of the model. The quality of the fits is quantified by averaged χ^2 values (see Eq. (7.1.16), p. 114) for each model. All three possibilities for $p_{AP}(\tau)$ fit the data equally well. However, only for the power-law decay, a narrow parameter distribution could be achieved. Therefore this power law model was used for all SPIM-FCS measurements and the consensus parameter $\beta_{AP} = 1.1$ was fixed in all cases. Then only the amplitude of the decay a_0 is added as a fit parameter to the FCS model functions. As shown in the last section, this method was successfully used to extract correct mobility parameters with SPAD arrays in a SPIM.

8.8.4. Concluding remarks

In summary the results in this section show that SPAD arrays are promising new image sensors for imaging FCS. They have a high temporal resolution around 10 μs , or even lower if only subregions are read out, which allows them to measure also fast moving particles with good accuracy. Still, the tested chips have some remaining problems that should be resolved in the future. It should be possible to reduce the afterpulsing, which was especially strong in *SwissSPAD*, by an improved quenching circuitry. The photon collection efficiency can be further improved, by optimized microlenses and possibly new SPADs with a larger active area. Back-illuminated sensors would also be beneficial, as these can improve the quantum efficiency dramatically. In addition to the good properties, that SPAD arrays exhibit for imaging FCS, they can also be used for other measurement schemes in the same setup. The gating circuit, present in the pixels of *SwissSPAD*, allows to perform fluorescence lifetime imaging microscopy (FLIM) measurements with the very same sensor [193]. Also an application to super resolution microscopy with methods such as super-resolution optical fluctuation imaging (SOFI) is possible [263–265].

8.9. Summary of the chapter

In summary this chapter shows that SPIM-FCS is a viable method to measure maps of mobility parameters. It can measure absolute diffusion coefficients and with additional calibrations also absolute concentrations. Using modern EMCCD cameras allows for routine application of SPIM-FCS to live cell measurements for intermediately fast and slow proteins. Standard cell culture protocols and fluorescent dyes (fluorescent proteins, as well as chemical dyes and QDots) can be used. In order to measure faster particles, faster image sensors than EMCCD cameras are required. SPAD arrays were shown to be a promising alternative to EMCCD cameras. They reach a temporal resolution of $\Delta t_{\text{frame}} = 10 \mu\text{s}$ and faster, but currently available sensors are just on the verge of applicability to live-cell measurements. Still it can be expected, that the next generation of chips will cross this border. Scientific CMOS (sCMOS) cameras, which have become available during the last years, are also promising candidates for high-speed detectors, but they are not as versatile as SPAD arrays and also still need to be improved in sensitivity.

9. Evaluation of the SPIM for FCCS measurements

Measurements in this chapter were performed in part together with Anand Pratap Singh (NUS, Singapore).

In the last chapter SPIM-FCS was thoroughly tested and characterized. This chapter will show a similar characterization of single plane illumination fluorescence cross-correlation spectroscopy (SPIM-FCCS). First the alignment of a SPIM for 2-color imaging FCCS measurements is discussed in section 9.1. The role of misalignment in this first step was explored using FCCS simulations, which are described in section 9.2. Section 9.3 compares the results of 2-color SPIM-FCCS on several *in vitro* samples with confocal FCCS measurements as a standard. The measurement of absolute concentrations in 2-color SPIM-FCCS is discussed in section 9.4. Section 9.5 discusses the application of 2-color SPIM-FCCS to live-cell measurements. Finally section 9.6 shows an representative flow measurement with two-focus SPIM-FCCS. Most of the results that are summarized in this chapter have been published in Ref. [132].

9.1. Alignment procedure for 2-color FCCS measurements

For SPIM-FCCS measurement the SPIM needs to be aligned for detection of two color channels. This includes adjusting the light sheets for a good overlay (see sections 6.1.2 and 6.3.1) and aligning the dual-view optics (see sections 6.1.4 and 6.3.2). Finally a beadscan with multi-fluorescent microspheres ($\varnothing = 100$ nm, T7279, Invitrogen, see appendix A.3.2) was performed to validate the alignment and obtain the displacement $\vec{\delta}$ between the MDEs of the two color-channels. For all measurements in this thesis, the average over each component of $\vec{\delta}$ was smaller than 100 nm (see section 6.3.2). If a larger displacement was obtained in the beadscans, the alignment was repeated.

Just as for SPIM-FCS, a calibration of the MDE parameters is required also for SPIM-FCCS. The same method, as for SPIM-FCS, was used, but for each color channel separately. The longitudinal $1/e^2$ half-widths of the MDE (z_g and z_r) were obtained from the beadscan. Then a SPIM-FCS measurement was performed with multi-fluorescent microspheres (again: $\varnothing = 100$ nm, T7279, Invitrogen, see appendix A.3.1), which are visible in both color channels. The SPIM-FCS calibration method from section 8.1 was applied to each color channel separately to yield the $1/e^2$ half-widths of the MDE (w_g and w_r). The diffusion coefficients D_g and D_r obtained for each color channel, were compared as an additional plausibility check. If D_g and D_r were not similar within their errors, the complete alignment was repeated.

The values of the MDE parameter (w_g , w_r , z_g and z_r) obtained in this alignment procedure, were comparable to those given for a single (green) focus in section 8.1, i.e. w_g , w_r were approximately 600 nm and z_g , z_r were approximately 1200 nm. For the SPIM-FCCS model functions from section 5.4, also the pixel size a in the image plane is required. It is given by the size of the pixels on the image sensor and the magnification of the microscope, which is nearly equal in both color channels.

At this point, the setup is aligned for the measurements. As an additional check, the cross-correlation curve from the calibration measurement was analyzed and the alignment was redone, if the cross-correlation amplitude was too low. The multi-fluorescent microspheres carry many molecules of each of their four different dyes and are thus near-perfect FCCS samples, that should consist of double-labeled particles only. Therefore the amplitude of their cross-correlation function $\hat{g}_{gr}(\tau_{\min})$ is expected to be

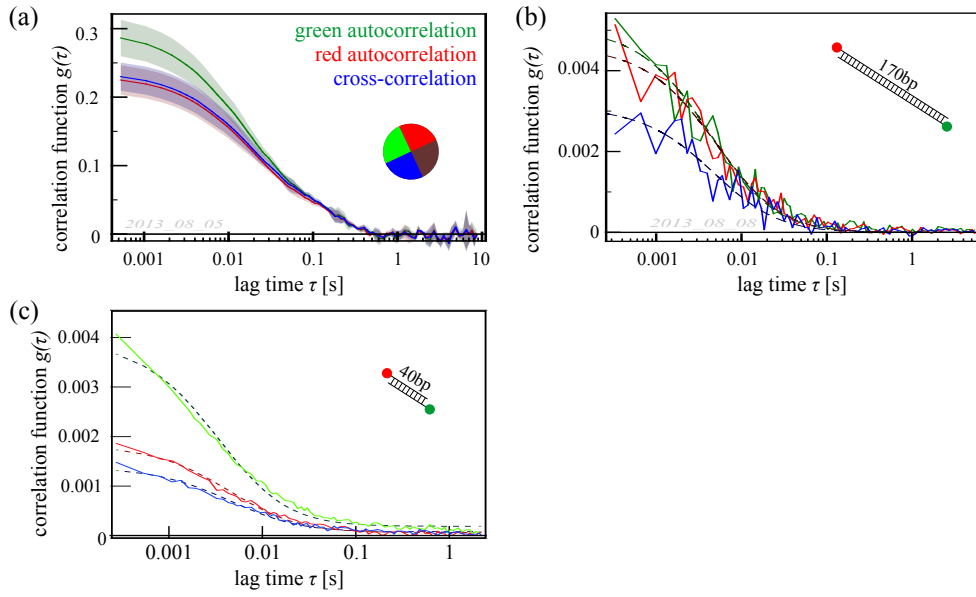


Figure 9.1. | Exemplary SPIM-FCCS autocorrelation (green/red) and cross-correlation curves (blue) of several test samples. (a) TetraSpec beads, $\tau_{\min} = 0.53$ ms, 3 runs. (b) 170 bp dsDNA, labeled with Alexa-488 and Alexa-594 on opposing ends, $\tau_{\min} = 0.29$ ms. (c) 40 bp dsDNA with 2×2 -binning, $\tau_{\min} = 0.27$ ms. The graphs show the correlation functions of a single pixel, or average and standard deviation over several runs. Dashed lines are fits to the data. All curves were acquired with an Andor iXon X3 860 EMCCD camera.

approximately on the level of the autocorrelation amplitudes $\hat{g}_{gg}(\tau_{\min})$ and $\hat{g}_{rr}(\tau_{\min})$ (see section 5.4.2). In the following experiments, this is quantified by:

$$q_{gr} = \frac{g_{gr}(\tau_{\min})}{\min[g_{gg}(\tau_{\min}), g_{rr}(\tau_{\min})]}. \quad (9.1.1)$$

Figure 9.1(a) shows representative auto- and cross-correlation curves of multi-fluorescent microspheres. Figure 9.1(b,c) shows the same curves for different double-labeled DNA samples, that can be produced with the polymerase chain reaction and are often used to calibrate confocal FCCS. Table 9.1 summarizes the relative cross-correlation amplitudes q_{gr} and diffusion coefficients $D_{20^\circ\text{C},\text{W}}$, that were obtained with SPIM-FCCS for these samples.

A further important factor in the 2-color SPIM-FCCS fit model is the crosstalk κ_{gr} between the green and the red detection channel (see section 5.4.2). It depends on the filter set, which is mounted in the microscope and the used fluorophores. Since κ_{gr} is a parameter of the SPIM-FCCS model functions,

sample	$D_{20^\circ\text{C},\text{W}}$ [$\mu\text{m}^2/\text{s}$]	q_{gr} [%]
40 bp dsDNA	(36 ± 8)	(75 ± 10)
170 bp dsDNA *	(22 ± 3)	(59 ± 8)
607 bp dsDNA *	(6.3 ± 0.9)	(46 ± 18)
TetraSpec*	(3.1 ± 0.2)	(104 ± 8)

* an average over 6 measurements during two week

Table 9.1. | Summary of typical diffusion coefficients $D_{20^\circ\text{C},\text{W}}$ and of the relative cross-correlation amplitudes q_{gr} obtained with different samples in SPIM-FCCS. Note that the values for q_{gr} were not corrected for the crosstalk κ_{gr} .

red channel transmission	fluorophore	κ_{gr} [%]
$\lambda > 568$ nm	Alexa-488	(11.8 ± 1)
	eGFP	(9.5 ± 1)
$\lambda > 594$ nm	Alexa-488	(5.4 ± 0.5)
	eGFP	(3.3 ± 0.5)

Table 9.2. | Crosstalk κ_{gr} for different fluorophores and filter sets. The fluorescence was always split at 565 nm with a dichroic mirror and the green channel was defined by a bandpass filter with transmission in the range of 500...550 nm. In the red channel a longpass filter was used, which had an edge as defined in the table.

it needs to be estimated before any fits can be performed. This was performed with a sample, that contains the green fluorophore only, either in aqueous solution, or expressed in cells. For both variants the same crosstalk coefficients were obtained. They are summarized in Tab. 9.2 for two different filter sets in the dual-view optics. The two channels were always split with a dichroic mirror with an edge at $\lambda = 565$ nm and the green channel was always defined by a bandpass filter with transmission in the range $\lambda = 500...550$ nm. For the red channel, two different long-pass filters were used, that start transmitting at 568 nm or at 594 nm. The latter filter was used for most of the measurements, as it minimized the lower crosstalk, while transmitting enough red fluorescence to obtain evaluable autocorrelation curves. The measured values for κ_{gr} also coincide with the values obtained from the spectra of the filters and the fluorophores.

9.2. Simulation of a misalignment in 2-color FCCS

In addition to the six parameters w_g , w_r , z_g , z_r , a and κ_{gr} , the SPIM-FCCS models from section 5.4.2 also depend on a possible displacement $\vec{\delta} = (\delta_x, \delta_y, \delta_z)^T$ between the green and the red focus. The displacements were assessed with beadscans and were routinely smaller than 100 nm (see above), which is significantly smaller than w_y and z_y . Therefore the displacement was fixed to $\vec{\delta} = 0$ in all fits in this thesis, which significantly simplifies the model functions. In order to justify this assumption and to estimate the error that it possibly introduces, FCCS simulations were carried out with the software described in appendix B.1. In these simulations, two foci were set up with a varying displacement δ_x . The MDE parameters in the simulation were chosen to match the values obtained for the real microscope. For each focus pair, different sets of Brownian particles were simulated. Either all particles carried a green and a red fluorophore, or only a fraction of them. In the latter case, the remaining particles were equally partitioned between a green-only and a red-only species. These simulations were also performed for two different values of the cross-talk $\kappa_{gr} = 3.5\%$ or $\kappa_{gr} = 11.2\%$, which are in the range of the experimentally observed cross-talks.

Figure 9.2 shows a set of representative correlation curves obtained from this simulation. For small displacements $\delta_x \leq 100$ nm, the cross-correlation amplitude $g_{gr}(\tau_{\min})$ does not change significantly (horizontal blue lines: $g_{gr}(\tau_{\min})$ for $\delta_x = 0$). For larger displacements $\delta_x \geq 200$ nm it drops considerably and nearly reaches 0 for $\delta_x = 1$ μ m. These correlation curves were evaluated with the fit models described in section 5.4.2 and the global fit, described in section 7.1.4. For each curve $\delta_x = 0$ was assumed and the diffusion coefficients of the three species were linked: $D_A = D_B = D_{AB}$. Each such fit then yielded the concentrations of the three species $\langle c_A \rangle$, $\langle c_B \rangle$ and $\langle c_{AB} \rangle$, from which the relative dimer concentration was obtained as a function of δ_x :

$$p'_{AB}(\delta_x) = \frac{\langle c_{AB} \rangle(\delta_x)}{\langle c_A \rangle(\delta_x) + \langle c_B \rangle(\delta_x) + \langle c_{AB} \rangle(\delta_x)}. \quad (9.2.1)$$

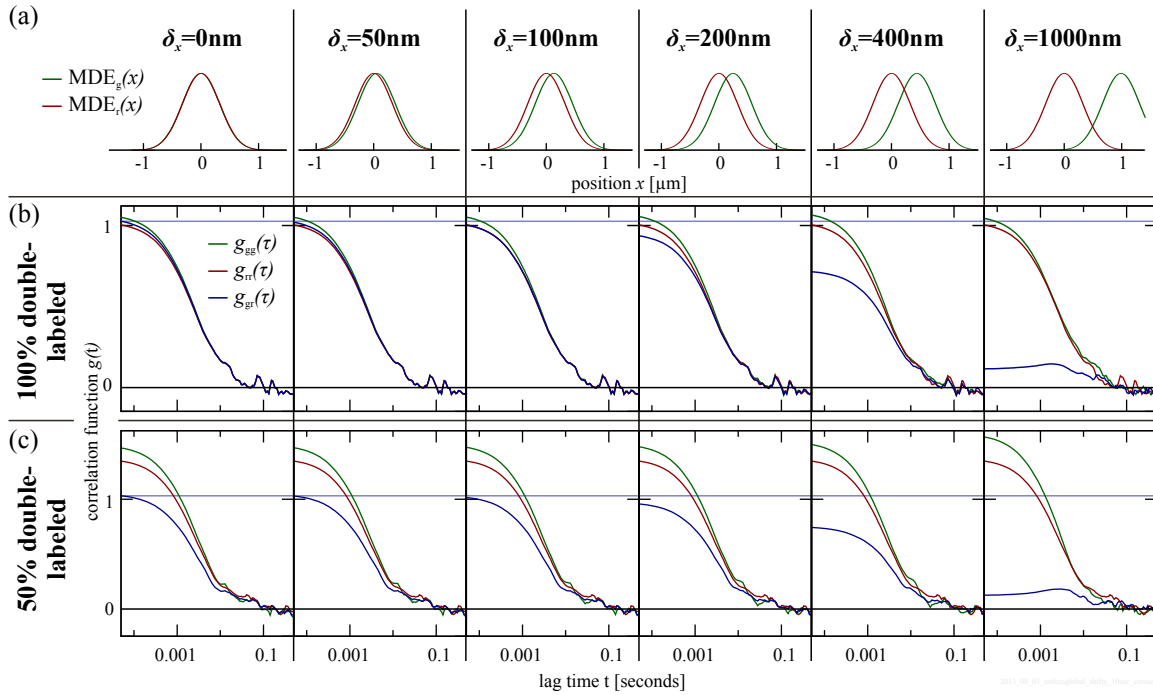


Figure 9.2. | Representative results of auto- and cross-correlation curves from an FCCS simulation with different amounts of double-labeled particles and for different displacements δ_x of the green and the red MDE. (a) Cuts through the MDEs along the x -axis. (b) Correlation curves for a 100% double-labeled sample. In (a,b) the blue horizontal line is $\hat{g}_{gr}(\tau_{\min})$ at $\delta_x = 0$. (c) Correlation curves for a 50% double-labeled sample. The crosstalk for this simulation was $\kappa_{gr} = 11.2\%$. All simulations were performed with the same trajectories, hence the similar noise structure on the correlation curves.

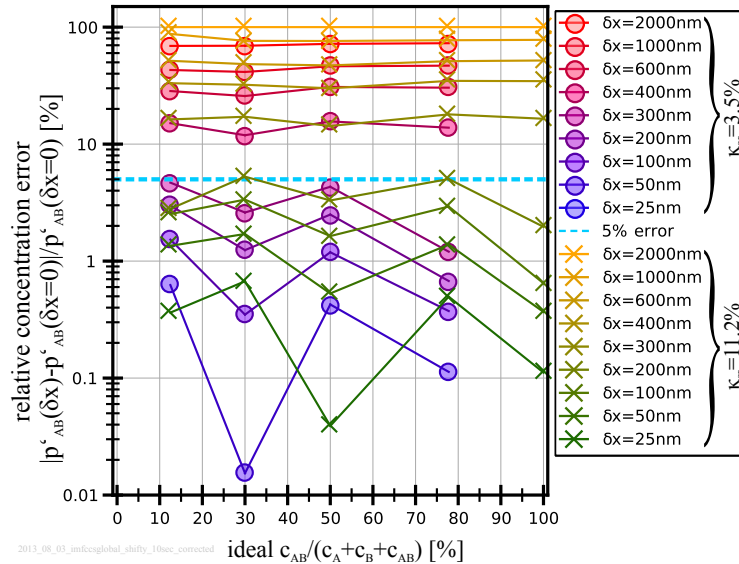


Figure 9.3. | Fit results from the simulation in Fig. 9.2, when assuming no shift $\delta_x = 0$ in the fit model, given that a shift $\delta_x > 0$ actually is present in the microscope setup. The graph shows the relative error, as defined by Eq. (9.2.2) at different crosstalk coefficients κ_{gr} and focal shifts δ_x (color-coded green-orange or blue-red). The thick orange line marks an error level of 5% which is still acceptable.

Here $\langle c_\chi \rangle(\delta_x)$ is the concentration of species χ , obtained from the simulation with focus displacement δ_x . The relative error, which is introduced by the assumption $\delta_x = 0$ in the fit models, can then be quantified as:

$$\text{err}(\delta_x) = \frac{|p'_{AB}(\delta_x) - p'_{AB}(0)|}{p'_{AB}(0)}. \quad (9.2.2)$$

Figure 9.3 shows a plot of this error as a function of the true relative dimer concentration of the sample, which was given by the simulation parameters. The results for the two values of the crosstalk κ_{gr} are approximately similar (color-coded from orange to green for $\kappa_{\text{gr}} = 11.2\%$ and blue to red for $\kappa_{\text{gr}} = 3.5\%$).

From Fig. 9.3 it is now possible to justify, that $\vec{\delta} = 0$ was set in the models. The typical displacement $\vec{\delta}$ in the alignment was on the order of 100 nm at the most. Therefore the error, introduced by fixing $\vec{\delta} = 0$ in the models is less than 3%, which is significantly smaller, than the widths of the usually obtained parameter distributions in SPIM-FCS (see measurements in last chapter). Note that 3% is the maximum error in the simulations and some runs are significantly below this value. If an error margin of $\text{err}(\delta_x) < 5\%$ for p'_{AB} is seen as acceptable (blue dashed line in Fig. 9.3), the required precision of the alignment alignment is only 200 nm. The diffusion coefficient D , that was obtained from the fits, did not show any dependence on the displacement δ_x , or the crosstalk κ_{gr} (data not shown). This is explained by the facts, that the decay times of the two autocorrelation functions are not affected by these parameters, and that the autocorrelations dominate the objective function $\chi^2(\cdot)$ of the linked fit.

In summary, these FCCS simulations allowed to define error margins on the effect of a misaligned instrument on the results of SPIM-FCCS fits. With the alignment precision, that was typically achieved for the SPIM described in chapter 6, the assumption $\vec{\delta} = 0$ could safely be used for all 2-color SPIM-FCCS fits in the remaining thesis. The systematic error, that is introduced by this assumption is less than 3%.

9.3. Comparison with confocal 2-color FCCS

As for SPIM-FCS, the results of SPIM-FCCS were compared to measurements on a confocal microscope as a reference. For this comparison, different samples of a 607 bp long dsDNA were prepared. The DNA molecules were single- and double-labeled with Alex-488 and Alexa-594 (see above). Seven samples with different relative concentrations of the dimers were prepared and measured on a SPIM and a confocal microscope. The data was evaluated with the global fit described in section 7.1.4 and the models from section 5.4.2. From the fit results, the relative dimer concentration was quantified with the parameter

$$p_{AB} = \frac{\langle c_{AB} \rangle}{\min[\langle c_A \rangle, \langle c_B \rangle]}. \quad (9.3.1)$$

Figure 9.4(a) shows a plot that compares p_{AB} obtained with SPIM-FCCS and confocal FCCS. Figure 9.4(b) shows the same plot, but for the relative cross-correlation amplitudes q_{gr} (see Eq. 9.1.1). Both plots are compatible with linear relationship between the two sets of measurements. For q_{gr} the values are close to the ideal slope of 1 and for p_{AB} a slope of ~ 1.2 was obtained with an outlier-robust regression. This indicates that the SPIM and the confocal FCCS measurement have about the same dynamic range and the SPIM-FCCS results are reasonable.

The fact, that in Fig. 9.4(a) the ideal slope of 1 was not reached has several reasons. Firstly, the correlation curves from the SPIM-FCCS measurement were noisy and the temporal resolution was lower than in confocal FCCS. Both effects increase the uncertainty on the fit results. Also an imperfect background and bleach correction can influence the results. A small amount of photo-bleaching (10–20% drop in amplitude) had to be corrected before correlating the SPIM measurement, which can impair the cross-correlation amplitude although the autocorrelation amplitudes are fully reconstructed (see section 5.5.4). Finally, as discussed in section 8.3, also the difference between the true focus geometry

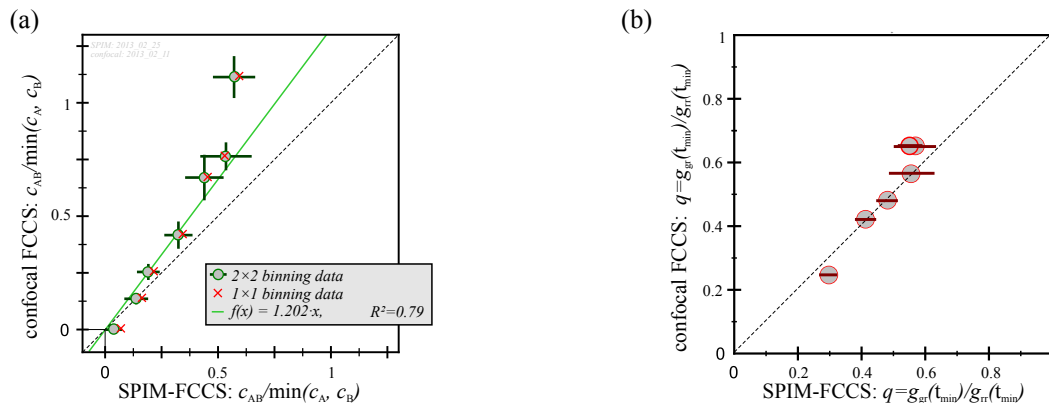


Figure 9.4. | Comparison between confocal and SPIM-FCCS measurements. (a) Relative dimer concentration p_{AB} . (b) Relative cross-correlation amplitude q_{gr} . The black dashed line represents the ideal result (slope 1). Acquisition settings for SPIM-FCCS: 700,000 frames, 128×6 pixels, no binning (red crosses) or 2×2 binning (green circles), $\tau_{\min} = 0.33$ ms. Data from the confocal measurements are average and standard deviation over 7 consecutive runs (30 s each). For SPIM they are average and standard deviation over all pixels from 3–4 separate experiments. The green line in (a) represents an outlier-robust linear fit to the data with 2×2 -binning.

and its model can severely influence the results in both the confocal and the SPIM-FCCS measurement. A detailed analysis of the different factors, that affect FCCS measurements in general, can be found in Ref. [220].

In conclusion, the results from both methods are impaired by several artifacts. Nevertheless, the relative concentrations measured on a confocal microscope and on a SPIM were very close. Also the dynamic ranges of both types of instruments were shown to be comparable. Therefore SPIM-FCCS can be used as a reliable tool for the measurement of molecular interactions, provided a proper alignment and calibration has been performed.

9.4. Absolute concentration measurements with 2-color FCCS

In the last section, it was shown that SPIM-FCCS and confocal FCCS yield approximately the same relative concentrations for a sample. In this section, the measurement of absolute concentrations with SPIM-FCCS will be discussed. To this end, a mixture of single- and double-labeled dsDNA fragments (fluorophores: Alexa-488 + Alexa-594, length: 170 bp) was prepared and diluted to different degrees. The different dilutions were then measured with a SPIM and a confocal microscope. Figure 9.5 shows the results. As for the autocorrelation analysis in section 8.3, the concentrations measured with SPIM-FCCS depend linearly on the concentrations obtained with confocal FCCS. The proportionality factors were determined with a robust regression and found to be in the range 8.8–11.2 for this sample. The variation of the factors around their mean was $\pm 10\%$, which agrees with the findings of the last section, that relative concentrations can be measured accurately. The absolute values of the proportionality factors are significantly higher than the ones that were obtained for the autocorrelation analysis in section 8.3, which were in the range of 3–4. In addition to the reasons for an overestimated concentration, that were discussed for the autocorrelation analysis, the focus geometry might play an even bigger role in SPIM-FCCS. Here the concentrations depend on the overlap of the two focal volumes, which can be significantly underestimated by a wrong model for the MDE. Also the temporal resolution of the EMCCD camera and the relatively dim samples may again impair the results.

Regardless of the different factors that influence the results of SPIM-FCCS, the relation between the concentrations measured with confocal FCCS and with SPIM-FCCS on the same sample was always

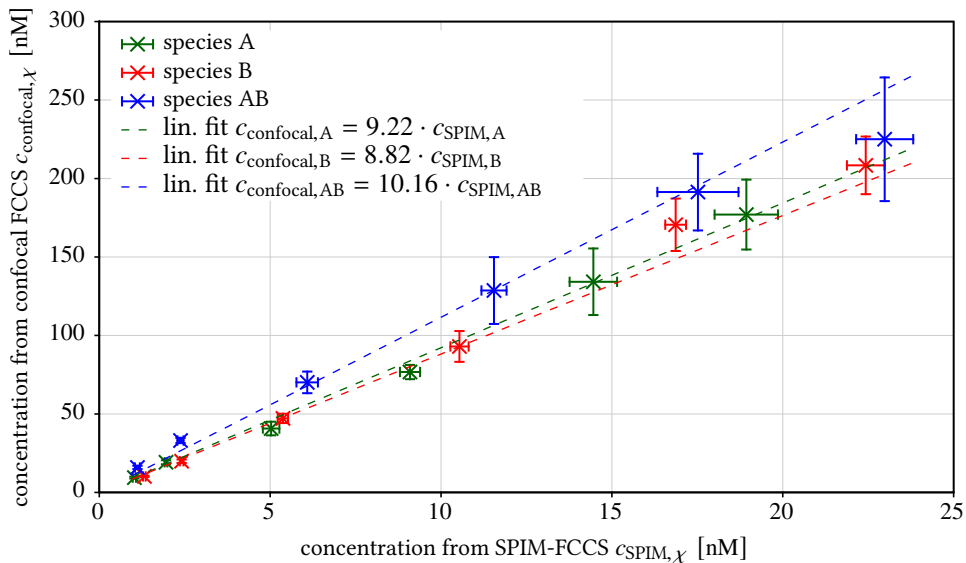


Figure 9.5. | **Calibration of the SPIM-FCCS concentration against concentrations measured in a confocal microscope.** Concentrations measured in a dilution series of a 170 bp dsDNA sample. Species A is Alexa-488 single-labeled, species B is Alexa-594 single-labeled and species AB is double-labeled. Datapoints are averages and standard deviations over fits to 6 runs (20 s each) in the confocal case and all pixels in 2 – 4 measurements in the SPIM-FCCS case ($\tau_{\min} = 330 \mu\text{s}$). A global fit with $D_A = D_B = D_{AB}$ was used in both cases. Linear functions (dashed lines) were fit with robust regression and forced to $c_{\text{SPIM}}(0) = 0$.

linear. In addition the relative concentrations were nearly the same with both methods (factor 1.2 between SPIM and confocal, instead of 1, see last section). Therefore SPIM-FCCS can be calibrated to yield the same concentrations, as confocal FCCS.

9.5. Applicability of 2-color FCCS in live-cells

Cells for this section were prepared by Gabriele Müller (DKFZ, Heidelberg).

The last sections discussed the applicability of SPIM-FCCS for *in vitro* samples. Here the method is tested on living mammalian cells, that express fluorescent proteins. Five different types of cells were prepared and measured (see appendix A.2 for details on cell culture methods and the plasmids). The first three samples are mono- and dimers of the fluorescent proteins eGFP and mRFP1. They are often used as controls for confocal FCCS measurements in the cytoplasm or the nucleus (e.g. in refs. [73, 95, 266]):

1. As a negative control, eGFP and mRFP1 monomers were expressed from a single plasmid (pCMV-eGFP-ires-mRFP1). This ensures that approximately equal amounts of both proteins are present in every cell, which is hard to achieve if the cells have to be double-transfected with two plasmids.
2. As a first positive control an eGFP-mRFP1 dimer was expressed in HeLa cells. In this fusion protein, the two separate fluorophores are connected by a short linker.
3. As a second positive control an eGFP-P30-mRFP1 dimer with a linker of 30 proline amino acids (P30) was expressed in HeLa cells. Since the poly-proline linker is relatively sturdy [267], this fusion protein is larger than the simple dimer (item 2). It is also expected to show less Förster resonance energy transfer (FRET) between the two fluorophores, due to their larger separation.

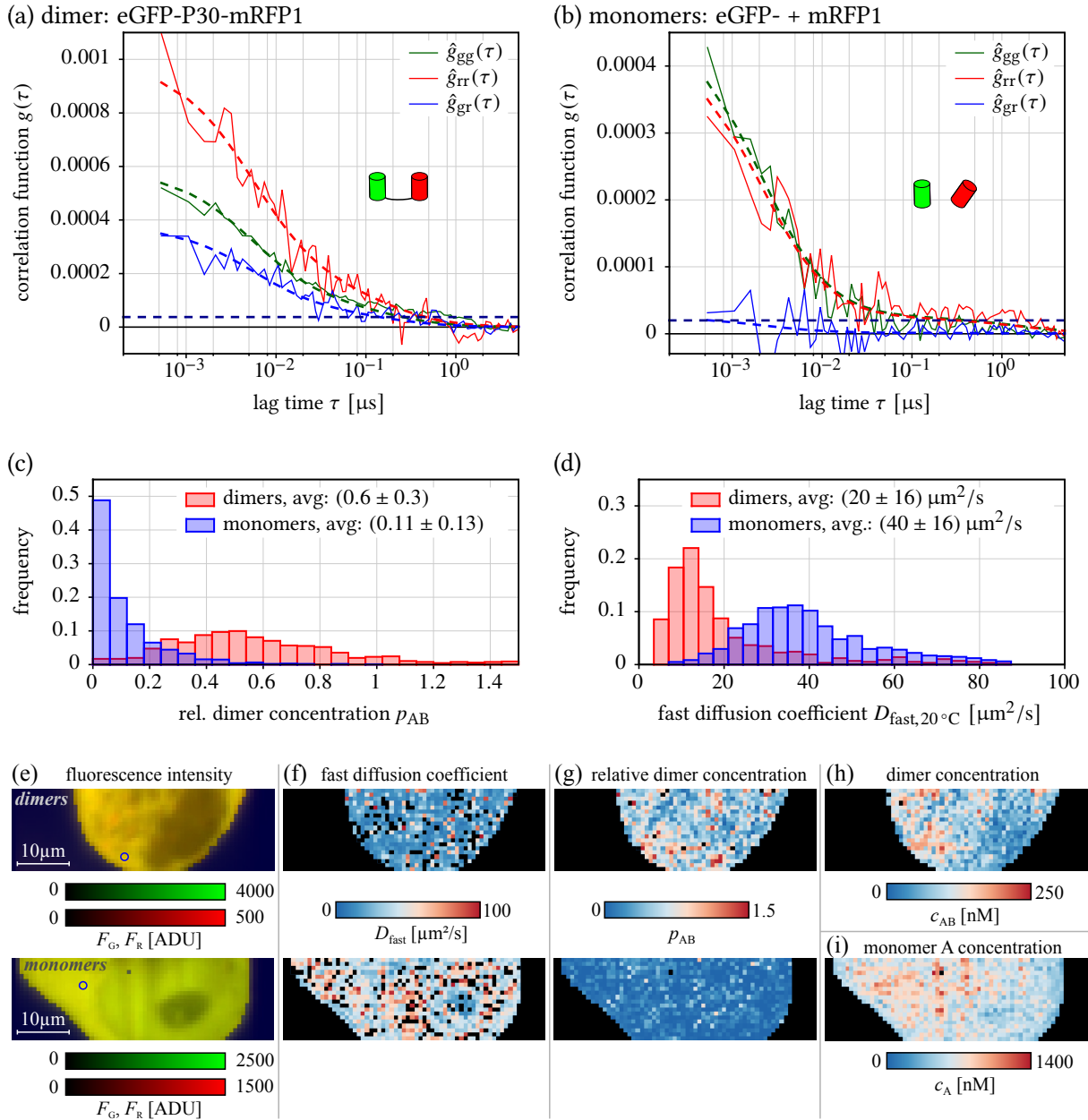


Figure 9.6. | SPIM-FCCS measurement of eGFP-P30-mRFP1-dimers and eGFP + mRFP1-monomers expressed in HeLa cells. (a,b) Representative correlation curves and fits for the dimer and monomer sample, horizontal dashed lines are the level of cross-talk, which is explained by crosstalk. (c) Histograms of the relative dimer concentration p_{AB} over the two cells. (d) Histogram of the fast diffusion coefficient $D_{fast,20^\circ C}$ over the two cells. (e) Fluorescence Intensity image (blue circles mark position of the measurements in a,b), (f) Maps of D_{fast} (at $\vartheta = 25^\circ \text{C}$). (g) Maps of p_{AB} . The first row of images in (e-g) shows a cell expressing eGFP-P30-mRFP1 and the second row a cell expressing eGFP + mRFP1-monomers. (h) Map of the dimer concentration c_{AB} in the cell, which expresses eGFP-P30-mRFP1-dimer. (i) Map of the monomer A concentration c_A in the cell, which expresses eGFP- and mRFP1-monomers. Acquisition settings: 128×20 pixel, $\tau_{min} = 530 \mu\text{s}$.

In addition to these samples, also the applicability of SPIM-FCCS in cell membranes was assessed:

1. As a negative control, PMT-eGFP and PMT-mRFP1 monomers were expressed in a double-transfection in HeLa and CHO-K1 cells. The PMT sequence, anchors the single fluorophores to the membrane (see section 8.6 for details).
2. As a positive control a double-labeled epidermal growth factor receptor (EGFR) (eGFP-EGFR-mRFP1)¹ was expressed in HeLa and CHO-K1 cells. The eGFP-EGFR-mRFP1 is a trans-membrane protein, which carries one fluorophore on the extra-cellular and one on the intra-cellular side [76, 262].

For each of these five samples, several cells were measured on different days. The SPIM-FCCS fit models from section 5.4.2 were used in a global fit (see section 7.1.4) to evaluate the data. Generally a two-component normal-diffusion model was used. The concentrations $\langle c_A \rangle$, $\langle c_B \rangle$ and $\langle c_{AB} \rangle$ were linked over the two auto- and the cross-correlation curve. Depending on the sample, the diffusion coefficients were treated differently.

Figure 9.6 shows representative results of one cell expressing the eGFP-P30-mRFP1 dimer and one cell expressing eGFP and mRFP1 monomers. The auto- and cross-correlation curves shown in Fig. 9.6(a,b) are comparable to those published for confocal FCCS studies of the same proteins (see e.g. Ref. [73, 268]). For the fits (dashed curves in the figure) a two-component normal diffusion model was used, which accounts for the complex environment in the cell. Furthermore, it was assumed that all visible proteins have the same size and thus also the same diffusion coefficients. Therefore the three fast diffusion coefficients, the three slow diffusion coefficients and the three fractions of the fast component were each linked together. This assumption also implies that the three species A, B and AB are only distinguished by their spectral properties. Figure 9.6(c-i) shows histograms and maps of the different fit results.

The diffusion coefficient distributions in Fig. 9.6(d) have two distinct peaks at $(40 \pm 16) \mu\text{m}^2/\text{s}$ for the monomers and $(20 \pm 16) \mu\text{m}^2/\text{s}$ for the dimers (both given at $\vartheta \approx 20^\circ\text{C}$). These values are also compatible with the diffusion coefficients listed in Fig. 8.17(b) on p. 137. The fact, that dimers are significantly slower than the monomers, serves as a control for the correct expression of the proteins.

Figure 9.6(c) shows a distribution of the relative dimer-concentrations p_{AB} . The average and standard deviation of p_{AB} for the monomers is (0.11 ± 0.13) , which is compatible with no dimers ($p_{AB} = 0$). The remaining small dimer fraction is explained by an imperfect background, crosstalk and bleach correction, as well as the noisiness of the correlation curves. Also motions inside the cell can lead to deformed correlation curves that are interpreted as representing a small dimer fraction.

The distribution of p_{AB} for dimers in Fig. 9.6(c) is significantly different from the distributions of the monomers. Its mean and standard deviation are (0.6 ± 0.3) . In an ideal sample, all proteins would carry both fluorophores (AB only) and $p_{AB} \rightarrow \infty$. This case is never encountered in a real cell. Due to several reasons, many proteins have only a single functioning fluorophore (species A or B). Firstly, the maturation time for the two fluorescent proteins in the cell is different, so it is possible, that one fluorophore is already fluorescent, whereas its partner is not yet in a fluorescent state. Secondly, proteins are never folded perfectly, so a certain amount of dimers will contain non-fluorescent partners. A third reason is that each fluorophore in a dimer is bleached independently. Therefore some double-labeled proteins are always converted to single-labeled proteins during the measurement. However, the measured relative cross-correlation amplitudes are comparable to those usually obtained from confocal FCCS, which is expected, since all given reasons for the low dimer concentration also apply to confocal microscopy.

Figure 9.7 shows representative results for the measurements in the membrane. Figure 9.7(a) illustrates the auto- and cross-correlation curves from a single pixel for the double-labeled EGFR. Figure 9.7(b) shows the same curves for a cell, expressing PMT-eGFP and PMT-mRFP1. The auto-

¹This construct was kindly provided by Thorsten Wohland (NUS, Singapore).

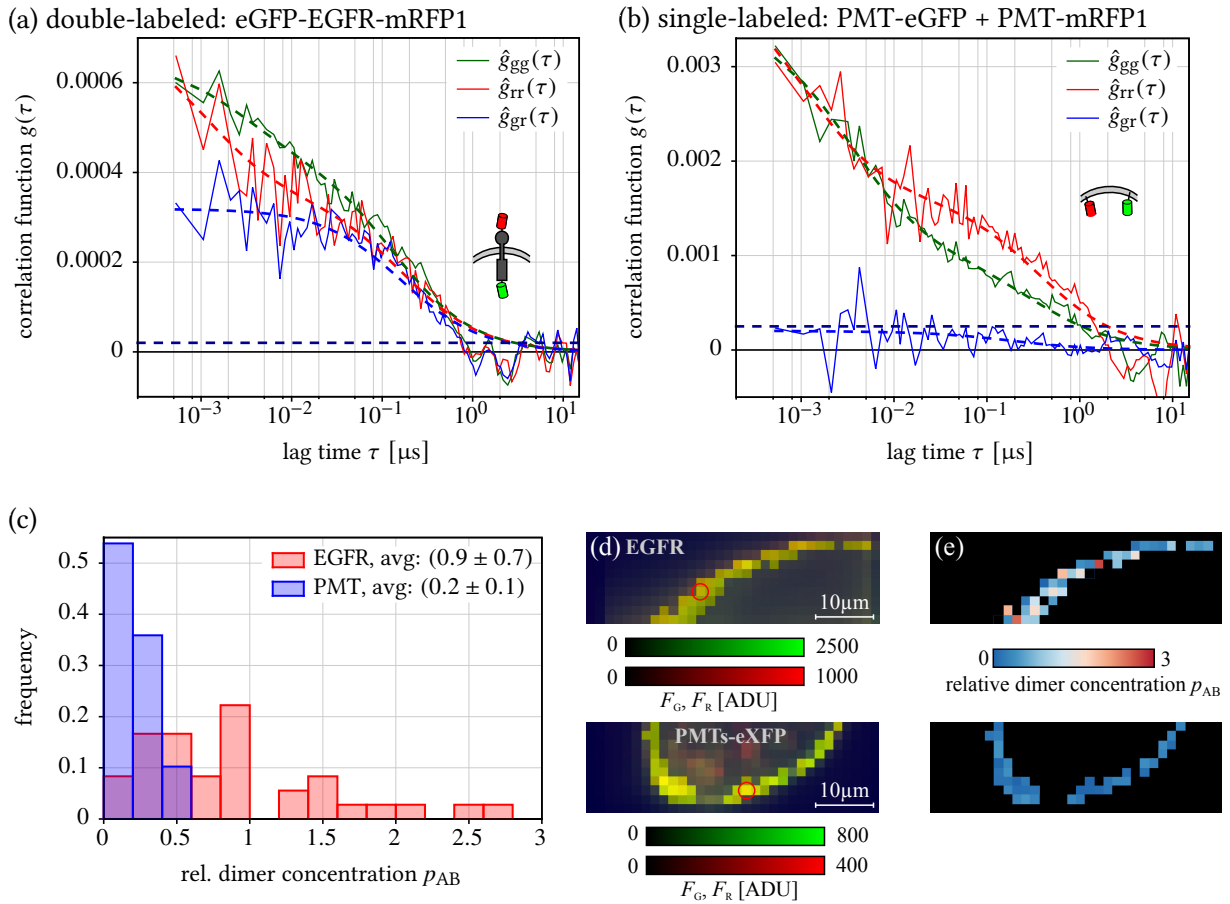


Figure 9.7. | SPIM-FCCS measurement of eGFP-EGFR-mRFP1 and PMT-eGFP + PMT-mRFP1-monomers expressed in CHO-K1 cells. (a,b) Representative correlation curves and fits for the EGFR and the PMT sample, horizontal dashed lines are the level of cross-correlation, which is explained by crosstalk. (c) Histograms of the relative dimer concentration p_{AB} over the two cells. (d) Fluorescence Intensity image (red circles mark position of the measurements in a,b), (e) Maps of p_{AB} . Acquisition settings: 128×20 pixel, 2×2 -binning, $\tau_{\min} = 530 \mu\text{s}$.

and cross-correlation curves are comparable to those shown in section 8.6 and those published for a confocal FCCS study on the very same proteins in Ref. [76]. The cross-correlation functions in Fig. 9.7(a,b) are significantly different. The level of cross-correlation, that can be explained by crosstalk is indicated by horizontal dashed lines. A comparison of these lines with the cross-correlation function $\hat{g}_{gr}(\tau)$ in Fig. 9.7(b) shows that $\hat{g}_{gr}(\tau)$ can be explained by crosstalk.

Membrane-bound proteins pose additional difficulties in the data processing. The membranes tend to move back and forth by a few 100 nm during the measurements. These motions manifest themselves as decay components in the correlation curves on very long timescales ($\tau_{\text{decay}} = 1..10$ s), which are misinterpreted as a certain amount of cross-correlation. Therefore only those cells were selected for further evaluation, in which these membrane motions were negligible. Also a 2×2 binning was used, which increases the size of the MDE and therefore helps reducing the influence of membrane motion.

For the SPIM-FCCS evaluation, a model function with two components of 2-dimensional normal diffusion was combined with the SPIM-FCCS framework from section 5.4.2. A global fit was used to extract the model parameters (see section 7.1.4) from pixels on the cell membrane (see masks in Fig. 9.7d,e). In this fit, the concentrations were linked over all curves. Linking also the diffusion coefficients did not yield good fits. Here again the membrane motions seem to impair the fits. Therefore two separate

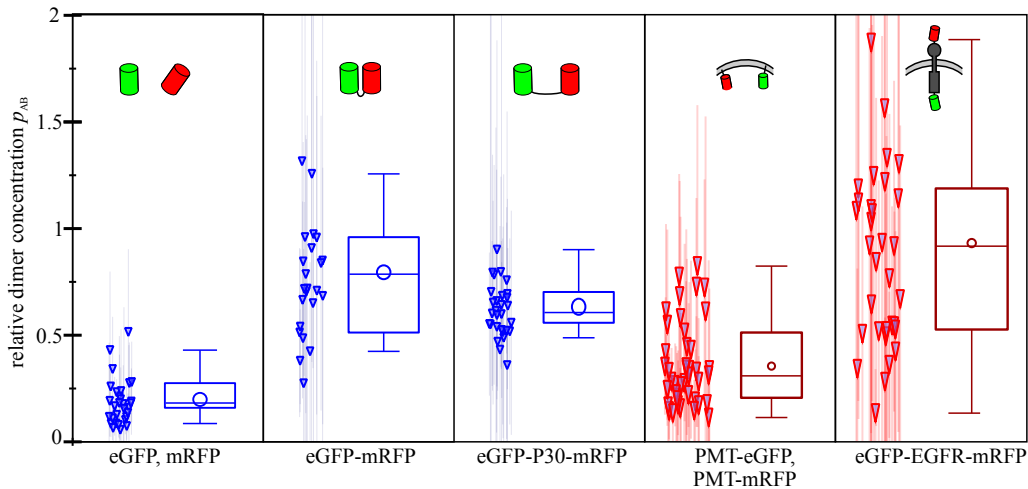


Figure 9.8. | Statistical summary of the relative dimer concentrations p_{AB} obtained for different proteins in cells, using SPIM-FCCS. For each protein, the averages and standard deviations of p_{AB} is shown as small triangles with error bars. The boxplot illustrates minimum and maximum (whiskers), the interquartile range (IQR), the median and the mean (circle) of the average values.

diffusion coefficients (fast & slow) were used per auto- or cross-correlation curve, i.e. altogether six coefficients for all three curves. With these settings, good fits were obtained, as shown with dashed lines in Fig. 9.7(a,b). Finally Fig. 9.7(c) shows a histogram of the average relative dimer concentrations p_{AB} obtained for both samples from different cells. The average of the two distributions are (0.2 ± 0.1) for the PMT-cells and (0.9 ± 0.7) for the EGFR-cells. Again the distributions are significantly different and the results are comparable to those found in confocal FCCS studies [76].

In summary these measurements have shown that SPIM-FCCS can be used to measure molecular interactions of proteins, that are localized in the cytoplasm, the nucleus and even the cellular membrane. The correlation curves that were obtained for a variety of positive and negative control samples are comparable to those published in confocal FCCS studies. Figure 9.8 summarizes the relative dimer concentrations p_{AB} measured in a larger set of cells for each of the mentioned samples (10 – 30 cells per sample). It shows the average and standard deviation of p_{AB} for each single cell as triangles together with the statistics of these averages as boxplots. Even though the variance between different cells is high, which is usually observed in in-vivo measurements, the dimer-samples are significantly different from the monomer samples. For the membrane-bound proteins, the separation is least significant and the errors are largest. As detailed above, this is mostly caused by membrane motion. These measurements also show that the constructs used here can serve as good control samples in cellular SPIM-FCCS studies.

9.6. Flow measurements with 2-focus SPIM-FCCS

In section 5.4.1, 2-focus SPIM-FCCS was introduced as a method that allows to determine directed flows. To test this, a simple experiment was set up. A sample bag at room temperature was mounted into the sample chamber, which was heated to 37°C . The temperature difference between the bag and the surrounding buffer induced a convective flow in the bag. The flow lasted for a few minutes, which was long enough to acquire a SPIM-FCCS measurement.

Figure 9.9 shows a single exposure of the sample with an exposure time $\Delta t_{\text{exp}} = 100$ ms. Three aggregates moved through the focus, which are clearly distinguishable as bright stripes. Their length is approximately $10\ \mu\text{m}$, which leads to a rough estimate of the flow speed of $\|\vec{v}\| = 100\ \mu\text{m/s}$.

Figure 9.10 shows the results of the 2-focus SPIM-FCCS measurement. In addition to the autocorrela-

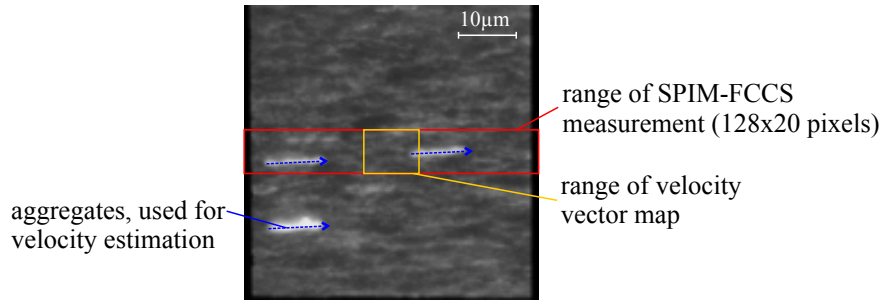


Figure 9.9. | A single exposure of $\Delta t_{\text{exp}} = 100$ ms of flowing microspheres. Three bright aggregates are marked with blue lines. The pixel range of the SPIM-FCCS measurement is shown as a red rectangle and the range of the flow vector map Fig. 9.10(b) is shown in yellow.

tion curve $\hat{g}(\tau; 0, 0)$, also the cross-correlation curves $\hat{g}(\tau; \delta_x, \delta_y)$ to the four directly adjacent pixels $(\delta_x, \delta_y) \in \{(-a, 0); (a, 0); (0, -a); (0, a)\}$ were calculated. These five curves are shown in Fig. 9.10(a). they have the typical shape, as discussed in section 5.4.1. The 2-focus SPIM-FCCS model in Eqs. (5.4.7, 5.4.8) was fitted to these five curves with a global fit. the diffusion coefficient D and the flow velocities v_x, v_y were linked over the curves.

Figure 9.10(b) shows the resulting flow vector map of (v_x, v_y) for each pixel in the magenta rectangle in Fig. 9.10. All vectors point in the same direction, as observed in the long exposed frame. Finally Fig. 9.10(c) shows histograms of the two flow-vector components v_x, v_y . Their averages are $\langle v_x \rangle = (73 \pm 3) \mu\text{m/s}$ and $\langle v_y \rangle = (6 \pm 5) \mu\text{m/s}$. This yields a length of the flow vector of $(73 \pm 3) \mu\text{m/s}$, which is comparable to the crude estimate of $100 \mu\text{m/s}$ from the aggregates. In order to obtain a better estimate of the flow speed, the image series, acquired for the SPIM-FCCS evaluation was also evaluated with

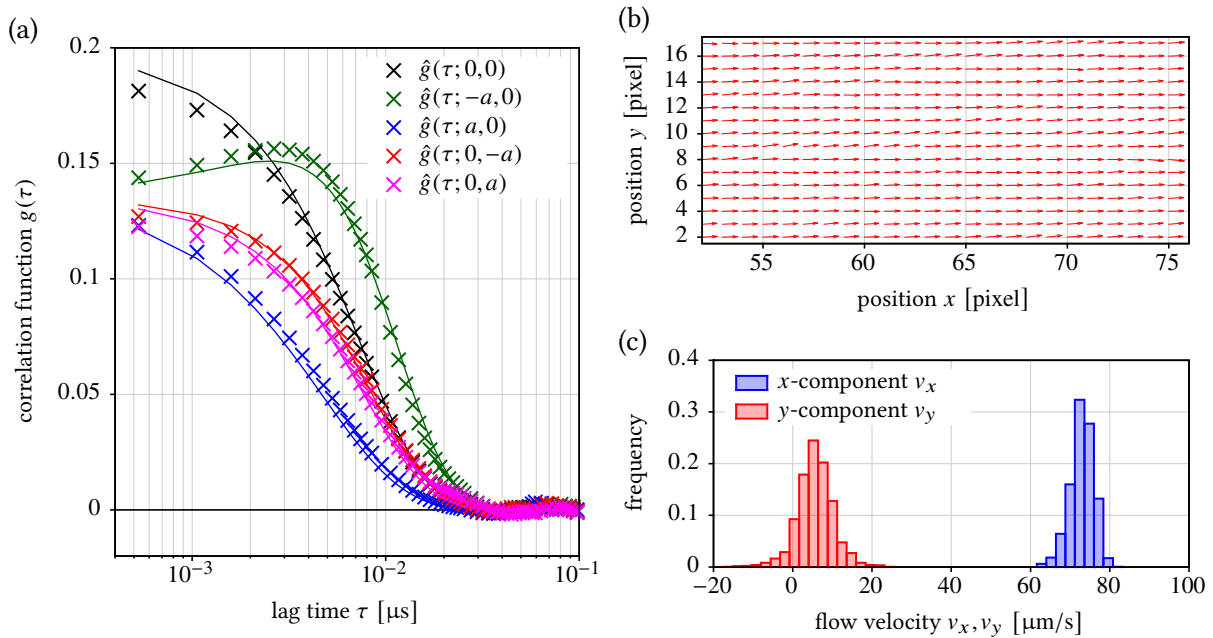


Figure 9.10. | Flow of fluorescent microspheres determined with 2-focus SPIM-FCCS. (a) Auto- and cross-correlation curves in a single pixel (points) together with the respective SPIM-FCCS fits (lines). (b) map of the flow velocity direction. (c) Histogram of the two flow velocity components v_x and v_y .

the algorithm of Lucas&Kanade [269], which calculates the planar optical flow in the image series. The implementation in the plugin “FlowJ” of the image processing package FIJI was used [270]. This algorithm yielded velocities of $v_x \approx 77 \mu\text{m/s}$ and $v_y \approx 5 \mu\text{m/s}$, which are very close to the results of the SPIM-FCCS measurement.

The diffusion coefficient, obtained from this measurement was $D_{20^\circ\text{C},\text{W}} = (5.1 \pm 0.3) \mu\text{m}^2/\text{s}$ (renormalized to 20°C , see appendix C.4). This is on the same order of magnitude as the value of $D_{20^\circ\text{C},\text{W}} = (3.3 \pm 0.3) \mu\text{m}^2/\text{s}$, which was obtained during the SPIM-FCCS calibration on the same day. For these particles the convective flow is significantly faster than normal diffusion. Therefore the contributions of the flow to the correlation curves outweigh the contributions of diffusion.

9.7. Summary of the chapter

2-color SPIM-FCCS: This chapter summarized several results that establish 2-color SPIM-FCCS as a method for spatially resolved measurements of molecular interactions. Alignment and calibration methods were developed, that allow to measure the same relative amounts of interaction, as with the established confocal FCCS technique. Also the dynamic range of both methods is comparable. All the same as SPIM-FCS, the cross-correlation analysis overestimates absolute concentrations. However a calibration is possible, because a linear relation was shown to exist between the results of confocal FCCS and SPIM-FCCS. Finally 2-color SPIM-FCCS was applied to fluorescent proteins, expressed in the cytoplasm, the nucleus and also the cellular membrane. In all three domains SPIM-FCCS yield qualitatively and quantitatively the same results as confocal FCCS. With these experiments it was also established, that standard cell culture techniques and common fluorescent proteins can be used for SPIM-FCCS analyses in live cells.

2-focus SPIM-FCCS: The last section of this chapter showed that the 2-focus SPIM-FCCS variant can be used to quantify directed molecular motion. For a simple test measurement, the results from SPIM-FCCS were successfully compared to an independent determination of the velocity field using the established algorithm of Lucas&Kanade [269].

Part IV.

***In vivo* applications**

10. Macromolecular dynamics in live cells

The cells for this chapter were prepared by Gabriele Müller (DKFZ, Heidelberg). Details on the cell culture protocols can be found in appendix A.2.

10.1. Protein mobility in live cells

As shown in sections 1.2 and 1.3, protein mobility in the cytoplasm and in the nucleus is of major importance to the functioning of living cells. Therefore it has been studied in several publications over the last years (see e.g. Refs. [16, 23, 25, 27, 33, 61, 99, 100, 102, 107, 271, 272]). In most studies, the diffusion of inert tracer molecules is observed, since this excludes binding and reaction effects, which could disturb the measurements. These tracers are either fluorescently labeled particles (e.g. dextrans or gold nanoparticles), that are microinjected into the cytoplasm of a cell, or autofluorescent proteins (e.g. eGFP oligomers and diverse fusion proteins), that are expressed by the cells themselves. Such measurements then form the basis for studies on molecules that are expected to interact with each other and with structures in the cell (see also chapters 11 and 12). In most of the mentioned publications, the measurements were performed using confocal fluorescence correlation spectroscopy (FCS) or fluorescence recovery after photo bleaching (FRAP), because these techniques allow to observe diffusion over a large range of timescales. Only in a few of these publications, spatially resolved measurements of protein diffusion are described [27, 33, 99, 100, 102, 107, 120]. Furthermore, simultaneous multi-spot measurements were reported in live cells only in Refs. [100, 102, 107, 120].

In this chapter, SPIM-FCS is applied to measure the diffusion of different inert tracer particles in live cells. In some sense, this extends section 8.6, in which the basic applicability of SPIM-FCS to autofluorescent proteins was demonstrated. First the diffusion of different tracers in HeLa cells is studied in section 10.2. Then measurements in different cell lines are compared in section 10.3. These measurements will form the basis for the interpretation of advanced applications of SPIM-FCS in chapters 11 and 12.

10.2. Mobility of different inert tracer molecules

10.2.1. Tracer molecules

This section summarizes measurements of diverse fluorescent molecules, that are believed not to interact, or only to interact weakly, with other particles and structures in the cell (see also Fig. 10.1):

- eGFP-1x monomer (molecular weight: 32.7 kDa, expressed from a plasmid encoding for eGFP-1x and mRFP1, plasmid description: [268])
- eGFP-mRFP1 dimer (molecular weight: 65.4 kDa, plasmid description: [268])
- eGFP-4x tetramer (molecular weight: 130.8 kDa, plasmid description: [276])
- eGFP-8x octamer (molecular weight: 261.6 kDa, plasmid was newly constructed by Gabriele Müller)

- β -gal-eGFP (molecular weight: 149 kDa per subunit, including the eGFP, plasmid description: [27, 277])

Figure 10.1(a-c) illustrates the crystal structures of the eGFP mono- and oligomers. The oligomers were constructed by inserting a short linker (5 amino acid for eGFP oligomers and 7 amino acids for eGFP-mRFP1) between two subsequent molecules [276]. The arrangements of the subunits, shown in the figures, is a hypothesis based on measurements of the oligomers in aqueous solutions, using FCS [33] and analytical ultra-centrifugation [278]. The geometric shape of the octamer eGFP-8x is not known. β -gal-eGFP is a fluorescently labeled variant of the bacterial protein β -galactosidase (β -gal), that hydrolyses β -galactosides into monosaccharids. All proteins, except β -gal-eGFP, were transiently transfected into HeLa cells. β -gal-eGFP was expressed from stably transfected rat prostate adenocarcinoma cells (AT-1s). Measurements were performed at room temperature (24 – 26 °C) in HBSS. The cells expressing eGFP-4x and eGFP-8x were co-transfected with an mRFP1-labeled histone H2A (see sections 1.1 and 12.1). This allows to assess the local chromatin density in the cells during the measurement, using the dual-view optics of the SPIM.

10.2.2. Measurement protocol

All measurements were performed with an Andor iXon X3 860. For each measurement, 100,000 frames with 64×20 pixels were acquired at a temporal resolution of $\tau_{\min} = \Delta t_{\text{frame}} = 530 \mu\text{s}$. The laser intensity in the center of the light sheet was in the range of 100 – 200 W/cm², which is a factor 5 – 10 below the laser intensities usually used in confocal FCS in living cells. Only those cells were selected for a measurement, that showed the typical shape of a healthy HeLa/AT-1 cell (no blebs, a recognizable nucleus, typical elongated shape, etc.), and that were not obviously in mitosis. The acquired data was corrected for photobleaching with the model in Eq. (7.1.5) (p. 109) with a polynomial degree of $N_f = 2 \dots 4$. Cells that had moved during the measurement, in which the bleach correction did not work, or that showed other uncommon artifacts (e.g. large internal rearrangements) were sorted out. This way $\sim 30\%$ of the cells were removed from the further evaluations. In the remaining datasets, the cells were masked by imposing a threshold on the fluorescence intensity. The exact value of the threshold was optimized for each cell. If necessary, the mask was corrected by hand to include also the nucleoli, or exclude regions with stripe artifacts (see section 8.5.1). The background intensity for the fits was then estimated as the average over all masked pixels for each cell (cf. section 8.6). Finally two SPIM-FCS models were fitted to the cell data: an anomalous diffusion model (Eq. (5.3.32), p. 63) and a 2-component normal diffusion model (Eq. (5.3.25) (p. 61) with Eq. (5.3.29), p. 62). These two models are usually used to describe FCS data from live cells. In a last step, the fit results were checked for proper convergence and sound values.

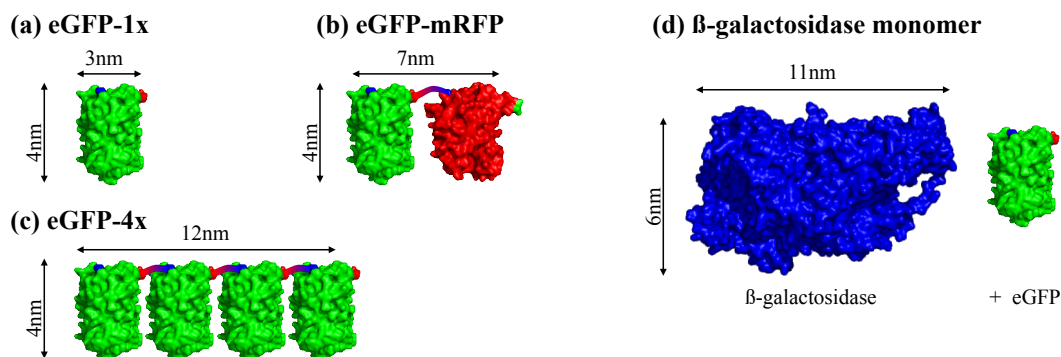


Figure 10.1. | Different inert probe particles for mobility measurements in live cells. (a) eGFP-1x, crystal structure taken from Ref. [273, 274]. (b) eGFP-mRFP1. (c) eGFP-4x. (d) β -gal, crystal structure taken from Ref. [275].

During this step, again $\sim 20\%$ of the cells were sorted out, since a motion of the cells often only become visible in the fit results.

10.2.3. Results

For each of the five different tracer proteins, Fig. 10.2 shows the fit results for one representative cell. Already the fluorescence images in the first row of Fig. 10.2 show, that the ratio between the fluorescence in the nucleus and the cytoplasm decreases with increasing size of the tracer. This is especially prominent in the fluorescence images for eGFP-4x and eGFP-8x. The exclusion from the nucleus is caused by the limited size of cargo that can freely diffuse through the nuclear pore complexes (NPCs). These bridge the nuclear membrane, which separates the nucleus from the cytoplasm, where the proteins are synthesized. Typically only proteins with a mass of less than ~ 60 kDa can freely pass these pores by diffusion. Larger proteins require a short polypeptide sequence, called nuclear localization sequence (NLS), that initiates an active transport of the protein into the nucleus [2]. The eGFP constructs, used here, lack this NLS. In addition, especially eGFP-4x and eGFP-8x are significantly larger than the given limit. Nevertheless, a relevant concentration of particles was still detected in the nuclei (see 1st and 3rd row in Fig. 10.2). This is in agreement with earlier publications using the same constructs [33, 276], and it supports the hypothesis, that the eGFP oligomers are built in a rod-like shape, and therefore still fit through the NPC, if oriented properly. Nevertheless the number of molecules transported into the nucleus is strongly

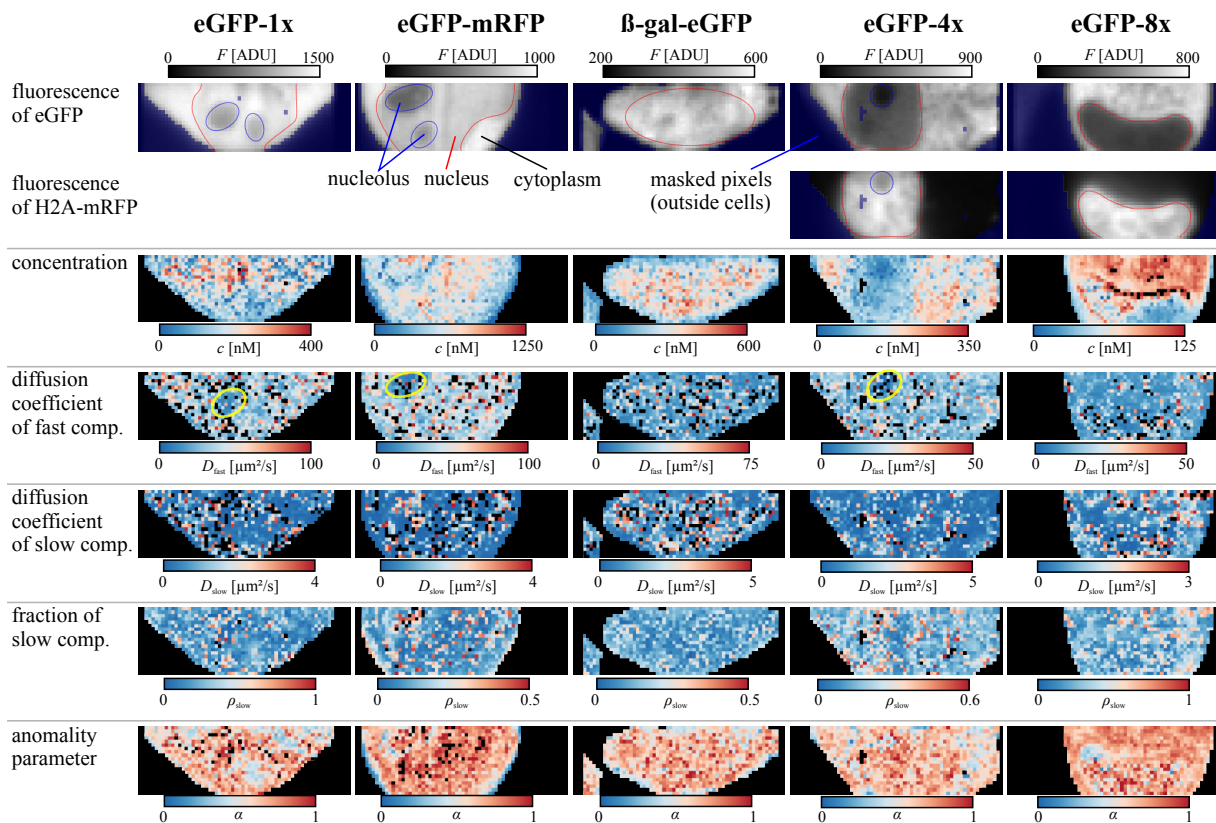


Figure 10.2. | Intensity images and fit parameter maps for one representative cell for each of the five inert tracer molecules. The proteins are sorted by increasing molecular mass. Thin red lines mark the nuclear envelope and thin blue lines the nucleoli. All images have a width of $25.6 \mu\text{m}$. The color scales of the parameter maps were optimized for each parameter separately, in order to make any large-scale structures in the data visible. A comparison of the absolute values of the parameters can be found in Fig. 10.5.

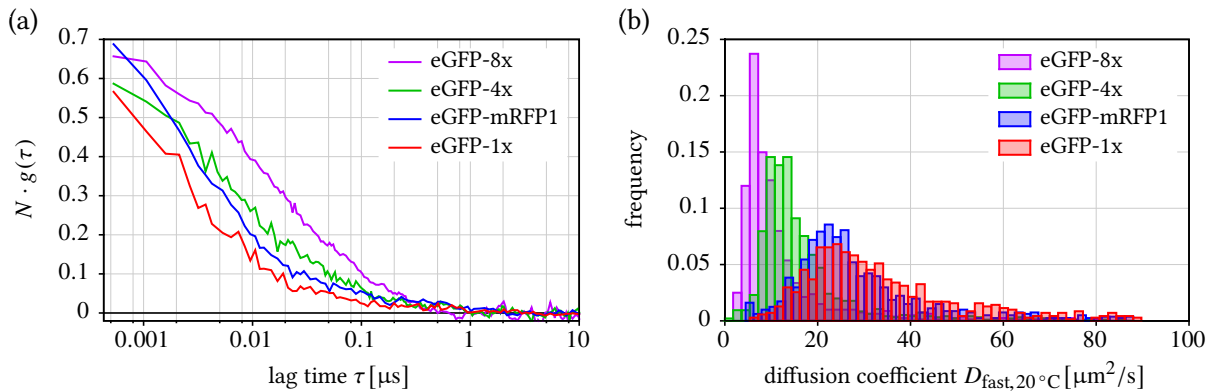


Figure 10.3. | (a) Representative autocorrelation curves from cells, expressing the different eGFP oligomers. (b) Histograms of the diffusion coefficient of the fast component, calculated using all pixels of the respective cell. Autocorrelation curves were averaged over 4 – 8 adjacent pixels. Diffusion coefficients have been recalibrated to $\vartheta = 20^\circ\text{C}$ (see appendix C.4). Acquisition parameters: $\tau_{\min} = 530 \mu\text{s}$, no binning, bleach correction with Eq. (7.1.5) (p. 109) with $N_f = 2 - 4$.

reduced for larger proteins.

As stated above, all autocorrelation curves were fitted with two different models. Figure 10.3 shows four representative autocorrelation curves and the histograms of the diffusion coefficient D_{fast} of the fast component in the normal diffusion fit. Figure 10.3(a) illustrates the increasing decay time with increasing tracer size. The histograms for D_{fast} in Fig. 10.3(b) quantify this effect. Comparable histograms were obtained for all parameters from the fits. In most cases, these histograms contain a certain number of outliers and often feature broad distributions of the parameters. Therefore, robust statistical measures, such as the median, were used for any further evaluation.

The two components of the normal diffusion model are usually interpreted in such a way, that the faster component of the two (D_{fast}) describes the random motion of the particles in a more or less viscous medium. The slow component (D_{slow}) summarizes the effects of crowding, of the complex cellular environment and of internal rearrangements of the cell. An increased impact of crowding is then usually reported as an increased fraction of the slow component ρ_{slow} . Figure 10.4 summarizes the fit results for these parameters from all measured cells. The figure shows the medians of the parameter distribution in each cell (red cross) and the average and the standard deviation over these medians (blue error bars). It can be seen again, that the fast diffusion coefficient D_{fast} decreases with increasing molecular mass (see Fig. 10.4a). The diffusion coefficient D_{slow} of the slow component does not show a clear dependence on the molecular mass (see Fig. 10.4b), but the fraction of this slow component ρ_{slow} is increased for heavier molecules (see Fig. 10.4c). This can be explained by a stronger hindrance of the molecular motion with increasing size of the molecules, which has e.g. been observed in simulations and confocal FCS measurements in Ref. [23].

The values obtained for the diffusion coefficients can be analyzed more closely. Figure 10.5 shows the diffusion coefficients D_{fast} for the different tracers as a function of the molecular mass (green squares). For comparison, the same curve is shown for diffusion coefficients $D_{\text{fast,W}}$ obtained with a confocal FCS measurement of an aqueous solution of the eGFP oligomers (blue stars). In general, both curves show the same dependence on the molecular mass, but the diffusion in the cell is significantly slower. Following the Einstein relation in Eq. (1.3.3) (p. 7), the ratio between the two diffusion coefficients in the cell and in water ($D_{\text{fast,cell}}$ and $D_{\text{fast,W}}$) directly equals the ratio between the viscosities of water $\eta_{\text{visc,W}}$

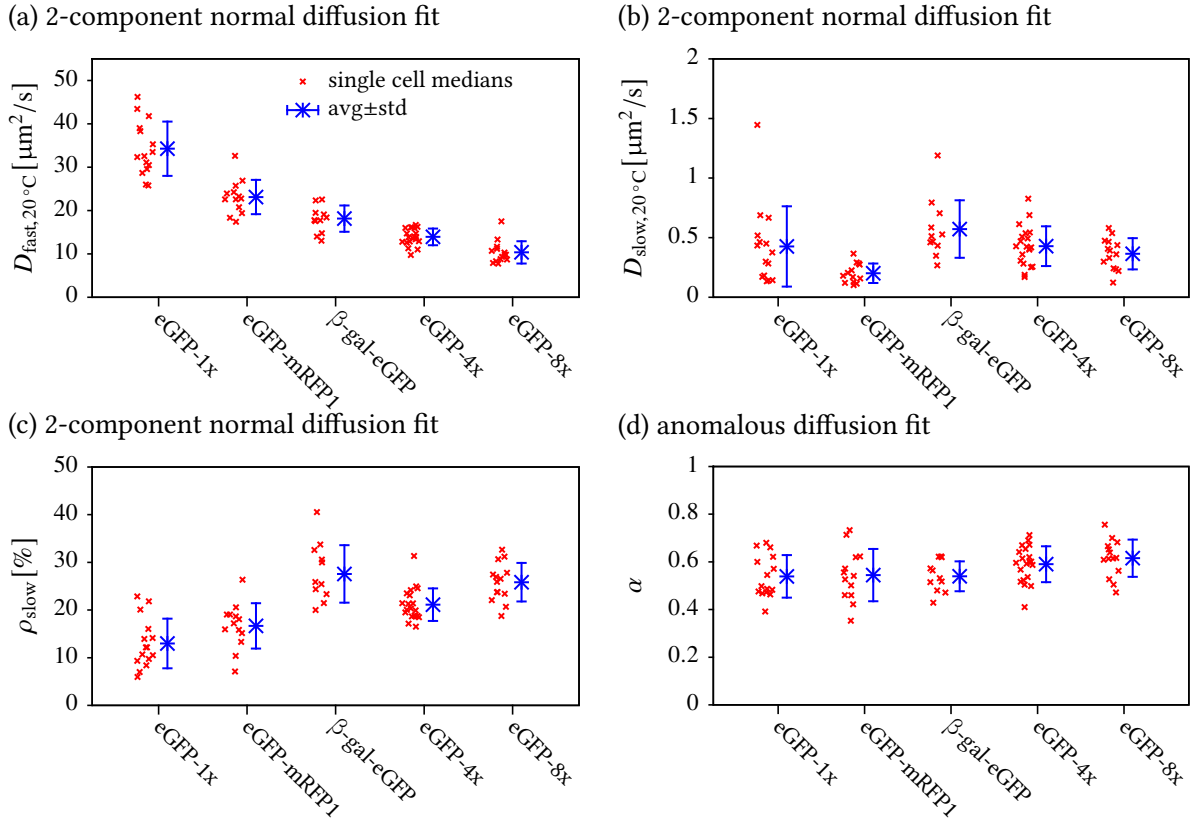


Figure 10.4. | Summary of fit results for different inert tracer molecules in HeLa cells. (a-c) Fast and slow diffusion coefficients ($D_{fast,20^\circ C}$ and $D_{slow,20^\circ C}$) and fraction ρ_{slow} of slow component from a 2-component normal diffusion fit. The diffusion coefficients were recalibrated to $\vartheta = 20^\circ C$ (see appendix C.4). (d) Anomaly parameter α from an anomalous diffusion fit. Red crosses are the medians of the parameter distribution in each cell and blue error bars show average and standard deviation over these medians.

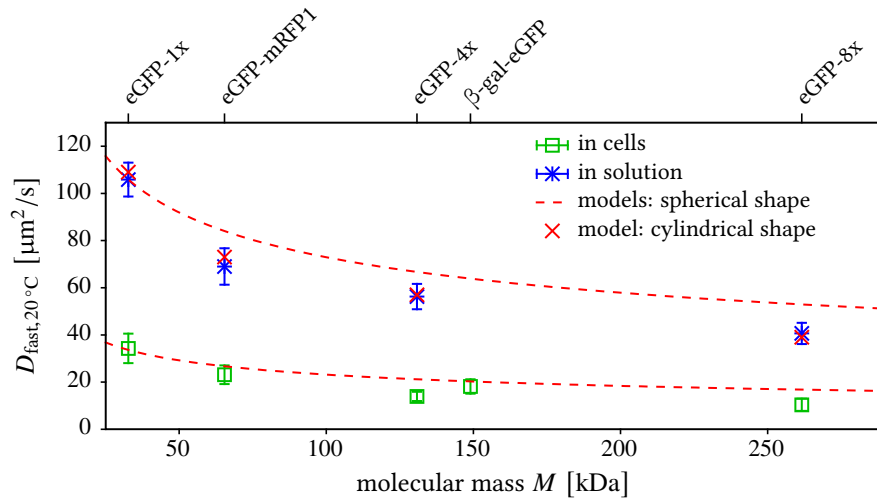


Figure 10.5. | Diffusion coefficient $D_{fast,20^\circ C}$ of the fast component, as a function of the molecular mass M for inert tracer particles in cells (green) and in water (blue). Dashed lines show the model for $D_{fast,20^\circ C}$ from Eq. 10.2.2. Red crosses are theoretical values, calculated with Eq. (C.5.5) (p. 225) for a cylindrical molecule of diameter $d_{cyl} = 4$ nm and different lengths $l_{cyl} \in \{7, 12, 24\}$ nm for the oligomers and $d_{cyl} = 3$ nm, $l_{cyl} = 4$ nm for the monomer.

and of the cytoplasm $\eta_{\text{visc,cell}}$:

$$\eta_{\text{rel}} := \frac{\eta_{\text{visc,cell}}}{\eta_{\text{visc,W}}} = \frac{D_{\text{fast,W}}}{D_{\text{fast,cell}}}. \quad (10.2.1)$$

From the eGFP mono- and dimer measurements, a value of $\eta_{\text{rel}} = (3.2 \pm 0.6)$ was obtained, and for the tetramers and octamers $\eta_{\text{rel}} = (4 \pm 1)$. These values are in agreement with several other published measurements [16–19]. The increase in viscosity with increasing size of the molecule can again be explained by the stronger impact of crowding on larger molecules [16, 23].

Figure 10.5 also shows theoretical estimates of the dependence of D_{fast} on the molecular mass M (dashed lines). For these curves, spherical particles with a constant mass density were assumed, for which the hydrodynamic radius scales like $R_{\text{h}} \propto \sqrt[3]{M}$. Then the Einstein relation Eq. (1.3.3) (p. 7) predicts the scaling of the diffusion coefficients:

$$D_{\text{fast}}(M) = D_{\text{eGFP-1x}} \cdot \sqrt[3]{\frac{M_{\text{eGFP-1x}}}{M}}. \quad (10.2.2)$$

Here $D_{\text{eGFP-1x}}$ and $M_{\text{eGFP-1x}}$ are the measured diffusion coefficient and the molecular mass of the monomer eGFP-1x. As shown in Fig. 10.5 the function Eq. (10.2.2) does not successfully predict the diffusion coefficients of the larger particles. The graph also contains theoretical predictions (red symbols) that were calculated for cylindrical particles (see Eq. (C.5.5) in appendix C.5) with a diameter $d_{\text{cyl}} = 4$ nm and different lengths $l_{\text{cyl}} \in \{7, 12, 24\}$ nm for the oligomers, as well as $d_{\text{cyl}} = 3$ nm and $l_{\text{cyl}} = 4$ nm for the monomer. These models were motivated by an approximately cylindrical shape of the oligomers (Fig. 10.1). The predicted values coincide better with the measured data, than those calculated with the spherical model in Eq. (10.2.2). These results support the shapes, assumed for the tracer particles, shown in Fig. 10.1.

The fit results also allow to quantify the anomaly of the molecular motion. This is possible by directly measuring the anomaly parameter α with an anomalous diffusion fitting model (see Fig. 10.4d). For all tracers, a value of $\alpha = 0.54 - 0.6$ was obtained, which is in general agreement with the values obtained in several other studies (see Ref. [25] for a good overview). For comparison, SPIM-FCS measurements of aqueous solutions of eGFP-1x and a dsDNA (length 170 bp) were also evaluated using the anomalous diffusion model. These measurements should yield $\alpha = 1$, but values of $\alpha = 0.85 - 0.9$ were obtained. Confocal FCS measurements on the same samples typically yield values of $\alpha = 0.9 - 0.95$. These values of $\alpha \leq 0.9$ are possibly due to the limited temporal resolution of the camera, which leads to a prevalence of any artifacts in the tail of the autocorrelation function (e.g. aggregates and dirt particles in the sample). Also the inaccuracy of the model for the MDE could play a role (see section 8.3).

As shown by the representative cells in Fig. 10.2, no interpretable large-scale structures could be observed in the maps of most of the different fit parameters. However, a closer look at the 4th row of Fig. 10.2 reveals a decrease of D_{fast} inside the nucleoli of some cells (thin yellow circle in Fig. 10.2). For the cell expressing eGFP-2x (2nd column), the relative decrease is approximately 50%. This corresponds to a further increase of the viscosity, which is explained by the high density of proteins in the nucleoli, that severely hinder the diffusion of the tracers. In order to test whether the density of chromatin influences the tracer diffusion, mRFP1-labeled histones (H2A-mRFP1) were co-expressed together with eGFP-4x and eGFP-8x. The intensity in the red color channel can then be interpreted as a measure of the chromatin density (see also section 12.1). However, no correlation between this parameter and any of the mobility parameters could be found in the measurements. This is in agreement with the earlier experimental study by Dross et al. and simulations by [33, 279]. In Ref. [279] the authors estimate that particles with a hydrodynamic radius R_{h} of less than 20 nm are not influenced by the chromatin in interface nuclei.

10.3. Diffusion in different cell lines

Most of the measurements in the last section were performed in HeLa cells. In order to evaluate the influence of the cell type, the experiments with transiently expressed eGFP-4x were repeated in different cell lines

- baby hamster kidney cells (BHKs)
- Chinese hamster ovary cells (CHO-K1s)
- transformed African green monkey kidney fibroblast cells (COS-7s)
- human embryonic kidney cells (HEK-293s)
- human breast carcinoma cells (MDA-MB231s)
- human cervical carcinoma cells (HeLas)

For the HeLa cells, the data from the last section was pooled together with additional measurements, hence their fit results show an increased standard deviation. The data was evaluated as described in section 10.2. Figure 10.6 summarizes the results of the measurements. As in section 10.2, the plots show a statistical evaluation of selected fit parameters. The medians of the parameter distributions in each single cell are shown as red crosses and the blue error bars give the average and standard deviation over these medians. Generally, the results are comparable to those in Fig. 10.4 and most of the parameters

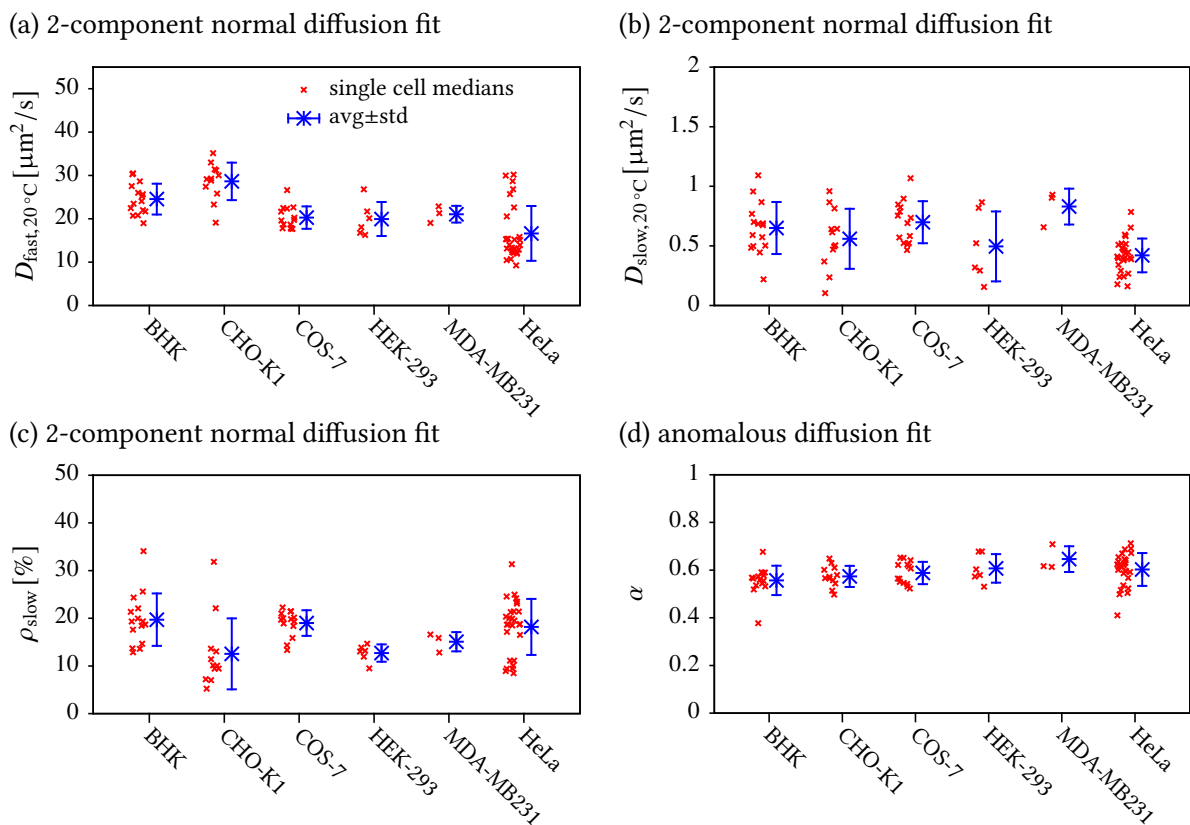


Figure 10.6. | Summary of fit results for eGFP-4x, expressed in different cell lines. (a-c) Fast and slow diffusion coefficients $D_{fast,20^\circ C}$ and $D_{slow,20^\circ C}$ and fraction of slow component ρ_{slow} from a 2-component normal diffusion fit. The diffusion coefficients were recalibrated to $\vartheta = 20^\circ C$ (see appendix C.4). (d) Anomaly parameter α from an anomalous diffusion fit. Red crosses are the medians of the parameter distribution in each cell and blue error bars show average and standard deviation over these medians. Note that more measurements on HeLa cells were pooled together here, than for Fig. 10.4.

cell line	η_{rel}
BHK	(2.2 ± 0.4)
CHO-K1	(1.9 ± 0.3)
COS-7	(2.7 ± 0.6)
HEK-293	(2.6 ± 0.4)
MDA-MB231	(2.5 ± 0.3)
HeLa	(3.2 ± 1.3)

Table 10.1. | Relative viscosities of the cellular medium in different cells, measured with transiently expressed eGFP-4x.

agree within their errors. From the diffusion coefficients of the fast component, again the relative viscosity η_{rel} could be calculated. The values obtained from that calculation are listed in Tab. 10.1. All values for η_{rel} were in the range of $\eta_{\text{rel}} = 1.9 - 3.2$.

10.4. Conclusions

In this section, several measurements were described, in which the mobility parameters of inert tracer proteins of different sizes were measured in living cells. The results generally agree with other measurements, published over the last 15 years (see e.g. [16, 23, 25, 27, 33, 61, 99, 100, 102, 107, 271, 272]). Those measurements were in most cases obtained in few consecutively measured spots (confocal FCS) or averaged over larger regions (FRAP). Together with the work of Wohland et al. [117] and by Capoulade et al. [120], the experiments in this section demonstrate for the first time a true imaging approach to FCS measurements of cytoplasmic proteins of different sizes. The fact, that several published results could be reproduced for normal and anomalous diffusion confirms the applicability of SPIM-FCS to these biological systems. The measurements in this section also show that the different artifacts and properties of SPIM-FCS (see chapter 8) are no obstacle to the applicability of this technique.

11. Keratin dynamics

The measurements in this chapter were performed in cooperation with Reinhard Windoffer (RWTH Aachen) and Norbert Mücke (DKFZ, Heidelberg).

11.1. The keratin intermediate filament system

As briefly mentioned in section 1.1, the shape of a cell is maintained by the cellular cytoskeleton. The latter consists of three different types of filament subsystems (see Fig. 11.1a-c), which are each built up from distinct protein monomers. These subsystems differ largely in their properties and in their function in the cell [2, 280]:

1. Actin filaments (also called microfilaments) are two-stranded helical polymers. A single fiber is 5 – 9 nm in diameter and very flexible. Actin filaments form a dense network below the cellular membrane and are especially enriched near cell protrusions. Since they interact with myosin motor proteins, actin filaments are also involved in active cellular transport.
2. Microtubules are hollow protein cylinders with a diameter of around 25 nm. These cylinders are very rigid and can span the whole diameter of a cell. They are involved in the segregation of the chromatids during mitosis (see Fig. 1.2, p. 5), and in active cellular transport via the motor protein families kinesin and dynein.
3. Finally, intermediate filaments (IFs) are rope-like structures with a diameter of around 10 nm [281]. They are constituted of a large variety of different protein monomers. The keratin family is the largest sub-group within these. IFs span the whole cytoplasm and give a certain mechanical

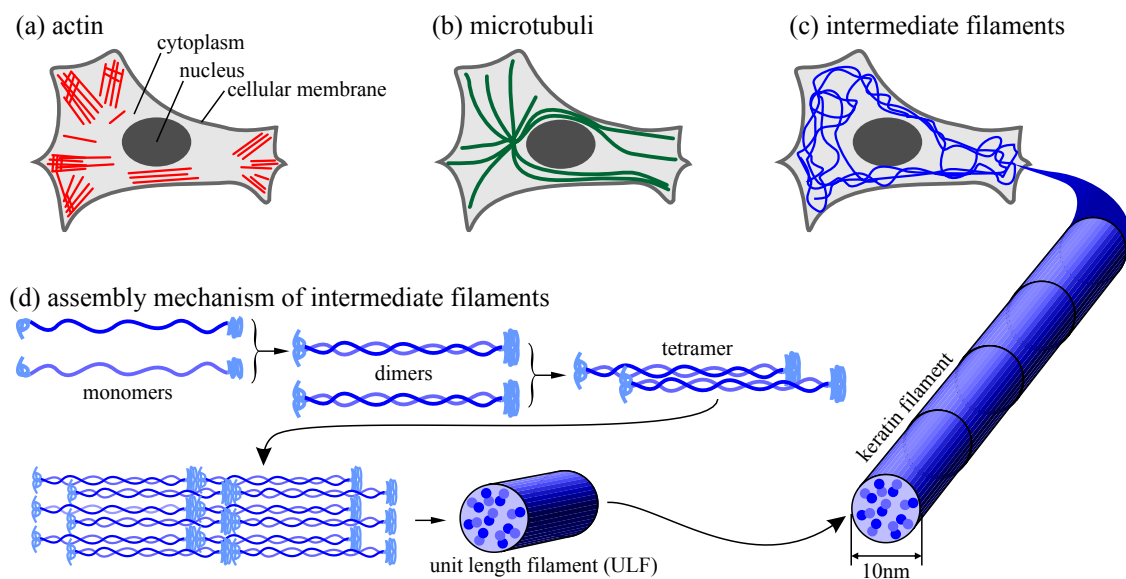


Figure 11.1. | (a-c) Filament networks in a mammalian cell. (d) Intermediate filament assembly. (a-c) Adapted from Ref. [2]. (d) Based on Ref. [280].

rigidity to the single cells. In epithelial tissue, the IF network can also span the whole space between two cell-cell junctions, thereby increasing the mechanical strength of the whole tissue. The lamins are a special group of IFs that form a meshwork on the inside of the nuclear membrane. This meshwork stabilizes the nucleus and interacts in many ways with nuclear proteins.

In this chapter SPIM-FCS is applied to the keratin intermediate filaments. The keratin network gives mechanical strength to many epithelial cells, such as keratinocytes. Nevertheless the network remains flexible and is constantly remodeled in order to adapt to changes in the cell and its environment. A general assembly mechanism, that explains how cytoplasmic IFs are formed from the protein monomers is depicted in Fig. 11.1(d) [280]. Data published by Lichtenstern et al. suggests that this mechanism also describes the assembly of keratin filaments [281]. First, two monomers form a dimer with a coiled-coil structure. These dimers can then laterally assemble into tetramers. Between 8 and 10 of these tetramers can further assemble to form so-called unit length filaments (ULFs), which have a length of $l_{ULF} = 43$ nm and a diameter of approximately 10 nm [281, 282]. These ULFs finally assemble into the longer filaments by end-to-end annealing [283, 284].

So far the assembly of a filament was described. In order to remodel and adapt the whole network, a higher-level process is required. A model for this remodeling process is depicted in Fig. 11.2 [285, 286]. Soluble precursors of the filaments diffuse through the cytoplasm. The nature of these precursors is unknown but candidates are dimers, tetramers, complete ULFs or even longer filaments. Near the periphery of the cell, the precursors start to assemble into small filamentous particles. These particles elongate and grow into larger and larger meshworks and bundles. During this process, they are actively transported towards the nucleus of the cell. This active transport has been observed with time-lapse fluorescence microscopy [55, 287]. Its average velocity was found to be in the range of 100 – 500 nm/min. When the large filament bundles arrive at the nucleus, they are either disassembled, or they are integrated into fixed structures, such as the perinuclear cage, which surrounds the nucleus. The fragments of the disassembled filaments spread through the cytoplasm by diffusive transport. Thereby they can return to the periphery of the cell, where the remodeling cycle begins again. This assembly/disassembly cycle allows the cell to keep the keratin filament network in a dynamic state. The disassembly of unused filaments helps the cell to maintain a pool of filament precursors in the cytoplasm. Therefore only a minor fraction of the proteins, that are needed to form new filaments, have to be newly synthesized by the cell.

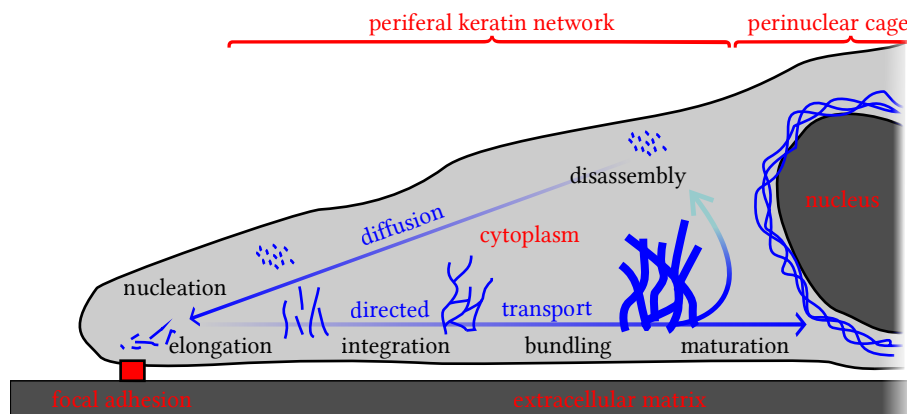


Figure 11.2. | The keratin remodeling cycle. Adapted from Fig. 1 in Ref. [285].

11.2. The free pool of keratin precursors

The nature of the free precursor molecules, that were mentioned in section 11.1, is not known. In Ref. [287], fluorescence recovery after photo bleaching (FRAP) was used to estimate a diffusion coefficient of $D_{\text{keratin,FRAP}} \approx 1 \mu\text{m}^2/\text{s}$ for the filament precursors in the cytoplasm. In these experiments one half of the cell was bleached, and subsequently the fluorescence recovery into regions without larger filaments was assessed. The fact, that the diffusion coefficient $D_{\text{keratin,FRAP}}$ is small in comparison to other diffusion coefficients measured in cells for this thesis, suggests that the free pool consists of larger particles.

Figure 11.3 shows an estimate of the expected diffusion coefficients of keratin filaments of different lengths and a diameter of $\sim 10 \text{ nm}$. On the upper border of the plot, the number of ULFs in such a filament is noted. The persistence length l_p of the filaments is also displayed (for keratin: $l_p \approx 300 \text{ nm}$ [281]). It corresponds to the length scale on which the filament behaves like a stiff rod, i.e. the length scale, on which a cylindrical shape can be assumed. The viscosity of the cytoplasm $\eta_{\text{visc, cytosol}}$ was assumed to be around 3-fold larger than that of water (see sections 10.2 and 10.3). With these preconditions an expected range of diffusion coefficients $D = 0.8 - 6 \mu\text{m}^2/\text{s}$ can be estimated from Fig. 11.3. This corresponds to filament lengths of $1 - 23 \cdot l_{\text{ULF}}$. For keratin monomers, dimers or tetramers, larger diffusion coefficients in the range of $7 - 14 \mu\text{m}^2/\text{s}$ (at $\vartheta = 20^\circ\text{C}$) are expected. From these estimations, the diffusion coefficient from the FRAP measurements of $\sim 1 \mu\text{m}^2/\text{s}$ would correspond to filaments, which are made up of $10 - 20$ ULFs. However, FRAP does not directly observe single particles, but evaluates how fast fluorescence is recovered in a larger region (see section 1.4.2). Therefore it cannot easily distinguish between several species of particles that are characterized by different diffusion coefficients. In such a case FRAP will usually report an averaged diffusion coefficient.

In this chapter, FCS measurements on the dynamics of keratin in a living cell are reported. In contrast to FRAP, FCS observes only a small volume and can resolve different species. For such FCS measurements, it is important to position the observation volume between large filament bundles. A large fraction of the FCS measurements will have to be sorted out due to filament bundles that move through the focus. Therefore confocal FCS measurements on the free pool of keratin precursors are cumbersome. SPIM-FCS was chosen as a method to circumvent these problems. It allows to record hundreds of positions in a cell simultaneously. This does not prevent some pixels from being affected by large filaments, but even if these are sorted out, enough points with evaluable measurements remain in every cell.

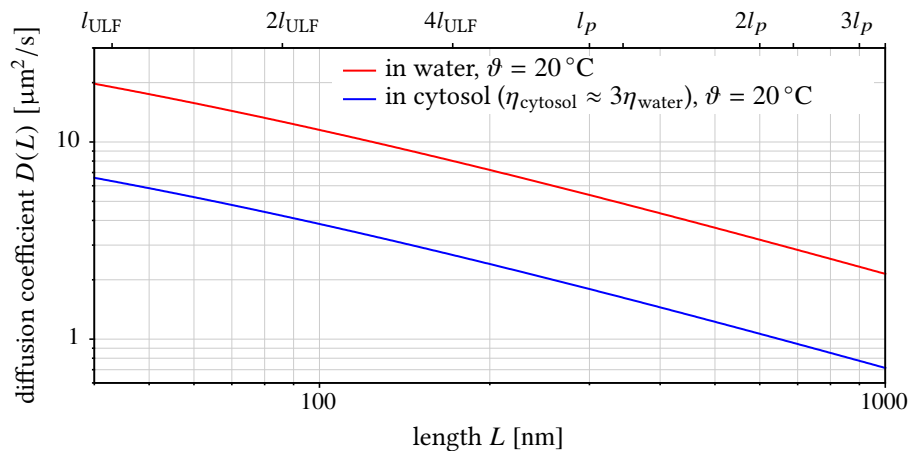


Figure 11.3. | Diffusion coefficient D of a cylinder of diameter $d = 10 \text{ nm}$ and length L . The diffusion coefficient is given at $\vartheta = 20^\circ\text{C}$ for water and for cytosol with viscosity $\eta_{\text{visc, cytosol}} \approx 3 \cdot \eta_{\text{visc, water}}$. The diffusion coefficient of the cylinder was estimated, as described in appendix C.5.

11.3. SPIM-FCS measurements of the free pool of keratin precursors

Two types of cells were provided by Reinhard Windoffer for the measurements (see also Fig. 11.4):

1. Adrenal cortex carcinoma-derived SW13 cell (SK8/18), stably transfected with Keratin8-CFP and Keratin18-YFP [288]
2. Humane keratinocyte cell (HaCat B 10), stably transfected with keratin5-YFP [289]

Both were stably expressing a protein from the keratin family, labeled with yellow fluorescent protein (YFP). The SPIM presented in section 6 is not optimized for this fluorescent protein (see section 2.5 for its spectra), but detection with a long-pass filter with transmission above 500 nm, together with excitation at 491 nm worked reasonably well. The cells were measured in a heated sample chamber at $\vartheta = (37 \pm 0.2)^\circ\text{C}$. For each cell one or more SPIM-FCS measurements were performed with the Andor iXon X3 860 EMCCD camera set to an EM-gain setting of 100 – 300. Each measurement comprised 128×32 pixels at a temporal resolution of $\tau_{\min} = 700 \mu\text{s}$. For bleach correction, the model in Eq. (7.1.5) (p. 109) with a degree of the polynomial of $N_f = 4$ was used. For the measurements, slices of the cell with a low density of large filament bundles were selected, in order to increase the chance of finding pixels that lie in between filaments.

Figure 11.5 shows an representative measurement on an SK8/18 cell. The thick filament bundles can be seen in Fig. 11.5(a), especially around the nucleus. Still enough pixels were found that were located between the filament bundles in this slice of the cell. Figure 11.5(b,d) shows autocorrelation curves and fluorescence intensity time traces from one of these bundle-free pixels. For a further statistical analysis, such pixels were selected by an automatic scheme, which is explained below. Figure 11.5(c,e) shows autocorrelation and fluorescence intensity curves for a pixel near the nucleus, which has to be sorted out. It is positioned directly on a large filament bundle. Here the motion of the filaments leads to a large-scale variation of the fluorescence intensity $F_g(t)$ with time. The long-term decay, caused by this intensity variation in the autocorrelation curve, outweighs any other contributions.

The autocorrelation function in Fig. 11.5(b) was best described by a 2-component normal diffusion model (Eq. (5.3.29), together with Eq. (5.3.24), see pages 60-62). It yielded a fast component with a diffusion coefficient of $D_{\text{fast},20^\circ\text{C}} = 5.7 \mu\text{m}^2/\text{s}$, a slow component with $D_{\text{slow},20^\circ\text{C}} = 0.06 \mu\text{m}^2/\text{s}$ and a fraction of the slow component of $\rho_{\text{slow}} = 53\%$. The meaning of the parameter ρ_{slow} in this context is discussed in more detail in section 11.4. The fast component can be interpreted as representing the pool of free precursors. In this interpretation, the slow component summarize two effects. Firstly, it accounts for the complex cellular medium and motions of the whole cell. Secondly, it may be caused by remaining motions of larger filaments through the focus or in its vicinity.

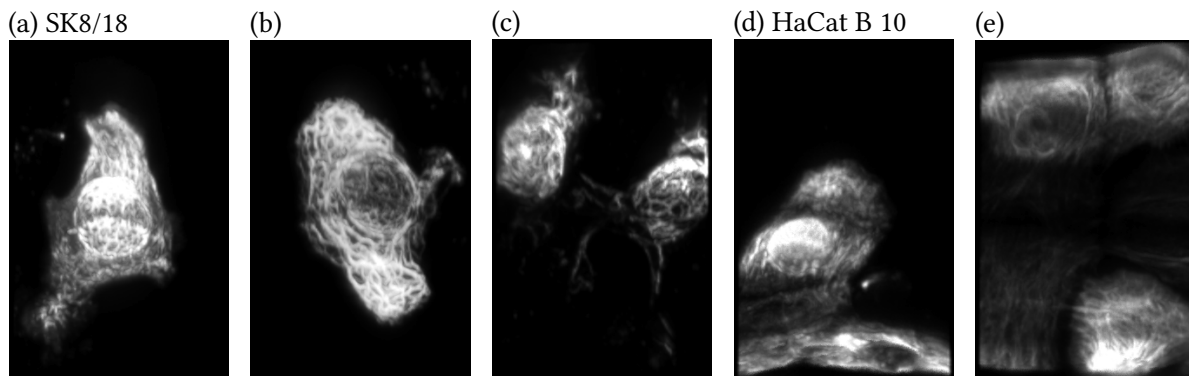


Figure 11.4. | Representative fluorescence images of (a-c) SK8/18 and (d-e) HaCat B 10 cells, expressing keratin. Image width: $51.2 \mu\text{m}$. Images are maximum intensity projections of z -stacks acquired with the SPIM, created with the plugin VOLUMEVIEWER of FIJI.

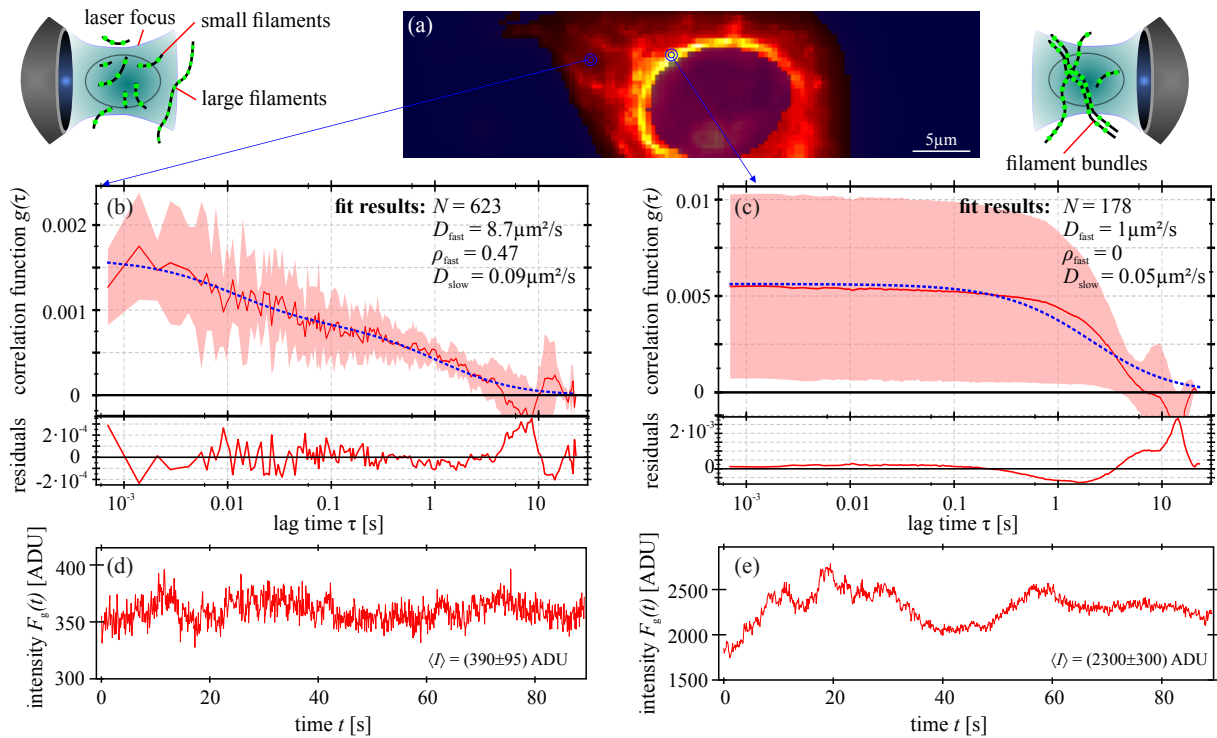


Figure 11.5. | Representative results from a SPIM-FCS measurement of YFP-labeled keratin in a SK8/18 cell. (a) Fluorescence image of the observed cell. (b,d) Autocorrelation curves, residuals and fluorescence intensity time trace of a pixel without contributions from large filaments. (c,e) the same for a pixel containing larger filaments.

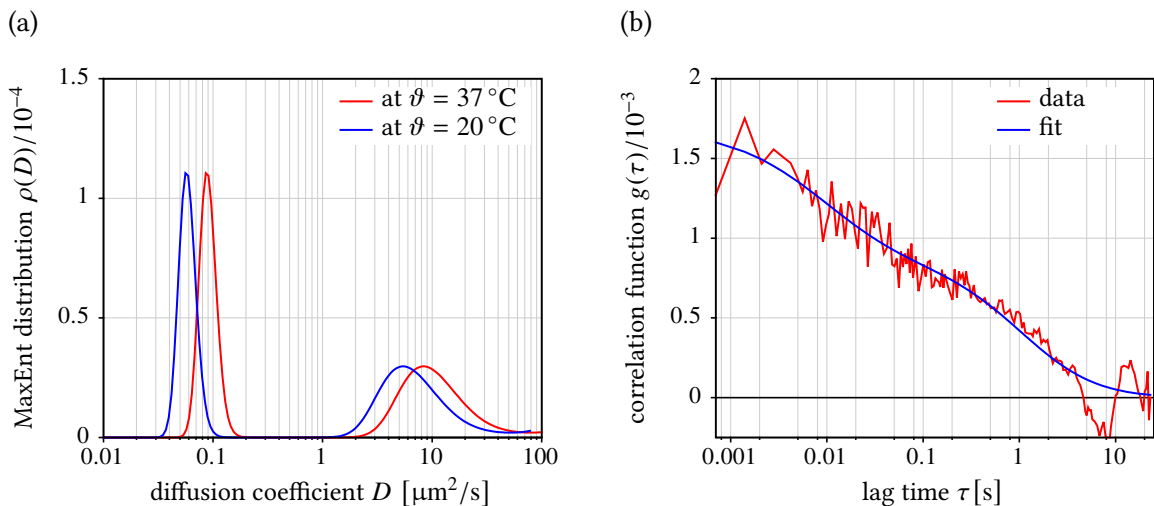


Figure 11.6. | Maximum Entropy fit to the same pixel as in Fig. 11.5(b,d). (a) MaxEnt distribution of diffusion coefficients at $\vartheta = 37^\circ\text{C}$ and recalibrated to $\vartheta = 20^\circ\text{C}$ (see appendix C.4). (b) Autocorrelation curve (red) and MaxEnt fit result (blue).

The choice of a fit model with 2-component normal diffusion in the data evaluation was checked by a maximum entropy data evaluation (MaxEnt) analysis (see section 7.1.5). It calculates a distribution of particles with different diffusion coefficients, that explain the shape of a given autocorrelation curve. Figure 11.6 shows its result for the very same pixel as in Fig. 11.5b. The MaxEnt distribution in Fig. 11.6(a) clearly shows two distinct peaks at approximately the same diffusion coefficients, as found by the 2-component fit. If the FCS autocorrelation curve would best be described by a single anomalous component, the MaxEnt distribution would contain a single, but broadened peak. Therefore the 2-component model was chosen for all remaining evaluations in this chapter.

For a final statistical analysis, a SPIM-FCS fit was performed for every pixel in all cells. Figure 11.7 shows the fit results for the same cell as in Figs. 11.5 and 11.6 as histograms and parameter maps. The histograms of the diffusion coefficient D_{fast} and the fraction ρ_{fast} of the fast diffusing component show sharp peaks at the edges of the parameter ranges (Note the discontinued axes in Fig. 11.7b,c) and a broad distribution in between. From the maps of the parameters, it can be seen that the peaks in the edges correspond to pixels, that contain large filaments. They are colored dark blue or dark red in the parameter maps. The other pixels are mostly positioned towards the periphery of the cell, where the density of filament bundles is lower. This feature was used to design an automatic selection procedure, which picks only those pixels, that meet all of the following conditions:

1. The diffusion coefficient of the fast component should be in a reasonable range, which excludes the edge peaks in its histograms: $D_{\text{fast}} \in [1.1 \dots 40] \mu\text{m}^2/\text{s}$ (at $\vartheta = 37^\circ\text{C}$)
2. The edge peaks were also excluded from the fraction of the fast diffusing component: $\rho_{\text{fast}} \in [0.1 \dots 0.9]$
3. The measured fluorescence intensity $\langle F_g \rangle$ in each pixel has to be in the lower third of the intensity distribution. This effectively excludes many of the bright filament bundles.
4. The molecular brightness $\langle F_g \rangle / N$ has to be in the main peak of its distribution (N is the particle number obtained from the measurement). The ranges for $\langle F_g \rangle / N$ were selected for each cell by hand, based on the parameter histogram.

This procedure could successfully select only pixels with autocorrelation curves as shown in Fig. 11.5(b).

Figure 11.8 shows the summary statistics (IQR, median, mean) of the filtered distributions of the diffusion coefficient $D_{\text{fast}, 20^\circ\text{C}}$ for each cell. The mean for most of the cells is significantly higher than the median. This implies that the distributions are skewed, which could already be seen in the raw distributions in Fig. 11.7(b). Comparable analyses were performed for several parameters in the measurements. Finally, a summarizing statistics was computed from the medians of the distributions of each cell. The median was chosen, because it is robust to outliers and a good measure of peak position of a skewed distribution. Table 11.1 shows the results. For all mobility parameters, approximately equal values were obtained in both cell types. They agree with the values shown above for a single SK8/18 cell.

parameter	from SK8/18 cells	from HaCat B 10 cells
diffusion $\langle D_{\text{fast}, 20^\circ\text{C}} \rangle$ coefficient of fast species	$(6.1 \pm 1.0) \mu\text{m}^2/\text{s}$	$(6.9 \pm 1.8) \mu\text{m}^2/\text{s}$
fraction $\langle \rho_{\text{fast}} \rangle$ of fast species	$(49 \pm 8)\%$	$(46 \pm 7)\%$
diffusion $\langle D_{\text{slow}, 20^\circ\text{C}} \rangle$ coefficient of slow species	$(0.10 \pm 0.03) \mu\text{m}^2/\text{s}$	$(0.10 \pm 0.03) \mu\text{m}^2/\text{s}$
number of cells	12	9

Table 11.1. | Summary of the SPIM-FCS fit results for SK8/18 and HaCat B 10 cells. The values in the table are average and standard deviation over the medians of the distributions in each cell. All diffusion coefficients were recalibrated to $\vartheta = 20^\circ\text{C}$ (see appendix C.4).

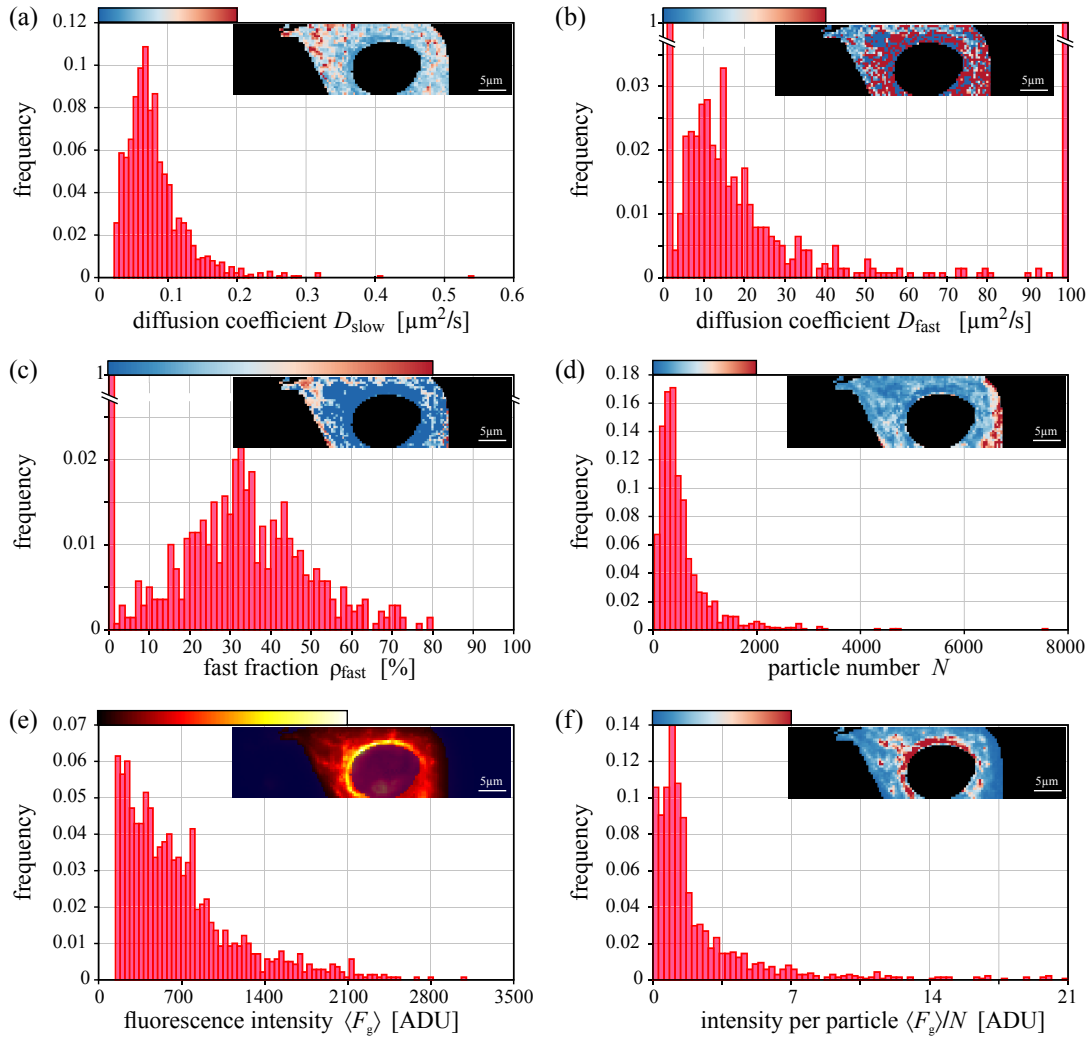


Figure 11.7. | SPIM-FCS fit result histograms from a representative SK8/18 cell, expressing YFP-labeled keratins. In each histogram, the inset show maps of the histogrammed parameter. The according colorscales are shown above the histograms. All diffusion coefficients are given at $\vartheta = 37^\circ\text{C}$.

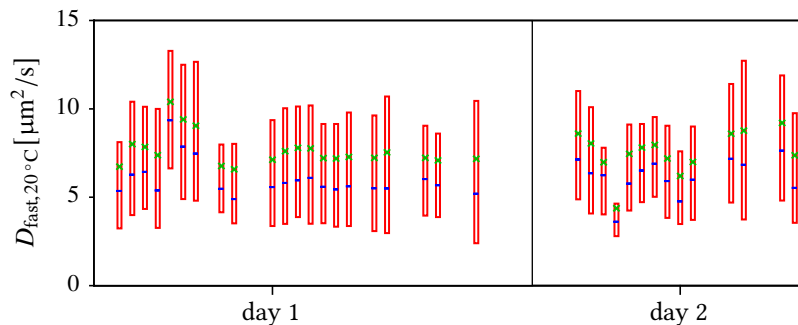


Figure 11.8. | Fast diffusion coefficient $D_{\text{fast},20^\circ\text{C}}$ extracted from all SK8/18 cells expressing Keratin18-YFP. The data was acquired on two consecutive days. The red boxes are the IQR of the filtered distribution of D_{fast} in each cell. The blue lines are its median. Green crosses mark the average from each cell. Only those pixels matching the mentioned conditions were used to calculate the statistics. All diffusion coefficients were recalibrated to $\vartheta = 20^\circ\text{C}$ (see appendix C.4).

11.4. Discussion of the results

The distributions of diffusion coefficients of the fast diffusing component span a large range of values (see Fig. 11.8). This reflects the large variability between different measurements in a single cell. The medians of the distributions are compatible with the diffusion coefficients estimated theoretically for small filaments consisting of one or two ULFs (see Fig. 11.3). They also agree with the peak of the MaxEnt distribution for a single pixel, shown in Fig. 11.6(a).

The diffusion coefficient of the fast component in the MaxEnt distribution spreads over a range of $D_{20^\circ\text{C}} \in [2\dots 30] \mu\text{m}^2/\text{s}$. This indicates that the pixels might contain a broad mixture of particles. The upper fraction of the distribution (between $7 \mu\text{m}^2/\text{s}$ and $30 \mu\text{m}^2/\text{s}$) is compatible with the diffusion coefficients that is expected for dimers, or tetramers. The slow fraction of the distribution represents single ULFs or filaments constituted from a few ULFs. The data shows no indication of particles in the free pool, that are significantly larger than a few ULFs.

The diffusion coefficients measured with FRAP ($D_{\text{keratin,FRAP}} \approx 1 \mu\text{m}^2/\text{s}$) are on a timescale between the two components that were observed in the SPIM-FCS measurements. A possible explanation is that FRAP measures an average over the two distinct dynamics, that could be resolved with FCS.

The concentration of particles in the free pool cannot easily be extracted from these measurements, because the autocorrelation function directly depends on the unknown brightnesses of the different molecules that make up this free pool. In addition, the interpretation of the slow component is complicated. If it is assumed to only describe the complexity of the medium, then the overall particle concentration $\langle c_{\text{all}} \rangle$, measured in the autocorrelation curve, can be interpreted to quantify the molecules in the free pool. The fraction ρ_{slow} can then be ignored. This interpretation seems sound, if the data for keratin and for inert tracers (chapter 10) is compared. Still, the interpretation of $\langle c_{\text{all}} \rangle$ is complicated by its implicit dependence on the brightness of the particles, which is not uniform in the free pool. Here longer polymer fragments are brighter than shorter fragments, because they carry more fluorophore molecules. This is already evident, if the autocorrelation function Eq. (5.3.12) (p. 58) is written for two species 1 and 2 with arbitrary brightnesses $\eta_{g,1}$ and $\eta_{g,2}$:

$$g_g(\tau) = \frac{\eta_{g,1}^2 G_g^{(1)}(\tau) + \eta_{g,2}^2 G_g^{(2)}(\tau)}{(\eta_{g,1} \langle c_1 \rangle + \eta_{g,2} \langle c_2 \rangle)^2} = \frac{\left(\frac{\eta_{g,1}}{\eta_{g,2}}\right)^2 \cdot G_g^{(1)}(\tau) + G_g^{(2)}(\tau)}{\left(\frac{\eta_{g,1}}{\eta_{g,2}} \cdot \langle c_1 \rangle + \langle c_2 \rangle\right)^2} \quad (11.4.1)$$

In simple systems, assumptions on $\eta_{g,1}/\eta_{g,2}$ can be made, such as $\eta_{g,1}/\eta_{g,2} = 2$ for a homo-dimerization reaction. In the case of keratin, a more sophisticated is required, which will be left to future work on this project. Note however, that only the correlation amplitudes are affected by this brightness issue. Therefore, the diffusion coefficients can be measured reliably.

12. Dynamics and interaction of chromatin-associated proteins

Most of the cells for this chapter were prepared by Gabriele Müller (DKFZ, Heidelberg). Details on the cell culture protocols can be found in appendix A.2.

In this chapter SPIM-FCS and SPIM-FCCS measurements on chromatin-associated proteins are described. First the dynamics of three histones (H2A, H4, H1) are examined. This forms the basis for the application of SPIM-F(C)CS to two other functional proteins, namely the transcription factor system activator protein 1 (AP-1) with its constituents c-Fos and c-Jun (chapter 12.2) and the nuclear receptor retinoid X receptor (RXR) (chapter 12.3).

12.1. Histone Dynamics

Measurements on histones were performed in cooperation with Tabea Elbel.

12.1.1. Introduction

The nucleosome was briefly introduced in section 1.1 as the basic packing unit of chromatin in a cellular nucleus during interphase. Figure 12.1(a) depicts the crystal structure of such a nucleosome, which is composed of a protein core (red/yellow/green/blue) and a stretch of DNA wound around it (gray) [290]. As shown in the figure, the core structure consists of two copies of four different proteins. H3 (green) and

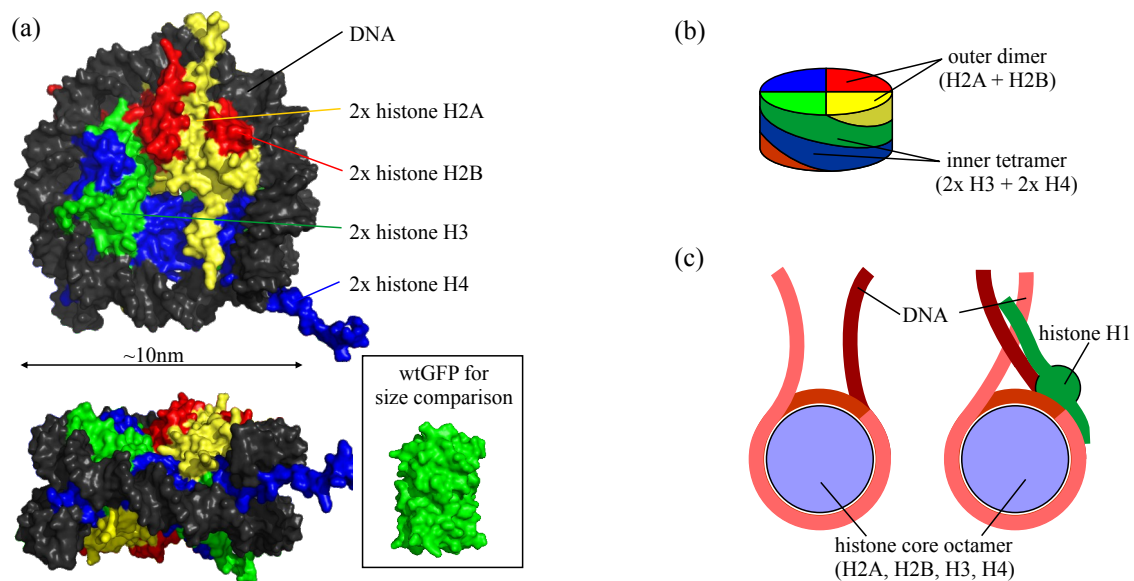


Figure 12.1. | (a) Crystal structure of the nucleosome. (b) Schematic drawing of the protein core of the nucleosome. (c) Interaction of the nucleosome with the linker histone H1. Crystal structures taken from Refs. [148, 290] and rendered using PyMOL. (c) adapted from Ref. [2].

H4 (blue) form the “inner tetramer”, H2A (yellow) and H2B (red) the two “outer dimers”. The stability of the nucleosome has been assessed with salt-induced destabilization experiments. There it was shown, that the H2A/H2B-dimer is evicted at lower salt concentrations, than the H3/H4-tetramer [291, 292].

The histone protein H1 (see Fig. 12.1c) is not a part of the nucleosome core structure. It is however often bound to the nucleosomes in cells, where it helps to package nucleosomes into higher-order structures [2, 293]. For this reason it is also called linker histone. As shown in Figure 12.1(c), H1 binds to the outer part of the nucleosome, where the two DNA-strands leave the core structure. It interacts with the DNA strands (and to tails of the core histone proteins) and thereby changes the exit angle of the DNA. This allows for a denser packaging of the chromosomes.

12.1.2. Measurement protocol

The dynamics of three eGFP- or YFP-tagged histone proteins in live cells are investigated. HeLa cells were transiently transfected with the following protein constructs [294]:

- H2A-eGFP (molecular weight of histone + eGFP: 14.1 kDa + 32.7 kDa = 46.8 kDa)
- H4-eGFP (molecular weight of histone + eGFP: 11.4 kDa + 32.7 kDa = 44.1 kDa)
- H1.0-YFP (molecular weight of histone + eGFP: 20.8 kDa + 32.7 kDa = 53.5 kDa)

All cells were also co-transfected with free mRFP1, in order to label the shape of the cells. SPIM-FCS measurements were performed in these cells at room temperature ($\vartheta \approx 24^\circ\text{C}$) in HBSS. An Andor iXon X3 860 EMCCD camera was used to acquire frames with 128×20 pixels at a temporal resolution of $\tau_{\min} = \Delta t_{\text{frame}} = 530 \mu\text{s}$. The laser intensity in the center of the light sheet was in the range of $100 - 200 \text{ W/cm}^2$. The dual-view optics was used to detect the eGFP/YFP and the mRFP1 signals simultaneously.

The data selection and evaluation process was comparable to the one described in section 10.2.2. The bleaching behavior of the slowly moving chromatin is relatively complex. Therefore the model Eq. (7.1.5) (p. 109) with a degree of the polynomial of $N_f = 4$ was used in all cases. For the final evaluation, two regions in each cell were selected. The nucleus was masked by a threshold of the intensity, which was optimized for each cell individually. In some of the cells, a significant part of the cytoplasm was visible in a measurement. In these case, also a region inside the cytoplasm was selected in order to measure the abundance and mobility of labeled histones in that compartment. Finally all data was fitted with a 2-component normal diffusion model (Eq. (5.3.25) with Eq. (5.3.29), p. 62). As described earlier, moving cells were excluded during the masking stage and after the fitting stage. For each fit parameter the outlier-robust median of the distribution in each cell was calculated, and then used for further statistical evaluations.

12.1.3. Results

Figure 12.2 shows the fit results and fluorescence images for three typical cells, expressing the histone fusion-proteins H2A-eGFP, H4-eGFP or H1.0-YFP. In all cases, the histones were localized mostly in the nucleus, and the concentrations measured in the cytosol were a factor 10 – 20 lower. The distribution of chromatin can be seen in the fluorescence images (Fig. 12.2f) and, likewise, in the maps of the particle concentration (Fig. 12.2g). The dependence between measured concentration and fluorescence intensity was approximately linear in all cases (cf. section 8.6).

The autocorrelation curves were best described by a two-component normal diffusion model in all cases. Table 12.1 gives a statistical summary of the fit results in the nucleus and the cytoplasm of all cells. In the cytoplasm, the diffusion coefficient of the fast component were $D_{\text{fast},20^\circ\text{C}} = 11 - 19 \mu\text{m}^2/\text{s}$ for all histone variants. These values are in the same range as those obtained for eGFP-mRFP1, β -gal-eGFP and eGFP-4x in section 10.2.3 (especially Fig. 10.4a). Assuming a relative viscosity of $\eta_{\text{rel}} = 3$ for the medium in the cell (see section 10.2), the diffusion coefficients $D_{\text{fast},20^\circ\text{C}}$ can be converted to hydrodynamic radii

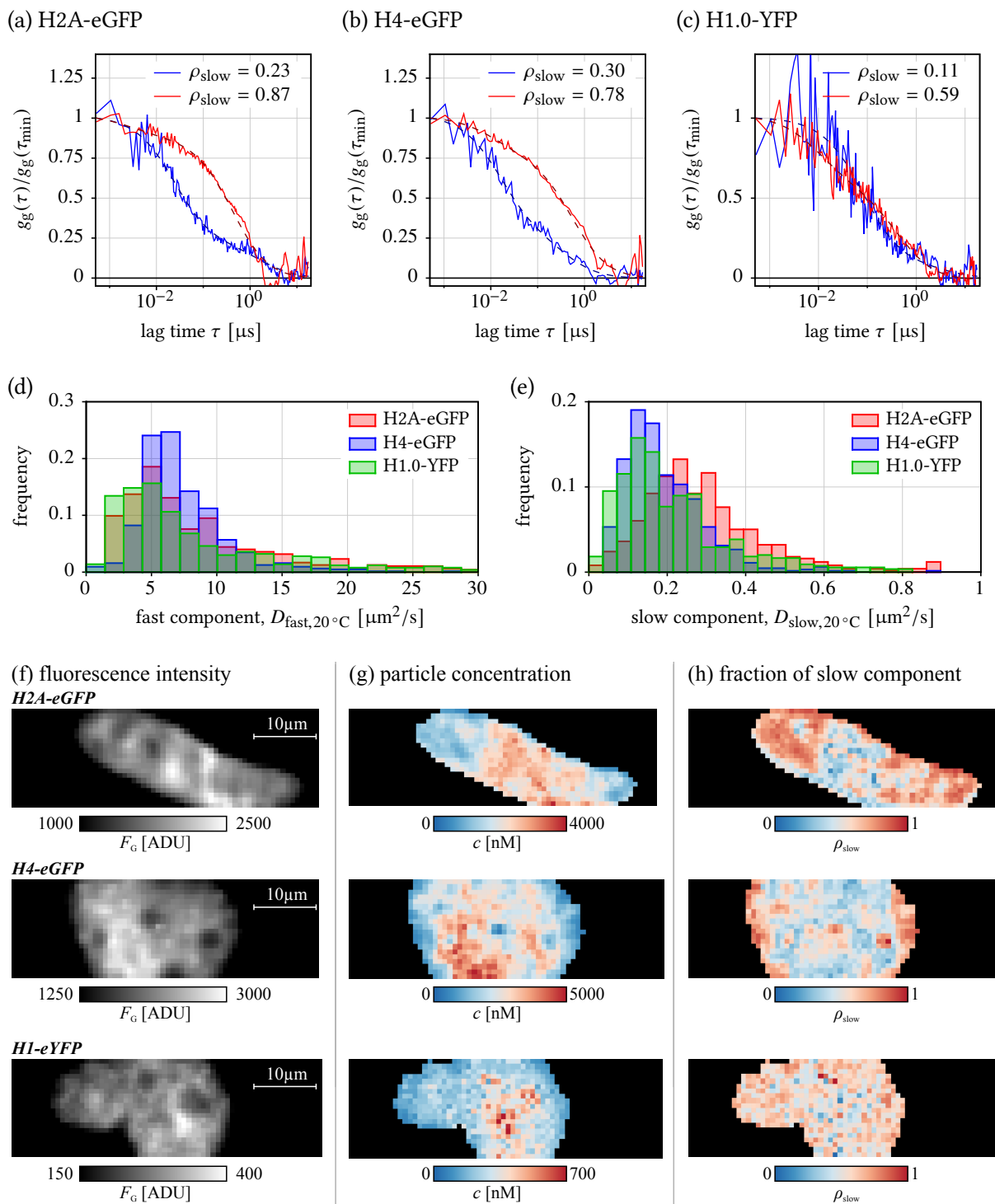


Figure 12.2. | SPIM-FCCS measurements of different labeled histones (H2A-eGFP, H4-eGFP, H1.0-YFP) in the nucleus of transiently transfected HeLa cells. (a,b,c) Representative correlation curves (solid lines) and fits (dashed lines). From each cell one pixel with a high and one pixel with a low value of ρ_{slow} was selected. (d) Fluorescence intensity images. (e) Maps of the fraction of the slow diffusing component ρ_{slow} in the green color channel. (f) Maps of the fraction of the slow component ρ_{slow} . In (d-f), the first row shows a cell, expressing H2A-eGFP, the second row a cell expressing H4-eGFP and the last row a cell expressing H1.0-YFP. Acquisition settings: 64×20 pixel, $\tau_{min} = 530 \mu\text{s}$.

parameter	location	H2A-eGFP	H4-eGFP	H1.0-YFP
$D_{\text{fast},20^\circ\text{C}}$ [$\mu\text{m}^2/\text{s}$]	nucleus	(7.3 \pm 2.1)	(7.8 \pm 4.2)	(5.8 \pm 1.9)
	cytoplasm	(18.2 \pm 7.1)	(19.0 \pm 4.8)	(11.5 \pm 6.7)
$D_{\text{slow},20^\circ\text{C}}$ [$\mu\text{m}^2/\text{s}$]	nucleus	(0.22 \pm 0.05)	(0.37 \pm 0.18)	(0.17 \pm 0.03)
	cytoplasm	(0.20 \pm 0.10)	(0.45 \pm 0.26)	(0.03 \pm 0.03)
ρ_{slow}	nucleus	(0.57 \pm 0.08)	(0.41 \pm 0.07)	(0.48 \pm 0.08)
	cytoplasm	(0.28 \pm 0.20)	(0.22 \pm 0.10)	(0.32 \pm 0.11)
number of cells	nucleus	8	13	22
	cytoplasm	8	11	9

Table 12.1. | **Summary of fit results for the labeled histones in HeLa cells.** The given values are average and standard deviation over the medians from each single cell. Diffusion coefficients were recalibrated to $\vartheta = 20^\circ\text{C}$ (see appendix C.4).

in the range of $R_h = 6.5 - 3.7$ nm. To summarize, the particle mobility in the cytoplasm is compatible with single tagged histones, or small aggregates of a few histone proteins. The values obtained for $D_{\text{fast},20^\circ\text{C}}$ were on the same order of magnitude as the values published in Refs. [295, 296].

For diffusion in the nucleus, the fast diffusion coefficient $D_{\text{fast},20^\circ\text{C}}$ was generally approximately a factor of 2 smaller than in the cytoplasm. The fraction of the slow component ρ_{slow} was significantly increased from ~ 0.2 to $0.4 - 0.5$ in the nucleus. The diffusion coefficient of this slow fraction was on the order of $0.2 \mu\text{m}^2/\text{s}$. Figure 12.2(h) shows maps of ρ_{slow} , as they were typically obtained in all cells. Figure 12.2(a-c) show representative autocorrelation curves obtained from one pixel with a relatively high value of ρ_{slow} and from one pixel with a low value of this parameter. The ρ_{slow} -maps demonstrate that the fraction of the slow component is significantly increased near the periphery of the nucleus for H2A-eGFP and H4-eGFP. For H1.0-YFP, no comparable large-scale structures could be detected in any cell. The parameter ρ_{slow} never correlated with the fluorescence intensity in the cells. Nevertheless it showed a significant anti-correlation (Pearson's correlation coefficient: $|r(\rho_{\text{slow}}, c)| > 50\%$) with the measured concentration within most cells for H2A-eGFP and H4-eGFP. This is also directly visible in the images in Fig. 12.2(g,h). For H1.0-YFP, no such correlation was observed (Pearson's correlation coefficient: $|r(\rho_{\text{slow}}, c)| < 20\%$).

The reduced mobility and the increased slow fraction of the diffusion in the nucleus confirm, that the labeled histone proteins interact with structures in the nucleus, most probably the chromatin. This is further backed by the large-scale structures, that are visible in the distribution of the fraction of the slow component ρ_{slow} . This parameter was significantly increased towards the periphery of the nuclei, which can be explained by heterochromatic regions. Such regions with a high density of silenced chromatin are usually found near the nuclear lamina [2, 297]. In addition, these distributions are comparable to the mobility maps of the heterochromatin-binding protein HP-1 α , which were also measured on a SPIM-FCS setup by Capoulade et al. [120]. In that publications, the authors reported patchy structures of slowed down mobility of HP-1 α in an interphase nucleus. The fact that both H2A-eGFP and H4-eGFP exhibit such patterns, also shows that these proteins are at least in part still functional, although the small histone proteins are fused to the rather large eGFP/YFP, which could prevent proper formation of the densely packed histone octamer and of nucleosomes (cf. Fig. 12.1).

For the linker histone H1.0-YFP, a significant slow-down of diffusion in the nucleus was also found (see values for $D_{\text{fast},20^\circ\text{C}}$ Tab. 12.1). This argues for an interaction of H1.0-YFP with structures in the nucleus. Nevertheless, no patterns could be observed in the parameter maps. The reason for this finding is unclear, as it contradicts other published results (e.g. Refs. [298, 299]).

12.2. The AP-1 transcription factor system

12.2.1. Introduction

An important group of chromatin-associated proteins are the transcription factors (TFs). These are a family of proteins, that can bind to specific DNA sequences (promoter sites). After binding to the DNA, they offer interaction sites for proteins of the RNA polymerase complex. Without such TFs, the RNA polymerase would not be able to initiate the transcription of a gene (see section 1.1). Since TFs are required for the binding of the RNA polymerase to nearly all promoter sites in the human genome, they are also called “general” transcription factors [2].

For this thesis, the activator protein 1 (AP-1) system was examined as an example, since extensive confocal FCCS studies have already been performed for this protein [73, 95, 268]. These can serve as reference for the results of SPIM-FCCS measurements. The structure of the transcription factor AP-1 is illustrated in Fig. 12.3. It consists of two proteins, c-Fos and c-Jun, that bind to each other via leucine residues in a coiled-coil structure (leucine zipper). This heterodimer then binds to DNA with its two DNA binding domain (DBD). The interaction with proteins from the polymerase complex is mediated by the trans-activation domains at the amino-terminal (N-terminal) ends of c-Fos and c-Jun.

The heterodimeric binding of AP-1 is an ideal test system for the SPIM-FCCS methods developed during this thesis project. Two differently labeled fusion proteins, c-Fos-eGFP and c-Jun-mRFP1, were used for the experiments. They consist of the full length c-Fos or c-Jun protein and an eGFP or mRFP1 fluorescent tag. These proteins are referred to as “wildtype” throughout this section. They are expected to exhibit a high relative dimer concentration, as shown in refs. [73, 268]. In addition the two deletion mutants c-Fos $\Delta\Delta$ -eGFP and c-Jun $\Delta\Delta$ -mRFP1 were measured, in which the DNA binding domain and the dimerization domains are missing. These proteins are known not to interact and only show a negligible cross-correlation amplitude.

12.2.2. Measurement protocol

HeLa cells were transiently co-transfected with a combination of c-Fos-eGFP and c-Jun-mRFP1 or with c-Fos $\Delta\Delta$ -eGFP and c-Jun $\Delta\Delta$ -mRFP1. The exact cell culture protocols are described in appendix A.2.

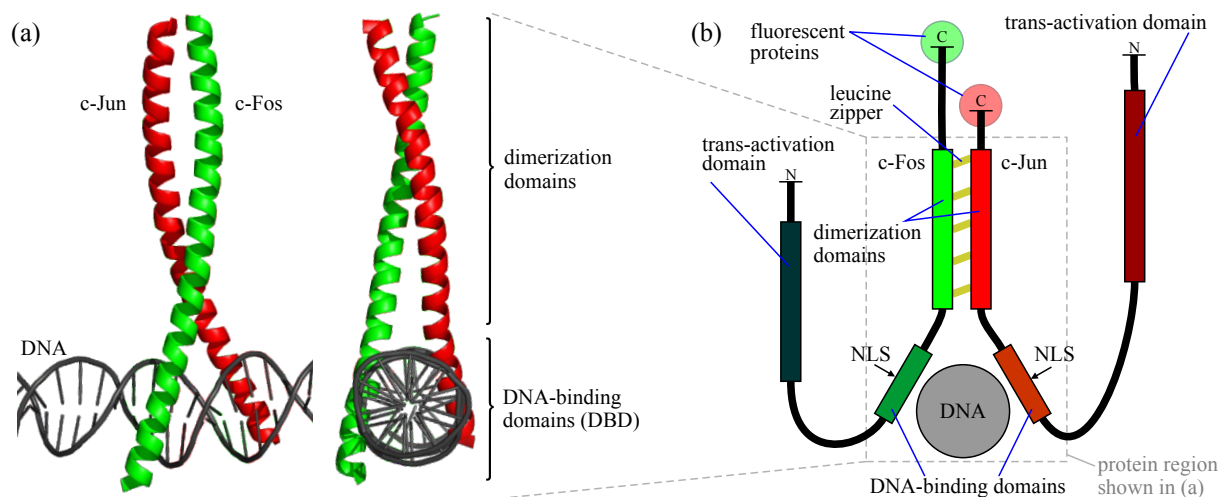


Figure 12.3. | (a) Two views of the crystal structure of the DNA-binding and trans-activation domains of c-Fos and c-Jun. (b) Structure of the transcription factor pair c-Fos and c-Jun. Crystal structures taken from Refs. [148, 300] and rendered using PyMOL. (b) adapted from Ref. [268]. NLS = nuclear localization sequence

SPIM-FCCS measurements were performed at room temperature ($\vartheta = 24^\circ\text{C}$) in HBSS. The Andor iXon X3 860 EMCCD camera was used to acquire frames with 128×20 pixels at a temporal resolution of $\tau_{\min} = \Delta t_{\text{frame}} = 530 \mu\text{s}$. The laser intensity in the center of the light sheet was in the range of $100 - 200 \text{ W/cm}^2$. The dual-view optics was used to detect the fluorescence of eGFP and mRFP1 simultaneously.

Cells were selected for the measurement, as described in section 10.2.2. For the evaluation, the bleach correction Eq. (7.1.5) (p. 109) with $N_f = 3$ was sufficient to yield evaluable results. The cells were masked, using a threshold on the intensity. The background intensities for both color channels were estimated from the masked pixels. Two auto-correlation curves $\hat{g}_{\text{gg}}(\tau)$ and $\hat{g}_{\text{rr}}(\tau)$ and the cross-correlation curve $\hat{g}_{\text{gr}}(\tau)$ were evaluated with the global fitting strategy described in section 7.1.4. The crosstalk factor $\kappa_{\text{gr}} = (2.9 \pm 0.9)$ between the green and the red color channel was determined on the day of the measurements, using a solute sample of eGFP. For the interaction, three distinct species A (green monomers, c-Fos-eGFP), B (red monomers, c-Jun-mRFP1) and AB (dimers, c-Fos-eGFP + c-Jun-mRFP1) were assumed in the model functions in Eqs. (5.4.12)-(5.4.14) (p. 71). For the non-normalized cross-correlation factors $G_{\gamma\rho}^x(\tau)$, a two-component normal-diffusion model was chosen. In order to reduce the complexity of this model (six linked diffusion coefficients), only the concentrations $\langle c_A \rangle$, $\langle c_B \rangle$ and $\langle c_{\text{AB}} \rangle$ were linked over all curves. The diffusion coefficients were specific to each detection channel and not to each species. With this simplifying approximation, Eqs. (5.4.12)-(5.4.14) can be rewritten to:

$$g_{\text{gg}}(\tau) = \frac{1}{\langle c_A \rangle + \langle c_{\text{AB}} \rangle} \cdot G_{\text{gg}}(\tau) \quad (12.2.1)$$

$$g_{\text{rr}}(\tau) = \frac{\eta_{\text{r}}^2 \cdot [\langle c_B \rangle + \langle c_{\text{AB}} \rangle] + \kappa_{\text{gr}}^2 \eta_{\text{g}}^2 \cdot [\langle c_A \rangle + \langle c_{\text{AB}} \rangle] + 2\kappa_{\text{gr}} \eta_{\text{r}} \eta_{\text{g}} \langle c_{\text{AB}} \rangle}{(\kappa_{\text{gr}} \eta_{\text{g}} \langle c_A \rangle + (\eta_{\text{r}} + \kappa_{\text{gr}} \eta_{\text{g}}) \cdot \langle c_{\text{AB}} \rangle + \eta_{\text{r}} \langle c_B \rangle)^2} \cdot G_{\text{rr}}(\tau) \quad (12.2.2)$$

$$g_{\text{gr}}(\tau) = \frac{\eta_{\text{g}} \eta_{\text{r}} \langle c_{\text{AB}} \rangle + \kappa_{\text{gr}} \eta_{\text{g}} \eta_{\text{r}} \langle c_A \rangle + \kappa_{\text{gr}} \eta_{\text{g}}^2 \cdot \langle c_{\text{AB}} \rangle}{(\eta_{\text{g}} \langle c_A \rangle + \eta_{\text{g}} \langle c_{\text{AB}} \rangle) \cdot (\kappa_{\text{gr}} \eta_{\text{g}} \langle c_A \rangle + (\eta_{\text{r}} + \kappa_{\text{gr}} \eta_{\text{g}}) \langle c_{\text{AB}} \rangle + \eta_{\text{r}} \langle c_B \rangle)} \cdot G_{\text{gr}}(\tau) \quad (12.2.3)$$

where the correlation factor $G_{\gamma\rho}(\tau)$ for a combination of channels $\gamma\rho$ is defined as:

$$G_{\gamma\rho}(\tau) := (1 - \rho_{\text{slow},\gamma\rho}) \cdot \frac{G_{\gamma\rho}^{\text{fast},\gamma\rho}(\tau)}{\langle c_{\text{fast},\gamma\rho} \rangle} + \rho_{\text{slow},\gamma\rho} \cdot \frac{G_{\gamma\rho}^{\text{slow},\gamma\rho}(\tau)}{\langle c_{\text{slow},\gamma\rho} \rangle}. \quad (12.2.4)$$

The functions $G_{\gamma\rho}^{\text{fast},\gamma\rho}(\tau)$ are defined by Eqs. (5.4.16, 5.4.17) (p. 71) with the diffusion coefficient $D_{\chi} \equiv D_{\text{fast},\gamma\rho}$. Dividing $G_{\gamma\rho}^{\text{fast},\gamma\rho}(\tau)$ by $\langle c_{\text{fast},\gamma\rho} \rangle$, formally removes its explicit dependence on the concentration. The dependence of $g_{\gamma\rho}(\tau)$ on the particle concentrations is modeled by Eqs. (12.2.1)-(12.2.3). For the cross-correlation curve, a single-component was sufficient to describe the data, therefore $\rho_{\text{slow},\text{gr}} \equiv 0$ and $D_{\text{fast},\text{gr}} \equiv D_{\text{gr}}$

In the fitting model described above, two diffusion coefficients $D_{\text{fast},\gamma\rho}$ and $D_{\text{slow},\gamma\rho}$ and a fraction $\rho_{\text{slow},\gamma\rho}$ are used to describe the correlation curves for each channel $\gamma\rho$ by a fast and a slow component. These cannot be directly assigned to the three species A, B and AB, but for each channel the species of major influence can be identified:

- In the autocorrelation curve from the green channel (gg), only the species A and AB have an influence on the diffusion coefficients.
- In the autocorrelation curve from the red channel (rr), mainly the species B and AB have an influence on the diffusion coefficients.
- The cross-correlation curve (gr) measures mainly the diffusion of species AB, if the crosstalk can be neglected.

The fit results were again treated as described previously. The outlier-robust medians of the distributions from each cell were calculated and then used for any further analysis.

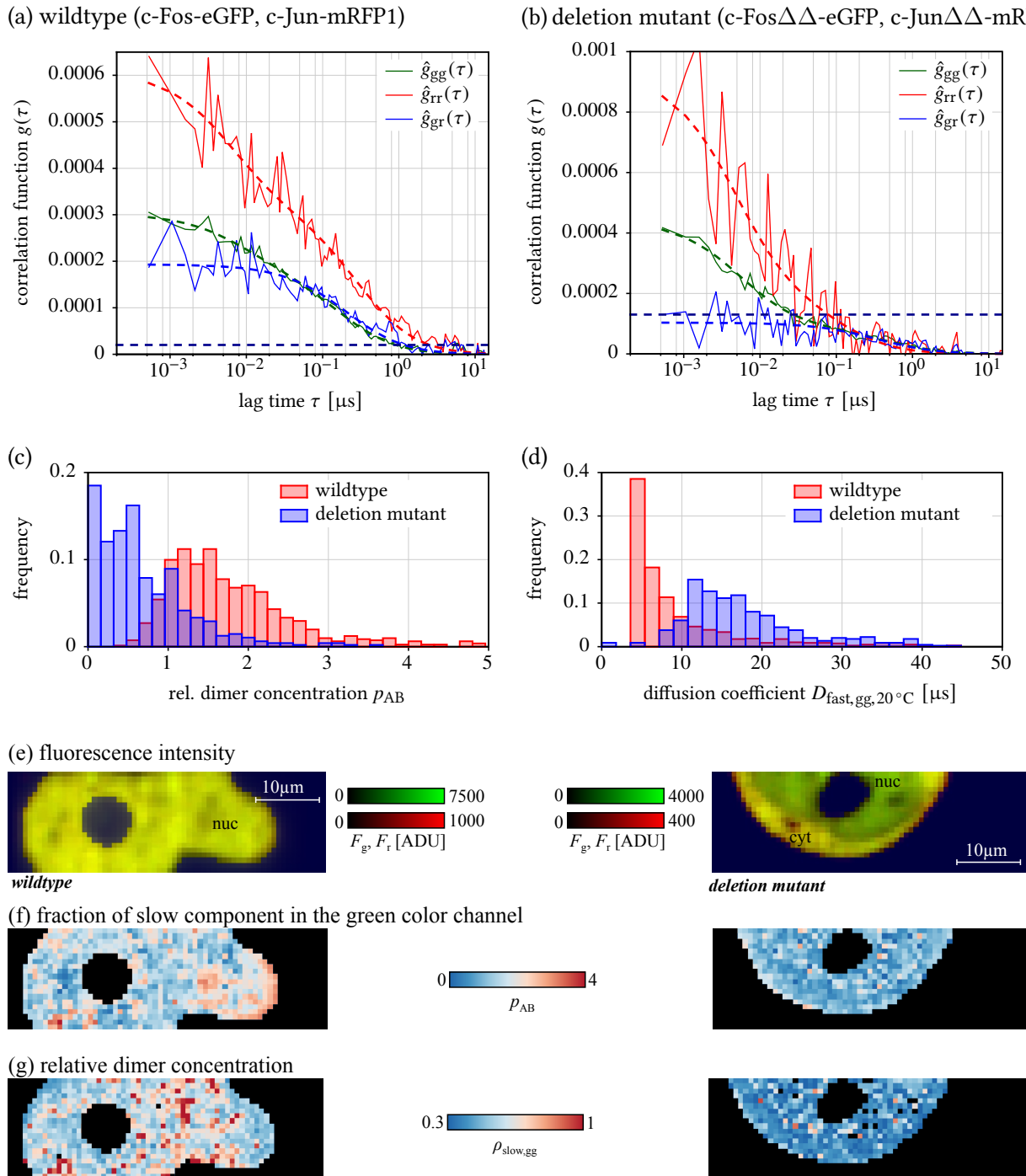


Figure 12.4. | SPIM-FCCS measurement of wildtypes (c-Fos-eGFP + c-Jun-mRFP1) and double-deletion mutants (c-Fos $\Delta\Delta$ -eGFP + c-Jun $\Delta\Delta$ -mRFP1) of AP-1 complex in HeLa cells. (a,b) Examples of correlation curves (solid lines) and fits (dashed lines), horizontal dashed lines are the level of cross-correlation, which is explained by crosstalk. (c) Histograms of the relative dimer concentration p_{AB} in the two cells. (d) Histogram of the fast diffusion coefficient $D_{fast,20^\circ C}$ in the two cells. (e) Overlay images of the green and red fluorescence intensity. In the upper images, only the nucleus (nuc) is visible, in the lower images, the nucleus and the cytosol (cyt) are visible. (f) Maps of the fraction $\rho_{slow,gg}$ of the slow diffusing component in the green color channel. (g) Maps of the relative dimer concentration p_{AB} . In (e-g), the first column shows a cell, expressing c-Fos-eGFP + c-Jun-mRFP1 (wildtype) and the second column a cell expressing c-Fos $\Delta\Delta$ -eGFP + c-Jun $\Delta\Delta$ -mRFP1 (deletion mutant). Acquisition settings: 128×20 pixel, $\tau_{min} = 530 \mu s$.

12.2.3. Results

Figure 12.4 shows typical results from one cell, expressing the wildtype AP-1 and one cell expressing the deletion mutant. The histograms in Fig. 12.4(c) demonstrate that the relative dimer concentration p_{AB} (see Eq. (9.3.1), p. 155) is significantly larger for the wildtype ($p_{AB} = (1.7 \pm 0.7)$) than for the deletion mutant ($p_{AB} = (0.7 \pm 0.6)$). This is also evident from the auto- and cross-correlation curves in Fig. 12.4(a,b). The dashed horizontal lines in these plots mark the cross-correlation amplitude that is explained by crosstalk only. A histogram of the diffusion coefficient $D_{\text{fast,gg},20^\circ\text{C}}$ of the fast species in the green channel (recalibrated to $\vartheta = 20^\circ\text{C}$, see appendix C.4) is illustrated in Fig. 12.4(d). It shows that $D_{\text{fast,gg},20^\circ\text{C}}$ is significantly lower for the wildtype ($D_{\text{fast,gg}} = (9 \pm 7) \mu\text{m}^2/\text{s}$) than for the deletion mutant ($D_{\text{fast,gg},20^\circ\text{C}} = (18 \pm 7) \mu\text{m}^2/\text{s}$). The statistics of all fit parameters over all measured cells are summarized in Tab. 12.2. They exhibit the same trends, as seen for the two cells in Fig. 12.4.

Figure 12.4(e-g) also shows fluorescence images and maps of the relative dimer concentration p_{AB} , as well as the fraction of the slow component $\rho_{\text{slow,gg}}$ in the green channel for two typical cells. For the deletion mutant (2nd column), no large-scale patterns are observable. Also the fluorescence is evenly distributed over the cytoplasm and the nucleus. This is explained by the fact, that the deletion mutants lack the NLS, which is positioned in the DNA binding domain [301]. In the images for the wildtype (1st column) however, the fluorescence is limited to the nucleus. The map of $\rho_{\text{slow,gg}}$ shows the same patchy structure, as the histone variants H2A-eGFP and H4-eGFP. Again the fraction of the slow component is increased near the nuclear envelope. A comparison between the values in Tab. 12.2 and the results for histones in Tab. 12.1 (p. 186) shows that the diffusion coefficient of the slow component of the wildtype AP-1 and especially the diffusion coefficient of the cross-correlation curve $D_{\text{gr},20^\circ\text{C}}$ are compatible with the slow components for the histones. The additional fact, that only a single diffusing component is required to describe the cross-correlation, indicates that most of the dimerized c-Fos and c-Jun molecules are also associated to chromatin.

All numeric fit results shown here are compatible with the results published in Refs. [73, 268], which shows that SPIM-FCCS is applicable to cellular systems beyond the simple fluorophore dimers, presented in section 9.5. The maps of $\rho_{\text{slow,gg}}$, which are available only by applying SPIM-FCCS, support the interpretation, that also the labeled variants c-Fos-eGFP and c-Jun-mRFP1 bind to the DNA in the cellular nucleus.

parameter	channel	wildtype	deletion mutant
$D_{\text{fast,gg},20^\circ\text{C}} [\mu\text{m}^2/\text{s}]$	green	(12 ± 4)	(16 ± 4)
$D_{\text{fast,rr},20^\circ\text{C}} [\mu\text{m}^2/\text{s}]$	red	(22 ± 5)	(25 ± 4)
$D_{\text{slow,gg},20^\circ\text{C}} [\mu\text{m}^2/\text{s}]$	green	(0.4 ± 0.1)	(0.4 ± 0.3)
$D_{\text{slow,rr},20^\circ\text{C}} [\mu\text{m}^2/\text{s}]$	red	(0.3 ± 0.1)	(0.4 ± 0.2)
$\rho_{\text{slow,gg}}$	green	(0.50 ± 0.12)	(0.23 ± 0.09)
$\rho_{\text{slow,rr}}$	red	(0.44 ± 0.10)	(0.18 ± 0.07)
$D_{\text{gr},20^\circ\text{C}} [\mu\text{m}^2/\text{s}]$	cross-correlation	(0.7 ± 0.3)	(2.0 ± 1.5)
p_{AB}	cross-correlation	(0.97 ± 0.32)	(0.33 ± 0.13)
number of cells		17	12

Table 12.2. | Summary of fit results for the AP-1 complex in HeLa cells. The given values are average and standard deviation over the medians from each single cell. Diffusion coefficients were recalibrated to $\vartheta = 20^\circ\text{C}$ (see appendix C.4).

12.3. Nuclear receptors

Measurements, described in this section were performed in collaboration with Peter Brázda (university of Debrecen, Hungary). Additional details can be found in Ref. [121, 302].

12.3.1. Introduction

The last example of a chromatin associated protein that was measured during this thesis project, is the nuclear receptor rhenoid X receptor (RXR). Nuclear receptors are a class of proteins that bind to DNA like transcription factors and can control the transcription of genes (see Fig. 12.5b). They are usually thought to exist in one out of two distinct states. In the repressed state, a nuclear receptor (NR) binds a group of corepressor molecules. They inhibit the transcription of the gene, the NR is bound to. If a NR in a repressed state binds a small, but specific ligand molecule, a structural transition switches it to an active state. It now releases the corepressor molecules and instead offers a binding site for coactivator molecules that help initiating the expression of the gene [2, 303].

In this section, measurements on the nuclear receptor RXR are described. It is a promiscuous NR, which conducts its function as a heterodimer with one of several partner NRs, such as rhenoidic acid receptor (RAR). It binds to the hormone response element, a short DNA base pair sequence, which is present in many genes. RXR is activated by metabolites of vitamin A. The basic structural units of RXR are illustrated in Fig. 12.5(a). The protein contains a ligand binding domain (LBD) for interaction with its dimer partner, a DNA binding domain (DBD) and an “activation function”, which contains the binding sites for the corepressor and coactivator. A nuclear localization sequence (NLS) ensures that RXR is enriched in the nucleus of a cell.

12.3.2. Measurement protocol

SPIM-FCS measurements were performed on two variants of RXR [121, 302]:

- RXR-eGFP is the full length RXR, fused to eGFP as fluorescent label.
- RXR-LBD-eGFP is a truncated version of RXR, which lacks the DBD but contains the LBD. It is also fused to eGFP.

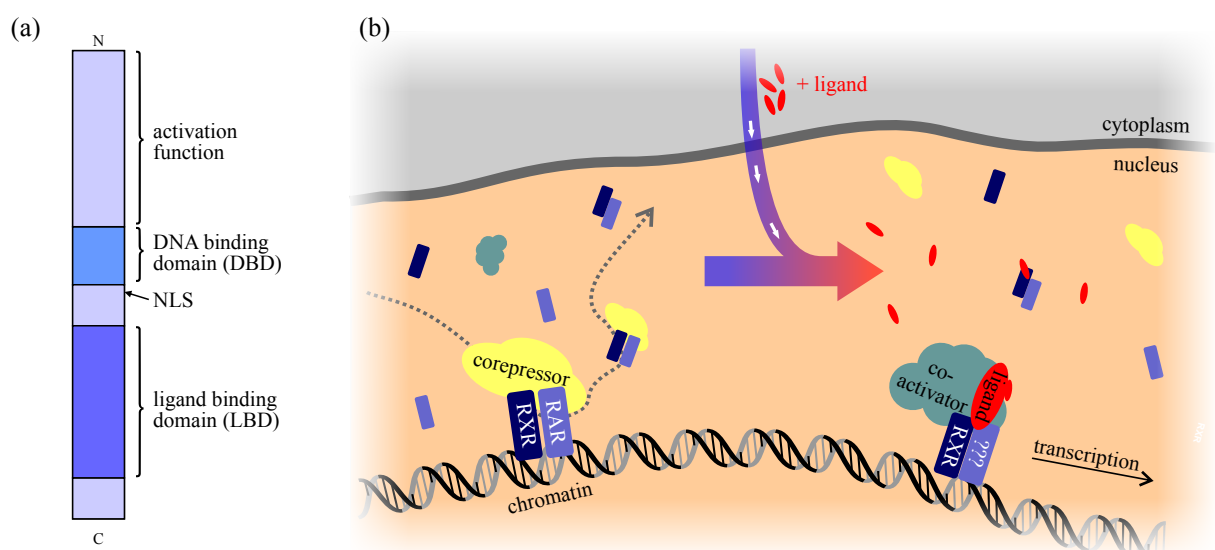


Figure 12.5. | (a) Structure of RXR. (b) Model for the functioning of RXR. (a) was modified from [303].

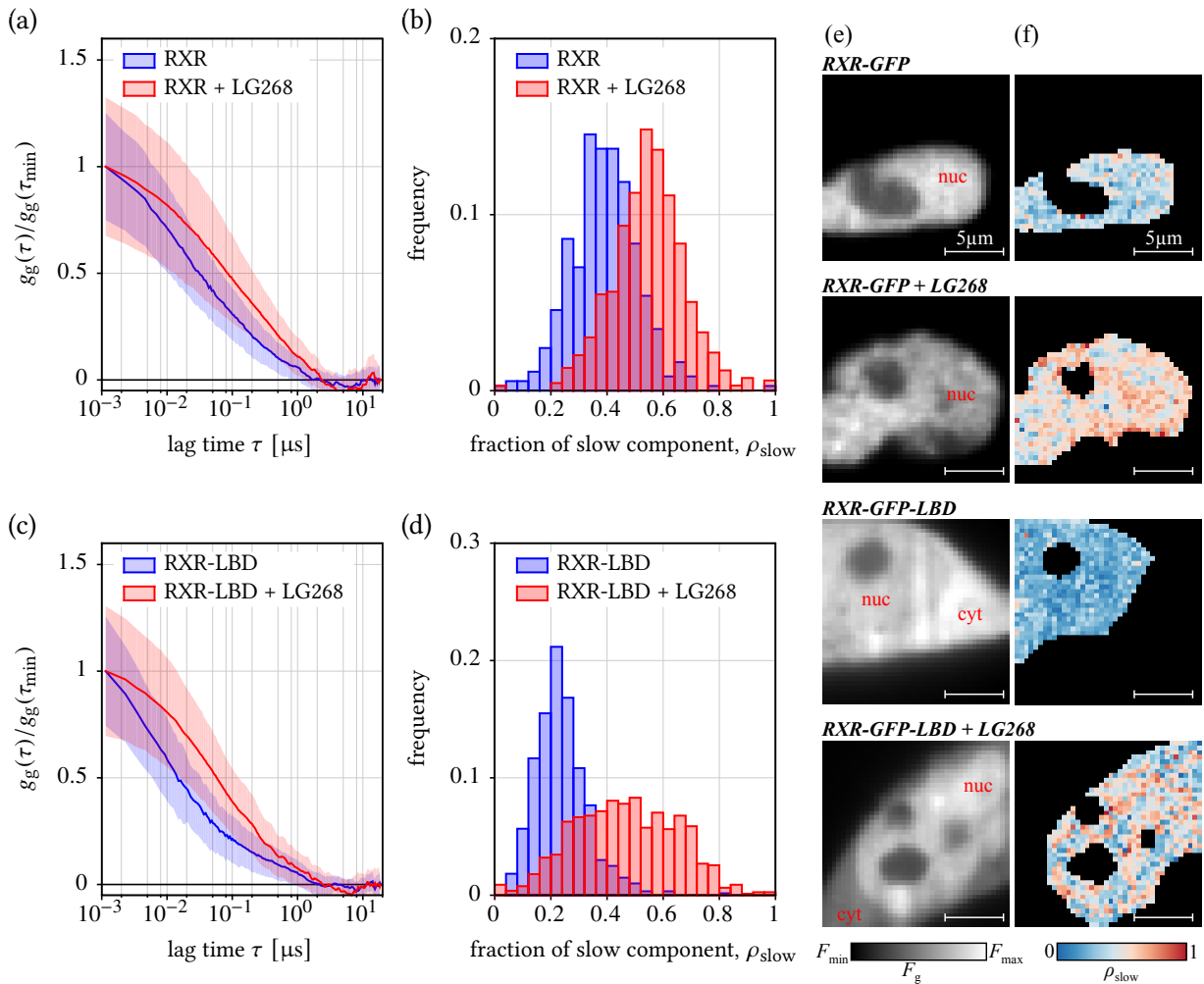


Figure 12.6. | SPIM-FCS measurement of RXR-eGFP and RXR-LBD-eGFP in HeLa cells with and without the ligand LG268. (a,c) Average and standard deviation over all autocorrelation curves in the nucleus of the cells. (b,d) Histograms of the fraction ρ_{slow} of the slow component. (e) Fluorescence intensity images (nuc=nucleus, cyt=cytoplasm). (f) Maps of the fraction of the slow component ρ_{slow} . Acquisition settings: 40×40 pixel, $\tau_{\text{min}} = 1150 \mu\text{s}$.

Both proteins were transiently expressed in HeLa cells. In order to activate RXR, an artificial but specific ligand LG268 was used. All SPIM-FCS measurements were performed in phenol red-free RPMI cell culture medium at room temperature ($\vartheta \approx 24^\circ\text{C}$). Data was acquired with the Andor iXon 860 X3 EMCCD camera (image size: 40×40 pixels, $\tau_{\text{min}} = 1150 \mu\text{s}$). The temporal resolution was lower, due to the larger number of rows in the image. The laser intensity in the center of the light sheet was in the range of 100 W/cm^2 .

The data was treated as described in section 12.1.2. Briefly, a bleach correction was applied and the nuclei of the cells were masked by a threshold on the intensity. If necessary, the masks were corrected by hand. Finally a two-component normal-diffusion fit was used (Eq. (5.3.25) with Eq. (5.3.29), p. 62) to extract information regarding the mobility of the proteins.

12.3.3. Results

In this study, the SPIM-FCS measurements supplemented confocal FCS, FRAP measurements. A detailed account of all measurements is given in Ref. [121]. Here mainly the SPIM-FCS results are detailed. FRAP

measurements showed, that the mobility of RXR on the timescale of several minutes depends on the presence of the ligand. In both, the full length and the truncated form, the addition LG268 significantly slowed down the fluorescence recovery, which indicates a stronger binding and slower dynamics of the receptor.

Comparable results were obtained in confocal and SPIM-FCS on shorter timescales. Figure 12.6 summarizes measurements of four cells, that expressed RXR-eGFP or RXR-LBD-eGFP. For each protein, two cells are shown: one untreated cell and one cell, which was measured ~ 10 min after treatment with LG268. The change in the receptor, which is induced by the ligand, is easily recognized in the autocorrelation curves in Fig. 12.6(a,c). The blue curves (no ligand) show the typical shape of two-component diffusion with a low fraction ρ_{slow} of the slow component. If the ligand is added, the fraction of the second component is increased, and the shape of the curve changes significantly. This can be seen even better in the histograms of ρ_{slow} in Fig. 12.6(b,d). As for AP-1 and histones, the slow component can be interpreted as the motion of RXR (in all cases: $D_{\text{slow},20^\circ\text{C}} \approx 0.4 \mu\text{m}^2/\text{s}$), when it is bound to chromatin. The fast component may be attributed to freely diffusing molecules. It was $D_{\text{slow},20^\circ\text{C}} = (10 \pm 7) \mu\text{m}^2/\text{s}$ for RXR-eGFP without ligand and $D_{\text{slow},20^\circ\text{C}} = (8 \pm 7) \mu\text{m}^2/\text{s}$ for the cell with added ligand. For the truncated version $D_{\text{slow},20^\circ\text{C}} = (13 \pm 8) \mu\text{m}^2/\text{s}$ and $D_{\text{slow},20^\circ\text{C}} = (6 \pm 6) \mu\text{m}^2/\text{s}$ were found respectively. In addition it can be seen that the distribution of the truncated RXR is initially homogeneous over the whole cell. After applying LG268, the receptor molecules start to accumulate in the nucleus (see the two fluorescence images at the bottom of Fig. 12.6e). In contrast to AP-1 and histones, no nuclear-structure dependent patterns were observed in the parameter maps.

These results show, that SPIM-FCS can be used to follow the function of a NR molecule in live cells. The change in binding affinity to DNA is clearly visible in a change of the shape of the autocorrelation curves. This change was successfully quantified with a 2-component normal-diffusion model and the same results were obtained, as in parallel confocal FCS measurements. The results of the imaging FCS measurements indicate that the mobility parameters are homogeneously distributed over the nucleus. Therefore, they do not seem to depend on the nuclear architecture.

Interestingly, the general behavior of the truncated and the full-length forms of RXR are equal. This is expected, since the missing DBD in RXR-LBD-eGFP can be balanced to a great extent by the dimer partner of the protein. In future work, the interaction of RXR with a dimer will be investigated using SPIM-FCCS.

12.4. Conclusions

In this chapter, SPIM-FCS and SPIM-FCCS was applied to three different types of chromatin-associated proteins: histones, the transcription factor pair *c-Fos/c-Jun* and the nuclear receptor RXR. The results for RXR were successfully published in Ref. [121]. In all cases, the results were similar to measurements with the established confocal FCS/FCCS techniques. This again shows the applicability of SPIM-FCS to different biological problems. All measurements were performed with an EMCCD camera. The limited temporal resolution of this type image sensor did not impair the application of SPIM-FCS in any of these cases.

The benefit of SPIM-FCS/SPIM-FCCS over the traditional confocal FCS is generally two-fold. Firstly, SPIM-F(C)CS allows to acquire extensive statistics, even in a single cell, in the same measurement duration that is required to record a single-point confocal FCS/FCCS measurement. Secondly, the imaging of mobility parameters can reveal additional information that is not accessible to single-point measurements. This was seen for the large-scale patterns in the fraction of the slow diffusing component in the histones H2A and H4, as well as for *c-Fos*. These patterns can possibly be attributed to the chromatin structure.

Part V.
Summary

13. Summary

SPIM-F(C)CS

Transport processes play a major role in the functioning of living cells. They are often investigated, by fluorescently labelling the molecules of interest and a subsequent observation with light microscopy methods. To obtain the mobility of molecules, fluorescence correlation spectroscopy (FCS) is often used. In FCS the time series of the fluorescence signal from a small subvolume ($\sim 1 \mu\text{m}^3$) of the whole cell is measured. In equilibrium, this time series exhibits no long-term trends, but shows small fluctuations around an average intensity. These fluctuations encode the motion of single particles through the observation volume. The parameters of motion of these particles (e.g. the diffusion coefficient or flow speeds) are finally extracted using an autocorrelation analysis. The autocorrelation function of the fluorescence fluctuations decays on a timescale, which is connected to the average dwell time of particles in the focus, and therefore also to their diffusion coefficient. In addition, the particle concentration can be extracted from the amplitude of the fluctuations, because of the Poissonian nature of the particle count in the observation volume. An extension of FCS is fluorescence cross-correlation spectroscopy (FCCS): it allows for the measurement of molecular interactions between two differently labelled molecules, by analysing the cross-correlation between two detection channels. In this case, the amplitude of the cross-correlation function directly depends on the number of dimerized molecules, that carry both fluorescent tags.

The aim of this PhD project was to develop methods for spatially resolved FCS and FCCS measurements, with the purpose to investigate the spatial organization of mobility in a cell. FCS and FCCS were combined with selective plane illumination microscopy (SPIM) and fast image sensors (SPIM-F(C)CS). This approach is based on initial work on SPIM-FCS by Wohland et al. [117]. The SPIM allows to evenly illuminate an arbitrarily positioned thin slice of the cell (width: $\sim 1 - 3 \mu\text{m}$). This microscopy technique exhibits good z -sectioning capabilities, while maintaining a very low background signal. The use of a fast, high-sensitivity electron-multiplying charge-coupled device (EMCCD) camera (temporal resolution $\sim 500 \mu\text{s}$) allows to resolve the motion even of relatively small fluorescent proteins (e.g. eGFP) inside cells. SPIM-FCCS was developed during this thesis and introduced in Ref. [132]. It extends SPIM-FCS and allows for the mapping of molecular interactions in addition to the mobility parameters.

Theory of SPIM-F(C)CS

The general theory of imaging FCS and imaging FCCS was presented in chapter 5. Usually this theory is formulated for a confocal microscope, in which the focal volume can be described by a three-dimensional Gaussian function. Here the theoretic framework is extended to a more realistic model, which takes into account the finite, rectangular shape of the camera pixels. Auto- and cross-correlation model functions were derived for several transport processes: normal diffusion, anomalous diffusion and directed motion/flow. In addition, a detailed model for two-color cross-correlation functions was presented, which allows for the quantification of molecular interactions. A variant, two-focus SPIM-FCCS, also makes it possible to quantify the direction and absolute value of a planar flow.

Instrumental setup

During this project, a light sheet microscope has been developed and built. Its design is optimized for the application of imaging F(C)CS in living cells. This microscope was described and a detailed characterization was shown in chapter 6. With an NA = 1 detection objective, the microscope realizes a focal volume with an $1/e^2$ -diameter of approximately 1.2 μm and an $1/e^2$ -height of approximately 2.4 μm . It is equipped with a blue and a green laser, as well as a dual-view optics. With this combination, two-color cross-correlation measurements can routinely be performed. The alignment of such a two-color setup was described in detail.

In chapter 7, the data evaluation methods necessary for imaging FCS were detailed. The multi- τ algorithm used to calculate all auto- and cross-correlation functions for this thesis was described and analyzed in detail. In addition, a global model fitting strategy was developed, which allows to extract the mobility parameters from the thousands of pixels in a typical imaging F(C)CS measurement. The devised strategy converges reliably and within reasonable processing times of a few minutes per measurement. Finally, a robust model function for the correction of photobleaching in imaging F(C)CS measurements was proposed, based on work by Ries et al. [98]. It allows for the reliable correction of bleaching in thousands of pixels without requiring a supervision of the process.

All data evaluation methods, that were developed for imaging FCS and imaging FCCS, were implemented in the extensive and user-friendly software package QUICKFIT 3.0¹.

Evaluation measurements

The combination of light sheet microscopy and imaging F(C)CS techniques was evaluated in detail in chapters 8 and 9. Notably, it was shown that SPIM-FCS is capable of determining absolute diffusion coefficients without relying on a calibration standard with a known reference diffusion coefficient. This is made possible by using the fixed pixel size and magnification of the microscope as a ruler [114, 130]. Also, the measurement of concentrations was discussed in detail. By comparison with confocal FCS measurements, it was shown, that concentrations, which are measured using SPIM-FCS, are a factor of 3 – 4 too high. Several reasons for this behavior were discussed. The most likely cause is an inaccurate model for the focal volume. Nevertheless, relative concentration measurements are possible and the values obtained can be recalibrated by using a concentration standard. Both, for the measurement of diffusion coefficients and of concentrations, limits on the required temporal resolution of the image sensor were derived. The data in section 8.2 and 8.3 show, that the temporal resolution of the image sensor should be at least a factor of 30 – 100 smaller than the average dwell times of particles in the observation volume. If this is the case, the mobility parameters can be measured with a systematic error of less than 10%. If an EMCCD camera is used, this is easily achieved for most fluorescently tagged proteins in living cells. Comparable evaluation measurements were performed for two-color imaging FCCS. They demonstrate that the methods yields accurate relative dimer concentrations and diffusion coefficients. For the extraction of absolute concentrations, the same limitations as for SPIM-FCS apply.

Finally the applicability of both techniques to live-cell measurements was demonstrated in detail. There, it was shown that SPIM-F(C)CS cannot only be used in the cytoplasm and the nucleus of live cells, but it is also applicable to measurements in the cellular membrane [132].

Different image sensors

As shown above, an image sensor with high temporal resolution and high photo-sensitivity is required for successful imaging F(C)CS measurements. In section 8.7, several commercially available high-speed

¹QUICKFIT 3.0 is available free of charge from <http://www.dkfz.de/Macromol/quickfit/>.

cameras were compared. In addition to these linear detectors, arrays of single-photon avalanche diodes (SPADs) were evaluated during this thesis. These feature a matrix of up to 512×128 pixels, which can be read out every $1 - 10 \mu\text{s}$. With these specifications, they exceed any commercially available high-sensitivity camera. A disadvantage of such SPAD arrays is however their low fill factor, which is due to the electronics, that is required in each pixel in addition to the SPAD. Nevertheless, it was demonstrated that the SPAD array *Radhard2* can successfully be used for accurate SPIM-FCS measurements of bright fluorescent microspheres.

The problem of low photo-sensitivity in SPAD arrays was approached during the last months of this thesis by a new sensor (*SwissSPAD*), which could be operated at higher excess voltages, and that contains a microlens array [193]. Using this new sensor, it was demonstrated in section 8.8.2, that SPIM-FCS measurements are feasible also for dim fluorescent samples (e.g. Alexa-488 labeled DNA). Nevertheless, a successful measurement in living cells was not yet achieved. Details of the applicability of SPAD arrays and other image sensors to imaging FCS were published in Refs. [130, 131].

In conclusion, EMCCD cameras currently offer the best trade-off between speed and photo-sensitivity. Nevertheless, the next generation of SPAD arrays can be expected to replace them as ideal image sensor in the near future.

In vivo applications

Finally SPIM-F(C)CS was applied to several cellular systems. Chapter 10 presents several mobility measurements of inert tracer particles in live cells. They demonstrated the possibility to obtain maps of the mobility parameters. From these the dynamic viscosity of the cytoplasm and nucleoplasm could be derived. Also the effect of crowding in the cytoplasm was shown. All results obtained in this section agree well with published results from confocal FCS measurements.

SPIM-FCS was used to quantify the free pool of keratin filament precursors (see chapter 11). This pool enables the cell to dynamically remodel its intermediate filament network. It needs to be measured at positions in the cell, that lie in between larger filament bundles. For this, the capability of SPIM-FCS to measure at thousands of positions in parallel was exploited. In this way, pixels with artifact-free measurements could be selected after data acquisition. Using a confocal microscope for this task, the experiments would have taken 10–100 times longer and would still have yielded less statistical relevance. Earlier FRAP measurements on the same system (see Ref. [287]) could be significantly refined with SPIM-FCS. The range of diffusion coefficients that were determined with SPIM-FCS could be used to give an estimate of the particle sizes in the free pool.

Finally in chapter 12, SPIM-F(C)CS was applied to three different chromatin-associated proteins. For histones, it could be shown, that the chromatin organization can be studied with mobility-parameter maps, obtained by SPIM-FCS. In addition, the function of the transcription factor system *c-Fos/c-Jun* (AP-1) and of the nuclear receptor retinoid X receptor (RXR) were successfully measured with these new approaches. The results on RXR were published in Ref. [121].

Part VI.
Appendix

A. Materials and methods

A.1. List of used materials and suppliers

Table A.1. | Optical components. This table lists all components used in the experiments, including their suppliers or manufacturers.

used for	component	part no.	manufacturer
illumination	blue DPSS laser $\lambda = 491$ nm, $P \leq 25$ mW	Calypso-25	Cobolt SE
	blue diode laser $\lambda = 488$ nm, $P \leq 60$ mW	MLD 488-60	Cobolt SE
	blue cleanup filter	ZET 488/10	Chroma
	blue beam expander	S6ASS2075/067	Sill Optics GmbH
	green DPSS laser $\lambda = 561$ nm, $P \leq 25$ mW	Jive-25	Cobolt SE
	green beam expander	bm.x VIS-YAG 5x	Qioptiq
	neutral density filters $\varnothing = 0.5$ "	NE5xxA	Thorlabs
	servo motors for beam shutters	HS5056MG	Hitec
	dichroic beam combiner	zt488/594rpc	Chroma
	1 st relais telescope lens L1, $f = 150$ mm	AC508-150-A-ML	Thorlabs
	2 nd relais telescope lens L2, $f = 250$ mm	AC508-250-A-ML	Thorlabs
	$\varnothing = 1$ " silver mirrors	BB1-E02	Thorlabs
	$\varnothing = 2$ " silver mirrors	PF20-03-P01	Thorlabs
	<i>optomechanics</i>	optical rail system	SYS65
gimbal mount		TRANS 65G-D38-MS	OWIS
piezo-driven beam combiner mount		customized MDI-H	Radiant Dyes
2-channel piezo-controller		RD2-16020	Radiant Dyes
standard mirror mounts		KS1D/M & KS2/M	Thorlabs
transmission illumination	1 W LED, warm white (6500 K, 100 lm)	W42182/U2	Seoul Semiconductor
	ground glass diffusor	DG10-1500	Thorlabs
	collimation lens		Thorlabs
lightsheet formation	cylindrical lens, $f = 150$ mm	LJ1629RM-A	Thorlabs
	alternative cylindrical lens, $f = 100$ mm	CKX18-C	Newport
	cylindrical lens rotation mount	CRM1P/M	Thorlabs
	objective lens, NA = 0.3, $f = 20$ mm	Plan Fluor 10x/0.3	Nikon
	objective lens translation mount	SM1Z	Thorlabs
detection beam path	objective lens, NA = 1.0, $f = 3.33$ mm	CFI Apo-W NIR 60x/1.0W	Nikon
	tube lens, $f = 200$ mm	MXA20696	Nikon
	alternative tube lens, $f = 100$ mm	AC254-100-A-ML	Thorlabs
	tube lens translation stage	07TXS723	CVI Melles Griot
	488 nm/491 nm notch filter	StopLine Notch 488	Semrock
	561 nm notch filter	ZET 561NF	Chroma

Continued on next page

Table A.1 – continued from previous page

used for	component	order no.	manufacturer
	50 : 50 beam splitter, $37.5 \times 25 \text{ mm}^2$		
	mirror prism		
	rotation stage	WV 40-D25-FGS	OWIS
<i>filter wheel (FW)</i>	filter wheel stepper motor	PD3-108-28-SE-485	Trinamic
	filter wheel computer interface	USB-RS485-WE-1800-BT	FTDI
	filter wheel hall stop switch	55100-3H-02-A	Hamlin
<i>FW filters:</i>	neutral density filter $OD = 3$	NE30A-A	Thorlabs
	neutral density filter $OD = 4$	NE40A-A	Thorlabs
	green longpass	Edge Basic 488 LP	Semrock
	green bandpass	BrightLine HC525/50	Semrock
	red longpass	EdgeBasic 561LP	Semrock
	red bandpass	BrightLine 641/75-25	Semrock
DualView & filterset	dual view assembly	DualView DV2	Photometrics
	beam splitter 565 mm	T565lpxr	Chroma
	green filter	BrightLine HC525/50	Semrock
	red filter	Brightline HC 593LP	Semrock
	alternative red filter	Edge Basic 561LP	Semrock
	1500 lines electron microscopy grid	AGG2785C	Agar Scientific
	2000 lines electron microscopy grid	AGG2786C	Agar Scientific
Camera	EMCCD camera	iXon X3 860	Andor
	water cooling for EMCCD camera	PREMIUM XXD	Innovatek
	sCMOS camera	pco.edge 5.5	pco
	SPAD array, 32×32 pixels	Radhard2	– [186]
	SPAD array, 512×128 pixels	CHSPAD	– [192]
	camera box construction	profil 5 system	Item Industrietechnik GmbH
sample mounting	x -, y - & z -translation stage	M-112.2DG	PI Physik Instrumente
	x -, y - & z -translation stage controller	C-863 Mercury	PI Physik Instrumente
	manual rotation stage	124-0315	Opto-Sigma
	No. 3 cover slips for adherent cells	16301	Neolab
	foil for sample bags	Lumox Folie 25 M	Sarstedt AG & Co
sample chamber	translation stage	SHTC 12	Igus
	No. 1 cover slips $\varnothing = 20 \text{ mm}$		
	No. 1 cover slips $\varnothing = 22 \text{ mm}$, borosilicate glass	631-0158	VWR
	O rings, MVQ70, 16×1.5		HUG Industrietechnik
	O rings, MVQ70, 17×1.5		HUG Industrietechnik
	O rings, MVQ70, 18×1.0		HUG Industrietechnik
	silicone grease Baysilicone Paste 35 g, low viscous		GE Bayer Silicones
	self-closing tweezers	HSC 516-10	Hammacher, Solingen
	fine tweezers	3c SA	Vomm, Solingen
	heating resistor 4.7Ω or 10Ω	RTO 20 F	Vishay
	PT100 temperature sensor MR828	32 209 340	Heraeus

Continued on next page

Table A.1 – continued from previous page

used for	component	order no.	manufacturer
	PT100 stainless steel probe, class B, 4-wire, Ø = 1.5 mm		TMH GmbH
control computer	6-core Processor	Phenom II X6 1090T	AMD
	16 GB RAM		
	mainboard	M4A785TD-V EVO	Asus
	graphics card	GeForce GTX 550 Ti	NVidia
	frame grabber for EMCCD	CCI-23	Andor

Table A.2. | Software used during this thesis work.

software	description/used for ...
Autodesk Inventor 2010-2013, Student License	computer aided design (CAD) software used for design and planning of all mechanical components
Target 3001! V14	electronics CAD software (schematic entry and printed circuit boards) used to develop all electronics
Corel Draw X4&X6	creation of figures for papers and thesis
MatLab 2010-2014	numerical computation, data evaluation and plotting
Mathematica 5	symbolic mathematics
PyMol 1.3	visualization of protein crystal structures
GNU compiler collection 4.4-4.8	C/C++ compiler used for software development on windows and Linux
GNU Scientific Library ≤ 1.16	library for scientific computation (special functions, optimization, statistics, ...)
LevMar ≤ 2.6	Levenberg-Marquardt least-squares optimization library [304]
LMFit ≤ 5.3	Levenberg-Marquardt least-squares optimization library [235]
Eigen 3.2	open source linear algebra library, http://eigen.tuxfamily.org/
Qt 4.4-4.8	open source widget toolkit http://www.qt-project.org/

Table A.3. | Chemicals used during this thesis.

description	name	part no.	manufacturer
Fluorescent Probes			
yellow-green fluorescent microspheres Ø = 200 nm, carboxylate modified	FluoSpheres YG	F8811	Invitrogen
yellow-green fluorescent microspheres Ø = 100 nm, carboxylate modified	FluoSpheres YG	F8803	Invitrogen
yellow-green fluorescent microspheres Ø = 40 nm, carboxylate modified	FluoSpheres YG	F8795	Invitrogen
yellow-green fluorescent microspheres Ø = 20 nm, carboxylate modified	FluoSpheres YG	F8787	Invitrogen

Continued on next page

Table A.3 – continued from previous page

description	name	part no.	manufacturer
red fluorescent microspheres $\varnothing = 200$ nm, carboxylate modified	FluoSpheres RT	F8810	Invitrogen
red fluorescent microspheres $\varnothing = 100$ nm, carboxylate modified	FluoSpheres RT	F8801	Invitrogen
red fluorescent microspheres $\varnothing = 40$ nm, carboxylate modified	FluoSpheres RT	F8794	Invitrogen
red fluorescent microspheres $\varnothing = 20$ nm, carboxylate modified	FluoSpheres RT	F8786	Invitrogen
multi-colored microspheres $\varnothing = 100$ nm	TetraSpec	T7279	Invitrogen
green quantum dots, streptavidin modified	QD525 ITK	Q10041MP	Invitrogen
yellow quantum dots, carboxyl modified	QD565 ITK	Q21331MP	Invitrogen
orange quantum dots, carboxyl modified	QD585 ITK	Q21311MP	Invitrogen
red quantum dots, carboxyl modified	QD605 ITK	Q21301MP	Invitrogen
deep red quantum dots, carboxyl modified	QD655 ITK	Q21321MP	Invitrogen
other chemicals			
transfection reagent	FuGENE HD		Roche Diagnostics
gel for bead scans	Phytigel	P8169	Sigma-Aldrich
Buffers/cell culture media			
DMEM growth medium			Invitrogen
Hanks balanced salts solution			PAN-Biotech
microsphere dilution buffer: 10 mM Tris, pH 8.5			—

A.2. Cell culture protocols

Most of the cell culture works for the experiments (growing cells, transfection, plasmid preparations, cloning) were performed by Gabriele Müller.

A.2.1. Cell growth and transfection

Cell growth conditions: Adherent cells were grown in phenol red-free Dulbecco's modified eagle medium (DMEM), supplemented with 10% fetal calf serum and 1% glutamine. The atmosphere in the incubator was held at a constant level of 5% CO₂, humidified and temperature-stabilized to 37 °C.

Transfection protocol:

1. The growth medium was removed from the flask and the cells are washed with 5 ml Hank's balanced salts solution (HBSS).
2. Cells were trypsinized, by incubating them for ~ 1 min with 5 ml of Trypsin/EDTA solution. In order to stop the trypsinization process 10 ml of fresh DMEM (supplemented with 5% fetal calf serum) were added to the cells.
3. The cells were diluted 20-fold in fresh medium, seeded in new cell culture flask and incubated for another 24 h. For SPIM measurements the cells were seeded on small glass pieces in a 35 mm petri dish. For confocal measurements the cells were seeded into 8-well NUNC chambered cover glasses (No. 155411, Nunc, Rochester).
4. Cells were transfected 24 h after trypsination (step 3). Transfection with mammalian expression vectors was generally carried out with FuGENE HD transfection reagent, as proposed by the

manufacturer. The exact amounts of FuGENE and plasmid are listed in tables Tab. A.4 and Tab. A.5 on the following pages.

5. Before measurement the cells were grown for another 24 – 48 h.

protein	plasmid	amount of plasmid	transfection	cells	reference
eGFP monomer	pCMV-1xGFP	50 ng	45 μ l medium 4 μ l FuGENE HD	HeLa	[18]
mRFP1 monomer	pSV-mRFP	100 ng	– ” –	HeLa	
eGFP-2x (dimer)	pCMV-2xGFP	25 ng	– ” –	HeLa	[18]*
eGFP-3x (trimer)	pCMV-3xGFP	50 ng	– ” –	HeLa	[18]*
eGFP-4x (tetramer)	pCMV-4xGFP	25 – 100 ng	– ” –	HeLa, COS-7, CHO-K1, BHK, HEK-293, MDA-MB231	[18]*
eGFP-8x (octamer)	pCMV-8xGFP	75 ng	– ” –	HeLa	†
eGFP-mRFP1 fusion protein	pSV-eGFP-mRFP1	100 ng	– ” –	HeLa	[73, 268]
eGFP-PolyP-mRFP1 fusion protein with poly proline linker	pCMV-eGFP-P30-mRFP	100 ng	– ” –	HeLa	†
IREs: eGFP and mRFP1 monomers from a single plasmid	pCMV-eGFP-ires-mRFP1	100 – 140 ng	– ” –	HeLa	[73, 268]
cFos-eGFP + cJun-mRFP1	pSV-Fos-mRFP + pSV-cJun-mRFP	1000 ng + 1000 ng	45 μ l medium 6 μ l FuGENE HD	HeLa	[73, 268]
cFos $\Delta\Delta$ -eGFP + cJun $\Delta\Delta$ -mRFP1	pSV-Fos $\Delta\Delta$ -mRFP + pSV-cJun $\Delta\Delta$ -mRFP	1000 ng + 1000 ng	– ” –	HeLa	[73, 268]
Histon H1-YFP	pSV-H1.0-YFP	25 – 75 ng	45 μ l medium 4 μ l FuGENE HD	HeLa	[294]
Histon H2A-eGFP	pSV-H2A-eGFP	25 ng	– ” –	HeLa	[294]
Histon H2A-mRFP1	pSV-H2A-mRFP	25 – 75 ng	– ” –	HeLa	[294]
Histon H4-eGFP	pSV-H4-eGFP	25 – 75 ng	– ” –	HeLa	[294]
β -galactosidase	pCMV-Neo-LacZ-GFP	permanent		AT-1	[27]

* these plasmids were provided by Dr. M. M. Nalaskowski (university medical center Hamburg-Eppendorf)

† these plasmids were newly constructed by Gabriele Müller (DKFZ)

Table A.4. | Listing of the transfection protocols used for cytosolic and nucleic proteins. The amounts in the table are given for standard 35 mm petri dishes.

protein	plasmid	amount of plasmid	transfection	cells	reference
PMT-eGFP and PMT-mRFP1		200 ng + 400 ng	45 μ l medium 6 μ l PuGENE HD	CHO-K1, HeLa	[76]*
GFP-EGFR-mRFP1		1000 – 1500 ng	– ” –	CHO-K1, HeLa	[76]*

* these plasmids were provided by Dr. Thorsten Wohland (NUS, Singapore)

Table A.5. | Listing of the transfection protocols used for membrane proteins. The amounts in the table are given for standard 35 mm petri dishes.

A.2.2. Cell types

The following cell lines were used for experiments throughout this thesis

- AT-1: rat prostate adenocarcinoma cell
- BHK: baby hamster kidney cell
- CHO-K1: Chinese hamster ovary cell
- COS-7: transformed African green monkey kidney fibroblast cell
- HaCat B 10: humane keratinocyte cell [289]
- HEK-293: human embryonic kidney cell
- HeLa: human cervical carcinoma cell (provided by F. Rösl, DKFZ, Heidelberg, Germany)
- MDA-MB231: human breast carcinoma cell
- SK8/18: adrenal cortex carcinoma-derived SW13 cell [288]

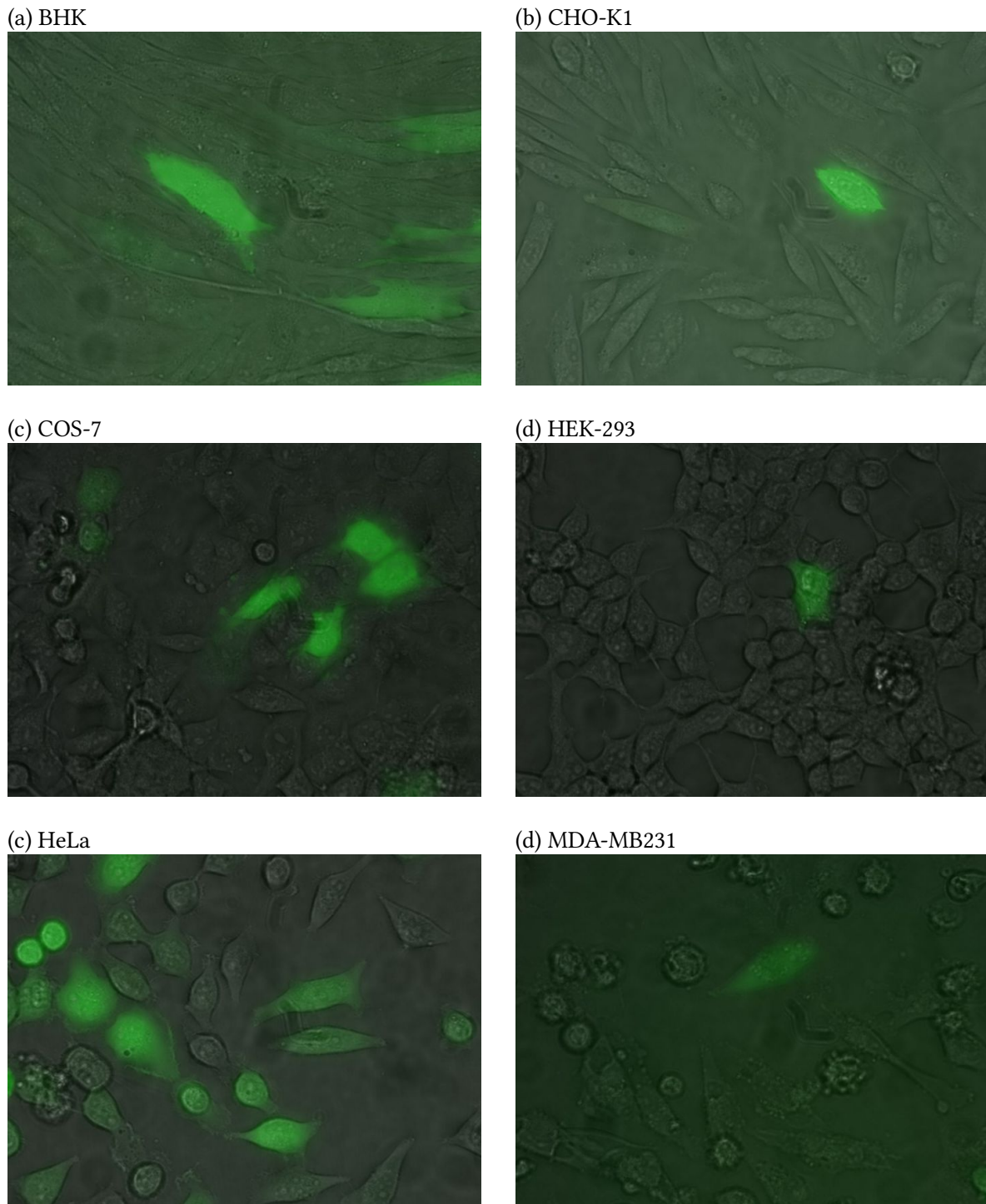


Figure A.1. | Combined transmission and fluorescence images of different cell lines, expressing eGFP-4x. The image width is 162 μm . All images were acquired on an epi-fluorescence microscope with a magnification of 40 \times on a Lumenera Infinity2-1R CCD camera. The images are contrast enhanced (power-law rescaling: $\gamma = 0.6$) and combined using COREL PHOTOPAINT.

A.3. SPIM sample mounting protocols

A.3.1. Preparation of sample bags for liquid samples

This section describes how the sample bags used to mount liquid samples in the SPIM sample chamber and briefly described in section 6.2.3, were made. they consist of LumoxFolie 25 M (Sarstedt AG & Co, [225]), a 25 μm thin plastic foil, which has the same refractive index as water. A soldering tweezer was modified and temperature regulated to 230 – 250 $^{\circ}\text{C}$ for this purpose. Powder-free latex gloves should be worn throughout the process to keep the foil clean and fat-free. The protocol is illustrated in Fig. A.2 and works as follows:

1. A ~ 5 cm long sleeve with the hydrophilic side inside is formed by bending a rectangular sheet around a 3 mm steel rod and heat-sealing the long, overlapping edge.
2. The sleeves are thoroughly washed with 70% ethanol and deionized water.
3. Each sleeve is heat-sealed at both ends and in the center, forming two independent air-filled pockets.
4. If an intermediate from step 3 proves to be airtight, it is cut into four equal pieces of $\sim 5 \times 10 \times 2 \text{ mm}^3$ in size, which are closed on three sides and open on the fourth.
5. For a measurement, 30 – 50 μl of the liquid sample are filled in and the last side is heat-sealed. If properly prepared, these sample bags may be stored and reused for months. At the welded edges they can be held by a self-closing tweezer and mounted in the sample chamber. Liquid sample

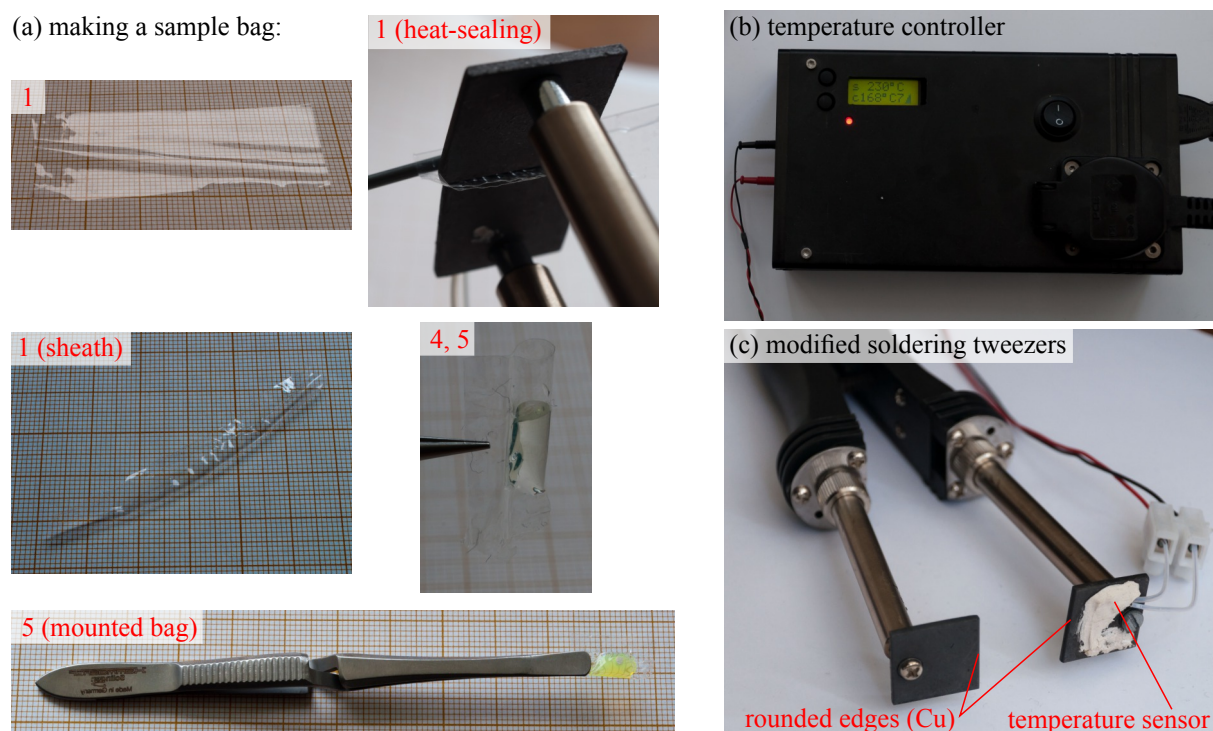


Figure A.2. | Illustration of the preparation of SPIM sample bags. (a) shows the actual process from a sheet of LumoxFolie, which is heat-sealed to form a sheath. Then small sample bags are formed which may be filled and held by a self-closing tweezer. (b) shows the controller built to control the temperature of a modified soldering tweezer, as shown in (c).

with QDots and microspheres were sonicated for 30 min in a bath sonicator, before they were filled into the sample bags. This helps to disperse them properly and reduces the number and size of aggregates.

A.3.2. Preparation of a gel cylinder for bead scans

For PSF determinations with z -scans, different beads were embedded in an 0.5% PhytaGel. The exact protocol was as follows:

1. Dissolving 200 mg PhytaGel in 40 ml of deionized water and add 400 μ l of a 10% stock solution of MgSO_4 .
2. Heat in the microwave until the PhytaGel has dissolved. Every few seconds, take the flask out of the oven and shake it, so the components mix well.
3. Let cool down to around 40 °C and mix with beads (e.g. 5 – 15 μ l of 100 nm-diameter TetraSpec Microsphere stock with 1 ml of gel) by vortexing the gel in an Eppendorf tube.
4. Cut the tip of a standard 1 ml syringe (inner diameter 4.6 mm) and draw up \sim 400 μ l of the fluid gel. Ensure that no air is trapped between the gel and the plug.
5. Let the gel solidify in the refrigerator for 5 min.

A.3.3. Preparation of cover slips for adherent cells

1. No. 3 glass cover glasses (thickness 0.28 – 0.32 mm) were cut into small pieces (size: \sim 5 \times 10 mm²) with a steel glass cutter.
2. The glass pieces were thoroughly washed in 70% ethanol or acetone to remove any remaining dirt.
3. In a second step the ethanol/acetone was removed by a second washing step in deionized water. The glass pieces are left to dry on low-lint cleaning paper.
4. Finally the glass pieces were sterilized before use.

B. Simulation software

B.1. Fluorescence correlation spectroscopy simulations

This software can simulate FCS and FCCS correlation curves for different focus geometries and is closely related to the FCS/FCCS theory as presented in chapter 5 and especially the modeling of fluorescence detection described in section 5.2. It starts from a set of N particle trajectories $\{\vec{r}_i(t)\}$, where i numbers the particles and $t = 1, 2, \dots$ numbers the equidistant timepoints with resolution Δt_{im} . The trajectories are either read from an external data file or are created internally by a configurable random walk. First $N_i \geq 1$ fluorophores are assigned to each particle, leading to an overall number of fluorophores

$$F = \sum_{i=1}^N N_i$$

fluorophores f , which are each characterized by the following set of properties (the functions $i(f)$ is the trajectory ID for every fluorophore f):

1. a position $\vec{r}_f(t) = \vec{r}_{i(f)}(t) + \Delta\vec{r}_f$, where $\vec{r}_{i(f)}(t)$ is the position of the particle and $\Delta\vec{r}_f$ is an arbitrary, but constant shift from this position. In the simplest case there is only one fluorophore per particle and $\Delta\vec{r}_f = 0$. Using $\Delta\vec{r}_f \neq 0$, moving finite-sized objects may be simulated that are e.g. labeled with a set of fluorophores on their surface or in their interior.
2. each fluorophore may be in one of S_f states. Each state may have different spectroscopic properties. The current state at time t is denoted by $s_f(t)$.
3. a wavelength-dependent absorption crosssection spectrum $\sigma_{\text{abs},i}(\lambda)$.
4. a normalized fluorescence spectrum $\eta_{\text{fl},f}(\lambda)$ and a fluorescence quantum yield $q_{\text{fluor},f,s_f(t)}$
5. a dipole orientation vector $\vec{p}_f(t)$ with $\|\vec{p}_f(t)\| = 1$.

The state trajectory $s_f(t)$ for each fluorophore either does not change (the default case), is read from an external file, or is simulated using a matrix of transition rates and a random decision in each simulation step. In this way photophysical blinking transitions may be simulated, if e.g. $s_f(t) \equiv 1$ is a bright state and $s_f(t) \equiv 2$ is a dark state with $q_{\text{fluor},f,2} = 0$. Also a simple bleaching process is implemented, by switching off (but never on again) a fluorophore with a certain low probability.

The simulation proceeds in steps of Δt_{sim} . For each time step and each focus in the simulation, first the expected number of fluorescence photons is calculated:

$$\overline{N}_{\text{phot}}(t) = \sum_{f=1}^F q_{\text{fluor},f,s_f(t)} \cdot \sigma_{\text{abs},i}(\lambda_{\text{ex}}) \cdot q_{\text{det}} \cdot \frac{\Delta t_{\text{sim}} \cdot I(\vec{r}_f(t))}{hc_0/\lambda_{\text{ex}}} \cdot \Omega(\vec{r}_f(t)) \cdot h_{\text{pol}}(\vec{p}_f(t)), \quad (\text{B.1.1})$$

where h is Planck's constant, c_0 is the velocity of light in vacuum and λ_{ex} is the excitation wavelength.

The shape of the illumination profile is described by the function $I(\vec{r})$ and the respective shape of photon collection efficiency by $\Omega(\vec{r})$. Several models are implemented for them:

1. **Gaussian:** The shapes of $I(\vec{r})$ and $\Omega(\vec{r})$ are cigar-like Gaussian functions with equal x - and y -width w_0 and z -width z_0 :

$$I(\vec{r}), \Omega(\vec{r}) \propto \exp\left(-2 \cdot \frac{x^2 + y^2}{w_0^2} - 2 \cdot \frac{z^2}{z_0^2}\right) \quad (\text{B.1.2})$$

2. **Gaussian beam:** The illumination/detection focus is described by a Gaussian beam, which has a lateral width $w(z)$ increasing with distance z from the focus and a Laurentzian shape in z -direction:

$$I(\vec{r}), \Omega(\vec{r}) \propto \left(\frac{w_0}{w(z)}\right)^2 \cdot \exp\left(-2 \cdot \frac{x^2 + y^2}{w^2(z)}\right), \quad \text{with } w(z) = w_0 \cdot \sqrt{1 + \left(\frac{z}{z_0}\right)^2} \quad (\text{B.1.3})$$

3. **Gaussian light sheet:** A simple model for a lightsheet is a Gaussian in z -direction, which does not depend on x or y :

$$I(\vec{r}) \propto \exp\left(-2 \cdot \frac{z^2}{z_0^2}\right) \quad (\text{B.1.4})$$

4. **Slit pattern light sheet:** To model the sidelobes observed in typical light sheets a slit function can be used:

$$I(\vec{r}) \propto \left(\frac{\sin(\pi \cdot z/z_0)}{\pi \cdot z/z_0}\right)^2 \quad (\text{B.1.5})$$

The first two patterns can be used for both, the illumination and detection foci, whereas the last two are designed to model the light sheet illumination.

The remaining influence of the detection process (signal loss at optical interfaces and filters, detector quantum efficiency, ...) is described by the factor

$$q_{\text{det}} = q_{\text{det},0} \cdot \frac{\int_{\lambda_{\text{det},\min}}^{\lambda_{\text{det},\max}} \eta_{\text{fl},f}(\lambda) \, d\lambda}{\int_0^{\infty} \eta_{\text{fl},f}(\lambda) \, d\lambda}, \quad (\text{B.1.6})$$

summarizing the loss of light due to optics and detector quantum efficiency $q_{\text{det},0}$, as well as the spectral width of the fluorescence detection window $\lambda_{\text{det},\min} \dots \lambda_{\text{det},\max}$. This detection window allows to also take into account crosstalk between two detection channels. The influence of the dipole direction $\vec{p}_f(t)$ and a possible laser polarization is modeled by the factor

$$h_{\text{pol}}(\vec{p}_f(t)) = (1 - \theta_{\text{pol}}) + \theta_{\text{pol}} \cdot (\vec{\epsilon}_{\text{ex}} \bullet \vec{p}_f(t))^2, \quad (\text{B.1.7})$$

where \bullet is a scalar product, $\theta_{\text{pol}} \in [0, 1]$ is the fraction of linear polarization of the excitation light source and $\vec{\epsilon}_{\text{ex}}$ (with $\|\vec{\epsilon}_{\text{ex}}\| = 1$) is the linear polarization direction of this light source.

From the average number of detected photons, the measured number of photons $N_{\text{det}}(t)$ is calculated, taking the detector statistics into account. In the simplest case of a photon counting detector, $N_{\text{det}}(t)$ is drawn from a Poissonian distribution with mean (and variance) $\overline{N}_{\text{phot}}(t)$. Other detection statistics are possible, such as a linear detector, where $N_{\text{det}}(t)$ is drawn from a Gaussian distribution with mean $\overline{G} \cdot \overline{N}_{\text{phot}}(t)$ and a variance comparable to Eq. (4.2.15):

$$\sigma_{\text{det}}^2 = \overline{G}^2 \cdot \mathcal{F}^2 \cdot N_{\text{det}}(t) + \sigma_{\text{read}}^2, \quad (\text{B.1.8})$$

where \bar{G} is the average detector gain, \mathcal{F}^2 the excess noise factor and σ_{read}^2 the read noise variance, summarizing all contributions, not depending on the number of incident photons. Also artifacts, such as a background intensity offset may be included in the detector simulation. Although intermediate results may be floating-point numbers, the finally detected number of photons (or ADU counts in a linear detector) is always an integer number.

Finally the time series $N_{\text{det}}(t)$ is post processed to yield count rate traces with arbitrary binning, auto- and cross-correlation functions (between different foci on the simulation) and other statistical properties. Also several test data sets are saved by the simulation program, such as particle MSDs, the raw detector statistics etc.

The complete program is split into modules that may be combined in different ways for a simulation. All these modules are either trajectory sources or sinks. In each time step first all sources generate a new set of fluorophore properties, e.g. by reading a new data set from a file or advancing a random walk simulation. The these new particle properties are forwarded to the sink objects, which simulate the actual detection process, as described above, or generate MSDs and other trajectory statistics. Every sink may be connected to several sources, and one source can feed several sinks. This can be used e.g. for simulations of fluorophore reservoir depletion, as in section 5.5.4, where a single trajectory source is fed into intermediate objects that simulate different bleaching rates on the same particle positions and finally detected by a set of identical sinks, which simulate FCS detection.

This software was initiated in the first year of the thesis and extended and improved in the following years. It was used to simulate different aspects of FCS/FCCS in several publications [82, 130–132].

B.2. Macromolecular crowding

To demonstrate the effect of macromolecular crowding on single-particle dynamics, a simple simulation software (“crowder2d_moleculardynamics”) was implemented in C++. The program was inspired by Ref. [23]. It integrates the overdamped Langevin equation for a set of spherical particles i with different radii r_i and masses m_i with a simple first-order Eulerian scheme with time step Δt and periodic boundary conditions:

$$\vec{x}_i(t + \Delta t) = \vec{x}_i(t) + \vec{\xi} + \Delta t \cdot \sum_{i \neq j} \frac{\vec{F}_{ij}}{6\pi\eta r_i} \quad \xi_k \sim \mathcal{N}(0, 2D_i\Delta t). \quad (\text{B.2.1})$$

Here η is the viscosity of the embedding medium. The vector $\vec{\xi}$ is a random vector, where each spacial component ξ_k is independently distributed according to a normal distribution with variance $2D_i\Delta t$ with a diffusion coefficient given by Einstein’s relation at temperature T :

$$D_i = \frac{k_B T}{6\pi\eta r_i}.$$

The repelling force \vec{F}_{ij} between two particles i and j is calculated using a softcore potential with cutoff radius r_c :

$$\vec{F}_{ij} = \begin{cases} F_0 \cdot \left(1 - \frac{\|\vec{x}_j - \vec{x}_i\| - r_i - r_j}{r_c}\right) \cdot \frac{\vec{x}_j - \vec{x}_i}{\|\vec{x}_j - \vec{x}_i\|} & \text{for } \|\vec{x}_j - \vec{x}_i\| - r_i - r_j < r_c \\ 0 & \text{else} \end{cases}. \quad (\text{B.2.2})$$

This definition leads to a linearly increasing force between any two particles, if their borders are closer than r_c . The force is depicted in Fig. B.1.

The simulation program follows these steps:

1. The particles are initialized by randomly drawing a mass or a radius from given distributions and then placing the particle without overlap in the simulation box. If a placement is not possible, a new mass and radius is drawn.
2. The simulation is equilibrated for a few thousand steps
3. The simulation is run for a given number of steps.
4. Time-averaged MSD curves are calculated from the trajectory of each particle. These are then averaged over groups of particles with comparable masses or radii.

To achieve good resolution for all numerical calculations, all distances were rescaled to nanometers. Typical simulation parameters are summarized in Tab. B.1.

The mass of each particle is estimated (in real units) by a reference particle with given mass m_{ref} and radius r_{ref} :

$$m_i = m_{\text{ref}} \cdot \begin{cases} r_i^2 / r_{\text{ref}}^2 & \text{in 2 dimensions} \\ r_i^3 / r_{\text{ref}}^3 & \text{in 3 dimensions} \end{cases} \quad (\text{B.2.3})$$

Typically, values resembling bovine serum albumin (BSA) were chosen for the reference particles: $m_{\text{ref}} = 66 \text{ kDa}$ and $r_{\text{ref}} = 2 \text{ nm}$.

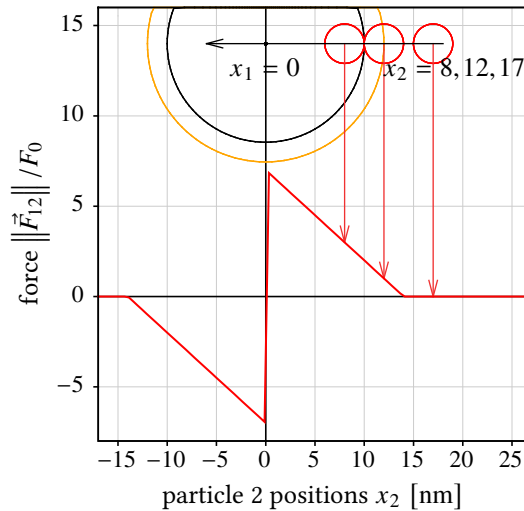


Figure B.1. | Softcore force between two particles, calculated for parameters $r_c = 2 \text{ nm}$, $r_1 = 10 \text{ nm}$ and $r_2 = 2 \text{ nm}$. Particle 1 is fixed at position $x_1 = 0$ and sketched in black. Particle 2 moves (position x_2 on x -axis) and is sketched in red. The critical radius around particle 1 is shown in orange.

parameter	symbol	value
simulation box dimension	L	500 nm
time step	Δt	10 ns
viscosity	η	5 mPa · s
temperature	T	283 K
interaction strength	F_0	$6\pi\eta \cdot 10 \mu\text{m}^2/\text{s}$
critical interaction radius	r_c	3 nm
reference particle radius (BSA)	r_{ref}	2 nm
reference particle mass (BSA)	m_{ref}	66 kDa
particle radius limits		$1 \text{ nm} \leq r_i \leq L/5$
equilibration steps	N_{init}	2000
simulation steps	N_{sim}	$10^5 \dots 10^7$

Table B.1. | Typical parameters for molecular crowding simulations.

B.3. Numerical integration for the PSF of a microscope

As described in section 3.1 and Ref. [158], the PSF of a fluorescence microscope can be estimated as:

$$\text{PSF}(\vec{r}) = |h(\vec{r})|^2,$$

$$\text{with: } h(u, v) = -\frac{2\pi i}{\lambda} \cdot \frac{\text{NA}^2}{n^2} \cdot A_0 \cdot e^{i\text{NA}^2 u/n^2} \cdot \int_0^1 J_0(v\rho) \cdot e^{-iu\rho^2/2} \cdot \rho \, d\rho,$$

$$u \equiv u(z) = \frac{2\pi\text{NA}^2}{n\lambda} \cdot z,$$

$$v \equiv v(x, y) = \frac{2\pi\text{NA}}{\lambda} \cdot \sqrt{x^2 + y^2}.$$

This integral can be solved numerically (up to prefactors) using the MATLAB R2013b code below:

```
function [ out ] = born_wolf_psf_integral( x, y, z, NA, lambda, n )

f = 300;
a = f .* NA / n;

u = 2 * pi * NA * NA * z / lambda / n;
v = 2 * pi * NA * sqrt( x.^2 + y.^2 ) / lambda;

F=@(rho) rho .* besselj(0, v .* rho) .* exp(-1i .* u .* rho .* rho ./ 2);
out=abs(integral(F, 0, 1)).^2;

end
```

B.4. Beam propagation method

The “split step beam propagation method” is used to calculate the solution of the paraxial wave equation in a medium with an arbitrary refractive index distribution $n \equiv n(\vec{r})$. A detailed description can be found in Refs. [305, 306]. The skalar wave equation is given by [178]:

$$\nabla^2 U(\vec{r}, t) - \frac{n^2}{c_0^2} \cdot \frac{\partial^2 U(\vec{r}, t)}{\partial t^2} = 0. \quad (\text{B.4.1})$$

One solution of this equation is the monochromatic plane wave with angular frequency ω , wavelength λ and vacuum wavevector $k_0 = \omega/c_0$:

$$U(\vec{r}, t) = A(\vec{r}) \cdot e^{i\omega t} \cdot e^{-ik_0 z}, \quad \text{with } k_0 = \frac{\omega}{c_0} = \frac{2\pi}{\lambda}. \quad (\text{B.4.2})$$

Plugging this solution into Eq. (B.4.1) yields:

$$\vec{\nabla}_{\perp}^2 A + \left(\frac{\partial^2}{\partial z^2} - 2ik_0 \frac{\partial}{\partial z} - k_0^2 \right) A + n^2 k_0^2 A = 0 \quad \text{with } \vec{\nabla}_{\perp}^2 = \frac{\partial^2}{\partial x^2} + \frac{\partial^2}{\partial y^2}. \quad (\text{B.4.3})$$

The paraxial approximation demands that the derivative $\partial A(\vec{r})/\partial z$ changes slowly over the distance of one wavelength λ , from which follows [178]:

$$\frac{\partial^2 A}{\partial z^2} \ll k_0 \cdot \frac{\partial A}{\partial z} = 2\pi \cdot \frac{1}{\lambda} \cdot \frac{\partial A}{\partial z}.$$

Using this result Eq. (B.4.3) can be further simplified, yielding a differential equation, which describes the propagation of the amplitude distribution $A(\vec{r})$:

$$\frac{\partial A}{\partial z} = \frac{1}{2ik_0} \cdot \vec{\nabla}_{\perp}^2 A + \frac{n^2 - n_0^2}{2i} \cdot k_0 \cdot A. \quad (\text{B.4.4})$$

The solution of this differential equation can formally be written as:

$$\begin{aligned} A(x, y, z) &= \exp\left(\frac{z}{2ik_0} \cdot \vec{\nabla}_{\perp}^2 + \frac{n^2 - 1}{2i} \cdot k_0 z\right) A(x, y, 0) = \\ &= \underbrace{\left[\exp\left(\frac{z}{2ik_0} \cdot \vec{\nabla}_{\perp}^2\right)\right]}_{=: e^{\hat{H}z}} \cdot \underbrace{\left[\exp\left(\frac{n^2 - 1}{2i} \cdot k_0 z\right)\right]}_{=: e^{\hat{G}z}} A(x, y, 0). \end{aligned} \quad (\text{B.4.5})$$

As shown by the underbraces, this can be interpreted as the sequential application of two differential operators $e^{\hat{H}z}$ and $e^{\hat{G}z}$. As stated in Refs. [305, 306] these operators do not commute, so the order of application is of importance.

The solution Eq. (B.4.5) can be used directly to propagate an arbitrary initial field distribution $A(x, y, 0)$ through an arbitrary refractive index distribution $n(x, y, z)$. In addition using, that derivatives can be expressed in a simple form in Fourier space (see appendix C.1, especially equation Eq. (C.1.6)), the following stepping algorithm can be devised [305, 306]:

1. Fourier transform the field at z :

$$\tilde{A}(k_x, k_y, z) = \mathcal{F}_{x,y} [A(x, y, z)] \quad (\text{B.4.6})$$

2. propagate the plane wave in Fourier space:

$$\tilde{A}(k_x, k_y, z + \Delta z) = \tilde{A}(k_x, k_y, z) \cdot \exp\left(\frac{i \cdot (k_x^2 + k_y^2)}{2k_0} \cdot \Delta z\right) \quad (\text{B.4.7})$$

3. backtransform the field at $z + \Delta z$:

$$A'(x, y, z + \Delta z) = \mathcal{F}_{x,y} [\tilde{A}(k_x, k_y, z + \Delta z)] \quad (\text{B.4.8})$$

4. apply the second operator, representing the changing refractive index distribution:

$$A(x, y, z + \Delta z) = A'(x, y, z + \Delta z) \cdot \exp\left(\frac{n^2 - 1}{2i} \cdot k_0 \cdot \Delta z\right). \quad (\text{B.4.9})$$

5. set:

$$z \leftarrow z + \Delta z \quad (\text{B.4.10})$$

and return to step 1 to calculate the next propagation step.

This algorithm calculates the (scalar) electrical field distribution $A(x, y, z)$, from which the full field distribution is given by Eq. (B.4.2). Usually the light intensity distribution $I(x, y, z)$ is of interest, not the electrical field distribution. The intensity can be calculated as

$$I(\vec{r}) = |A(\vec{r})|^2. \quad (\text{B.4.11})$$

Note that the method, presented here, can only calculate forward scattering, but not backward scattering. Still it is useful for cases like scattering cell organelles in a lightsheet illumination setup, as discussed in section 3.3.3 or intensity distributions in microlenses, as shown in section 4.2.2.

This algorithm was implemented for the 2-dimensional case of the xz -plane using MATLAB R2013b:

```
function [ E, xx, zz ] = beam_propagation1d( n, Nz, E0, dx, wavelength)
%beam_propagation1d( n, Nz, E0, dx, wavelength) propagate an scalar field
%
%      electrical distribution a medium of varying refractive index
%
%  n(x,z):      refractive index distribution
%  Nz:          number of steps to iterate
%  E0:          initial field distribution
%  dx:          step size in x- and z-direction
%  wavelength:  wavelength if the monochromatic light

% vacuum wave vector
k0=2*pi/wavelength;
% point in x-direction
Nx=length(E0);
% k_x wavevectors, defining fourier space
kvec=(2*pi*linspace(-0.5,0.5,Nx)*Nx/(Nx*dx))';
% x positions definig real space
xx=((-(Nx-1)/2*dx):dx:((Nx-1)/2*dx))-1/2*dx;
% z-positions
zz=(1:Nz)*dx;

% initiate scalar field
E=ones(Nx, Nz, 'like', 1+1i);
E(:,1)=E0;
E(:,2)=E0;

% propagate field
for z=2:Nz
    nfac=exp(-0.5i.*k0.*(n(:,z).^2-1).*dx);
    kfac=exp(1i*kvec.^2.*dx./k0);
    E(:,z)=ifft(fft(E(:,z-1)).*fftshift(kfac)).*nfac;
end
end
```


C. Formulary

C.1. Fourier transform

Definition: The **Fourier transform** of a L^2 function $f(t)$ is defined as

$$\tilde{f}(\omega) = \mathcal{F}_t [f(t)] (\omega) := \int_{-\infty}^{\infty} f(t) \cdot e^{-i\omega t} dt. \quad (\text{C.1.1})$$

$$f(t) = \mathcal{F}_\omega^{-1} [\tilde{f}(\omega)] (t) := \frac{1}{2\pi} \cdot \int_{-\infty}^{\infty} \tilde{f}(\omega) \cdot e^{i\omega t} dt. \quad (\text{C.1.2})$$

The Fourier transform has some interesting properties:

- **Linearity:**

$$\mathcal{F}_t [a \cdot f(t) + b \cdot g(t)] (\omega) = a \cdot \tilde{f}(\omega) + b \cdot \tilde{g}(\omega) \quad (\text{C.1.3})$$

- **Shift:**

$$\mathcal{F}_t [f(t - \tau)] (\omega) = e^{-i\tau\omega} \cdot \tilde{f}(\omega) \quad (\text{C.1.4})$$

$$\mathcal{F}_t [e^{i\kappa t} \cdot f(t)] (\omega) = \tilde{f}(\omega - \kappa) \quad (\text{C.1.5})$$

- **Differentiation:**

$$\mathcal{F}_t \left[\frac{d^n f}{dt^n} \right] (\omega) = (i \cdot \omega)^n \cdot \mathcal{F}_t [f] (\omega) = (i \cdot \omega)^n \cdot \tilde{f}(\omega) \quad (\text{C.1.6})$$

Some common Fourier transforms (see e.g. [307]):

$$\mathcal{F}_t [e^{-\alpha \cdot t^2}] (\omega) = \sqrt{\frac{\pi}{\alpha}} \cdot e^{-\omega^2/(4\alpha)} \quad (\text{C.1.7})$$

$$\mathcal{F}_t [e^{-\alpha \cdot |t|}] (\omega) = \frac{2\alpha}{\alpha^2 + \omega^2} \quad (\text{C.1.8})$$

$$\mathcal{F}_t [\delta(t - t_0)] (\omega) = e^{-i\omega t_0} \quad (\text{C.1.9})$$

C.2. Convolution

Definition: The convolution of two functions $f(t)$ and $h(t)$ is defined as:

$$(f \otimes h)(\tau) := \int_{-\infty}^{\infty} f(t) \cdot h(t + \tau) dt. \quad (\text{C.2.1})$$

Convolution Theorem: The convolution has a close relation to the Fourier transform, which is expressed in the convolution theorem:

$$(f \otimes h)(\tau) = \mathcal{F}^{-1} [\mathcal{F}[f] \cdot \mathcal{F}[h]]. \quad (\text{C.2.2})$$

C.3. Statistical measures

Pearson's Correlation Coefficient: The Pearson's Correlation Coefficient is a measure of the linear dependence between two sets of measurements X and Y . It is defined as:

$$r(X, Y) \equiv r_{X, Y} = \frac{\langle (X - \langle X \rangle) \cdot (Y - \langle Y \rangle) \rangle}{\sqrt{\text{Var}(X)} \cdot \sqrt{\text{Var}(Y)}}, \quad (\text{C.3.1})$$

where average and variance are defined as:

$$\langle X \rangle = \frac{1}{N} \sum_i X_i \quad \text{and} \quad \text{Var}(X) = \langle (X - \langle X \rangle)^2 \rangle$$

C.4. Recalibration of diffusion coefficients to a different temperature

The Einstein relation Eq. (1.3.3) (p. 7) was used to recalibrate diffusion coefficients D_1 from one temperature and solvent ($T_1, \eta_{\text{visc}, 1}$) to a different temperature and solvent ($D_0, T_0, \eta_{\text{visc}, 0}$):

$$\frac{D_0}{D_1} = \frac{T_0}{T_1} \cdot \frac{\eta_{\text{visc}, 1}}{\eta_{\text{visc}, 0}}. \quad (\text{C.4.1})$$

Often the diffusion coefficients were recalibrated to the standard conditions of $T = 293 \text{ K}$ and water as a solvent. Then D_0 is also denoted as $D_{20^\circ\text{C}, \text{W}}$. The viscosity of water between 0°C and 100°C can be approximated by approximations like

$$\eta_{\text{visc}, \text{W}}(T) = A \cdot 10^{B/(T-C)}, \quad \text{with } A = 2.41 \cdot 10^{-5} \text{ Pa} \cdot \text{s}, B = 247.8 \text{ K}, C = 140 \text{ K} \quad (\text{C.4.2})$$

The viscosity of an aqueous solution of known composition can be estimated as described in Ref. [308] from tabulated viscosity data (e.g. from [309]).

In many of the live-cell measurements presented in this thesis cases, Eq. (C.4.1) was used to only recalibrate the temperature. The medium (e.g. the cytosol) was not corrected. This is possible, if it is assumed, that the general scaling of $\eta_{\text{visc}}(T)$ is proportional to that of water, i.e. $\eta_{\text{visc}}(T) = \eta_{\text{rel}} \cdot \eta_{\text{visc}, \text{W}}(T)$. Then Eq. (C.4.1) can be reformulated to:

$$\frac{D_0}{D_1} = \frac{T_0}{T_1} \cdot \frac{\eta_{\text{visc}, \text{W}}(T_1)}{\eta_{\text{visc}, \text{W}}(T_0)}, \quad (\text{C.4.3})$$

which can be evaluated using Eq. (C.4.2).

C.5. Estimation of diffusion coefficients for particles of different geometries

In section 1.3.1 the Einstein relation was introduced, which allows to estimate the diffusion coefficient of spherical particles of radius R_h in a solvent with viscosity η_{visc} at an absolute temperature T :

$$D = \frac{k_B \cdot T}{6\pi \cdot \eta_{\text{visc}} \cdot R_h}. \quad (\text{1.3.3})$$

Variants of this equation exist, which allow to also estimate D for more complex particle geometries. These have the general form

$$D = \frac{k_B \cdot T}{6\pi \cdot \eta_{\text{visc}} \cdot F_p \cdot R_e}, \quad (\text{C.5.1})$$

where R_e is an effective hydrodynamic radius of the particles and the Perrin factor F_p corrects for the changed geometry. Relations for R_e and F_p have been published for different particle geometries:

- **ellipsoids with rotation axis diameter a and perpendicular axis diameter b :** Using $p = a/b$ and $q = 1/p$ the effective radius and the Perrin factor are [310–313]:

$$R_e = (a \cdot b^2)^{1/3} \quad (\text{C.5.2})$$

$$F_p = \begin{cases} \frac{\sqrt{1-q^2}}{q^{2/3} \cdot \ln \left[\left(1 + \sqrt{1-q^2} \right) / q \right]} & \text{for } p > 1 \\ \frac{\sqrt{q^2-1}}{q^{2/3} \cdot \tan^{-1} \left[\sqrt{q^2-1} \right]} & \text{for } p < 1 \end{cases} \quad (\text{C.5.3})$$

- **cylinder with diameter d_{cyl} and length l_{cyl} :** Using $p = l_{\text{cyl}}/d_{\text{cyl}}$ and $q = 1/p$ the effective radius and the Perrin factor are [311, 312]:

$$R_e = \left(\frac{3}{4p^2} \right)^{1/3} \cdot \frac{l_{\text{cyl}}}{2} \quad (\text{C.5.4})$$

$$F_p = 1.0304 + 0.0193 \cdot x + 0.06229 \cdot x^2 + 0.00476 \cdot x^3 + 0.00166 \cdot x^4 + 2.66 \cdot 10^{-6} \cdot x^5, \quad \text{with } x \equiv \ln[p] \quad (\text{C.5.5})$$

Nomenclature

Constants

c_0	speed of light in vacuum, $c_0 = 299792458$ m/s [314]
k_B	Boltzman's constant $k_B = 1.3806488 \cdot 10^{-23}$ J/K [314]
N_A	Avogadro's number $N_A = 6.02214129 \cdot 10^{23}$ mol ⁻¹ [314]
q_e	elementary charge, $q_e = 1.602176565 \cdot 10^{-19}$ C [314]
$h, \hbar = h/(2\pi)$	Planck constant, $h = 6.62606957 \cdot 10^{-34}$ Js [314]
R	molar gas constant $R = 8.3144621$ J/(K · mol) [314]

Mathematical Notation

$(f \otimes h)(\cdot)$	convolution of functions $f(\cdot)$ and $h(\cdot)$ see sec. C.2
$ x $	absolute value of x
~ 123.456	approximately 123.456
$\mathbb{N} = \{1, 2, \dots\}, \mathbb{N}_0 = \mathbb{N} \cup \{0\}$	set of positive integer numbers (with or without 0)
$\delta(\cdot)$	Dirac's δ -distribution
\hat{f}	statistical estimator for the quantity f
$O(f) \ni g$	The function $g(\cdot)$ grows considerably faster than function $f(\cdot)$ (Landau O-notation)
$\lfloor \cdot \rfloor$	lower Gaussian brackets: rounding to the next lower integer number
$\langle \cdot \rangle$	average
$\langle f(t) \rangle_t$	average over variable t , e.g. for time t : $\langle f(t) \rangle_t = \lim_{T \rightarrow \infty} \int_0^T f(t) dt$
$\ \vec{x}\ $	Euclidean norm (length) of vector \vec{x}
$\tilde{f}(\omega) = \mathcal{F}_t [f(t)](\omega)$	Fourier transform of function $f(t)$ see sec. C.1
$\text{Var}(X)$	variance of random variable X
$\vec{\nabla}$	gradient operator $\vec{\nabla} = \left(\frac{\partial}{\partial x}, \frac{\partial}{\partial y}, \dots \right)^t$
$\vec{\nabla}^2$	Laplace operator $\vec{\nabla}^2 = \left(\frac{\partial^2}{\partial x^2} + \frac{\partial^2}{\partial y^2} + \dots \right)$
$f(t) = \mathcal{F}_\omega^{-1} [\tilde{f}(\omega)](t)$	inverse Fourier transform of function $\tilde{f}(\omega)$, see sec. C.1
$J_\nu(x)$	Bessel function of first kind, with order ν , evaluated at x
q_p , e.g. $q_{25\%}, q_{75\%}$	p -quantile of a random number distribution, $q_{25\%}$ and $q_{75\%}$ are the lower and upper quartile
$r(X, Y), r_{X, Y}$	Pearson's correlation coefficient see Eq. (C.3.1)
$x \sim \mathcal{N}(\bar{x}, \sigma^2)$	random variable x is normally distributed with mean \bar{x} and variance σ^2

Variables

\mathcal{A}_{ADC}	conversion factor between electrons and analog-to-digital converter values (ADUs) in units of ADU/electron
$A_{\text{eff}}, A_{\text{eff}, \gamma}$	effective area laterally spanned by a FCS focus (in color channel γ) <i>see Eq. (5.3.27)</i>
$p_{\text{AP}}(\tau)$	afterpulsing probability after a delay τ <i>see sec. 5.5.3</i>
\mathbb{S}	set of molecular species in FCS theory
β_{AP}	exponent of a power-law afterpulsing decay <i>see sec. 5.5.3</i>
χ^2	(normalized) sum of squared deviations in a model fit <i>see Eq. (7.1.16)</i>
$\kappa_{\gamma\rho}$	spectral crosstalk between the microscope detection channels γ and ρ . . <i>see Eq. (5.4.11)</i>
d_{Det}	half aperture diameter: detection objective
d	dimensionality of a random walk <i>see Eq. (1.3.2)</i>
\emptyset	diameter of a circle or sphere
d_{∞}	length of infinity space in an infinity corrected microscope
d_{LS}	$1/e^2$ half depth of field of a light sheet
d_{Obj}	half aperture diameter: any objective
d_{Proj}	half aperture diameter: light sheet projection objective
d_{SPAD}	circular SPAD diameter <i>see sec. 4.1.3</i>
d_{TL}	half aperture diameter: tube lens
$D_{20^\circ\text{C}, \text{W}}$	diffusion coefficient of a substance, dissolved in water at a temperature of 20°C
$\eta_{\text{fl}, \chi}(\lambda)$	fluorescence emission spectrum of fluorophore χ
$\eta_{\text{det}}, \eta_{\text{det}, \gamma}$	detection efficiency (in channel γ)
$\eta_{\gamma, \chi}$	fluorescence detection efficiency (of species χ in channel γ)
\mathcal{F}^2	excess noise parameter of an analog detector <i>see Eq. (4.2.7)</i>
ε_{abs}	extinction coefficient
$\varepsilon_{\text{abs}, \chi}(\lambda)$	fluorescence absorption (extinction) spectrum of fluorophore χ
$F_{\text{back}}, F_{\text{back}, \gamma}$	background signal in fluorescence detection (in channel γ)
f_{CL}	focal length: cylindrical lens <i>see Fig. 6.3</i>
f_{DO}	focal length: detection objective
FF	fill factor of an image sensor pixel (active are / pixel area) <i>see Eq. (4.1.5)</i>
$f_{\text{L1}}, f_{\text{L2}}$	focal length: relay lenses L1 and L2 in the SPIM light sheet shaping <i>see Fig. 6.3</i>
f_{Obj}	focal length: objective lens
f_{PO}	focal length: light sheet projection objective <i>see Fig. 6.3</i>
f_{TL}	focal length: tube lens
$\text{FWHM}_{\text{microscope}, xy}$	lateral full width at half maximum of the PSF of a given microscope (perpendicular to optical axis)
$\text{FWHM}_{\text{microscope}, z}$	longitudinal full width at half maximum of the PSF of a given microscope (along optical axis)
Γ	radiative decay rate of the excited state in molecular fluorescence <i>see Eq. (2.1.3)</i>
Γ, Γ_{χ}	generalized diffusion coefficient in anomalous diffusion (of species χ)
h_{LS}	$1/e^2$ height of a light sheet

I_{phot}	signal photo current
λ_{eff}	effective wavelength in a confocal microscope see Eq. (3.2.2)
λ_{fl}	fluorescence light wavelength
λ_{ill}	illumination light wavelength in a microscope
l_p	persistence length of a polymer
IC	image cross-correlation coefficient between two images see Eq. (6.1.6)
$\langle \Delta r \rangle(\tau)$	mean displacement at lag time τ
M_{xy}	lateral magnification of an optical system see Eq. (3.1.3)
MSD(τ)	mean squared displacement at lag time τ
NA	numerical aperture see Eq. (3.1.6)
N_{back}	background signal in an image sensor
N_{dark}	dark count of an image sensor pixel in electrons
\dot{N}_{dark}	rate of dark photons in an image sensor
OD	optical density of a filter, transmission: $T = 10^{-OD}$
\bar{G}	average gain of an analog detector see sec. 4.2
p_{AB}	describes the relative dimer concentration see Eq. (9.3.1)
p'_{AB}	alternative relative dimer concentration see Eq. (9.2.1)
Φ	photon flux
$\phi_{\chi, \chi'}(\vec{r}, \vec{r}', \tau)$	van-Hove self correlation function of two species χ and χ' , positions \vec{r} and \vec{r}' at a time lag τ see Eq. (5.3.8), (5.3.12)
a	pixel size of image sensor in the object plane ($a = a_{\text{sensor}}/M$, if M is the magnification of the optics)
PSF(\vec{r})	general point spread function of a microscope
PSF _{det} (\vec{r})	detection point spread function of a microscope
PSF _{ill} (\vec{r})	illumination point spread function of a microscope
$q_{\text{fluor}}, q_{\text{fluor}, \gamma, \chi}$	fluorescence quantum yield (of species χ in channel γ)
q_{gr}	describes the relative cross-correlation amplitude see Eq. (9.1.1)
\mathcal{R}_{ADC}	resolution of an analog to digital converter in bits
R_h	hydrodynamic radius of a particle
a_{sensor}	image sensor pixel pitch
$\sigma_{\text{abs}}, \sigma_{\text{abs}, \gamma, \chi}$	absorption crosssection (of species χ in channel γ)
σ_{ADC}^2	quantization noise by the ADC in a photodetector see Eq. (4.2.13)
σ_{back}^2	variance of the background signal of a photodetector
σ_{cic}^2	variance of the clock-induced charges of a CCD image sensor see Eq. (4.2.12)
σ_{dark}^2	variance of the dark current signal of a photodetector
σ_{photon}^2	photon shot noise variance in a photodetector
σ_{read}^2	variance of the readout noise of an image sensor
SNR	signal-to-noise ratio
τ_{AP}	decay time of an exponential afterpulsing decay see sec. 5.5.3

τ_B	(exponential) decay time of a fluorophore bleaching decay see Eq. (5.5.15)
$\tau_D, \tau_{D,\chi}$	diffusion correlation time (of species χ) see Eq. (5.3.22) & (5.3.26)
τ_F	flow correlation time see Eq. (5.3.41)
τ_{fl}	fluorescence lifetime see Eq. (2.1.3)
τ_{min}	minimum lag time of correlation
τ_T	triplet correlation time
Δt_{exp}	exposure time
Δt_{frame}	frame repetition time of an image sensor
θ_T	equilibrium fraction of particles in a triplet state
Δt_{read}	readout time of an image sensor
$\vartheta = T - 273.15 \text{ K}$	temperature in $^{\circ}\text{C}$
U_{bias}	bias voltage of a semiconductor photodetector or (reverse) bias voltage of a SPAD . see sec. 4.1.1
U_{break}	breakdown voltage of a SPAD see sec. 4.1.1
$V_{eff}, V_{eff,\gamma}$	effective focal volume in FCS (in color channel γ). see Eq. (5.3.4)
$U_{excess} = U_{bias} - U_{break}$	excess bias voltage of a SPAD
η_{visc}	dynamic viscosity
V_{obs}	observation volume
w_{Laser}	$1/e^2$ half width of a laser beam
w_{LS}	$1/e^2$ half width of a light sheet
w_{obs}	size (diameter) of the observation volume
$B(x, y; t)$	background image series in an FCS/FCCS measurement see sec. Eq. (7.1.2)
$c(\vec{r}, t)$	particle concentration at position \vec{r} and time t
D, D_{χ}	diffusion coefficient (of species χ) see Eq. (1.4.1),(1.3.3),(1.3.2)
$f(t)$	function describing a fluorophore bleaching decay see sec. 5.5.4
$F(x, y; t)$	full image series in an imaging FCCS data acquisition
$F_{\gamma}(t), \delta F_{\gamma}(t)$	fluorescence time trace and fluctuations from color channel γ in FCS/FCCS
$F_{\gamma}(t; x, y), \delta F_{\gamma}(t; x, y)$	fluorescence time trace and fluctuations of a pixel (x, y) from color channel γ in imaging FCS see Eq. (5.2.9),(5.2.11)
$F_{\gamma}^{(c)}(t)$	bleach-corrected fluorescence time trace from color channel γ in FCS/FCCS see sec. 5.5.4
F_B	background fluorescence signal
$g(\tau)$	normalized autocorrelation function in FCS see Eq. (5.1.2)
$g_{\gamma\rho}(\tau; x, y)$	normalized two-color cross-correlation function of a pixel (x, y) in imaging FCS/imaging FCCS
$h_{pixel}(\vec{r})$	characteristic function of a camera pixel see Eq. (5.2.5)
I_{ADC}	signal from an image sensor in analog-to-digital converter values (ADUs)
k_{nr}	non-radiative decay rate of the excited state in molecular fluorescence ... see Eq. (2.1.3)
$L(x, y), L(x, y; t)$	single left half image and image series acquired with a dual-view optics
N_{cic}	clock-induced charges in a CCD image sensor per cycle/frame see Eq. (4.2.12)
N_e	number of detected photo-electrons in an image sensor

N_e	number of secondary electrons in a photodetector
$R(x, y), R(x, y; t)$	single right half image and image series acquired with a dual-view optics
T	absolute temperature
T_B	number of frames in a background measurement $B(x, y; t)$ for imaging FCCS
T_F	number of frames in an imaging FCCS acquisition $F(x, y; t)$
w_γ	lateral $1/e^2$ -half width of a Gaussian PSF in FCS theory
z_γ	axial $1/e^2$ -half width of a Gaussian PSF in FCS theory

Glossary

β -gal β -galactosidase.

ADC analog-to-digital converter.

ADU analog-to-digital converter unit.

AP-1 activator protein 1.

AT-1 rat prostate adenocarcinoma cell.

ATP adenosine triphosphate.

BHK baby hamster kidney cell.

BM Brownian motion.

BSA bovine serum albumin.

CAD computer aided design.

CCD charge-coupled device.

CHO-K1 Chinese hamster ovary cell.

CMOS complementary metal oxide semiconductor.

COS-7 transformed African green monkey kidney fibroblast cell.

CPU central processing unit.

CSV comma separated values.

DBD DNA binding domain.

DCR dark count rate.

DMEM Dulbecco's modified eagle medium.

DNA deoxyribonucleic acid.

DPSS diode-pumped solid state.

dsDNA double-stranded deoxyribonucleic acid.

eGFP enhanced green fluorescent protein.

EGFR epidermal growth factor receptor.

EMCCD electron-multiplying charge-coupled device.

eYFP enhanced yellow fluorescent protein.

FCCS fluorescence cross-correlation spectroscopy.

FCS fluorescence correlation spectroscopy.

FITC fluorescein isothiocyanate.

FLIM fluorescence lifetime imaging microscopy.

FOV field-of-view.

FPGA field programmable gate array.

FRAP fluorescence recovery after photo bleaching.

FRET Förster resonance energy transfer.

HaCat B 10 humane keratinocyte cell.

HBSS Hank's balanced salts solution.

HEK-293 human embryonic kidney cell.

HeLa human cervical carcinoma cell.

ICS image correlation spectroscopy.

IF intermediate filament.

imaging FCCS imaging fluorescence cross-correlation spectroscopy.

imaging FCS imaging fluorescence correlation spectroscopy.

IQR interquartile range.

IRLS iteratively reweighted least squares.

iSPIM inverted selective plane illumination microscope.

ITIR-FCS imaging total internal reflection fluorescence correlation spectroscopy.

LBD ligand binding domain.

LED light emitting diode.

LM fit Levenberg-Marquardt fit.

LSFM light sheet fluorescence microscope.

MaxEnt maximum entropy data evaluation.

MDA-MB231 human breast carcinoma cell.

MDE molecular detection efficiency function.

MIS metal-insulator-semiconductor.

MOSFET metal oxide semiconductor field-effect transistor.

mRFP1 monomeric red fluorescent protein.

MSD mean squared displacement.

mSPIM multi-directional selective plane illumination microscopy.

NA numerical aperture.

NLS nuclear localization sequence.

NPC nuclear pore complex.

NR nuclear receptor.

OPFOS orthogonal-plane fluorescence optical sectioning.

OPM oblique plane microscopy.

PCB printed circuit board.

PCR polymerase chain reaction.

PDE partial differential equation.

PMT plasma membrane targeting sequence.

PSF point spread function.

PTFE polytetrafluoroethylene.

QDot quantum dot.

RAM random access memory.

RAR retinoic acid receptor.

RNA ribonucleic acid.

ROI region of interest.

RXR retinoid X receptor.

- sCMOS** scientific complementary metal oxide semiconductor camera.
- SK8/18** adrenal cortex carcinoma-derived SW13 cell.
- SLM** scanning light sheet microscope.
- SNR** signal-to-noise ratio.
- SOFI** super-resolution optical fluctuation imaging.
- SPAD** single-photon avalanche diode.
- SPIM** selective plane illumination microscope.
- SPIM-FCCS** single plane illumination fluorescence cross-correlation spectroscopy.
- SPIM-FCS** single plane illumination fluorescence correlation spectroscopy.
- SPT** single particle tracking.
- TDC** time-to-digital converter.
- TF** transcription factor.
- TIFF** tagged image file format.
- TIRF** total internal reflection fluorescence.
- TOF** time-of-flight.
- ULF** unit length filament.
- USB** universal serial bus.
- wtGFP** wildtype green fluorescent protein.
- YFP** yellow fluorescent protein.

List of Figures

1.1.	Sketch of an eukaryotic cell.	3
1.2.	Illustration of the cell cycle.	5
1.3.	Typical transport processes in a cell	7
1.4.	Mean squared displacements for different types of transport.	8
1.5.	Anomalous transport in an environment with a given amount of excluded volume.	9
1.6.	(a) Principle of SPT. (b) SPT in an image series. (c) SPT on a laser scanning microscope.	11
1.7.	Illustration of fluorescence recovery after photo bleaching.	12
1.8.	(a) Transition of the time-dependent concentration into an equilibrium state. (b) Illustration of fluorescence correlation spectroscopy	13
1.9.	(a) Confocal microscope. (b) TIRF microscope. (c) LSM.	14
2.1.	Jablonski diagram of a fluorescent molecule.	22
2.2.	Molecular structures (a,b) and absorption and fluorescence spectra (c) of Alexa-488 and Alexa-594 dyes.	23
2.3.	(a) Molecular structure of wtGFP. (b) Absorption and fluorescence spectra of the fluorescent proteins eGFP, eYFP and mRFP1.	25
2.4.	Properties of CdSe/ZnS quantum dots.	26
3.1.	(a) Basic setup of an epi-fluorescence microscope and (b) principle of infinity-corrected optics.	27
3.2.	(a) Definition of the quantities used to calculate the PSF of a focusing lens. (b) Point spread function of a fluorescence microscope for different numerical apertures NA.	29
3.3.	Two versions of dual-color detection. In (a) the light is split into two image sensors and in (b) a “dual-view” optics images the two color channels onto one image sensor.	30
3.4.	(a) Schematic setup of a confocal microscope. (b) Out-of-focus light exclusion with a pinhole. (c) Modification for dual-color-detection.	31
3.5.	(a) Cut through the PSF of an epi-fluorescence and a confocal microscope in the focal plane. (b) PSF of an epi-fluorescence and a confocal microscope.	32
3.6.	Principle of light sheet fluorescence microscopy in a 3-dimensional view (a) and a top view (b) and comparison of the illumination schemes of epi-fluorescence microscopy (c), confocal fluorescence microscopy (d) and light sheet microscopy (e).	33
3.7.	Examples of the system PSF of a light sheet fluorescence microscope with a numerical aperture $NA_{\text{det}} = 1.0$ for detection and different numerical apertures $NA_{\text{ill}} \in \{0.1, 0.3, 1.0\}$ for illumination.	34
3.8.	(a) Stripe artifacts in light sheet microscopy. (b) Pivoting of the light sheet, which is used to reduce stripe artifacts.	36
3.9.	Overview of different schemes of light sheet microscopes implemented in the last 20 years.	36
3.10.	Two LSM variants with a horizontal support for the samples: (a) iSPIM and (b) OPM.	37
4.1.	(a) Cross-section of a typical single-photon avalanche diode, showing the charge distribution in the device. (b) Formation of an avalanche of electron-hole pairs in a single-photon avalanche diode.	39

4.2.	(a) Passive quenching circuit for a single-photon avalanche diode. (b) Signals in that circuit.	40
4.3.	(a,b) Different structures and (c-e) Different pixel designs of SPAD array image sensors.	41
4.4.	(a) Intensity distribution in a microlens array for an image sensor with low fill factor. (b) 3-dimensional illustration of the microlens array and the sensor.	42
4.5.	Structure of a typical CMOS image sensor.	44
4.6.	(a,b) Operation of a CCD structure as a shift register for charges. (c) CCD sensor with a single readout register. (d) Interline transfer sensor. (e) Frame-transfer CCD sensor. . .	45
4.7.	(a) Structure of a frame-transfer EMCCD image sensor. (b) Electron multiplication process in an EM gain register.	45
4.8.	Quantum efficiency η_{det} of different image sensors, as a function of the light wavelength λ .	48
4.9.	Theoretical signal-to-noise ratios of different image sensors.	49
5.1.	Illustration of the principle of FCS.	51
5.2.	Illustration of the principle of imaging FCS.	53
5.3.	Schematic of the optics model used for the derivation of FCS theory.	54
5.4.	Plots of cuts through the MDE of a SPIM in Eq. (5.2.6) along one coordinate axis.	55
5.5.	Plots of the autocorrelation function for a confocal microscope and 3-dimensional normal diffusion, as defined in Eq. (5.3.20).	60
5.6.	Plots of the SPIM-FCS autocorrelation function for 3-dimensional normal diffusion, as defined in Eq. (5.3.25).	61
5.7.	Plots of the SPIM-FCS autocorrelation function for a two-component system $\chi = 1, 2$ with $\eta_{\gamma,1} = \eta_{\gamma,2}$, as defined by Eq. (5.3.25).	62
5.8.	Plots of the SPIM-FCS autocorrelation function for single-component anomalous diffusion, as defined in Eq. (5.3.24).	63
5.9.	Impact of flow on FCS autocorrelation curves for 3D diffusion in a Gaussian focus.	64
5.10.	Illustration of two-focus fluorescence cross-correlation spectroscopy.	66
5.11.	Impact of flow on the FCCS cross-correlation curves for 3D diffusion between two Gaussian foci (Eq. (5.4.6)).	68
5.12.	Two-focus FCCS cross-correlation curves for 3D diffusion without flow (Eq. (5.4.6)).	68
5.13.	Schematic illustration of two-color fluorescence cross-correlation spectroscopy	69
5.14.	Absorption and fluorescence spectra of Alexa-488 and Alexa-594 together with the excitation laser wavelengths and typical fluorescence emission detection channels.	70
5.15.	(a) 2-color FCCS correlation curves for different concentrations of monomers (A,B) and dimers (AB). (b) Dependence of the zero-lag amplitudes $g_{\gamma\rho}(0)$ of the different correlation functions on the relative dimer concentration $\langle c_{AB} \rangle / (\langle c_A \rangle + \langle c_B \rangle + \langle c_{AB} \rangle)$ with $\langle c_A \rangle + \langle c_B \rangle + \langle c_{AB} \rangle = 5 \text{ nM}$ and $\langle c_A \rangle = \langle c_B \rangle$	72
5.16.	Influence of fluorophore blinking on the confocal FCS autocorrelation function for 3D diffusion.	74
5.17.	Influence of a constant background signal on the FCS autocorrelation amplitude $g_{\gamma\gamma}(0)$.	75
5.18.	Simulation of SPIM-FCS curves showing a depletion of the fluorophores by bleaching.	77
6.1.	Photograph of the SPIM instrument.	81
6.2.	Schematic of the optics and computer control system of the SPIM instrument.	82
6.3.	Detailed schematic of the illumination beam path: (a) top view and (b) a side view.	83
6.4.	(a) Geometry of a light sheet. (b) Width (blue) and peak intensity (red) of a light sheet as a function of the displacement x from the focus (at $x = 0$).	84
6.5.	Overview of the detection assembly.	86
6.6.	Illustration of the alignment of the DualView DV2.	87

6.7.	(a) 3D view of the sample chamber and the sample mounting assemblies. (b) Exploded view of the sample chamber.	89
6.8.	Properties of the temperature control system: (a) Heating curve and stability of the temperature. (b) Temperature distribution in the sample chamber.	90
6.9.	Different methods for sample mounting in a SPIM: (a) samples embedded in a gel cylinder, (b) adherent cells on a cover slip, (c) sample bags for liquid samples.	91
6.10.	Autofluorescence of sample bags made from LumoxFolie 25 M.	91
6.11.	Details on adherent cells mounted in a SPIM.	93
6.12.	Light sheet analysis with a mirror.	94
6.13.	Typical properties of the light sheet of the SPIM described in this thesis.	94
6.14.	Determination of the MDE of the microscope, using a bead scan.	96
6.15.	Typical results of a light sheet analysis.	97
6.16.	Stability of the MDE parameters over a timespan of more than one year.	98
6.17.	Examples of SPIM images of cells.	98
6.18.	(a) SPAD array <i>SwissSPAD</i> , mounted in the SPIM. (b,c) Pixel circuits of the two SPAD arrays (b) <i>Radhard2</i> and (c) <i>SwissSPAD</i>	99
6.19.	Structure of the readout circuit used for the two SPAD arrays <i>Radhard2</i> and <i>SwissSPAD</i>	101
6.20.	Effect of the excess bias voltage U_{excess} on the quantum efficiency of a <i>SwissSPAD</i> chip without microlenses.	102
6.21.	The breakdown voltage of <i>SwissSPAD</i>	102
6.22.	Histograms of the dark count rate of the SPAD arrays <i>Radhard2</i> and <i>SwissSPAD</i>	102
6.23.	Simulation of the light intensity distribution in a microlens, which is comparable to the microlenses on <i>SwissSPAD</i>	103
6.24.	(a,b) Hot pixels and broken columns in the same dark frame, acquired with <i>SwissSPAD</i> for two different gray scales (two different color scales!). (c) A SPIM image of HeLa cells expressing eGFP tetramers, acquired with <i>SwissSPAD</i> and corrected for broken pixels with the online correction method described in the text.	104
6.25.	Intensity profile along the longer axis of <i>SwissSPAD</i> without microlenses in (a) and with microlenses in (b), at comparable illumination intensities.	105
7.1.	Evaluation chain for imaging FCCS.	107
7.2.	Example of a bleach correction according to Eq. (7.1.2).	109
7.3.	Illustration of the splitting of a single frame from an FCCS measurement.	110
7.4.	Effect of triangular averaging in a multi- τ correlation on the estimated correlation curve.	113
7.5.	Screenshots of <i>QUICKFIT</i> 3.0.	117
7.6.	Overview of the SPIM control software and its connections to the microscope.	118
8.1.	Results of an imaging FCS calibration with increasing pixel size.	120
8.2.	Lateral PSF width w_g over more than one year and for several different calibration samples.	121
8.3.	(a) Correlation curves from SPIM-FCS (blue) and confocal FCS measurements (red) on fluorescent microspheres with $\varnothing = 100$ nm. (b) Averaged MSD and (c) diffusion coefficient distribution obtained with SPT on the same sample.	122
8.4.	(a,b) Normalized SPIM-FCS autocorrelation functions acquired with an Andor iXon X3 EMCCD camera for different samples and binnings. (c) Histograms of the diffusion coefficients from single SPIM-FCS measurements.	123
8.5.	(a) Comparison of diffusion coefficient measured for different samples with SPIM-FCS and confocal FCS. (b) Diffusion coefficient $D_{20^\circ\text{C,W}}$, as a function of ratio between minimum lag time τ_{min} and diffusion correlation time τ_D , measured with SPIM-FCS.	125

8.6.	(a) Effect of different ratios τ_{\min}/τ_D on the concentration c , measured with SPIM-FCS. (b) Comparison of concentration measurements with SPIM-FCS and confocal FCS.	126
8.7.	(a,c) EMCCD signal $F(t)$ and autocorrelation function measured on a single pixel of a dark EMCCD camera with the baseline clamp activated. (b,d) The same without activated baseline clamp.	127
8.8.	(a) Results of FCS simulations for linear detectors with different gains \bar{G} and excess noise factors \mathcal{F}^2 . (b) Relative error $(c_{300} - c_{500})/c_{300}$ between concentrations c_{300} and c_{500} , measured at an EM-gain setting of 300 and 500, respectively.	128
8.9.	Representative result of an extended bead scan analysis.	129
8.10.	(a) $1/e^2$ -isosurface plot of 3-dimensional Gaussian function. (b) $1/e^2$ -isosurface plot of a Gaussian beam as in Eq. (8.3.1).	130
8.11.	Different focus geometries used for FCS simulations.	131
8.12.	Results of anomalous diffusion FCS simulation.	132
8.13.	Stripe artifacts in (a-f) a SPIM-FCS measurement of QDot-565 ITK and (g-i) a cell expressing a an eGFP tetramer (eGFP-4x).	133
8.14.	Simulation results of a 2D simulation of light beam propagation in a medium with $\bar{n} = 1.33$, which contains a few circular regions of changed refractive index n'	134
8.15.	Influence of the sample bags on SPIM-FCS measurements.	135
8.16.	Influence of the width of the light sheet on SPIM-FCS measurements.	135
8.17.	(a) Confocal FCS autocorrelation curve acquired from HeLa cell expressing eGFP-1x or eGFP-4x. (b) Table of diffusion coefficients for eGFP-1x– eGFP-4x acquired with confocal FCS.	137
8.18.	(a) SPIM-FCS autocorrelation curves acquired from HeLa cells expressing eGFP-1x and eGFP-4x with an EMCCD camera. (b) Histograms of fast diffusion coefficient of eGFP-1x and eGFP-4x in the same cells. (c) Fluorescence intensity image of a cell, expressing eGFP-4x. (d) Map of the fast diffusion coefficient D_{fast} and (e) map of the concentration c in the same cell.	137
8.19.	SPIM-FCS measurement of the particle concentration c in a cell, which expressing eGFP-4x. (a) Map of c without a background offset F_{back} . (b) Fluorescence intensity (F) image. (c) Map of c with background intensity F_{back} estimated in the nucleolus (blue circle in b). (d,e) Correlation plot between c and F from (a) and (b).	138
8.20.	(a) SPIM-FCS autocorrelation curves acquired from CHO-K1 cells expressing PMT-eGFP with an EMCCD camera. (b) Histograms of fast diffusion coefficient. (c) Histogram of the fraction ρ_{slow} of the slow component. (d) Fluorescence image of the cell. (e) Map of the fast diffusion coefficient D_{fast} . (f) Map of the fraction ρ_{slow} of the slow diffusion component.	139
8.21.	SPIM-FCS autocorrelation curves of green fluorescent microspheres ($\varnothing = 100$ nm), obtained with several different cameras.	141
8.22.	(a-c) Autocorrelation curves from a HeLa cell, expressing eGFP-4x, acquired on a pco.edge sCMOS camera. (d-f) Intensity images of the same cell at different binning stages.	144
8.23.	(a) SPIM-FCS autocorrelation curves of fluorescent microspheres ($\varnothing = 100$ nm) and QDot-525 streptavidin ITK, obtained with <i>Radhard2</i> . (b,c) Distribution of diffusion coefficients, obtained for the two samples.	145
8.24.	Autocorrelation functions for different samples, acquired with the SPAD array <i>SwissSPAD</i>	146
8.25.	Comparison of concentration measurements with SPIM-FCS with the SPAD array <i>SwissSPAD</i> and confocal FCS.	147
8.26.	Autocorrelation functions from the SPAD array <i>SwissSPAD</i> , that show afterpulsing.	148
8.27.	Evaluation of afterpulsing in the SPAD array <i>SwissSPAD</i> : (a) with a power-law fit, (b) with a mono-exponential fit and (c) with a double-exponential fit.	149

9.1. Exemplary SPIM-FCCS autocorrelation (green/red) and cross-correlation curves (blue) of several test samples.	152
9.2. Representative results of auto- and cross-correlation curves from an FCCS simulation with different amounts of double-labeled particles and for different displacements δ_x of the green and the red MDE.	154
9.3. Fit results from the simulation in Fig. 9.2, when assuming no shift $\delta_x = 0$ in the fit model, given that a shift $\delta_x > 0$ actually is present in the microscope setup.	154
9.4. Comparison between confocal and SPIM-FCCS measurements.	156
9.5. Calibration of the SPIM-FCCS concentration against concentrations measured in a confocal microscope.	157
9.6. SPIM-FCCS measurement of eGFP-P30-mRFP1-dimers and eGFP + mRFP1-monomers expressed in HeLa cells.	158
9.7. SPIM-FCCS measurement of eGFP-EGFR-mRFP1 and PMT-eGFP + PMT-mRFP1-monomers expressed in CHO-K1 cells.	160
9.8. Statistical summary of the relative dimer concentrations p_{AB} obtained for different proteins in cells, using SPIM-FCCS.	161
9.9. A single exposure of $\Delta t_{\text{exp}} = 100$ ms of flowing microspheres.	162
9.10. Flow of fluorescent microspheres determined with 2-focus SPIM-FCCS.	162
10.1. Different inert probe particles for mobility measurements in live cells.	168
10.2. Intensity images and fit parameter maps for one representative cell for each of the five inert tracer molecules.	169
10.3. (a) Representative autocorrelation curves from cells, expressing the different eGFP oligomers. (b) Histograms of the diffusion coefficient of the fast component, calculated using all pixels of the respective cell.	170
10.4. Summary of fit results for different inert tracer molecules in HeLa cells.	171
10.5. Diffusion coefficient $D_{\text{fast}, 20^\circ\text{C}}$ of the fast component, as a function of the molecular mass M for inert tracer particles in cells (green) and in water (blue).	171
10.6. Summary of fit results for eGFP-4x, expressed in different cell lines.	173
11.1. (a-c) Filament networks in a mammalian cell. (d) Intermediate filament assembly.	175
11.2. The keratin remodeling cycle.	176
11.3. Diffusion coefficient D of a cylinder of diameter $d = 10$ nm and length L	177
11.4. Representative fluorescence images of (a-c) SK8/18 and (d-e) HaCat B 10 cells, expressing keratin.	178
11.5. Representative results from a SPIM-FCS measurement of YFP-labeled keratin in a SK8/18 cell.	179
11.6. Maximum Entropy fit to the same pixel as in Fig. 11.5(b,d).	179
11.7. SPIM-FCS fit result histograms from a representative SK8/18 cell, expressing YFP-labeled keratins.	181
11.8. Fast diffusion coefficient $D_{\text{fast}, 20^\circ\text{C}}$ extracted from all SK8/18 cells expressing Keratin18-YFP.	181
12.1. (a) Crystal structure of the nucleosome. (b) Schematic drawing of the protein core of the nucleosome. (c) Interaction of the nucleosome with the linker histone H1.	183
12.2. SPIM-FCCS measurements of different labeled histones (H2A-eGFP, H4-eGFP, H1.0-YFP) in the nucleus of transiently transfected HeLa cells.	185
12.3. (a) Two views of the crystal structure of the DNA-binding and trans-activation domains of c-Fos and c-Jun. (b) Structure of the transcription factor pair c-Fos and c-Jun.	187

12.4. SPIM-FCCS measurement of wildtypes (c-Fos-eGFP + c-Jun-mRFP1) and double-deletion mutants (c-Fos $\Delta\Delta$ -eGFP + c-Jun $\Delta\Delta$ -mRFP1) of AP-1 complex in HeLa cells.	189
12.5. (a) Structure of RXR. (b) Model for the functioning of RXR.	191
12.6. SPIM-FCS measurement of RXR-eGFP and RXR-LBD-eGFP in HeLa cells with and without the ligand LG268.	192
A.1. Combined transmission and fluorescence images of different cell lines, expressing eGFP-4x.	211
A.2. Illustration of the preparation of SPIM sample bags.	212
B.1. Softcore force between two particles, calculated for parameters $r_c = 2$ nm, $r_1 = 10$ nm and $r_2 = 2$ nm.	218

List of Tables

1.1.	Examples of reaction rates k_r and half-life times $\tau_{r,1/2}$ for enzyme-catalyzed reactions.	6
1.2.	Transport timescales for the diffusion of several typical particles inside a living cell over a given distance r	8
2.1.	Spectroscopic properties of some fluorescent dyes.	24
6.1.	Geometric properties of the image sensors used.	85
6.2.	Properties of the SPAD arrays <i>Radhard2</i> and <i>SwissSPAD</i>	100
8.1.	Diffusion coefficients $D_{20^\circ\text{C},\text{W}}$ measured by SPIM-FCS and other methods on two samples of green fluorescent microspheres of different diameter.	123
8.2.	Summary of diffusion coefficients measured for different samples using SPIM-FCS and confocal FCS.	125
8.3.	Fit results obtained from simulated FCS autocorrelation curves with different focus geometries and for particles with $D_{\text{real}} = 50 \mu\text{m}^2/\text{s}$	131
8.4.	Properties of the different image sensors and fit results for green fluorescent microspheres ($\varnothing = 100 \text{ nm}$) in water, obtained with each sensor.	142
8.5.	Summary of diffusion coefficients measured for different samples using the SPAD array <i>SwissSPAD</i> and comparison to data from an Andor iXon X3 860 and confocal FCS.	147
9.1.	Summary of typical diffusion coefficients $D_{20^\circ\text{C},\text{W}}$ and of the relative cross-correlation amplitudes q_{gr} obtained with different samples in SPIM-FCCS.	152
9.2.	Crosstalk κ_{gr} for different fluorophores and filter sets.	153
10.1.	Relative viscosities of the cellular medium in different cells, measured with transiently expressed eGFP-4x.	174
11.1.	Summary of the SPIM-FCS fit results for SK8/18 and HaCat B 10 cells.	180
12.1.	Summary of fit results for the labeled histones in HeLa cells.	186
12.2.	Summary of fit results for the AP-1 complex in HeLa cells.	190
A.1.	Optical components.	203
A.2.	Software used during this thesis work.	205
A.3.	Chemicals used during this thesis.	205
A.4.	Listing of the transfection protocols used for cytosolic and nucleic proteins.	208
A.5.	Listing of the transfection protocols used for membrane proteins.	209
B.1.	Typical parameters for molecular crowding simulations.	219

Bibliography

Parts of this thesis have been published in the following peer-reviewed journal papers (* marks equally contributing authors). A detailed account of the new contributions to SPIM-FCS, presented in this thesis are given in section 1.6 on page 16.

- T. Wocjan, JW. Krieger, O. Krichevsky, and J. Langowski. **Dynamics of a fluorophore attached to superhelical DNA: FCS experiments simulated by brownian dynamics.** *Physical Chemistry Chemical Physics*, 11(45):10671, 2009. doi:10.1039/B911857H.
- J. Buchholz, JW. Krieger, G. Mocsár, B. Kreith, E. Charbon, G. Vámosi, U. Kebschull, and J. Langowski. **FPGA implementation of a 32x32 autocorrelator array for analysis of fast image series.** *Optics Express*, 20(16):17767, 2012. doi:10.1364/OE.20.017767.
- G. Mocsár, B. Kreith, J. Buchholz, JW. Krieger, J. Langowski, and G. G. Vámosi. **Note: Multiplexed multiple-tau auto- and cross-correlators on a single field programmable gate array.** *Review of Scientific Instruments*, 83(4):046101, 2012. doi:10.1063/1.3700810.
- AP. Singh*, JW. Krieger*, J. Buchholz, E. Charbon, J. Langowski, and T. Wohland. **The performance of 2D array detectors for light sheet based fluorescence correlation spectroscopy.** *Opt. Express*, 21(7):8652–8668, 2013. doi:10.1364/OE.21.008652.
- JW. Krieger*, AP. Singh*, CS. Garbe, T. Wohland, and J. Langowski. **Dual-Color fluorescence Cross-Correlation spectroscopy on a single plane illumination microscope (SPIM-FCCS).** *Optics Express*, 22(3):2358, 2014. doi:10.1364/OE.22.002358.
- P. Brazda, JW. Krieger, B. Daniel, D. Jonas, T. Szekeres, J. Langowski, K. Toth, L. Nagy, and G. Vámosi. **Ligand binding shifts highly mobile retinoid x receptor to the Chromatin-Bound state in a Coactivator-Dependent manner, as revealed by Single-Cell imaging.** *Molecular and Cellular Biology*, 34(7):1234–1245, 2014. doi:10.1128/MCB.01097-13.

The following main bibliography for this thesis is sorted by the order of their appearance in the text.

- [1] Jacob Grimm and Wilhelm Grimm. *Deutsches Wörterbuch*. Verlag von S. Hirzel, 1854. available at <http://woerterbuchnetz.de/DWB/>.
- [2] B. Alberts, A. Johnson, J. Lewis, M. Raff, K. Roberts, and P. Walter. *Molecular Biology of the Cell*. Garland Science, 5 edition, 2008.
- [3] Helmut Schiessel. *Biophysics for Beginners*. Pan Stanford Publishing (CRC press), 2013. ISBN 9789814241656.
- [4] Christopher K. Mathews, Kevin G. Ahern, and K. E. Van Holde. *Biochemistry*. Benjamin Cummings, 3 edition, 2000. ISBN 9780805330663.
- [5] Paul Hertz. Über den gegenseitigen durchschnittlichen Abstand von Punkten, die mit bekannter mittlerer Dichte im Raume angeordnet sind. *Mathematische Annalen*, 67(3):387–398, 1909. doi:10.1007/BF01450410.
- [6] S. Chandrasekhar. Stochastic problems in physics and astronomy. *Reviews of Modern Physics*, 15(1):1–89, 1943. doi:10.1103/RevModPhys.15.1.
- [7] Jeremy M. Berg, John L. Tymoczko, and Lubert Stryer. *Biochemistry*. W.H. Freeman, 2007. ISBN 0716787245.
- [8] Peter Atkins and Julio de Paula. *Physical Chemistry for the Life Sciences*. Macmillan, 2 edition, 2011. ISBN 9781429231145.
- [9] Robert Brown. A brief account of microscopical observations made in the months of june, july and august 1827, on the particles contained in the pollen of plants; and on the general existence of active molecules in organic and inorganic bodies. *The Philosophical Magazine and Annals of Philosophy*, 4(21):161–173, 1828.

- [10] A. Einstein. Über die von der molekularkinetischen theorie der wärme geforderte bewegung von in ruhenden flüssigkeiten suspendierten teilchen. *Annalen der Physik*, 322(8):549–560, 1905. doi:10.1002/andp.19053220806.
- [11] M. von Smoluchowski. Zur kinetischen theorie der brownschen molekularbewegung und der suspensionen. *Annalen der Physik*, 326(14):756–780, 1906. doi:10.1002/andp.19063261405.
- [12] Jean Perrin. L'agitation moléculaire et le mouvement brownien. *Comptes rendus hebdomadaires des séances de l'académie des sciences*, 146:967–970, 1908.
- [13] Paul Langevin. Sur la théorie du mouvement brownien. *CR Acad. Sci. Paris*, 146(530-533), 1908.
- [14] Jean Perrin. Mouvement brownien et réalité moléculaire. *Annales de Chimie et de Physique*, 18:5–104, 1909.
- [15] M. Jean Perrin and F. Soddy (translator). *Brownian movement and molecular reality. Translated from Annales de Chimie et de Physique 8^{me} series, September 1909.* Taylor & Francis, 1910.
- [16] Katherine Luby-Phelps, Philip E. Castle, D Lansing Taylor, and Lanni Frederick. Hindered diffusion of inert tracer particles in the cytoplasm of mouse 3t3 cells. *Proceedings of the National Academy of Sciences*, 84(14):4910–4913, 1987.
- [17] K.M. Berland, P.T. So, and E. Gratton. Two-photon fluorescence correlation spectroscopy: method and application to the intracellular environment. *Biophysical Journal*, 68(2):694–701, 1995. doi:10.1016/S0006-3495(95)80230-4.
- [18] Nicolas Dross. *Mobilität von eGFP-Oligomeren in lebenden Zellkernen.* doctoral thesis, University of Heidelberg, 2009. URL http://archiv.ub.uni-heidelberg.de/volltextserver/volltexte/2010/10470/pdf/Dross_Mobilitaet_von_eGFP_Oligomeren_in_lebenden_Zellkernen.pdf.
- [19] Heike Glauner, Ivo R Ruttekolk, Kerrin Hansen, Ben Steemers, Yi-Da Chung, Frank Becker, Stefan Hannus, and Roland Brock. Simultaneous detection of intracellular target and off-target binding of small molecule cancer drugs at nanomolar concentrations. *British Journal of Pharmacology*, 160(4):958–970, 2010. doi:10.1111/j.1476-5381.2010.00732.x.
- [20] Ralf Metzler and Joseph Klafter. The random walk's guide to anomalous diffusion: a fractional dynamics approach. *Physics Reports*, 339(1):1–77, 2000.
- [21] Ralf Metzler and Joseph Klafter. The restaurant at the end of the random walk: recent developments in the description of anomalous transport by fractional dynamics. *Journal of Physics A*, 37:R161–R208, 2003.
- [22] Matthias Weiss, Hitoshi Hashimoto, and Tommy Nilsson. Anomalous protein diffusion in living cells as seen by fluorescence correlation spectroscopy. *Biophysical Journal*, 84(6):4043–4052, 2003. doi:10.1016/S0006-3495(03)75130-3.
- [23] Matthias Weiss, Markus Elsner, Fredrik Kartberg, and Tommy Nilsson. Anomalous subdiffusion is a measure for cytoplasmic crowding in living cells. *Biophysical Journal*, 87(5):3518–3524, 2004. doi:10.1529/biophysj.104.044263.
- [24] Margaret R. Horton, Felix Höfling, Joachim O. Rädler, and Thomas Franosch. Development of anomalous diffusion among crowding proteins. *Soft Matter*, 6(12):2648–2656, 2010. doi:10.1039/B924149C.
- [25] Felix Höfling and Thomas Franosch. Anomalous transport in the crowded world of biological cells. *Reports on Progress in Physics*, 76(4):046602, 2013. doi:10.1088/0034-4885/76/4/046602.
- [26] Petra Schwille, Jonas Korlach, and Watt W. Webb. Fluorescence correlation spectroscopy with single-molecule sensitivity on cell and model membranes. *Cytometry*, 36(3):176–182, 1999. doi:10.1002/(SICI)1097-0320(19990701)36:3<176::AID-CYTO5>3.0.CO;2-F.
- [27] Malte Wachsmuth, Waldemar Waldeck, and Jörg Langowski. Anomalous diffusion of fluorescent probes inside living cell nuclei investigated by spatially-resolved fluorescence correlation spectroscopy. *Journal of Molecular Biology*, 298(4):677–689, 2000. doi:10.1006/jmbi.2000.3692.

- [28] Takahiro Fujiwara, Ken Ritchie, Hideji Murakoshi, Ken Jacobson, and Akihiro Kusumi. Phospholipids undergo hop diffusion in compartmentalized cell membranes. *The Journal of Cell Biology*, 157(6):1071–1082, 2002. doi:10.1083/jcb.200202050.
- [29] Nina Malchus and Matthias Weiss. Elucidating anomalous protein diffusion in living cells with fluorescence correlation spectroscopy: Facts and pitfalls. *Journal of Fluorescence*, 20(1):19–26, 2010. doi:10.1007/s10895-009-0517-4.
- [30] Frederik W Lund, Michael A Lomholt, Lukasz M Solanko, Robert Bittman, and Daniel Wüstner. Two-photon time-lapse microscopy of BODIPY-cholesterol reveals anomalous sterol diffusion in chinese hamster ovary cells. *BMC Biophysics*, 5(1):20, 2012. doi:10.1186/2046-1682-5-20.
- [31] Gurpreet Kaur, Mauro W Costa, Christian M Nefzger, Juan Silva, Juan Carlos Fierro-González, Jose M Polo, Toby D M Bell, and Nicolas Plachta. Probing transcription factor diffusion dynamics in the living mammalian embryo with photoactivatable fluorescence correlation spectroscopy. *Nature communications*, 4:1637, 2013. doi:10.1038/ncomms2657.
- [32] Petra Schwille, Ulrich Haupts, Sudipta Maiti, and Watt W. Webb. Molecular dynamics in living cells observed by fluorescence correlation spectroscopy with one- and Two-Photon excitation. *Biophysical Journal*, 77(4):2251–2265, 1999. doi:10.1016/S0006-3495(99)77065-7.
- [33] N. Dross, C. Spriet, M. Zwerger, G. Müller, W. Waldeck, and J. Langowski. Mapping egfp oligomer mobility in living cell nuclei. *PLoS ONE*, 4(4):e5041, 2009.
- [34] A Kusumi, Y Sako, and M Yamamoto. Confined lateral diffusion of membrane receptors as studied by single particle tracking (nanovid microscopy). effects of calcium-induced differentiation in cultured epithelial cells. *Biophysical journal*, 65(5):2021–40, 1993. doi:10.1016/S0006-3495(93)81253-0.
- [35] Thomas Bürli, Kristin Baer, Helge Ewers, Corinne Sidler, Christian Fuhrer, and Jean-Marc Fritschy. Single particle tracking of alpha7 nicotinic AChR in hippocampal neurons reveals regulated confinement at glutamatergic and GABAergic perisynaptic sites. *PLoS one*, 5(7):e11507, 2010. doi:10.1371/journal.pone.0011507.
- [36] Nadia Ruthardt, Don C Lamb, and Christoph Bräuchle. Single-particle tracking as a quantitative microscopy-based approach to unravel cell entry mechanisms of viruses and pharmaceutical nanoparticles. *Molecular therapy : the journal of the American Society of Gene Therapy*, 19(7):1199–211, 2011. doi:10.1038/mt.2011.102.
- [37] R H Köhler, P Schwille, W W Webb, and M R Hanson. Active protein transport through plastid tubules: velocity quantified by fluorescence correlation spectroscopy. *Journal of cell science*, 113(22):3921–3930, 2000.
- [38] Roop Mallik and Steven P. Gross. Molecular motors: Strategies to get along. *Current Biology*, 14(22):R971–R982, 2004. doi:10.1016/j.cub.2004.10.046.
- [39] Harukata Miki, Yasushi Okada, and Nobutaka Hirokawa. Analysis of the kinesin superfamily: insights into structure and function. *Trends in Cell Biology*, 15(9):467–476, 2005. doi:10.1016/j.tcb.2005.07.006.
- [40] James R Sellers and Claudia Veigel. Walking with myosin v. *Current Opinion in Cell Biology*, 18(1):68–73, 2006. doi:10.1016/j.ceb.2005.12.014.
- [41] A Mehta. Myosin learns to walk. *Journal of cell science*, 114(11):1981–1998, 2001.
- [42] D. H. Schott. Secretory vesicle transport velocity in living cells depends on the myosin-v lever arm length. *The Journal of Cell Biology*, 156(1):35–40, 2002. doi:10.1083/jcb.200110086.
- [43] Teruo Shimmen and Etsuo Yokota. Cytoplasmic streaming in plants. *Current Opinion in Cell Biology*, 16(1):68–72, 2004. doi:10.1016/j.ceb.2003.11.009.
- [44] Lin Guo, Pramit Chowdhury, Jiyu Fang, and Feng Gai. Heterogeneous and anomalous diffusion inside lipid tubules. *The Journal of Physical Chemistry B*, 111(51):14244–14249, 2007. doi:10.1021/jp076562n.
- [45] H Qian, M P Sheetz, and E L Elson. Single particle tracking. analysis of diffusion and flow in two-dimensional systems. *Biophysical journal*, 60(4):910–21, 1991. doi:10.1016/S0006-3495(91)82125-7.

- [46] Michael J. Saxton and Ken Jacobson. SINGLE-PARTICLE TRACKING: Applications to membrane dynamics. *Annual Review of Biophysics and Biomolecular Structure*, 26(1):373–399, 1997. doi:10.1146/annurev.biophys.26.1.373.
- [47] Valeria Levi, QiaoQiao Ruan, and Enrico Gratton. 3d particle tracking in a Two-Photon microscope: Application to the study of molecular dynamics in cells. *Biophysical Journal*, 88:2919–2928, 2005. doi:10.1529/biophysj.104.044230.
- [48] Kevin Braeckmans, Dries Vercauteren, Jo Demeester, and Stefaan De Smedt. Single particle tracking. In Alberto Diaspro, editor, *Nanoscopy and multidimensional optical fluorescence microscopy*, pages 5–1–5–17. CRC Press, 2010. ISBN 9781420078862. doi:10.1201/9781420078893-c5.
- [49] Maxine Dahan, Sabine Lévi, Camille Luccardini, Philippe Rostaing, Béatrice Riveau, and Antoine Triller. Diffusion dynamics of glycine receptors revealed by single-quantum dot tracking. *Science*, 302:442–444, 2003.
- [50] M Suomalainen, M Y Nakano, S Keller, K Boucke, R P Stidwill, and U F Greber. Microtubule-dependent plus- and minus end-directed motilities are competing processes for nuclear targeting of adenovirus. *The Journal of cell biology*, 144(4):657–72, 1999. doi:10.1083/jcb.144.4.657.
- [51] Valeria Levi and Enrico Gratton. Chromatin dynamics during interphase explored by single-particle tracking. *Chromosome research : an international journal on the molecular, supramolecular and evolutionary aspects of chromosome biology*, 16(3):439–49, 2008. doi:10.1007/s10577-008-1240-8.
- [52] P. J. Keller, A. D. Schmidt, J. Wittbrodt, and E. H.K. Stelzer. Reconstruction of zebrafish early embryonic development by scanned light sheet microscopy. *Science*, 322(5904):1065–1069, 2008. doi:10.1126/science.1162493.
- [53] Pakorn Kanchanawong and Clare M Waterman. Localization-based super-resolution imaging of cellular structures. *Methods in molecular biology (Clifton, N.J.)*, 1046:59–84, 2013. doi:10.1007/978-1-62703-538-5_4.
- [54] Kim Pham, Raz Shimoni, Mandy J Ludford-Menting, Cameron J Nowell, Pavel Lobachevsky, Ze’ev Bomzon, Min Gu, Terence P Speed, C Jane McGlade, and Sarah M Russell. Divergent lymphocyte signalling revealed by a powerful new tool for analysis of time-lapse microscopy. *Immunology and cell biology*, 91(1):70–81, 2013. doi:10.1038/icb.2012.49.
- [55] M. Moch, G. Herberich, T. Aach, R. E. Leube, and R. Windoffer. Measuring the regulation of keratin filament network dynamics. *Proceedings of the National Academy of Sciences*, 110(26):10664–10669, 2013. doi:10.1073/pnas.1306020110.
- [56] S Boitano, E. Dirksen, and M. Sanderson. Intercellular propagation of calcium waves mediated by inositol trisphosphate. *Science*, 258(5080):292–295, 1992. doi:10.1126/science.1411526.
- [57] Eric A. Newman. Propagation of intercellular calcium waves in retinal astrocytes and müller cells. *The Journal of Neuroscience*, 21(7):2215–2223, 2001.
- [58] G Katona, G Szalay, P Maák, A Kaszás, M Veress, D Hillier, B Chiovini, ES Vizi, B Roska, and B. Rózsa. Fast two-photon in vivo imaging with three-dimensional random-access scanning in large tissue volumes. *Nature Methods*, 9(2):201–208, 2012. doi:10.1038/nmeth.1851.
- [59] D Axelrod, D E Koppel, J Schlessinger, E Elson, and W W Webb. Mobility measurement by analysis of fluorescence photobleaching recovery kinetics. *Biophysical journal*, 16(9):1055–69, 1976. doi:10.1016/S0006-3495(76)85755-4.
- [60] Tom K. L. Meyvis, Stefaan C. De Smedt, Patrick Van Oostveldt, and Joseph Demeester. Fluorescence recovery after photobleaching: A versatile tool for mobility and interaction measurements in pharmaceutical research. *Pharmaceutical Research*, 16(8):1153–1162, 1999. doi:10.1023/A:1011924909138.
- [61] Thomas Kühn, Teemu O. Ihalainen, Jari Hyväluoma, Nicolas Dross, Sami F. Willman, Jörg Langowski, Maija Vihinen-Ranta, Jussi Timonen, and Sudha Agarwal. Protein diffusion in mammalian cell cytoplasm. *PLoS ONE*, 6(8):e22962, 2011. doi:10.1371/journal.pone.0022962.

- [62] Malte Wachsmuth. Molecular diffusion and binding analyzed with FRAP. *Protoplasma*, 251(2):373–382, 2014. doi:10.1007/s00709-013-0604-x.
- [63] Lin Guo, Jia Yi Har, Jagadish Sankaran, Yimian Hong, Balakrishnan Kannan, and Thorsten Wohland. Molecular diffusion measurement in lipid bilayers over wide concentration ranges: A comparative study. *ChemPhysChem*, 9(5):721–728, 2008. doi:10.1002/cphc.200700611.
- [64] Brian L Sprague, Robert L Pego, Diana A Stavreva, and James G McNally. Analysis of binding reactions by fluorescence recovery after photobleaching. *Biophysical journal*, 86(6):3473–95, 2004. doi:10.1529/biophysj.103.026765.
- [65] J Ellenberg, E D Siggia, J E Moreira, C L Smith, J F Presley, H J Worman, and J Lippincott-Schwartz. Nuclear membrane dynamics and reassembly in living cells: targeting of an inner nuclear membrane protein in interphase and mitosis. *The Journal of cell biology*, 138(6):1193–206, 1997. doi:10.1083/jcb.138.6.1193.
- [66] J White and E Stelzer. Photobleaching GFP reveals protein dynamics inside live cells. *Trends in cell biology*, 9(2):61–5, 1999. doi:10.1016/S0962-8924(98)01433-0.
- [67] Malte Wachsmuth, Thomas Weidemann, Gabriele Müller, Urs W Hoffmann-Rohrer, Tobias A Knoch, Waldemar Waldeck, and Jörg Langowski. Analyzing intracellular binding and diffusion with continuous fluorescence photobleaching. *Biophysical journal*, 84(5):3353–63, 2003. doi:10.1016/S0006-3495(03)70059-9.
- [68] D Magde, E L Elson, and W W Webb. Fluorescence correlation spectroscopy i: Conceptual basis and theory. *Biopolymers*, 13(1):1–27, 1974.
- [69] D Magde, E L Elson, and W W Webb. Fluorescence correlation spectroscopy. ii. an experimental realization. *Biopolymers*, 13(1):29–61, 1974.
- [70] R. Rigler, Ü. Mets, J. Widengren, and P. Kask. Fluorescence correlation spectroscopy with high count rate and low background: analysis of translational diffusion. *European Biophysics Journal*, 22(3):169–175, 1993. doi:10.1007/BF00185777.
- [71] Michael Wahl, Hans-Jürgen Rahn, Ingo Gregor, Rainer Erdmann, and Jörg Enderlein. Dead-time optimized time-correlated photon counting instrument with synchronized, independent timing channels. *Review of Scientific Instruments*, 78(3):033106, 2007. doi:10.1063/1.2715948.
- [72] Oleg Krichevsky and Grégoire Bonnet. Fluorescence correlation spectroscopy: the technique and its applications. *Reports on Progress in Physics*, 65:251–297, 2002.
- [73] Nina Baudendistel, Gabriele Müller, Waldemar Waldeck, Peter Angel, and Jörg Langowski. Two-hybrid fluorescence cross-correlation spectroscopy detects protein-protein interactions in vivo. *Chemphyschem : a European journal of chemical physics and physical chemistry*, 6(5):984–90, 2005. doi:10.1002/cphc.200400639.
- [74] Kirsten Bacia, Sally A. Kim, and Petra Schwille. Fluorescence cross-correlation spectroscopy in living cells. *Nature Methods*, 3(2):83–89, 2006.
- [75] Elke Haustein and Petra Schwille. Fluorescence correlation spectroscopy: Novel variations of an established technique. *Annu. Rev. Biophys. Biomol. Struct.*, 36:151–169, 2007.
- [76] Ping Liu, Thankiah Sudhakaran, Rosita M.L. Koh, Ling C. Hwang, Sohail Ahmed, Ichiro N. Maruyama, and Thorsten Wohland. Investigation of the dimerization of proteins from the epidermal growth factor receptor family by single wavelength fluorescence Cross-Correlation spectroscopy. *Biophysical Journal*, 93(2):684–698, 2007. doi:10.1529/biophysj.106.102087.
- [77] Ping Liu, Sohail Ahmed, and Thorsten Wohland. The f-techniques: advances in receptor protein studies. *Trends in Endocrinology & Metabolism*, 19(5):181–190, 2008. doi:10.1016/j.tem.2008.02.004.
- [78] Douglas Magde, Watt W. Webb, and Elliot L. Elson. Fluorescence correlation spectroscopy. iii. uniform translation and laminar flow. *Biopolymers*, 17(2):361–376, 1978.

- [79] D. Lumma, S. Keller, T. Vilgis, and J. O. Rädler. Dynamics of large semiflexible chains probed by fluorescence correlation spectroscopy. *Physical Review Letters*, 90(21):218301, 2003.
- [80] Roman Shusterman, Sergey Alon, Tatyana Gavrinov, and Oleg Krichevsky. Monomer dynamics in double- and single-stranded dna polymers. *Physical Review Letters*, 92(4):048303, 2004.
- [81] Roman Shusterman, Tatyana Gavrinov, and Oleg Krichevsky. Internal dynamics of superhelical dna. *Physical review Letters*, 100:098102, 2008.
- [82] Tomasz Wocjan, Jan Krieger, Oleg Krichevsky, and Jörg Langowski. Dynamics of a fluorophore attached to superhelical DNA: FCS experiments simulated by brownian dynamics. *Physical Chemistry Chemical Physics*, 11(45):10671, 2009. doi:10.1039/B911857H.
- [83] Dominik Wöll. Fluorescence correlation spectroscopy in polymer science. *RSC Advances*, 4(5):2447, 2013. doi:10.1039/C3RA44909B.
- [84] Jerker Widengren, Rudolf Rigler, and Ülo Mets. Triplet-state monitoring by fluorescence correlation spectroscopy. *Journal of Fluorescence*, 4(3):255–259, 1994.
- [85] Ulrich Haupts, Sudipta Maiti, Petra Schwill, and Watt W. Webb. Dynamics of fluorescence fluctuations in green fluorescent protein observed by fluorescence correlation spectroscopy. *PNAS*, 95:13573–13578, 1998.
- [86] Romey F. Heuff, Jody L. Swift, and David T. Cramb. Fluorescence correlation spectroscopy using quantum dots: advances, challenges and opportunities. *Phys. Chem. Chem. Phys.*, 9:1870–1880, 2007. doi:10.1039/b617115j.
- [87] S. R. Aragón and R. Pecora. Fluorescence correlation spectroscopy and brownian rotational diffusion. *Biopolymers*, 14:119–138, 1975.
- [88] P. Kask, P. Piksarv, Ü. Mets, M. Pooga, and E. Lippmaa. Fluorescence correlation spectroscopy in the nanosecond time range: rotational diffusion of bovine carbonic anhydrase b. *European Biophysical Journal*, 14:257–261, 1987.
- [89] P. Kask, P. Piksarv, M. Pooga, Ü. Mets, and E. Lippmaa. Separation of the rotational contribution in fluorescence correlation experiments. *Biophysical Journal*, 55:213–220, 1989.
- [90] James M. Tsay, Sren Doose, and Shimon Weiss. Rotational and translational diffusion of peptide-coated cdse/cds/zns nanorods studied by fluorescence correlation spectroscopy. *J. Am. Chem. Soc.*, 128(5):1639–1647, 2006.
- [91] P. Schwill, F.J. Meyer-Almes, and R. Rigler. Dual-color fluorescence cross-correlation spectroscopy for multicomponent diffusional analysis in solution. *Biophysical journal*, 72(4):1878–1886, 1997. doi:10.1016/S0006-3495(97)78833-7.
- [92] Ling Chin Hwang, Michael Gösch, Theo Lasser, and Thorsten Wohland. Simultaneous multicolor fluorescence Cross-Correlation spectroscopy to detect higher order molecular interactions using single wavelength laser excitation. *Biophysical Journal*, 91(2):715–727, 2006. doi:10.1529/biophysj.105.074120.
- [93] Ling Chin Hwang and Thorsten Wohland. Single wavelength excitation fluorescence cross-correlation spectroscopy with spectrally similar fluorophores: Resolution for binding studies. *The Journal of Chemical Physics*, 122(11):114708, 2005. doi:doi:10.1063/1.1862614.
- [94] U Kettling, A Koltermann, P Schwill, and M Eigen. Real-time enzyme kinetics monitored by dual-color fluorescence cross-correlation spectroscopy. *Proceedings of the National Academy of Sciences of the United States of America*, 95(4):1416–20, 1998.
- [95] György Vámosi, Nina Baudendistel, Claus-Wilhelm von der Lieth, Nikolett Szalóki, Gábor Mocsár, Gabriele Müller, Péter Brázda, Waldemar Waldeck, SÁndor Damjanovich, Jörg Langowski, and Katalin Tóth. Conformation of the c-Fos/c-Jun complex in vivo: A combined FRET, FCCS, and MD-Modeling study. *Biophysical Journal*, 94(7):2859–2868, 2008. doi:10.1529/biophysj.107.120766.

- [96] Jonas Ries, Zdeněk Petrášek, Anna J García-Sáez, and Petra Schwille. A comprehensive framework for fluorescence cross-correlation spectroscopy. *New Journal of Physics*, 12(11):113009, 2010. doi:10.1088/1367-2630/12/11/113009.
- [97] Qiaojiao Ruan, Melanie A Cheng, Moshe Levi, Enrico Gratton, and William W Mantulin. Spatial-temporal studies of membrane dynamics: scanning fluorescence correlation spectroscopy (SFCS). *Biophysical Journal*, 87(2):1260–7, 2004. doi:10.1529/biophysj.103.036483.
- [98] Jonas Ries, Salvatore Chiantia, and Petra Schwille. Accurate determination of membrane dynamics with Line-Scan FCS. *Biophysical Journal*, 96(5):1999–2008, 2009. doi:10.1016/j.bpj.2008.12.3888.
- [99] Christian M. Roth, Pia I. Heinlein, Mike Heilemann, and Dirk-Peter Herten. Imaging diffusion in living cells using Time-Correlated Single-Photon counting. *Analytical Chemistry*, 79(19):7340–7345, 2007. doi:10.1021/ac071039q.
- [100] Gerrit Heuvelman, Fabian Erdel, Malte Wachsmuth, and Karsten Rippe. Analysis of protein mobilities and interactions in living cells by multifocal fluorescence fluctuation microscopy. *European Biophysics Journal*, 38(6):813–828, 2009. doi:10.1007/s00249-009-0499-9.
- [101] Felix Bestvater, Zahir Seghiri, Moon Sik Kang, Nadine Gröner, Ji Young Lee, Im Kang-Bin, and Malte Wachsmuth. EMCCD-based spectrally resolved fluorescence correlation spectroscopy. *OPTICS EXPRESS*, 18(23):23818–23828, 2010.
- [102] Daniel J. Needleman, Yangqing Xu, and Timothy J. Mitchison. Pin-Hole array correlation imaging: Highly parallel fluorescence correlation spectroscopy. *Biophysical Journal*, 96(12):5050–5059, 2009. doi:10.1016/j.bpj.2009.03.023.
- [103] Daniel R. Sisan, Richard Arevalo, Catherine Graves, Ryan McAllister, and Jeffrey S. Urbach. Spatially resolved fluorescence correlation spectroscopy using a spinning disk confocal microscope. *Biophysical Journal*, 91(11):4241–4252, 2006. doi:10.1529/biophysj.106.084251.
- [104] Michael Gösch, Alexandre Serov, Tiemo Anhut, Theo Lasser, Alexis Rochas, Pierre-André Besse, Radivoje S. Popovic, Hans Blom, and Rudolf Rigler. Parallel single molecule detection with a fully integrated single-photon 2x2 CMOS detector array. *Journal of Biomedical Optics*, 9(5):913, 2004. doi:10.1117/1.1781668.
- [105] Ryan A. Colyer, Giuseppe Scalia, Ivan Rech, Angelo Gulinatti, Massimo Ghioni, Sergio Cova, Shimon Weiss, and Xavier Michalet. High-throughput FCS using an LCOS spatial light modulator and an 8x1 SPAD array. *Biomedical Optics Express*, 1(5):1408, 2010. doi:10.1364/BOE.1.001408.
- [106] Ryan A Colyer, Giuseppe Scalia, Federica A Villa, Fabrizio Guerrieri, Simone Tisa, Franco Zappa, Sergio Cova, Shimon Weiss, and Xavier Michalet. Ultra high-throughput single molecule spectroscopy with a 1024 pixel SPAD. In Jörg Enderlein, Zygmunt K. Gryczynski, and Rainer Erdmann, editors, *Single Molecule Spectroscopy and Imaging IV*, volume 7905 of *SPIE Proceedings*. SPIE, 2011. doi:10.1117/12.874238.
- [107] M. Kloster-Landsberg, D. Tyndall, I. Wang, R. Walker, J. Richardson, R. Henderson, and A. Delon. Note: Multi-confocal fluorescence correlation spectroscopy in living cells using a complementary metal oxide semiconductor-single photon avalanche diode array. *Review of Scientific Instruments*, 84(7):076105, 2013. doi:10.1063/1.4816156.
- [108] Balakrishnan Kannan, Lin Guo, Thankiah Sudhaharan, Sohail Ahmed, Ichiro Maruyama, and Thorsten Wohland. Spatially resolved total internal reflection fluorescence correlation microscopy using an electron multiplying Charge-Coupled device camera. *Analytical Chemistry*, 79(12):4463–4470, 2007. doi:10.1021/ac0624546.
- [109] Jagadish Sankaran, Xianke Shi, Liang Yoong Ho, Ernst H. K. Stelzer, and Thorsten Wohland. Im-FCS: a software for imaging FCS data analysis and visualization. *Optics Express*, 18(25):25468, 2010. doi:10.1364/OE.18.025468.
- [110] Daniel Boening, Teja W. Groemer, and Jürgen Klingauf. Applicability of an EM-CCD for spatially resolved TIR-ICS. *OPTICS EXPRESS*, 18(13):13516–13528, 2010.

- [111] Nirmalya Bag and Thorsten Wohland. Imaging fluorescence fluctuation spectroscopy: New tools for quantitative bioimaging. *Annual Review of Physical Chemistry*, 65(1):131213171031009, 2012. doi:10.1146/annurev-physchem-040513-103641.
- [112] Jagadish Sankaran, Nirmalya Bag, Rachel Susan Kraut, and Thorsten Wohland. Accuracy and precision in Camera-Based fluorescence correlation spectroscopy measurements. *Analytical Chemistry*, 85(8):3948–3954, 2013. doi:10.1021/ac303485t.
- [113] Nirmalya Bag, Ashraf Ali, Virander Singh Chauhan, Thorsten Wohland, and Aseem Mishra. Membrane destabilization by monomeric hIAPP observed by imaging fluorescence correlation spectroscopy. *Chemical Communications*, 49(80):9155, 2013. doi:10.1039/C3CC44880K.
- [114] Nirmalya Bag, Jagadish Sankaran, Alexandra Paul, Rachel S. Kraut, and Thorsten Wohland. Calibration and limits of Camera-Based fluorescence correlation spectroscopy: A supported lipid bilayer study. *ChemPhysChem*, 13(11):2784–2794, 2012. doi:10.1002/cphc.201200032.
- [115] Nirmalya Bag, Darilyn Hui Xin Yap, and Thorsten Wohland. Temperature dependence of diffusion in model and live cell membranes characterized by imaging fluorescence correlation spectroscopy. *Biochimica et Biophysica Acta (BBA) - Biomembranes*, 1838(3):802–813, 2014. doi:10.1016/j.bbamem.2013.10.009.
- [116] Syuan-Ming Guo, Nirmalya Bag, Aseem Mishra, Thorsten Wohland, and Mark Bathe. Bayesian total internal reflection fluorescence correlation spectroscopy reveals hIAPP-Induced plasma membrane domain organization in live cells. *Biophysical Journal*, 106(1):190–200, 2014. doi:10.1016/j.bpj.2013.11.4458.
- [117] Thorsten Wohland, Xianke Shi, Jagadish Sankaran, and Ernst H. K. Stelzer. Single plane illumination fluorescence correlation spectroscopy (SPIM-FCS) probes inhomogeneous three-dimensional environments. *Optics Express*, 10(8):10627–10641, 2010. doi:10.1364/OE.18.010627.
- [118] Jan Huiskens, Jim Swoger, Filippo Del Bene, Joachim Wittbrodt, and Ernst H. K. Stelzer. Optical sectioning deep inside live embryos by selective plane illumination microscopy. *Science*, 305(5686):1007–1009, 2004. doi:10.1126/science.1100035.
- [119] K. Greger, J. Swoger, and E. H. K. Stelzer. Basic building units and properties of a fluorescence single plane illumination microscope. *Review of Scientific Instruments*, 78:023705, 2007.
- [120] Jérémie Capoulade, Malte Wachsmuth, Lars Hufnagel, and Michael Knop. Quantitative fluorescence imaging of protein diffusion and interaction in living cells. *Nature biotechnology*, 29:835–839, 2011. doi:10.1038/nbt.1928.
- [121] P. Brazda, J. Krieger, B. Daniel, D. Jonas, T. Szekeres, J. Langowski, K. Toth, L. Nagy, and G. Vamosi. Ligand binding shifts highly mobile retinoid x receptor to the Chromatin-Bound state in a Coactivator-Dependent manner, as revealed by Single-Cell imaging. *Molecular and Cellular Biology*, 34(7):1234–1245, 2014. doi:10.1128/MCB.01097-13.
- [122] Paul W. Wiseman, Jeffrey A. Squier, and Kent R. Wilson. Dynamic image correlation spectroscopy (ICS) and two-color image cross-correlation spectroscopy (ICCS): concepts and application. In Jose-Angel Conchello, Carol J. Cogswell, Andrew G. Tescher, and Tony Wilson, editors, *Three-Dimensional and Multidimensional Microscopy: Image Acquisition Processing VII*, volume 3919 of *SPIE Proceedings*, pages 14–20. SPIE, 2000. doi:10.1117/12.384193.
- [123] Paul W. Wiseman, Claire M. Brown, Donna J. Webb, Benedict Hebert, Natalie L. Johnson, Jeff A. Squier, Mark H. Ellisman, and A. F. Horwitz. Spatial mapping of integrin interactions and dynamics during cell migration by image correlation microscopy. *Journal of Cell Science*, 117(Pt 23):5521–5534, 2004. doi:10.1242/jcs.01416.
- [124] Michelle A. Digman, Parijat Sengupta, Paul W. Wiseman, Claire M. Brown, Alan R. Horwitz, and Enrico Gratton. Fluctuation correlation spectroscopy with Laser-Scanning microscope: Exploiting the hidden time structure. *Biophysical Journal*, 88(5):L33, 2005. doi:10.1529/biophysj.105.061788.

- [125] Michelle A. Digman, Claire M. Brown, Parijat Sengupta, Paul W. Wiseman, Alan R. Horwitz, and Enrico Gratton. Measuring fast dynamics in solutions and cells with a laser scanning microscope. *Biophysical Journal*, 89(2):1317–1327, 2005. doi:10.1529/biophysj.105.062836.
- [126] Benedict Hebert, Santiago Costantino, and Paul W Wiseman. Spatiotemporal image correlation spectroscopy (STICS) theory, verification, and application to protein velocity mapping in living CHO cells. *Biophysical journal*, 88(5):3601–14, 2005. doi:10.1529/biophysj.104.054874.
- [127] David L Kolin, David Ronis, and Paul W Wiseman. k-space image correlation spectroscopy: a method for accurate transport measurements independent of fluorophore photophysics. *Biophysical journal*, 91(8): 3061–75, 2006. doi:10.1529/biophysj.106.082768.
- [128] David L. Kolin and Paul W. Wiseman. Advances in image correlation spectroscopy: measuring number densities, aggregation states, and dynamics of fluorescently labeled macromolecules in cells. *Cell Biochemistry and Biophysics*, 3(49):141–164, 2007. doi:10.1007/s12013-007-9000-5.
- [129] P. Wiseman. Image correlation spectroscopy: mapping correlations in space, time, and reciprocal space. *Methods in enzymology*, 518:245–67, 2013. doi:10.1016/B978-0-12-388422-0.00010-8.
- [130] Anand Pratap Singh, Jan Wolfgang Krieger, Jan Buchholz, Edoardo Charbon, Jörg Langowski, and Thorsten Wohland. The performance of 2D array detectors for light sheet based fluorescence correlation spectroscopy. *Opt. Express*, 21(7):8652–8668, 2013. doi:10.1364/OE.21.008652.
- [131] Jan Buchholz, Jan Wolfgang Krieger, Gábor Mocsár, Balázs Kreith, Edoardo Charbon, György Vámosi, Udo Kbschull, and Jörg Langowski. FPGA implementation of a 32x32 autocorrelator array for analysis of fast image series. *Optics Express*, 20(16):17767, 2012. doi:10.1364/OE.20.017767.
- [132] Jan Wolfgang Krieger, Anand Pratap Singh, Christoph S. Garbe, Thorsten Wohland, and Jörg Langowski. Dual-Color fluorescence Cross-Correlation spectroscopy on a single plane illumination microscope (SPIM-FCCS). *Optics Express*, 22(3):2358, 2014. doi:10.1364/OE.22.002358.
- [133] Andreas Schenk, Sergey Ivanchenko, Carlheinz Röcker, Jörg Wiedenmann, and G. Ulrich Nienhaus. Photodynamics of red fluorescent proteins studied by fluorescence correlation spectroscopy. *Biophysical Journal*, 86:384–394, 2004.
- [134] Mark Bates, Bo Huang, and Xiaowei Zhuang. Super-resolution microscopy by nanoscale localization of photo-switchable fluorescent probes. *Current Opinion in Chemical Biology*, 12(5):505–514, 2008. doi:10.1016/j.cbpa.2008.08.008.
- [135] Molecular Probes (Invitrogen). Alexa fluor 488 carboxylic acid, succinimidyl ester, mixed isomers, 2014. URL <http://www.lifetechnologies.com/order/catalog/product/A20000>. accessed 2014-02-27.
- [136] Molecular Probes (Invitrogen). Alexa fluor 594 carboxylic acid, succinimidyl ester, mixed isomers, 2014. URL <http://www.lifetechnologies.com/order/catalog/product/A20004>. accessed 2014-02-27.
- [137] Markus Sauer, Johan Hofkens, and Jörg Enderlein. *Handbook of Fluorescence Spectroscopy and Imaging*. Wiley-VCH, 2011. ISBN 9783527316694.
- [138] Molecular Probes (Invitrogen). FluoSpheres - fluorescent microspheres, 2005. URL <http://tools.lifetechnologies.com/content/sfs/manuals/mp05000.pdf>. accessed 2014-02-18.
- [139] Roger Y. Tsien. The green fluorescent protein. *Annual Review of Biochemistry*, 67(1):509–544, 1998. doi:10.1146/annurev.biochem.67.1.509.
- [140] Nathan C Shaner, Paul A Steinbach, and Roger Y Tsien. A guide to choosing fluorescent proteins. *Nature Methods*, 2(12):905–905–909, 2005. doi:10.1038/nmeth819.
- [141] Molecular Probes (Invitrogen). The molecular probes® handbook, 2014. URL <http://www.lifetechnologies.com/us/en/home/references/molecular-probes-the-handbook.html>. accessed 2014-02-19.

- [142] Molecular Probes (Invitrogen). Qdot ITK carboxyl quantum dots, 2007. URL <http://tools.lifetechnologies.com/content/sfs/manuals/mp19020.pdf>. accessed 2014-02-18.
- [143] Yang Wu, Gabriel P. Lopez, Larry A. Sklar, and Tione Buranda. Spectroscopic characterization of streptavidin functionalized quantum dots. *Analytical Biochemistry*, 364(2):193–203, 2007. doi:10.1016/j.ab.2007.02.007.
- [144] Joseph R. Lakowicz. *Principles of fluorescence spectroscopy*. Springer, 2006. ISBN 9780387463124.
- [145] Osamu Shimomura, Frank H. Johnson, and Yo Saiga. Extraction, purification and properties of aequorin, a bioluminescent protein from the luminous Hydromedusan, Aequorea. *Journal of Cellular and Comparative Physiology*, 59(3):223–239, 1962. doi:10.1002/jcp.1030590302.
- [146] Haruki Niwa, Satoshi Inouye, Takashi Hirano, Tatsuki Matsuno, Satoshi Kojima, Masayuki Kubota, Mamoru Ohashi, and Frederick I. Tsuji. Chemical nature of the light emitter of the aequorea green fluorescent protein. *Proceedings of the National Academy of Sciences*, 93(24):13617–13622, 1996.
- [147] R. E. Campbell, O. Tour, A. E. Palmer, P. A. Steinbach, G. S. Baird, D. A. Zacharias, and R. Y. Tsien. A monomeric red fluorescent protein. *Proceedings of the National Academy of Sciences*, 99(12):7877–7882, 2002. doi:10.1073/pnas.082243699.
- [148] M. Ormö, A. B. Cubitt, K. Kallio, L. A. Gross, R. Y. Tsien, and S. J. Remington. Crystal structure of the aequorea victoria green fluorescent protein. *Science*, 273(5280):1392–1395, 1996. doi:10.1126/science.273.5280.1392.
- [149] George Patterson, Rich N. Day, and David Piston. Fluorescent protein spectra. *Journal of Cell Science*, 114(5):837–838, 2001.
- [150] IGEM. Team:Paris/Construction - 2008.igem.org, 2014. URL <http://2008.igem.org/Team:Paris/Construction>. accessed 2014-02-19.
- [151] Warren C. W. Chan and Shuming Nie. Quantum dot bioconjugates for ultrasensitive nonisotopic detection. *Science*, 281:2016–2018, 1998. doi:10.1126/science.281.5385.2016.
- [152] Rebecca C. Somers, Mounqi G. Bawendi, and Daniel G. Nocera. CdSe nanocrystal based chem-/bio- sensors. *Chemical Society Reviews*, 36(4):579, 2007. doi:10.1039/B517613C.
- [153] Varun K A Sreenivasan, Andrei V Zvyagin, and Ewa M Goldys. Luminescent nanoparticles and their applications in the life sciences. *Journal of Physics: Condensed Matter*, 25(19):194101, 2013. doi:10.1088/0953-8984/25/19/194101.
- [154] Claude Cohen-Tannoudji, Bernard Diu, and Franck Laloë. *Quantenmechanik. 1 (1997)*. Walter De Gruyter, 2 edition, 1999. ISBN 9783110135923.
- [155] M. Pelton, G. Smith, N. F. Scherer, and R. A. Marcus. Evidence for a diffusion-controlled mechanism for fluorescence blinking of colloidal quantum dots. *Proceedings of the National Academy of Sciences*, 104(36):14249–14254, 2007. doi:10.1073/pnas.0706164104.
- [156] Pavel Frantsuzov, Masaru Kuno, Boldizsár Jankó, and Rudolph A. Marcus. Universal emission intermittency in quantum dots, nanorods and nanowires. *Nature Physics*, 4(7):519–522, 2008. doi:10.1038/nphys1001.
- [157] W. Demtröder. *Experimentalphysik 2 Elektrizität und Optik*. Springer-Verlag, 1999.
- [158] Max Born and Emil Wolf. *Principles of Optics*. Cambridge University Press, 7 edition, 1999. ISBN 0521642221.
- [159] Kazuhiko Kinosita Jr., Hiroyasu Itoh, Shin'ichi Ishiwata, Ken'ichi Hirano, Takayuki Nishizaka, and Tsuyoshi Hayakawat. Dual-View microscopy with a single Camera: Real-Time imaging of molecular orientations and calcium. *The Journal of Cell Biology*, 115(1):67–73, 1991. doi:10.1083/jcb.115.1.67.
- [160] Robert H. Webb. Theoretical basis of confocal microscopy. *Methods in Enzymology*, 307:3–20, 1999.

- [161] Guy Cox and Colin J.R. Sheppard. Practical limits of resolution in confocal and non-linear microscopy. *Microscopy Research and Technique*, 63(1):18–22, 2004. doi:10.1002/jemt.10423.
- [162] Alexander Rohrbach. Artifacts resulting from imaging in scattering media: a theoretical prediction. *Optics Letters*, 34(19):3041, 2009. doi:10.1364/OL.34.003041.
- [163] Jan Huisken and Didier Y. R. Stainier. Even fluorescence excitation by multidirectional selective plane illumination microscopy (mSPIM). *Optics Letters*, 32(17):2608, 2007. doi:10.1364/OL.32.002608.
- [164] H. Siedentopf and R. Zsigmondy. Über sichtbarmachung und größenbestimmung ultramikroskopischer teilchen, mit besonderer anwendung auf goldrubingläser. *Annalen der Physik*, 315(1):1–39, 1902. doi:10.1002/andp.19023150102.
- [165] Timo Mappes, Norbert Jahr, Andrea Csaki, Nadine Vogler, Jürgen Popp, and Wolfgang Fritzsche. The invention of immersion ultramicroscopy in 1912—the birth of nanotechnology? *Angewandte Chemie International Edition*, 51(45):11208–11212, 2012. doi:10.1002/anie.201204688.
- [166] Richard A. Zsigmondy. Properties of colloids, 1925. URL http://www.nobelprize.org/nobel_prizes/chemistry/laureates/1925/zsigmondy-lecture.pdf. accessed 2014-03-08.
- [167] Charlotte Bigg. Evident atoms: visuality in jean perrin’s brownian motion research. *Studies in History and Philosophy of Science Part A*, 39(3):312–322, 2008. doi:10.1016/j.shpsa.2008.06.003.
- [168] A. H. Voie, D. H. Burns, F. A. Spelman, A. H. Voie, D. H. Burns, and F. A. Spelman. Orthogonal-plane fluorescence optical sectioning: Three-dimensional imaging of macroscopic biological specimens. *Journal of Microscopy*, 170(3):229–236, 1993. doi:10.1111/j.1365-2818.1993.tb03346.x.
- [169] Florian O. Fahrbach and Alexander Rohrbach. A line scanned light-sheet microscope with phase shaped self-reconstructing beams. *OPTICS EXPRESS*, 18(23):24229–24244, 2010. doi:10.1038/nphoton.2010.204.
- [170] Thomas A Planchon, Liang Gao, Daniel E Milkie, Michael W Davidson, James A Galbraith, Catherine G Galbraith, and Eric Betzig. Rapid three-dimensional isotropic imaging of living cells using bessel beam plane illumination. *Nature methods*, 8(5):417–423, 2011. doi:10.1038/NMETH.1586.
- [171] Tom Vetterburg, Heather I C Dalgarno, Jonathan Nytk, Clara Coll-Lladó, David E K Ferrier, Tomáš Cizmar, Frank J Gunn-Moore, and Kishan Dholakia. Light-sheet microscopy using an airy beam. *Nature methods*, eбуд ahead of print, 2014. doi:10.1038/nmeth.2922.
- [172] Uros Krzic, Stefan Gunther, Timothy E Saunders, Sebastian J Streichan, and Lars Hufnagel. Multiview light-sheet microscope for rapid in toto imaging. *Nature Methods*, 9(7):730–733, 2012. doi:10.1038/nmeth.2064.
- [173] Fernando Amat, Raju, Philipp J Keller, Khaled Khairy, Tomer, and Raju Tomer. Quantitative high-speed imaging of entire developing embryos with simultaneous multiview light-sheet microscopy. *Nature Methods*, 9(7):755–763, 2012. doi:10.1038/nmeth.2062.
- [174] Terrence F. Holekamp, Diwakar Turaga, and Timothy E. Holy. Fast Three-Dimensional fluorescence imaging of activity in neural populations by Objective-Coupled planar illumination microscopy. *Neuron*, 57(5):661–672, 2008. doi:10.1016/j.neuron.2008.01.011.
- [175] Y. Wu, A. Ghitani, R. Christensen, A. Santella, Z. Du, G. Rondeau, Z. Bao, D. Colon-Ramos, and H. Shroff. Inverted selective plane illumination microscopy (iSPIM) enables coupled cell identity lineaging and neurodevelopmental imaging in *caenorhabditis elegans*. *Proceedings of the National Academy of Sciences*, 108(43):17708–17713, 2011. doi:10.1073/pnas.1108494108.
- [176] C. Dunsby. Optically sectioned imaging by oblique plane microscopy. *Optics Express*, 16(25):20306, 2008. doi:10.1364/OE.16.020306.
- [177] Makio Tokunaga, Naoko Imamoto, and Kumiko Sakata-Sogawa. Highly inclined thin illumination enables clear single-molecule imaging in cells. *Nature methods*, 5(2):159–61, 2008. doi:10.1038/nmeth1171.

- [178] Bahaa E. A. Saleh and Malvin Carl Teich. *Fundamentals of Photonics*. John Wiley & Sons, 1991. ISBN 0-471-83965-5.
- [179] Ekbert Hering and Rolf Martin, editors. *Photonik*. Springer, 2005. ISBN 9783540234388.
- [180] S. Cova, M. Ghioni, A. Lacaita, C. Samori, and F. Zappa. Avalanche photodiodes and quenching circuits for single-photon detection. *Applied Optics*, 35(12):1956, 1996. doi:10.1364/AO.35.001956.
- [181] Mingguo Liu, Chong Hu, Joe C. Campbell, Zhong Pan, and Mark M. Tashima. Reduce afterpulsing of single photon avalanche diodes using passive quenching with active reset. *IEEE Journal of Quantum Electronics*, 44(5):430–434, 2008. doi:10.1109/JQE.2007.916688.
- [182] Cristiano Niclass and Mineki Soga. A miniature actively recharged single-photon detector free of afterpulsing effects with 6ns dead time in a 0.18 μm CMOS technology. In *2010 International Electron Devices Meeting*, pages 14.3.1–14.3.4. IEEE, 2010. ISBN 978-1-4424-7418-5. doi:10.1109/IEDM.2010.5703360.
- [183] Salvatore Tudisco, Francesco Musumeci, Luca Lanzano, Agata Scordino, Simona Privitera, Angelo Campisi, Luigi Cosentino, Giovanni Condorelli, Paolo Finocchiaro, Giorgio Fallica, Salvatore Lombardo, Massimo Mazzillo, Delfo Sanfilippo, and Emilio Sciacca. A new generation of SPAD Single-Photon avalanche diodes. *IEEE Sensors Journal*, 8(7):1324–1329, 2008. doi:10.1109/JSEN.2008.926962.
- [184] Mark A. Itzler, Xudong Jiang, and Mark Entwistle. Power law temporal dependence of InGaAs/InP SPAD afterpulsing. *Journal of Modern Optics*, 59(17):1472–1480, 2012. doi:10.1080/09500340.2012.698659.
- [185] Cristiano Niclass, Claudio Favi, Theo Kluter, Marek Gersbach, and Edoardo Charbon. A 128 \times 128 Single-Photon image sensor with Column-Level 10-bit Time-to-Digital converter array. *IEEE JOURNAL OF SOLID-STATE CIRCUITS*, 43:2977–2989, 2008. doi:10.1117/12.685974.
- [186] L. Carrara, C. Niclass, N. Scheidegger, H. Shea, and E. Charbon. A gamma, x-ray and high energy proton radiationtolerant cmos image sensor for space applications. In *IEEE International Solid-State Circuits Conference*, pages 40–41. Solid-State Circuits Conference - Digest of Technical Papers, 2009. ISSCC 2009. IEEE International, 2009. doi:10.1109/ISSCC.2009.4977297.
- [187] M. Gersbach, R. Trimananda, Y. Maruyama, M. Fishburn, D. Stoppa, J. Richardson, R. Walker, R. K. Henderson, and E. Charbon. High frame-rate TCSPC-FLIM using a novel SPAD-based image sensor. In *Society of Photo-Optical Instrumentation Engineers (SPIE) Conference Series*, volume 7780, page 38, 2010.
- [188] Gerard Giraud, Holger Schulze, Day-Uei Li, Till T. Bachmann, Jason Crain, David Tyndall, Justin Richardson, Richard Walker, David Stoppa, Edoardo Charbon, Robert Henderson, and Jochen Arlt. Fluorescence lifetime biosensing with DNA microarrays and a CMOS-SPAD imager. *Biomedical Optics Express*, 1(5):1302, 2010. doi:10.1364/BOE.1.001302.
- [189] Peter Seitz and Albert J. P. Theuwissen. *Single-Photon Imaging*. Springer, 2011. ISBN 9783642184420.
- [190] Simone Tisa, Nick Bertone, and Franco Zappa. A 32 \times 32 photon counting camera. *Optik & Photonik*, 6(2): 43–46, 2011. doi:10.1002/opph.201190329.
- [191] S. Bellisai, D. Bronzi, F. A. Villa, S. Tisa, A. Tosi, and F. Zappa. Single-photon pulsed-light indirect time-of-flight 3d ranging. *Optics Express*, 21(4):5086, 2013. doi:10.1364/OE.21.005086.
- [192] Samuel Burri, Damien Stucki, Yuki Maruyama, Claudio Bruschini, Edoardo Charbon, and Francesco Regazzoni. Jailbreak imagers: Transforming a Single-Photon image sensor into a true random number generator. In *International Image Sensor Workshop*, 2013. URL http://www.imagesensors.org/Past%20Workshops/2013%20Workshop/2013%20Papers/07-20_099_regazzoni_paper_revised.pdf. accessed 2014-03-25.
- [193] Samuel Burri, Yuki Maruyama, Xavier Michalet, Francesco Regazzoni, Claudio Bruschini, and Edoardo Charbon. Architecture and applications of a High Resolution, gated SPAD image sensor. *Optics Express*, submitted, 2014.

- [194] Ivan Rech, Stefano Marangoni, Daniele Resnati, Massimo Ghioni, and Sergio Cova. Multipixel single-photon avalanche diode array for parallel photon counting applications. *Journal of Modern Optics*, 56(2-3):326–333, 2009. doi:10.1080/09500340802318309.
- [195] A. Ingargiola, R. A. Colyer, D. Kim, F. Panzeri, R. Lin, A. Gulinatti, I. Rech, M. Ghioni, S. Weiss, and X. Michalet. Parallel multispot smFRET analysis using an 8-pixel SPAD array. *Proceedings of the SPIE*, 8228:82280B–82280B–8, 2012. doi:10.1117/12.909470. URL <http://www.chem.ucla.edu/~michalet/papers/SPIE2012a.pdf>.
- [196] C. Niclass, A. Rochas, P.-A. Besse, and E. Charbon. Design and characterization of a CMOS 3-d image sensor based on single photon avalanche diodes. *IEEE Journal of Solid-State Circuits*, 40(9):1847–1854, 2005. doi:10.1109/JSSC.2005.848173.
- [197] Juan Mata Pavia, Martin Wolf, and Edoardo Charbon. Measurement and modeling of microlenses fabricated on single-photon avalanche diode arrays for fill factor recovery. *Optics Express*, 22(4):4202, 2014. doi:10.1364/OE.22.004202.
- [198] Jun Ohta. *Smart CMOS Image Sensors And Applications*. CRC Press, 2008. ISBN 9780849336812.
- [199] C. Coates, Boyd Fowler, and Gerhard Holst. sCMOS: scientific CMOS technology. Technical report, Andor, 2009. URL <http://www.andor.com/pdfs/learning/technical/neo/New%20sCMOS%20vs.%20Current%20Microscopy%20Cameras.pdf>. accessed 2014-03-25.
- [200] Andor. *Andor sCMOS Brochure*, 2014. URL http://www.andor.com/pdfs/literature/Andor_sCMOS_Brochure.pdf. accessed 2014-03-25.
- [201] Simon M. Sze and Kwok K. Ng. *Physics of Semiconductor Devices*. Wiley-Interscience, 3 edition, 2006. ISBN 9780471143239.
- [202] Gerald C. Holst. *CCD arrays, cameras and displays*. SPIE Optical Engineering Press, 2 edition, 1998. ISBN 0-9640000-4-0.
- [203] Eric Lantz, Jean-Luc Blanchet, Luca Furfaro, and Fabrice Devaux. Multi-imaging and bayesian estimation for photon counting with EMCCDs. *Monthly Notices of the Royal Astronomical Society*, 386(4):2262–2270, 2008. doi:10.1111/j.1365-2966.2008.13200.x.
- [204] Donal J. Denvir and Emer Conroy. Electron multiplying CCDs. In Andrew Shearer, Fionn D. Murtagh, James Mahon, and Paul F. Whelan, editors, *Opto-Ireland 2002: Optical Metrology, Imaging, and Machine Vision*, volume 4877 of *SPIE Proceedings*, pages 55–68. SPIE, 2003. doi:10.1117/12.463677.
- [205] Michael Hirsch, Richard J. Wareham, Marisa L. Martin-Fernandez, Michael P. Hobson, Daniel J. Rolfe, and Chin-Tu Chen. A stochastic model for electron multiplication Charge-Coupled devices – from theory to practice. *PLoS ONE*, 8(1):e53671, 2013. doi:10.1371/journal.pone.0053671.
- [206] Y. Reibel, M. Jung, M. Bouhifd, B. Cunin, and C. Draman. CCD or CMOS camera noise characterisation. *The European Physical Journal Applied Physics*, 21(1):75–80, 2003. doi:10.1051/epjap:2002103.
- [207] Michael J. DeWeert, Jeffrey B. Cole, Andrew W. Sparks, and Andrew Acker. Photon transfer methods and results for electron multiplication CCDs. In Andrew G. Tescher, editor, *Applications of Digital Image Processing XXVII*, volume 5558 of *SPIE Proceedings*, pages 248–259. SPIE, 2004. doi:10.1117/12.562223.
- [208] Ulrich Tietze and Christoph Schenk. *Halbleiter-Schaltungstechnik*. Springer, 12 edition, 2002. ISBN 3540428496.
- [209] B.M. Oliver, J.R. Pierce, and C.E. Shannon. The philosophy of PCM. *Proceedings of the IRE*, 36(11):1324–1331, 1948. doi:10.1109/JRPROC.1948.231941.
- [210] Andor. *Andor Clara Series Specifications*, 2014. URL http://www.andor.com/pdfs/specifications/Andor_Clara_Series_Specifications.pdf. accessed 2014-03-25.
- [211] Andor. *Andor iXon Ultra and iXon 3 EMCCD Brochure*, 2014. URL http://www.andor.com/pdfs/literature/Andor_iXon3_EMCCD_Brochure.pdf. accessed 2014-03-25.

- [212] Jean Pierre Hansen and Ian Ranauld McDonald. *Theory of Simple Liquids*. Academic Press, 4 edition, 2013. ISBN 9780123870322. doi:10.1016/B978-0-12-387032-2.00015-5.
- [213] Paul Hopkins, Andrea Fortini, Andrew J. Archer, and Matthias Schmidt. The van hove distribution function for brownian hard spheres: Dynamical test particle theory and computer simulations for bulk dynamics. *The Journal of Chemical Physics*, 133(22):224505, 2010. doi:10.1063/1.3511719.
- [214] M.L. Boas. *Mathematical methods in the physical sciences*. John Wiley & Sons New York, 1983.
- [215] E. P. Petrov, T. Ohrt, R. G. Winkler, and P. Schwille. Diffusion and segmental dynamics of double-stranded dna. *Physical Review Letters*, 97:258101, 2006.
- [216] A G 3rd Palmer and N L Thompson. Theory of sample translation in fluorescence correlation spectroscopy. *Biophysical Journal*, 51(2):339–43, 1987.
- [217] Jerker Widengren, Uelo Mets, and Rudolf Rigler. Fluorescence correlation spectroscopy of triplet states in solution: a theoretical and experimental study. *Journal of Physical Chemistry*, 99(36):13368–13379, 1995.
- [218] Ming Zhao, Lei Jin, Bo Chen, Yao Ding, Hui Ma, and Dieyan Chen. Afterpulsing and its correction in fluorescence correlation spectroscopy experiments. *Applied Optics*, 42(19):4031, 2003. doi:10.1364/AO.42.004031.
- [219] Jörg Enderlein and Ingo Gregor. Using fluorescence lifetime for discriminating detector afterpulsing in fluorescence-correlation spectroscopy. *Review of Scientific Instruments*, 76:033102, 2005. doi:10.1063/1.1863399.
- [220] Yong Hwee Foo, Nikolaus Naredi-Rainer, Don C. Lamb, Sohail Ahmed, and Thorsten Wohland. Factors affecting the quantification of biomolecular interactions by Å fluorescence Cross-Correlation spectroscopy. *Biophysical Journal*, 102(5):1174–1183, 2012. doi:10.1016/j.bpj.2012.01.040.
- [221] National Semiconductors. *Application NOte 1559: Practical RTD interface solutions*, 2007. URL <http://www.ti.com.cn/cn/lit/an/zhca271/zhca271.pdf>. accessed on 2014-04-02.
- [222] Emmanuel G. Reynaud, Uros Krzic, Klaus Greger, and Ernst H. K. Stelzer. Light sheet-based fluorescence microscopy: more dimensions, more photons, and less photodamage. *HFSP Journal*, 2(5):266–275, 2008.
- [223] Alexis Maizel, Daniel von Wangenheim, Fern A;n Federici, Jim Haseloff, and Ernst H.K. Stelzer. High-resolution live imaging of plant growth in near physiological bright conditions using light sheet fluorescence microscopy. *The Plant Journal*, 68(2):377–385, 2011. doi:10.1111/j.1365-313X.2011.04692.x.
- [224] Annaïck Desmaison, Corinne Lorenzo, Jacques Rouquette, Bernard Ducommun, and Valérie Lobjois. A versatile sample holder for single plane illumination microscopy. *Journal of microscopy*, 251(2):128–32, 2013. doi:10.1111/jmi.12051.
- [225] Greiner Bio One. *Lumox multiwell Platten*, 2014. accessed on 2014-04-02.
- [226] Jan Huisken. *Multi-view microscopy and multi-beam manipulation for high-resolution optical imaging*. doctoral thesis, Albert-Ludwigs-Universität Freiburg, 2004. URL http://www.freidok.uni-freiburg.de/volltexte/1533/pdf/huisken_phd.pdf.
- [227] Uros Krzic. *Multiple-view microscopy with light-sheet based fluorescence microscope*. doctoral thesis, University Heidelberg, 2009. URL http://archiv.ub.uni-heidelberg.de/volltextserver/9668/1/Uros_Krzic_PhD_Thesis_Heidelberg_University_July_2009_v40.pdf.
- [228] P. Török, P. Varga, and G. R. Booker. Electromagnetic diffraction of light focused through a planar interface between materials of mismatched refractive indices: structure of the electromagnetic field. i. *J. Opt. Soc. Am. A*, 12(10):2136–2144, 1995.
- [229] P. Török and P. Varga. Electromagnetic diffraction of light focused through a stratified medium. *Appl. Opt.*, 36(11):2305–2312, 1997.

- [230] Olivier Haeberlé. Focusing of light through a stratified medium: a practical approach for computing microscope point spread functions. part i: Conventional microscopy. *Optics Communications*, 216(1-3): 55–63, 2003. doi:10.1016/S0030-4018(02)02282-4.
- [231] Francois Aguet, Dimitri Van De Ville, and Michael Unser. An accurate PSF model with few parameters for axially shift-variant deconvolution. In *2008 5th IEEE International Symposium on Biomedical Imaging: From Nano to Macro*, pages 157–160. IEEE, 2008. ISBN 978-1-4244-2002-5. doi:10.1109/ISBI.2008.4540956.
- [232] Jan Buchholz. *tba.* doctoral thesis, Ruprecht-Karls-Universität Heidelberg, 2014. in preparation.
- [233] G H Patterson and D W Piston. Photobleaching in two-photon excitation microscopy. *Biophysical journal*, 78(4):2159–62, 2000. doi:10.1016/S0006-3495(00)76762-2.
- [234] Louis Hodgson, Perihan Nalbant, Feimo Shen, and Klaus Hahn. Imaging and photobleach correction of Mero-CBD, sensor of endogenous cdc42 activation. *Methods in enzymology*, 406:140–156, 2006. doi:10.1016/S0076-6879(06)06012-5.
- [235] Joachim Wuttke. *lmfit - a c/c++ routine for levenberg-marquardt minimization with wrapper for least-squares curve fitting, based on work by b. s. garbow, k. e. hillstrom, j. j. moré, and s. moshier.* version 5.3, retrieved on 2013-08-12 from ., 2013. URL <http://apps.jens.fz-juelich.de/lmfit>. accessed on 2013-08-12.
- [236] Donald W. Marquardt. An algorithm for Least-Squares estimation of nonlinear parameters. *Journal of the Society for Industrial and Applied Mathematics*, 11(2):431–441, 1963. doi:10.1137/0111030.
- [237] Jorge Nocedal and Stephen Wright. *Numerical Optimization*. Springer Series in Operations Research and Financial Engineering. Springer Verlag, 2 edition, 2006. ISBN 978-0387303031.
- [238] James E. Gentle. *Matrix algebra*. Springer, 2007. ISBN 9780387708737.
- [239] Klaus Schätzel, Martin Drewel, and Sven Stimac. Photon correlation measurements at large lag times: Improving statistical accuracy. *Journal of Modern Optics*, 35(4):711–718, 1988.
- [240] Klaus Schätzel. Noise on photon correlation data: I. autocorrelation functions. *Quantum Opt.*, 2:287–305, 1990.
- [241] S.L. Miller and D.G. Childers. *Probability and random processes: with applications to signal processing and communications*. Academic Press, 2004.
- [242] Z. Kojro, A. Riede, M. Schubert, and W. Grill. Systematic and statistical errors in correlation estimators obtained from various digital correlators. *Review of Scientific Instruments*, 70(12):4487–4496, 1999. doi:10.1063/1.1150101.
- [243] Dennis E. Koppel. Statistical accuracy in fluorescence correlation spectroscopy. *Physical Review A*, 10(6): 1938–1945, 1974. doi:10.1103/PhysRevA.10.1938.
- [244] T Wohland, R Rigler, and H Vogel. The standard deviation in fluorescence correlation spectroscopy. *Biophys J*, 80(6):2987–99, 2001. doi:10.1016/S0006-3495(01)76264-9.
- [245] A. Corana, M. Marchesi, C. Martini, and S. Ridella. Minimizing multimodal functions of continuous variables with the “simulated annealing” algorithm. *ACM Transactions on Mathematical Software*, 13(3):262–280, 1987. doi:10.1145/29380.29864.
- [246] Parijat Sengupta, K. Garai, J. Balaji, N. Periasamy, and S. Maiti. Measuring size distribution in highly heterogeneous systems with fluorescence correlation spectroscopy. *Biophysical Journal*, 84:1977–1984, 2003. doi:10.1016/S0006-3495(03)75006-1.
- [247] Kóroly Módos, Rita Galántai, Irén Bárdos-Nagy, Malte Wachsmuth, Katalin Tóth, Judit Fidy, and Jörg Langowski. Maximum-entropy decomposition of fluorescence correlation spectroscopy data: application to liposome-human serum albumin association. *European Biophysics Journal*, 33(1):59–67, 2004. doi:10.1007/s00249-003-0343-6.

- [248] J. Skilling and R. K. Bryan. Maximum entropy image reconstruction - general algorithm. *Monthly Notices of the Royal Astronomical Society*, 211:111–111, 1984.
- [249] I.F. Sbalzarini and P. Koumoutsakos. Feature point tracking and trajectory analysis for video imaging in cell biology. *Journal of Structural Biology*, 151(2):182–195, 2005. doi:10.1016/j.jsb.2005.06.002.
- [250] MOSAIC group at ETH Zürich. ParticleTracker 2d and 3d, 2013. URL <http://mosaic.mpi-cbg.de/ParticleTracker/>. accessed on 2014-04-16.
- [251] Zdenek Petrásek and Petra Schwille. Precise measurement of diffusion coefficients using scanning fluorescence correlation spectroscopy. *Biophysical Journal*, 94:1437–1448, 2008.
- [252] Amanda P. Siegel, Nicole M. Hays, and Richard N. Day. Unraveling transcription factor interactions with heterochromatin protein 1 using fluorescence lifetime imaging microscopy and fluorescence correlation spectroscopy. *Journal of Biomedical Optics*, 18(2):025002, 2013. doi:10.1117/1.JBO.18.2.025002.
- [253] J.R. Unruh and E. Gratton. Analysis of molecular concentration and brightness from fluorescence fluctuation data with an electron multiplied ccd camera. *Biophysical journal*, 95(11):5385–5398, 2008.
- [254] Jorg Enderlein, Ingo Gregor, Digambara Patra, Thomas Dertinger, and U. Benjamin Kaupp. Performance of fluorescence correlation spectroscopy for measuring diffusion and concentration. *Chem. Phys. Chem.*, 6: 2324–2336, 2005. doi:10.1002/cphc.200500414.
- [255] Thomas Dertinger, Anastasia Loman, Benjamin Ewers, Claus B Muller, Benedikt Kramer, and Jorg Enderlein. The optics and performance of dual-focus fluorescence correlation spectroscopy. *Optics Express*, 19(16): 14353–14368, 2008. doi:10.1364/OE.16.014353.
- [256] C. B. Müller, A. Loman, V. Pacheco, F. Koberling, D. Willbold, W. Richtering, and J. Enderlein. Precise measurement of diffusion by multi-color dual-focus fluorescence correlation spectroscopy. *EPL (Europhysics Letters)*, 83(4):46001, 2008. doi:10.1209/0295-5075/83/46001.
- [257] Christian C. Fritsch and Jörg Langowski. Kinetic lattice monte carlo simulation of viscoelastic subdiffusion. *The Journal of Chemical Physics*, 137(6):064114, 2012. doi:10.1063/1.4742909.
- [258] Maxim Kalashnikov, Wonshik Choi, Chung-Chieh Yu, Yongjin Sung, Ramachandra R. Dasari, Kamran Badizadegan, and Michael S. Feld. Assessing light scattering of intracellular organelles in single intact living cells. *Optics Express*, 17(22):19674, 2009. doi:10.1364/OE.17.019674.
- [259] Jing-Wei Su, Wei-Chen Hsu, Cheng-Ying Chou, Chen-Hao Chang, and Kung-Bin Sung. Digital holographic microtomography for high-resolution refractive index mapping of live cells. *Journal of Biophotonics*, 6(5): 416–424, 2013. doi:10.1002/jbio.201200022.
- [260] Christopher Fang-Yen, Wonshik Choi, Yongjin Sung, Charles J. Holbrow, Ramachandra R. Dasari, and Michael S. Feld. Video-rate tomographic phase microscopy. *Journal of Biomedical Optics*, 16(1):011005, 2011. doi:10.1117/1.3522506.
- [261] J E Aubin. Autofluorescence of viable cultured mammalian cells. *The journal of histochemistry and cytochemistry : official journal of the Histochemistry Society*, 27(1):36–43, 1979. doi:10.1177/27.1.220325.
- [262] Thorsten Wohland and Anand Prataph Singh. private communications, 2013.
- [263] T. Dertinger, R. Colyer, G. Iyer, S. Weiss, and J. Enderlein. Fast, background-free, 3d super-resolution optical fluctuation imaging (SOFI). *Proceedings of the National Academy of Sciences*, 106(52):22287–22292, 2009. doi:10.1073/pnas.0907866106.
- [264] Thomas Dertinger, Ryan Colyer, Robert Vogel, Jörg Enderlein, and Shimon Weiss. Achieving increased resolution and more pixels with superresolution optical fluctuation imaging (SOFI). *Optics Express*, 18(18): 18875, 2010. doi:10.1364/OE.18.018875.

- [265] Thomas Dertinger, Mike Heilemann, Robert Vogel, Markus Sauer, and Shimon Weiss. Superresolution optical fluctuation imaging with organic dyes. *Angewandte Chemie (International ed. in English)*, 49(49):9441–3, 2010. doi:10.1002/anie.201004138.
- [266] B. D. Slaughter, J. W. Schwartz, and R. Li. Mapping dynamic protein interactions in MAP kinase signaling using live-cell fluorescence fluctuation spectroscopy and imaging. *Proceedings of the National Academy of Sciences*, 104(51):20320–20325, 2007. doi:10.1073/pnas.0710336105.
- [267] Sören Doose, Hannes Neuweiler, Hannes Barsch, and Markus Sauer. Probing polyproline structure and dynamics by photoinduced electron transfer provides evidence for deviations from a regular polyproline type II helix. *Proceedings of the National Academy of Sciences of the United States of America*, 104(44):17400–5, 2007. doi:10.1073/pnas.0705605104.
- [268] Nina Baudendistel. *Zwei-Hybrid-Fluoreszenz Kreuzkorrelationspektroskopie: In vivo Charakterisierung von Protein-Protein-Wechselwirkungen im AP-1-System*. doctoral thesis, University of Heidelberg, 2004. URL http://archiv.ub.uni-heidelberg.de/volltextserver/5105/1/Diss_unibib.pdf.
- [269] Bruce D Lucas, Takeo Kanade, et al. An iterative image registration technique with an application to stereo vision. In *Proceedings of the 7th international joint conference on Artificial intelligence-Volume 2*, pages 674–679, 1981.
- [270] M.A. Viergever, W.J. Niessen, and M.D. Abramoff. Objective quantification of the motion of soft tissues in the orbit. *IEEE Transactions on Medical Imaging*, 19(10):986–995, 2000. doi:10.1109/42.887614.
- [271] O Seksek, J Biwersi, and A S Verkman. Translational diffusion of macromolecule-sized solutes in cytoplasm and nucleus. *The Journal of cell biology*, 138(1):131–42, 1997. doi:10.1083/jcb.138.1.131.
- [272] Gernot Guigas, Claudia Kalla, and Matthias Weiss. The degree of macromolecular crowding in the cytoplasm and nucleoplasm of mammalian cells is conserved. *FEBS Letters*, 581(26):5094–5098, 2007. doi:10.1016/j.febslet.2007.09.054.
- [273] M A Wall, M Socolich, and R Ranganathan. The structural basis for red fluorescence in the tetrameric GFP homolog DsRed. *Nature structural biology*, 7(12):1133–8, 2000. doi:10.1038/81992.
- [274] Antoine Royant and Marjolaine Noirclerc-Savoye. Stabilizing role of glutamic acid 222 in the structure of enhanced green fluorescent protein. *Journal of Structural Biology*, 174(2):385–390, 2011. doi:10.1016/j.jsb.2011.02.004.
- [275] R. H. Jacobson, X.-J. Zhang, R. F. DuBose, and B. W. Matthews. Three-dimensional structure of β -galactosidase from e. coli. *Nature*, 369(6483):761–766, 1994. doi:10.1038/369761a0.
- [276] Nicole Maria Seibel, Jihane Eljouni, Marcus Michael Nalaskowski, and Wolfgang Hampe. Nuclear localization of enhanced green fluorescent protein homomultimers. *Analytical biochemistry*, 368(1):95–9, 2007. doi:10.1016/j.ab.2007.05.025.
- [277] Malte Wachsmuth. *Fluoreszenzfluktuationmikroskopie*. doctoral thesis, Universität Heidelberg, 2001. URL http://archiv.ub.uni-heidelberg.de/volltextserver/1666/1/wachsmuth_2001.pdf.
- [278] Norbert Mücke, 2013. personal communication.
- [279] Christian C. Fritsch and Jörg Langowski. Anomalous diffusion in the interphase cell nucleus: The effect of spatial correlations of chromatin. *The Journal of Chemical Physics*, 133(2):025101, 2010. doi:10.1063/1.3435345.
- [280] Harald Herrmann and Ueli Aebi. Intermediate filaments: Molecular structure, assembly mechanism, and integration into functionally distinct intracellular scaffolds . *Annual Review of Biochemistry*, 73(1):749–789, 2004. doi:10.1146/annurev.biochem.73.011303.073823.
- [281] Tanja Lichtenstern, Norbert Mücke, Ueli Aebi, Monika Mauermann, and Harald Herrmann. Complex formation and kinetics of filament assembly exhibited by the simple epithelial keratins k8 and k18. *Journal of Structural Biology*, 177(1):54–62, 2012. doi:10.1016/j.jsb.2011.11.003.

- [282] P.M. Steinert, L.N. Marekov, and D.A. Parry. Diversity of intermediate filament structure. evidence that the alignment of coiled-coil molecules in vimentin is different from that in keratin intermediate filaments. *The Journal of biological chemistry*, 268(33):24916–25, 1993.
- [283] Stefan Winheim, Aaron R. Hieb, Marleen Silbermann, Eva-Maria Surmann, Tatjana Wedig, Harald Herrmann, Jörg Langowski, and Norbert Mücke. Deconstructing the late phase of vimentin assembly by total internal reflection fluorescence microscopy (TIRFM). *PLOS ONE*, 6(4):e19202, 2011. doi:10.1371/journal.pone.0019202.
- [284] Stéphanie Portet. Dynamics of in vitro intermediate filament length distributions. *Journal of Theoretical Biology*, 332:20–29, 2013. doi:10.1016/j.jtbi.2013.04.004.
- [285] Beil Windoffer and Leube Magin. Cytoskeleton in motion: the dynamics of keratin intermediate filaments in epithelia. *The Journal of cell biology*, 194(5):669–78, 2011. doi:10.1083/jcb.201008095.
- [286] Reinhard Windoffer, Stefan Wöll, Pavel Strnad, and Rudolf E Leube. Identification of novel principles of keratin filament network turnover in living cells. *Molecular biology of the cell*, 15(5):2436–48, 2004. doi:10.1091/mbc.E03-09-0707.
- [287] A. Kolsch, R. Windoffer, T. Wurflinger, T. Aach, and R. E. Leube. The keratin-filament cycle of assembly and disassembly. *Journal of Cell Science*, 123(13):2266–2272, 2010. doi:10.1242/jcs.068080.
- [288] Stefan Wöll, Reinhard Windoffer, and Rudolf E. Leube. Dissection of keratin dynamics: different contributions of the actin and microtubule systems. *European Journal of Cell Biology*, 84(2-3):311–328, 2005. doi:10.1016/j.ejcb.2004.12.004. URL http://www.moca.rwth-aachen.de/pubs/24/Woell_et_al._2005_JCB.pdf.
- [289] Reinhard Windoffer, 2013-08-27. personal communication.
- [290] K Luger, A W Mäder, R K Richmond, D F Sargent, and T J Richmond. Crystal structure of the nucleosome core particle at 2.8 a resolution. *Nature*, 389(6648):251–60, 1997. doi:10.1038/38444.
- [291] V. Böhm, A. R. Hieb, A. J. Andrews, A. Gansen, A. Rocker, K. Toth, K. Luger, and J. Langowski. Nucleosome accessibility governed by the dimer/tetramer interface. *Nucleic Acids Research*, 39(8):3093–3102, 2011. doi:10.1093/nar/gkq1279.
- [292] Tabea Elbel. *Packing and unpacking nucleosomal DNA: The role of DNA torsion*. doctoral thesis, University of Heidelberg, 2014. in preparation.
- [293] J. Bednar, R. A. Horowitz, S. A. Grigoryev, L. M. Carruthers, J. C. Hansen, A. J. Koster, and C. L. Woodcock. Nucleosomes, linker DNA, and linker histone form a unique structural motif that directs the higher-order folding and compaction of chromatin. *Proceedings of the National Academy of Sciences*, 95(24):14173–14178, 1998. doi:10.1073/pnas.95.24.14173.
- [294] Tobias A. Knoch. *Approaching the tree-dimensional Organization of the Human Genome*. doctoral thesis, Universität Heidelberg, 2002. URL http://archiv.ub.uni-heidelberg.de/volltextserver/3105/1/TAKnoch-EDiss-Edit_020914.pdf.
- [295] Thomas Weidemann, Malte Wachsmuth, Tobias A Knoch, Gabriele Müller, Waldemar Waldeck, and Jörg Langowski. Counting nucleosomes in living cells with a combination of fluorescence correlation spectroscopy and confocal imaging. *Journal of molecular biology*, 334(2):229–240, 2003. doi:10.1016/j.jmb.2003.08.063.
- [296] Dipanjan Bhattacharya, Aprotim Mazumder, S. Annie Miriam, and G. V. Shivashankar. EGFP-Tagged core and linker histones diffuse via distinct mechanisms within living cells. *Biophysical Journal*, 91:2326–2336, 2006. doi:10.1529/biophysj.105.079343.
- [297] Aurélien Bancaud, Sébastien Huet, Nathalie Daigle, Julien Mozziconacci, Joël Beaudouin, and Jan Ellenberg. Molecular crowding affects diffusion and binding of nuclear proteins in heterochromatin and reveals the fractal organization of chromatin. *The EMBO journal*, 28(24):3785–98, 2009. doi:10.1038/emboj.2009.340.
- [298] M A Lever, J P Th'ng, X Sun, and M J Hendzel. Rapid exchange of histone h1.1 on chromatin in living human cells. *Nature*, 408(6814):873–6, 2000. doi:10.1038/35048603.

- [299] Thomas Weidemann. *Quantitative Untersuchung der Verteilung, Mobilität und Bindung von fluoreszenzmarkierten Histonen in vitro und in vivo mit Fluoreszenzfluktationsmikroskopie*. doctoral thesis, University of Heidelberg, 2002. URL http://archiv.ub.uni-heidelberg.de/volltextserver/2217/1/Dis_THW_02.pdf.
- [300] J. N. Mark Glover and Stephen C. Harrison. Crystal structure of the heterodimeric bZIP transcription factor c-Fos–c-Jun bound to DNA. *Nature*, 373(6511):257–261, 1995. doi:10.1038/373257a0.
- [301] I Mikaélian, E Drouet, V Marechal, G Denoyel, J C Nicolas, and A Sergeant. The DNA-binding domain of two bZIP transcription factors, the Epstein-Barr virus switch gene product EB1 and jun, is a bipartite nuclear targeting sequence. *Journal of virology*, 67(2):734–42, 1993.
- [302] Peter Brazda. *Determination of dynamic properties of nuclear receptors*. doctoral thesis, university of Debrecen, 2014. URL <http://hdl.handle.net/2437/179680>.
- [303] Laszlo Nagy and John W R Schwabe. Mechanism of the nuclear receptor molecular switch. *Trends in biochemical sciences*, 29(6):317–24, 2004. doi:10.1016/j.tibs.2004.04.006.
- [304] M.I.A. Lourakis. levmar: Levenberg-marquardt nonlinear least squares algorithms in C/C++, 2004. URL <http://www.ics.forth.gr/~lourakis/levmar/>. accessed on 2011-09-03.
- [305] M. D. Feit and J. A. Fleck Jr. Light propagation in graded-index optical fibers. *Applied Optics*, 17(24):3990, 1978. doi:10.1364/AO.17.003990.
- [306] Herbert Gross, Wolfgang Singer, and Michael Totzeck. *Handbook of Optical Systems: Physical image formation*, volume 2. Wiley-VCH, 2005. ISBN 3527403787.
- [307] L. Papula. *Mathematik für Ingenieure und Naturwissenschaftler*, volume 1. Vieweg+ Teubner, 2007.
- [308] TM Laue, BD Shah, TM Ridgeway, and SL Pelletier. Computer-Aided interpretation of analytical sedimentation data for proteins. In S. E. Harding, A.J. Rowe, and J.C Horton, editors, *Analytical Ultracentrifugation in Biochemistry and Polymer Science*. Royal Society of Chemistry, 1992.
- [309] David R. Lide and W. M. Mickey Haynes. *CRC handbook of chemistry and physics*. CRC Press/Taylor and Francis, 90 edition, 2010.
- [310] Francis Perrin. Mouvement brownien d’un ellipsoïde - i. dispersion diélectrique pour des molécules ellipsoïdales. *Journal de Physique et le Radium*, 5(10):497–511, 1934. doi:10.1051/jphysrad:01934005010049700.
- [311] M.M. Tirado and J.G. de la Torre. Translational friction coefficients of rigid, symmetric top macromolecules. application to circular cylinders. *J. Chem. Phys.*, 71:2581–2587, 1979. doi:10.1063/1.438613.
- [312] Steen Hansen. Translational friction coefficients for cylinders of arbitrary axial ratios estimated by monte carlo simulation. *The Journal of Chemical Physics*, 121(18):9111, 2004. doi:10.1063/1.1803533.
- [313] Victor A. Bloomfield. On-Line biophysics textbook, volume: Separations and hydrodynamics, chapter 1: Survey of biomolecular hydrodynamics, 2000. URL <http://www.biophysics.org/portals/1/pdfs/education/vbloomfield.pdf>. accessed 2014-02-03.
- [314] NIST. Codata internationally recommended values of the fundamental physical constants, 2010. URL <http://physics.nist.gov/cuu/Constants/>. accessed 2014-03-25.

Aknowledgements

It would not have been possible to complete my PhD project and to write this thesis without the help and kind support of numerous people and colleagues. Here I can only name a few.

- Foremost I would like to thank my PhD advisors Prof. Jörg Langowski and PD Dr. Christoph Garbe for providing the opportunity and the means to follow this interesting project. I would also like to thank them for their support and confidence during the last six years.
- I also want to express my gratitude to the international graduate college IGK 710 “Complex processes: Modeling, Simulation and Optimization” and the Heidelberg graduate school for mathematics and computation in the sciences (HGS MathComp) for their financial support during the first three years of my project. I also acknowledge the German National Academic Foundation for their sponsorship.
- I am very grateful to Prof. Ulrich Schwarz, who agreed to review my thesis on very short notice.
- A special thanks goes to my colleagues and friends Jan Buchholz (DKFZ) and Anand Prataph Singh (NUS, Singapore) with whom I worked closely together in this interdisciplinary project. It was always great to work with you, discuss with you ... and generally have fun with you. For sure I will not forget Anand’s first crêpe in Toulouse and the great tour through Singapore, he gave me. Also I will remember long hours behind a hot barbecue grill on every single TP3 summer festival.
- I also want to thank Prof. Thorsten Wohland (NUS Singapore), Prof. Edoardo Charbon (EPFL Lausanne/TU Delft) and Dr. Gyögy Vámosi (university of Debreczen) for the great cooperation during the project and many helpful discussions.
- Building the SPIM would not have been possible without the great support of Rüdiger Schmidt and all his colleagues from the DKFZ workshop. You did a great work on all the strange little aluminum and stainless steel parts that I needed. Also your support in designing the SPIM was invaluable. A special thanks goes to Paul Spiegel from the workshop of the KIP, who taught me how to properly operate a lathe and a mill without injuring myself.
- An invaluable help during the last six years was Gabriele Müller. She perfectly performed all cell culture work for this thesis, was a great help in all questions concerning cellular biology and a great company in general. Sorry for all the trouble I caused by strange plasmids and cells, that I brought into your lab.
- A huge thank you also goes to all the other people that I collaborated with during this thesis: Péter Brázda, Reinhard Windoffer, Norbert Mücke, Christian Fritsch, Tomasz Wocjan, Samuel Burri, Nikoletta Szalóki, Gábor Mocsár, Katalin Tóth
- I also want to thank all my friends, who showed me that there is a life outside the lab, especially Nicolas Dross, who taught me FCS and was never short on coffee and good advice.
- Also a huge thank you to all the people that read and corrected this thesis and helped me during the writing with their invaluable advice.

- I want to thank all the members of our group whom I haven't named so far: You made my years in B040 worthwhile.
- I also want to mention all the interns, master and bachelor students, that contributed to my project: Benedikt Häusele, Niko Schnellbacher, Sebastian Isbaner, Randolph Beerwert, Artjom Zern, Jan Soldat, Katharina Joachimsmeier.
- A huge thank you goes to my parents who supported me during the last 32 years and without whom I would never have arrived at this point in life.
- Finally I want to thank Tabea for everything she gives me on every single day. You are the greatest person to share the lab, the office, the flat and the life with!

Ich erkläre hiermit, dass ich die vorgelegte Dissertation selbst verfasst und mich keiner anderen als der von mir ausdrücklich bezeichneten Quellen und Hilfen bedient habe.

Heidelberg, den _____

Unterschrift